Alteration and transformation of As-hosting iron phases in redox transition zones of the red river sediments, Vietnam

Zur Erlangung des akademischen Grades eines

DOKTORS DER NATURWISSENSCHAFTEN

von der KIT-Fakultät für

Bauingenieur-, Geo- und Umweltwissenschaften

des Karlsruher Instituts für Technologie (KIT)

genehmigte

DISSERTATION

von

Magnus Christopher Schneider, M. Sc. Geoscience

aus Pforzheim

Tag der mündlichen Prüfung:

10.07.2023

Hauptreferent: Prof. Dr. Thomas Neumann

Korreferentin: Prof. Dr. Agnes Kontny

Korreferent: Prof. Dr. Thomas Pichler

Karlsruhe 2024

Abstract

Iron (Fe) minerals are highly reactive and play a major role in controlling the contaminant dynamics in natural and anthropogenic environments. In particular, the behaviour of oxyanions like arsenic (As) in near-surface aquifers is known to be controlled by redox-sensitive Fe-phases. Geogenic As-contaminated drinking water from shallow groundwater (GW) bodies remains one of the major global health risks of our time and it is particular important to understand As mobilization and retention mechanisms in near-surface environments. In this regard, the present study investigated the dynamic of ferruginous As hosting phases within the delta sediments of the Red River (RR) in Vietnam, which is known for its patchy distribution of dissolved GW As. This thesis presents the Fe mineralogy and related As concentrations of two sediment cores (approx. ~50m) across a sharp natural redox boundary separating an As-contaminated and an uncontaminated shallow sandy aquifer in order to describe the Fe dynamic and identify related As release and storage mechanisms.

Like in many other As polluted areas in South and Southeast Asia (SSEA), heavily As polluted (> 500 mg/L As) and almost As free (< 0.5 mg/L As) GW bodies border directly on each other at the study site. Although local GW flow (~40 m/yr) leads from the As-rich GW body to the adjunct low-As aquifer, a GW-monitoring program lasting from 2010 to 2017 was unable to detect any entry of As in the uncontaminated aquifer down-stream which is used for local water supply. GW data indicate a redox-induced accumulation of Fe and As in the solid phase of the narrow (~35m) redox transition zone (RTZ) as GW concentration for both elements decrease dramatically across the redox boundary while redox potential (Eh) increases from reduced (Eh=10-40mV) to moderately reduced (Eh > 110mV) conditions. Despite extensive research investigating the coupled Fe and As dynamic along redox boarders, it is largely unknown how Fe and As are present in the solid phase of a natural redox interface. It is widely speculative what alterations Fe minerals as main As carriers experience along redox boundaries under advective flow conditions and to what extent and in which way secondary Fe minerals affect the As-cycle across the interface. In particular, the influence of local geology in heterogeneous delta sediments on the complex biogeochemical processes determining the Fe and As cycle has so far hardly been analysed on a small scale. Therefore, this study focused on analysing the distribution and (trans-) formation of ferruginous As host phases along a natural redox gradient. The work followed the approach to gradually map type, occurrence, distribution, frequency and properties of Fe minerals and related As content along two vertical core profiles collected at the transition of a high-As grey coloured (presumably Holocene) aquifer and a low-As yellow-brown coloured (presumably Pleistocene) aquifer located horizontally adjacent. Sinking of the cores directly in the fringy and overlapping redox interface allowed a cross-section from the high-As across the transition zone to the low-As aquifer sediments in one core profile covering both the reduced and the moderately reduced GW environments. This approach enables to draw conclusions about horizontal GW induced transformation processes from vertical core profiles. By preserving the original sediment texture and redox state in a series of thin sections and bulk samples across the redox boundary, it was possible to map the Fe phases and related As concentrations spatially resolved from µm to m scale. A comprehensive set of high-resolution mineralogical and geochemical investigations by a combination of microscopic, spectroscopic and magnetic techniques revealed the redox-specific distribution of primary and secondary Fe minerals along the redox gradient as well as their contribution to As sequestering.

The study found that As is mobilized in the Holocene sediments up-stream of the core site most likely caused by reductive dissolution of Fe(III) oxyhydroxide mineral coatings on primary quartz (Qtz) grains. As soon as the highly reduced As-rich GW reaches the boarder to the moderately reduced Pleistocene sands As gets immobilized by various secondary Fe minerals formed across the redox interface in a specific order. The first stage is defined by the formation of secondary Fe(II)-phases. Most prominent are Fe- and Fe-Mn- carbonates with As concentrations up to 140 mg/kg. To a lesser extent pyrite (Py)

is formed with As concentrations up to 4700 mg/kg. The Fe(II) minerals are found to be transformed and dissolved again. In a second stage abundant Fe(III)-dominated oxyhydroxide precipitates hosting up to 480 mg/kg As form as dominant As-carrier. The outcome demonstrates that metastable secondary Fe(II)-sulphides, Fe(II)-carbonates and in particularly the extensive Fe(III)-dominated precipitates composed of microcrystalline (mc) goethite (Gt), hematite (Hem), and magnetite (Mt) of variable amounts largely control the Fe and As dynamic across the redox gradient. There is clear evidence that these metastable secondary products formed by coupled biogeochemical processes retain significant amounts of As. The formation of the mixed valance Fe(II)/(III) precipitates is most likely coupled to the oxidative behaviour of residual Fe(III) and Mn(IV) phases within the reducing environment. The high As absorption capacity and sensivity to hydrogeochemical variations of the mc Fe precipitates offers an excellent explanation for the high temporal and spatial variability of dissolved As GW concentrations that are observed in many study areas worldwide. Especially the Fe(III)-dominated precipitates which were shown to be the key retention mechanism controlling Fe and As flux across the redox boundaries offer an explanatory approach to understand the coupled redox dynamic of the two elements in natural environments. The mc character of the phases offers a new and conclusive explanation for the often strongly contrasting Fe and As GW concentrations across short distances, which has not yet been taken into account in most models. Since mc Fe-precipitations can show substantial variations in regard to their reactivity and (reductive) dissolution kinetics compared to crystalline counterparts the work clarifies that the clear demarcation of crystalline and mc phases is necessary to describe the redox-driven Fe and As cycle across sharp natural redox boundaries and to assess the stability and As hosting capacity of the secondary products. Furthermore, the study identified Fe-bearing phyllosilicates (PS) to be involved in both the As and Fe cycle. The study shows the Fe-rich PS act as source and sink for both As and Fe and as important Fe(III) reservoir disintegrating primary PS support the formation of the secondary mixed valance Fe(II)/(III) precipitates. Although the contribution of primary PS to overall As and Fe dynamic is hard to quantify the secondary formation of Fe-rich PS in the submicron range was shown to be an important intermediate step in the Fe cycle. They are clearly involved in the (trans-)formation of secondary Fe minerals and are closely entangled in the biogeochemical evolution of the Fe phases. The almost ubiquitous presence of the submicron PS clearly shows that the Fe mineral dynamic in natural delta sediments is more complex than many models depict.

These findings underline the importance of comprehensive mineralogical and geochemical investigation which go beyond the standard bulk analysis to characterize a study side. The results validate a complex interaction of hydro- and biogeochemical processes control the accumulation and (trans-) formation of Fe minerals along the natural redox boarder. The findings show that the appearance of Fe(II), Fe(II/III) and Fe(III) minerals as well as complex mixed valence mc Fe precipitates and Fe-rich PS is coupled to microscale sedimentology and GW hydrogeochemistry which create highly variable biogeochemical microenvironments across the redox interface. Different GW flow regimes, advective flow induced alterations along preferential flow paths and decoupled microenvironments in the complex structured and heterogeneous sediments provide highly variable micro milieus. Related to sedimentology the geochemical conditions vary significantly on the µm to cm scale and the observations suggest a dynamic system with oscillating hydrogeochemical conditions. Fluctuating conditions introducing strong redox and hydrochemistry gradients were shown to be crucial for the formation of extensive mc precipitates controlling Fe and As flus across the redox boundary. Therefore, the study provides a better understanding of redox-controlled Fe and As cycling in near-surface sedimentary aquifer systems and sheds new light on small-scale redox processes in heterogeneous delta sediments. The presented sequence of Fe phases across the redox transition zone in Van Phuc is suggested to play a significant role for As retardation in sandy near-surface aquifers of delta and floodplain regions all over SSEA.

Kurzfassung

Eisen- (Fe) Minerale sind hochreaktiv und haben eine wichtige Kontrollfunktion bei der Schadstoffdynamik in natürlichen und anthropogenen Umgebungen. Insbesondere das Verhalten von Oxyanionen wie Arsen (As) in oberflächennahen Aquiferen wird bekanntermaßen durch redoxsensitive Fe-Phasen gesteuert. Geogen As-kontaminiertes Trinkwasser aus oberflächennahen Grundwasser- (GW) Körpern ist nach wie vor eines der größten globalen Gesundheitsrisiken unserer Zeit, und es ist deshalb unumgänglich, As-Mobilisierungs- und Retentionsmechanismen in oberflächennahen Aquiferen besser zu verstehen. In diesem Zusammenhang untersucht die vorliegende Studie die Dynamik eisenhaltiger As-Trägerphasen in den Deltasedimenten des Roten Flusses (RR) in Vietnam, der für seine heterogene Verteilung von gelöstem As im GW bekannt ist. Diese Dissertation präsentiert die Fe-Mineralogie und die damit verbundenen As-Konzentrationen von zwei Sedimentkernen (ca. 50 m) über eine scharfe natürliche Redoxgrenze hinweg, die einen As-kontaminierten und einen nicht kontaminierten flachen sandigen Aquifer trennt, in Hinblick auf die Fe-Dynamik und die damit verbundene As-Freisetzung und As-Speicherung.

Wie in vielen anderen As-belasteten Gebieten Süd- und Südostasiens (SSEA) grenzen stark As-belastete (> 500 mg/L As) und nahezu As-freie (< 0,5 mg/L As) GW-Körper am Studienort direkt aneinander an. Obwohl der lokale GW-Fluss (~40 m/yr) vom As-reichen GW-Körper zum angrenzenden As-armen Aquifer führt, konnte ein GW-Überwachungsprogramm von 2010 bis 2017 keinen Eintrag von As in den unkontaminierten Aquifer feststellen, der für die lokale Wasserversorgung verwendet wird. GW-Daten weisen auf eine redoxinduzierte Akkumulation von Fe und As in der Festphase der schmalen (~35 m) Redox-Übergangszone (RTZ) hin, da die GW-Konzentration für beide Elemente über die Redoxgrenze hinweg drastisch abnimmt, während das Redoxpotential (Eh) vom reduzierten (Eh=10-40mV) zum mäßig reduzierten (Eh > 110mV) Aquifer ansteigt. Trotz umfangreicher Forschung zur gekoppelten Fe-As Dynamik entlang von Redoxgrenzen ist weitgehend unbekannt, wie Fe und As in der Festphase einer natürlichen Redoxgrenzfläche vorliegt. Es ist weitgehend spekulativ, welche Veränderungen Fe-Minerale als Hauptarsenträger entlang Redoxgrenzen unter advektiven Strömungsbedingungen erfahren und in welchem Ausmaß und auf welche Weise sekundäre Fe-Minerale den As-Zyklus entlang der Überganszone beeinflussen. Insbesondere der Einfluss der lokalen Geologie der heterogenen Deltasedimente auf die komplexen biogeochemischen Prozesse, die den Fe- und As-Kreislauf bestimmen, wurde bisher kaum auf kleinen Skalen analysiert. Daher konzentriert sich diese Studie auf die Analyse der Verteilung und (Trans-)Formation von eisenhaltigen As-Trägerphasen entlang eines natürlichen Redoxgradienten. Die Arbeit folgte dem Ansatz, Typ, Vorkommen, Verteilung, Häufigkeit und Eigenschaften von Fe-Mineralen und den zugehörigen As-Gehalt entlang zweier vertikaler Kernprofile, die am Übergang eines grau gefärbten (vermutlich holozänen) Grundwasserleiters mit hohem As-Gehalt und eines gelbbraun gefärbter (vermutlich pleistozäner) As-armen horizontal angrenzenden Grundwasserleiters erbohrt wurden, zu erfassen. Das abteufen der Kerne direkt in die fransige und sich überlappende Redoxgrenzfläche ermöglichte einen Querschnitt über die die gesamte Übergangszone, von den As-reichen zu den As-armen Aquifersedimenten in einem Kernprofil, welcher sowohl die reduzierten als auch die mäßig reduzierten GW-Bereiche abdeckt. Dieser Ansatz ermöglicht es, aus vertikalen Kernprofilen Rückschlüsse auf horizontale GW-induzierte Transformationsprozesse zu ziehen. Durch die Konservierung der ursprünglichen Textur und des Redoxzustands der Sedimente in einer Reihe von Dünnschliffen und Sedimentproben über die Redoxgrenze hinweg war es möglich, die Fe-Phasen und die damit verbundenen As-Konzentrationen räumlich aufgelöst im µm- bis m-Maßstab zu erfassen. Eine umfassende Sammlung hochauflösender mineralogischer und geochemischer Untersuchungen durch eine Kombination aus mikroskopischen, spektroskopischen und magnetischen Techniken ermöglichte es die redoxspezifische Verteilung von

primären und sekundären Fe-Mineralen entlang des Redoxgradienten sowie deren Beitrag zur As-Sequestrierung zu erfassen.

Die Studie ergab, dass As in den holozänen Sedimenten stromaufwärts der Bohrung durch reduktive Auflösung von Fe(III)-Oxyhydroxid-Mineralummantelungen um primären Quarzkörnern (Qtz) mobilisiert wird. Sobald das stark reduzierte As-reiche GW die Grenze zu den mäßig reduzierten pleistozänen Sanden erreicht, wird As durch verschiedene sekundäre Fe-Minerale immobilisiert, die in einer spezifischen Reihenfolge über die Redox-Grenzfläche hinweg gebildet werden. Die erste Stufe ist durch die Bildung sekundärer Fe(II)-Phasen definiert. Am weitesten verbreitet sind Fe- und Fe-Mn-Carbonate mit Arsenkonzentrationen bis 140 mg/kg. In geringerem Umfang konnte Pyrit (Py) mit Arsenkonzentrationen bis 4700 mg/kg dokumentiert werden. Die Fe(II)-Minerale werden umgewandelt und wieder aufgelöst. In einer zweiten Stufe bilden sich ausgedehnte Fe(III)-dominierte Oxyhydroxid-Präzipitate mit bis zu 480 mg/kg As als dominante Arsenträger. Das Ergebnis zeigt, dass metastabile sekundäre Fe(II)-Sulphide, Fe(II)-Carbonate und insbesondere die weit verbreiteten Fe(III)-dominierten Präzipitate aus mikrokristallinem (mc) Goethit (Gt), Hämatit (Hem) und Magnetit (Mt), in variablen Mengen, weitgehend die Fe- und As-Dynamik über den Redoxgradienten steuern. Es gibt klare Hinweise, dass diese metastabilen Sekundärprodukte, die durch gekoppelte biogeochemische Prozesse gebildet werden und erhebliche Mengen an As enthalten. Die Bildung der gemischtvalenten Fe(II)/(III)-Präzipitate ist höchstwahrscheinlich an das oxidative Verhalten von residualen Fe(III)- und Mn(IV)-Phasen in der reduzierenden Umgebung gekoppelt. Die hohe As-Absorptionskapazität und Empfindlichkeit gegenüber hydrogeochemischen Schwankungen der mc Eisenpräzipitate bietet eine hervorragende Erklärung für die hohe zeitliche und räumliche Variabilität von gelösten As-GW-Konzentrationen, die in vielen Untersuchungsgebieten weltweit beobachtet wird. Insbesondere die Fe(III)-dominierten Präzipitate, die sich als der Schlüsselretentionsmechanismus erwiesen haben, welcher den Fe- und As-Fluss über die Redoxgrenzen hinweg steuert, bieten einen Ansatz, um die gekoppelte Redoxdynamik der beiden Elemente in natürlichen Umgebungen besser zu verstehen. Der mc Charakter der Phasen bietet eine neue und schlüssige Erklärung für die oft stark kontrastierenden Fe- und As-GW-Konzentrationen über kurze Distanzen, die in den meisten Modellen noch nicht berücksichtigt werden. Da mc Eisenpräzipitate im Vergleich zu ihren kristallinen Pendants erhebliche Unterschiede hinsichtlich ihrer Reaktivität und (reduktiven) Auflösungskinetik aufweisen können, verdeutlicht die Arbeit, dass die klare Abgrenzung von kristallinen und mikrokristallinen Phasen notwendig ist, um den redoxgetriebenen Fe- und As- Zyklus entlang scharfer, natürliche Redoxgrenzen zu beschreiben und die Stabilität und As-Aufnahmefähigkeit der Sekundärprodukte zur erfassen. Darüber hinaus identifizierte die Studie Fe-haltige Schichtsilikate (PS), die sowohl am As- als auch am Fe-Zyklus beteiligt sind. Die Studie zeigt, dass das Fe-reiche PS sowohl als Quelle als auch als Senke für As und Fe fungiert und als wichtiges Fe(III)-Reservoir unterstützen alterierende primäres PS die Bildung der sekundären Fe(II)/(III)-Präzipitate. Obwohl der Beitrag von primärem PS zur Gesamtdynamik von As und Fe schwer zu quantifizieren ist, zeigt die Studie, dass die sekundäre Bildung von Fe-reichen PS im sub-µm Bereich ein wichtiger Zwischenschritt im Fe-Zyklus ist. Sie sind eindeutig an der (Um-) Bildung sekundärer Fe-Minerale beteiligt und eng mit der biogeochemischen Evolution der Fe-Phasen verwoben. Die fast allgegenwärtige Präsenz von Submikron-PS zeigt deutlich, dass die Mineraldynamik von Fe in natürlichen Deltasedimenten komplexer ist, als viele Modelle darstellen.

Diese Ergebnisse unterstreichen die Bedeutung umfassender mineralogischer und geochemischer Untersuchungen, die über die standardmäßige Mischprobenanalyse hinausgehen, um einen Standort zu charakterisieren. Die Ergebnisse bestätigen ein komplexes Zusammenspiel von hydro- und biogeochemischen Prozessen, welche die Akkumulation und (Trans-)Formation von Fe-Mineralen entlang der natürlichen Redoxgrenze steuern. Die Ergebnisse zeigen, dass das Auftreten von Fe(II)-, Fe(II/III)- und Fe(III)-Mineralen sowie von komplexen gemischtvalenten mikrokristallinen Fe-

Präzipitaten und Fe-reichen PS an die kleinräumige Sedimentologie und GW-Hydrogeochemie gekoppelt ist, welche hochgradig variable biogeochemische Mikroumgebungen über die Redox-Grenzfläche hinweg erzeugen. Unterschiedliche GW-Strömungsregime, durch advektive Strömung induzierte Veränderungen entlang bevorzugter Strömungspfade und entkoppelte Mikroumgebungen in den komplex strukturierten und heterogenen Sedimenten erzeugen hochvariable Mikromilieus. In Hinblick auf die Sedimentologie variieren die geochemischen Bedingungen erheblich auf der µm- bis cm-Skala und die Beobachtungen deuten auf ein dynamisches System mit oszillierenden hydrogeochemischen Bedingungen hin. Es wurde gezeigt, dass schwankende Bedingungen, die starke Redox- und Hydrochemiegradienten erzeugen, entscheidend für die Bildung umfangreicher mikrokristalliner Präzipitate sind, die den Fe- und As-Fluss über die Redoxgrenze hinweg kontrollieren. Daher liefert die Studie ein besseres Verständnis des redoxkontrollierten Fe- und As-Kreislaufs in oberflächennahen sedimentären Aquifersystemen und wirft ein neues Licht auf kleinräumige Redoxprozesse in heterogenen Deltasedimenten. Es kann vermutet werden, dass die präsentierte Abfolge von Fe-Phasen in der Redox-Übergangszone von Van Phuc eine bedeutende Rolle für die As-Speicherung in sandigen oberflächennahen Grundwasserleitern von Delta- und Flussgebieten in ganz SSEA spielt.

Eidesstattliche Versicherung

Eidesstattliche Versicherung gemäß § 6 Abs. 1 Ziff. 4 der Promotionsordnung des Karlsruher Instituts für Technologie für die Fakultät für Bauingenieur-, Geo- und Umweltwissenschaften (BGU).

1. Bei der eingereichten Dissertation zu dem Thema „Alteration and transformation of As-hosting iron phases in redox transition zones of the red river sediments, Vietnam" handelt es sich um meine eigenständig erbrachte Leistung.

2. Ich habe nur die angegebenen Quellen und Hilfsmittel benutzt und mich keiner unzulässigen Hilfe Dritter bedient. Insbesondere habe ich wörtlich oder sinngemäß aus anderen Werken übernommene Inhalte als solche kenntlich gemacht.

3. Die Arbeit oder Teile davon habe ich wie folgt/ bislang nicht an einer Hochschule des In- oder Auslands als Bestandteil einer Prüfungs- oder Qualifikationsleistung vorgelegt.

Titel der Arbeit: Natural As retention along sharp redox boarders in shallow deltaic aquifers – Alteration and (trans-)formation of As hosting iron phases under advective flow conditions in the Red River sediments of Van Phuc, Vietnam

Hochschule und Jahr: Karlsruher Institut für Technologie 2023

Art der Prüfungs- oder Qualifikationsleistung: Monographie

4. Die Richtigkeit der vorstehenden Erklärungen bestätige ich.

5. Die Bedeutung der eidesstattlichen Versicherung und die strafrechtlichen Folgen einer unrichtigen oder unvollständigen eidesstattlichen Versicherung sind mir bekannt.

Ich versichere an Eides statt, dass ich nach bestem Wissen die reine Wahrheit erklärt und nichts verschwiegen habe.

Karlsruhe, den Unterschrift

Acknowledgement & Funding

This thesis would not have been possible without the support of many individuals. Therefore, I would like to express my gratitude towards all of the people who made this study possible with helpful comments, practical advice, support and inspiration.

First and foremost, I would like to thank my **supervisors, advisers and members of my PhD commission**.

Prof. Dr. Thomas Neumann, *Head of Applied Geochemistry Department* at the TU Berlin, 10587 Berlin, Germany *(bevor 2018 Acting Head of the Institute of Mineralogy and Geochemistry at KIT)*

Prof. Dr. Agnes Kontny, *Division of Structural Geology and Tectonophysics* at Karlsruhe Institute of Technology, 76131 Karlsruhe, Germany

Prof. Dr. Thomas Pichler, *Head of Geochemistry & Hydrogeology group* at University of Bremen, 28334 Bremen, Germany

I want to express my special thanks to **Dr. Elisabeth Eiche**, *Division of Geochemistry & Economic Geology*, Head of Laboratory for Environmental and Raw Materials Analysis (LERA) at the Institute of Applied Geosciences (AGW) at Karlsruhe Institute of Technology, 76131 Karlsruhe, Germany. Without your tireless support throughout the entire project, this work would not have been possible!

Next, I want to thank all young scientists of the AdvectAs team (doctoral students and post-docs) with whom I spent many enjoyable days, weeks and months in the field and in the laboratory. The cooperation was excellent at all times and I look back on the project with a lot of nostalgia.

Dr. Martyna Glodowska, Radboud University Nijmegen, Netherlands (before Geomicrobiology Group at Center for Applied Geoscience, Eberhard-Karls-University Tuebingen)

Dr. Monique Patzner, Colorado State University (before Geomicrobiology Group at Center for Applied Geoscience, Eberhard-Karls-University Tuebingen)

Dr. Alex Lightfoot, Eawag Swiss Federal Institute of Aquatic Science and Technology

Dr. Emiliano Stopelli, Project Manager Hydrochemistry, Consulting & International Projects at Nagra - Nationale Genossenschaft für die Lagerung radioaktiver Abfälle (before at Eawag Swiss Federal Institute of Aquatic Science and Technology)

Dr. Bhasker Rathi, Senior Geochemical Modeler at Environmental Geochemistry International (before University of Western Australia)

As the work is part of an interdisciplinary approach investigating solid phase geochemistry, mineralogy, microbiology, hydrochemistry and hydrology due lab and field experiments as well as an accompanying modelling approach the study of related publications from Emiliano Stopelli, Martyna Glodowska, Alex Lightfoot and Bhasker Rathi is highly recommended.

I would also like to thank all AdvectAs project and cooperation partners for the numerous discussions and suggestions and the fantastic time during the coring campaigns and the various meetings.

Prof. Dr. Michael Berg, *Head of Department Water Resources & Drinking Water at* Eawag Swiss Federal Institute of Aquatic Science and Technology, 8600 Dübendorf, Switzerland

Prof. Dr. Andreas Kappler, *Chair of Geomicrobiology at* Eberhard Karls University Tuebingen, 72074 Tübingen, Germany

Prof. Dr. Lenny Winkel, *Head of Inorganic Environmental Geochemistry Group at the Institute of Biogeochemistry and Pollutant dynamics (IBP) at ETH Zürich &* Eawag Swiss Federal Institute of Aquatic Science and Technology

Prof. Dr. Henning Prommer, CSIRO Land and Water & Winthrop Research Professor at School of Earth Sciences, University of Western Australia, 6014 Floreat, Western Australia, Australia

Prof. Dr. Rolf Kipfer, Water Resources and Drinking Water, Eawag Swiss Federal Institute of Aquatic Science and Technology, 8600 Dübendorf, Switzerland

Prof. Dr. Olaf Cirpka, Centre for Applied Geosciences, Eberhard Karls University Tuebingen, 72074 Tübingen, Germany

Prof. Dr. Sara Kleindienst, Microbial Ecology, Centre for Applied Geosciences, Eberhard Karls University Tuebingen, 72074 Tübingen, Germany

Prof. Dr. Ben Bostick Lamont-Doherty Earth Observatory, Columbia University, New York, United States

PD Dr. Harald Neidhardt, Geooecology Research Group of Prof. Dr. Yvonne Oelmann, Geography, Department of Geosciences, University of Tuebingen, , 72074 Tübingen, Germany

I would also like to thank for an excellent scientific cooperation

Dr. Jörg Göttlicher, Institute for Photon Science and Synchrotron Radiation (IPS), Karlsruhe Institute of Technology (KIT), Eggenstein-Leopoldshafen, Germany

Prof. Dr. Stefan Norra, *Head of Environmental Mineralogy & Environmental System Analysis Group* at Karlsruhe Institute of Technology, 76131 Karlsruhe, Germany and *Head of Soil Science and Geoecology Group* at Institute of Environmental Science and Geography at University of Potsdam, Germany

Dipl.-Ing. Volker Zibat, Laboratory for Electron Microscopy (LEM), Karlsruhe Institute of Technology (KIT), Germany

Dipl.-Ing. (FH) Jörg Nissen, Zentraleinrichtung Elektronenmikroskopie (ZELMI), Technische Universität Berlin (TUB), Germany

Furthermore, I want thank all project partners from the **Key Laboratory of Analytical Technology for Environmental Quality and Food Safety Control (KLATEFOS), Vietnam National University of Science (VNU), Hanoi, Vietnam** for the unforgettable time in Vietnam and the tireless efforts that made the field work possible in the first place. My gratitude also goes to the **villagers of Van Phuc** for their friendly and generous help during our field work.

Further I want to thank all technicians of the Institute of Applied Geosciences (AGW) at Karlsruhe Institute of Technology for the support with the technical implementation, sample preparation and countless measurements:

Ralph Wachter for technical assistance with regard to the CAD construction and 3D-printing of the stitch rings.

The geoscientific preparators **Kristian Nikoloski** and **Stephan Unrein** for their tireless efforts in preparing the numerous thin sections.

Beate Oetzel for providing helpful advices regarding sample preparation and solving analytical difficulties with regard to the XRD measurements.

I also want to thank **Reto Britt** and **Matthias Brennwald** (Eawag) for the help during the field campaign.

Finally I want to thank **all unmentioned colleagues at KIT, TU Berlin, University of Tubingen, ETH Zurich and Eawag** for four unforgettable years.

This thesis was created at the section of Geochemistry & Economic Geology (before 2019 section of Aquatic Geochemistry) at the Institute of Applied Geoscience at the Karlsruhe Institute of Technology (KIT) and at the section of Applied Geochemistry at the Technical University of Berlin (TUB) and originates from a joined German-Swiss (DACH) research project co-funded by the **German Research Foundation** (DFG) and the **Swiss National Fond** (SNF) entitled "Retardation and mobilization of arsenic at redox fronts under advective flow conditions - a concerted multidisciplinary approach (AdvectAs)". I want to thank the DFG and SNF for funding the AdvectAs project through DACH (grant # 200021E-167821 -http://gepris.dfg.de/gepris/projekt/320059499) and enable this thesis.

My final thank goes to **Andres Schenk and the Graduate School for Climate and Environment** (GRACE) at KIT and the Karlsruhe House of Young Scientists (KHYS) for a scholarship and financial support for participation in summer schools, curses, conferences and workshops.

Table of content

List of Figures

Table index

List of abbreviations

Abbreviation	Definition
Al	aluminum
ANKA	Angströmquelle Karlsruhe
As	arsenic
bgs	below ground surface
C	carbon
C/N	carbon-nitrogen-ratio
Ca	calcium
CH_4	methane
C_{inorg}	inorganic carbon
cm	centimeter
C_{org}	organic carbon
CSA	carbon sulphur analyzer
DOC	dissolved organic carbon
Eawag	Swiss Federal Institute of Aquatic Science and Technology
ED-XRF	Energy Dispersive X-Ray Fluorescence
Eh	reducing potential (mV)
EMPA	Electron probe microanalysis
EXAFS	X-ray absorption fine structure
Fe	iron
GS	grain size
GW	groundwater
H	hydrogen
ICDP	International Continental Scientific Drilling Program
IRMS	isotope-ratio mass spectrometry
K	potassium
k	volume dependent magnetic susceptibility
kg	kilogram
KIT	Karlsruher Institut für Technologie
kt	temperature dependent magnetic susceptibility
L	liter
LOD	limit of detection
m	meter
mc	microcrystalline
mg	milligram
Mn	manganese
nm	nanometer
O	oxygen
OM	organic matter
P	phosphorous
pfp	preferential flow paths
RB	redox boundary
RI	redox interface
RR	Red River
RRD	Red River Delta

RTZ	redox transition zone
S	sulphur
SEM-EDX	Scanning Electron Microscope - Energy dispersive X-ray spectroscopy
Si	silicon
SOM	sedimentary organic matter
ssa	specific surface area
SSEA	South and Southeast Asia
SSRL	Stanford Synchrotron Radiation Light Source
SUL-X	Beamline for Combining Microfocused X-ray Techniques, Institute for Synchrotron Radiation (ISS), KIT
TC	total carbon
TN	total nitrogen
TS	total sulphur
UN	United Nations
UNESCO	United Nations Educational Scientific and Cultural Organization
UNICEF	United Nations Children's Fund
WD-XRF	Wavelength Dispersive X-ray Fluorescence
WHO	World Health Organization
XANES	X-ray absorption near edge structure
XAS	X-ray absorption spectroscopy
XRD	X-ray diffraction
XRF	X-ray fluorescence
yr	year
µg	microgram
µm	micrometer

Mineral abbreviations are based on Siivola & Schmid (2007) and Whitney & Evans (2010). An overview on all mineral abbreviations can be found in Table 20. An exception are the following abbreviations, for which there is no official abbreviation in the sources mentioned.

Abbreviation	**Definition**
Greru	green rust
Grei	greigite
PS	phyllosilicates

1. Introduction

In 2022 the greatest global health hazard remains the lack of access to clean drinking water. According to the World Health Organization (WHO) and the United Nations Children's Fund (UNICEF) one in three people globally does not have access to safe drinking water (WHO 2019). The United Nations (UN) estimates the total number of people without access to clean and continuously available drinking water at around 2.1 billion (UN World Water Report 2020). In addition to areas affected by acute water shortages, many supposedly water-rich countries are affected which are not to be expected at first glance. Especially in South and Southeast Asia (SSEA) geogenic, As-contaminated drinking water from shallow groundwater bodies represents a threat for millions of people (Smith et al., 1992; Kapaj et al., 2006; WHO 2022; Muehe & Kappler 2014; Karagas et al., 2015; Podgorski & Berg 2020). Groundwater plays a key role in global water supply and worldwide, more than two billion people depend on GW for their daily supply and over half of the world's population depends on GW for drinking water (The Groundwater Project 2020). Especially in developing countries, easily available and inexpensive near-surface GW is an indispensable source of drinking water. The natural As contaminated GW in the densely populated river floodplains and delta regions of the major Asian river systems with probably over 200 million affected people (Ravenscroft et al., 2009; WHO 2022; Podgorski & Berg 2020) represents one of the major global health risks of our time (Smith et al., 2000; Harvey et al., 2002; Berg et al., 2007; Fendorf et al., 2010; Hug et al., 2020; van Geen et al., 2011; McArthur et al., 2001; Murcott 2012). Massive population growth, accelerated economic development and a rising standard of living over the past decades has created a considerable pressure to accessible water resources in many areas. Due to the increased demand for drinking and process water the easily attainable As-contaminated near-surface GW reserves are still used intensively in many countries in SSEA. The often-precarious economic situation in the affected areas prevents the use of alternative, As-free lower-lying GW resources or the use of adequate water cleaning systems. The decentralized water supply with thousands of small household wells additionally complicates the widespread use and aftercare of water treatment technologies in the often poorly developed rural areas. Poorly trained and equipped national authorities and inadequate public administration further hamper conceptual development for sustainable water usage in these regions.

But more like all other factors the patchy occurrence of the As contaminated GW and the high spatial heterogeneity of As GW concentrations is the major challenge for the sustainable use of near surface GW across many regions in SSEA. As-free and As-polluted GW bodies lie often directly next to each other. This greatly complicates the use of the limited As-free water resources. The immediate neighbourhood of high and low As GW bodies poses a constant danger that punctual GW abstraction changes the local GW flows in a way that As contaminated water is drawn into previously As-free aquifers causing a permanent contamination. The continual risk of further reducing the already limited water resources makes the sustainable development of water resources in context of an increasing demand considerably more difficult. Especially since a reliable hazard assessment is almost impossible because the mineralogical and biogeochemical processes along the interfaces under (changing) advective flow conditions have hardly been understood. This lack of knowledge aggravates the effective use of the water resources considerably. Many cases are known in which As contaminated and uncontaminated aquifers directly adjoin one another without mixing. There are numerous examples for aquifers with contrasting As concentrations and redox conditions located adjacent to each other, separated by sharp redox boarders in vertical, inclined or lateral orientation (Larsen et al., 2008; Jung et al., 2012, van Geen et al., 2006; van Geen et al., 2013; Eiche et al., 2008; Wallis et al., 2020). Periods of almost a decade are documented without a noteworthy amount of As crossing the interfaces, even if it represents the local GW flow direction (Stopelli et al., 2020). GW analysis suggest As is held back by natural retention processes but the reason for this phenomenon is not well

understood. Up to date, it is largely unknown which processes retains As at the interface of these high and low As GW bodies. Yet understanding the natural remediation processes could make a significant contribution for a better management and sustainable use of the GW resources and could prevent large numbers of people from consuming contaminated water. Furthermore, the transition interfaces could act as natural As-barriers if they turn out to be stable. Embedding natural retention mechanisms in the local water abstraction concepts could enable the development of large-scale renovation and water management strategies that can be used reliably and inexpensively across locations all over SSEA. Easy applicable As mitigation strategies through the use of natural retention mechanisms due controlled GW pumping could make an important contribution to safe water supply and significantly reduce the number of people affected by As contaminated drinking water worldwide. Both the sustainable use and the development of As removal and management strategies require an understanding of the formation and structure of the transition zones as well as identification and assessment of the As sequestering mechanisms. Understanding the solid phase processes at the redox transition zone between the two contrasting aquifers is fundamental in order to promote further development. In order to reach that goal this thesis tries to characterize the close interrelation between Fe mineral (trans-)formation and As (im)mobility and describe the related mineralogical and biogeochemical mechanisms. These findings can be implemented in reactive transport models to better predict future As contamination scenarios in the GW of the Red River delta (RRD) and other affected areas where reduced As-rich waters are in danger to be drawn into uncontaminated aquifers.

It is common to most locations with patchy As distribution that narrow transition zones separate usually hydrogeochemical contrasting aquifers, which differ mainly in terms of their redox conditions and their dissolved element (e.g. Fe, As, Mn) concentrations. The most important As carriers in these environments characterized by highly variable redox conditions are redox-sensitive Fe phases. Yet such a location characterized by highly contrasting dissolved As and Fe concentrations and Eh conditions has rarely been investigated with regard to the transformation and new formation of Fe phases in order to identify As retention mechanisms. The focus of most of the previous and recent publications is on the search for the As sources in the sediment and the identification of the As mobilization processes in order to explain As liberation and distribution in GW. For this purpose, the As content, the As-hosting capacity and the dissolution kinetics of multiple As carrier phases were investigated under different hydrobiogeochemical conditions. In consequence, natural mobilization pathways of geogenic As from saturated aquifer sediments, especially under anaerobic conditions by water-rock-microbe interactions, are understood quit well (see chapter 3). The small number of studies investigated As retardation were either based on large scale GW analyses (Van Geen et al., 2013; Chakraborty et al., 2014; Rathi et al., 2017; Stopelli et al., 2020; Mozumder et al., 2020) or investigated the retention capacity for As(III) and/or As(V) through specific minerals and other potential sorbents under different hydrogeochemical conditions in controlled and simplified experiments. A wide range of natural and synthetic mineral phases were investigated in this context. In consequence the As storage capacity and stability under certain environmental conditions for almost all potential As carrier phases are relatively well known. In particular, the most prominent natural phases, Fe-, Mn- and Al-minerals, as well as diverse phyllosilicates (PS) are well characterized. However, the formation, structure and composition of natural redox barriers remains largely unknown. Although in the past, it has often been mentioned that heavily contaminated As and uncontaminated GW bodies lie in the immediate vicinity of one another, potential natural As retention processes have so far been neglected to a wide extent. Therefore, secondary retardation processes at the redox front between the solid and liquid interface are largely unexplored. Although it has been known for years that redox-sensitive Fe-minerals largely control the speciation, mobility and degradation of As (Cornell & Schwertmann 2003; Smedley & Kinniburgh 2002) up to present only a small number (Banning et al., 2013; Hsu et al., 2010; Jung et al., 2012b) of studies have focused on analysing the actual mineralogy and solid-phase

geochemistry of sediment samples across a redox gradient in high resolution. The coupled As & Fe dynamic at a redox interface in natural environment was hardly described on mineral scale and research that explicitly considers the variable composition across the redox interface is still lacking. Further there is uncertainty over the extent to which the Fe minerals most commonly studied in the laboratory reflect the Fe minerals found in the field (Smedley & Kinniburgh 2002). Though redox transition zones have been described mineralogically up to now, mineral characterization of natural As hosts was carried out using X-ray-based bulk analyses. Although this procedure specifies the mineral composition and also allows basic quantitative statements, the lack of spatial allocation does not allow any statements about the association of the phases. Moreover, only limited to none statements could be made about the crystallinity and texture of the host phases. Classic mineralogical analyses, especially spatially resolved, were not carried out and most model based studies use the properties of well-crystalline Fe phases. In fact, relatively little is known about the actual crystallinity of the phases in natural redox boundaries. However, information about the texture, crystallinity and position of the phases in the sediment allow important conclusions to be drawn about the (trans-) formation of the phases and the identification of additional influencing factors such as, different GW flow regimes, preferential flow paths and decoupled microenvironments related to local sedimentological heterogeneity. Yet these small-scale processes can play an important role in the As cycle. Especially the crystallinity of hosting phases has huge impact on the reactivity and stability of As hosting phases (Voegelin et al., 2019). The highly variable As uptake and storage capacity of differently crystalline As carrier phases can have a decisive influence on the overall As dynamics. Especially if the different As species are taken into account. This in turn provides important insights on the efficiency and long-term stability of the retention process.

In summary, it can be stated that it is largely unknown how the mineralogy of potential As carriers evolves across sharp natural redox boarders. It is widely speculative which secondary minerals form across the redox boundaries and how much As is retained (incorporated or adsorbed) in this phases (So et al., 2018 a & b). The actual (trans-) formation products of redox-sensitive As host-minerals as well as the distribution of redox-sensitive Fe minerals and their As contents across the redox interface is unexplored. Therefore, coupled Fe and As-sequestering mechanisms and their effect on Fe and As GW concentrations across a redox interface are unknown to a great extent. This lack of knowledge creates high uncertainties in predicting the future behaviour of As contamination in context of different usage or climate scenarios. In order to address this knowledge gaps the study presents the solid phase composition of two drill-cores from a shallow aquifer of the RRD in Vietnam and introduces a multi-stage process model to describe the spatial variabilities of Fe and As concentrations in shallow delta and floodplain GW resources on small spatial scales. This thesis deals with the redox-controlled As and Fe dynamics in natural near-surface environments at the sediment-GW boundary. The study focuses on conditions as found in Holocene and Pleistocene alluvial and deltaic floodplains and inland basins of SSEA and tries to explain the sharp transition from high to low As contaminated aquifers by identification of previously unmentioned retardation mechanisms. The clear, spatially resolved distinction between the Fe phases involved provides a broader understanding of redox controlled pollutant dynamic and could help to set up new more detailed process models describing mineral transformation schemes and contaminant behaviour. I am fortunate to approach these questions in an already well-characterized study area. The solid-phase geochemistry up- and downstream of the transition zone has already been characterized (Berg et al., 2007; Eiche 2010). Further the hydrochemistry of the field site was investigated in a multi-year GW monitoring program in a series of wells along the redox gradient (Berg et al., 2007; Stopelli et al., 2020) and a model based study (Wallis et al., 2020) which also allowed to identify the position of the redox boarder. Finally the dominant microbial processes are were investigated by Glodowska et al. (2020).

The **working hypothesis** of this study is based on the assumption that As release originates from reductive dissolution of Fe oxyhydroxide coatings through microbial mediated redox changes up-stream of the study area (Eiche 2009). Changing hydrogeochemical conditions across the redox interface cause dissolution, alteration, transformation and secondary formation of new Fe minerals by coupled biogeochemical processes, which incorporate or release As. The heterogeneity of the pending fluvial and marine deposits, complex GW flow regimes, microbial activity and alternating redox conditions suggest highly variable (hydro)geochemical subsurface conditions and therefore multiple mineralization pathways after As and Fe release from primary Fe oxyhydroxide coatings. Accordingly, it can be assumed that a broad variety of secondary As hosting Fe phases can be present across a redox-controlled retardation front in small-scale microenvironments. Nevertheless, it is reasonable to assume that a specific sequence of main secondary ferruginous (Fe-rich) As carrier phases controls the As and Fe flux across the redox gradient. It was assumed that a comprehensive description of the solid phase geochemistry and mineralogy will allow to explain the highly variable As GW concentrations on small spatial scales observed in many study sites worldwide. **Primary target of this study** is to identify the most important Fe and As retention mechanisms along the redox boundary and name the most important As carriers. The term ``Fe oxyhydroxides´´ in this thesis includes all mixed-valance and trivalent Fe-oxides, mixed oxide-hydroxides and hydroxides. Stated aim of this study to disclose mineralogical (trans-)formation of ferruginous As-carrier phases to describe retention mechanisms that prevent both elements from migrating with the GW across the redox boarder. The scientific focus is on the alteration and secondary formation of ferruginous As hosting phases in order to explain Fe and As accumulation indicated by long-term GW monitoring data. Further this study tries to identify the dominant Fe phases that lead to As fixation under advective flow conditions and prevent the entry of As in uncontaminated aquifers. Specifically the thesis tries to answer which carrier phases do form and how much As is stored in which mineral. For this purpose, the type, frequency, texture and the As distribution within the secondary As carries were recorded. Based on this results the study tries to predict the long-term capacity and stability of the retention front. Further the study try's to reconstruct formation, structure and extension of the redox front based on solid phase composition. Linking small-scale mineralogy with sedimentological and geochemical properties of the two cores will allow to estimate local effects caused by varying grain size and permeability, preferential flow paths, microenvironments, embedded OM or other potential electron donors and acceptors relevant for biogeochemical processes. Final aim of the work is to record the abundance of the relevant small and large-scale processes to create an overview of biotic and abiotic factors controlling Fe and As dynamic along the shallow natural redox front. For this purpose, the study presents the geochemical and sedimentological core data and the related Fe mineralogy in order to understand the interrelation between Fe mineral (trans-)formation and As (im)mobilisation across the redox interfaces. In order to achieve these goals, an approach was chosen that differs from previous works particularly in the small-scale description of the ferruginous As-hosting phases by a combination of microscopic, spectroscopic and magnetic techniques in a series of thin sections and bulk samples across the entire redox boundary. Combined spatially resolved synchrotron based EXAFS and XANES analysis merge information on As species and type of carrier phases and microprobe analysis deliver punctual total As concentrations. The application of magnetic susceptibility measurements as well as the almost full-coverage microscopic analysis allows the mineral phases to be characterized in a resolution and sensitivity not achieved previously. The additional description of sedimentology and solid phase geochemistry allows combining sedimentological, geochemical and mineralogical findings to a comprehensive picture.

2. Arsenic contaminated drinking water – a global health hazard

Arsenic contaminated drinking water is a well-known health concern affecting millions of people worldwide (Ravenscroft et al., 2009). From a global perspective, inorganic As exposure has become the most dangerous environmental health hazard (McCarty et al., 2011). The "largest mass-poisoning in human history" is one of the major physical health problems of our time and of global relevance (Smith et al., 2000) with almost 70 affected countries worldwide (Wang et al., 2018). Especially the densely populated river valleys and delta regions of SSEA are affected by dangerously high geogenic As GW concentrations far above the WHO limit of 10 µg/L (Kim et al., 2011; Benner & Fendorf 2010; McCarty et al., 2011). The consequences of As contaminated thinking water are disastrous. Long-term exposure to inorganic As above the guideline level poses a significant risk for irreversible health effects. Examples where polluted GW bodies exceed the limit value by a factor up to 500 or more are well documented for many different areas (Sarkar & Paul 2016) summing up to an estimated 150-220 million affected people worldwide (Ravenscroft et al., 2009; WHO 2022). The WHO estimated in 2008 that above 200 million persons worldwide might be chronically exposed to As in drinking water at concentrations above the safety standard of 10 µg/L (WHO 2008; Naujokas et al., 2013). A recent study (Podgorski & Berg 2020) confirms this numbers and finds 94 million to 220 million people are potentially exposed to high As concentrations (> 10 µg/L) in GW based on machine-learning model with vast majority (94 %) being in Asia. The unclear dimension and (future) extent of the health threat represents a substantial economic and social risk for many developing countries. The consumption of As contaminated drinking water leads to great suffering in the often poor and remote areas and hinders development.

The origin of the As crisis in SSEA dates back to a well drilling program to develop easily accessible near-surface GW bodies of the UN (Battling Arsenic Poisoning in Southeast Asia 2018). The wells were meant to replace sewage-laced surface water that still represented the main drinking water source for the majority of people. Due to the tropical to subtropical climate, the surface water was highly contaminated with pathogens and opening up the easy accessible GW resources to access germ-free water should improve the health situation. The partly man-made crisis took its origin in the 1960s and 1970s when water extraction from shallow (< 50m) aquifers started on a significant scale. Consequently, millions of tube wells have been installed with support of international developing aid (UN/UNICEF program) and private parties to replace surface water by supposedly clean GW resources (Smith et al., 2000). For example Unicef and the Bangladesh's Department of Public Health and Engineering, launched a campaign to sink a massive number of tube wells across the country to pump, as everyone assumed, unencumbered drinking water up from the shallow aquifers (Akbar 1998). One has to keep in mind that at that time it was top priority to replace the traditional village ponds which were the primary source of drinking water for a large portion of the population. Wastewater was not treated and cholera and diarrhoea were omnipresent. Consequently international institutions and national authorities in the affected countries were working hand in hand to improve the situation pragmatically. Large-scale naturally occurring As-contaminated GW had not been documented at this time and all cases of As contamination known at that time were highly concentrated point sources related to geologic anomalies or anthropogenic input. Also methodologically As was still quite difficult to detect. In consequence, a strong growing population all over South and Southeast Asia has been exposed to As enriched GW for decades (Smith et al., 2004).

How little was known at the time about the potential danger posed by As is also reflected in the legislation. Although the toxic effects of As have been known since ancient times, it took until the 1950s until the first limit values were adopted. First international standards for As in drinking water date back to 1958 when WHO first recommended a maximum contaminant level (MCL) of 200 µg/L (Smith et al., 2004). After Blackfoot disease was discovered by Chen & Wu (1962) and as

epidemiological evidence on chronic As toxicity emerged WHO set the guideline level for As on 50 µg/L in 1963 (Smith et al., 2004). Finally Tseng et al. (1968) described the relationship between long-term exposure to a high-level of As in drinking water and characteristic disease symptoms, including skin lesions, skin cancer, and Blackfoot disease. The characteristic symptoms led to the fact that after 10 to 20 years of incubation time in the early 1980s the first awareness of As induced health problems arose in SSEA. The nature of the problem was first spelt out in 1982 by the Indian medicine Professor Saha and published in 1984 (Saha 1984). Analytical problems and related errors made the determination of total As and As compounds in drinking water still very difficult in that time (Irgolic 1994) but as symptoms of chronic As exposure had been diagnosed frequently in the local populations, international research began in the early nineties to monitor scale and origin of this calamity (British Geological Survey 2001). In the early 1990s arrived the first scientific publications addressing the As problem. Results soon revealed that As in GW is inorganic and geogenic in nature, and microbes were identified as key players in the biogeochemical cycling of As in alternating redox conditions (Islam et al., 2004). Consequently the WHO reduced the guideline value for inorganic As in drinking water from 50 µg/L to 10 µg/L in 1993 (WHO 2022) and the United States Environmental Protection Agency (US EPA) followed in 2001. Before the turn of the millennium, the first As hotspot in the Bengal delta – later on ground zero – was scientifically described (Bhattacharya et al., 1997; Van Geen et al., 2003). It quickly became clear that the worst affected areas were the densely populated deltaic floodplains and inland basins of SSEA (Rahmen et al., 2009; Benner & Fendorf 2010; Charlet & Polya 2006; Kim et al., 2011; Muehe & Kappler 2014). Numerous monitoring studies quickly showed that As contamination is ubiquitous in the shallow GW of deltas and floodplains in SSEA (Agusa et al., 2010). Other affected areas all over the world were identified quickly in the following years (Fig. 1) (Ravenscroft et al., 2001; Amini et al., 2008; Huq et al., 2018; Nriagu et al., 2007; Mandal & Suzuki 2002). Today the As problem spans across all continents. Cases of naturally occurring high As levels in the GW are documented in American and European countries (Ravenscroft et al., 2009; Apata et al., 2017; Robinson & Ayotte 2006; Bundschuh et al., 2004), in Africa (Bretzler et al., 2017) and Australia (Medunic et al., 2020). In Asia, the list of countries affected was expanded to include India (Chakraborti et al., 2017; Alam et al., 2016), China (Rodríguez-Lado et al., 2013; He & Charlet 2013) and Cambodia (Phan et al., 2014). Especially in Bangladesh and West Bengal, tens of millions of people have been proven to have no permanent access to an alternative clean drinking water source and are dependent on As-contaminated GW. About 97 percent of Bangladesh's rural population depends on modest community and private GW wells for drinking water supply (Smith et al., 2000; Alam et al., 2002; Brinkel et al., 2009). Also in **Vietnam**, millions of people are potentially exposed to As bearing GW along the Red River and the Mekong River (Agusa et al., 2007 & 2014). In the Vietnamese Red River Delta (RRD), including the metropole region of Hanoi, above 3 million people are potentially endangered by As concentrations above the WHO limit (Winkel et al., 2011) reaching concentrations up to 3000 µg/L (Berg et al., 2001 & 2007).

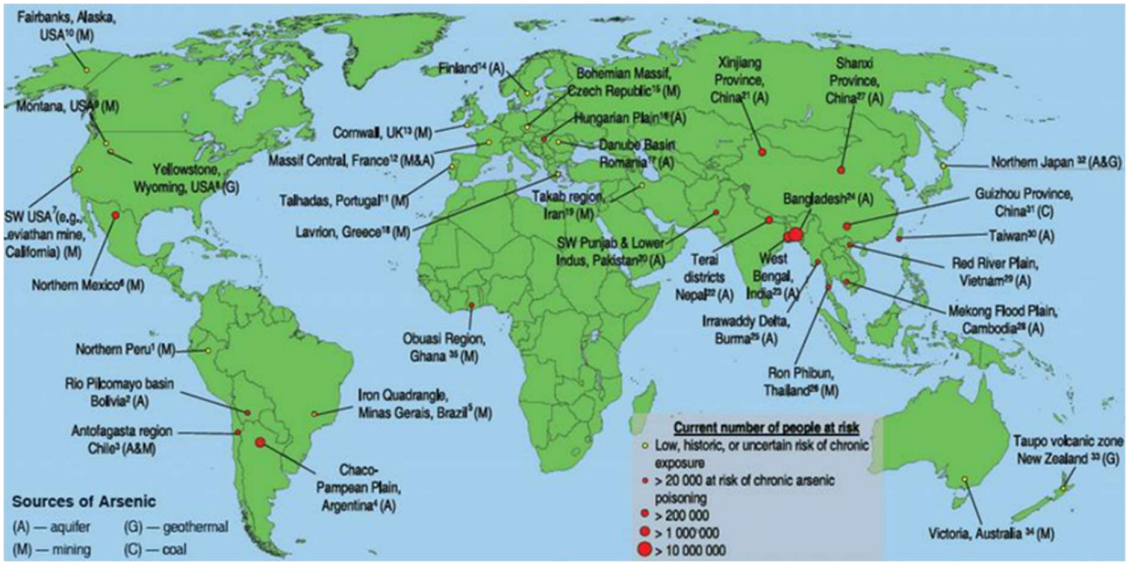

Figure 1: Worldwide distribution of arsenic contaminated regions and people at risk of chronic exposure (Thakur et al., 2011)

The millions of people affected all over the world quickly got attention in science and increasingly also in public. Since the "millennium peak" in 2000 the "largest mass poisoning of a population in history" drew a lot of interest. A high number of publications, reports and articles covering all fields from geoscience to medicine got published annually. A bibliometric analysis of research on As in drinking water by Abejon & Garea (2015) show a rising flow of new publications mainly in the field of Environmental sciences/ and Ecology which account for 38.1 % of the total publications. Based on an identification by a Web of Science study the field has experienced a massive increase since the millennium (Fig. 2) and has an annual publication output of more than 400 publications since 2010. Despite the substantial body of literature, research on As is still continuing and the number of publications is still increasing.

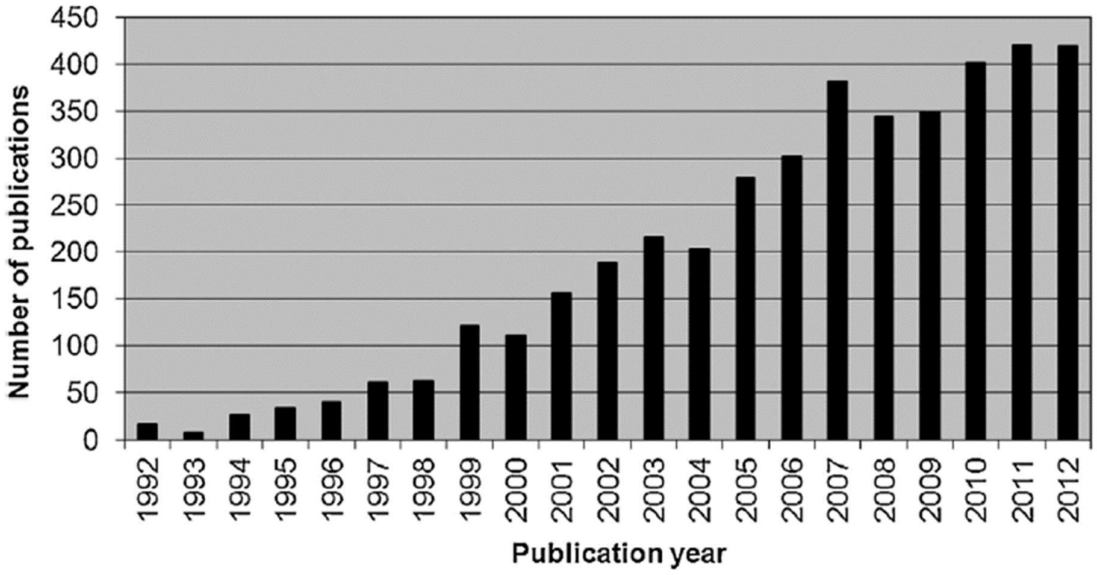

Figure 2: Annual publication output of research on arsenic in drinking water (Abejon & Garea 2015)

Despite extensive research and problem awareness among the authorities, the risk of As contaminated GW is still present. Constant rising demands (drinking, sanitary, industry, agricultural water) in context to growing populations, advancing industrialization and rising standards of living cause excessive water requirement and thus hamper sustainable use of limited GW resources. However, dealing with the natural source of danger of geogenic As contaminated GW has made significant progress in many areas. Today As contaminated GW is easy and inexpensive to clean with simple sand filter systems (Luzi et al., 2004; Berg et al., 2006; Nitzsche et al., 2015; Callegari et al., 2018) or other cost effective natural solids (Elizalde-González et al., 2001; Guo et al., 2007 & 2007b; Zhang et al., 2004; Devi et al., 2014; Gallegos-Garcia et al., 2012;Gupta et al., 2005). Up to date a broad range of low-cost adsorbents (Mohan & Pittman 2007; Chiban et al., 2012; Jovanovic et al., 2011) or alternative technologies for As removal from water are available (Nicomel et al., 2015). However, the actual effectiveness and reliability of the solutions has not yet been conclusively clarified. Especially the effectiveness of low-cost solutions in remote areas can hardly be determined. But in general decentralized solutions and increasingly widespread central drinking water facilities work effectively and the As levels in drinking water dropped considerably. However, it is important to consider that, unlike most international regulations the limit for As in drinking water in many developing countries is still at 50 µg/L As what is still based largely on analytical capability. The lack of adequate testing facilities for lower concentrations hinder many national authorities bringing the limits in line with the WHO guideline value (Bowell et al., 2014). In this context it is important to note that the most modern standards and recommendations for water consumption are based on an average body weight and water intake per day. The hard manual work in hot climate can cause the actual water requirement to be exceeded by a factor of 2 to 3. For this people, even the 10 µg/L As limit would still have to be decreased (Chakraborti et al., 2015). Nevertheless, decades of intensive research, raising awareness of national and international authorities and institutions around the world and comprehensive monitoring programs have most likely led to the fact that the intensively used As contaminated GW sources are identified. A drastic increase in the number of cases is therefore not to be expected although up to date As is regularly discovered in new areas. Yet still up to this day, As is not part of the standard suite of tested water quality parameters in most countries.

The effects of As on the human organism have been well researched. As one of the most prevalent toxic elements in environment As has diverse effects on human health (Bowell et al., 2014). While it forms numerous of poisonous compounds the toxicity and bioavailability of the tasteless, odourless and colourless element depends mainly on its chemical form and its oxidation state (Oremland & Stolz 2003) whereas both inorganic species are significantly more dangerous than methylated organic forms (Hopenhayn 2006; WHO 2022). The soluble inorganic arsenic is highly toxic and is supposed to act genotoxic, carcinogenic and teratogenic while it does not serve any beneficial metabolic function (WHO 2022). The trivalent compounds are generally more mobile and is said to be 2 to 10 times more toxic than the pentavalent compounds (Wasiuddin et al., 2002; Hong et al., 2014). Common to both As species is their persistence and propensity to bio-accumulate in higher trophic levels (von der Heyden & Roychoudhury 2015). In contrast its metallic form it is practically insoluble and therefore harmless to organisms since there is hardly any interaction with the organism (Oremland & Stolz 2003). Further the toxicity of As is dependent on a large variety of influencing factors including the exposure amount, length and frequency of exposure, the biological species, age and sex, individual sensitivity and genetics and nutritional factors (Abernathy et al., 1999). Due to its chemical similarity the pentavalent Arsenate (AsO_4^{3-}) can act as an analogous for phosphate (PO_4^{3-}) and interact with up to 200 enzymes, what affects numerous biochemical pathways (Goyer 2001). Arsenate uses the phosphate transport system to enter cells and hinders the adenosine-tri-phosphate (ATP) synthesis and the DNA synthesis and repair system (Abernathy et al., 1999; Islam & Islam 2011). Arsenate can also substitute for phosphate in various biomolecules, thus disrupting key pathways, including glycolysis (Fendorf et al.,

1997). Reduced inorganic Arsenite (AsO_3^{3-}) is considered even more toxic to the human organism (Meng et al., 2004), resulting from its high affinity for reactive thiol groups of enzymes (Knowles & Benson 1983). Trivalent arsenite suppresses and inactivates the activity of more than 200 enzymes after bonding with thiol or sulfhydryl groups, thus hindering intermediate metabolism (Fendorf et al., 1997; Tamaki & Frankenberger 1992) consequently causing cell damage (Chen et al., 1998; Duker et al., 2005) and affecting numerous organs (Goyer 2001). Further the binding of Arsenite with glutathione, a key enzyme in mammalian metabolism disrupts the function of many proteins (Mukhopadhyay et al., 2002; Bowell et al., 2014).

Chronic arsenic exposure in humans have been well documented and reviewed for decades and known to entail severe diseases (Kapaj et al., 2006). Consequence of chronic intake are serious health hazards up to death. The clinical picture is typically arsenicosis involving different sorts of cancer and skin lesions (Smith,et al., 1992; Chen et al., 1992; Kapaj et al., 2006; Muehe & Kappler 2014; WHO 2022; Madhukar et al., 2016). Its carcinogenic character was proven beyond any doubt and chronic uptake promotes an increased appearance of cancer even in low doses (Chen et al., 1992; Kapaj et al., 2006; Smith et al., 2000). Most affected are those organs involved in As absorption, accumulation and/or excretion (Kapaj et al., 2006). This includes the complete gastrointestinal tract and the circulatory system. Particularly affected organs are lung, bladder liver, kidney and the skin (Squibb & Fowler 1983). Signs of chronic As toxicity include dermal lesions (e.g. hyperpigmentation, hyperkeratosis, desquamation and loss of hair), peripheral neuropathy, skin cancer and peripheral vascular disease (Fig. 3 & 4) (Tseng 1977; Tseng et al., 1968; Zaldivar & Ghai 1980; Smith et al., 2000). Chronic As contamination is reflected on the skin in particular what is called arsenicosis. The expression arsenicosis, is a collective term for skin lesions like keratosis, hyperkeratosis and pigmentary abnormalities of the extremities that are characteristic for chronic As exposure. To the present day, no proper therapy for arsenicosis exists, therefore mitigation and removal strategies are the only available possibilities to avoid diseases related to chronic As uptake. Long-term cohort studies imply that chronic As uptake may also trigger a broad range of additional effects. They range from foetal loss and infant death, development of diabetes mellitus, cardio-vascular disease up to neurotoxic effects and inhibition of children's mental development (Alam et al., 2002; Argos et al,. 2010; Rahman et al., 2009; Kapaj et al., 2006). While acute As poisoning is rare and is usually caused anthropogenically chronic intoxication is mainly derived from oral ingestion of As-enriched water (Meliker & Nriagu 2007). Studies of As in human hair and urine suggest that drinking water is the most important source of As (Agusa et al., 2014). In addition to As contaminated water used for drinking and food preparation irrigation of food crops poses another threat (WHO 2022). Especially the uptake through rice has been shown to be a further potential As source (Mondal et al., 2010; Halder et al., 2014; Meharg et al., 2009). Like with As-contaminated drinking waters, the broad public attention and intensive research activities lead to simple and cost-effective methods to reduce the As content also in the area of As-contaminated food. A recently published study demonstrates that the As content in rice can be drastically reduced through a specific cooking process (Menon et al., 2021). As serious as the problem of As-contaminated food is, there are numerous ways to counteract the risk. As with the thinking water the challenge lies rather in the communication and implementation of possible solutions.

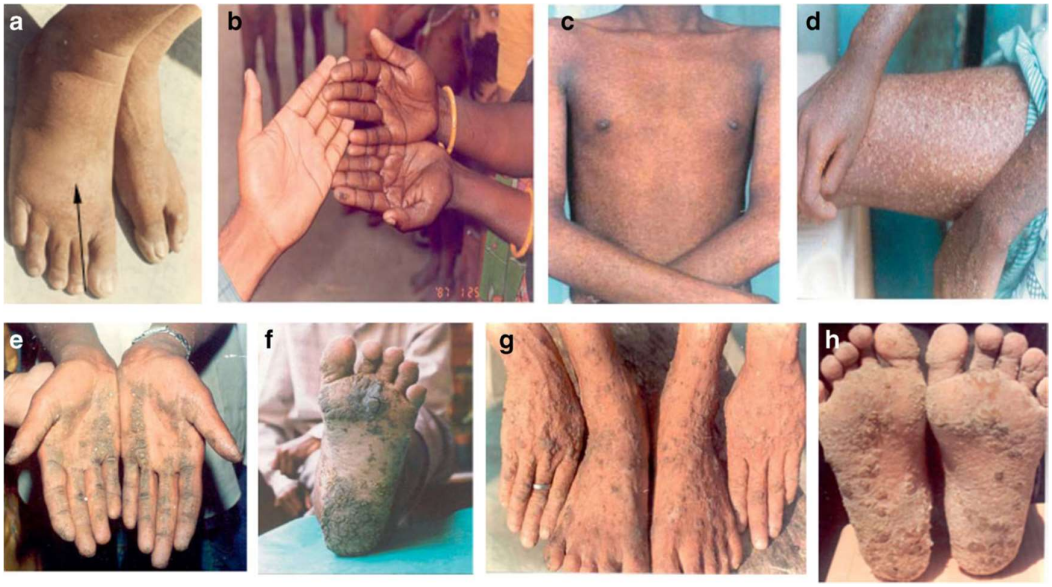

Figure 3: Arsenical skin lesions (Chakraborti et al., 2017)

Figure 4: Bowens and cancer from arsenic affected villages of West Bengal (Chakraborti et al., 2017)

3. Environmental Arsenic

3.1 Arsenic Chemistry

Arsenic (As - atomic number 33) has a molecular weight of 74.9 g/mol and is widely distributed throughout the geosphere (Matschullat 2000). Albertus Magnus, who is traditionally known as the discoverer of the element arsenic, first described the redox sensitive oxyanion-forming trace element around 1250 by isolating the element from the As sulphide orpiment (As_2S_3). The element has with ^{75}As one naturally occurring isotope and belongs to Group 5A of the periodic table (Matschullat 2000). Arsenic is classified as a metalloid with a chemical nature intermediate between that of metals and non-metals with an electronic configuration of $[Ar]3d^{10}4s^24p^3$. The five valence electrons, allow four oxidation states: As(-III) (arsenide), As(0) (elemental arsenic), As(III) (arsenite) and As(V) (arsenate). It commonly occurs naturally in the inorganic As species As(III) and As(V) while the oxidation states As(0) and As(–III) play only a subordinate role under the environmental conditions examined in this study. Similar to other metalloids the predominant species largely determines the bioavailability, mobility, reactivity and toxicity of the element (Garelick et al., 2008; Bowell et al., 2014) and transformations between arsenate and arsenite species can lead to As release or retention (Chatterjee et al., 2017). Under reducing and moderately reduced conditions, the trivalent As(III) is thermodynamically stable and predominant, whereas the pentavalent As(V) is stable and predominant under more aerobic conditions. Similar to many metalloids, the prevalence of particular species depends greatly on the pH and redox conditions and can summarised in Eh-pH diagrams (Fig. 5a) (Smedley & Kinniburgh 2002; Garelick et al., 2008; Borch et al., 2010; Bowell et al., 2014). In solution, As exists primarily as oxyanionic acids (Fig. 5b & 5c). Under oxidising conditions the arsenate species $H_2AsO_4^-$ is dominant at low pH (less than about pH 6.9), whilst at higher pH, $HAsO_4^{2-}$ becomes dominant. $H_3AsO_4^0$ and AsO_4^{3-} may be present in extremely acidic and alkaline conditions respectively. Under reducing conditions at pH < 9.2 the uncharged arsenite species $H_3AsO_3^0$ is predominate (Berg 2007). Lesser amount of $H_2AsO_3^-$ are possible with increasing pH (Bowell et al., 2014; Smedley & Kinniburgh 2002; Goldberg & Johnston 2001; Smith et al., 1998). Further Cullen & Reimer 1989 reported that plant and microbial activity may methylate As(V) or As(III). In consequence dimethylarsenic acid (DMAA) and monomethylarsonous acid (MMAA) can be formed. However, Fendorf et al. (2010) summarized that “methylated species are usually not abundant in aqueous solutions compared to inorganic forms of As (Smedley & Kinniburgh 2002; Smith et al., 1998)”. Additionally Fendorf et al. (2010) mentions that “thio- and carbonate- complexes of As also exist within anaerobic systems” and that “thiolate forms of As may, in fact, represent an important reactive component within sulfidic environments” already described by Wilkin et al. (2003).

In natural environments different As species often co-occur in both anoxic and oxic soils, sediments and GW. Reasons are kinetic inhibition or microbial induced catalytic reactions (Smedley & Kinniburgh 2002; Chatterjee et al., 2017; Anderson & Bruland 1991 Dowdle; et al., 1996; Nriagu et al., 2007). The chemical species of As in aqueous systems usually are not at equilibrium status because of slow rates of redox reactions (Meng et al., 2003). Slow rates of redox reactions were documented by Johnson & Pilson (1974) in seawater who give half-lives for As(III) oxidation the range from several months to a year in seawater. Also for freshwater environments modelled based results suggest that the oxidation of As(III) by dissolved oxygen can be slow and can reach a half-life of 1-3 years (Eary & Schramke 1990). On the other hand the prevailing As species can change quickly in dynamic environmental conditions. Reaction times of several hours after redox conditions changes from anaerobic to aerobic are reported for As(III) oxidation in GW by atmospheric oxygen (Hall et al., 1999; Berg et al., 2006). Further Sanders (1980) described the rapid oxidation of arsenite to arsenate, in the presence of oxygen, in coastal waters within 0.5 to 10 days. In summary, the reaction speed for As(III) oxidation and AS(V) reduction reactions is strongly dependent on the hydrogeochemical environment and microbial activity. Interactions with mineral surfaces, especially manganese (Mn) oxides, can have a catalytic effect on

redox kinetics and dramatically accelerate the transformation process while reactions due to Fe oxyhydroxides are much slower (Oscarson et al., 1981; Peterson & Carpenter 1983). Suspended particles such as OM has a great influence on the kinetic of As species and is able to accelerate the transformation process of the prevailing As species in both oxidation and reduction reactions (Redman et al., 2002). Also chemical parameters like pH, salinity, temperature and arsenite concentration can increase the rate of arsenite oxidation (Johnson & Pilson 1974). In addition, biotic reactions have a strong influence on the prevailing species and their transformation, in natural systems. It was shown that the biotic transformation rates for arsenite oxidation is at least seven orders of magnitude faster than the abiotic rate (Welch & Stollenwerk 2007). The same applies for arsenate reduction reactions. Timespan of 1-3 days have been reported for coupled biogeochemical processes (Xu et al., 2007) as well as pure microbial reductions (Langner et al., 2000). Therefore, As transforming bacteria can change the predominant species within hours to days. The transformation processes of the As species in natural systems thus cover a wide time window, depending on the geochemical environment. The complex interplay of coupled biogeochemical processes (Smith et al., 1998) and the multitude of possible catalytic reactions in heterogeneous sediments therefore leads to a broad variety of options. In complex structured near-surface sediments with successive hydrogeochemical variations, the As species composition is difficult to predict on a small scale and can be subject to a constant dynamic that change the relative proportion of As species continually. A comprehensive overview of factors controlling the As dynamic in natural near-surface sediments is given in chapter 3.3.

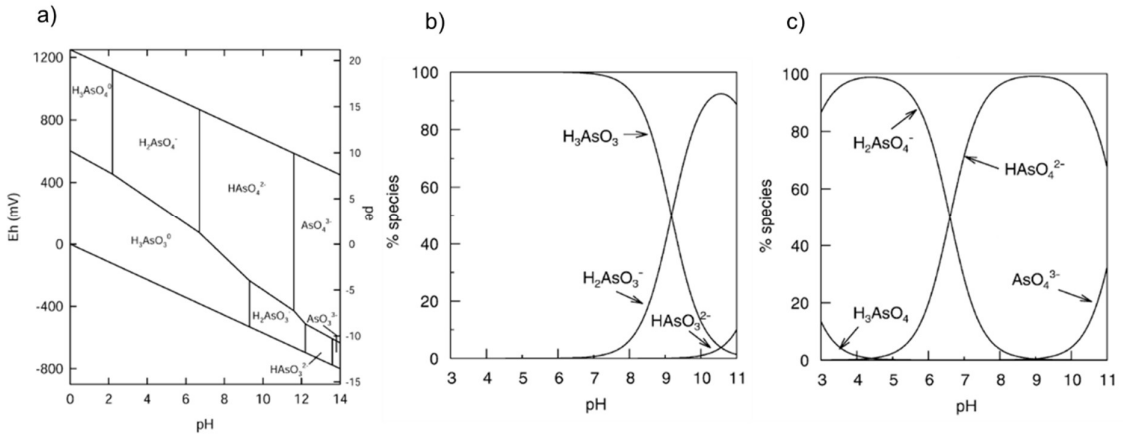

Figure 5: a) Eh-pH diagram for aqueous arsenic species in the system As– O_2–H_2O at 25 °C and 1 bar total pressure b) Arsenite, and c) Arsenate speciation as a function of pH at an ionic strength of about 0.01 M (Smedley & Kinniburgh 2002)

3.2 Occurrence and distribution of As in the lithosphere and hydrosphere

Arsenic is the 47th most abundant element on our planet (Bowell et al., 2014) and ranks 20th in crustal abundance of elements (WHO 2022). It is ubiquitous in the **lithosphere** as a result of geological contribution. Virtually all rocks, sediments, soils and natural waters contain at least traces of As whereby the geogenic background concentrations fluctuate considerably (Smedley & Kinniburgh 2002; Smith et al., 1998; Matschullat 2000). The As concentration range in the Earth's crust is given from 1.5 to 5.0 mg/kg (Smedley & Kinniburgh 2002; Chatterjee et al., 2017) with an estimated average of 2.5 mg/kg (Bowell et al., 2014). In the upper continental crust, As is concentrated by magmatic and hydrothermal processes and averages 5.7 mg kg^{-1} (Hu & Gao 2008). While the average As content for **ingenious rocks** lies usually between 0.5 and 3 mg/kg (average 1.5 mg/kg for all igneous rock types, Table 1) and rarely exceed 5 mg/kg (Ure & Berrow 1982; Garelick et al., 2008; Smedley & Kinniburgh 2002) **sediments** can contain significant higher As concentrations. In general, the As content in sediments is determined by the specific mineral composition, which can lead to enormous fluctuations in concentration in individual cases. The concentration range extends from 1.7 to 400 mg/kg (Bhumbla

& Keefer 1994) with an average of 5-10 mg/kg (Webster 1999; Garelick et al., 2008; Smedley & Kinniburgh 2002). The As concentration in sediments and soils is usually higher than in parent rocks because it accumulates due to weathering and translocation in colloid fractions (Smith et al., 1998). The wide range in sediments is mainly related to the variable proportion of As hosting phases in different sedimentological environments. Especially sulphides, oxides, organic matter (OM) and clays tend to host As and are mainly responsible for high As concentrations. Relatively pure **sands and sandstones** tend to have with 4 mg/kg the lowest sediment concentrations, reflecting their dominant mineral components quartz and feldspars. **Argillaceous deposits** have a broader range and higher average As concentrations and average typically around 13 mg/kg (Smedley & Kinniburgh 2002). However, **carbonates** show significantly lower average concentration of 3 mg/kg and the As concentrations are mainly attributed to constituent minerals (Garelick et al., 2008). **Iron- or organic-rich sediments** can far exceed the average concentrations mentioned so far and contain As concentrations up to 120 mg/kg in sandstones, up to 490 mg/kg in marine shales and mudstones, up to 800 mg/kg in chamosite-limonite oolites, up to 2,900 mg/kg in Fe-rich sediments and up to 35,000 mg/kg in coal (Boyle & Jonasson 1973; Garelick et al., 2008; Matschullat 2000; Smedley & Kinniburgh 2002). However, these extreme cases are extremely rare and accordingly only play a minor role when considering geogenic As contamination on the earth's surface. Concentrations of As in **unconsolidated sediments** lie with typically 3–10 mg/kg in the same range from those in their indurated equivalents. Depending on texture and mineralogy the As content varies but rarely exceeds 50 mg/kg (Smedley & Kinniburgh 2002; Garelick et al., 2008). Sediment concentrations documented from Acharyya et al. (1999) in sediments from the River Ganges average 2.0 mg kg1 (range 1.2–2.6 mg/kg), from the Brahmaputra River average 2.8 mg/kg (range 1.4–5.9 mg/kg) and from the Meghna River average 3.5 mg/kg (range 1.3–5.6 mg/kg). Benner & Fendorf (2010) summarizes that solid-phase As concentrations typically range from 1 to 15 mg/kg (Kocar et al., 2008; Swartz et al., 2004) and are therefore in general very near the global average As concentration in river sediments of 5 mg/kg (Boyle & Jonasson 1973; Smedley & Kinniburgh 2002). Within the **Pedosphere** As concentrations in the range of 5-10 mg/kg are usually documented with average concentration of 7.2-7.4 mg/kg (Boyle & Jonasson 1973). Soils that are particularly rich in organic matter, clays, and Fe minerals can also have significantly higher As concentrations up to 40 mg/kg (Kabata-Pendias 2000). Similar to sediments, the average As concentration given for soils in the literature fluctuate greatly due to the geographic location and mineral composition. Ure & Berrow 1982 give an average value of 11.3 mg/kg for clay-rich soils. Concentration above 100 mg/kg to about 170 mg/kg are documented by Smith et al. (1998) and Yamazaki et al. (2003). However, these high concentrations are extremely rare.

Table 1: Background concentration of arsenic in crustal materials (Madhukar et al., 2016)

Rock Type	Range (mg of As/kg)	Rock Type	Range (mg of As/kg)
Igneous Rock		**Oxide Minerals**	
Ultra basic	0.3-16	Haematite	Up to 160
Basalt	0.18-113	Fe(III) oxyhydroxide	Up to 76000
Gabbro	0.06-28	Magnetite	02.07.1941
Latite, Andesite, trachyte	0.5-5.8	Ilmenite	Less than 1
Granites/silicic volcanic	0.2-13.8	**Silicate Minerals**	
Rhyolite	3.2-5.4	Quartz	0.4-1.3
Diorite, granodiorite, Syenite	0.09-13.4	Feldspar	0.1-2.1
Sedimentary Rocks		Biotite	1.4
Shales and Clays	0.3-490	Amphibole	1.1-2.4
Phophorites	0.4-188	Olivine	0.08-0.17
Sandstones	0.6-120	Pyroxene	0.05-0.8
		Carbonates	
Limestones	0.1-20	**Minerals**	
Coals	0.5-80	Calcite	1-8
Bituminous Shale	100-900	Dolomite	Less than 3
Metamorphic Rocks		Siderite	Less than 3
Quartzite	2.2-7.6	**Sulphate Minerals**	
Hornfels	0.7-11	Gypsum/ Anhydrite	1-6
Slate	0.5-143	Barite	1-12
Schist	0.1-19	Jarosite	34-1000
Amphibolite and Greenstone	0.4-45	**Other Minerals**	
Sulphide Minerals		Apatite	1-1000
Pyrite	100-77000	Halite	3-30
Marcasite	20-12600	Fluorite	Less than 2
Pyrrhotite	5-100		
Galena	5-10000		
Sphalerite	5-17000		
Chalcopyrite	10-5000		

The widespread natural occurrence of As is related to the large amount of minerals that can host As. As is a major constituent in more than 200 **minerals** (Smedley & Kinniburgh 2002). Though not a major component, As is present in varying concentrations in many common rock-forming minerals. In many rock-forming minerals As is present as metal arsenate and arsenite where it substitutes for P(V), Si(IV), Al(III), Fe(III), and Ti(IV) in various mineral structures (Ure & Berrow 1982; Smedley & Kinniburgh 2002; Bowell et al., 2014). Up to July 2014, there are 568 known minerals for which As is a critical component (Bowell et al., 2014). Most are ore minerals or their alteration products (Smedley & Kinniburgh 2002). As the chemistry of As follows closely that of sulphur, the greatest concentrations of the element tend to occur in sulphide minerals. Especially high As concentrations are found in **sulphides** and mixed sulphides of the M(II)AsS type where M(II) stands for two-valent metal such as Fe or Mn (Nollet & Lambropoulou 2019). Most abundant are **arsenopyrite (FeAsS2), realgar (AsS) and orpiment (As_2S_3)**. It is generally believed that arsenopyrite, together with the other As-sulphide minerals realgar and orpiment, are mainly formed under high temperature conditions in the earth's crust (Smedley & Kinniburgh 2002). Arsenopyrite tends to be the earliest-formed mineral, derived from hydrothermal solutions followed by the formation of rarer native As and thereafter arsenian pyrite. Realgar and

orpiment generally form later still (Smedley & Kinniburgh 2002). However, these minerals are relatively rare in the natural surface environments (Reimann & Caritat 1998). The most important source of As in is most likely **arsenian ('As-rich') pyrite** (Fe(S,As)2) which seems to be the largest reservoir of As in crustal and ingenious rocks (Nordstrom 2000). Trace to minor contents up to 10 wt% As in natural pyrite are documented whereby As appears either as major components in sulphide mineral or as an isomorphous replacement for other elements in the crystal lattice. Isomorphous replacement occurs within the lattice between arsenic and sulphur due to their chemical similarity (Bowell et al., 2014; Reich et al., 2006; Neumann et al., 2013; Smedley & Kinniburgh 2002; Garelick et al., 2008). Weathering of arsenopyrite, base metal sulphides, realgar and orpiment and As-rich pyrite after transport to earth surface via tectonic, volcanic and hydrothermal processes is believed to be the main source of surface As (Nordstrom 2000; Smedley & Kinniburgh 2002; Garelick et al., 2008). At the earth surface high As concentrations can be found in addition to primary and secondary sulphides mainly in **oxide minerals, hydrous metal oxides and phosphates**, either as a component of the mineral structure or as sorbed species (Smedley & Kinniburgh 2002; Garelick et al., 2008; Bowell et al., 2014). The by far most important As carriers in surface environments are various **Fe minerals**. Therefore, the role of Fe phases (oxyhydroxides, sulphides, carbonates and phosphates) in near-surface environments is discussed in the chapter 4. Adsorption to hydrous **Al and Mn oxides** can also be important but due their low quantity, these oxides normally play a subordinate role (Peterson & Carpenter 1983; Brannon & Patrick 1987). Arsenic concentrations in **phosphate minerals** are variable but can reach high concentration, up to 1000 mg/kg in apatite. As-phosphate minerals are much less abundant than oxide minerals and make therefore only a small contribution to the As concentration in most sediments. Also important for the As dynamic are **carbonate minerals**. Although they usually contain less than 10 mg/kg of As they are much more abundant and therefore can host in sum significant amounts of As (Boyle & Jonasson 1973). Most **silicate minerals** contain approximately 1 mg/kg or less As and therefore only play a minor role in As cycle (Smedley & Kinniburgh 2002). An exception are **phyllosilicates** (PS), which can have somewhat higher concentration from in general 3-10 mg/kg but individual organic-rich clay layers are reported to reach 30-50 mg/kg (Smedley & Kinniburgh 2002). In addition to the fixation of As in the crystal lattice As may also be sorbed to the surface of clays (Goldberg & Glaubig 1988). An overview on important primary and secondary As hosting minerals can be found in Table 2.

Table 2: Important primary and secondary As bearing minerals (Madhukar et al., 2016)

Mineral	Formula	Occurrence	References
Native Arsenic	As	Hydrothermal Veins	Ko et al. 2012
Arsenopyrite	FeAsS	Lode Gold, Cu Sulfide, Sn, most abundant As mineral, dominantly mineral veins	Meunier et al. 2010
Cobaltite	CoAsS	Cu, Zn ores, high temperature deposits, metamorphic rocks	Kwong et al. 2007
Gersdorffite	NiAsS	High temperature deposits, metamorphic rocks	Senior et al. 2009
Enargite	Cu_3AsS_4	Hydrothermal Veins and Replacement	Lattanzi et al. 2008
Niccolite	NiAs	Hydrothermal modification of ultramafic rocks, vein deposits and norties	Anita 2011
Orpiment	As_2S_3	Hydrothermal Veins, hot springs, volcanic sublimation product	Zhu et al. 2011
Realgar	AsS	Vein deposits, Clay, Lime stone and Hot springs	Jin et al. 2000
Tennanite	$(Cu,Fe)_{12}As_4S_{13}$	Hydrothermal Veins	Bruckard et al. 2010
Arsenolite	As_2O_3	Secondary mineral formed by oxidation of arsenopyrite, native As & other As minerals	Islama et al. 2013
Claudetite	As_2O_3	Secondary mineral formed by oxidation of realgar and arsenopyrite, native As & other As minerals	Pichler et al. 1999
Scorodite	$FeAsO_4\ 2H_2O$	Secondary Mineral	Kossoff et al. 2012
Annabergite	$(Ni, Co)_3(AsO_4)_2\ 8H_2O$	Secondary Mineral	Cook 2010
Hoernesite	$Mg_3(AsO_4)_2\ 8H_2O$	Secondary Mineral	Voigt 1999
Conichalcite	$CaCu(AsO_4)(OH)$	Secondary Mineral	Henderson 2008

Pharmacosiderite	$Fe_3(AsO_4)_2(OH)_3\ 5H_2O$	Oxidation product of arsenopyrite and other As minerals	Tutor et al. 2013
Kankite	$Fe^{3+}As^{5+}O_4\ 3.5H_2O$	-	Walker et al. 2009
Loellingite	$Fe_3(AsO_4)_2(OH)_3\ 5H_2O$	Mesothermal vein deposits	Borba et al. 2000
Adamite	$Zn_2(OH)(AsO_4)$	Secondary Mineral	Armienta et al. 2000, 2005
Seligmannite	$PbCuAsS_3$	Hydrothermal vein	Mandal & Suzuki 2002
Safflorite	$(Co,Fe)As_2$	Mesothermal vein, Hornfels	Senior & Sloto 2006, Murcott 2012
Rammelsbergite	$NiAs_2$	Mesothermal vein	Nriagu et al. 2007

Arsenic is also omnipresent in natural waters and can be found throughout the **hydrosphere.** Both species, arsenite and arsenate, are widely present in liquid phase of near-surface waters and As concentrations in natural waters reach from 0.5 µg/L up to more than 5000 µg/L (Smedley & Kinniburgh 2002; Chatterjee et al., 2017; Reimann et al., 2009). Typical As concentrations in **fresh water** lies in the range between 1 and 2 µg/L (Hindmarsh & McCurdy 1986). Baseline concentrations of As in **river waters** are usually between 0.1–0.8 µg/L but can range up to 2 µg/L in consequence of geothermal activity or in connection with high-As GW. Arsenic concentrations in river waters from geothermal areas have been reported typically at around 10–70 µg/L with very rare cases in which the concentrations were significantly exceeded (Smedley & Kinniburgh 2002). Only in single cases like the geothermal springs of Yellowstone National Park As concentrations can reach 1 mg/L (McCleskey et al., 2022). Regionally, **geothermal waters** can represent extensive As sources. The Madison River down gradient the source area in Yellowstone reaches up to 0.36 mg/L (McCleskey et al., 2022). But these high values are extremely rare. Concentrations of As in **lake waters** are typically less than or equal to those found in rivers with As concentrations below 1-2 µg/L (Smedley & Kinniburgh 2002). The suggested background concentration for As in **GW** is given as 0.5-0.9 µg/L, but with a very high variance (Smedley & Kinniburgh 2002). The concentrations of GW As varies by more than four orders of magnitude and depend largely on the local hydrobiogeochemical environment. The reason for the high variance and the high maximum values lie in the tendency of aquifer environments to create physical and geochemical conditions that favour for As mobilization and accumulation (Smedley & Kinniburgh 2002). Concentrations and relative proportions of As(V) and As(III) in GW vary but under certain conditions, As concentrations of several thousand µg/L As can be achieved (Zhu et al., 2014; Bowell et al., 2014). The most common high As concentrations in aqueous surface environments are related to **porewaters** extracted from unconsolidated sediments. They frequently exceed typical freshwater ranges and often form sharp contrasts to the concentrations observed in surrounding ground and surface waters. High porewater As concentrations (up to several 1000 µg/L), are usually to linked to strong redox gradients that occur below the sediment-water interface (Smedley & Kinniburgh 2002).

3.3 Arsenic dynamic in sedimentary environments

While the usually low geospheric As background concentrations are harmless, it gets potentially dangerous when inorganic As gets mobilized and accumulates in GW. The As dynamic in near surface sedimentary environments is controlled through a large variety of processes. Through the huge variety of feasible processes the circumstances controlling natural As flux and content in sedimentary environments are in principle location-specific and result from a complex interplay of input sources, transport mechanisms, depositional history and present hydrobiogeochemical processes (Zhu et al., 2014; Bowell et al., 2014; Benner & Fendorf 2010). The behaviour of As in subsurface environments has been reviewed frequently and numerous partly coupled biotic and abiotic processes that introduce As into GW from As-bearing sediments are documented (Fendorf et al., 2010; Cullen & Reimer 1989; Mandal & Suzuki 2002; Smedley & Kinniburgh 2002). With regard to As contaminated delta and floodplain deposits of SSEA there are several main factors that widely control As GW concentration.

The predominant As species, the predominant mineralogy and the local microbiological activity (and their effect on local hydrochemistry) are usually considered to be the most important factors that determine mobility and fate of As in sedimentary environments (Wang et al., 2018; Bowell et al., 2014). On large spatial and temporal scales the dynamic of As in natural environments is largely controlled by alteration of carrier phases. Minor amounts of As are introduced in the environment continuously during sediment transport and deposition. During erosion, weathering or diagenetic alteration processes As-bearing primary phases are gradually altered and liberate As in the environment (Schwertman & Cornell 2000). Within secondary sedimentary systems the transformation of As carrier phases is the main mechanism mobilising As. Dissolution of As-hosting phases through changing hydrogeochemical environments are typical reasons for steady As-liberation in sedimentary environments. In this context the mobility of As in the near surface and surface environment is largely controlled by the redox potential Eh that determines both the prevailing As species and the stability of most carrier phases (Lear et al., 2007; Oremland & Stolz 2005). Changes in water redox chemistry often cause As release from solid phases through various desorption pathways and changing Eh conditions are widely accepted to be the main mechanism of As liberation in SSEA (Fendorf et al., 2010). As release by desorption and reductive dissolution of As-bearing Fe(III) oxyhydroxides are generally assumed as the dominant mobilization process from the solid phase into an aquatic environment during the onset of reducing conditions (McArthur et al., 2001; Smedley & Kinniburgh 2002; Nickson et al., 2000; Postma et al., 2012; Garelick et al., 2008; Oremland & Stolz 2003; Harvey et al., 2002; Dixit & Hering 2003; Ahmed et al., 2004; Kocar et al., 2006; Fendorf et al., 2010; Saunders et al., 2008). Many studies demonstrate the ability of shallow delta sediments to release As when subjected to reducing conditions. Also there is no clear consensus on the precise mechanisms involved, yet. Particularly with respect to the roles played by reductive desorption, reductive dissolution and the additional effect of diagenetic changes to the mineral structure (Smedley & Kinniburgh 2002).

3.3.1 Microbial mediated As dynamic

Most processes controlling the fate of As in hydrogeochemical environments are determined by a complex interplay of processes of which the majority are directly or indirectly driven by microbial activity (Huang 2014). In recent past, a conception established that both predominate As species and As carrier phase transformation are primarily determined by biogeochemical processes. In order to explain high As-contaminated GW concentrations of several hundred or thousand µg/L the **biotic onset of reducing conditions** through OM consumption is thought to be the dominant process in shallow sedimentary aquifer environments. Positive correlations between As and Fe(II) GW contents emphasize As is released passively through microbial oxidation of OM (Smedley & Kinniburgh 2002). Thus recent research describes microbial induced redox changes as main process controlling As and Fe dynamic in organic-rich floodplain and delta sediments of SSEA (McArthur et al., 2001; Dowling et al., 2002; Harvey et al., 2002; Akai et al., 2004; Islam et al., 2004; Swartz et al., 2004; Postma et al., 2007 & 2010 & 2012; Fendorf et al., 2010; Stuckey et al., 2016; Nickson et al., 1998 & 2000; Kocar et al., 2006; Ravenscroft et al., 2001; Wagner et al., 2005). Microbiological induced reducing conditions promote the principal mechanism largely determining the behaviour of As at the solid-liquid interface (Huang 2014). Therefore, it is widely accepted that As mobilisation from sediments into shallow reducing GW requires **active metal-reducing microbes** and electron donors such as OM (Lawati et al., 2012). While aquifers are usually carbon limited systems (Cozzarelli & Weiss 2007) marine transgressions and high sedimentation rates in the deltas and floodplains of SSEA caused rapid burial of considerable amounts of OM (Smedley & Kinniburgh 2002; Quicksall et al., 2008). Humic substances function as important electron shuttles and often dominate the dissolved organic carbon (DOC) fraction in reduced aquifers. The DOC serves as main electron donor in microbial respiration (Muehe & Kappler 2014; Mladenov et al., 2010) as the dissolved organic molecules are mobile and can be easily transported along hydrological flow paths. This makes them readily available in the deltaic near surface

aquifers of SSEA. Surface derived water from ponds and fields may serve as additional OC source. Infiltrating OM, especially during monsoon rains, when the surface recharge drastically increases may enhance microbial activity, too (Kocar et al., 2008).

Dissimilatory iron-reducing bacteria have shown to be able to create widespread reducing conditions and release of Fe(III)-bound As and Fe(II) (Borch et al., 2010). Much of the redox disequilibrium observed in the near-surface sediments of SSEA has been attributed to the role of microorganisms (Zhu et al., 2014; Bowell et al., 2014). In this context microbiological promoted Fe-mineral transformations through oxidation or reduction reactions are particular important. In particular the microbial mediated Fe redox cycling significantly influences the availability As (Zobrist et al., 2000; Islam et al., 2004; Oremland & Stolz 2005). There is broad agreement that reductive dissolution of detrital Fe(III)-oxyhydroxides is the main As and Fe mobilization process within the delta and floodplain sediments (McArthur et al., 2001; Dowling et al., 2002; Harvey et al., 2002; Akai et al., 2004; Islam et al., 2004; Swartz et al., 2004; Postma et al., 2007 & 2010 & 2012; Fendorf et al., 2010; Stuckey et al., 2015; Nickson et al., 2000; Kocar et al., 2006; Lovley 1995 & 1997). Many species of biota are involved in the turnover of Fe and especially microbes participate in the mobilization and immobilization of As by reduction and oxidation and by complexation and de-complexation (Schwertmann & Fitzpatrick 1992). Up to date a large number of isolated microbes are known who manipulate biologically the hydrochemical conditions within GW systems and interfere with the mineralogical inventory of the aquifer sediments. Numerous new interaction mechanisms between microbes and minerals have been discovered within the last two decades (Kocar et al., 2006). Involved organism mainly belong to the domain of Bacteria and therein to the heterotrophic dissimilatory Fe(III)-reducing bacteria, which couple the reduction of Fe(III) with the oxidation of alcohols, short- and long-chain fatty acids, mono-aromatic compounds or H2. These substances can be metabolic products released by synergistic bacteria or come directly from reactions with the OM (Konhauser et al., 2011; Lovley et al., 1989). At circum-neutral pH, available dissolved Fe(III) is quite rare since Fe(III)-minerals are poorly soluble. In consequence, many Fe-reducing bacteria adsorb onto Fe(III)-bearing mineral surfaces and excrete organic compounds that serve as Fe(III)-electron shuttles and thereby mobilise Fe(III) via surface complexion (Wolf et al., 2009; Konhauser et al., 2011). In general, Fe-reducing bacteria are able to release different kinds of electron shuttles, depending on the present mineral phases and some bacteria are able to directly mobilise and uptake Fe(III) after adsorption to the mineral surface (Wolf et al., 2009).

In addition to bacteria distinct **archaea** can respire on Mn(III/IV)- and Fe(III)-oxides leading to their dissolution with the potential for concomitant displacement of As into the aqueous phase (Cummings et al., 1999). Further archaea have shown to use additional metabolic mechanisms and therefore change the local hydrochemical cycle and open up new pathways. Recent studies by Glodowska et al. (2020), (2020b), (2021) and (2021b) could show bacteria and archaea contribute to the overall element cycle in the study area. However, Glodowska et al. (2021) revealed fermentation and methanogenesis as important processes providing electron donors, fuelling the microbially mediated reductive dissolution of As bearing Fe(III) minerals and ultimately promoting As mobilization**.** Glodowska et al. (2020b) could demonstrate that methane (CH_4) functions as electron donor for methanotrophs, triggering the reductive dissolution of As-bearing Fe(III) minerals and therefore identify a CH_4-mediated mechanism for As mobilization that is distinct from previously described pathways. Finally, the study of Glodowska et al. (2021) underlined the role of SO_4^{2-} reducing and putative Fe(II)-/As(III)-oxidizing bacteria as a sink for As, particularly at the RTZ. Another study in Van Phuc by Glodowska et al. (2020) could show that microbial processes in Van Phuc are fuelled by in-situ NOM from the upper aquitard (clayey silt) and lower sandy aquifer sediments. Although less efficient in stimulating microbial

Fe(III) reduction than highly bioavailable acetate/lactate, it ultimately has the potential to mobilize the same amount or even more As.

In addition individual microbes have shown to directly change the predominant As species or intact with organic As compounds. The ability of microorganism to interact with As covers respiratory oxidation and reduction processes as well as methylation of organic As compounds (Huang 2014; Campbell & Nordstrom 2014) and up to date many organisms have been isolated that transform As either through respiratory and/or detoxification pathways (Oremland & Stolz 2003). Microbial As mobilization through As species transformation is essentially driven by As(V) reduction and includes As(V) in solution or adsorbed on the surfaces of As hosting phases (Zobrist et al., 2000). As As(III) is the predominating GW As species the reduction of As(V) is of minor importance in shallow Asian aquifers. Since highest total As concentrations usually remain below necessary threshold concentration of 100 µmol/L that are needed to operate the methylation reactions this process is also of minor importance in SSEA (Smedley & Kinniburgh 2002). Arsenic-oxidizing bacteria oxidize As(III) to As(V) in order to yield metabolic energy and encompass two main groups. Heterotrophic arsenide oxidising bacteria (HAO) are capable to directly oxidise As(III) (Oremland & Stolz 2005; Salmassi et al., 2002) while Chemolitho-autotrophic bacteria (CAO) couple the oxidation of As(III) to the reduction of O_2 or NO_3^-. Both reactions are independent from organic matter as electron donor but play a subordinate role in the aquifer systems of SSEA analysed so far (Jackson et al., 2001).

However, the biogeochemical element cycling is never based on the activity of a single microbial species rather than **complex networks of microbial communities** (Cozzarelli & Weiss 2007; Lovley et al., 1989; Glodowska et al., 2021). Microbes form species-independent, connected networks (consortiums or communities) that are adapted to the present environment (quality of OM, prevailing Fe minerals, pH, temperature, intra-species interactions, etc.) and to respond to continuous changes in hydrogeochemical conditions with changing bacterial communities enable their members to degrade OM continually (Konhauser 2009). Furthermore, the cycling of As in most shallow aquifers are largely determined by **coupled biogeochemical processes**. The abiotic framework such as heterogeneity of dynamic delta and floodplain sediments with decoupled microenvironments, variable GW currents and constantly changing the hydrochemical conditions create a broad range of possibilities for hydrobiogeochemical processes. Biotic activity, indirect mineral phase transformation by reduction or direct interaction with microbes change the mineral inventory and local GW hydrochemistry frequently. In consequence a broad range of multiple interrelated microbial and abiotic processes are relevant to asses the subsurface element dynamic as dissolution or formation of secondary minerals release or sequester adsorbed and incorporated major and trace elements constantly (Lovley 1995 & 1997). In addition to Fe and As the cycling of potential nutrients like S, N and C as well as many major and trace elements including MnO, Al_2O_3 , TiO_2, SiO_2, MgO, Na_2O, P_2O_5, K_2O, CaO is widely influenced by this activities (Smedley & Kinniburgh 2002). This in turn affects the GW hydrochemistry by limiting or providing electron donors or acceptors. In addition to the release of Fe(II) and As, microbial metabolic reaction causes formation and release of protons and bicarbonate, which trigger in turn subsequent geochemical reactions like carbonate dissolution. Depending on the availability of terminal electron acceptors (TEA) and OM, microbial communities and resulting geomicrobiological reactions can evolve over time. In redox controlled high As aquifers in SSEA successive consumption of TEA and formation of specific redox layers as a result of a dynamic competition between different heterotrophic microbes with different metabolic pathways is well documented (Borch et al., 2010; Chapelle 2000; Mc Mahon & Chapelle 2008). As a result, communities are formed according to the available redox couples in a specific sequence (redox ladder) is called the Ecological redox sequence (Fig. 6).

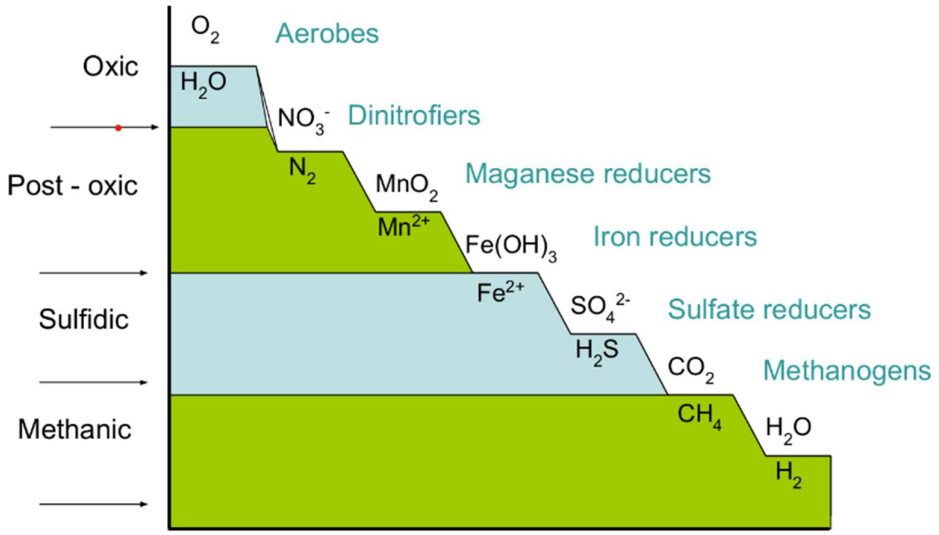

Figure 6: Redox Ladder showing redox conditions on the left and most effective redox-couples and involved microorganisms on the right (HP University of Vermont)

3.3.2 Hydrogeochemical mediated As dynamic

Within the biological mediated aquifers a broad range of **abiotic hydrogeochemical reactions** effects the As dynamic. Beside the immediate microbial activity the As dynamic in shallow aquifers is controlled by **hydrogeochemical parameters** which are usually regulated by a complex interplay of biotic and abiotic processes. The extent to which **pH** influences As dynamic differs depending on hydrogeochemical environment and mineralogical inventory (Fitz & Wenzel 2002; Mahimairaja et al., 2005; Masscheleyn et al., 1991). Dissolution of As-carrier phases due changing pH conditions can cause further As release (Smedley & Kinniburgh 2002) although this process is less important for most near-neutral and widely pH-stable delta and floodplain deposits of SSEA. The influence of pH on As dynamics is mainly related to sorption processes and dependent on the **prevailing As species**. While As(V) adsorption decreases with increasing pH, in particular above pH 8.5, the opposite occurs for As(III). In general it is assumed that in anoxic environments with near-neutral pH the As mobility is increased after reduction to As(III) (Bowell et al., 1994; Harvey et al., 2002; Smedley & Kinniburgh 2002) although Dixit & Hering (2003) could show that the effect of As(V) reduction on As mobility is strongly dependent on solution composition. However, a general statement on As mobility based on predominant species cannot generally be applied one to one to complex natural systems. Laboratory experiments have demonstrated that this statement is an oversimplification and that an estimation of the species dependent As mobility is very difficult to assess in natural aquifer systems (Frankenberger 2002; Mohan & Pittman 2007). Studies that examined the sorption behaviour of As used strongly simplified experimental setups (Mohan & Pittman 2007). In addition to pH and redox state (Dixit & Hering 2003; Goh & Lim 2004) the sorption behaviour of dissolved As(III) and As(V) strongly depends on the **solid-to-solution ratio** of both As species, quantity and **type of ad- and desorbing mineral phases** and **hydrochemical composition** of local GW (anion sorption competition) (Dixit & Hering 2003; Mohan & Pittman 2007; Lear et al., 2007; Oremland & Stolz 2005). Therefore, results from simplified experimental setups should be viewed with caution. Despite the extensive research on microbiological controls on As mobilisation, there is no consensus regarding the potential influence of consecutive abiotic reactions (Neidhardt et al., 2012).

With regard to the **solid phase** the As dynamic in shallow sedimentary aquifers is widely governed by interaction of dissolved As species with the **mineral inventory** at solid-liquid interface. This processes can either fix As in the solid phases or release As into GW. Partitioning of As onto solids is foremost dependent on its oxidation state. Fendorf et al. (2010) states that “in general, As(V) binds extensively

and strongly to most mineral constituents of soils and sediments, while As(III) retention is more convoluted and dependent on specific chemical conditions" and the “constituents inducing precipitation vary dramatically” between the two species. However, the fate of As and adsorption and desorption reactions with mineral surfaces are closely related. Sorption processes can either accelerate or slow down the mobilization and transport of As compared with the GW flow and in the best of cases can even stop further spread (Appelo & Postma 2004). Adsorption and desorption mechanisms largely depend on solid properties of potential As-hosting minerals. Changes in crystallinity and available surface area govern the As binding capacities to a wide extent (Kocar et al., 2006). Especially for redox-sensitive Fe minerals, the main As carriers in SSEA, mineral transformation reactions causes changes in hosting capacity for various competing adsorbents including As (Voegelin et al., 2019). The most **important As carriers** for both arsenate and arsenite in sediments are metal oxides and hydroxides. In particularly Fe, Al and Mn oxides and hydroxide minerals and various (Fe-rich) PS widely control the fate of As in natural sedimentary aquifer environments (O’Day 2006; Sullivan & Aller 1996). To a lesser extent, As in sediments can be associated calcium carbonates and organic acids (O’Day 2006). High sorption affinity for both As species are found especially for Mn oxides like birnessite (Garelick et al., 2008). Mn-phases were observed to own the same regulating role as Fe minerals in the As dynamic if present in high quantities (Smedley & Kinniburgh 2002; O’Day 2006). Fendorf et al. (2010) summarizes that “especially the reaction of arsenite in solutions with Mn oxides results in extensive and rapid uptake. Arsenite is oxidized by Mn(III/IV) and retained as arsenate surface complexes (Manning et al., 2002; Oscarson et al., 1981b). Aluminium hydroxides and aluminosilicate clay minerals may also retain appreciable concentrations of arsenite, although they exhibit a strong preference for arsenate relative to arsenite (Manning & Goldberg 1997)”. The publications Smith et al. 1998 and Garelick et al. 2008 confirm this determination. The role of Fe minerals as dominant As carriers is discussed in the following chapter in more detail. Further the dissolution or precipitation of As carriers due under- or oversaturated GW is a potential mechanism relevant for the As dynamic. Especially in heterogeneous sediment bodies with complex GW flows, the concentration for different elements can fluctuate considerably and consequently influence the solid and liquid phase. This process however is mainly governed by the solution composition.

In addition to the solid phase composition the As dynamic at the solid-liquid interface is dependent on present **GW hydrology and hydrochemistry**. Competition for sorption sites of competitive anions has a significant effect on the kinetics of both arsenate and arsenite. Ad- and desorption processes depend on respective flow velocities as well as concentrations of competing ions and solutes (Smedley & Kinniburgh 2002). The similar sorption behaviour of As oxyanions and other anions plays an important role regulating competitive ion exchange and adsorption reactions between the two As species, competing adsorbents and minerals (Postma et al., 2007). Also Fendorf et al. (2010) mentioned that “competitive ion displacement can represent an important mechanism by which As is released to the aqueous phase and subjected to transport”. Both As oxyanions are subjected to sorption-competitive reactions with competing adsorbents. These include phosphate, silicate, (bi-) carbonate, sulphate and organic matter (OM) (Chowdhury et al., 1999; Nordstrom 2000; Garelick et al., 2008; Oremland & Stolz 2003; Biwas et al., 2018; Smedley & Kinniburgh 2002; Bauer & Blodau 2006). In particular, adsorbed inorganic ions such as Ca^{2+}, Mg^{2+}, PO_4^{-3} and CO_2^{-3} will interact with As when adsorbed on the sites of metal oxides surfaces (Smedley & Kinniburg 2002; British Geological Survey 2001). Type and extent of the interaction of the different As species with mineral surfaces and competitive anions depends primary on the type of bonding. Surface adsorbed As, which is either weakly adsorbed (electrostatic attraction) or strongly bound (ligand exchange), is easily accessible to interactions with dissolved compounds and microbes. Ligand exchange processes and complexation reactions are generally considered as important mechanisms mediating the As mobility (Smedley & Kinniburgh 2002). In contrast, As, which is firmly integrated into the crystal lattice, is not so easily available. Arsenic

adsorption can be significantly decreased by the presence of Fe binding organic ligands like dissolved organic matter (Redman et al., 2002) and inorganic ligands such as phosphates (Zhu et al., 2011) which compete for surface bonding sites on Fe oxyhydroxides surfaces (Heyden & Roychoudhury 2015).

In the competition for sorption sites, **phosphate** (PO_4^{3-}) occupies a special role in the As dynamic (Manning & Goldberg 1996; Violante & Pigna 2002; Dixit & Hering 2003). Phosphate is a major competitor for arsenate as well as arsenite binding sites and the presence of phosphate in GW controls the fate of As to a wide extent as it can trigger displacement and mobilization of As (Fendorf et al., 2010; Mohan & Pittman 2007). Adsorbed and dissolved phosphate ions have a interaction with both As species and therefore phosphate is of critical importance for the As behaviour in natural waters. Therefore, the As dynamic at the sediment-GW interface is strongly depend on the GW phosphate level (Stachowicz et al., 2008). Especially for arsenates, after all considered a subclass of the phosphate mineral group mineralogically (Dana classification). Because of the similarity in size, charge and chemical structure under equilibrium-oxidized conditions over the pH range of 6-8 observed in most natural waters (O'Day 2006). Both ions form oxyanions (AsO_4^{3-} & PO_4^{3-}) and compete for chemical binding sites, especially on Fe oxyhydroxides. The competition between arsenate and phosphate for sorption sites is a significant factor for the GW As dynamic (Dixit & Hering 2003; Garelick et al., 2008; Stachowicz et al., 2008; Biwas et al., 2018). High phosphate concentrations is calculated to severely reduce As(V) sorption on Fe oxyhydroxide phases while As(III) sorption remains largely unaffected (British Geological Survey 2001; Smedley & Kinniburgh 2002; Hoa et al., 2014). Stachowicz et al. 2008 claims that "the interaction between **arsenite** and phosphate is less important and the sensitivity of arsenite oxyanions for changes in the phosphate concentrations is smaller than the sensitivity of arsenate oxyanions for phosphate" and that in general "it responses less strongly to changes in the phosphate concentration compared to arsenate. The difference in sensitivity of both As species for the presence of phosphate is caused by different electrostatic interaction". However, the phosphate concentration is also of crucial importance for the arsenite dynamics. In 3-component experiments with As(OH)3–, PO3−4 and divalent cations Stachowicz et al. (2008) could show that the "arsenite concentration is dominantly regulated by phosphate with some influence of Ca^{2+} and Mg^{2+} concentrations".

Beside phosphate the concentration and distribution of the two As species in GW is influenced by competitive sorption behaviour with several other ions and oxyanions. **Ca^{2+} and Mg^{2+}** both promote phosphate and arsenate absorption on Gt and comparable mineral sites in the pH range relevant for natural GW (pH 5–9). An Increase in AsV adsorption capacity of 26-37 % in sediments was observed after the addition of Calcium (Ca) (Stachowicz et al., 2008; Hafeznezami et al., 2017). Especially at high pH (8.5) Ca was shown to dramatically increase arsenate sorption to amorphous iron hydroxide (Smith & Edwards 2005). Stachowicz et al. 2008 wrote that "a similar (electrostatic) effect is expected for the Magnesium (Mg) ions interaction with As(V) oxyanions" also calculations predict a larger effect of Ca^{2+} compared to Mg^{2+}. Both ions have no significant effect on arsenite oxyanion adsorption (Stachowicz et al., 2008). Stachowicz et al. 2008 also mentions that "other anions, such as **Cl^- , SO_4^{2-}, and NO_3^-** have minimal impact on As sorption", yet these "ions can contribute to ionic strength and salinization effects on As retention in soils and sediments (Smith et al., 1998) that are potentially important in the desorption of arsenite". In addition to the chemical similarities of As to P chemical similarities also exists for **sulphur** (S) which control the As dynamic to a significant extent (Bowell et al., 2014; Reich et al., 2006; Neumann et al., 2013; Smedley & Kinniburgh 2002; Garelick et al., 2008). The similarities towards S favour the As incorporation in sulphide minerals. In terms of sorption competition, **sulphate** may have a small competitive effect on As adsorption to oxide surfaces (Gustafsson & Bhattacharya 2007). Stachowicz et al., 2008 also names **(bi-)carbonate** (HCO_3^-) as "a another weak competitor for sorption sites on mineral surfaces (Van Geen et al., 2013; Kim et al, 2000; Villalobos & Leckie 2001;

Appelo & Postma 2004)". For both types of As oxyanions the presence of **carbonate** (CO_3^{2-}) ions is theoretically relevant also compared to the dominant role of phosphate the role of bicarbonate is almost negligible (Radu et al., 2005). Radu et al. (2005) found increasing aqueous carbonate concentrations had relatively little effect on As mobility and transport in the subsurface. Even when present in significant higher concentrations than phosphate the competitive release of As from Fe oxides under natural GW conditions was very little (Stachowicz et al., 2008). Only Gustafsson & Bhattacharya 2007 documented a noteworthy competition of carbonate in the circumneutral pH range. Another competitor in the circumneutral pH range for As is **silicic acid** (Gustafsson & Bhattacharya 2007). The contribution of dissolved silicate to As desorption is lower than that of phosphate and bicarbonate (Radu et al., 2005) and the adsorption process of arsenite on Gt was found to be significantly slower compared to the other competitors (Luxton et al., 2008). Desorption experiments where silicate was introduced to previously adsorbed arsenite indicated that silicate was able to irreversibly displace between 0.3 and 1.5 % of the adsorbed arsenite resulting in an As release into GW. Dissolved silicate is therefore able to competitively limit As adsorption or promote desorption (Luxton et al., 2008). Although there is disagreement about the necessary concentrations. In this context Stachowicz et al. 2008 refers to Luxton et al. (2008) which assume "that concentrations common to soils and sediments having an appreciable impact on dissolved As concentrations". In other studies silicate is thought to reduce arsenite adsorption rates and quantity and displace adsorbed arsenite on most Fe oxyhydroxides only in much higher concentrations (Smedley & Kinniburgh 2002). Also for **organic matter** (OM) there is disagreement about the necessary concentrations in natural systems. Especially dissolved organic carbon (DOC) may also compete with As for adsorption sites on mineral surfaces. While Grafe et al. (2001) & (2002) expects OM to limit As adsorption or promote desorption, with concentrations common to soils and sediments other studies presuppose high concentrations of OM are necessary to enhance desorption of As (Smedley & Kinniburgh 2002). In general, the sorption of DOM has a strong potential to mobilize both As species from soils and sediments (Bauer & Blodau 2006). NOM samples are known compete with As and inhibit As adsorption onto Fe oxyhydroxides due to competitive adsorption and to displace sorbed arsenate and arsenite (Xu et al., 1991; Redman et al., 2002). Competition between NOM and As for sorption thus appears to be a potentially important process in natural waters, suggesting that NOM may play a greater role in As mobility than all other competitors apart from phosphate. Especially the trivalent arsenite was observed to be consistently desorbed or prevented from sorbing by NOM (Redman et al., 2002). The competition for sorption sites of dissolved organic anions and As species represents a substantial mechanism to release As from solid phases into GW due sorption competition for probably all metal oxyhydroxide surfaces. Also in most aquifers, Fe mineral–As interactions are likely to dominate over organic matter–As interactions (Smedley & Kinniburgh 2002). Beside competition for sorption sites OM influences the As dynamic in several other ways. NOM is known to form aqueous complexes, affect the redox potential of site surfaces and the As speciation (Wang & Mulligan 2006). The formation of aqueous complexes through humic acids might enhance As mobility and change electrostatic interactions (Wang & Mulligan 2006). Especially fulvic acids may promote As−Fe−FA complexation reactions that may enhance As mobility (Mladenov et al., 2015). On the other hand, Wang & Mulligan (2006) assumed that organic acids could also reduce As mobility by serving as a binding agent and/or by forming insoluble complexes, especially when saturated with metal cations. But up to date little is known about this processes. Fendorf et al. (2010) compiles the current state of knowledge and states that both As species "may also bind to organic material, with **arsenate and arsenite** having maximum adsorption on humic acids at pH 5.5 and 8.0, respectively (Grafe et al., 2001 & 2002). Arsenate adsorbs onto solid phase humic acids more extensively than arsenite (Thanabalsingam & Pickering 1986). Arsenic adsorption by humic substances is also enhanced by cation addition, particularly Fe, Al and Mn (Lin et al., 2004). Nevertheless, organic matter tends to be poorly correlated with total As in

comparison to Fe, Al, or P (Chen et al., 2002), suggesting that its contribution to As retention in soils and sediments is limited". Even so, important uncertainties still remain in relation to the interactions of As(III) and As(V) and in the presence of the large variety of interacting ions of natural systems (Smedley & Kinniburgh 2002). Due to the complex interplay of different competitors with the multitude of potential carrier phases, sorption competition reactions are basically location-specific and change over time and cannot be named in general. Overall, the sorption distribution coefficient of As(V) onto geological media is much larger than that of As(III), and a reduction of As(V) to As(III) will lead to GW enrichment with As. The different sorption behaviour of As(III) and As(V) strongly affects the geochemical cycling of the redox-sensitive As species in the subsurface (Hu et al., 2012). Based on most studies the order of sorption competition for both As species follows the order phosphate > OM > silicate > sulphate > bicarbonate.

4. Fe minerals in natural near-surface environments

The large range of Fe minerals occurring in various surface environments is not surprising in view of the ubiquity of the element. Iron is the fourth most abundant element in the earth's crust and makes up by mass about 5.1 %. It is the most abundant transition metal on the Earth's surface and ubiquitous in most sediments and soils (Schwertmann & Fitzpatrick 1992). **Sedimentary iron** originates from Fe(II) bound in the lattice structures of Fe-rich ferro-magnesian silicate minerals such as olivine, pyroxene, biotite and amphiboles (Heyden & Roychoudhury 2015). The most common primary Fe-minerals in sedimentary settings are Mt and Py (Schwertmann & Cornell 2000; Cornell & Schwertmann 2003). Fe is released into surface environments by weathering and oxidation of primary minerals. Mainly, by weathering of primary silicate and sulphide minerals. In the presence of O_2 and H_2O and in the usual pH range of surface environments, the released Fe(II) will be oxidized to Fe(III) and immediate hydrolysis cause the transformation into widespread secondary Fe(III) oxyhydroxides and clay minerals (Cornell & Schwertmann 2003; Schwertmann & Fitzpatrick 1992). Especially **Fe(III) oxyhydroxides** are common constituents of geologic surface materials (Murad 1996) as Fe oxyhydroxide minerals in sediments are almost ubiquitous secondary products (Stucki et al., 1988). In presence of oxygen, ferric Fe is the thermodynamically favourable oxidation state and predominantly forms highly insoluble Fe oxyhydroxides (Heyden & Roychoudhury 2015). Because the Fe mineral stability is strongly dependent on the ambient redox properties Fe oxyhydroxides often form in natural waters and sediments at oxic-anoxic boundaries (Dixit & Hering 2003) where they precipitate either as discrete crystals (including nano particles) or as coatings on other mineral phases, and due to their ubiquity, redox activity and amphoteric surface reactivity, they are known to have a strong control on the chemical properties of soils and sediment (Heyden & Roychoudhury 2015; Cornell & Schwertmann 2003). Depending on the climatic conditions, the most common soil and sediment Fe oxyhydroxides are goethite (α-FeOOH), hematite (Fe_2O_3), magnetite (Fe_3O_4), lepidocrocite (γ-FeOOH) and amorphous to poorly crystalline phases like ferrihydrite ($Fe_{10}O_{14}(OH)_2$) (Heyden & Roychoudhury 2015, Cornell & Schwertmann 2003). Which oxyhydroxides are formed depends mainly on Eh, pH and the concentration of the relevant anions (hydroxyl, carbonate, phosphate and sulphide) (Schwertmann & Fitzpatrick 1992). The redox stability of Fe(III) oxyhydroxides is rather low. They dissolve under reducing conditions whereby their stability against redox changes mainly depends on their crystallinity (Schwertmann & Cornell 2000; Cornell & Schwertmann 2003). The mineral stability and binding capacities are mainly governed by the solid mineral properties (Schwertmann & Fitzpatrick 1992; Kocar et al., 2006). This involves crystallinity as well as mineral form, size, surface area, porosity and degree and kind of isomorphous substitution. These factors control dissolution rates (Schwertmann 1991) as well as the ability to retain contaminants. Different Fe(III) minerals show a substantial variability of solid properties which depend on the conditions under which crystal growth takes place and the recent interaction with GW and are mineral-specific and may also vary within a mineral class (Cornell & Schwertmann 2003). Beside Fe(III)

oxyhydroxides sedimentary Fe is present in near surface environments in form of **Fe(II) sulphides and carbonates** as well as **Fe(II), Fe(II/III) and Fe(III) (phyllo-)silicates.** Only minor amounts are present in other phases of which phosphates are the most important ones. Almost all of these phases are products of secondary processes related to surface exposure and biological activity which create a broad range of often metastable Fe minerals.

4.1 Most relevant Fe-minerals in natural near-surface sediments

The most common **crystalline Fe phases in oxic near-surface sediments** are goethite and hematite. They are thermodynamically the most stable Fe oxyhydroxides under aerobic surface conditions and therefore the most widespread Fe oxyhydroxides in aerated surface conditions (Schwertmann & Cornell 2000). Once formed, Fe(III) oxides, due to their high thermodynamic stability, will usually persist in an aerobic environment for long periods of time (Schwertmann & Fitzpatrick 1992). Other Fe(III) phases found frequently in surface environments are ferrihydrite (Fh) and lepidocrocite (Lep). Although thermodynamically less stable locally they may be kinetically favoured (Ostwald stage rule) depending on local conditions (Steefel & Van Cappelen 1990). In addition, their transformation into more stable forms may be kinetically hindered because the dissolution of the metastable form may be slow and nucleation of the stable phase hampered by contaminating compounds in the system. Metastable Fe(III) forms may, therefore, persist for long periods of time, too (Schwertmann & Fitzpatrick 1992). Alternatively, the occurrence of the metastable phases may be bound to a redox-active zone where they appear as freshly formed precursor phases or they appear in coupled biogeochemical processes. The stable Fe(III) oxyhydroxides Gt and Hem occur regular as single Fe minerals whereas associations of various Fe oxyhydroxides such as goethite, hematite, lepidocrocite and ferrihydrite are more common. Especially the metastable forms appear in dynamic environments usually in close association with other Fe oxyhydroxides reflecting recent transformation reactions (Schwertmann & Fitzpatrick 1992).

Goethite (Gt), usually yellow-brown coloured, is considered a stable and most widespread form of Fe (III) oxyhydroxides and is ubiquitous in almost every surface environment. It is generally accepted that Gt precipitates from solution via a nucleation-crystal growth process or due transformation reactions of precursor Fe-phases (Schwertmann & Fitzpatrick 1992; Cornell & Schwertmann 2003). The specific surface area (ssa) of natural Gt ranges from 8 to 200 m^2/g and varies related to the formation process. Gt grown from Fh usually shows smaller ssa between 9 and 88 m^2/g while higher ssa of 80-150 was observed on Gt formed by oxidation of $Fe(II)_{aq}$. They are therefore good adsorbents towards trace elements like As, Al and phosphate (Cornell & Schwertmann 2003; Mamindy-Pajany et al., 2009). Also it has no internal surfaces Gt is known to be a good adsorbents towards both As species at near-neutral pH. While As(III) is mainly bound as inner sphere, bidentate As(V) is present in low loading as monodentate and at high loading as bidentate (Borggaard 1983, Gimenez et al., 2007; Manning et al., 1998; Dixit & Hering 2003; Matis et al., 1997; Mohan & Pittmann 2007; Mamindy-Pajany et al., 2009).

The red coloured **hematite** (Hem) is almost equally present in surface sediments is considered the most stable Fe(III) oxyhydroxide phase. Sedimentary Hem is usually associated with Gt and originates mainly from oxidation of 2-line Fh in aqueous media at neutral pH. Structural rearrangement and dehydration of Fh and via-solution transformation of Fh are possible pathways. Another Hem formation process in sedimentary environments is the internal reorganisation and oxidation of Mt (Schwertmann & Fitzpatrick 1992). The ssa is with 10 to 90 m^2/g significantly lower than the average Gt surface area (Cornell & Schwertmann 2003). In view of its high crystallinity without internal surfaces and low ssa Hem is regarded as a moderate As carrier phase (Borggaard 1983; Gimenez et al., 2007; Mohan & Pittmann 2007) although compared to other non-Fe mineral phases, Hem still has a high As adsorption capacity Only Mn and Al oxides have higher capacities (Mamindy-Pajany et al., 2009).

Although less frequent than Gt and Hem, **lepidocrocite** (Lep), a bright orange coloured polymorph of Gt, occurs widespread in aqueous surface environments as metastable transition phase. Lep forms as temporarily phase as a partial process during the dehydration of Fh and its transformation to Hem. In particularly in sediments with dynamic hydrogeochemical interfaces, the phase is often associated with Gt and sometimes with Fh. A association with Hem is very rare. The occurrence of Lep is usually associated with partially or temporarily oxygen deficiency. The ssa lies between 15-260 m^2/g depending on formation process. Like Gt the polymorph forms either by precipitation from solution or as transformation product whereby the oxidation of aqueous Fe(II) is the dominate process. The oxidation process forms generally low area Lep (Cornell & Schwertmann 2003). Lep is no good As carrier and mainly binds arsenate to the surface as inner sphere, bidentate (Borggaard 1983; Pederson et al., 2006).

Magnetite (Mt) is the most common mixed-valance Fe oxide in near-surface environments and the most widely spread primary Fe mineral. Sedimentary Mt can be a residual detrital phase or form secondary by precipitation of mixed Fe(II)/Fe(III) solution, oxidation of Fe(II) or interaction of Fe(II) with Fh (Cornell & Schwertmann 2003) and Mt in surface environments is often associated with microbial processes (Schwertmann & Cornell 2000; Cornell & Schwertmann 2003). Since the discovery of so-called magnetotactic bacteria, which form very fine-grained (up to 50 nm) crystals biologically formed Mt has been established as common Fe mineral component in near-surface sediments (Cornell & Schwertmann 2003). The redox stability of the mixed valence Fe-oxide is rather high compared to the other Fe oxyhydroxides mentioned so far. It is stable in oxic environments and it can overcome reducing conditions. Abiotic Mt formation is related to redox state and aqueous Fe(II) concentration. Mt formation will be favoured as the Fe(II) concentration increases (Schwertmann & Fitzpatrick 1992) and can form until reducing conditions appear (Guerin & Blakemore 1992). Authigenic Mt has commonly been identified in anaerobic sediments (Fredrickson et al., 1998) and only under strongly reducing conditions, Mt becomes unstable and dissolves. In the presence of high concentrations of H_2S, it slowly converts to Py (Smedley & Kinniburgh 2002). Another formation process is the reduction of Hem (Cornell & Schwertmann 2003). In dynamic environments with alternating redox conditions Mt formation can happen due multiple pathways. The ssa of Mt is in usually quite low compared to Fe(III) oxyhydroxides and is usually well below 100 m^2/g although there can be significant differences depending on the formation mechanism (Cornell & Schwertmann 2003). Low ssa are characteristic for primary Mt and for Mt formed by reduction of Hem while small biogenic produced Mt produced by precipitation show high ssa that can exceed the 100 m^2/g significantly. Crystalline Mt phases are assumed as bad As carrier phases with regard to both As species which can only absorb small amounts of As as surface precipitates. As(V) as well as As(III) are thought to form inner-sphere surface adsorption complex on Mt. However, the specific characterises of small bio Mt differs from the crystalline phases in this respect and offers large surface space for surface precipitates (Schwertmann & Cornell 2000; Cornell & Schwertmann 2003; Jönsson & Sherman 2008; Wang et al., 2008; Dixit & Hering 2003).

In oxygen-free environments Fe(II) carbonates and sulphides dominate the Fe mineralogy in near surface sediments. In particular, **Fe sulphides** are common Fe minerals under reducing conditions. Especially **pyrite** (Py) is widespread and can exist in near-surface sedimentary environments as detrital fragments or as secondary products. Py is frequently formed in low-temperature sedimentary environments under reducing conditions. Authigenic Py is common in many aquifer sediments and plays a very important role in the present-day biogeochemical Fe cycle (Bowell et al., 2014). Heyden & Roychoudhury 2015 described how sulphate reduction leads to the precipitation of various sulphide mineral phases under anoxic conditions and it is generally accepted that the formation of near-surface Fe sulphides is intimately associated with biological activity in anaerobic surface environments

(Schwertmann & Fitzpatrick 1992) and Py forming sulphate reducing bacteria are known to contribute to sedimentary Fe and As dynamic substantially (Phan et al., 2018). Fendorf et al. (2010) further noted that the "solubility of As(III) is often controlled by sulphide precipitates. Particularly in extremely reducing environments where sulfidogenesis occurs". Moore et al. 1988 showed already in the 1980s that As(III) concentrations in GW are often limited by Py formation. Especially in organic-rich surface environments, Fe sulphides were identified to host significant amounts As in form of biogenic framboidal Py (Postma & Jakobsen 1996) and are considered as one of the key factors for GW As immobilization under reducing conditions (Wilkin & Ford 2006; Wang et al., 2020). Arsenic substitution into early diagenetic Py is commonly proposed as a mechanism to account for removal of dissolved As from pore water in marine and fresh water sediment (Sullivan & Aller 1996; Saunders et al., 1997; Saunders et al., 2005; Wilkin & Ford 2006; Lowers et al., 2007). Lowers et al. (2007) reported that "As assimilation into forming sulphides commonly occurs as sediment is buried below the suboxic and sulfidic redox boundary. While reduced As(III) can undergo ligand displacement and be incorporated into the Py structure (Bostick & Fendorf 2003; Heyden & Roychoudhury 2015) inner sphere complex formation, apparently involving bidentate (bridging) for both As species seems to be more common (Farquhar et al., 2002). Although usually less frequent than other As hosting phases the usually strong influence of Py on the As dynamic is mainly related to its ability to reach As concentrations. Py is known to be the best natural As carrier and As concentrations of several 1000 mg/kg As are quiet common and due to the high hosting capacity Py may control the As dynamic to a wide extent in reduced environments (Das et al., 1996; Acharyya et al., 1999; Oremland & Stolz 2003). As for all redox-sensitive Fe phases, the redox stability of Py is low and in aerated surface environments oxidizing Fe sulphides can also act as As source. Especially within partly oxidized heterogenic sediments the oxidation of arsenical Py and other As-bearing sulphides can represent an important As pathway into GW (Das et al., 1996; Acharyya et al., 1999; Oremland & Stolz 2003). Other Fe sulphides like marcasite, mackinawite and its analogues pyrrhotin and troilit or greigite are likely to co-exist as precursor minerals in dynamic redox controlled environments. This metastable monosulphides are also able to host significant amounts of As and therefore influence the Fe-As GW cycle (Schwertmann & Fitzpatrick 1992; Bostick & Fendorf 2003).

Further **Fe carbonates** are common Fe minerals under anoxic conditions. **Siderite** (Si), which often appears as whitish, poorly crystalline deposits is stable under reducing conditions is the most common Fe carbonate in near surface sedimentary systems. Vuillemin et al. 2019 states that in present day sediments, "early diagenetic growth of Si crystals is most likely coupled to degradation of sedimentary organic carbon and the accumulation of dissolved inorganic carbon in pore waters. It is suggested that Si formation proceeds through syntaxial growth on pre-existing Si crystals, or possibly through ageing of precursor carbonate green rust. Crystal growth ultimately leads to spar-sized (> 50 µm) mosaic single Si crystals that form twins, bundles, and spheroidal aggregates". The redox stability of Si is low and Si is likely to be transformed in Fe(III) oxyhydroxides in oxidising environments (Schwertmann & Fitzpatrick 1992). It is widely accepted that Si is able to limit the As concentrations in GW (Smedley & Kinniburgh 2002) and is established as good As carrier (Guo et al., 2007a) whereby As(II) is sorbed as outer-sphere and As(V) as inner-sphere surface adsorption complex (Jönsson & Sherman 2008). Also common in sediments is **ankerite** (Ank) an Fe-Mn-carbonate with largely similar properties with regard to the As interaction. Due to the increased redox sensitivity of Mn compared to Fe the stability field of Ank is slightly shifted towards reducing conditions.

A special role with regard to dynamics in near surface sedimentary aquifers with active redox dynamic and strong Fe turnover play **amorphous and poorly to microcrystalline Fe (oxyhydroxide) phases.** In addition to the distinct crystalline minerals mentioned so far Fe phases in natural surface environments are frequently present as less crystalline phases (Schwertmann & Fitzpatrick 1992; Schwertmann &

Cornell 2000). In dynamic natural sediments, both crystalline and amorphous to poorly crystalline Fe phases typically coexist with crystalline solids also crystalline solids are typically 2 to 10 times more abundant (based on Fe content) than less crystalline or amorphous phases (Dixit & Hering 2003). In natural surface environments, amorphous and poorly to microcrystalline Fe phases are ubiquitous in form of precipitations. Fe oxyhydroxides often occur in sediments as alteration products in form of partial coatings around detrital mineral phases like Qtz and act as important sinks for many trace elements (Eiche at al., 2010; Guo et al., 2007a). Typical representatives of amorphous and poorly to microcrystalline Fe in sedimentary freshwater reservoirs are **hydrous Fe oxides (HFO)**. Especially along natural redox boundaries with strong Fe_{aq} gradients Fe oxyhydroxides occur frequently as complex mixture of sub-µm phases. Natural HFO are usually composed of a mixture of amorphous to poorly crystalline phases like Fh and more crystalline phases, such as Lep, Gt, and Hem (Fortin et al., 1993; Perret et al., 2000). In the aqueous milieu HFO occur as small granular particles in the range of 1 to 100 nm in diameter whereas especially biotic HFO minerals tend to have very small diameters in the range of 2 to 10 nm and are often found in close association with bacterial cells (Fortin et al., 1993; Mavrocordatos & Fortin 2002). Due to their abundance, large specific surface, high porosity and iso-electric point at neutral pH, HFO play an important role in the transport of (micro) pollutants in the environment and are very effective for removing both As(III) and As(V) from aqueous solution (Fortin et al., 1993; An et al., 2005). The large adsorption capacity of HFO and sorption affinity for both As species makes them very strong As sorbents (Smedley & Kinniburgh 2002; Dixit & Hering 2003; Garelick et al., 2008). Arsenate adsorption is particularly strong even at very low GW concentrations (Goldberg, 1986; Manning & Goldberg 1996) and the sorption affinity of As(V) towards HFO is significantly higher compared to crystalline adsorbents like Gt (Hingston et al., 1971). The poorly crystalline Fe oxyhydroxides have a chemical reactivity that is far out of proportion to their abundance (Borch et al., 2010). Due to their high level of activity, the phases are often referred to as 'reactive' iron and it is assumed that around 20 % of the Fe in dynamic freshwater sediments is present as 'reactive' Fe while about 50 % is present in the form of Fe oxyhydroxides (Smedley & Kinniburgh 2002). Along active redox boarders, the proportion of 'reactive' iron can presumably be higher. By definition poorly crystalline phases have very small nano-sized (5-100 nm in size) crystals, do not clearly exhibit the typical morphology of well-crystalline forms, are rich in defects and contain impurities. Due their small size the phases exhibit a large and reactive surface area and they carry functional groups at their surface which can adsorb a large range of ions and molecules such as As and organic acids. Despite their small particle size they have very low solubility (Schwertmann & Fitzpatrick 1992; Schwertmann & Cornell 2000). Their formation is typical of weathering surface environments. During sediment transport sedimentary Fe turns progressively into Fe oxyhydroxides and precipitates on the surface of primary particles such as silt and sand in form of nanoparticles, colloids and coatings (Raiswell et al., 2011; Hasselhöv & Kammer 2008; Eiche et al,. 2010). They are particularly common in biogeochemical dynamic areas such as redox transition zones, as strong hydrogeochemical gradients and high microbial activity promote the dissolution and precipitation of Fe phases. Due the broad variety of processes involved at redox boundaries natural Fe-precipitation often consist of a multitude of different phases with different size and crystallinity, which often merge directly into one another. Especially in dynamic superficial aquifer systems, the phases are subject to constant alterations that change their solid properties (crystallinity, stability, reactivity, surface area and porosity) and cause continuous phase transformation and formation of new mineral phases. In contrast to amorphous to poorly crystalline phases like ferrihydrite **microcrystalline phases** show a characteristic crystal structure and can be assigned to a specific phase such as Gt, Hem or Mt. Due to their small size they are hard to identify by classical mineralogical techniques like XRD or microscopy. Especially since they often form multi-phase complexes, miss the typical morphology of well-crystalline minerals, and are rich in defects and impurities. Fe-precipitation complexes share many features of poorly crystalline phases and are very

reactive. Although the ubiquitous presence and importance of non-crystalline Fe phases in the pollutant cycle is known for decades, their high reactivity and small size make analytical investigations difficult. Due to poor crystallinity, their identification is often difficult and needs a combination of physical, chemical and mineralogical techniques. Particularly in concentrations < 10 % is their identification rather difficult (Schwertmann & Fitzpatrick 1992). Consequently, the actual properties with regard to pollutant dynamic and redox stability of the often heterogeneously structured natural precipitates are hard to assess in individual cases. Therefore, it is difficult to quantify their role in the overall As cycle. The role of poorly to microcrystalline oxyhydroxide phases in the As cycle has so far only been viewed marginally, although some exciting works indicate the importance of the phases (Voegelin et al., 2019). The association of As with amorphous to weakly crystalline phases has long been known through leaching experiments and pronounced formation of poorly and microcrystalline Fe phases along redox interfaces and high As uptake affinity and capacity underline their importance in natural redox environments. Although only marginally assessed their presence offers an excellent retention and release mechanism to explaining strongly variable As and Fe GW concentrations on small spatial scales. Calculated sorption and retardation factors indicated already 20 years ago that highly variable sorption capacities in surface sediments largely depend on the content of weakly crystalline phases if hydrochemical factors such as As speciation, As concentration, pH and concentration of competitors such as phosphate are excluded (British Geological Survey 2001). For the As dynamic in near surface sedimentary aquifers amorphous and poorly to microcrystalline Fe precipitates are of great importance as their high surface reactivity and pronounced presence at biogeochemical interfaces force the interaction with mobile As. Eiche at al. (2010) and Guo et al. (2007a) showed that Fe alteration products especially in form of partial coatings act as important As sinks and the affinity of As oxyanions for secondary Fe coatings with heterogeneous crystallinity has been demonstrated multiple times (Charlet & Polya 2006; Charlet et al., 2011). The sorption affinity of most likely weakly crystalline Fe- precipitates towards As is thought to be particular strong in GW aquifers (O'Day 2006; Berg et al., 2007; Eiche 2010). For amorphous Fe hydroxides it is known that it has the highest adsorption capacities towards both arsenate and arsenite of all natural Fe phases (Lenoble et al., 2002; Smedley & Kinniburgh 2002). On the other hand diffusion limitations within µm-sized Fe particles decrease their adsorption rate and available capacity (Gupta wt al 2012).

However, **amorphous and poorly to microcrystalline Fe phases** are essential with regard to the element dynamic in redox influenced natural systems. They react very sensitive to hydrogeochemical changes and are also preferred by microorganisms over more crystalline forms. Most natural amorphous to poorly crystalline phases such as hydrous ferric oxide (HFO) are unstable and tend to transform with time toward more crystalline forms, either by ageing or possibly by dissolution and re-crystallization (Cornell and Giovanoli 1988). It is assumed that ageing reactions and early diagenesis in near-surface sediments cause "stability and speciation changes" and transform the amorphous and poorly to microcrystalline Fe phases (Heyden & Roychoudhury 2015). While the initially formed poorly crystalline solids have high specific surface areas, over time, the amorphous and weakly crystalline phases are transformed into less reactive more crystalline minerals. The decrease in specific surface area and hence site density can increase the mobility of As. The metastable character and sensivity to changes in the hydrobiogeochemical environment make the good absorbents also to susceptible player in the As dynamic (Dixit & Hering 2003). The most common poorly crystalline Fe phase and the main diagenetic oxidation product in near-surface sediments is thought to be **ferrihydrite** (Fh). Fh is typical in surface environments especially in alternating redox conditions with an active Fe turnover (Schwertmann & Cornell 2000 Schwertmann & Fitzpatrick 1992) which are often found in young sediments with high amounts of organic matter. In this environments Fh can be an important component (Schwertmann 1991). Often termed as hydrous ferric oxide the abundant metastable Fe hydroxide nanoparticle is thought to play an important role in sedimentary trace-element cycling

(Jambor and Dutrizac 1998; Benner et al., 2002; Hansel et al., 2003). The short-range order material (Benner et al., 2002; Hansel et al., 2003) has usually very small, poorly ordered crystals about 2-5 nm in size and a large surface area up to 700 m^2/g. Small size, high porosity and characteristic surface properties make Fh highly reactive towards many important GW components such as As or organics (Schwertmann & Fitzpatrick 1992, Cornell & Schwertmann 2003 Jambor and Dutrizac 1998). In contrast to the crystalline Fe(III) oxyhydroxide phases, Fh has absorption available internal surfaces which drastically increase the receptivity for As (Mohan & Pittmann 2007). Their surface reactivity also differs. Compared to bulk Fe atoms, which are bonded to bridging oxo (O) and hydroxo (OH) ligands, surface Fe atoms of Fh are also octahedrally coordinated to HzO ligands (Manceau & Gates 1997) and is therefore considered as particular effective sorbent. Fh "is known to have the highest sorption capacity for As" of all common natural Fe phases (Heyden & Roychoudhury 2015) although As in mainly surface bound and not strongly fixed (Pederson et al., 2006; Mohan & Pittman 2007). Therefore, As mobilization from Fh is most likely driven by reductive dissolution and transformation of the phase instead of desorption (Zhang et al., 2017). Fh is most likely formed by rapid oxidation and hydrolysis of Fe(II) and usually precipitates directly from solution. Significant occurrences are normally linked to Fe-rich fluids and abrupt redox changes and are often associated with microbial processes (Schwertmann & Fitzpatrick 1992; Cornell & Schwertmann 2003). The poorly crystalline character and specific adsorption properties are closely linked to the formation process with high rate of oxidation and the presence of numerous inhibitors in complex natural systems (Schwertmann & Cornell 2000). The higher the rate of oxidation and/or the higher the concentration of nuclei and/or crystallisation inhibitors in the system, the more likely Fh will be favoured over more crystalline minerals such as Gt (Schwertmann & Fitzpatrick 1992). Fh is the least stable of the Fe(III) oxyhydroxides in surface environments (Schwertmann & Fitzpatrick 1992). In nature, Fh will slowly transform to crystalline Gt, Hem or Lep (Schwertmann & Cornell 2000; Zhang et al., 2017) and like other poorly crystalline Fe phases Fh is considered to be a metastable phase. It is usually assumed that the these phases are young and recently formed (Schwertmann & Cornell 2000). Therefore, Fh is often associated with Gt and Lep but not with Hem (Schwertmann & Fitzpatrick 1992). Other less common poorly crystalline Fe mineral phases are schwertmannite and green rust which primarily play a role as precursor minerals in complex natural systems.

Beside as distinct Fe minerals sedimentary Fe is present as **(phyllo-) silicate minerals** in distinct amounts. In particular, (**Fe-rich) clay minerals** can act as important Fe and As sink and source minerals in near surface sediments. Clays can adsorb As(III) and As(V) (Manning & Goldberg 1997; Garelick et al., 2008) and both As species have a great affinity for clays which is only a little inferior to Fe phases (Manning & Goldberg 1997). The ability of various clays to adsorb As is linked the oxide-like character of their edges (Smedley & Kinniburgh 2002) and especially clays with substantial amounts of Fe (up to several wt% Fe) show a high As hosting capacity (Botto et al., 2013). Ubiquity and large surface areas of clay minerals promote the interaction with dissolved oxyanions like As also their role in sediments in terms of As binding is unclear at present. Typical Fe-rich PS in near-surface sedimentary environments are chamosite, chlorite, phengite and greenalite and nontronite, a Fe(III)-rich member of the smectite group. Depending on the individual mineral Fe can be present as Fe(II), Fe(III) or in mixed valance oxidation state. Although clays in which Fe is a main component are in general rare (Schwertmann & Fitzpatrick 1992) their occurrence at redox boundaries with strong Fe GW gradients was observed frequently. Close associations between Fe oxyhydroxides and Fe-rich PS are common in near-surface sediments in features such as concretions, pipe stems, ferricretes, and lateritic crusts. **Cementations** occur where Fe oxyhydroxide crystals grow in pores, gradually filling up the pore space and developing large areas of contact between the Fe oxyhydroxide crystals and other matrix particles. Association of Fe and clay minerals seems to be a crucial part of this process (Stucki et al., 1988).

4.2 Fe mineral mediated As dynamic

Due its high abundance, Fe plays a particularly important role in environmental biogeochemistry (Borch et al., 2010) and sedimentary pollutant cycle (Sherman & Randall 2003) and coupled in-situ mobilization or retention of As and Fe at the sediment-GW interface largely control the fate of the contaminant (Cornell & Schwertmann 2003). Especially Fe(III) oxyhydroxides "are well known for their propensity for adsorbing various inorganic and organic pollutants" (Heyden & Roychoudhury 2015) and the importance of Fe(III)-oxyhydroxides in controlling the concentration of As in natural waters has been appreciated for a long time (Livesey & Huang 1981; Matisoff et al., 1982; Smedley & Kinniburgh 2002). The ubiquitous mineral phases are the most important As adsorbents in most aquifers due to their great abundance and the strong binding affinity towards As (Smedley & Kinniburgh 2002) and are usually the dominant As carrier in oxic sedimentary surface conditions (Fendorf et al., 2010). Iron oxyhydroxides are well known to accumulate As up to concentrations of several percent of weight (Bowell et al., 2014) and the mobility of As in aerated natural waters was shown to depend largely on the availability of Fe oxyhydroxides as adsorption phases (Lear et al., 2007; Oremland & Stolz 2005 Cornell & Schwertmann 2003). As liberation from Fe oxyhydroxides is coupled to desorption and dissolution processes (Smedley & Kinniburgh 2002; Zhang et al., 2017). As mobilization from Fe(III) oxyhydroxides at redox interfaces is most likely to occur in two steps. The release of sorbed As, is followed immediately by the dissolution of the Fe phases Both processes can hardly be separated because dissolution and desorption occurred almost simultaneously (Masscheleyn et al., 1991; Guo et al., 1998). With regard to the overall As dynamic Fe(II) sulphides are mainly considered as important As sources in the sedimentary environments of SSEA. The release of As from Fe sulphides like Py is mainly coupled to the oxidation of arsenical Py and other As-bearing sulphides and will be mentioned in the next chapter. Meanwhile Fe(II) carbonates were hardly described as significant As source minerals and are mainly related to recent biogeochemical processes.

As mentioned in the previous chapter the As and Fe dynamics in sedimentary environments are essentially driven by reactions at the **solid-liquid interface.** To understand and predict the element dynamic in sedimentary aquifers it is crucial to understand the solid-liquid phase interactions of the mineral inventory with surrounding GW. Aqueous-solid-phase-interactions between aquifer sediments and the surrounding GW are the key process to predict As concentration and mobility in aquifer systems (Smedley & Kinniburgh 2002). With regard to As behaviour in near-surface sedimentary environments of SSEA the solid-liquid phase interactions are mostly controlled by (transformation of) various Fe minerals, the by far most important As hosting phases in near surface environments (Smedley & Kinniburgh 2002; Fendorf et al., 2010). Especially in young sedimentary deposits Fe-phases widely control the As mobility (Smedley & Kinniburgh 2002; O'Day 2006) and their importance only decreases in low-iron settings (O'Day 2006). The broad variety of (secondary) Fe(II) and Fe(III) phases in natural near-surface sediments is related to the geochemical heterogeneity of surface sediments and the large number of biogeochemical processes in which Fe is involved. Especially complex fluviatile sediments are often characterized by multiple biogeochemical interfaces that act as hotspot for (Fe) mineral transformation (Stucki et al., 1988). In particular redox interfaces have a major impact on Fe mineralogy and determine the exchange processes between Fe minerals, associated elements and the GW to a wide extent as redox-sensivity is a specific characteristic of most Fe-phases. Type as well as quantity and properties of As-hosting Fe minerals can change fundamentally across oxic-anoxic boundaries within short spatial and temporal scales. Redox induced alteration of Fe minerals involves dissolution, transformation and formation of new Fe minerals. The geochemical behaviour of Fe in the sedimentary environment is largely determined by its considerably higher mobility in the divalent than in the trivalent state. While under oxic conditions the solubility of Fe is very low and Fe precipitates as Fe(III) minerals the GW-mobile Fe(II) is dominant under anoxic conditions. Changes in the oxidation state result in inevitably mobilization or precipitation of Fe minerals (Stucki et al., 1988; Cornell &

Schwertmann 2003; Schwertmann & Fitzpatrick 1992). Therefore, the oxygen availability widely controls mobility and predominant mineralogy of Fe and changes in Fe redox chemistry are particularly important since they directly affect the mobility of associated contaminates like As by releasing or sequestering the element (Smedley & Kinniburgh 2002). Redox transformations of Fe mineral phases, in particular Fe oxyhydroxides, Fe-bearing clay minerals, and Fe sulphides largely control the dynamic of As and other redox sensitive major and trace elements (Borch et al., 2010). As Fe minerals control speciation, mobility, bioavailability and toxicity of As, sequestration and liberation of both As species is closely linked to transformation redox-sensitive Fe phases (Cornell & Schwertmann 2003; Smedley & Kinniburgh 2002; Borch et al., 2010). The close coupling between the Fe and As redox cycles extends to both the solid and the liquid phase. Frequently, the element which correlates best with As in delta and floodplain sediments is Fe (Smedley & Kinniburgh 2002) and several experimental studies demonstrated the close relationship between Fe mineralogy and As sequestration (Giménez et al., 2007; Sun et al., 2016; Voegelin et al., 2019) and also in natural GW environments a strong correlation between ferrous Fe and As was routinely documented (Nickson et al., 2000; McArthur et al., 2001) indicating that both mobilization and retention mechanisms of As and Fe are closely linked. Therefore, alteration, dissolution and formation of new Fe minerals are of great importance since the pollutant dynamics are largely determined by the transformation of the Fe mineral inventory (Stucki et al., 1988). With regard to the As dynamic Fe mineral transformation processes control the behaviour of the oxyanion at many locations almost completely (Smedley & Kinniburgh 2002). Different liberation and sequestering mechanisms, different affinity toward As and different storage capacity for As of various Fe carrier phases control the release and retention of the toxic element. Dissolution, alteration and new formation of ferruginous As carrier phases cause variable exchange reactions that influence the As dynamic fundamentally.

The **(trans-) formation, dissolution and (re-)precipitation** of the various Fe oxyhydroxides in the environment depends predominately on hydrobiogeochemical factors such as dissolved Fe(II) concentration, pH, Eh, temperature, GW ions and biological activity (Schwertmann & Cornell 2000; Pedersen et al., 2006). The formation of Fe(III) oxyhydroxides involves two basic mechanisms. They either form by direct precipitation from Fe(II) or Fe(III) in solution or they form as the result of the transformation of a precursor mineral. A characteristic of the Fe oxyhydroxide system is the variety of possible interconversions between the different Fe(III) phases. Dehydration, dehydroxylation and electron turnover (oxidation/reduction) can lead to the formation of transition and mixing phases and promote the phases merge into one another. Especially alternating oxidation and reduction conditions change the Fe oxyhydroxides frequently. The conversion can involve a topotactic transformation (internal atomic rearrangements) or more common in the context of strong redox alterations are reconstructive transformation what involves dissolution (complete breakdown of initial phases) and reprecipitation of new phase precipitates from solution (Cornell & Schwertmann 2003). Secondary Fe mineral formations in redox-controlled systems encompass a high degree of diversity with multiple processes and phases that can form. Also the stability of the secondary phases and ability to host As can vary significantly. Further the Fe mineralogy along dynamic natural redox boundaries is subject to constant changes. Formation of new minerals and transformation processes constantly affect As storage affinity and capacity and the way As is hosted in or on the mineral phase and either enhance or lower their ability to retain As. Secondary Fe oxyhydroxides, for example, go through ageing processes, which generally increases crystallinity but reduces the ssa what consequently results in release of As to the GW (Dixit & Hering 2003; Eiche 2009). This applies to crystalline but especially to amorphous to weakly crystalline phases. Transformation of precursor phases like Fh into more stable minerals like Gt or Mt, however, does not always lead to a release of As, because it can also get incorporated into the newly evolving mineral structure becoming even better fixed (Pedersen et al., 2006; Eiche 2009). However, there is always the danger of releasing As during transformation

reactions. For example phases with particularly high initial As concentrations or during particularly rapid transformation processes As is likely liberated to GW. As the Fe mineral evolution along natural redox boundaries depends on a broad range of factors, in complex non-linear, often oscillating aquifer sediments the future development is usually hard to predict. **Co-precipitation** of dissolved As and Fe from solution represents an important As retention mechanisms at redox boundaries where reconstructive transformation of potential carrier phases in common. If GW holds high concentrations of dissolved Fe(II), As(III) and As(V) can rapidly coprecipitate with Fe oxyhydroxides (Berg et al., 2006). During the formation process As can become incorporated or adsorbed in/on the new mineral phases. In contrast to surface adsorption the incorporation of As into crystal lattice during mineral formation leads to a particularly secure fixation of As. Compared to adsorption this fixation process is more stable as the liberation of the incorporated element requires the dissolution of the hosting phase. The incorporation is a typical phenomenon of redox interfaces with high Fe turnover and represents an important As retention mechanisms coupled to the formation of new mineral phases. Both As species can precipitate out of solution and become incorporated or adsorbed on or into newly formed minerals (Smedley & Kinniburgh 2002; Mandal & Suzuki 2002; Drahota & Filippi 2009). The precipitation of arsenate is likely coupled to the precipitation of ferric Fe under low to neutral pH conditions. Arsenate is also known to replace sulphate or phosphate in minerals, due to the similar stereochemistry and charge and become therefore part of the crystal structure (Fendorf et al., 2010; Smedley & Kinniburgh 2002). Fendorf et al. (2010) also highlighted that "various heavy metals (Mn, Cd, Pb) and alkali earth metals (Ca, Mg, Ba) have the capacity to precipitate with arsenate, albeit that these phases tend to be relatively soluble and thus have a limited impact on dissolved concentrations of As, particularly in anaerobic environments (Rochette et al., 1998)". Arsenite precipitates mainly with sulphides, thus decreasing soluble arsenite concentration in very reducing environments (Moore et al., 1988; Oremland et al., 2002). Furthermore, Fendorf et al. (2010) emphasised that "adsorption of As(III) onto metal sulphides is often followed by incorporation of As into mineral structures (Bostick & Fendorf 2003)". Further As becomes incorporated in the mineral structure when oxyhydroxides form as the oxidation products of primary phases, like As-rich Fe sulphide minerals (O'Day 2006). Another As retention mechanism in sediment systems with high As concentrations, is the formation of various "discreet coprecipitated mineral phases ($FeAsO_4^-$, H_2O, $FeAsO_4.2H_2O$ and $Fe_3(AsO_4)_2$). Many of which are more stable and less soluble than the complexes that form when As is merely adsorbed to Fe oxyhydroxide surfaces" (Heyden & Roychoudhury 2015). The As mobility in natural sedimentary environments is primarily controlled by **sorption** onto Fe oxyhydroxide surfaces under oxic conditions and various Fe(II)-phases under reducing conditions (Benner & Fendorf 2010; Smedley & Kinniburgh 2002). The adsorption processes strongly depend from the solid mineral properties that largely determine surface exchange reactions. Adsorption processes on Fe oxyhydroxide surfaces with gaseous and soluble species, the surfaces of other oxides and bacterial cells is governed by structural and functional groups (sites) which interact with the various binding partners. The number of available sites per unit mass of oxyhydroxide depends upon the nature of the oxide and its specific surface area (Cornell & Schwertmann 2003). In addition, specific surface area (ssa) and porosity are crucial factors for determining the activity of Fe oxide catalysts (Cornell & Schwertmann 2003). The ssa influences the reactivity of the Fe oxyhydroxide. Particularly its dissolution and dehydroxylation behaviour, phase transformations, thermodynamic stability and interaction with sorbents. The ssa of Fe minerals significantly controls the sorption of As (Dixit & Hering 2003). Within surface sediments high rates of growth at low temperatures lead frequently to small, poorly ordered crystals with high surface are, porosity and yet high reactivity towards contaminates and other GW constituents (Cornell & Schwertmann 2003). Along dynamic hydrobiogeochemical interfaces, the adsorption kinetics of Fe oxyhydroxides have therefore to be assessed as particularly high, but are subject to constant changes. In addition to rapid sorption processes on the mineral surface, which essentially depend on the crystal

size and surface area, diffusion into and out of pores is often considered responsible for slow adsorption and desorption processes related to porosity or "internal" surface area of the sample (Cornell & Schwertmann 2003). Sorption processes with regard to pollutant interactions of Fe oxyhydroxides are also influenced by cation substitution (Cornell & Schwertmann 2003). In particular Al substitution for Fe(III) in the various oxyhydroxide mineral structures has been shown to decrease As adsorption (Masue et al., 2007; Cornell & Schwertmann 2003). Especially the adsorption of As(V) decreased due Al incorporation (Heyden & Roychoudhury 2015). In contrast low levels of Al incorporation enhanced the adsorption of As (Tufo et al., 2016). However, high binding affinities and capacities of Fe oxyhydroxides towards As are the reason for the widespread use of natural and synthetic Fe products in water treatment for the removal of As and other pollutants (Smedley & Kinniburgh 2002). Due to their wide range of commercial uses Fe oxyhydroxides have been well researched. In particular, their ability to absorb and fix aqueous contaminants is well known. A wide range of studies measured adsorption isotherms for natural and synthetic oxyhydroxide minerals and established sorption processes at the molecular scale (Smedley & Kinniburgh 2002). Also the effect of potential competitive sorption of inorganic anions on Fe oxyhydroxides has been analysed compressively (Cornell & Schwertmann 2003).

In summary, ad- and desorption processes are the most important As mobilization and retention mechanisms under redox cycling and depend on respective available binding sites and adsorption partners and the predominate As species (Smedley & Kinniburgh 2002; Dixit & Hering 2003). Iron oxyhydroxides retain both As(V) and As(III) and thus often control the dissolved GW concentration of both As species (Smedley & Kinniburgh 2002). Especially the crystallinity, specific surface area and the amount of substituted Al affect the ability of Fe oxyhydroxides to adsorb or integrate contaminates like As (Cornell & Schwertmann 2003). Further the reactivity, structure and chemistry of the hydroxyl groups on the mineral surfaces has a huge impact on adsorption processes (Waychunas et al., 2005; Heyden & Roychoudhury 2015). The most important external factors (related to GW conditions) for the adsorption of contaminants on Fe oxyhydroxides are governed by the ambient Eh, pH conditions and hydrochemical GW composition and present (bio)geochemical processes (Waychunas et al., 2005; Cornell & Schwertmann 2003). The stability of the adsorption interactions can vary significantly and depends largely on the exchange reactions. Contaminant adsorption to Fe mineral surfaces can occur through inner-sphere and outer-sphere complexation reactions, ligand exchange reactions and through the formation of ternary complexes (Waychunas et al., 2005; Manning & Goldberg 1997; Heyden & Roychoudhury 2015). As and other trace metals are not as strongly adsorbed to Fe oxyhydroxide mineral surfaces and the stability of these various adsorption complexes is often more strongly dependent on GW parameters other than the Fe mineralogy and concentration (Atkinson et al., 2007; Heyden & Roychoudhury 2015). The interaction of As with Fe mineral inventory is further dependent on the predominate As species that has a strong influence especially on adsorption processes. Both, As(III) and As(V), have a strong, pH dependent sorption affinity towards Fe oxyhydroxide minerals and form strong bidentate complexes via ligand exchange (Cornell & Schwertmann 2003; Dixit & Hering 2003; Müller et al., 2010; Ona-Nguema et al., 2005; O'Day 2006). Near pH 7, arsenite is bound less strongly than arsenate in the major range of phosphate concentrations and reaches its maximum adsorption around pH 8–9 for most Fe oxyhydroxides. In consequence, arsenite is more mobile than arsenate and at neutral pH range typical for most natural waters (Stachowicz et al., 2008). Arsenite tends to adsorb less strongly than arsenate often causing arsenite to be present at higher concentrations (Nordstrom 2002).In contrast to As(V) the As(III) adsorption is full reversibility (Hoa et al., 2014). The adsorption maximum for AsV on Fe oxyhydroxides lies around pH 4, whereas for AsIII the maximum is found at approximately pH 7-8.5 (Fitz & Wenzel 2002; Mahimairaja et al., 2005; Masscheleyn et al., 1991). Although both forms show a strong geochemical association with Fe, the oxidised form As(V) is more strongly bound to Fe oxyhydroxide

surfaces than As(III) (Heyden & Roychoudhury 2015). Because of arsenate's strong retention, As tends to impose a limited impact on environmental quality in aerobic environments except at very high pH (Fendorf et al., 2010). This is achieved through the formation of bidentate inner-sphere bonding coordination of As(V) at the Fe(III) mineral surface at near-neutral pH (Sherman & Randall 2003; Jain et al., 1999; Heyden & Roychoudhury 2015). Although monodentate bonding has also been reported, typically when the pH is above eight (Jain et al., 1999; Heyden & Roychoudhury 2015). Under fully oxidized conditions, it is established that As(V) binds strongly to Fe(III) oxyhydroxide minerals as an inner-sphere complex (O'Day 2006). The interaction kinetics of the two As species is not known for all Fe phases. Since the mineral-specific, exchange reactions are in turn dependent on a large number of hydrochemical factors and can therefore change depending on the location or over time. "In contrast to arsenate, arsenite exhibits a limited binding to most minerals" (Fendorf et al., 2010) and is much more mobile in natural environments. "The adsorption maxima of arsenite is also with Fe(III) oxyhydroxides" (Fendorf et al., 2010) and in fact, "arsenite has a greater adsorption maximum on ferric oxyhydroxides and Mt than arsenate at all but acidic conditions" (Fendorf et al., 2010). Similar to arsenate, arsenite, in part, also forms a bidentate, binuclear complex on all Fe(III) oxyhydroxides (Manning et al., 1998; Ona-Nguema et al., 2005). Fendorf et al. (2010) further explicates, that on Fh and Hem, As(III) is also "present in bidentate, mononuclear and, to a small degree, monodentate coordination on the mineral surface (Ona-Nguema et al., 2005)". Despite the wide range of binding mechanisms, inner-sphere complexes appear to be most important for arsenite retention (Ona-Nguema et al., 2005; Dixit & Hering 2003). The "combination with outer-sphere and H-bonded moieties" (Fendorf et al., 2010) enable various binding mechanisms. "However, surface complexes of arsenite, although extensive, are far more fragile than for its oxidized counterpart, arsenate (Kocar et al., 2006; Tufano et al., 2008)" states Fendorf et al. (2010). Fendorf et al. (2010) concludes that "as a consequence, an appreciable fraction of arsenite appears to reside in weakly adsorbed complexes that rapidly desorb in response to decreases in aqueous concentrations. The observation that arsenite forms more labile complexes on ferric oxyhydroxides challenges the presumption that Fe reduction is the primary factor liberating As to the aqueous phase. Arsenic reduction, in fact, may have a more pronounced role in destabilizing As and allowing its transport within soils. Although Fe reduction has been suggested as a means for As desorption, and in fact would lead to the depletion of a prominent sorbent, As reduction may be more influential".

5. Geogenic Arsenic in Asia: sources, transport & release

Searching the origin of the widespread As contamination in SSEA is an ongoing process for more than three decades now. With regard to the initial As source a look at the areas affected by As GW contamination in SSEA revealed significant similarities. Almost all affected areas are located in two major types of depositional environments. The delta and floodplain deposits of the main Asian rivers draining the Himalayas and connected mountain ranges (Smith et al., 2000; Harvey et al., 2002; Berg et al., 2007; Fendorf et al., 2010b; Hug et al., 2020; van Geen et al., 2011; McArthur et al., 2001; Zhang et al., 2017) and inland basins like the Hetao basin (Guo et al., 2012; Zhang et al., 2018). Both sedimentary environments share the same source area and result from the terrestrial deposition of these sediments (Saunders et al., 2005; Wang et al., 2018). The depositional areas were gradually filled with eroded sediments sourced from the Himalayas and hydrogeological analogous as a result of the uplifting mountain range since the Miocene (Saunders et al., 2005; Wang et al., 2018). Accordingly it is reasonable to assume that the As-bearing sediments deposited along the main Asian river systems (Indus, Ganges- Brahmaputra-Meghna, Mekong and Red River) and the inland basins have their origin in As-hosting primary mineral phases in the Himalaya Mountains and connected mountain ranges (Fig. 7)(Benner & Fendorf 2010). So weathering of As-loaded primary rocks, minerals and ores appeared to be the major As source in SSEA (Bowell et al., 2014). Especially outbreaks of As-rich bedrocks coupled

to the uplifting processes of the Himalayas were believed to be mainly responsible for the widespread As contamination (Acharyya et al., 1999; Benner & Fendorf 2010). But up to date it was not possible to identify a specific As source across the postulated source region that could explain As contamination in all affected areas.

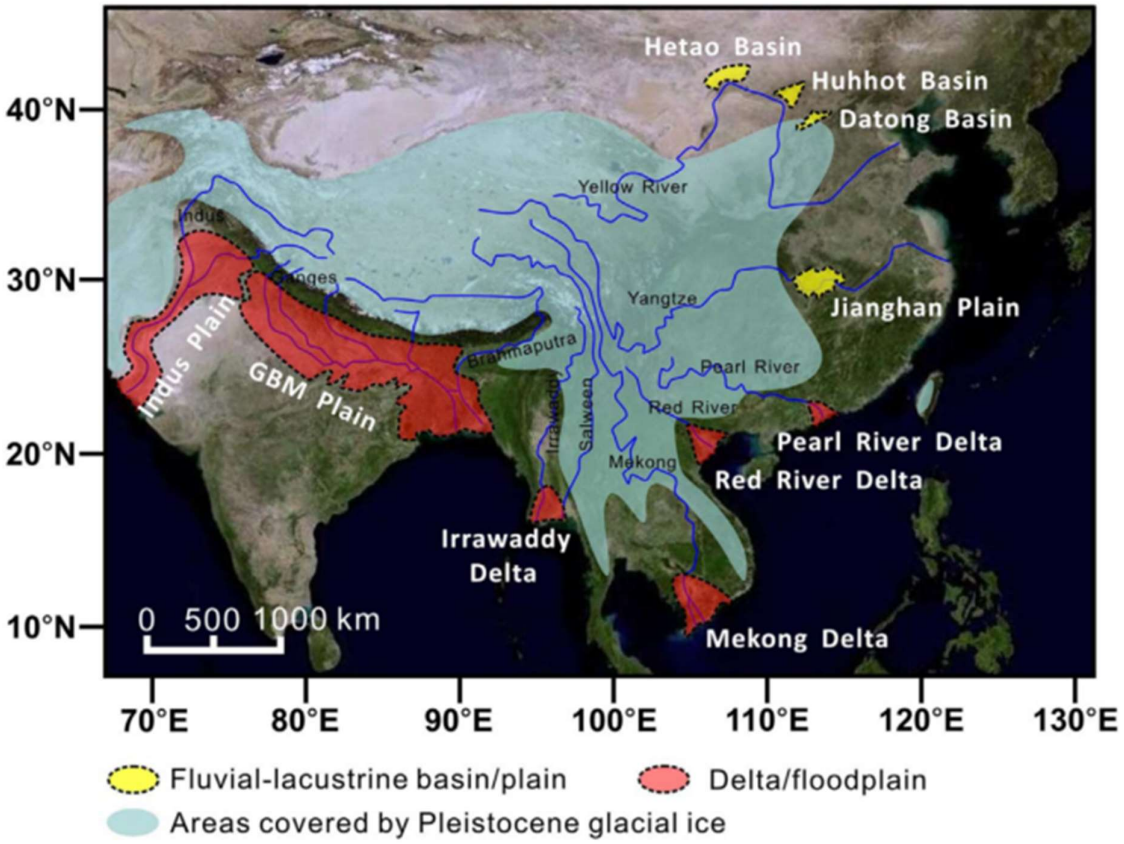

Figure 7: Major Asian river systems and As-contaminated basins, plains, floodplains and deltas originating from the Himalayan Mountains (Wang et al., 2017)

Metamorphic rocks and magmatic intrusions form a complex geological setting all across the Himalayas and include As-bearing primary phases like apatite and pyrite. They form the only known, widespread As-containing geological structure and are therefore viewed as an important source material. However, their presence is not sufficient to explain the high As-contamination observed in the secondary sedimentary environments of SSEA (Mailloux et al., 2009). Rather, it is assumed that the high As exposure results from a combination of different As sources. A number of regionally anchored studies identified potential As sources which give an impression of the supposedly diverse origin of the As. Guillot et al. (2015) showed that **black schists** from the Lesser Himalaya highly contributed to the As pollution in in the Nawalparasi district (Terai, Nepal). Further Guillot & Charlet 2007 postulated that the original source of As in the Bengal region could be related to **ophiolitic As-rich rocks** in the Indus-Tsangpo suture zone. They describe large volume of As enriched **serpentinites** as one potential primary As reservoir. Also As-enriched **geothermal deposits** linked to large scale tectonic processes are named as potential As source in the Himalayan region (Bundschuh & Maity 2015). Another popular explanation assumes that **coal seams and sulphide outcrops** could be a crucial source of As (Das et al., 1996; Acharyya et al., 1999). Both are widespread As enrichments and got exposed all over the Himalayas during the uplifting process and especially the sulphides offer a promising approach to explain the origin of As. **Arsenic-rich (arsenian) pyrite** is the most common As carrier in the earth's crust and is able to host high concentrations. Also arsenopyrite, realgar orpiment and base metal

sulphides are widespread and likely to host As (Garelick et al., 2008). Uplifting of these As-rich sulphides followed by oxidation in near-surface environments could be a major source of As in SSEA depositional environments. Studies in other parts of the world have shown that sulphide enrichments can cause extensive As contamination in subsequent sedimentary environments (Goldhaber et al., 2003). As in early studies, As-rich pyrite was found along the transport routes of many Asian rivers it was assumed that oxidation of these phases during erosion and transport up-stream the deposition area are primary responsible for As release in the sedimentary environment (Nickson et al., 1998; Das et al., 1996). The oxidation of arsenical pyrite and other As-bearing sulphides was firstly proposed by Das et al. (1996) in order to explain As contaminated GW bodies of SSEA. According to Das et al. (1996) As is released in partly oxic GW fluctuation zones through the oxidation of As-containing Fe sulphides. Subsequent As enriched GW is transported downward during surface recharge. However, the As-containing sulphides up-stream could never be detected across the affected study sites in SSEA in greater extent. Although most delta sediments contain As-rich Fe-sulphides, usually within organic-rich silt layers between the aquifer and the surface, it is assumed, that the fine-grained layers are usually not hydraulically connected to the aquifers. Moreover, the As-rich pyrites are too rare to explain the widespread As contamination. Therefore, the theory has only a subordinate meaning for the explanation of the As-contaminated GW in SSEA. A few years after Harvey et al. (2002) postulated that lowered GW levels in depositional areas due to intensive GW abstraction caused As mobilization from in-situ oxidation of As-bearing sulphides and therefore mentioned a different oxidation pathway in the densely populated areas. Since As-enriched GW was subsequently reported from areas which are considered unaffected by GW extraction this approach did not offer a generally applicable solution to the origin of high As GW, too (Harvey et al., 2006; van Geen et al., 2003).

In summary, none of the above-mentioned sources provides a general explanation for the widespread As pollution in the sedimentation regions of SSEA. Although the publications were able to give an indication of the origin of As, they were not able to directly link source and sink regions in a coherent process. Within the source and depositional areas of the deltas and floodplains As-rich source rocks or minerals are in general rare and insufficient to explain widespread As contamination. As a result, the assumption that high concentrations of dissolved As require high sedimentary As contents had been abandoned. Instead of regional or supra-regional As-rich formations or high-As point sources within the sediments **efficient As liberation from source rocks with inconspicuous As background concentrations** were increasingly discussed as crucial process responsible for high-As GW in SSEA (Berg et al., 2007; Benner & Fendorf 2010). To explain the As contamination, the research focus progressively turned on efficient mobilization processes able to cause high As GW concentrations even with low solid background levels. A simple calculation to assume potential As mobilization from low-As sediments was presented by Neidhardt et al. (2012). Excluding flow and influences of transport and re-adsorption, the release of one mg/kg As in one m^3 of sediments will result in a concentration increase of 2,650 µg/L in GW, assuming a pore volume of 50 % and a sediment density of 2.65 g cm-3. Another calculation demonstrated that complete dissolution of 1 mg/kg As from sandy Bangladesh aquifer sediment could increase GW As concentration up to 7950 µg/L (Smedley & Kinniburgh 2002). Both calculations clarify that high As GW concentrations can arise from successive As release from sediments with low As background concentrations. Decisive in this process is the effective As mobilization mechanism and it could be shown that high dissolved GW concentrations do not need high sedimentary As contents.

In this context As-containing **Fe-coatings** offered a good explanation to connect As-rich source areas with the sedimentation areas through a capable As transport mechanism. Attempting to reconstruct the transport chain of the As from the source area to the polluted sedimentation environments, a coupling to the Fe cycle is obvious. The most widely accepted model (Fig. 8) assumes that during the transport sedimentary Fe turns progressively into Fe oxyhydroxides and precipitates on the surface of

primary particles (Raiswell et al., 2011; Hasselhöv & Kammer 2008; Eiche et al., 2010). The breakdown of primary-rocks due to erosion, weathering and transport creates to a combination of primary and secondary As-hosting mineral phases (Benner & Fendorf 2010). Weathering and oxidation through surface exposure lead to a gradual release of As from multiple primary sources. After release from primary phases, As co-precipitates and/or adsorbs onto the Fe oxyhydroxides precipitates (Eiche at al., 2010; Guo et al., 2007a; Charlet & Polya 2006; Charlet et al., 2011). The coatings scavenge dissolved As from water and fix it most likely by inner-sphere bidentate complexes (Manning & Goldberg 1997; Berg 2007) and act as new-formed carrier phases for As (Raiswell et al., 2011). Subsequent As is transported within the Fe precipitates via surface runoff and accumulates continuously in the depositional areas. According to today's status, the dominant large scale As transport mechanisms is most likely coupled to suspended particles with Fe oxyhydroxide coatings and adsorbed As that are washed into rivers and transported downstream (Berg 2007). Only to a minor extent As is directly transported by the drainage system in fragments of As(V) and/or As(III) hosting primary minerals (Neidhard et al., 2012). Finally As gets deposited with the settling sediments as a mixture of individual As-rich primary mineral fragments but mostly secondary As-hosting Fe-coatings in the final sedimentation areas due decreasing relief energy (Smedley & Kinniburgh 2002) together with high amounts of organic matter (Berg et al., 2007). The uniform distribution of As on the ubiquitous coatings leads to a relatively low, homogeneous As bulk concentration in the sediments.

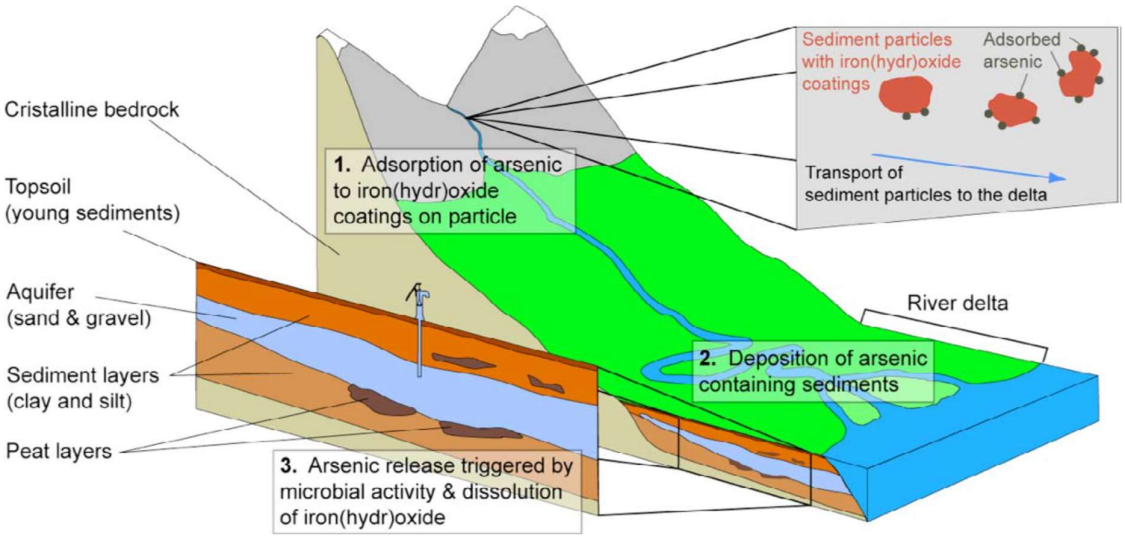

Figure 8: Simplified illustration of the widely accepted theory on the origin of arsenic in groundwater of Asian river deltas (Berg 2007)

Subsequent sedimentological processes and (paleo) climatic conditions have created favourable conditions for As-release within the late Pleistocene-Holocene deposits. The most widely accepted theory assumes microbial decomposition of co-buried organic carbon generates **reducing conditions** in the subsurface. The onset of reducing conditions seems to have evolved as a consequence of OM biodegradation in the slow flowing GW (Berg et al., 2001; Kocar et al., 2008; McArthur et al., 2004; Polizzotto et al., 2008; Postma et al., 2007; Stuckey et al., 2016). The co-deposition of As-bearing Fe coatings and reactive OM promote As release in reduced geochemical environments (Wang et al., 2018). As the heavily As contaminated GW bodies don't show high As background concentration in the solid phase it is assumed that the onset of reducing conditions finally (re-) dissolves the As-enriched redox-sensitive Fe-coatings and releases accumulated As entirely into GW (Benner & Fendorf 2010). The supposed mechanism is supported by the fact that all As contaminated sites show characteristic redox properties and low solid phase bulk As-concentrations. The large-scale cases of geogenic high-As GW in SSEA typically occur under strongly reducing conditions in aquifers composed of Late

Pleistocene-Holocene alluvial material deposited in flat, low-lying, sedimentary environments of deltaic plains and inland basins (Wang et al., 2018; Mandal & Suzuki 2002; Nordstrom 2000; Smedley & Kinniburgh 2002; Charlet & Polya 2006; Fendorf et al., 2010b). The As remained fixed in the coatings until the GW got reduced. As soon as the coatings came into contact with reduced GW Fe reduction started, Fe oxyhydroxides got dissolved, causing a passive release of adsorbed and incorporated trace elements including As (Lovley 1995 & 1997). Although the As amount in primary oxyhydroxides had never been determined on a comprehensive scale (Xie et al., 2008; Kocar & Fendorf 2009; Postma et al., 2010 & 2012; Stuckey et al., 2015 & 2016; So et al., 2018b) and attempts to directly link high As concentrations within Holocene aquifers to the respective mineralogy have failed, (British Geological Survey 2001) the mechanism is widely accepted.

The reductive dissolution of redox-sensitive Fe precipitates represents an effective transport and mobilization process that is capable to produce high As GW concentrations from sediments with low to moderate As background concentrations. Due to the complete dissolution of the precipitates, low As concentrations from 1–20 µg/kg found in most affected aquifers (Smedley & Kinniburgh 2002) are sufficient to cause GW concentrations far above the recommended guideline levels. Reductive dissolution further explains why As liberation is limited to highly reduced organic-rich sediments of Holocene and late Pleistocene age. The limitation of high-As GW to environments characterized by strong redox alterations reinforces the impression that the origin of the high As GW concentration is related to successive mobilization from Fe precipitates with low-As background values. The unique geographical setting of the South Asia deltas produce conditions highly conducive to the creation of naturally occurring, high-As concentrations in reduced GW. Local hydrology, sedimentology and biogeochemical processes lead to the release of As from near-surface sediments to the aquifer waters, where it then enters the drinking water supply via shallow GW wells in the densely populated river valleys of SSEA (Fig. 9) (Benner & Fendorf 2010). This approach offers a holistic picture of the As dynamic including origin, transport and final release mechanisms. The widespread As contamination in secondary sedimentary aquifers of SSEA can therefore be traced back to the mobilization of various As sources. The dominant As sources vary regionally but the most important are most likely As-hosting parent rocks (e.g. igneous and highly metamorphic), coals, hydrothermal systems and sulphide outcrops. The relevant As-rich minerals include arsenian pyrite, arsenopyrite, realgar, orpiment, base metal sulphides and apatite. But only through the interaction of efficient enrichment and transport in secondary Fe precipitations during subsequent erosion and weathering as well as the comprehensive re-mobilization under redox conditions in the final deposition areas that the high As GW loads in near the surface aquifers could be achieved.

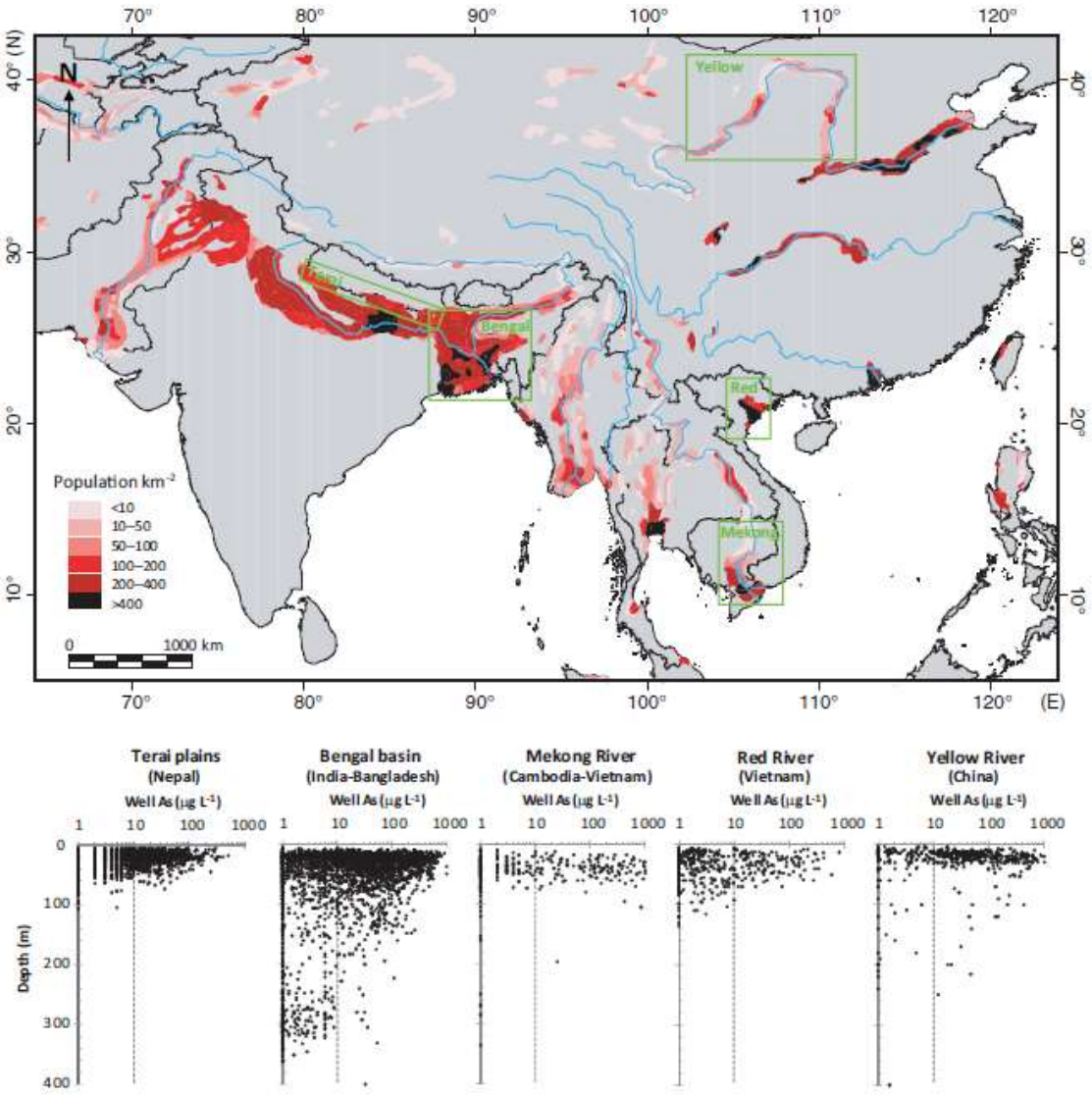

Figure 9: Map of population density within Asian regions where groundwater As concentrations are potentially elevated and distribution of arsenic in groundwater as a function of depth within five areas (Van Geen 2011)

6. Red River (RR) & Red River Delta (RRD)

The Sông Hồng (**Red River - RR**) is the major waterway of northern Vietnam with a catchment area of approximately 169.000 km^2. The name of the river originates from its high load of particles rich in Fe oxyhydroxides that generally exhibit a characteristic red to yellowish brown colour (Berg 2007). The Red River and his three major tributaries Da, Thao and Lo originate in the Yunnan province, a mountainous region of southeaster China, where its name is the Hóng Hé. The source area of the main tributary, the Black River (Sông Đà), is a mountain range southeast of the city of Dali from where he runs to the southeast (Fig. 10). The mountainous terrain to the East and North with an average altitude above 1000 m dominates the upper catchment area. The sources of the various tributaries are up to 1.776 m high. The regional topography slopes in a northwest to southeast direction and in consequence, the river flows into the South China Sea near the Island of Hainan through the four diffluent branches Day, Lach Giang, Ba Lat and Tra Ly. The main arm of the river reaches a length of about 1.175 km before it discharges into the Gulf of Tonkin (also known as the Gulf of Bac Bo) via a great delta. Especially during the rainy season, the Red River carries large quantities of water and

sediments. The total flow volume of the entire Red River system is estimated with about 135.7 km^3/yr and drains a considerable part of SSEA (Zhang et al., 2019; Mathers & Zalasiewicz 1999; Tanabe et al., 2003; Simons et al., 2016). The **Red River Basin** is one of the largest river basins in the world and stretches across Vietnam, China and Laos from approximately 20°00 to 25°30 N and from 100°00 to 107°10 E. With 890000 $km^{2,}$ Vietnam accounts for around 51 % of the area while about 48 % of the basin is located in China and less than 1 % in Laos. To the north the basin borders with the Yangtze River basin, to the East with the Thai Binh basin, to the West with the Mekong River basin and in the south, it is enclosed by Tonkin Bay. The Đồng Bằng Sông Hồng (**red river delta - RRD**) is the fourth largest delta in Southeast Asia and is about 500 km long and 50 to 60 km wide and comprises a ~10.000 km^2 deltaic complex (Tanabe et al., 2006). The total GW resources in the Vietnamese part of the RRD are estimated at 18.219 billion m^3 and are fundamental for the development of the northern part of the country (Zhang et al., 2019; Mathers & Zalasiewicz 1999; Tanabe et al., 2003).

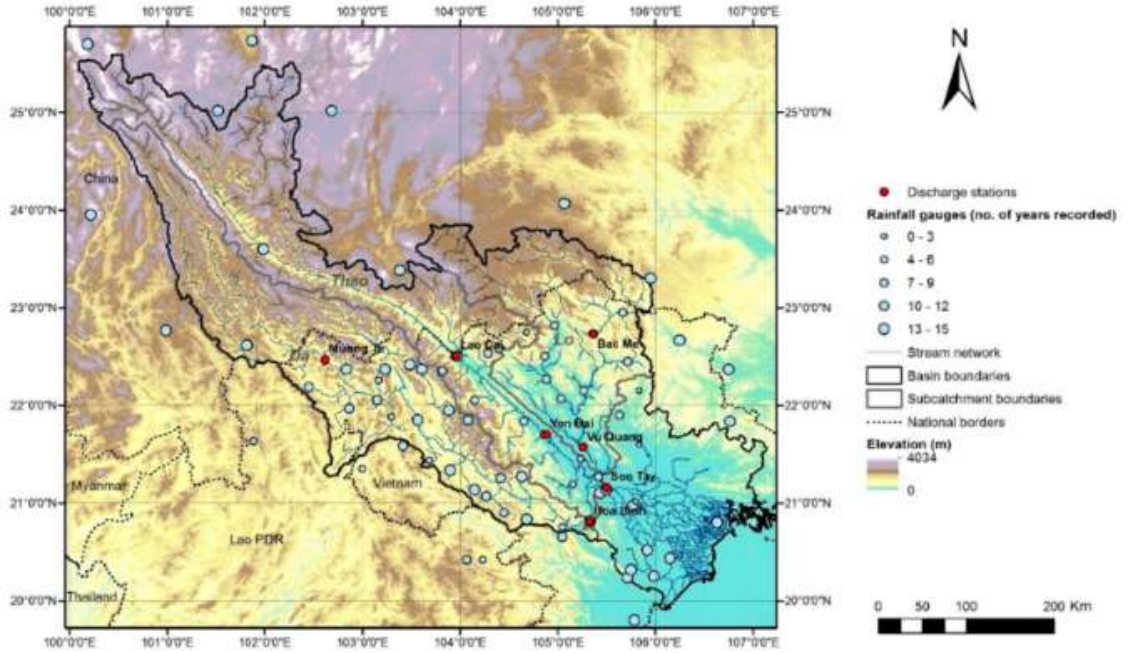

Figure 10: Red River Basin elevation map showing Red River catchment area and his three major tributaries Da, Thao and Lo originate in the mountainous Yunnan province in south-eastern China (Simons et al., 2016)

The development of the red river system is mainly controlled by the NW-SE aligned **Red River Fault system**, which stretches from Tibet to the South China Sea over more than 1.000 km as a result from the collision of the Indian and Asian tectonic plates in the Eocene (Rangin et al., 1995; Mathers & Zalasiewicz 1999; Tanabe et al., 2003 & 2006). There are many indications that the Paleogenic and Neogene fillings of the RRD are directly linked to the uplift of the Himalayas and the deltaic complex is thought to be composed of sediments from the eastern Tibetan plateau. Studies of the paleo drainage evolution of the large rivers in SSEA (Fig. 11) indicate that the Paleo Red River could have been directly connected to the rising Tibetan plateau during the Paleogene and Neogene and drained large parts of the eastern (paleo) Himalayas (Zhang et al., 2019). Although the sedimentological evidence is not sufficient to make a definitive statement about a Red river of continental proportions, dating the drainage fragmentation revealed the timing of uplift of Tibet (Zhang et al., 2019). However, the Paleo Red River had most likely a much larger catchment area than the modern river. The stable, fault-controlled system has become increasingly smaller since ~ 50Myr due to the northern migration of the east Himalayan syntaxis (Clark et al., 2004; Zhu et al., 2009; Leloup et al., 2007; Weinman 2010). The river is thought to have been depositing continuous sequences to the delta since the Eocene (Weinman

2010). Ongoing uplift, incision, and river reorganization have provided large amounts of erosion material especially since the Miocene (Clark et al., 2004; Weinman 2010). The major river systems transported huge quantities of sediments derived from the Himalaya to form great plain complexes in the low-lying areas (Ahmed et al., 2004). In consequence, the whole basin is filled with Neogene and Quaternary deposits, typically ≥ 3 km thick with low recent subsides rates of 0.04 - 0.12 mm/yr (Mathers & Zalasiewicz 1999; Tanabe et al., 2003).

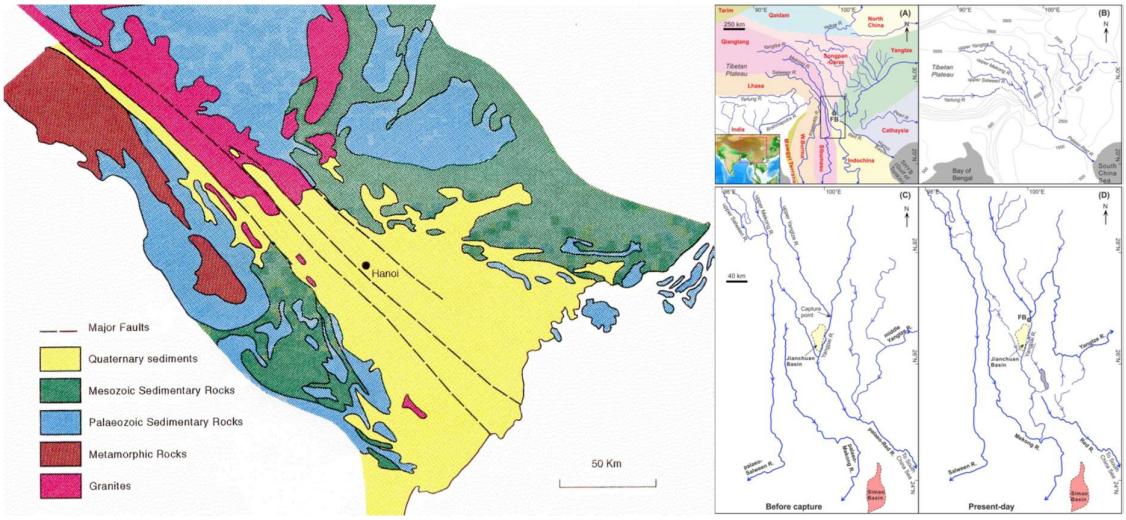

Figure 11: Generalized geological map of the Red River delta and the surrounding mountainous area (Mathers et al., 1996) and river history of the Red River in context of the rising Tibetan plateau (Zhang et al., 2019)

During the **Quaternary**, the source area shifted to the far eastern edge of the Himalayan in today's Yunnan region, which was uplifted in the Pleistocene (Zhang et al., 2019). Studies on the delta evolution suggest that the uppermost sediments originated from the mountains in the upstream river catchment and have been deposited entirely during Holocene and Pleistocene (Tanabe et al., 2006). The rapid tectonic uplift of the Himalaya and connected mountain ranges of the alpine orogenesis, coupled with high precipitation in the drainage basins, have led to large sediment loads during delta formation (Berg 2007; Benner & Fendorf 2010). During the last approximately 2.5 million years, deposits of river sediments have created thick sediment layers that form the delta as it is known today and the Red River's catchment got limited to the proximal terrains surrounding the RRB (Tanabe et al., 2006; Weinman 2010). In the modern upper reaches of the RR, Precambrian crystalline (Granites, Metamorphic rocks) as well as Palaeozoic sedimentary rocks are present, whereas the flat delta plain is surrounded by Mesozoic and Palaeozoic sedimentary rocks (Mathers et al., 1996; Berg et al., 2001; Eiche 2009). All these rocks act as source for the sediment deposited in the RRD today (Eiche et al., 2008). In its modern headwaters, the Yunnan Mountains, several sediments such as red sandstones, mudstones, siltstones of the Mesozoic - paleogens could serve as possible As and Fe sources (British Geological Survey 1996). However, their influence on the recent As dynamic in the RR delta flood plains is still to validate. The quaternary geology of the flat delta (in average 5 - 8 m above mean sea level) was essentially shaped by the deposition of alluvial material from the RR (Mathers et al., 1996; Berg et al., 2001). Constant shifts in the course of the river and fluctuations in the eustatic sea level and the estuary position have led to a continual interplay of terrestrial and marine deposition and erosion since beginning Quaternary forming characteristic sequences of fluvial, marine and transition sediments. Marine sediments have occasionally been introduced in context marine transgressions whereby the boundary between marine and fluvial-dominated sediments has always shifted (Tanabe et al., 2003). However, the marine transgressions never went beyond Hanoi into the further inland (Tanabe et al., 2003). At the last sea level high about 4 kyr years ago the sea level was 5 to 6 meters higher than today

and the RR estuary was west of Hanoi (Higham 1989). After the last regression, it is thought that the river maintained its current course southward of Hanoi (Tanabe et al., 2006). The intermediate stages were generally characterized by the formation of mangrove forests, which led to the formation of organic-rich clay deposits in the Holocene (often referred to as peat) (Mathers et al., 1996). The last large mangrove flats developed between 9 - 4 kyr BP as a result of the overall sea-level rise (Tanabe et al., 2003). Due to the multitude of processes occurring, the sedimentology of the RRD is highly complex and varies considerable within short distances. Some layers can be missing totally in some parts while they comprise thick layers in other areas (Eiche 2009). Especially the Late Pleistocene-Holocene aquifers have shown to have a complex inhomogeneous multi-layered structure with aquifer materials generally consisting of fine to coarse sands with occasional gravels, silts and (organic rich) clays (Winkel et al., 2008). Due to the complex sedimentation history, the time sequence in the vertical profile is often disturbed and Holocene and Pleistocene sediments can lie both on top of and next to each other and often cannot be clearly distinguished without specific dating technique (Funabiki et al., 2007). Especially lenses of silts and (organic rich) clays appear throughout the delta in an irregular pattern (Mathers et al., 1996). In consequence the Quaternary sediments in the basin, which normally unconformably overlie the Neogene deposits, are composed of Pleistocene and Holocene sequences of sands and gravels with minor lenses of silt and clay (Weinman 2010). The sediments deposited since the last glacial maximum are comprised of thick layers of alluvium (van Geen et al., 2013) and the fine layers are often rich in organic matter (Mathers & Zalasiewicz 1999; Tanabe et al., 2006). The thickness if the individual layers spreads from a few meters in the north-western part of the delta to almost 200 m in coastal areas and depending on their depths, the sediments are unconfined or semiconfined (Mathers & Zalasiewicz 1999; Tanabe et al., 2003). In the greater Hanoi area, the Quaternary sequence generally has a thickness of 50 - 100 m (British Geological Survey 2001; Mathers et al., 1996; Mathers & Zalasiewicz 1999; Weinman 2010).

With regard to **drinking water supply of the Hanoi region** the Quaternary sequence contains several aquifer units which are of great importance as GW is the only resource of drinking water and Hanoi depends almost 100 % on the local GW resources (Jusseret et al., 2010; Du Bui et al., 2012). Hanoi's GW resources are spread across the topmost Holocene and the shallow Pleistocene aquifers (Du Bui et al., 2012) and simplified, the sequence can be divided into a lower (LAS) and an upper aquifer system (UAS) (British Geological Survey 2001). The UAS usually stretches roughly from 20 - 40 m bgs and consist of sand, silt and clay as well as occasionally peat layers. The UAS includes both Holocene and Pleistocene aquifers and is mainly exploited in rural areas by shallow dug wells (British Geological Survey 1996). Especially near-surface Holocene aquifers are the source of widespread As poisoning across the region (Ravenscroft et al., 2009; Fendorf et al., 2010b; British Geological Survey 2001). The LAS is dominated by coarser fractions of sand and gravel and reaches a thickness of up to 50 m around Hanoi. Clay and silt lenses derived mainly from Pleistocene sea-level low stands are less abundant. Underlying follow sediments from the Neogene. Water transfer between the lower and upper aquifer system takes place to a certain degree, but the different aquifers are not hydraulically connected across the board and therefore water exchange between the units is limited (British Geological Survey 1996). In consequence the As contamination is usually limited to the OAS. As most LAS sediments are also highly permeable they form the main drinking water source for central water supply in the Hanoi region (British Geological Survey 1996).

7. Field site: Greater Hanoi area in Vietnam

The developing country of Việt Nam (Vietnam) was the 15th most populous country in the world in 2019 with a growing population reaching an expected 100 million people in 2020. Based on the CIA world fact book the Vietnamese population counted 98.7 million in July 2020. The General Statistics Office of Vietnam named 96.2 million people based on the Census from 2019. The Vietnamese

population increased from 1979 to 1999 by 24 million accounting for an increase of about 1 Mil/year (Hai & Yamaguchi 2008) and in contrast to many other developing countries, the trend continues until present and will likely continue for the next decades. In the 10 years from 2009 to 2019, the population of Vietnam has increased by 10.4 million people (Census 2009-04-01 of the General Statistics Office of Vietnam). According to FAO statistics (FAO 2009), the total population in Vietnam increased from 27.4 million in 1950 to 83.6 million in 2005, and could reach 118 million in the 2050s. The total area of the country is 329.566 km^2 whereby the social, economic and political life concentrates mainly in the two centres Hà Nội (Hanoi city) and Thành phố Hồ Chí Minh (Ho Chi Minh city) (Fig. 12). The Socialist Republic has undergone a remarkable development in the past 30 years. Economic and political reforms launched in 1980s, have spurred rapid economic growth, transforming what was then one of the world's poorest nations into a lower middle-income country (Worldbank). The GDP reached 650 million $ in 2017 with an average annual growth between 6 and 7 % during the last decade. The country is now one of the 35 largest economic nations in the world and has the ninth largest economy in Asia (CIA world fact book). The middle income country could decline the poverty rate sharply during the last three decades from above 70 % to below 6 % in 2019 (Worldbank). Since the signing the free trade agreement with Europe on august 1, 2020, Vietnam has been the largest trading partner of the European Union in Asia after China. In 2018, the trade volume between the EU and Vietnam was 49.3 billion euros - 38.2 billion euros imports from Vietnam and 11.1 billion exports to Vietnam. Based on an assessment of the German federal government, It can be expected that these values will increase significantly as a result of the free trade agreement in the coming years (bundesregierung.de). Strong population growth, rapid industrialization and digitalization, economic growth and the promise of rising standards of living have led to a massive population shift from the countryside to the two major cities. In consequence, the booming centres create an increased strain on regional natural resources (Norrman et al., 2008; Luu et al., 2019). Water supply in particular is an increasing challenge for the rapidly growing cities of millions as beside the number of people also the average daily water consumption in Vietnam significantly increased during the last three decades through rising standard of living and economic activity (Luu et al., 2019). To ensure the growing demand for clean drinking water for public and private use, sustainable management of natural resources is prerequisite and is increasingly taken into account in both political and economic decisions (Luu et al., 2019) reflecting the extensive development and growing education of the country.

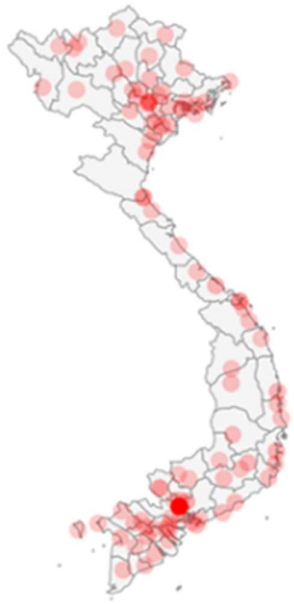

Figure 12: Population density across Vietnam (http://worldpopulationreview.com/countries/vietnam-population)

The field site lies in northern Vietnam in the Red River Delta (RRD) near the metropolis Hanoi. The national capital, **Hà Nội** (Hanoi) accounts for a total population of 8 (Census 2009 of the General Statistics Office of Vietnam) to 11 million (Luu et al., 2019) people. The metropole city of Hanoi is the economic, political and social centre of northern Vietnam. With 2.398 people/km^2 it has one of the highest population densities in the world (Census 2009 of the General Statistics Office of Vietnam). In combination with the surrounding RRD the population accounted for an estimated 11 to 15 million people near the millennium (Mathers et al., 1996; Berg et al., 2001) and increased to above 22.5 million people according to the 2019 Population and Housing Census (Population and Housing Census 2019 of the United Nations Population Fund p. 127). Therefore, nearly a quarter of the total Vietnamese population lives in the metropolis' direct catchment area. The most important cities in the RRD besides Hanoi are Hải Phòng, Thái Bình and Nam Định. Hanoi is a good example of a quickly expanding city in a developing country. The greater Hanoi area has experienced rapid urbanization and population growths during the last decades. From 1975-2003 the urban area increased from nearly 1000 ha to almost 6000 ha (Fig. 13) (Hai & Yamaguchi 2008). Especially from the beginning 1990s on urbanization in the Hanoi area increased rapidly. Mainly in response to housing needs several new urban districts have been created in the south and west of the city center (Dang et al., 2014).

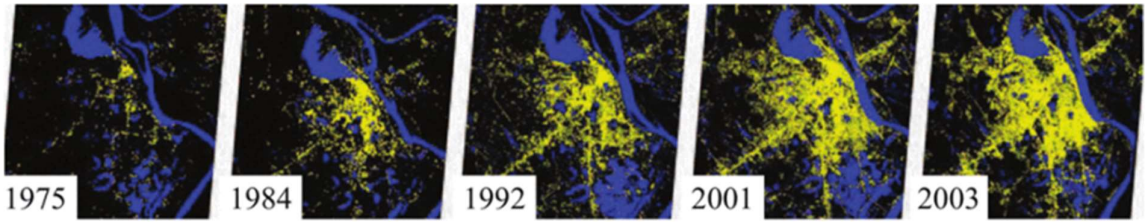

Figure 13: Hanoi city urban area increase from 1975 until 2003 (Hai & Yamaguchi 2008)

The **study area of Vạn Phúc** (Van Phuc), a small village approximately 15 km SE of Hanoi, is located on a meandering arch of the Red River (N20.920810° E105.896130) within the delta complex (Fig. 14 a & b). The rural commune in the Thanh Trì district of Hanoi municipality belongs to the wider Hanoi area and has a population of almost 10000 inhabitants. The population density of the 4.93 km² area lies at 1.950/km² in 2009 (Census 2009-04-01 General Statistics Office of Vietnam). Beside the small settlement, the land use is dominated agriculture and ponds for coupled duck breeding and fish farming. The most common crops are corn, medicinal plants, and cabbage (Eiche et al., 2008). In addition, bananas and a variety of herbs and fruits for the local kitchen are grown. To a lesser extent livestock farming of chickens and pigs could be observed. The village lies 11 m above sea level and thus about 5 m lower than the average height of Hanoi right on the river. A Network of dams to protect the city of Hanoi separates the small traditional village directly on the shore of the river and the densely populated urban Hanoi. The Van Phuc village is located in between the riverbed and the dike that protects the south-western parts of Hanoi from annual flooding. Unprotected by the dike, the village undergoes “occasional floods during the rainy season” (Weinman 2010). The **local climate** the northern part of Vietnam, including the RRD and the Hanoi area, is classified as tropical-subtropical climate of the East Asia monsoonal type (Tanabe et al., 2003; Li et al., 2006) with an annual temperature of about 23.4 °C (Hanoi). The average daily temperature vary from 14 – 16 °C in winter to 26 – 27 °C during summer. Relative humidity is high throughout the year, averaging 82 – 84 %. The annual precipitation is about 1800 mm/yr whereby the rainfall shows substantial variations from 700-4800 m/yr. The rainfall is mainly related to the Southeast Asian monsoon regime from May to September delivering about 80 % of the annual precipitation. During rainy season daily precipitation ranges from 10 to almost 200 mm/day. During the dry season from October to April the North East monsoon creates cooler, dryer weather (Larsen et al., 2008). The high variance in annual precipitation is reflected in the variable water level of the Red River. The annual fluctuations in the Hanoi area lie

between 7-9 m and lead to extensive flooding during the rainy season (Berg et al., 2008; Eiche 2009) while the river discharge fluctuates between 700 – 23.000 m^3/s depending on the season (Tanabe et al., 2003 & 2006) and Water table variations up to 4 m in the aquifers were observed between the seasons (Eiche 2009).

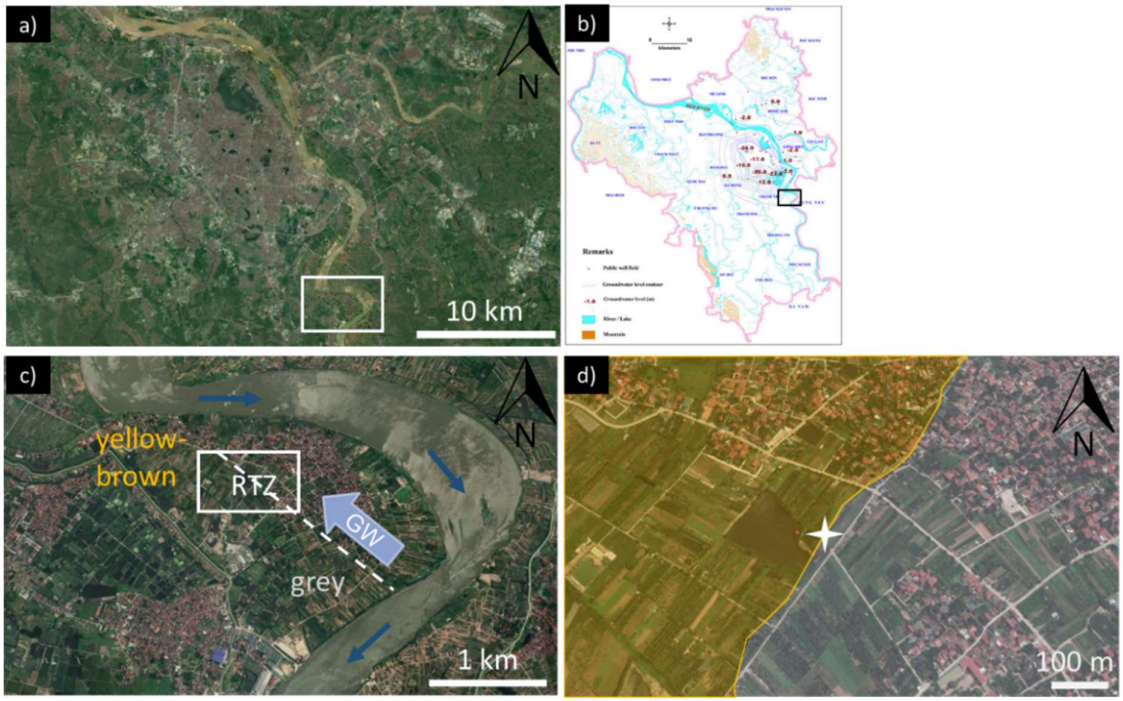

Figure 14: Field site: Position of Van Phuc Peninsula and the redox transition zone

a) Google earth image sowing the city of Hanoi and the position of the study side (white frame) at the Red River in the south-east. The white frame shows the area of c). b) Map showing the lowered groundwater level in Pleistocene complex below Hanoi city in 2010 (Phi & Strokova 2015). The position of the study is indicated by the black square. c) Google earth image sowing the Peninsula of Van Phuc Village (centre) with grey high As aquifer in the south-east and yellow-brown low As aquifer in the north-west and the redox transition zone (RTZ) in between. The arrows in dark blue indicate the flow direction of the Red River and light blue arrow the local GW flow direction. The dashed white line shows the SE to NW transect presented in Stopelli et al. (2020). The white frame shows the d) drilling position of RD42 & RD54 as well as the incubation experiment at the redox interface (course indicated by orange line).

With regard to the **local geology** Van Phuc has been the subject of intensive research for around two decades. Various drilling programs were carried out by the Swiss federal institute of aquatic science and technology (eawag) (Berg et al., 2001 & 2003 & 2007; Stopelli et al., 2020), the Karlsruhe Institute of Technology (KIT) (Eiche et al., 2008; Eiche 2010) and the Lamont-Doherty Earth Observatory of the Columbia University (VanGeen et al., 2013) creating a network of boreholes and wells across Van Phuc. Most boreholes were sunk along a transect extending from the river in the southeast towards Hanoi in the northwest across the meandering arch of the Red River (Fig. 14c). The local near-surface geology of Van Phuc has been described by previous studies with a structure of three distinct sediment units for the top 40-50m (Eiche et al., 2010; Berg et al., 2007; van Geen et al., 2013). The thickness of the individual units showed substantial variations throughout all coring campaigns reflecting the heterogeneous subsurface build as a result of frequent riverbed migrations and marine trans- and regressions (British Geological Survey 1996; Tanabe et al., 2006). The obtained young alluvial delta sediments are composed of clay, silt, sand and minor amounts of pebbles and isolated gravel (Eiche et al., 2010; Berg et al., 2007; van Geen et al., 2013). All drilling campaigns identified a top aquitard composed of clayey silt with a thickness of 10-20 m with individual organic-rich layers as uppermost unit below the soil. The aquifer below was described as a loose bedding of Holocene and Pleistocene sands up to a depth of 40-50 m. Coarse and fine-grained layers regularly traverse both the aquitard and the aquifer in an undefined pattern. Below the sandy aquifer, the campaigns reported a coarse gravel layer of unknown extent as coring techniques did not enable further penetration (Eiche et al., 2008; Berg et al., 2007; Van Geen et al., 2013). An exact sediment recording never took place since most of the corings were designed to build wells for a GW measuring network. Generally sediment sampling by core flushing were carried out which did not allow a precise description of the sediments and their location in the depth profile. Investigations in the immediate surrounding of Van Phuc provided a comparable picture for the subsurface. Investigations beneath Hanoi (British Geological Survey 1996) and a study location at the Red River 30 km upstream north of Hanoi (Postma et al., 2007) revealed a similar structure of the underground. Depending on the location, the Van Phuc aquifer is completely or partially greyish in colour. The proportion of grey decreases with increasing distance from the river and turns to yellowish-brownish-orangish colour along the transect from the south-east to north-west (Fig. 14d) (Eiche et al., 2008; van Geen et al., 2013). Sediment dating along the transect in Van Phuc suggest that low dissolved As concentrations are in general related to orange/yellow/brown-coloured Pleistocene sands deposited over 12.000 years ago, whereas high-As GW is typically in contact with grey reduced Holocene sands deposited less than 5.000 years ago (Weimann 2010; Eiche et al., 2008; Berg et al., 2007; Funabiki et al., 2007). Based on these results Van Geen et al., (2013) assumed that the grey sands represent channel fillings both above and next to yellowish-brownish- orangish sediments. However, the dated samples in Van Phuc never covered the whole depth profile of the aquifer and for the position of the redox interface, which is discussed in this thesis, are no dating information available at all. Therefore, it is widely speculative to assume that grey sediments in Van Phuc are in general Holocene while yellow brown and orange sediments represent Pleistocene deposits. Hence, the sediments will be referred according to the colour throughout the thesis.

The **local hydrology** is strongly influenced by the water supply of the capital. In response to the rapid growth, Hanoi experienced since the 1970s groundwater abstraction below the city of Hanoi has been rapidly increasing in response to rising demands for drinking and process water. The increasing demand was met with the construction of additional water production plants. An intensive GW abstraction for decades through several GW-pumping fields followed (Dang et al., 2014). Since 2005 ten major well fields of Hanoi water works exploited more than ~650.000 m^3GW/day through the pumping fields (Berg et al., 2007 & 2008; Jusseret et al., 2010). That from the 1990s to the 2000s the pumping rates reached a maximum of 430.000 to 473.780 m^3/day (RIGMR 2006; database) shows the

dramatic increase in water consumption. In the years 2002 to 2005 three additional water production plants were added with a total capacity of 30 000 m^3/day each. The rapid exploitation of the GW without an appropriate management system has reportedly caused a series of adverse impacts such as changing GW flow conditions (Berg et al., 2001; Postma et al., 2007; Van Geen et al., 2013) decline of GW level and drying up of shallow wells (Du Bui et al., 2012), and land subsidence (Dang et al., 2014; Thu & Fredlund 2000; Phi et al., 2015; Du Bui et al., 2012). These developments pose major problems for the local authorities and will enlarge if sustainable use of natural resources is not enforced promptly. The comprehensive consequences illustrate that the maximum sustainable exploitable GW quantity has been reached (Du Bui et al., 2012). The massive water consumption of the capital has influenced the local GW hydrology far beyond the city limits. Also the local GW hydrology in Van Phuc has been strongly influenced by water withdrawals by the city of Hanoi. Intense pumping of drinking water lowered the GW table below the city and created GW depression cones of up to 17 m (Dang et al., 2014). The GW table continuously drops roughly 0.30 m/year (Du Bui et al., 2012) and creates a radial GW inflow towards Hanoi. The result is a relatively constant inverse GW flow against the main GW flow direction of the Red River towards the northwest in the study site of Van Phuc. In consequence, to the large withdrawal GW migrates from a reduced grey As-rich aquifer towards the yellow-brown aquifers up-stream used for local water supply (Fig. 14c). Modelling of the GW flow for the Van Phuc area suggests average GW advection rates towards Hanoi of about 40 m/yr for the time span 1951-1971 (van Geen et al., 2013). Berg et al. (2008) assumed that the excessive abstraction of water from deep wells also caused the downward shift of Fe-reducing conditions. After Berg et al. (2008) the drawdown of Holocene water to the Pleistocene aquifer promotes reducing conditions in Pleistocene GW and it is believed that associated with this process highly reduced As-rich GW could be pulled into moderately reduced GW bodies with low As concentration used for irrigation and drinking water production.

In this context, it was also discussed whether the reduced area expands and whether additional As is mobilized by a migrating redox front and an expanding redox zone. As deep GW abstraction beneath Hanoi causes not only GW migration from the UAS to the LAS but also river water is directly drawn into both aquifers (British Geological Survey 1996; Berg et al., 2007 & 2008). Previous analyses could show both aquifers recharged predominantly by Red River water (Berg et al., 2007 & 2008; Stopelli et al., 2020; Wallis et al., 2020). As the RR incises deeply into the sediment both aquifers are connected to the river along a 5 km wide zone while in the rest of the delta leakage from the UAS is believed to be the main water source for LAS (British Geological Survey 1996; Berg et al., 2007 & 2008; Eiche 2009). Recent numerical model simulations by Wallis et al. (2020) illustrate that in consequence the As plume most likely migrated > 1700 m over the past 60 years, starting from the river–groundwater interface to its current position. The sharp decline in dissolved As concentrations was observed at the redox interface, which can be modelled by an As retardation factor of 16 to 20 relative to the movement of GW. In this context van Geen et al. (2013) assumed that less than 100 m of the formerly orange Pleistocene sediment became grey, indicating that not only As but also the movement of the whole redox front has been retarded in recent years. The near-surface GW bodies are also affected by the highly variable annual water level of the river. It can be assumed that GW flow velocities and hydrochemistry change over the course of the year as both hydrological systems are connected. Therefore, the hydrodynamic of the shallow aquifer is influenced by a complex interplay of annual water level variations and tidal variations of the nearby river as well GW abstraction beneath Hanoi and local pumping for irrigation. This assumption was approved during GW monitoring program from 2010-2017 by Stopelli et al. (2020) who documented a constant GW level while advective flow conditions and hydrochemistry showed minor variations in annual cycle and transport as well as spatial distribution of As in the GW system is mostly controlled though local flow regimes.

At the time of this work, the Village of van Phuc is partially connected to the central water supply of the city of Hanoi, which delivers As free drinking water from deep wells. Many residents still rely on the use of their own shallow wells for drinking water supply. Although it is planned to expand the central water supply (personal communication with local population), it will take years to come before all households in Van Phuc have been connected. Even then, it can be assumed that in the poor, rural region, the almost free local GW is preferred to the expensive tap water to irrigate the gardens and fields. Comprehensive irrigation networks are typical in the Red River basin. Numerous irrigation wells are also documented in Van Phuc. At regular intervals of 10-20 meters there are irrigation wells align across the fields. Depending on the crops, they are used daily during the dry season (personal communication with local farmers). Previous studies also reported that in the absence of the monsoon, the village fields are irrigated during the dry season either by water from ponds or by GW from frequent wells (Weinman 2010). It can be assumed that these wells influence the local hydrological regime of below Van Phuc. However, it is hard to quantify the impact on local hydrology as no numbers with regard to the amount of wells, depth and amount of pumped water across the time are available.

With regard to the **local drinking water supply** no health effects are to be expected in Van Phuc in present days. As mentioned, there is already a partial connection to the central water supply of the city of Hanoi and reconnaissance and monitoring have also created an awareness of the problem. The local residents of Van Phuc have switched from using surface water or unfiltered water from shallow dug wells using deeper tubewells as their primary sources of drinking water several decades ago (Berg et al., 2001; Tobias & Berg 2011). For the construction of the wells colour of aquifer sands and spectral reflectance measurements are used as indicators to identify safe well locations (van Geen et al., 2013; Nghiem et al., 2020). In addition households commonly treat raw GW through household sand filters (Fig. 15) which lower As concentrations on average by 80 % due to co-precipitation with Fe oxy-hydroxides (Berg et al., 2006). The application of this cheap and effective filter technology is now common all over Van Phuc (Nitzsche et al., 2015; Thuan et al., 2014). The use of sand filters is currently the only way to ensure a safe water supply due to the widespread As contamination of household wells. A study of tubewells in the greater Hanoi area showed that 72 % of the examined tubewells had As levels that exceeded the current WHO standard of 10 µg /L (Agusa et al., 2007).

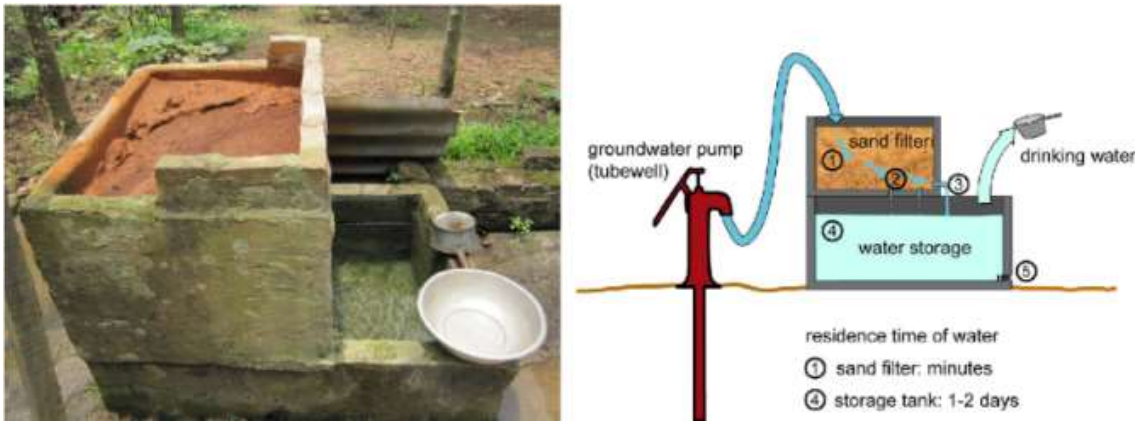

Figure 15: Household sand filter for point-of-use arsenic removal in the backyard of a rural household in Vietnam (Tobias & Berg 2011)

The **field and core site selection** was based on knowledge gained in previous works. Van Phuc was chosen as a study site because of the highly contrasting As concentrations ranging from < 1 - 540 µg/L over short distances discovered by Berg et al. (2001). The detailed characterization of the study site (Berg et al., 2001 & 2007 & 2008; Eiche 2009; Eiche 2010; Van Geen et al., 2013; Bostick et al., 2010; Stahl et al., 2016; Neidhardt et al., 2018; Litter et al., 2014; Rathi et al., 2017; Nghiem et al., 2020;

Stopelli et al., 2020; Glodowska et al., 2020; Lawati et al., 2012; So et al., 2018a; Weinman 2010; Wallis et al., 2020; Winkel et al., 2011) during the last two decades and a running GW monitoring program lasting for almost 10 years further allowed to precisely determine the position of the redox interface and therefore the coring position. Based on GW data of a monitoring program from 2010-2017 (Stopelli et al., 2020) the position of the transition area between the heavily As contaminated and the As-free aquifers could be determined to within a few meters (Table 3). Therefore, it was possible to situate the core directly at the redox interface where high and low As GW aquifers are juxtaposed. Both drill cores RD42 and RD54 are situated directly in the redox transition zone where high and low As GW aquifers are juxtaposed distanced 10 m away from each other. Further the GW data clearly suggested As and Fe retardation by the redox front and accumulation of both elements in the solid phase of the transition area. Therefore, Van Phuc allowed to investigate coupled As and Fe retention mechanisms related to abrupt redox changes in a natural sedimentary environment. Finally, the sedimentology, typical for many As-contaminated sites in SSEA, allows for good comparability with other sites. Restrictions in the selection of the core site arose from the high population density and intensive landuse of Van Phuc which has limited the choice for coring locations. Thanks to the mediation of our, long-term project partners of the Hanoi University of Sciences, the core could be drilled where it was suspected based on the GW data.

During the time of this work Stopelli et al. (2020) identified five hydrogeochemical zones along an approx. 2000 m long transect with highly variable GW As and Fe concentrations. Each zone is characterized by specific As mobilization and retardation processes and highly variable GW hydrochemistry. At the transition zone (zone D), As and Fe GW concentrations decreased significantly across a sharp redox boarder while Eh increased. Based on this work the RTZ extends over a total of 135m and covers a large range of hydrogeochemical parameters (Table 3). The As concentration drops from 509 µg/L to below 1.4 µg/L and the Fe from 13 mg/L to 1.3 mg/L while Eh increases from 36 to 113. A central area of the greatest changes over a short spatial distance provides a sharp decrease of dissolved As (from 393 to 1.4 µg/L) and Fe (from 11 to 1.3 mg/L) while the redox conditions change from highly (17 mV) to moderately reducing (113 (mV) over a distance of about 35 m. This section was defined as the central area of the RTZ. Both cores were drilled slightly offset in the center of this area.

Table 3: Horizontal and vertical GW gradient across the RTZ (Data Stopelli et al., 2020; GW flow from right to left)

Total horizontal distance for the wells in the top Table is 365m. The transition sediments (AMS-11-25 to AMS-36) stretch about 35 m. Total horizontal distance for bottom Table (AMS-11-25-D1 to AMS-32-D2) is about 20 m.

aquifer unit	yellow-brown		transition			grey
well ID	VPLMA-24	AMS-36	AMS-32	AMS-31	AMS-11-25	AMS-5
depth	23/24m		23/24m			23/24m
↓As	↑3.8	↓1.4	↓97	↓295	↓393	509
↓Fe	↓0.4	↓1.3	↓9.4	←11	↓11	13
↑Mn	↓2	↓2.3	↑3.9	↑0.9	↑0.4	0.1
↓DOC	↓1.4	↓1.6	↓3.4	←3.9	↓4	9.2
C-alka	↓2.3	9.5	←10	←10	↓9.7	13
↓CH_4	↓<0.1	↓4.3	↑37	↑31	↓18	46
↓NH_4^+	↓0.1	↓13	←19	←23	↓21	67
↓PO_4^{3-}	←0.04	↓0.03	←0.3	←0.4	↓0.5	1.6
Eh	↓85	113	↓10	↓11	↓17	36
↓S	↑2.7	↓<0.1	↓<0.1	↓<0.1	<0.1	0.1
↑CA^+	↓5	116	↑103	↑91	↑87	83
Mg	↓6	↓16	↓26	↑28	↑27	26
Na	↑32	↓10	←12	↑12	↑11	10
↓K	↓2	↓4	←5	←5	↓5	9
Si	↑16	12	↓7.5	↓8.5	↓9.5	15
pH	↓6.8	7.1	↑7.2	↑7.2	↑7.1	7
O	↓0.018	↑0.047	←0.014	←0.013	↑0.014	0.008

aquifer unit	yellow-brown	gravel?	transition		grey		
well ID	AMS-32-D2	AMS-11-47	PC44	AMS11-32	PC43	AMS-31	AMS11-25-D1
depth	23/24m	47m	38m	32m	28m	23/24m	23/24m
↓As	↓97	↑8	←0.5	↓0.5	↓61	↓295	↓393
↓Fe	↓9.4	↑17	←0.1	↓0.1	↓9	←11	↓11
↑Mn	↑3.9	↓1.1	↑2.6	↓1.6	↑2.8	↑0.9	↑0.4
↓DOC	↓3.4	↓1.6	↑1.9	↓1.6	↓3.4	←3.9	↓4
C-alka	←10	↓6.3	↑13	←10	←10	←10	↓9.7
↓CH_4	↑37	<0.1	←<0.1	↓<0.1	↓18	↑31	↓18
↓NH_4^+	←19	↓0.6	↓1.8	↓9.7	↓17	←23	↓21
↓PO_4^{3-}	←0.3	↑0.25	↓0.02	↓0.04	←0.5	←0.4	↓0.5
Eh	↓10	↑108	↓82	↑173	↑52	↓11	↓17
↑S	<0.1	↓0.04	↑0.2	←0.02	<0.1	↓<0.1	<0.1
↑CA^+	↑103	↓30	↓65	←101	↑102	↑91	↑87
Mg	↓26	↓20	↑66	←33	↑33	↑28	↑27
↑Na	←12	↑39	↑17	↑15	↑13	↑12	↑11
↓K	←5	↓3.7	↑5.6	↓4.8	↑6.4	←5	↓5
↑Si	↓7.5	↑16	↑15	↑14	↑9.1	↓8.5	↓9.5
↓pH	↑7.2	↓6.5	↓6.8	←7.1	↓7	↑7.2	↑7.1
←O	←0.014	↓0.012	↑0.474	↓0.071	↑0.19	←0.013	0.014

8. Materials and methods

A broad set of mineralogical and geochemical methods and techniques were combined to get a comprehensive picture of the mineralogy and geochemistry of the sediment cores. Especially with regard to Fe mineralogy challenging conditions with redox sensitive samples and complex small-scale variations in Fe mineralogy with probably poorly crystalline Fe phases present as coatings were expect based on the results previous works (Berg 2007; Eiche 2009). To characterize the lithological parameters of the sediment sequence, identify the various Fe minerals and their related As content a combination of bulk analysis and spatially resolved measurements was applied (Fig. 16). In addition to standard sedimentological (colour, grain size), mineralogical (XRD, microscopy) and geochemical (ED- & WD-XRF, CSA) characterization bulk analysis with high sensivity towards Fe phases (magnetic susceptibility, Mößbauer spectroscopy and synchrotron based Fe EXAFS) were used to identify and quantify Fe minerals and species. Related bulk As species composition was determined by As XANES. Spatially resolved µ-XANES measurements at the Fe and As k edge in combination with SEM-EDX and EMPA analysis made it possible to characterize the As-Fe associations in the sedimentological context.

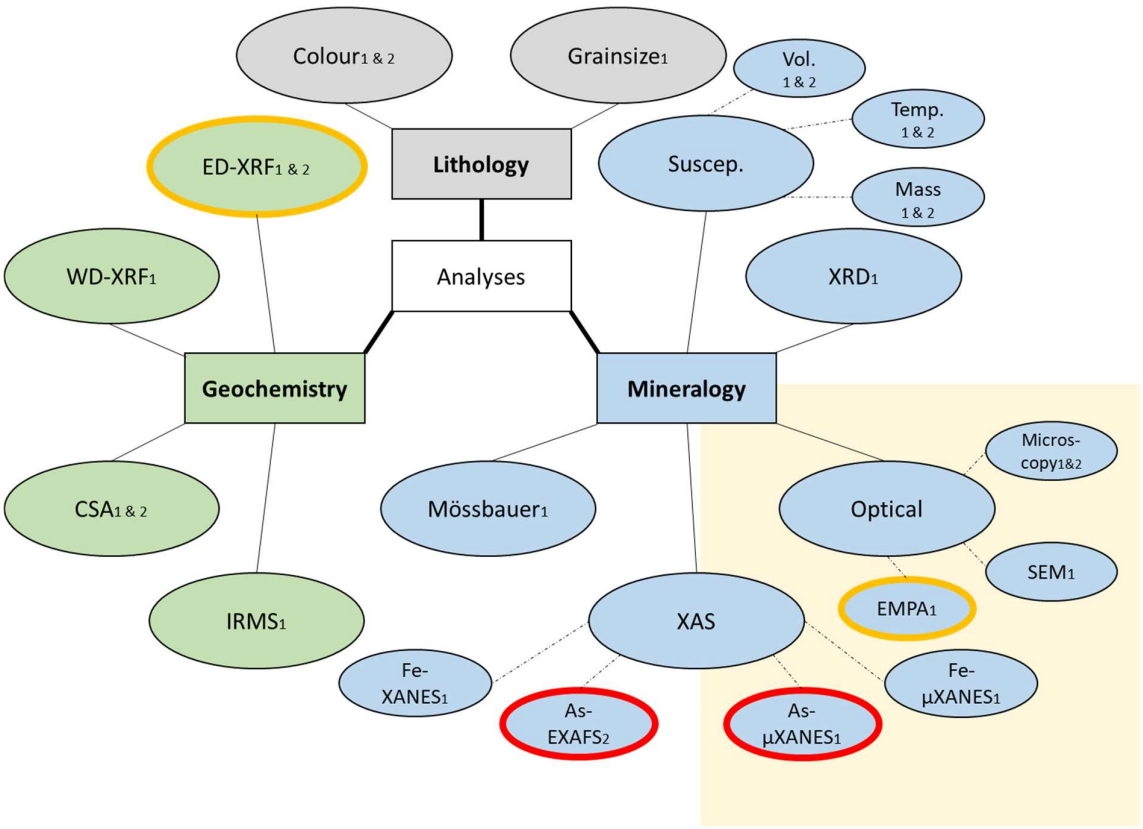

Figure 16: Overview on lithological (grey), geochemical (green) and mineralogical (blue) methods used in this study

Spatially resolved methods are highlighted in yellow and methods which allow to determine the arsenic concentration or the arsenic species are marked orange and red respectively. Numbers indicate sediment core RD42=1 and RD54=2.

8.1 Sediment cores

8.1.1 Coring & lithological characterization

During two field campaigns in 2017 and 2018 two sediment cores (RD42 2017 & RD54 2018) were gained by a rotary drilling technique (Fig. 17).

Figure 17: Rotary drilling in Van Phuc (RD42, 2017)

The individual core segments were 1.0 to 1.5 m long with a diameter of 20 cm. The location of the first drilling position (RD42) is N: 20°55'18.5'' E: 105°53'38.2'', the second core (RD54) was located 10 m northeast (N: 20°55'18.76'' E: 105°53'38.42''). Immediately after core recovery, the segment length was measured and potential core loss determined. The lithological core characterization and description took place in the field right after the core segments were opened and included a photo documentation. The subsequent core description followed the International Continental Drilling Program (ICDP) protocol and involved colour (Munsell), grain size (KA5/WRB), distribution of special features (e.g. concretions, fossils, roots, organic-rich layers, etc.) and measuring magnetic susceptibility (Fig. 18, 29, 30, 31; Table 16).

Figure 18: Field site a) core description and b) magnetic susceptibility measurements (RD42, 2017)

8.1.2 Bulk sediment sampling

The **sampling procedure** covered every distinct layer (not fixed intervals) based on a set of criteria involving sediment colour, grainsize, magnetic susceptibility and sedimentological features. Sampling intervals did not exceed intervals of 100 cm. Sampling frequency increased along small-scaled transitions in colour, grainsize or characteristic visible features such as Fe-precipitates. Especially along the redox transition zones sampling resolution was increased to cover intervals of several centimetres. Multiple **sample types** were collected: a) unflushed bulk samples for grain size analysis (nRD42=78),b) N_2-flushed bulk samples for determination of mineralogy, geochemistry and magnetic susceptibility (nRD42=74, nRD54=69), and c) N_2-flushed undisturbed stitch ring samples for optical analysis (nRD42=27, nRD54=30). Sampling took place immediately after the core description. A ceramic knife as used to cut the core segments into two halves split along the length of the core. Samples were collected with plastic spoons from the central area of the core in order to keep the contact time with oxygen as short as possible and avoid contamination with drilling fluid remains or other contaminations (Fig. 16). In the field all samples were packed and N_2-flushed (Air liquid UN 1066, ≥ 99,8 Vol.%, H_2O ≤ 40 mg/kgv/v, O_2 ≤ 100 mg/kgv/$v_{atmosphere}$), for all except the grain size samples, immediately after extraction. After packing the samples were cooled with ice packs and stored in a cooling box before they could be transferred into a fridge at the Hanoi University of Science. The sample temperature did not exceed 12 °C after they were cooled down. The samples were kept in this state until the transport to the KIT lab was completed. In order to minimize sample alteration during transport and storage Water- and air-tight zip log bags (PET/PE-LD/Aluminium stand-up pouches LamiZip bags from the company DAKLAPACK) with high barrier properties against oxygen and water vapour and protection against UV radiation were used. The procedure corresponds to the description published in Glodowska et al. (2021). Sample material that was not used immediately after the field campaign was split in half and was frozen at -20 °C or put in a fridge at 6 °C, both in nitrogen (N_2) flushed sample bags.

Figure 19: Bulk sediment sampling for EXAFS based Fe mineral composition (RD54, 2018)

8.1.3 Thin section preparation

To preserve the original sediment texture and redox state 3-D printed stitch rings were used to enable spatially resolved geochemical measurements and microscopic analysis. We used an Ultimaker 3 3D-printer and Ultimaker PLA - M0751 Transparent 750 - 211399 PLA 2.85 mm filament to print the molds. The molds were 35 mm wide, 55 mm long, and 30 mm high. The final size of the thin sections was aligned to fit 28x48 mm glass carriers. In isolated cases there was enough sample material available to use larger metal stitch rings which allowed thin sections in the size of 48x48 mm (Fig. 20 a-c). After storage and transport in N_2 atmosphere (Air liquid UN 1066, ≥ 99,8 Vol.%) the stitch rings were dried in a desiccator with drying granulate (Roth Silica gel orange 1-3mm) under N_2 atmosphere (Air liquid

UN 1066, ≥ 99,8 Vol.%) at 40 °C to avoid any alteration of redox and temperature sensitive samples. Afterwards the samples were impregnated with the synthetic resin Araldite 2020. The resin was chosen because its high viscosity at low temperatures allowed impregnation at temperatures below 40 °C. The subsequent hardening process was conducted under vacuum to ensure in-depth impregnation and exclusion of oxygen. After splitting the massive blocks one side was used to produce a classic thin section (30 µm thick) for microscopy and the mirror side for removable thick sections (100 µm thick) for spatially resolved synchrotron analysis. In total n_{RD42}=27 thin sections representing 22 depth levels, and n_{RD54}=30 thin sections representing 23 depth levels have been produced and analysed.

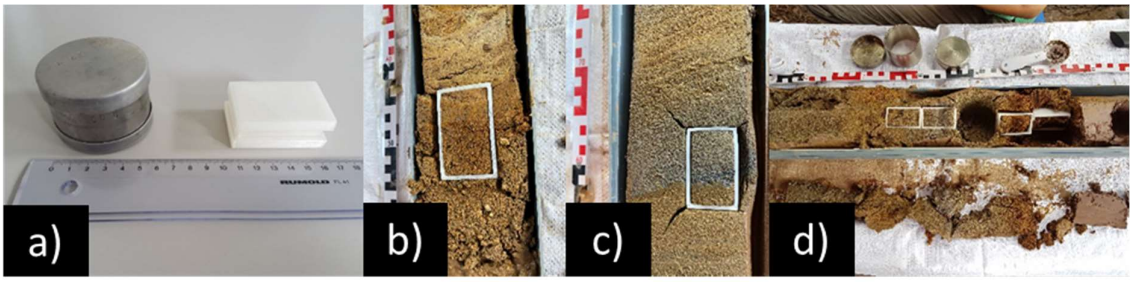

Figure 20: a) Metal stich ring and 3d-printed molds for thin sections and sampling position in b) RD54 in 34.1 m & c) 42.4 m bgs and d) RD42 in 41 m bgs

8.1.4 Grain size analyses

Grain size distribution was analysed by a combination of sieving (> 63 µm) and laser granulometry (< 63 µm) with a CILAS PSA 1064 at "Materials Testing and Research Institute" (MPA) at KIT. The procedure followed the standard protocol for grainsize analysis based on German DIN4220/KA5/LUFA (Ad-hoc Arbeitsgruppe Boden, 2005) and international WRB (World Reference Base)/FAO (Food and Agriculture Organization of the United Nations) standards. The four categories clay (< 2 µm), silt (2 - 63 µm), sand (63 µm – 2 mm) and pebbles (> 2 mm) were used to describe grainsize composition. In total n_{RD42}=78 samples were analysed. All subsequent grain size percentages are wt%.

8.1.5 Solid phase geochemistry

Bulk samples for geochemical analysis were oven dried for 48 h at 40 °C and grinded to a homogenous fine powder (< 63 µm) using a ball mill or disc mill (both made of agate), depending on sample quantity. The sediment geochemistry characterization that included major and trace element analyses was carried out in the Laboratory for Environmental and Raw Material Analysis (LERA; AGW) of the Karlsruhe Institute of Technology (Germany). **Trace element** concentrations of grinded sample material was analysed using energy dispersive X-Ray fluorescence (**ED-XRF**) (Epsilon 5, PANanlytical). The ED-XRF limit of detection (LOD) for As in this study is 1.2 mg/kg. For all other elements, the LOD is well below 1 wt%. In RD54 the precision of the As measurements with ED-XRF, which is based on 3 repeated measurements of 8 certified reference materials (BE-N, GXR-2, GXR-3, GXR-4, GXR-5, GXR-6, Soil-V, Soil-VII), was ± 1 % for higher As concentrations (13.4-3970 mg/kg) and 5.3-26 % for lower As concentrations of 1.8 and 11.3 mg/kg As respectively. The accuracy, determined with the same certified reference samples, is between 83 and 132 %, and can be considered as reasonably good. One exception is standard BE-N with 1.8 mg/kg As where 350 % of the certified concentration were measured. The precision of Fe_2O_3 measurements (certified concentration range: 2.7 to 27 wt%) by ED-XRF show a standard deviation between 0.2 and 1.9 % and an accuracy between 98 and 117 %. The precision of the MnO measurements for concentrations from 0.02 to 2.88 wt% is between 1-12 % and the accuracy is 98 to 128 %. The precision of the CaO measurements for concentrations from 0.25 to 13.9 wt% is between 0.1-1.9 % and the accuracy is 108 to 148 %. The precision of the TiO_2 measurements for concentrations from 0.2 to 2.6 wt% is between 0.1-6.6 % and the accuracy is 107 to

126 %. The precision of the K_2O measurements for concentrations from 0.9 to 4.8 wt% is between 0.1-2.6 % and the accuracy is 99 to 120 %. The precision of the SiO_2 measurements for concentrations from 13 to 66 wt% is between 0.5-28 % and the accuracy is 91 to 130 %. The precision for ED-XRF As measurements of the **RD42** samples, which was determined based on 2 repeated measurements of the certified reference material SOIL-V is ±1 %. The accuracy is between 98 and 108 %. At low As concentrations of 1.8 mg/kg As the accuracy increases to 210 % for the standard BE-N.

Wavelength dispersive X-Ray fluorescence (**WD-XRF**) (S4 Explorer, Bruker) of fused beads was used to determine the **major element** geochemistry. The LOD is well below 1 wt% for all observed elements. The accuracy of the Fe_2O_3 measurements of the RD42 samples (reference materials MA-N, GS-N, MAG, SDO-1, SDC1, certified concentrations range 3.75 - 12.17 wt%) using WD-XRF is between 90 and 104 %. For low Fe_2O_3 concentrations (0.47 wt%), the accuracy was 128 %. The precision was not determined. Based on the experiences in our lab the precision for Fe_2O_3 measurements are well below ± 1 %. The accuracy for the Al_2O_3 measurements is between 92-96 % and the precision is below ± 0.5 %. The accuracy for the CaO measurements is between 94-102 % and the precision is below ± 0.5 %. The accuracy for the P_2O_5 measurements is between 89-103 % and the precision is below ± 4.5 %. The accuracy for the MnO measurements is between 78-94 % with two standards showing accuracies of 130 % (MAG) and 180 % (SDO-1). The precision is below ± 1.5 %. The accuracy for the TiO_2 measurements is between 89-94 % except the standard MA-N with 227 %. The precision is below ± 0.5 %. The accuracy for the K_2O measurements is between 90-99 % and the precision is below ± 2 %. The accuracy for the SiO_2 measurements is between 91-97 % and the precision is below ± 0.5 %.

Total carbon (TC) and total sulphur (TS) contents were determined with the carbon sulphur analyser (CSA) CS-2000 from ELTRA. A **total inorganic carbon** (TIC) Module for CS-2000 was used to determine the TIC in 25 selected samples of RD42. **Total organic carbon (TOC)** was calculated by subtracting inorganic carbon from total carbon. Element analyser EuroEA 3000 from Hekatech was used to determine the **total nitrogen (TN) and total organic carbon (TOC)** (n=25 for core RD42). The isotopic $\boldsymbol{\delta^{13}C_{org}}$ value was determined by a combination of the EuroEA3000 and the isotopes ratio mass-spectrometer (IRMS) IsoPrime from GVInstruments. The precision calculated from three repeated sample measurements was better than ±0.19 ‰ for C. For all methods mentioned so far the number of samples was n=74 for RD42 and n=69 for RD54 which corresponds to an average depth resolution of 0.58 m for RD42 and 0.62 m for RD54.

8.1.6 Mineralogy

The work encompass a detailed mineralogical characterization of the sediment core material using a combination of microscopic, spectroscopic and magnetic techniques. Bulk samples for mineralogical analysis were dried in a desiccator with drying granulate (Roth Silica gel orange 1-3mm) under N_2 atmosphere (Air liquid UN 1066, ≥ 99,8 Vol.%) at 40 °C for 48h to avoid alteration of redox and temperature sensitive phases. The **bulk mineral composition** including semi quantitative evaluation of major and minor phases was determined on bulk powder by **XRD** (Bruker D8 Discover) at the LERA (KIT). $Cu_{K\alpha}$-radiation was used and the samples were scanned from 2° 2θ to 82° 2θ with an increment of 0,02° 2θ at 0.4 sec. The relative mineral abundances were estimated from integrated peak areas using the HighScore-Plus software from Malvern Panalytical GmbH and the Inorganic Crystal Structure Database (ICSD) for phase identification. **Volume susceptibility** was measured in field (nRD42=349, nRD54=374) with a handheld SM-30 Kappameter (ZH Instruments) along the halved cores in order to detect the Fe mineral distribution which corresponds to 10 cm intervals. **Mass specific magnetic susceptibility** measurements were done on wet and dry bulk samples (n=74 for RD42) to test potential sample alteration due to storage with a KLY-2 Kappabridge (Geofyzika/Agico). **Temperature dependent mass susceptibility** was determined on N_2 flushed bulk samples (nRD42=56) with a KLY-4S Kappabridge (Geofyzika/Agico) from -196 °C (liquid N_2 temperature) to 710 °C for Fe mineral

identification. High temperature measurements (room temperature – 710 °C) were measured in an inert argon atmosphere to minimize oxidation, as also described in Glodowska et al. (2021b). In total 46 samples cover the entire sandy aquifer and additional 9 samples give a representative picture from the top silt layer and 1 from the bottom silt layer. All magnetic analysis were done in the laboratories of the Structural Geology Division at KIT.

Mößbauer spectroscopy was applied on four samples in 20, 21, 30, 37m depth of RD42 at Laboratory of Geomicrobiology of the University of Tübingen in order to observe short-range associations of Fe minerals. The samples were loaded in Plexiglas holders under N_2 atmosphere prior to loading inside a closed-cycle exchange gas cryostat (Janis cryogenics). Measurements were collected at 5 and 77 K with a constant acceleration drive system (WissEL) in transmission mode with a ^{57}Co/Rh source and calibrated against a 7µm thick α-^{57}Fe foil measured at room temperature. All spectra were analysed using the software Recoil (University of Ottawa) by applying a Voight Based Fitting (VBF) routine (Rancourt et al., 1991). The half width at half maximum (HWHM) was fixed to a value of 0.130 mm/s for all samples.

Petrographic microscopic investigations (reflected and transmitted light) on thin sections were carried out in order to identify major and minor mineral composition with special focus on Fe mineralogy. Polarized microscopy was further used to describe micromorphology of Fe mineral assemblages and sediment properties. All analysis were done at the laboratories of KIT-AGW. The **Scanning Electron Microscope** coupled to ED-XRF (SEM-EDX) measurements were done using a Tescan Vega 2. The SEM is equipped with an Oxford Instruments Silicon Drift Detector (SDD) INCAx-act for Energy Dispersive X-ray Spectroscopy (ED-XRF) analysis (KIT-AGW) for quantitative elemental analyses operating at an accelerating voltage of 15 kV at a working distance of 15 mm, using the secondary electron (SE) and backscatter (BS) signal. Thin sections were mounted on specific 3D-printed sample holders and sputtered with carbon or gold coatings. Identification of elements in spot analyses and their distribution using the mapping option of automatic or manual search of elements were performed using the analytical software SwiftED (version 1.2). Element abundances were determined from the ED-XRF spectra by integrating peak areas and normalizing the results to 100 wt%. Selected spots were analysed at the Laboratory for Electron Microscopy (LEM) at KIT with a FEI Quanta 650 FEG ESEM coupled to a Bruker QUANTAX, Esprit 1.9 ED-XRF to obtain higher spatial resolution (the same equipment was used in Glodowska et al. (2021b)). **Electron probe microanalysis** (EMPA) was done at „Zentraleinrichtung Elektronenmikroskopie“ (ZELMI) of the TU Berlin with a JEOL JXA-8530 F. Chemical Information were gained by wavelength dispersive X-ray fluorescence (WD-XRF) measured at 15.0 kV. The detection limit of the method for As is 70 mg/kg. In total n_{RD42}=3 samples in 22, 30 and 41 m depth were analysed. The spot size of the ED-XRF (SEM) and WD-XRF (EMPA) point measurements is in the sub µm-range.

X-ray absorption spectra (XAS) were collected at the SUL-X beamline of the Institute for Photon Science and Synchrotron Radiation (IPS) at KIT (Germany) and the X-ray Absorption Spectroscopy Beamline 4-1 at the Stanford Synchrotron Radiation Lightsource (SSRL) facility (USA). At the **SUL-X beamline** quick scan XRF mappings were used in order to pre-identify Fe- and As-rich spots on the 100 µm thick sections of RD42 along the undisturbed sediment texture. Spatially resolved X-ray absorption near edge structure (µXANES) spectra were collected at the Fe (7.112 eV, calibrated against Fe metal foil), Mn (6.539 eV, calibrated against Mn metal foil) and As (11.919 eV, calibrated against Au metal foil) K-edges at room temperature using a Double Crystal Monochromator DCM (Si111). The spotsize is 40 x 30µm (horizontal x vertical). Subsequent linear combination fitting (LCF) allowed identifying the Fe mineral composition and As(III):As(V) ratio for 21 spot measurements on the Fe precipitates in 41 m depth. In total 6 reference spectra were used to identify the Fe phases (Gt, Hem, Mt, Lep, Magh, Fh). The reference spectra for As in included the species As(0), As(III) and As(V). At the **SSRL Beamline**

4-1 18 bulk samples from RD54 were measured. About 2 to 3g of fresh sediment material was taken from the core directly in the field. Blotting paper was used to remove entrained water. Samples were soaked in glycerol (bidistilled 99,5 %from VWR Chemicals) in centrifugation tubes, sealed with parafilm and stored under N_2 atmosphere to avoid oxidation. The samples were cooled during subsequent storage and transport to 8-12 °C. The As speciation was determined using XANES spectra for 22 samples (Au foil, Ge filter, Ge detector). Iron mineralogy was investigated at the K-edge in the EXAFS (X-ray absorption fine structure) range (Mn filter, Fe foil, PIPS detector). The spectra were processed to obtain normalised absorbance before the spectra have been analysed using the ''fingerprint'' method, by comparing spectra from samples with those from reference compounds.

8.2. Incubation experiment

In-situ incubation experiments with Fe oxyhydroxide coated sands were carried out in order to investigate the effect of the actual hydrochemical and microbiological subsurface conditions on a set of synthetic and biogenic minerals. To analyse redox sensitivity, As retention capacity and microbiological activity the mineral samples were placed in two depth levels (25 and 32 m bgs) with contrasting hydrogeochemical conditions for a period of 21 days in a well close to the drilling position. The monitoring well used for the experiment (AMS11) is located 7.5 m away in the SE direction from the drilling position. The set involves in total 9 biotically and abiotically synthesized Fe minerals (Fig. 21) and covers low crystallinity (Fh) and well-crystallized minerals (Gt, Hem, Mt) as well as biotic phase mixtures (Lep/Gt, Lep/Mt) produced by microbes isolated in the study site before (Glodowska et al., 2021). The biotic mineral coatings were characterized prior to the experiment by temperature dependent magnetic susceptibility measurements (Fig. 58) as relatively pure biogenic Gt, Fh and three phase mixtures composed of Lep and Mt (Lep/Mt) as well as two variants of Gt and Lep (Gt/Lepbio1 & Gt/Lepbio2) in variable amounts. None of the biogenic coatings is absolutely pure. The incubation experiment was part of the second field campaign in order to compare biosynthesised phases from the field site and synthetic minerals usually used in laboratory experiments in the natural environment of Van Phuc. The incubation experiment was designed to compare different biogenic and synthetic minerals. Two sets of different Fe(III) minerals were compared with regard to the bioavailability, their (trans)formation and/or dissolution resulting from (microbial) oxidation or reduction, and the microbial community that is involved under environmental conditions. The study aimed to identify the key Fe(III) reducers and asses Fe(III) reducing capacity of the native microbial communities. The experiment was designed to compare the evolution of biogenic and synthetic minerals in a natural hydrogeochemical environment with regard to the dissolution and transformation kinetics. By incubating the biotic and abiotic minerals in the moderately reduced and reduced aquifer environment both hydrogeochemical environments across the RTZ are covered. The methods and results were published in Glodowska et al. (2021b).

8.2.1 Mineral synthesis and coating procedure

In order to coat the quartz (Qtz) grains synthetic Fe minerals (Gt-Bayferrox 920, Hem-Bayferrox 110, Mt-Bayferrox 360) from the company Lanxess/Bayferrox (LANXESS Inorganic Pigments, Krefeld, Germany) were used. All minerals have been characterized with XRD prior to their usage. The coating process followed the procedure described in Scheidegger et al. (1993), Schwertmann & Cornell (2000) and Hanna (2007). To obtain the coating solution 100 mg of each Fe oxyhydroxide was mixed with 10 ml $NaNO_3$ solution in a 50 ml polyethylene tube and diluted with $HN0_3$ to adjust the pH. In order to obtain the maximum coating thickness the ionic strength of the $NaNO_3$ solution was adjusted to 0.01M and the pH to 7 for Gt (Schwertmann & Cornell 2000), pH 5 for Mt (Hanna 2007) and pH 2,5 for Hem (Schwertmann & Cornell 2000). Afterwards the mineral solution was shaken to obtain a homogeneous suspension at 25 °C for 24 h. Before mixing with the Fe minerals, the sand was pre-treated (washed) with 1.0 M HCl solution for 24 h, rinsed several times with distilled water and dried at 100 °C. Then 2.5

g of acid washed Qtz grains (0.4-0.8 mm Roth) were added to the mineral suspension. The Fe mineral-sand mixtures were shaken for another 24 h. After the mineral coated sand settled the supernatant was removed and the coated sand washed several times with a $NaNO_3$ solution with an ionic strength and pH equal to that of the reaction medium. Finally, the coated sand was washed with a salt solution and afterwards with pure water using a nylon sieve (63 pm) to remove any unattached Fe oxyhydroxide. The samples with a pH above 5 (Gt, Mt) were additionally washed with 1 M $NaNO_3$ solution of pH 3 to remove weakly attached Fe oxyhydroxide aggregates. The Gt-, Hem and Mt-coated sand was finally dried in an oven at 110 "C for 24 h. To test the strength of Fe oxyhydroxide attachment to the Qtz particles, small amounts of the dried coated sand was re-suspended and then shaken at pH 3 for 24 h. All ingredients were analysed with regard to the As concentration before the coating procedure. In order to quantify the As content of the reaction components inductively coupled plasma mass spectrometry (ICP-MS, , X-Series 2, ThermoFisher) was used to analyse the initial $NaNO_3$ solution and the Qtz sand and the synthetic Fe minerals were analysed by energy dispersive X-ray fluorescence (ED-XRF). The abiogenic Fh and the biogenic mineral coatings were prepared in the laboratories of geomicrobiology of the University of Tübingen in context of a cooperation project. The biogenic mineral coatings were produced by microbes native to Van Phuc which were isolated during the first field campaign. All information on the coating synthesis can be found in the publication (Glodowska et al., 2021). The mineralogy of the biogenic Fe mineral coatings was determined by temperature dependent magnetic susceptibility. The geochemistry and mineralogy of the Fe mineral coated sand grains was determined before and after the incubation experiment. The As und Fe content of the Fe mineral coated sand grains before and after the incubation experiment was determined with energy dispersive X-ray fluorescence (ED-XRF). Temperature dependent magnetic susceptibility (k-t) and scanning electron microscope (SEM) microscopy were used to analyse the synthetic mineral coatings before and after the experiment.

8.2.2 Field setup

Two identical sets the synthesized biogenic and abiogenic Fe mineral sand coatings were transported to the field site and exposed to the GW. In order to maximize GW contact 4.5 g of coated sand was placed in ramekins (3D printed frames) and covered with a well-permeable fine (0.2 mm) nylon mesh membrane as previously described in Neidhardt et al. (2018) (Fig. 21). The wafers were attached to a 55 mm nylon fishing line, weighed down with stainless steel hex nuts and placed in the well. One set was incubated in the strongly reducing As-contaminated, Fe(II) and CH_4-rich aquifer water (25m bgs), while the other one was located in suboxic water with low As-, Fe(II) and CH_4-concentrations in 32 m depth. In addition 4.5 g of uncoated HCL washed sand in bags of the same 0.2 mm nylon was exposed to GW as blank sample at the same depth levels. Further information about GW hydrochemistry and microbiology can be found in Glodowska et al. (2020).

Figure 21: Incubation setup showing the various biotic (bio) and abiotic (abio) mineral coatings in the characteristic mineral colours before the experiment

8.2.3 Sampling

After 21 days of incubation in the natural environment the samples were recovered from the wells. Immediately after extraction from the wells the samples were N_2-flushed and placed on dry ice in water- and air-tight zip log bags (PET/PE-LD/Aluminium stand-up pouches LamiZip, bags from the company DAKLAPACK) with high barrier properties against oxygen and water vapour and protection against UV radiation. The samples were kept in this state until the transfer to the laboratories of KIT was completed to minimize sample alteration during transport and storage.

8.2.4 Solid phase geochemistry

At the Laboratory for Environmental and Raw Material Analysis (LERA) the samples were extracted from the zip log bags in a glovebox and dried in a desiccator with drying granulate (Roth Silica gel orange 1-3mm) under N_2 atmosphere (Air liquid UN 1066, ≥ 99,8 Vol.%) at 40 °C for 72h to avoid alteration of redox and temperature sensitive phases. Samples for geochemical analysis were grinded to a homogenous fine powder (< 63 µm) using a ball mill before being analysed. Trace element concentrations of grounded sample material was analysed using **energy dispersive X-ray fluorescence** (Epsilon 5, PANanlytical).

8.2.5 Mineralogy

Bulk mineral composition of reaction components was determined by **XRD** (Bruker D8 Discover) at the LERA (KIT). $Cu_{K\alpha}$-radiation was used and the samples were scanned from 2° 2θ to 82° 2θ with an increment of 0,02° 2θ at 0.4 sec. The relative mineral abundances were estimated from integrated peak areas using the HighScore-Plus software from Malvern Panalytical GmbH and the Inorganic Crystal Structure Database (ICSD) for phase identification. **Temperature dependent mass susceptibility** was determined on N_2 flushed bulk samples with a KLY-4S kappabridge (Geofyzika/Agico) in the structural geology division at KIT from -196 °C (liquid N_2 temperature) to 710 °C. High temperature measurements (room temperature – 710 °C) were done in an inert argon atmosphere to minimize oxidation. Due the limited sample quantity **thin section preparation** for microscopically analyses followed a different approach than for the sediment samples and the wafer samples were embedded directly into small volumes of the synthetic resin Araldite 2020 to avoid any oxidation. The subsequent hardening process was conducted under vacuum to ensure in-depth impregnation and exclusion of oxygen. The sample material was cut out of the hardened block, fixed on the object carrier and ground and polished afterwards. The temperature during the whole process was always below 40 °C to avoid any thermal alteration of the Fe phases. The **Scanning Electron Microscope** (SEM-EDX) measurements were done using a Tescan Vega 2 SEM with an Oxford Instruments Silicon Drift Detector (SDD) INCAx-act for Energy Dispersive X-ray Spectroscopy (EDS) analysis for quantitative elemental analyses operating at an accelerating voltage of 15 kV, in combination with imaging using the secondary electron (SE) and backscatter (BS) signal. The thin sections were mounted on specific 3D-printed sample holders and measured with carbon or gold coatings. Identification of elements in spot analyses and their distribution using the mapping option of automatic or manual search of elements were performed using the analytical software SwiftED (version 1.2). Element abundances were determined from the EDX spectra by integrating peak areas and normalizing the results to 100 %. Selected spots were additionally analysed at the Laboratory for Electron Microscopy (LEM) at KIT with a FEI Quanta 650 FEG ESEM coupled to a Bruker QUANTAX, Esprit 1.9ED-XRF to obtain higher resolution. Unless otherwise described all analysis were done in the Laboratory for Environmental and Raw Material Analysis at KIT.

9. Results

Both sediment cores are 43.2 m long. Core RD42 reaches from 3.1- 46.3 m below ground surface (bgs) and RD54 from 3-46.2 m bgs respectively. Sampling started at a depth of around 3 m because the overlying material could neither be sampled undisturbed nor assigned to a clear depth level. Therefore, it was not taken into account in the study. Both drill cores could not be obtained without core loss. The total loss of core RD42 amounts to 748 cm and is concentrated on the upper 20 m while for core RD54 a total of 340 cm was lost mainly between 25 and 30 m depth. The core loss was always at the upper end of the segments and the material was most likely washed out during drilling and recovery process. The length of the individual segments reaches from 70 to 160 cm for both cores. RD42 was drawn in 35 runs while RD54 consists of 39 segments. The sampling for the mineralogical and geochemical investigations extended over the entire vertical profile in both sediment cores. An overview of the position of the various samples along the two vertical core profiles is provided in Fig. 22. An overview of individual segment lengths, core losses as well as position of samples and special features can be found in Table 16.

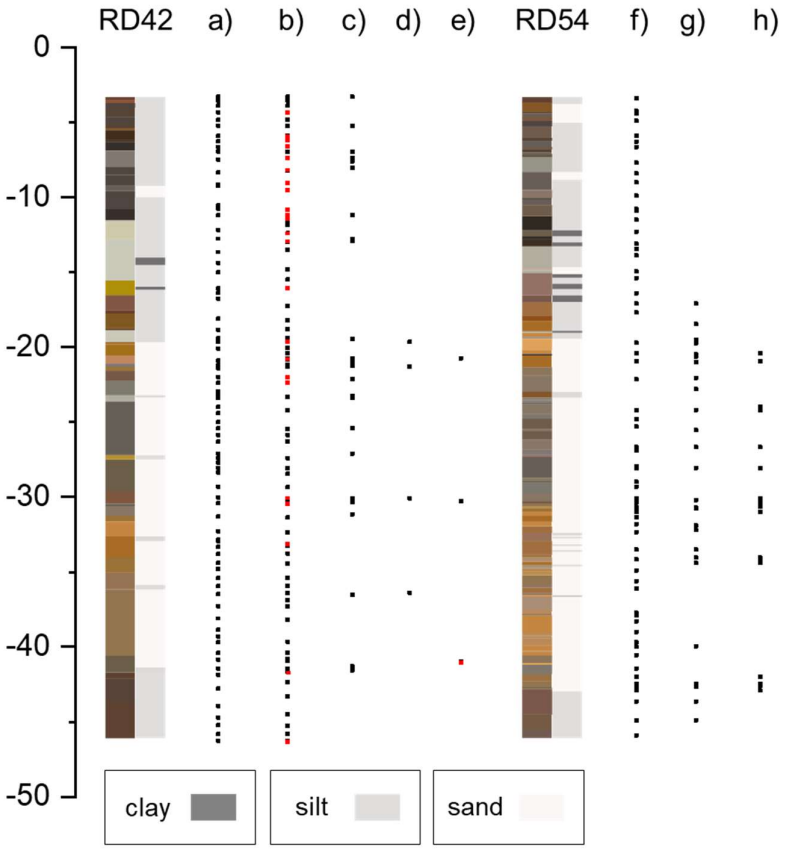

Figure 22: Sample position along the two vertical core profiles of RD42 & RD54.

On the left core RD42 with sediment colour (Munsell colours) and dominant grain size a) unflushed grain size samples b) N_2-flushed bulk samples for ED & WD-XRF, CSA, XRD, Susceptibility (mass, temperature). Selected samples for additional IRMS analyses are indicated in red. c) N_2-flushed thin sections for optical investigations with petrographic microscope and SEM. d) Position of selected Mossbauer samples. e) Position of selected samples for EMPA analyses. Selected sample for additional µ-XANES is indicated in red.

The right side shows core RD54 with sediment colour (Munsell colours) and dominant grain size f) N_2-flushed bulk samples for ED-XRF and CSA g) N_2-flushed thin sections for optical investigations with petrographic microscope and SEM and h) Glycerol-flushed bulk samples for Fe-EXAFS and As-XANES.

9.1 Lithology: colour, grain size & micro-morphology

The lithology of both sediment cores is highly variable across the depth profile. Colour and grain size change frequently on cm scale. Both sediment cores are composed of clastic to argillaceous fluvial and marine sediments presumably deposited during Holocene and Pleistocene. A comparison of the two sediment cores reveals numerous similarities. Both cores show widely similar lithological characteristics along the vertical profile. Colour and large-scale grain size gradients of the two cores are almost congruent and features like concretions, organic-rich layers or organic residues like fossils and roots are largely present in the same depth levels. The maximum vertical offset for one of these characteristics between the two cores is below 1 m over a horizontal distance of about 10 m. Both cores show a characteristic quarter division and based on grain size distribution and colours, the sediment cores can be subdivided from top to bottom into **four lithological units** (Fig. 23):

1. silt-clay aquitard
2. sandy aquifer
3. silt aquitard
4. gravel aquifer

Sharp colour and grainsize boarders separate the four lithological units almost at the same depth level. Only at the lower aquifer-aquitard transition shows an offset of around one meter. Small-scale differences between the two cores arise only in a direct comparison of the depth levels in cm-scale. Numerous coarse and fine-grained intercalated layers with variable thickness in the cm range interrupt the top aquitard, the aquifer and the bottom aquitard regularly in both cores. The position, thickness and frequency of the intercalated layers vary within and in-between the two cores without systematic pattern. RD42 is in general more homogeneous both in grain size distribution and sediment colour. Furthermore, the sediment colours are well pronounced in core RD42. Core RD54 has more pale colours and, compared to the homogeneous sediment layers of RD42, RD54 shows more and finer intercalated layers. Micro-morphological analysis revealed poorly sorted angular to sub-rounded grains with great range in particle size throughout both cores. Microscopic analysis showed further that sorting, rounding and grain size composition varies continuously along the vertical profiles of both cores and larger homogeneous sections are restricted to the aquitards. As the field description revealed almost similar grainsize composition the laboratory analysis was only carried out for RD42. Differences between the two sediment cores occur only in terms of position and location of the intercalated layers that vary somewhat in depth, thickness and frequency (Fig. 23).

Since statements from this thesis are partly derived from comparisons with results from previous studies, it is important to consider the **nomenclature used in the various publications**. Note that yellow-brown aquifer sands of this study most likely match the “orange samples” of previous studies (Berg 2007; Eiche 2009; van Geen et al., 2013). This is mainly related to the fact that interface sediments were described for the first time in this study. These samples show much stronger colours and since this study focused on analysing sediments in high resolution it was necessary to make further subdivisions to describe the samples.

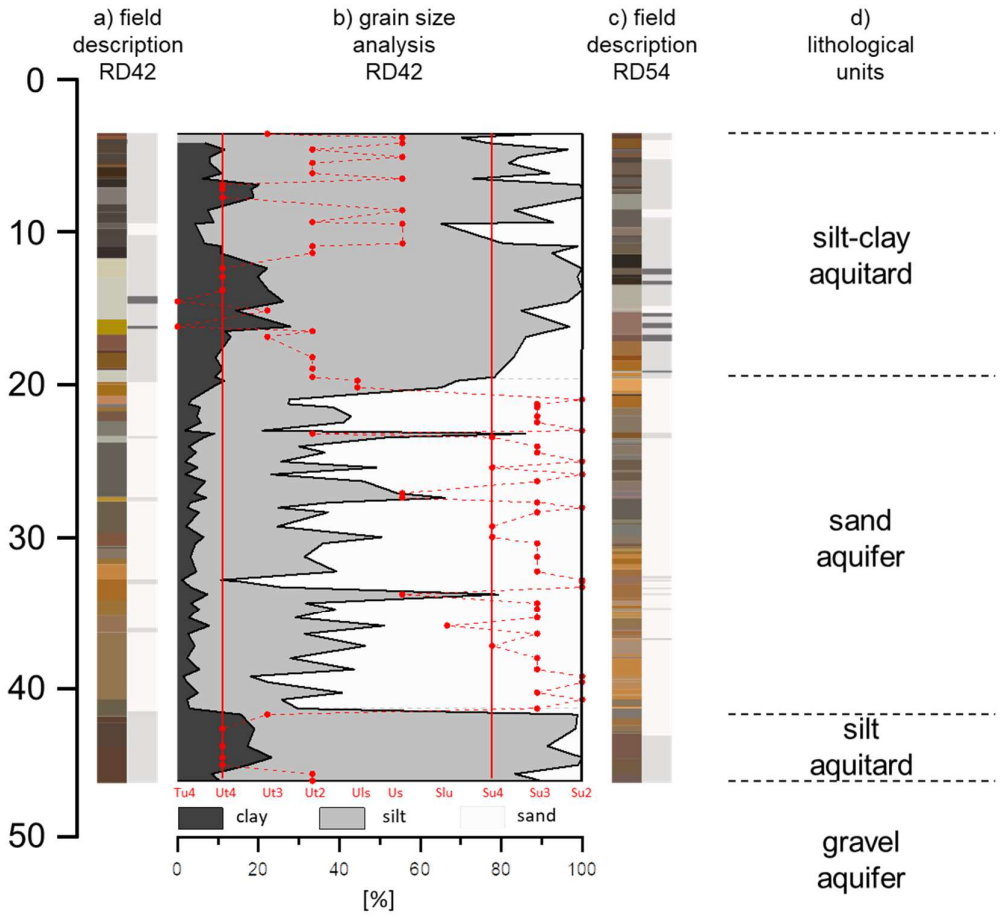

Figure 23: Vertical colour and grain size gradient of RD42 & RD54

a) field description of core RD42: left bar shows Munsell colours, right bar shows dominant grain size (clay, silt or sand) determined by finger probe. b) grain size composition (percentage of clay, silt and sand) of RD42 based on sieving & laser granulometry (n=78). In red the division into one of 10 present grain size classes corresponding to German classification system (KA5). c) field description of core RD54: left bar shows Munsell colours, right bar shows dominant grain size (clay, silt or sand) determined by finger probe. d) division of the cores into 4 lithological units

The **top aquitard** spreads to 19.5 m bgs for both cores (RD42, RD54). The dominant grainsize of the section determined on core **RD42** is silt with an average content of 75 % (n_{RD42}=28, 57-88 %) for the top 19.5 m. The clay content varies between 4 and 28 % (n=28) with an average of 13 %. 18 samples contain more than 10 % clay and 8 samples stand out with a clay content between 18 and 28 %. From 6.5-8 m and 12-15 m bgs two distinct clay layers are present with 26-28 % clay, 70 % silt and less than 4 % sand and intersect the silt unit (Fig. 23). The clay layers contrast with their bright beige colour significantly from the predominantly dark grey to black organic-rich silt layers above and the brown to yellowish silt layers below 15.5 to 19 m bgs (Fig. 24 & 25). The sand content in the top aquitard shows substantial variations with 0-34 % and averages 13 %. There are nine layers with a sand content between 20 and 35 % with an average of almost 27 %. Five are in the first 10 m and form well-permeable layers, especially between 8.5 and 10 m bgs. The remaining four samples represent the transition to the aquifer. Below 16.5 m the silt content continuously decreases and at around 19.5 m depth sand dominates. From 16.5 to 21 m bgs the sand content gradually increases from below 10 to above 70 % and continuously increases the permeability of the layers towards the aquifer. The average sand content of the other 21 samples lies at 7 % where the 15 samples with lowest sand content average 3.9 % and the lowest 11 samples 1.4 %. The aquitard is therefore mainly made up of poorly permeable silt-dominated layers. During field description thin sandy layers, which are less than 1 cm thick were identified throughout the whole aquitard in irregular sequences. Only the orange dotted beige clay layers (Fig. 24a) are free of intercalated sandy layers. The grain size analysis is not able to cover the recurring fine layers as sampling resolution could not reach the fine intervals. The usually less than a centimetre thick sandy layers have a potential to increase the permeability of the aquitard significantly if they form a connected network. Whether this is the case could not be determined in the course of the work. The silt layers are also regularly criss-crossed with thin clay layers. Like the sand layers, they occur irregularly, are usually only a few mm thick, and are only partially covered by the particle size analysis. However, they have also the ability to effect the permeability auf the aquifer unit. The top aquitard of core **RD54** differs from RD42 primarily in its finer lithological sequence. While the top aquitard of core RD42 is composed of 27 colour/grainsize units, 42 different units were documented in RD54. The biggest differences between the two cores occur with regard to the clay layers. While in core RD42 the characteristic beige clayey layers extend from 11.5-15.5m these layers are less pronounced in core RD54 and only extend from 13.3 to 15m bgs. In contrast, core RD54 shows more intercalated clay layers than core RD42, between 10 and 20 m bgs. But this are only minor differences with regard to the basic structure of the aquitard. The aquitard/aquifer transition is at the same depth in both cores and extends from about 19-19.5m. Also the overall colour sequence with mainly darker layers in the upper 12 meters, followed by beige and finally brownish layers at the transition to aquifer is similar in both cores (Fig. 24 & 25). The top aquitard of both cores is further characterized by regularly occurring clay and Fe concretions along sharp colour and grainsize transitions. The iron-clay concretion are particularly pronounced at the transition to the underlying aquifer where they reach a thickness of several cm and form a clearly visible hard layer (Fig. 24 b).

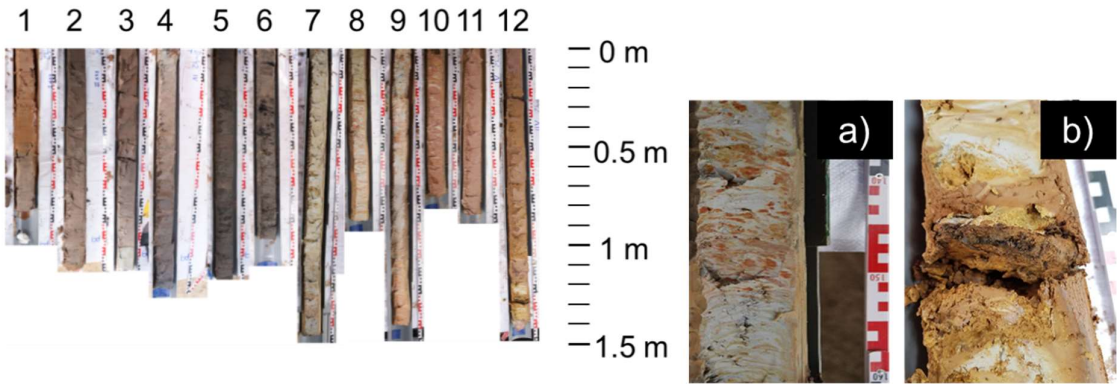

Figure 24: RD42 top aquitard core segments (run 1-12) from 3-19.5 m bgs

Particular striking are the black organic-rich layers in run 5 and 6 as well as the bright beige clay and clay-rich silt layers in run 7-9. The transition to the sand aquifer (run 10-12) is characterized by continuously increasing sand content and recurring clay and Fe concretions. Close up of a) clay to clay-rich silt layer of run 7 and b) clay-iron concretion near the transition of the top aquitard to the aquifer in run 12.

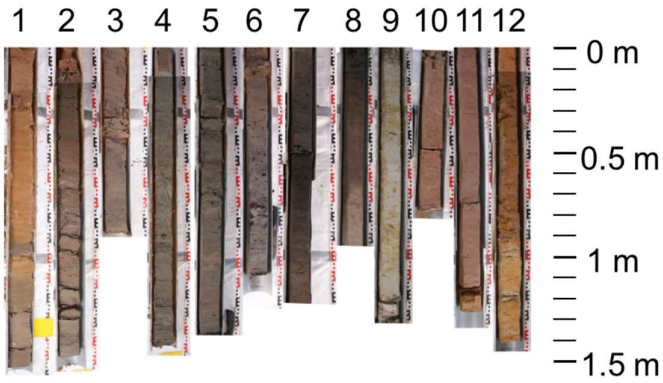

Figure 25: RD54 top aquitard core segments (run 1-12) from 3-19.5 m bgs

The core shows largely the same sequence as RD42 with varying layer thickness and stronger colours.

The central **sandy aquifer** reaches from 19.5 to 42 m for core RD42 and until 43 m bgs for core RD54. The average grain size composition determined on core RD42 is 63 % sand (n_{RD42}=41, 14-89 %), 33 % silt (10-77 %) and 4 % clay (1-9 %). Excluding four silty intercalations with in average 65 % silt, 7 % clay and 28 % sand (n=5) at 23, 27, 34 and 36m bgs (Fig. 23) the average sand content of the aquifer increases to 67 % while silt decreases to 30 % and the clay content drops below 4 % (n=37). In addition to the four silty layers further fine-grained layers with an average of 44 % silt and 6 % clay (n = 4) can be found in 23.5, 25.5, 30 and 37 m bgs. Within the aquifers of both two cores, the depositional conditions changes in mm to cm scales and numerous mm to cm thick fine-grained layers are intercalated periodically in the sandy matrix throughout the entire aquifer. They are present across the entire depth profile but only at 23, 27, 30, 34 and 36 m bgs the fine-grained layers reach an appreciable thickness of 20-50 cm and can clearly be separated by colour from surrounding sediments. These intercalated fingers contain significantly more silt and clay than the surrounding sediments, which predominantly consist of coarse sand. Due to limitations in sample resolution the numerous narrow, fine-grained layers in the mm-cm width are only partially covered by the grain size analysis. The same accounts for intercalated coarser layers with isolated pebbles which pervade the aquifer in the same irregular pattern although far less frequent (Fig. 26 & 27). Based on sediment colour the aquifers can be divided into three major segments which are referred as **aquifer units**:

1. grey sediments
2. yellow-brown sediments
3. transition sediments

A homogeneous sequence of grey reducing sediments expands from approx. 20 to 30m bgs and sits on top of yellow-brown less reduced sediments, which expand from approx. 30-40m. A grey sand layer also occurs at the bottom of the yellow-brown sand directly above the bottom silt aquitard at about 41 m depth. The grey and yellow-brown sediments are mainly composed of sand and have a good permeability. The third aquifer unit are transition sediments that occur at the interfaces between the grey and yellow-brown sediments and the boundaries the aquitards (Fig. 29 &30). The transitions sediments are characterized by distinct colour and grainsize gradients and clearly separate from the surrounding material with increased hardness. The colour spectrum of the transition sediments ranges from strong orange to brown and with regard to the grain size the layers reach least at 44 % silt while the sand content decreases accordingly. The kf-values of the silt-rich layers drops to an estimated range of 10^{-5} - 10^{-6} m/s. They are most pronounced in 19.5, 21, 23, 27, 30, 34 and 41 m bgs and coincide with colour and grain size boarders. Microscopic analyses on the mm to cm scale reveals an interplay of fine grey and yellow-brown layers and irregular occurring solid Fe and clay concretions. The concretions are responsible for the characteristic orange colouring and the increased hardness and can be recognized by eye. A close look at the transition sediments of the aquifer units reveals a network of preferential flow paths creating a complex fingering. Yellow-brown coloured as well as grey coloured flow paths pass several cm into the transition areas before the colours blend in with the surrounding material. As the colour change between the different aquifer units is sharp variations in the redox conditions within the aquifer seem to be largely controlled by differences in grain size composition and therefore hydrology. It is noticeable that the extent of the grey sediments between 20 and 30 m bgs is limited by the appearance of fine-grained transition sediments which frame the reduced grey area. The lower redox finger at 41 m bgs is also surrounded by fine-grained transition sediments. The yellow-brown sediments between 30 and 40 m bgs, apart from the colour, hardly differ from the grey sediments in terms of their grain size composition. Both consist mainly of well-drained sands and are criss-crossed by fine layers of deviant colour and grain size composition. Fine horizontal grey layers pervade the entire yellow-brown lower area of the aquifer between 30 and 40m bgs. Since the sequence of layers is irregular and small-scale, the naked eye impression of a homogeneous yellow-

brown section is wrong as in fact, the sediment composition and colour changes in the mm to cm scale. The thin layers with a thickness of a few cm are congruent to the prevailing grain size and thus permeability. The reduced grey layers are exclusively related to coarse sands while yellow and brownish colours are linked to finer grain size fractions. The recurring sequence of these layers leads to the pale yellow-brown colour in the lower part of the aquifer and is indicated in Fig. 29 and 30 by yellow and grey bars. The grey sediments between 20 and 30 m bgs also show grain sizes and colour variations, but are, in general much more homogeneously in structure. A slight stratification can only be seen in the upper part up to about 23.5m bgs, while most of the grey sediments below are largely homogeneous in colour and grain size. In this respect, both cores are largely identical with regard to grain size distribution. Based on sediment colour the aquifer redox process in core RD54 seem not to be as far advanced as in core RD42. The difference between the individual aquifer units are not as clear and a coherent grey redox front has not developed. Instead, reduced grey layers and less reduced yellow-brown and transition sediments alternate and form a complex fingering which however at no point achieve the high contrasts that occur in RD42 at depths of 22, 27 and 30 m. The pale yellow-brown aquifer sands between 20 and 22 m and below 30 m depth, are typical for the suboxic Holocene-Pleistocene fluvio-deltaic sand deposits while the grey sediments clearly indicate reducing conditions. In contrast, the strong coloured transition sediments indicate conditions that are more oxic (Eiche et al., 2008; van Geen et al., 2013).

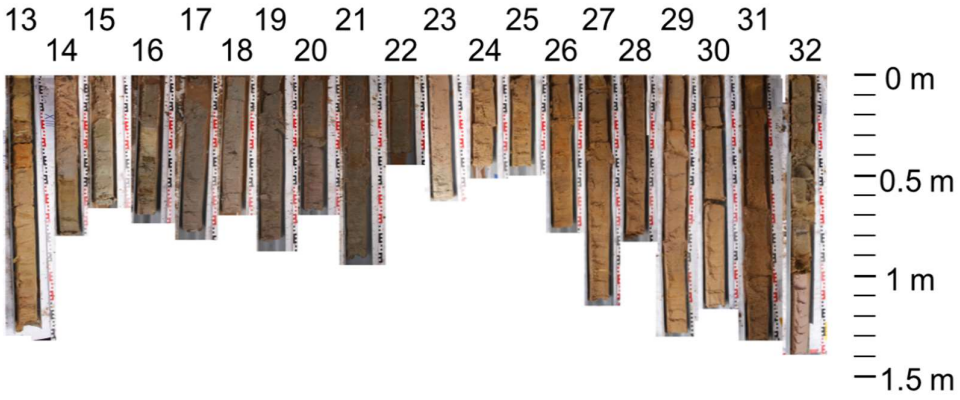

Figure 26: RD42 aquifer core segments (run 13-32) from 19.5-42 m bgs

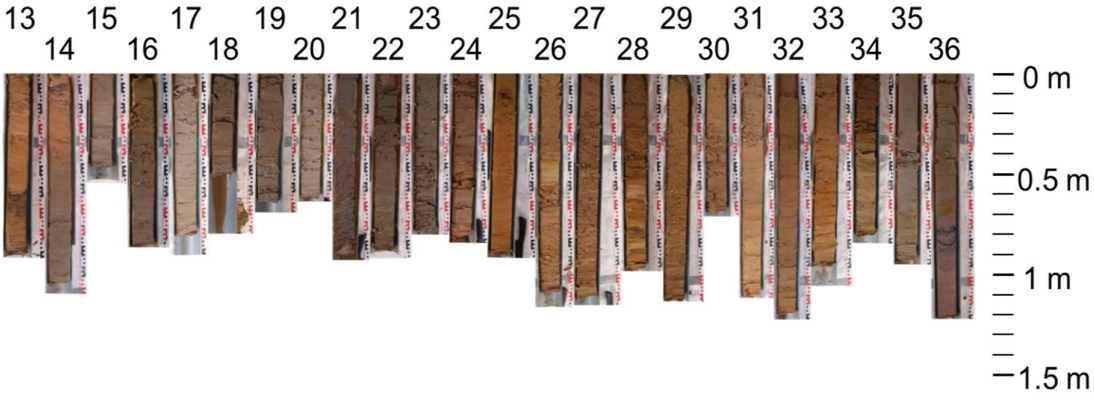

Figure 27: RD54 aquifer core segments (run 13-36) from 19.5-43 m bgs

The **bottom aquitard** consists almost completely of homogeneous pure brown silt from 42 up to 46.3 m bgs for core RD42 and 43 to 46.2 for core RD54 (Fig. 28 a & c). Based on grain size analysis of core RD42 the aquitard has an average silt content of 79 %. About 16 % is clay and the sand content is below 5 % (n_{RD42}=7). The four central samples average a sand content below 1 % and consist almost completely of silt and clay. Also the sand content increases towards the edges the permeability of this 3m thick layer has to be assessed as low. Derivation of the permeability coefficient K after DIN 4040-5 results in kf-values in the range between 10^{-5} - 10^{-8} m/s. Below 46m coarse gravel, which made deeper coring impossible (Fig. 28 b) marks the beginning of a **gravel aquifer**. All the results of the grain size analysis of core RD42 is available in Table 17 & 18.

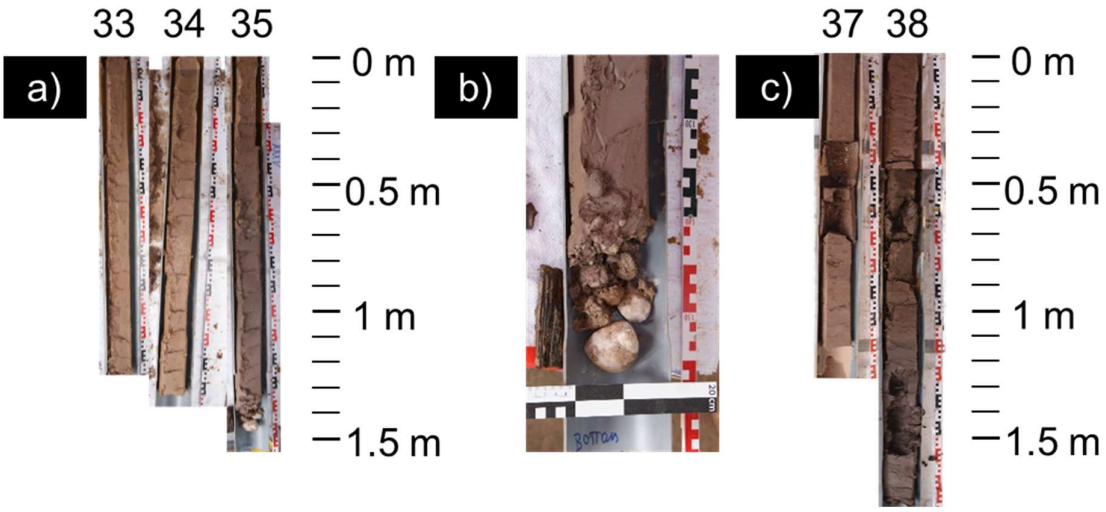

Figure 28: a) RD42 bottom aquitard core segments (run 33-35) from 42-46.3 m bgs. b) Close-up up of the transition from bottom aquitard to gravel aquifer at 46.3 m bgs in RD42 were coarse gravel stopped further coring. c) RD54 bottom aquitard core segments (run 37-38) from 43-46.3 m bgs

9.2 Sediment geochemistry

The geochemistry of the two cores is very similar along the depth profile and correlates well with the lithological and aquifer units described before. The elemental concentrations differ significantly across these units. Avergae concentrations of Fe_2O_3, Al_2O_3, P_2O_5 or As are clearly higher in the top and bottom aquitard compared to the aquifer. Within the aquifer the yellow-brown, grey and transition sediments each show a characteristic geochemical composition (Fig. 29 & 30 and Table 4). In a direct comparison the two drill cores RD42 and RD54 show comparable concentrations for most of the elements in the vertical profile. Therfore the division of the drill cores according to the geochemical results is consistent with the results of the lithological characterization. The complete geochemical results and information on the methods used are availible in Table 17-19.

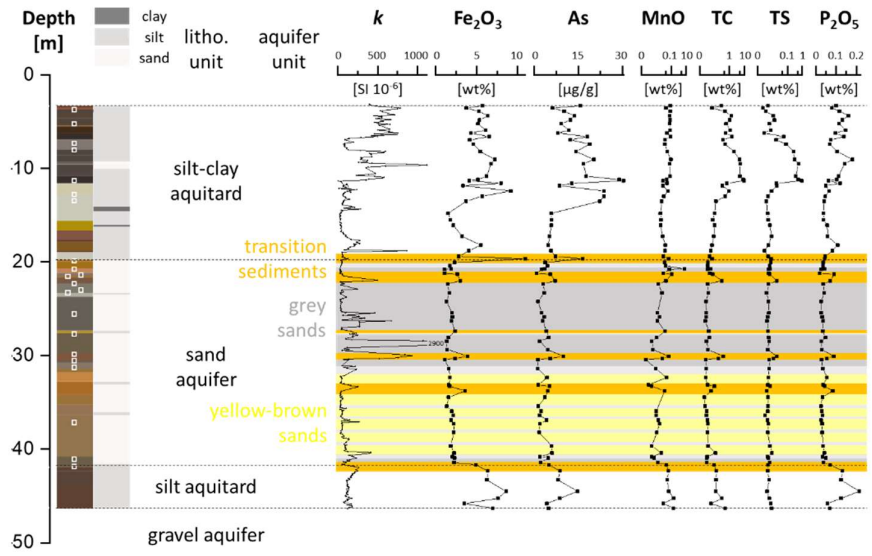

Figure 29: Sediment core RD42 with Munsell colours, dominant grain size, division into lithological and aquifer units, magnetic susceptibility log (k; n=349) and concentration of selected elements (n=74)

MnO, TC and TS have a logarithmic scale for better visibility, and k is cut off at 1000 x 10^{-6} SI. The white squares along the core profile indicate the position of the thin sections for optical investigation and spatially resolved measurements. Yellow, orange and grey colours indicate the aquifer units.

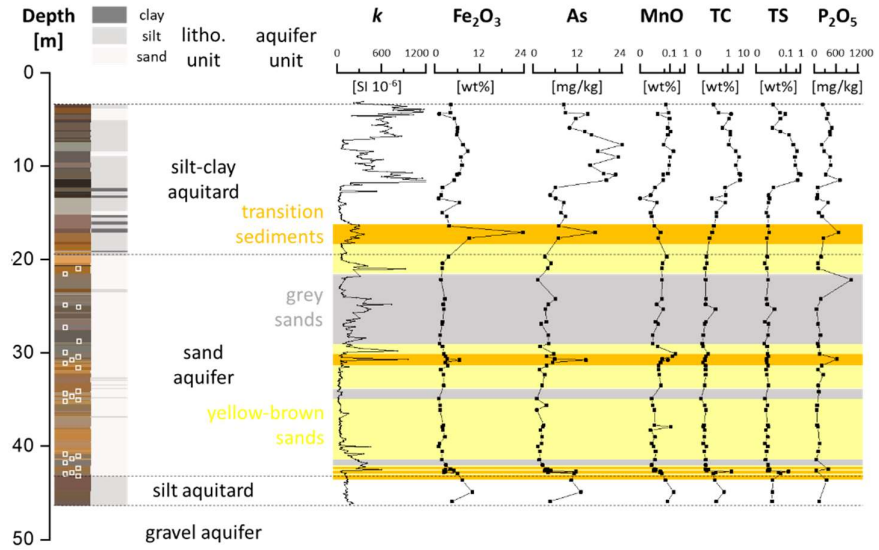

Figure 30: Sediment core RD54 with Munsell colours, dominant grain size, division into lithological and aquifer units, magnetic susceptibility log (k; n=374) and concentration of selected elements (n=69)

MnO, TC and TS have a logarithmic scale for better visibility. The white squares along the core profile indicate the position of the thin sections for optical investigation and spatially resolved measurements. Yellow, orange and grey colours indicate the aquifer units.

The geochemical composition of the upper and bottom **aquitards** is largely similar for both cores, with respect to the concentrations for the following elements (given as oxides): Fe_2O_3, MnO, Al_2O_3, TiO_2, MgO, Na_2O, P_2O_5, K_2O and SiO_2. However, the aquitards show clear differences with respect to TS, TC, CaO and As concentration, which are significantly lower in the bottom aquitards. The concentration of As and Fe are higher throughout the aquitards compared to the aquifer. The TC, TS, and P_2O_5 concentrations are also well above the aquifer concentrations (Fig. 29 & 30). The relatively high **As concentrations** in the upper aquitards of both cores are particularly noteworthy. In core RD42 in total the 29 samples average 13.8 mgAs/kg with 20 samples above 10 mg/kg which average of 17 mg/kg. The highest As concentrations with more than 30 mg/kg can be found in the dark organic-rich layers. The high values extend over the first 13.5 m until the concentrations decrease below the beige clay layers around 15 m bgs. The top aquitard of core RD54 averages 12.8 mg/kg As (n=23) with a maximum value of 24 mg/kg As and 7 samples from 7.5 to 11.5 m bgs average 20.2 mg/kg As. The As values below 13.5 m bgs are significantly lower (5.8 mg/kg n_{RD42} = 7) until they rise again at around 19.5 m bgs at the transition to the aquifer in RD42. The top aquitard in core RD54 shows the same basic trend. The As concentration decreases significantly below 12 m bgs before it increases again at the transition to the aquifer. In the depth between 12 and 19.5 m, the As concentrations average 6.9 mg/kg As (n = 8). An exception is the sample at a depth of 17 m with around 18.8 mg/kg As. The bottom aquitard of RD42 averages 7.8 mg/kg As (n=7). The four central samples average 10 mg/kg while the three outer samples and average with 4.7 mg/kg only half the As. Core RD54 averages 9.3 mg/kg As (n=3). Accorss all aquitards in both cores the As concentrations are closely linked to Fe, C, S and P_2O_5 concentrations. As and Fe_2O_3 concentrations show an almost identical course in both cores, which indicates a close association between the two elements. The **Fe_2O_3 concentration** is relatively high for boths cores and avergages almost 5 wt% for the top aquitard of RD42 (n=29) and almost 6 wt% for the top aquitard of RD54 (n=23). In the bottom aquitard the Fe_2O_3 cncentration is at 6.3 wt% for RD42 (n=7) and and 7.3 for RD54 (n=3). In the topping aquitard in particular, the Fe_2O_3 content is very unevenly distributed. In the top aquitard of RD54 the Fe-rich area extends from 5 to 12 m and avergages 6.5 wt% (n=11). Above and below the Fe content is sigificant lower until the Fe_2O_3 content rises again at the tranistion to the aquifer. In RD42 the increased Fe_2O_3 values are distributed more evenly and extend to a depth of 13 m with an average of 5.6 wt% (n = 21). Below the values also drop significantly until they rise again at the aquitard-aquifer transition. The juxtaposition of core RD42 and RD54 geochemical data reveals clear differences between the two cores only in the transition area between the upper aquitard and the aquifer from 16 to 22 m bgs where both the As and Fe peaks are about 3m offset. Both cores have the highest Fe_2O_3 concentrations in this upper transition sediments. In both cases, the high values can be assigned to well-developed Fe-concretions which, with their strong red-brown to organge colour, that clearly differs from the surrounding sediment. The As concentration follow a similar pattern.The **total carbon (TC)** content changes even more in the depth profile and significantly increased values are limited to a few depths in both cores. Particularly noticeable in the top aquitard of core RD42 are the depth levels between 9 and 12 m with an average of almost 7 wt% TC (n = 5). Although the carbon levels are high in the entire upper part of the top aquitard of RD42, the dark areas stand out particularly. The section consists almost entirely of organic carbon (OC). A total of 11 samples were analysed between 4 and 12 m depth for their OC content and revealed on average almost 90 % OC. Between 4 and 7 m depth, the OC content is around 70 % (n = 4). Between 8 and 12 m, the carbon consists almost entirely of organic carbon (98 % n = 7). The beige clays between 12 m (80 %) and 13 m (85 %) are dominated by inorganic carbon and create a clear contrast. Below the dark areas at around 11.5 m, the carbon content in the top aquitard of RD42 is significantly lower and shows an average of 0.3 wt% (n = 12) without strong fluctuations up to the aquifer transition. The average carbon concentration across the whole top aquitard of RD42 decrease to 1.6 % because the carbo content below 11.5 m bgs declines significantly towards the aquifer (0.3 % n = 12) until the concentration close

to the aquifer are well below 0.1 %. The bottom aquitard of RD42 has with on average 0.2 wt% significantly lower TC contents without major variations in concentration. While at the transition to the sand aquifer above the carbon consists entirely of organic carbon, the transition to the gravel aquifer below has only 16 % organic carbon. RD54 shows a similar picture in terms of Tc concentration. In the upper aquitard, layers between 8 and 12 m also stands out with particularly high TC content of 5.3 wt% (n = 6) in average. The upper 12 m show higher values overall and towards the aquifer the c concentration decreases significantly, which leads to an average of 1.8 wt% (n = 23). The bottom aquitard shows significantly lower concentration with 0.28 wt% (n = 3). The **total sulphur** (TS) content largely follows the trend of carbon in both cores. In RD42 the highest TS concentration with an average of around 0.5 wt% are between 8 and 11 m (n = 6). The areas of 12 m have an average of 0.166 wt% TOS while the depth between 12 and 19 m only has 0.006 wt% (n = 10). The average for the total aquitard is 0.111 (n = 29). The lower aquitard of RD42 shows significantly lower concentration with an average of 0.006 wt% (n = 7). In RD54 the highest values are between 6 and 12 m bgs and show an average of around 0.5 wt% (n = 8). The concentrations are generally higher in the upper area of the aquitard than near the aquifer. Between 13 and 19 m depth the average is only 0.007 (n = 8) which leads to an overall average for the upper aquitard of 0.2 (n = 23). In the lower aquitard of RD54 the TS concentrations are on average at 0.01 (n = 3). The **total nitrogen** (TN) content determined in core RD42 largely coincides with the depth profile of the TC and TS. The highest concentrations occur in the upper aquifer between 5 and 12 m depth. The maximum content of 0.18 and 0.23 wt% (n = 5) can be found in the dark organic-rich silt layers between 8 and 12 m bgs. In the further vertical course, the TN concentration is continuously between 0.01 and 0.06 wt%, on average 0.03 wt% (n = 12). The overall average of the 23 samples over the depth profile of RD42 is 0.08 wt%. The high TC, TS and TN concentrations can be related to the high proportion of embedded organic material in different states of decomposition that permeate the fine-grained clay and silt layers. The organic material gives the sediment of both drill cores in the upper 12m (RD42) and 13m (RD54) their dark colour. The organic material is mostly present as a greasy, no longer identifiable black mass. Occasionally, however, fossils and well-preserved plant residues (root remains and pieces of wood) could also be documented. Combined analysis of **TOC-TN ratio** and $\delta^{13}C$ **‰** in RD42 allow to assign individual core sections to a deposition environment and to classify them chronologically. The bright layer from 7 to 8 m bgs shows a C/N ration of 9 and a $\delta^{13}C$ of -27.4 what points to freshwater plankton and therefore fluviatile environment and was deposited most likely about 5 kyr BP. The results (C/N: 2-3; $\delta^{13}C$: -35-50) suggest that the dark organic-rich sediments with high concentrations of C, S and P_2O_5 from 8 to 11.5 m bgs derive from C3-plants of a mangrove forest or comparable estuarine sediments. A corresponding event can be dated to a period between 8 and 5 kyr BP (Tanabe et al., 2003 & 2006; Nguyen 2006, Funabiki et al., 2007). The beige As-rich clays directly beneath from 12 to 13.5 m bgs which can be clearly separated by colour from surrounding sediments could be assigned to a marine environment. The only sediments, which show high inorganic carbon concentrations and are low in S and P_2O_5. The contrasting geochemistry is a clear indication for changing depositional conditions. C_{org}/TN ratio of 2-3 and $\delta^{13}C$ of -22-23 ‰ confirm these beige deposits origin from marine phytoplankton related to a marine transgression. A marine transgression can be dated to a period between 9 and 6.5 kyr BP. Based on other results from the greater area an age of 8.5 kyr BP is likely (Tanabe et al., 2003 & 2006; Nguyen 2006). C/N ratio and $\delta^{13}C$ could only be determined to a limited extent in the aquifer due to the lack of sample material. Only in the upper part of the aquifer at a depth of 21m bgs two samples could be assigned to a fluviatile freshwater environment (C/N: 4; $\delta^{13}C$: -26.8‰). However, no deposition age could be assigned to these samples due to a lack of dating. It remains to be noted that the majority of sediments is related to freshwater deposition. This applies in particular to the entire aquifer. The position of the boundary between Holocene and Pleistocene sediments was not be determined in this study.

Within the **aquifer**, the geochemical results show a characteristic three-part division that corresponds to the division from the lithological description (Fig. 23). In the aquifer average, the element concentrations for all elements except SiO_2 are lower than in the two aquitards in both cores. Especially with regard to the **As and Fe_2O_3 concentrations** the aquifer geochemistry shows significantly lower values. The average As content is 3.9 mg/kg and the average Fe_2O_3 content is 2.2 wt% (n = 38) for core RD42 and 3.9 mg/kg As and 2.5 wt% Fe (n = 40) for core RD54. A special feature of both aquifers are high internal variations for most element concentrations. In particular, the Fe_2O_3 and As concentrations fluctuate strongly in the vertical profile. Corresponding to variations in sediment colour and grainsize distribution the solid phase composition varies largely in both cores. In RD54 the Fe_2O_3 aquifer concentration varies between 1.0 and 6.5 wt% in for most parts of the aquifer and between 1.0 and 4.0 wt% in core RD42. Significantly, higher concentrations are achieved in the transition sediments. In particular, the upper aquifer-aquitard transition shows very high Fe concentrations peaking at remarkable 11 wt% (RD42) and 24 wt% (RD54). The aquifer As concentrations largely correlate with the Fe concentrations and vary in both cores between 1 and 17 mg/kg. The highest As concentrations above 16 mg/kg are also found in the upper aquifer-aquifer transition in both cores. The **TC and TS** aquifer averages are low (RD42: TC 0.061, TS 0.006; RD54: TC 0.081, TS 0.001) but show some variation and increase significantly towards the transition sediments. MnO averages 0.04 wt% in the aquifer of RD42 and the course in the depth profile correlates with the depth profile of As and Fe and increased concentrations are mainly found at the colour and grain size boundaries. All three elements show peak concentrations at 20, 21, 27, 30 and 34 m bgs. The silt and silt-rich layers described in the previous chapter also show higher concentrations of characteristic elements such as Al_2O_3, MgO, TiO while the SiO_2 concentration decreases. The elements usually associated with PS in near-surface sediments vary according to the lithology and support the initial description. Also CaO has the highest concentrations in the transition sediments. The two dark brown layers at depths of 21 and 30 m in RD42 have high levels of TC, TS and TN that are otherwise only to be found in aquitards. At a depth of around 20.5 m there is an isolated MnO peak with 0.8 wt%, the highest Mn concentration in the entire profile. It is located directly under the transition to the aquitard above. Otherwise, the element distribution in the aquifer follows the described pattern. The comparison of RD42 and RD54 reveals only slight differences in the avergae element concentrations in the course of the aquifer sediments. Both cores show, recurring, increased As, Fe and Mn concentrations, which can usually be located in a fine-grained layer that also differs in colour from the surrounding material. The position of some of these layers is varies soewhat between the two drill cores but the significantly increased As, Fe and Mn concentrations along the redox and lithology boundaries are common to both cores. Like RD42, RD54 shows significantly increased As and Fe concentrations along the aquitard-aquifer boarders and the redox boundary in around 30 m. When comparing the two cores, there are slight differences in the position of the peaks in the depth profile. In the upper aquitard-aquifer transition, the maximum Fe_2O_3 and As concentrations in RD42 are around 20 m, around 3 m lower than in RD54. The silt layers in depths of 21 and 27 m do not appear in core RD54 and the geochemical analysis of RD54 shows a horizon with increased Fe, As, Mn, TC and TS concentrations at a depth of around 25m. However, the location does not differ from the surrounding sediments in terms of grain size or colour. The reduced grey area of core RD54 is only crossed once by a brown silt layer at a depth of around 23m, which geochemically, however, is only minimally different from the surrounding area. The transition between the grey and yellow-brown sands is as in core RD42 at a depth of 30 m. In contrast to RD42, the geochemistry of RD54 shows a broader transition area with 3 sections. A clear Fe peak at around 29.5 m bgs is followed by an equally clear and isolated Mn peak. Both show no correlation to As. It is the only example in both aquifers that a significant increase in the Fe content does not go hand in hand with an increase in the As concentration. Otherwise, both elements are closely linked. Below this follows a third horizon in around 30.5 with increased Fe_2O_3, MnO and As concentrations. A further

isolated Mn peak follows at a depth of around 38 m. Below the reduced finger at a depth of around 41 m, the Fe_2O_3 and As concentrations finally rise again on the transition to the lower aquitard. A Mn layers is also included in the lower transition area of RD42 at a depth of around 32 m and especially well pronounced in the top transition area around 20.5 m bgs. The isolated Mn-peaks at the edge of the reduced zone are always embedded in-between two Fe-rich layers. The aquifer pattern is very similar for both sediment cores. The comparison of the two drill cores reveals the same picture with large internal variations coupled to lithology and sediment colour as indicator for redox conditions.

The **transition sediments,** located along the entire colour-indicated redox interface can be clearly distinguished from the surrounding sediments. They either separate the grey and yellow-brown aquifer sediments or mark the boarder of the lithological units. In terms of geochemistry, the transition sediments are characterized by the highest Fe and As concentrations, some of which are 3 to 5 times higher than the concentrations of the immediately adjacent sediments. In **RD42**, the transition sediments frame the redox front and are present at depths of 20, 21, 27, 30, 34 and 41m. Geochemical results confirm the visual identification and validate the observation that transition sediments are best developed at the upper and lower end of the central redox front, where the spread of the redox front seems to be limited by the occurrence of finer grain sizes. The significant increase in As and Fe concentrations along the redox boundaries is remarkable. Especially at the upper aquitard-aquifer transition around 20 m bgs where redox and grain size boundaries coincide, extremely high Fe_2O_3 (11 wt%) and As (16 mg/kg) concentrations were detected. With around 4 wt% Fe_2O_3 and 20 mg/kg As, the lower end of the reduced area at 30 m bgs also stands out very clearly from the surrounding sediments. The fingers in the reduced layers at depths of 21 and 27 m show concentrations up to 3 wt% Fe_2O_3 and 7 mg/kg As. The transition sediments at depths of 21 and 30 m differ from the surrounding material by increased MnO, TC, TS and TN concentrations indicating organic material. The high proportion of organic carbon reinforces this impression. The highest TS concentration reach 0.02 wt% and the maximum TC concentration 0.39 wt%. The horizon at a depth of 34 m contains As (4.6 mg/kg) and Fe 3.6 (wt%). It is the only layer that is not directly associated with adjacent grey sediments and seems to belong to the lower redox transition. At the lower aquifer-aquitard transition at a depth of 41m, the Fe content in the sediment increases drastically along the redox and grain size boundary. As in the layer at 20 m bgs, Fe concretions could be documented in the lithological description that match the geochemical data. At the upper aquitard-aquifer transition at 20 m, a well-developed laterite layer could be assigned to the extremely high Fe_2O_3 concentration of 11 wt%. **RD54** shows the same picture. The transition sediments primarily border the grey layers between 20 and 30 m and at a depth of 41 m. The depth of the upper aquifer-aquifer transition varies somewhat and the maximum Fe concentrations of 24 wt% between 17 and 18 m depth are associated with As concentrations of approximately 17 mg/kg. The position of the remaining transition sediments largely coincides with core RD42. At a depth of around 30 m, the transition sediments of core RD54 contain almost 7 wt% Fe and around 14 mg/kg As. The lower aquifer-aquitard transition with around 5 wt% Fe and 5 mg/kg As is roughly in the same range as in RD42. In comparison to RD42, the transition sediments are limited to three horizons. The upper and lower redox and grainsize boundary along the upper and lower aquitard-aquifer transition and the redox boundary at 30 m bgs. RD54 shows comparable TS concentrations with a maximum of 0.02 wt%. The TC content of 0.15 wt% is slightly lower than in core RD42. The high TC and TS concentrations in core RD54 are limited to a layer at a depth of 25 m.

The **reduced grey sediments** show significantly concentrations for most elements in comparison to the other aquifer units and form a nearly coherent redox front between 20 and 30 m bgs. Compared to adjunct transition sediments the Fe_2O_3 and As concentrations are only around a third in RD42. For RD54 the difference is even greater. The grey sediments of RD54 contain only a fifth of the Fe_2O_3 concentration of the transition sediments and less than a third of As (Table 4). While the grey layers in

core RD42 only contain a fifth of the MnO, the difference in RD54 is only around 50 %. The same applies to the CaO concentrations. While an increase of around 300 % can be observed in RD42 from the grey to the transition sediments, the difference in RD54 is only around 15 %. The TS content in the transition sediments is around twice as high as in the grey sediments in both cores. The TC content in RD42 in the transition sediments is increased by a factor of 5 compared to the grey ones, while RD54 only shows an increase of 50 %. The element concentrations of the grey sediments are very low for sandy aquifer sediments in SSEA. In particular, the As (2.6 mg/kg RD42, 3.1 mg/kg RD54) and Fe_2O_3 (1.4 wt% RD42, 1.8 wt%) concentrations are far below typical literature values for delta sediments (Polizzotto et al., 2008; Benner & Fendorf 2010). The combination of geochemistry and lithological description clearly shows that the central redox front in core RD42 forms a homogeneous area. RD54, on the other hand, shows a heterogeneous structure between 20 and 30 m bgs with numerous easily distinguishable layers. In addition, core RD54 shows some greyish layers between 34 and 37 m depth, which indicate reducing conditions and do not occur in core RD42.

In the **yellow-brown sediments** of RD42, the element concentrations for As, Fe, Mn, Al_2O_3 and CaO lie almost exactly in the middle between the grey and transition sediments. The P_2O_5, TC and TS concentrations of the yellow-brown sediments are only slightly higher than the grey sediments and increase to the transition sediments by a factor of about 3 for P_2O_5 and TS and about a factor of 4 for TC. In RD54 As and Fe_2O_3 show a comparable trend while Mn, CaO and TS in the yellow-brown and the transition sediments are about the same. The TC content in the yellow-brown sediments of RD54 is even twice as high as in the transition sediments. The relatively high average TS and TC content in the yellow-brown sediments of core RD54 are related to an organic-rich layer at a depth of 43 m. If this layer is excluded the values fit into the pattern previously described. Compared to the grey sediments of RD54, the yellow-brown sediments show significantly higher concentrations for all elements. Al_2O_3 and P_2O_5 were not determined in RD54. The average element concentrations are in a low range compared to typical clastic near-surface sedimentary aquifers. This is especially true for As and Fe_2O_3. The yellow-brown sediments occupy the entire aquifer range below 30 m, but also occur above the redox front between 19 and 22 m and may represent the initial aquifer sediments but are most likely also affected by recent redox processes. The significantly increased standard deviation especially for As and Fe_2O_3 (Table 4) in the transition sediments of the two cores can be attributed to the high spatial heterogeneity of the samples. The Fe- and As-rich transition sediments often appear as fine layered structures that could not be sampled separately. As a result, the analyses reveal a broad range of concentrations.

Table 4: Dominant grain size and solid phase geochemistry of lithology and aquifer units of sediment core RD42 and RD54

Bold numbers give the average concentrations with standard deviation (SD) in brackets and range of values below. Numbers on the left give number of analyzed samples.

n_{RD42}	unit	sediment type	dominant grain size	As	Fe_2O_3	MnO	Al_2O_3	CaO	P_2O_5	TS	TC
				[mg/kg]	[wt%]						
29	aquitard	beige to black top silt	silt (75%)	**13.6** (7.18) 4.8-30.3	**4.9** (1.77) 1.5-9.2	**0.05** (.03) 0.02-0.09	**15.2** (2.87) 9.4-20.6	**0.62** (.53) 0.1-1.7	**0.09** (.04) 0.04-0.18	**0.111** (.22) 0.002-0.913	**1.61** (2.52) 0.05-9.68
8	aquifer	orange redox interface	sand (50%)	**7.3** (3.87) 4.2-16.5	**4.2** (2.68) 2.3-11.0	**0.05** (.03) 0.03-0.11	**9.8** (2.95) 6.1-16.2	**0.28** (.18) 0.1-0.7	**0.07** (.02) 0.03-0.09	**0.010** (.01) 0.004-0.019	**0.15** (.12) 0.04-0.39
20		yellow-brown sand	sand (70%)	**3.2** (1.50) 1.3-6.0	**1.9** (.33) 1.1-2.3	**0.06** (.17) 0.01-0.79	**6.4** (1.50) 4.1-11.6	**0.19** (.07) 0.1-0.3	**0.04** (.01) 0.03-0.08	**0.006** (.00) 0.003-0.009	**0.04** (.02) 0.02-0.12
11		grey sand	sand (66%)	**2.6** (1.26) 1.0-4.9	**1.4** (.32) 1.1-2	**0.01** (.01) 0.01-0.03	**5.3** (.90) 4.1-7.1	**0.10** (.02) 0.08-0.13	**0.03** (.01) 0.02-0.05	**0.005** (.00) 0.004-0.005	**0.03** (.01) 0.02-0.05
6	aquitard	brown bottom silt	silt (79%)	**7.8** (3.39) 4.3-14.7	**6.3** (1.58) 3.5-8.6	**0.08** (.04) 0.03-0.15	**15.9** (2.72) 12.0-19.9	**0.28** (.05) 0.2-0.34	**0.11** (.05) 0.06-0.21	**0.006** (.00) 0.004-0.009	**0.20** (.16) 0.06-0.53

n_{RD54}	unit	sediment type	dominant grain size	As	Fe_2O_3	MnO	Al_2O_3	CaO	P_2O_5	TS	TC
				[mg/kg]	[wt%]						
21	aquitard	beige to black top silt	silt	**12.9** (6.00) 4.6-24.1	**4.8** (2.23) 1.0-8.8	**0.05** (.05) 0.01-0.18	-	**0.84** (.55) 0.20-1.90	-	**0.217** (.29) 0.005-0.990	**2.02** (2.28) 0.09-6.60
6	aquifer	orange redox interface	sand	**9.6** (4.82) 3.9-16.8	**9.1** (6.69) 4.1-23.7	**0.03** (.02) 0.01-0.07	-	**0.28** (.09) 0.10-0.40	-	**0.013** (.01) 0.005-0.045	**0.06** (.03) 0.03-0.11
23		yellow-brown sand	sand	**3.6** (2.11) 1.2-5.9	**2.4** (.63) 1.0-3.6	**0.04** (.05) 0.01-0.07	-	**0.31** (.08) 0.16-0.45	-	**0.014** (.03) 0.004-0.150	**0.12** (.35) 0.02-1.74
13		grey sand	sand	**3.1** (1.47) 1.0-6.0	**1.8** (.46) 1.1-2.7	**0.02** (.01) 0.01-0.04	-	**0.24** (.06) 0.19-0.39	-	**0.006** (.00) 0.004-0.007	**0.04** (.03) 0.02-0.15
3	aquitard	brown bottom silt	silt	**9.3** (3.45) 4.6-12.9	**7.3** (2.23) 4.6-10.0	**0.10** (.06) 0.05-0.18	-	**0.35** (.05) 0.32-0.42	-	**0.012** (.00) 0.012-0.013	**0.28** (.19) 0.13-0.55

The analysis of the geochemical data using **descriptive statistics** reveals clear differences in the correlation between elements of the different lithological and aquifer units and supports the previously described observations (Table 5). For the entire vertical profile, there are positive correlations for both cores for As with TC (RD42 r=0.71, RD54 r=0.77), TS (RD42 r=0.63, RD54 r=0.71) and Fe_2O_3 (RD42 r=0.69, RD54 r=0.62). In addition, a correlation with aluminium (r=0.75), titanium (r=0.69) and magnesium (r=0.69) could be observed in RD42. These elements could point towards the presence of PS. If the lithological units are considered separately, there are clear differences for the aquifer and the aquitards (top and bottom aquitard combined). While As is mainly correlated with Fe in both aquifers (RD42 r=0.85, RD54 r=0.75), the aquitards show the highest correlation with TC (RD42 r=0.71, RD54 r=0.79) and TS (RD42 r=0.65, RD54 r=0.80). Within the aquifer**,** the different aquifer units also show clear differences. In the transition sediments, As shows a high correlation with Fe in both cores (RD42 r=0.89, RD54 r=0.70) and with phosphorous (P) in RD54 (r=0.82). The grey sediments show only a relatively low correlation of As with all considered elements. For Fe the correlation is r=0.47 in RD42 and r=0.52 in RD54. In core RD42 As instead shows a strong correlation with P (r=0.76) in the grey sediments. The yellow-brown sediments also differ significantly from the other aquifer units. For As, similar to the aquitards, the yellow-brown sediments show the highest correlation with TC (RD42 r=0.55, RD54 r=0.82), TS (RD42 r=0.63, RD54 r=0.81) and P (RD42 r=0.50, RD54 r=0.59). The comparison of the two sediment cores reveals a comparable picture. Clear differences emerge only for the correlation of As with P in the transition sediments and the grey sands.

Table 5: As correlation with other elements within lithology and aquifer units of sediment core RD42 and RD54

whole core correlation RD42 (n=74)										
Arsenic	Al	C	Ti	Mg	Fe	S	P	Ca	Mn	Pearson
	0,75	0,71	0,69	0,69	0,69	0,63	0,53	0,44	0,08	
	C	Fe	Al	Mg	Ti	P	Mn	Ca	S	Spearman
	0,88	0,80	0,79	0,79	0,78	0,78	0,64	0,49	0,45	
aquifer (n=38)										
Arsenic	Fe	Ti	S	C	Al	P	Mg	Ca	Mn	Pearson
	0,85	0,60	0,53	0,52	0,51	0,51	0,47	0,30	0,08	
	P	C	Fe	Mn	S	Mg	Al	Ti	Ca	Spearman
	0,70	0,66	0,57	0,47	0,46	0,39	0,35	0,35	0,24	
top + bottom aquitard (n=36)										
Arsenic	C	S	Mg	Ti	Fe	Ca	P	Al	Mn	Pearson
	0,71	0,65	0,38	0,38	0,35	0,21	0,14	0,14	0,03	
	C	Al	S	Mg	Fe	Ca	Ti	P	Mn	Spearman
	0,75	0,53	0,47	0,47	0,41	0,40	0,40	0,26	0,26	
transition sediments (n=8)										
Arsenic	Fe	Ti	Mn	S	C	Al	Ca	Mg	P	Pearson
	0,89	0,33	0,28	0,27	0,17	0,01	-0,04	-0,12	-0,21	
	S	C	Fe	Mn	Ca	P	Ti	Al	Mg	Spearman
	0,81	0,62	0,52	0,43	0,19	0,05	0,02	0,00	-0,19	
grey sediments (n=11)										
Arsenic	P	Ca	Fe	Ti	C	Al	Mg	Mn	S	Pearson
	0,76	0,50	0,47	0,26	0,26	0,26	0,24	0,00	-0,43	
	P	Fe	Ca	Al	C	Mg	Ti	Mn	S	Spearman
	0,81	0,61	0,58	0,36	0,34	0,28	0,24	0,18	-0,54	
yellow-brown sediments (n=20)										
Arsenic	S	C	P	Fe	Ca	Ti	Al	Mn	Mg	Pearson
	0,63	0,55	0,50	0,15	0,09	0,08	0,07	0,06	0,04	
	S	P	C	Mn	Fe	Al	Mg	Ti	Ca	Spearman
	0,58	0,49	0,49	0,27	0,22	0,08	0,05	0,04	0,01	

whole core correlation RD54 (n=66)										
Arsenic	C	S	Fe	P	Mn	Al	Ti	Mg	Ca	Pearson
	0,77	0,74	0,62	0,46	0,38	-	-	-	-	
	C	Fe	S	P	Mn	Al	Ti	Mg	Ca	Spearman
	0,77	0,70	0,66	0,59	0,50	-	-	-	-	
aquifer (n=42)										
Arsenic	Fe	S	C	P	Mn	Al	Ti	Mg	Ca	Pearson
	0,75	0,41	0,38	0,37	0,16	-	-	-	-	
	Fe	Mn	C	P	S	Al	Ti	Mg	Ca	Spearman
	0,63	0,42	0,38	0,33	0,21	-	-	-	-	
top + bottom aquitard (n=24)										
Arsenic	S	C	Fe	P	Mn	Al	Ti	Mg	Ca	Pearson
	0,80	0,79	0,56	0,56	0,35	-	-	-	-	
	S	C	Fe	P	Mn	Al	Ti	Mg	Ca	Spearman
	0,84	0,78	0,62	0,59	0,52	-	-	-	-	
transition sediments (n=6)										
Arsenic	P	Fe	Mn	C	S	Al	Ti	Mg	Ca	Pearson
	0,82	0,70	0,66	0,48	0,12	-	-	-	-	
	Fe	Mn	P	C	S	Al	Ti	Mg	Ca	Spearman
	0,83	0,77	0,40	0,31	-0,09	-	-	-	-	
grey sediments (n=13)										
Arsenic	Fe	Mn	C	S	P	Al	Ti	Mg	Ca	Pearson
	0,52	0,22	0,07	0,06	-0,32	-	-	-	-	
	P	Fe	Mn	S	C	Al	Ti	Mg	Ca	Spearman
	0,36	0,34	0,06	-0,03	-0,10	-	-	-	-	
yellow-brown sediments (n=23)										
Arsenic	C	S	P	Fe	Mn	Al	Ti	Mg	Ca	Pearson
	0,82	0,81	0,59	0,40	0,21	-	-	-	-	
	Fe	Mn	C	P	S	Al	Ti	Mg	Ca	Spearman
	0,64	0,61	0,48	0,44	0,24	-	-	-	-	

9.3 Magnetic core profiles

Volume, mass and temperature dependent magnetic susceptibility were recorded to identify individual mineral phases (temperature dependent susceptibility measurement) and distinct between para, ferro and ferrimagnetic Fe mineral classes (volume and mass dependent susceptibility measurement) (Tarling & Hrouda 1993). Accordingly the combined volume and mass dependent susceptibility parameters reflect the type and amount of magnetic minerals in the sediment and therefore, its lithology (Horneman et al., 2004) and can be used to describe and subdivide the sediment cores. **Volume susceptibility (*k*)** was measured in field every 10 cm along both vertical core profiles (Fig. 31) and revealed largely similar magnetic profiles for both cores. Both the course in the depth profile and the range of values are largely analogous for RD42 and RD54 and correspond to the Fe_2O_3 solid phase content (Fig. 29 & 30). Both profiles show significant fluctuations along the vertical profile that can be linked to the lithology and aquifer units described in chapter 9.1 and 9.2. The course widely matches the previous lithological and geochemical parameters and supports the classification of lithology and aquifer units. The observed *k*-range indicates that Fe is predominantly bound in paramagnetic minerals such as (phyllo-) silicates and carbonates along both core profiles. Since the method is not able to map the entire Fe mineral inventory, the results are not to be understood as a comprehensive inventory. The totality of the Fe phases can only be achieved by combining the measurements with other methods. Both the lithological and the aquifer units can be distinguished based on the value ranges. Volume susceptibility measurements reveal that the combined aquitards of RD42 (top and bottom) have with 241.8 x 10^{-6} SI (n=185) significantly higher average values than the aquifer. The wide range of values with 6-1120 x 10^{-6} SI within the aquitard sediment is striking and matches the heterogeneity of the sediments of variable depositional conditions in cm-scale described before. With an average of 271 x 10^{-6} SI (240 SD) (n = 142), the top aquitard is significantly higher than the bottom aquitard, which shows in average 144 x 10^{-6} SI (45 SD) (n = 43). Within the top aquitard, the beige-coloured clay intercalations (average 88 x 10^{-6} SI, 62 SD) and the dark, organic-rich sediments (359 x 10^{-6} SI average; 224 SD) can be clearly distinguished. The highest values all occur in the dark organic-rich upper 12 m and refer to ferrimagnetic Fe minerals like Mt (Tarling & Hrouda 1993). The significantly higher aquitard average values of 352.2 x 10^{-6} SI (n = 156) in RD54 with values from 19-1280 x 10^{-6} SI can be related to the top 12 m where SI values above 1000 occur frequently in dark organic-rich layers. With 149 x 10^{-6} SI (n = 162) the aquifer of RD42 shows significantly lower average values. The aquifer average of RD54 is, however, almost identical at 146 x 10^{-6} SI (n = 218). While in RD42 colour, lithology and aquifer units are represented well by the volume susceptibility (k), the relationship in core RD54 is not as clear. The differences in SI values between the individual units are significantly smaller and colour information and magnetic properties do not correlate as good as in RD54.The results of the **mass specific bulk susceptibility** measurements of wet & dry samples of core RD42 in the lab coincide with the results of the volume susceptibility measured in field and support the division of the sediment cores based on lithology and geochemistry (Fig. 31). Further the vertical magnetic profiles underline the importance of transition sediments for the Fe cycle. Although the three curves in Fig. 31 are not completely congruent, there is a clear increase in the signal in the depth ranges around 19, 22, 27, 30 and 41 m depth. Mass specific magnetic susceptibility measurements were not carried out for core RD54.

In summary, it can be stated that the magnetic profiles of the different lithology and aquifer units can be clearly distinguished from one another. The highest values occur in the transition zones and are in accordance with the high Fe content. The higher values for the silty aquitards and transition sediments compared to the sandy aquifer sediments reflect type and amount of magnetic Fe minerals and therefore lithology and coincide with the results of the lithological and geochemical investigations. The high standard deviation within the volume susceptibility measurements of the different core units show the high sensivity of the magnetic susceptibility measurements and displays the heterogeneity

of the sediments on small spatial scales. In this context, it must be taken into account that the high spatial resolution of 10 cm cannot be captured by the other methods.

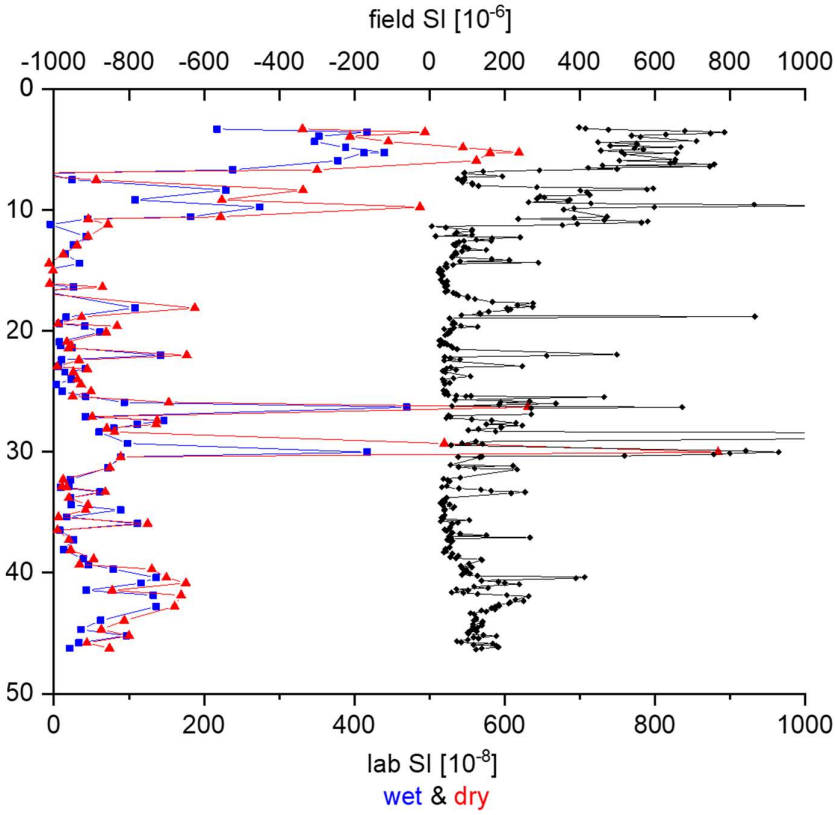

Figure 31: Vertical magnetic core profile of core RD42

Showing mass susceptibility of wet (blue) & dry (red) bulk material (n=78) and volume susceptibility (black, n=349)

The individual lithology and aquifer units can also be clearly distinguished using the **temperature dependent magnetic susceptibility (kt) measurements.** The 40 kt measurements across the aquifer of RD42 can be divided into three groups that correspond to the three aquifer units. A detailed explanation of the individual kt-patterns will follow in the next chapter.

9.4 Aquifer (iron) mineralogy and arsenic distribution

Based on reflected and transmitted light microscopy, SEM-EDX, EMPA and XRD analysis the bulk mineralogy of the two sediment cores is as follows. The **major phases** over the entire core profiles are **tectosilicates** namely quartz (Qtz), (alkali) feldspars (Afs, Fsp) (microcline (Mc), albite/analbite (Ab), orthoclase (Or), sanidine (Sa), anorthite (An)) and **phyllosilicates** (PS) which involve micas (Mca) (muscovite (Ms)) and various clay minerals (kaolinite (Kln), illite (Il) and clinochlor (Clc), chamosite (Chm), chlorite (Chl)). Qtz dominates the aquifer sediments, followed by feldspars while the PS content increases towards the aquitards and transition sediments. **Phosphates** (apatite (Ap)) and **carbonates** (calcite (Cal), dolomite (Dol)) only reach detectable concentrations in the upper aquitard. **Accessories** are heavy minerals like rutile, zircon, amphibole, olivine, monazite and titanite. The relative proportions of the various minerals change between the lithology and aquifer units.

With regard to the Fe mineralogy the picture is much more challenging. The identification of **Fe phases** in natural samples is always difficult. High variety, low quantity, often in trace amounts, inhomogeneous distribution, small size and sometimes low crystallinity set methodological demands. Along active redox transition zones in heterogeneous delta sediments with diverse microbiology and fluctuating GW chemistry, the crystallinity of Fe phases varies and ranges from amorphous to well crystalline phases. In addition especially natural Fe minerals often appear as complex phase mixtures that can neither be identified nor quantified by classical mineralogical methods. Consequently, a combination of several bulk and space-resolved methods was used for their identification and characterization. Because of the high effort required, the focus of the Fe mineralogical investigation was placed on the aquifer sediments. Table 6 summarizes the most important Fe minerals in the sandy aquifer and the method(s) used for their identification. A more detailed Table showing all documented Fe & As minerals is shown in Table 20.

Table 6: Occurrence and frequency of identified Fe minerals and Fe-hosting PS and the respective methods used

(Legend: X=rare, XX=moderate, XXX=abundant, + = present, ? = no clear evidence, - = not present, Fe valance state indicated by colour)

Fe-minerals	formula	aquifer unit			methods					
		yellow - brown sand	transition zones	grey sand	Microscopy/ SEM/EMPA	XRD	µ-XANES	bulk XANES	Magnetic	Mössbauer
Siderite (Sd)	$Fe^{2+}CO_3$	X	XXX		+	+	-	+	+	-
Ankerite (Ank)	$Ca(Fe^{2+},Mg,Mn)(CO_3)_2$	X	XXX		+	-	-	-	+	-
Pyrite (Py)	$Fe^{2+}S_2$		XXX		+	+	-	+	-	-
Ilmenite (Ilm)	$Fe^{2+/3+}TiO_3$	XX	X	X	+	-	-	-	-	-
Magnetite (Mt)	$Fe^{2+}Fe^{3+}{}_2O_4$	X	X	XX	+	+	+	+	+	-
Goethite (Gt)	alpha-$Fe^{3+}O(OH)$	XX	XXX	X	+	+	+	+	+	+
Lepidocrocite (Lep)	gamma-$Fe^{3+}O(OH)$		X		-	+	-	-	?	?
Ferrihydrite (Fh)	$Fe^{3+}{}_{10}O_{14}(OH)_2$	X	XXX		?	-	-	+	?	?
Hematite (Hem)	$Fe^{3+}{}_2O_3$	XX	XXX	X	+	+	+	+	+	+
Clinochlore (Clc)	$(Mg,Fe^{2+})_5Al(Si_3Al)O_{10}(OH)_8$	freqency linked to occurrence of fine-grained layers			+	+	-	-	-	+
Biotite (Bt)	$K(Mg,Fe^{2+})_3(Si_3Al)O_{10}(OH,F)_2$				+	+	-	+		
Chamosite (Chm)	$(Fe^{2+},Mg,Fe^{3+})_5Al(Si_3Al)O_{10}(OH,O)_8$				+	+	-	-		
Hornblende (Hbl)	$(Ca,Na,K)_{2-3}(Mg,Fe^{2/3+},Al)_5[(OH,F)_2/(Si,Al)_2Si_6O_{22}$				-	-	-	+		
Glauconite (Glt)	$(K,Na)(Fe^{3+},Al,Mg)_2(Si,Al)_4O_{10}(OH)_2$				+	-	-	-		

It can be stated that the type and quantity of the different Fe minerals within the aquifer is closely linked to the different aquifer units. The distribution and frequency of Fe and Fe-containing minerals along the vertical profile is in line with the lithological and magnetic findings and supports the geochemical results of three geochemical zones. Corresponding to the solid phase elemental composition the Fe mineralogy follows colour and grainsize gradients and the mineralogical analyses confirm the division of the aquifer into three units. Bulk and the spatially resolved analysis show clear differences between the individual units, both in terms of the Fe mineral inventory, composition and quantity. The results for the individual units are explained separately in the following chapters after a brief overview of the cores has been given.

The combined analysis revealed a broad set of primary and secondary Fe-bearing phases of different valence state across the RTZ (Table 6). The occurrence of the specific Fe phases is mainly limited to certain aquifer units of which the transition sediments show the highest quantity and diversity. **Fe(II) sulphides and carbonates** could be identified under the microscope and well as by spectroscopic techniques and occur only in the transition sediments. Combined optical and spectroscopic analysis revealed that **crystalline Fe(III) and Fe(II/III) oxyhydroxides** in the form of Gt, Hem and Mt are very rare in the entire profile and are essentially limited to the yellow-brown sediments. Synchrotron-based spectroscopic analysis (µXANES) showed that the Fe mineralogy across the redox interface is dominated by **microcrystalline Fe(III)-dominated precipitates** in form of coatings and complex cementations which could not be addressed by optical methods. The secondary precipitates are ubiquitous in the transition sediments and based on their occurrence and quantity they control the Fe cycle across the redox boarder to a wide extent. The grey sediments are depleted with regard to Fe minerals and seem to contain only remaining redox stable Fe phases essentially in the form of very fine-grained Mt. In addition to pure Fe minerals, several mixing phases could be detected that reach significant concentrations. Mixed **Fe-(Mn-) carbonates** (siderite, ankerite), **Fe-(Ti)-oxides** (ilmenite (Ilm)) could be detected in the yellow-brown sands as well as in the transition sediments and contribute to the Fe cycle as they show clear signs of (redox) alteration. The rare crystalline Fe(III) and Fe(II/III) oxyhydroxides share this characteristic. The mineralogical analyses also showed that a significant part of the solid Fe is bound in **Fe-rich phyllosilicates**. Fe-bearing PS appear in a wide variety and show regular signs of recent weathering or growth. The formation of **Fe-PS complexes** (Fe-rich PS form complex intergrowths with Fe-precipitates) is a prominent feature in the transition sediments often associated with mc Fe(III)-dominated precipitates. Most important for the Fe-cycle in the sheet silicate-bound fraction are the ferruginous PS chamosite and chlorite that are present along the entire core profile, followed by illite, clinochlor and glauconite. Further small amounts of greenalite (Gre) and phengite (Phen) were identified. Smectite (Smc) and nontronite (Non) could not be identified by XRD but microscopic analyses in combination with ED-/WD-XRF based elemental ratios suggest their presence. A large variety of further PS can be assumed in the sub-µm range. Relevant for sediment Fe content are also regularly occurring **inosilicates** (e.g. amphiboles like hornblende). Fe-bearing **cyclosilicates, sorosilicates and nesosilicates** could also be identified. In contrast to the Fe-rich PS, the Fe-bearing cyclosilicates, sorosilicates and nesosilicates show no signs of weathering and thus, seem not to contribute significantly to the recent Fe dynamic. **Borates, sulphates, phosphates, arsenates and vanadates** play a subordinate role and can be neglected both with regard to the Fe and the As cycle.

Further noticeable is the evidence of the **As minerals** arsenopyrite, auripigment and svabite in the sediment cores. Traces of **arsenopyrite** (Apy) were found in the aquitard and the aquifer of both cores. XRD analysis reveals the mineral is most prominent in the organic-rich sediments from 10-12 m bgs in RD42. Bulk XANES in aquifer sediments of RD54 reveals further Apy in small amounts across the transition sediments. Minimal amounts of the calcium-arsenic phase **svabite** (Sva) are indicated in the top aquitard until 11 m bgs and the top redox boundary at 20 to 22 m bgs of RD42 by XRD. XANES further revealed the presence of minor amounts **auripigment** (Aup) in two transitions sediments of RD54. The mineral, however, only reaches at the bottom transition around 43 m bgs a noteworthy concentration. The pure As minerals occur only occasionally and do not coincide with high As concentrations in the solid phase and therefore probably only play a subordinate role for the As dynamics.

9.4.1 Grey sediments

The grey aquifer sediments not only show the lowest Fe solid concentration but also the simplest Fe mineralogy. Based on the combined analyses the grey sands contain Mt and Hem as most prominent Fe-phases. The **microscopic investigations** indicate that the Fe II/III & III oxyhydroxides Mt and Hem occur very rarely as isolated strongly altered crystalline phases all across the grey sediments. Gt shows the same signs of alteration, such as cracks or dissolved rims, but is much rarer. The size of the crystalline oxyhydroxides is usually well below 10 µm. In addition, isolated Fe-rich PS and Fe-Ti-oxides could be identified as further ferruginous minerals. The Fe(III)-phases and the Fe-rich PS show clear signs of (redox) alteration and weathering. Attacked surfaces and cracks that often permeate the entire mineral most likely indicate weathering of primary phases due to recent redox processes and starting dissolution. That the crystalline primary phases have primarily lasted in areas with a fine-grained matrix with presumably lower permeability reinforces the impression that these phases are detrital phases. Mt and Hem are the two most redox-stable Fe oxyhydroxide phases and were therefore able to withstand the incipient reducing conditions. Further Fe mineral features like Fe-precipitations, Fe-coatings on primary grains and poorly crystalline phases like Fh are absent. Interestingly, also Fe(II)-phases are absent and no Fe(II) carbonates or sulphides could be found in these sediments. The microscopic results suggest that the two grey sediment units of the two cores are largely comparable. Despite slight colour differences, the grey sediments in both cores show a Fe mineralogy that is to be expected under reducing conditions. In addition, Fe bearing silicates could be detected microscopically, but the specific Fe content could not be assessed. The **XRD** investigation on the bulk sediments of core RD42 (Table 21-23) provides evidence of Hem but due to the small amounts (trace amounts) of the Fe phases, well below 5 wt%, detection with XRD is difficult. Nevertheless, the XRD shows around 1 wt% Hem in grey sediments at a depth of around 25.5 m. Further Fe or Fe-rich phases could not be detected with XRD in the grey sediments. The fact that in the majority of the grey sediments no Fe phases could be detected by XRD is in line with the small amount of Fe_2O_3 and represents the methodical limits. The **Fe EXAFS** measurements on the bulk sediments of RD54 (Table 7) reveal that in the grey sediments of RD54, the most important (on average 0.30 %, n = 7) ferruginous minerals are primary Fe(II/III) silicates (amphiboles, pyroxenes). It is unclear whether these phases contribute to the recent redox controlled Fe cycle but the fact that the proportion of redox stable phases is higher than in the other aquifer units could be interpreted as hint for redox-controlled dissolution of Fe phases. Gt is present in about the same amount (0.29 %) followed by 0.07 % Hem and 0.07 % Mt. These proportions are not in par with the previous results obtained by microscopy and XRD. A possible explanation could be slightly different redox progress in core RD54 which was used for Fe EXAFS analyses. In addition, the Fe EXAFS measurements revealed Fh/amorphous Fe(III) phases with 0.16 and small amounts of Fe sulphide minerals, which could not be detected by other methods. Based on the EXAFS analyses the mackinawite accounts for 0.05 % and in green rust for 0.03 %. However, the peaks are so low that this information should be considered with caution. Fe-containing PS such as biotite seem to play only a minor role in the grey sediments and account with 0.03 % only a tenth of the amount of Gt. The detection of Fh / amorphous Fe(III) and Fe sulphides in the bulk Fe EXAFS measurements could be explained by the less reduced character of RD54 compared to RD42. Both mineral phases can be seen as typical for the transition sediments along the redox boundary. This, it can be assumed that the samples for the Fe EXAFS investigations do not completely represent the grey sediments and are superimposed by adjacent transition sediments. **Volume susceptibility (*k*)** measured in the grey sediments of RD42 reveal significantly lower values compared to the other aquifer units and show in average 120.5 x 10^{-6} SI (327 SD) (n = 59), which reflects the lower overall Fe content. The wide spread of 27-673 x 10^{-6} SI can be attributed to the occurrence of ferrimagnetic Fe minerals like Mt and heterogeneous sedimentology. The grey sediments partly show remarkably high values of several 100 x 10^{-6} SI. However, in these layers the SD is high. Two extremely high values of

1070 and 2900 x 10^{-6} SI at a depth of around 28 m are especially noticeable. The values could be confirmed by repeated measurements and can only be traced back to a high content of ferrimagnetic Fe minerals like Mt. They lie in grey sediments, but have been excluded from the average calculation presented in chapter 8.5 as they do not follow the otherwise common pattern and do not separate from the surrounding sediment layers by colour or GS. The results show how much the actual small-scale Fe mineralogy can deviate within the large-scale aquifer unit. That the susceptibility in the Fe-poor grey sediments od RD42 is higher than that of the yellow-brown sediments is also most likely explained by the presence of redox-resistant ferrimagnetic Mt. The **grey sediments of RD54** have in average 147.8 x 10^{-6} SI (n = 86) with values between 12-734 x 10^{-6} SI and are therefore significantly higher than the volume susceptibility (k) measurement in RD42 (Fig. 30). The range of values in both cores indicates that predominantly paramagnetic minerals such as Fe (phyllo-) silicates and carbonates are present and occasionally Mt-rich layers occur. This findings support the results of the EXAFS measurements indicating that the redox status of the two cores is not identical. The **temperature dependent magnetic susceptibility** (*kt*) measurements confirm an increasing Mt content in the reduced sediments. The low-temperature measurements shows a clearly pronounced Mt peak in all grey sediments between 22 and 30m depth (Fig. 32) as well as a course of the high-temperature measurements that clearly indicates Mt (n = 7). The Verwey transition (TV) at around -150 °C, indicates a monoclinic to cubic first order structural transition and the Curie temperature at around 580 °C characteristic for the mixed valance mineral (Dunlop & Özdemir 1997; Dearing 1999; Hunt et al 2013). Further the high-temperature measurements indicate Hem due its characteristic Néel temperature around 675 °C (Dearing 1999; Hunt et al 2013; Dunlop & Özdemir 2007; Just & Kontny 2011; Petrovsky & Kapicka 2005). In accordance with previous results (Microscopy, XRD, EXAFS) Hem is present across the entire redox front and the separated grey fingers. In accordance with the bulk Fe EXAFS measurements (Table 7), the kt measurements also indicate Fh. The sharp drop in the low temperature measurement (Fig. 32) right at the beginning can be interpreted as an indication for Fh. However, the specific detection of Fh is not possible with the setup used because the necessary temperature range cannot be reached with the liquid nitrogen cooling used here (Berquo et al., 2007; Liu et al., 2008). It should also be noted that the alleged Fh signal occurs in all areas except the beige clays at a depth of 12-14m.

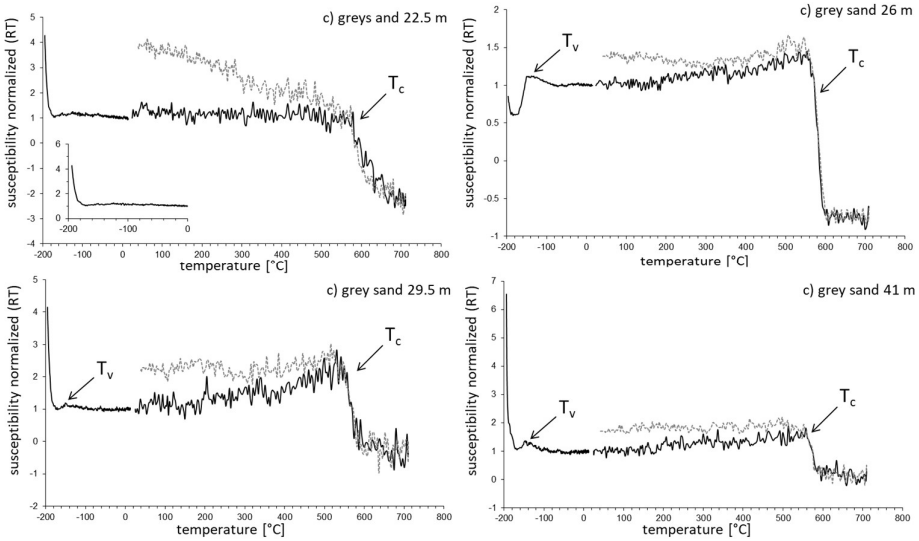

Figure 32: Temperature dependent magnetic susceptibility (kt) diagrams of the grey sediments

Characteristic Verwey transition (T_V) and Curie temperature (T_C) indicate the presence of Mt in all samples. Heating curve is indicated in black and cooling curve in dotted grey. Values are normalized to value at room temperature.

EMPA and SEM-EDX analysis revealed no **As** concentrations above detection limit for any potential carrier phases in the grey sediments. The **As XANES bulk analysis** across the vertical core profile of RD54 show for the As species ratios considerable variations in between the different aquifer units. The As(III):As(V) ratio is 59:33 in the grey sediments (n=7). Especially the depth between 20 and 30m are As(III) dominated with an average of 70 % (n = 5). Further the As XANES analysis revealed arsenopyrite (FeAsS) and auripigment (As_2S_3) in isolated samples. Overall, one or both minerals could be detected in 6 samples (Table 8) most of them in the grey sediments. Arsenopyrite as most important As mineral was detected at depths of 21, 27 and 28 m. However, the small quantity indicates a low contribution to the As dynamics with exception of 28 m depth. Other As minerals could not be observed.

9.4.2 Yellow-brown sediments

Based on the **microscopic evaluation**, the yellow-brown sediment units of the two cores are largely identical. The most important Fe and Fe-bearing minerals identified in the yellow-brown sands are Gt, Mt, Hem and Ilm. Microscopic investigations have shown that Fe(III) & (II/III) oxides and hydroxides, such as, Gt, Hem and Mt are present as coatings around detrital grains as well as autonomous crystalline detrital phases within the moderately reduced yellow-brown sediments. Overall, crystalline Fe phases occur more frequently than in the grey sediments but do not dominate the Fe mineralogy. Gt seems to be the most common phase and is followed by Hem and Mt. The distribution and texture is comparable to that of grey sediments. Microscopic analyses show that most Fe minerals show signs of weathering along their surface. Some minerals also show clear signs of dissolution, such as cracks. The size of the oxyhydroxides is usually between 5 and 10 µm in diameter. In contrast to the grey sediments, the kt bulk analyses suggest that the yellow-brown sands also contain Fe-carbonates (siderite) in low concentrations. However, this could not be confirmed microscopically. Based on microscopic investigations the most frequent ferruginous crystalline phases are Fe-Ti and Fe-Ti-Mn oxides such as Ilm. Fe-Ti oxides are much more abundant than in other aquifer units and usually show clear signs of redox alterations comparable to the Fe oxyhydroxides. Fe-rich PS are ubiquitous in the yellow-brown sediments. Clay layers pervade the entire aquifer unit and accordingly PS can often be found microscopically. In accordance with the grey sediments, most PS show signs of alteration and disintegration. Moreover, the Fe mineral inventory of the yellow-brown sediments is composed of additional Fe-features. In rare cases Fe-coatings around detrital Qtz and Fsp grains occur in the yellow-brown sediments. The thin superficial coatings usually do not completely enclose the primary grains and have numerous interruptions. Due to small grain size, optical properties cannot be determined and spatially resolved methods cannot resolve the narrow rims individually but the coatings seem to consist of a single layer and visual investigations do not reveal any internal structure. SEM-EDX based estimated atomic ratios across partially coated Qtz grains suggest Fe(III)-oxyhydroxides like Gt and Hem or Mt in variable composition. This approach inevitably leaves some room for speculation, as it is very difficult to distinguish between different Fe oxyhydroxides in small structures. Therefore, the presence of further Fe oxyhydroxide precursor phases like Fh or Lep in the coatings cannot be excluded. However, mineral composition and homogeneous structure could point, at least partly, towards detrital coatings.

The most prominent Fe-features identified by microscopy are **iron-phyllosilicate (Fe-PS) complexes**. Along the entire yellow-brown aquifer profile, associations between Fe-rich PS minerals and Fe oxyhydroxides are widespread. Based on the large size and quantity of these complexes the Fe dynamics is probably strongly influenced by these features. The Fe-PS complexes appear in various forms. Specimen analysis with backscattered electron (BSE) contrast revealed large Fe-rich structures, which frequently sit on the surface of primary Qtz grains regularly extending over 100 µm and more. A structure covering an area of about 100 x 50 µm is shown in Fig. 33. It is uncertain whether the Fe-

rich PS minerals were formed in this way or whether they were subsequently impregnated by Fe-rich fluids. they often co-occur together with small-scale Fe oxyhydroxides.

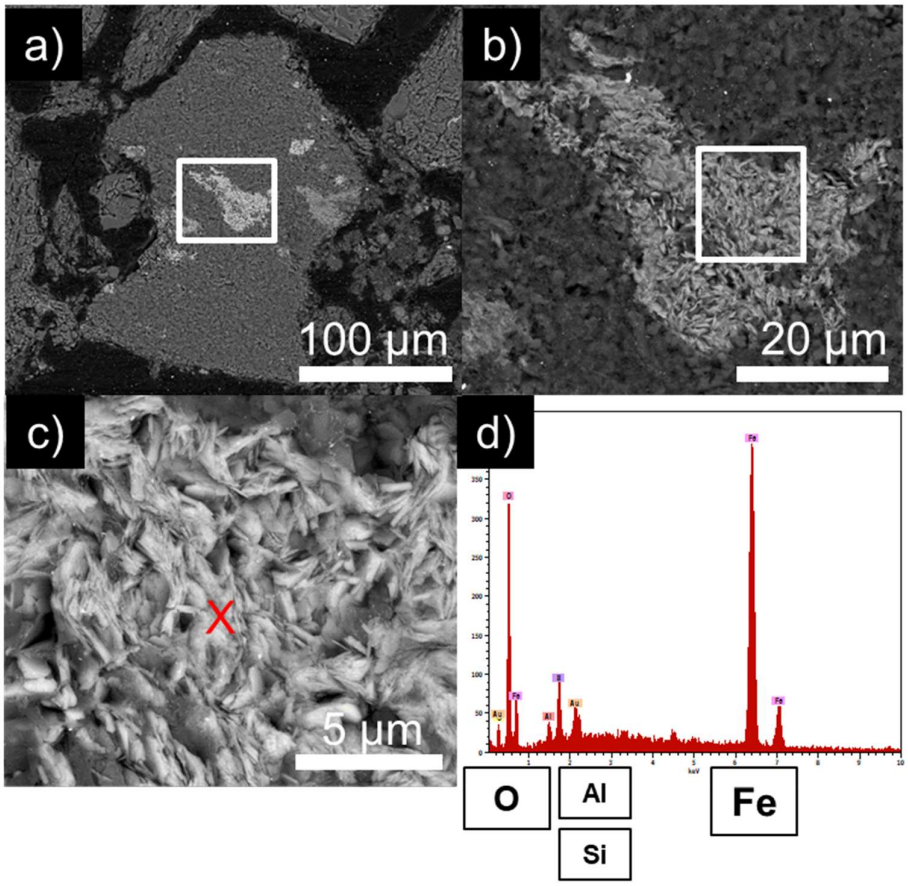

Figure 33: Backscatter micrographs of Fe-impregnated phyllosilicate mats in the yellow-brown sediments in 36.6 m depth of core RD42

a) Shows the phyllosilicate mat on top of a Qtz grain. b) and c) show a magnification of the area indicated by the white rectangle. The ED-XRF spectra d) measured at the red X reveals significant amounts of Al and Si in addition to Fe and O. The Au signal is related to the coating of the sample.

The dominant feature with regard to the Fe-dynamic in the yellow-brown sediments are **intergrowths between Fe precipitates and Fe-rich PS** (Fig. 34). The structures can expand over several 10s of µm and are present in the entire aquifer except the reduced sediments in recurring order in and along mm-scale fine-grained layers. They are extremely widespread and seem to largely control recent Fe-cycle. As the Fe precipitates and PS create complex adhesions the conglomerates cannot be separated and identified by optical techniques. Neither the extinction angle nor the colour allows a clear assignment and the precipitates appear without clear textural properties. Small isolated crystals can be overserved but due to their small size, they cannot be determined. The PS minerals within the complexes appear usually as elongated and layered minerals in the sub-µm range, which are surrounded by Fe precipitates (Fig. 33). The spatially resolved geochemical analysis shows Fe-dominated Al and Si-rich structures. Based on the elemental composition the precipitates and isolated crystals can be assigned as Fe oxyhydroxides while the PS minerals are indicated by continuous Al and Si admixtures. Based on texture and elemental composition a broad range of PS minerals could be identified. Chamosite and chlorite are regularly present, followed by phengite and greenalite. In addition clinochlor, nontronite and smectite–illite mixed-layer PS minerals occur regularly. The Fe oxyhydroxides could not be further distinguished quantitatively and the composition of the Fe

precipitates remains unknown. Position and texture of the PS minerals and precipitates show that the phases influence each other reciprocally. The Fe precipitates have accumulated along PS and Fe-rich rims around the presumably primary PS indicate that the PS serve as condensation nuclei for the formation of precipitates. Secondary PS minerals in the sub-µm range are embedded in precipitates and seem to grow within the precipitates most likely as a result of a recrystallization process. The texture suggests the Fe-PS-complexes are mainly composed of small sub-µm Fe oxyhydroxide crystals and embedded PS minerals. Shape and composition suggest redox-sensitive structures with huge surface areas. The small mineral phases in the precipitates and changing crystallinity within the complexes suggest a young age and inclusion in recent processes. Young age and high reactivity of the Fe-PS-complexes provide a clear indication of an active Fe-dynamic within the yellow-brown aquifer. All Fe-PS complexes seem to be secondary phenomena and the frequency of the structures not only suggests an active and comprehensive Fe dynamic, but also shows that, in addition to classic Fe minerals, Fe-rich PS play an important role in both release and (at least temporary) storage of Fe during the redox processes at the field site. The Fe-PS complexes show signs of dissolution and precipitation of Fe from GW in the yellow-brown sediments. The dissolution mainly takes place in coarser, slightly discoloured pale yellow-brown to greyish sections, while the Fe-PS complexes are increasingly present along fine-grained layers with rather strong yellow-brown colours. That the processes cannot be spatially separated could point to oscillating redox conditions.

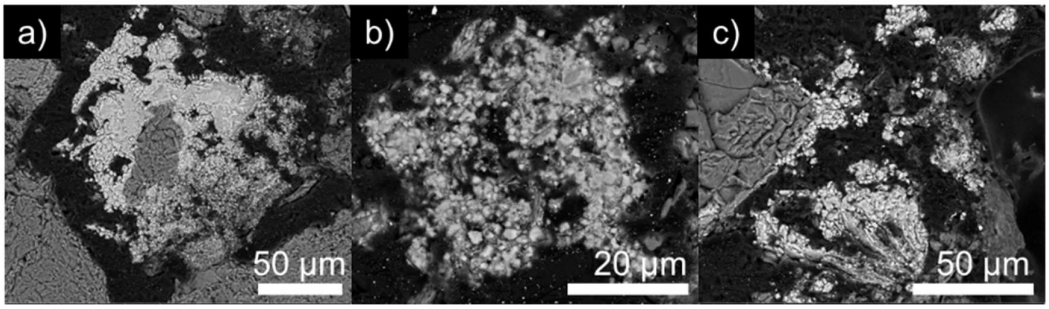

Figure 34: Backscatter micrographs of Fe-PS-complexes in the yellow-brown sediments

a) Fe-PS-complex in between Qtz grains. b) Numerous white structures in the sub-µm-range indicate formation of secondary Fe phases within the Fe-PS-complexes. c) Fe oxyhydroxide - PS intergrowths on the surface of primary grains

The **bulk Fe EXAFS** results on the sediments of RD54 (Table 7) are in accordance with the microscopical observations. Based on the XAS analyses Gt is the dominant Fe-phase in the yellow-brown sediments and accounts for 0.32 % (n = 7). That about the same amount of Fh (0.32 %) is present points towards the Fe-PS complexes, as they seem to form recently (trans-)formed and therefore likely contain poorly crystalline precursor phases. As the Fe-coatings seem to be detrital, it is unlikely that they contain Fh unless secondary processes affect them. Amphiboles/mixed Fe(II/III) silicates account for 0.21 %. Therefore, a notable amount of Fe is stored in stable phases, which are not involved in the recent Fe redox cycle. In according with the microscopic examination, Hem (0.05 %) and Mt (0.03 %.) could also be documented in small amounts. Surprisingly Fe-containing PS such as biotite play practically no role in the yellow-brown sediments based on the EXAFS analyses. This clearly contradicts the results of the microscopic analyses and might be attributed to the standards used. As a reference, only one Fe(II)-containing PS was available with biotite. However, clinochlor and chlorite, mostly mixed valence Fe(II/III) minerals, were documented associated with Illite, chamosite and probably smectite. In addition, ferrous PS such as glauconite are probably also present. Therefore, the missing standard is likely to explain the low measured PS concentrations in the bulk Fe EXAFS analysis.

In accordance to the other mineralogical analysis **Mossbauer results** from yellow-brown sediments from 36.4 m bgs (Fig. 35) confirm the presence of Gt and Hem. Further the spectra indicate another Fe(III) oxyhydroxide and Fe-containing PS mineral. The oxyhydroxide has the best agreement with Fh or Lep while the PS is probably a mixed valence Fe-bearing PS. With regard to the third Fe oxyhydroxide, Lep has typically a lower quadrupole splitting than Fh. Therefore, Lep seems more likely although it is difficult to distinguish these two phases even at low temperature and although the samples were measured at 77 and 5 K, the two phases cannot be clearly distinguished. Based on the area determined by integration under the curve at the 77k measurement the relative abundance of the phases comes as follows. Gt is the dominant phase and accounts for 24 % while the Hem content is significantly lower with 9 %. The other Fe phases are difficult to differentiate and to quantify, but Lep or Fh could contribute up to around 3 %. The minor doubling of the 5K measurements corresponding to Fe(III) in PS is noticeable as it occupies up to 26 % of the spectral area. This is supplemented by a minor doublet corresponding to Fe(II) in PS and stands for around 8 % of the spectral area. The Mossbauer analyses thus point to significant amounts of Fe(III) -rich PS and therefore supports the previous observations. In general the Mossbauer analyses in the yellow-brown sediments at 36.4 m bgs show the same characterises as the sample in 30 m depth, described in the next chapter, and indicate the presence of Gt, Hem, Fh/Lep and a Fe-bearing PS.

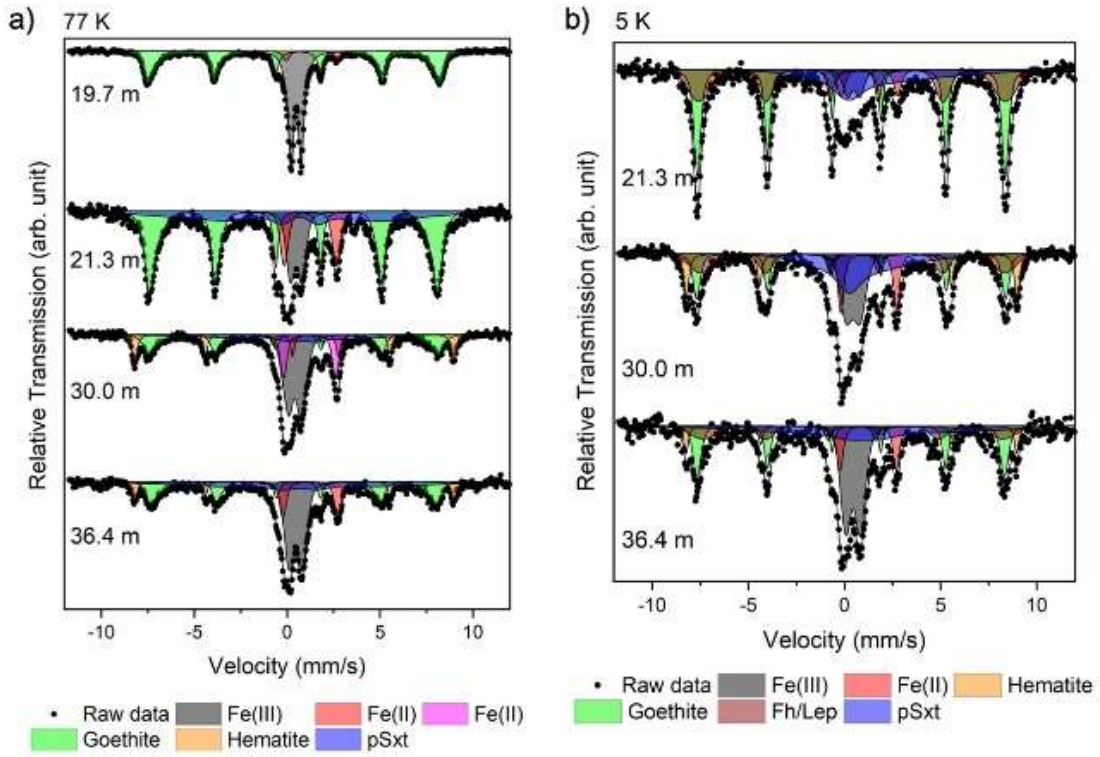

Figure 35: a) 77 K and b) 5K Mossbauer spectra of bulk samples taken at around 20, 21, 30 and 36 m depth

Figure was already shown in Kontny et al. (2021).

The **temperature dependent magnetic susceptibility** (kt) across the yellow-brown sediments reveal two alternating groups of sediment layers (Fig. 36). At 31-32, 34-35, 37-39 and 41 m depth the high temperature pattern is similar to the results in the grey sediments and indicates Hem and Mt (Fig. 36b). The less clear to absent Mt-peak in the low temperature measurements indicates that crystalline Mt occurs in smaller amounts than in the grey sediments. Most likely, the signal points towards detrital Mt in the sediment. This observation agrees with the microscopic results that showed small amounts

of crystalline Mt. The presence of Hem is also in accordance with the other results and the signal can be attributed to detrital Hem or Hem within the Fe-precipitates. Interposed in at 33-34 and 36, m depth, the sediments show a uniform pattern that can be assigned to a second group. The high temperature measurement differs significantly from the first group and show a strong increase of k at around 380 °C (Tt2). This indicates the transformation of a Fe-phase into Mt (Fig. 36a). Through comparison with measurements of pure minerals the initial phase was identified as Fe-carbonates such as Si (Tt2). This interpretation explains the irreversibility of the heating and cooling phase. In addition, the indication of a second increasing signal at around 280 °C (Tt1) could occasionally be documented (Fig. 37). Through comparison with measurements of pure minerals the phase was identified as Lep (Tt1). The low temperature heating curve shows no Mt peak. However, the common occurrence of the Lep and Mt in this aquifer unit could not be confirmed microscopically and agrees with the Mossbauer results (Fig. 35). The magnetic method is very sensitive so that even small quantities generate a clear signal. This can explain why the results could not be confirmed microscopically. The kt measurements suggest that the yellow-brown sediments consist of alternating layers with a different Fe mineralogy. Based on susceptibility results Fe-carbonates/Lep or Mt/Hem dominated layers regularly traverse the yellow-brown sediments. This could correspond to the described alternation of stronger and weaker coloured yellow-brown sediment layers in the lithological characterization. The fact that the effect in the kt measurements is not shown regularly on a small scale can be attributed to the sampling amounts and intervals. Both the detection of Mt/Hem and Si could indicate the onset of redox processes in the yellow-brown sediments. However, the correspondence of the group 1 signal with the reduced layers suggests that detection of Mt/Hem in the alternating layers can be interpreted as penetrating reduced GW that leave only the most redox-stable Fe phases unaltered. This indicates that the Fe carbonates are located in the less reduced layers. This might imply that at least some Fe carbonates could belong to the detrital mineral inventory of the yellow-brown sediments. The fact that Si is usually associated with Lep reinforces this assumption. kt shows Fe-carbonates at 33-34, 36-37 and 40 m depth. The kt measurements further indicate Fh as in the previous aquifer unit. Its verification using the kt method is subjected to the same restrictions mentioned before.

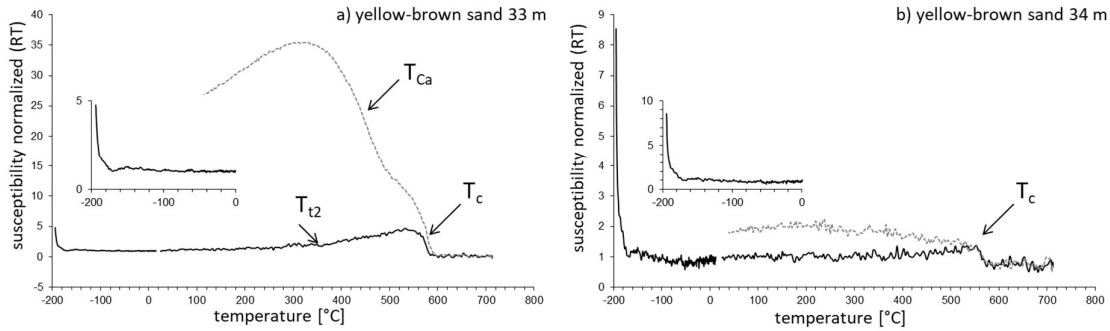

Figure 36: Temperature dependent magnetic susceptibility (kt) diagrams of the yellow-brown sediments

The two diagrams exemplify a repeating sequence from 30-40 m bgs. a) Transformation of Fe-carbonate (T_{t2}) into magnetite. b) Curie temperature (Tc) suggests Mt formation during heating from unidentified Fe-phase or primary Mt. Heating curve is indicated in black and cooling curve in dotted grey. Values are normalized to value at room temperature.

The **Volume susceptibility (*k*)** measurements in RD42 (Fig. 29) within the **yellow-brown sediments** is in average 83.8 x 10^{-6} SI (51 SD) (n = 88) and a range from 26-413 x 10^{-6} SI. The values are lower than in the grey sediments. The fact that the values are lower in spite of the higher average Fe solids concentrations can be attributed to two aspects. Firstly, ferrimagnetic Fe minerals are more common in the grey sediments. Secondly, the yellow-brown sediments show just as low Fe concentrations over

long stretches as the grey sediments, although this is not reflected in the sediment colour. The yellow-brown sediments of RD54 average with 128.4 x 10^{-6} SI (n = 128) higher values and a broader range from 19-919 x 10^{-6} SI (Fig. 30). This could indicate that the redox-driven Fe relocation processes in RD54 are not as advanced as in core RD42. The results indicate predominantly paramagnetic minerals such as (phyllo-) silicates and carbonates which are occasionally supplemented by ferro- (Gt, Hem, Ilm) and ferrimagnetic (Mt) Fe phases. The only identified ferrous mineral by **XRD** (Table 21-23) in the yellow-brown sediments is chamosite, which was detected in 33 and 40 m depths with around 1 wt%. At the lower aquifer-aquitard transition at 41 m the concentration increases to 2wt%.

EMPA and SEM-EDX analysis revealed no **As concentrations** above detection limit for any potential carrier phases in the yellow-brown sediments. Like in the grey sediments As appears to be homogeneously distributed in small quantities across different ferric and ferrous minerals. However, it must be taken into account that the methods are not able to resolve the often small spatial structures. The **As XANES bulk analysis** measurements across the vertical core profile of RD54 (Table 7) show the As(III):As(V) ratio is relatively balanced in the yellow-brown sediments with a As(III):As(V) ratio of 42:57 in(n=7). The yellow-brown sediments between 30 and 31 m are dominated by As(V) with an average of 68 % (n = 5). The samples between 34 and 35 m (n = 4) consist of yellow-brown and slightly discoloured sediments and show a balanced to As(V) dominated As species ratio (Table 7 & 8). Noticeable in this context, however, is the consistently high $\mathbf{P_2O_5}$ content in the Fe-PS complexes and the rare coatings. As the presence of Fe-phosphates can be excluded based on the spatially resolved synchrotron measurements, it is likely that P is adsorbed on the Fe oxyhydroxide and Fe-rich PS. However, the chemical similarity between As and P suggests that As is also sorbed on the mineral surfaces.

9.4.3 Transition sediments

The high Fe solid concentrations as well as quantity and diversity of Fe minerals in the transition sediments revealed by microscopic, geochemical and magnetic analysis are reflected in the most complex and diverse mineralogy along the core profiles. The transition sediments clearly stand out from the other aquifer units with regard to the Fe mineralogy. Both type and quantity of Fe phases differ significantly from the other aquifer units. The most noticeable result of the microscopic analysis are extensive Fe precipitations, which are primarily responsible for the high Fe solids concentrations. Along colour and GS boundaries **Fe(III) dominated precipitates** and **Fe-PS complexes** prevail the Fe mineralogy. They are much more frequent than in the yellow-brown sediments and form significantly larger complexes. They are most pronounced around 20 m bgs at the aquifer-aquitard interface which is accompanied by a redox transition. In addition, significant amounts of Fe-PS-complexes are present at the lower aquifer-aquitard transition at 41 m bgs and the redox boundaries at 22, 27 and 30 m bgs. **Fe(Mn)(II)-carbonate** and **Fe(II)-sulphide** minerals appear frequently in the transition sediments and highly altered texture of this phases imply the (trans)formation of these phases is linked to recent redox processes. In addition, the transition sediments also contain primary Fe phases in form of isolated well crystalline detrital **Fe(III)-oxyhydroxides** (Gt, Hem, Mt) and Fe-Ti Oxides. These phases occur about as frequently as in the yellow-brown sediments and show often signs of advanced weathering such as cracks and heavily altered edges. The appearance of the secondary phases follows a relatively fixed pattern that seems to be based on microscale depositional conditions. Individual Fe phases contain high **As concentrations** that significantly exceed the background content of the bulk sediments, reaching up 300 mg/kg in Fe-carbonates, 800 mg/kg in Fe-precipitations and up to 6000 mg/kg within Fe-sulphide. Bulk As XANES analysis show a dominance of As(III) at the redox interface is As(III) dominated but with variable contribution.

Also the mineralogical **bulk methods** draw a diverse picture of the Fe mineralogy within the transition sediments and therefore confirm the optical observations. Based on the **XRD bulk analyses** (Table 21-

23) the transition sediments show the highest concentrations and the widest variety of Fe phases. XRD analysis indicate Gt is the most common Fe mineral in the transition sediments. Gt was detected at the upper and lower end of the redox front and at the lower aquifer-aquitard boundary. While about 1 wt% is determined at a depth of around 20 and 41 m, the redox boundary at 30 m depth showed 8 wt% Gt. The results are in line with the high Fe in solid phase concentrations (Table 4) and microscopical results (Fig. 39) which show extensive yellowish to orange coloured Fe-precipitations in the corresponding depth levels. Further the XRD analysis show 1 wt% Hem at a depth of 21-22 and 41 m bgs. Furthermore, 1 wt% Lep could also be detected at the upper lithology and redox boundary at a depth of 20 m. Although Lep cannot be confirmed microscopically, it is in line with the temperature-dependent magnetic susceptibility measurements (Fig. 37). 2 wt% chlorite was determined at a depth of 30 m and chamosite at a depth of 21, 30, 34 and 41 m, with variable concentration between 1 and 4 wt%. The highest concentration are reached at the aquifer-aquitard transitions at around 21 and 41m where the Fe-rich PS represent a noteworthy Fe pool. The evidence of Fe-rich PS is in agreement with the microscopic findings. Fe-containing PS were regularly documented (Fig. 46 and 47) and could also be precisely determined via the atomic ratio at the EMPA and via SEM-EDX. Chamosite, chlorite, clinochlor and glauconite are the most common representatives and therefore include all Fe valance states and contain Fe(III), Fe(II) and Fe(II/III) (Table 20).

The **Fe EXAFS** measurements on the bulk sediments of RD54 (Table 7) reveal similarities in the transition sediments and in the grey sediments. The sequence of the Fe phases according to their quantity is almost identical. The most common Fe-bearing minerals are amphibole/mixed Fe(II/III) silicates (on average 0.32 %). The most important Fe mineral is Gt (0.27 %) followed by Fh/amorphous Fe(III) phases (0.13 %). The percentage of both phases is significantly lower than in the yellow-brown sediments. The concentration of Hem (0.08 %) and Mt (0.06 %) is slightly higher than in the yellow-brown sediments but still does not reflect the microscopically and geochemically documented Fe concentrations. That the Fe(III) oxyhydroxide concentrations are not significantly higher than the other aquifer units can attributed to the limited possibilities of sampling the often small-scale structures. As a minimum sample amount of about 3 g is necessary it is almost impossible to sample the small structures separately. The fact that the transition zones in RD54 are not as distinct as in RD42 can provide a further explanation for the relatively low Fe(III) oxyhydroxide concentrations. This means formation of extensive Fe-precipitations is not as advanced as in RD42. In contrast to the other aquifer units, the Fe EXAFS measurements also indicate Fe sulphides. 0.05 % mackinawite and 0.03 % green rust were detected, however, in extremely low concentrations, near the LOD. Py could not be detected although the presence of small amounts of Fe sulphide and in particular the precursor phase green rust is typical for active redox boundaries. This result does not coincide with the microscopic examinations showing framboidal Py frequently (see chapter 9.4.3.3). However, the occurrence of pyrites is limited to 2 sulphate-rich layers above and below the redox front in core RD42 which do not occur in core RD54. Furthermore, the bulk Fe EXAFS measurements suggest that PS in the form of biotite or similar phases account in the transition sediments for around 0.05 % while Si accounts for about 0.03 %. Also these results only partially agree with the other analyses. Both PS and Fe carbonates could be observed frequently with the microscope. Rather, the bulk Fe EXAFS imply that the redox conditions in core RD54 differ from those in core RD42. **As XANES bulk analysis** across the vertical core profile of RD54 reveal a As(III):As(V) ratio of 40:29 in the orange transition sediments (n=3) with As(III) and As(V) dominated layers. There is also one noticeable sample in which almost the entire As is in arsenopyrite (81 %) and auripigment (12 %) at the bottom aquifer-aquitard transition (Table 8).

Table 7: EXAFS based bulk Fe mineral composition (blue) and related total Fe_2O_3 (yellow) content in core RD54

Corresponding depth level, Munsell colour and aquifer unit is given on the left. EXAFS: 1 = 100 %.

depth & colour	aquifer-unit	Fe EXAFS										ED-XRF
		$Fe(OH)_3$	Gt	Hem	Mt	GR	Si	FeS	FeS_2	PS	silicates	Fe_2O_3
		[%]										[wt%]
20,4		**0,523**	0,141	0,117	0,000	0,029	0,013	0,000	0,003	0,000	0,173	2,021
20,95	grey	0,335	0,188	0,060	0,032	0,050	0,018	0,020	0,000	0,023	0,274	1,953
23,95	grey	0,024	0,285	0,054	0,085	0,000	0,000	0,103	0,000	0,008	**0,441**	
24,2	grey	0,333	0,155	0,133	0,002	0,000	0,000	0,074	0,006	0,000	0,296	2,651
26,67	grey	0,029	0,256	0,221	0,111	0,117	0,000	0,051	0,000	0,001	0,213	2,028
28,1	grey	0,285	0,169	0,031	0,063	0,053	0,032	0,066	0,046	0,157	0,098	1,367
30,1	yellow-brown	0,369	0,376	0,028	0,015	0,021	0,042	0,000	0,000	0,006	0,143	2,404
30,35	yellow-brown	0,238	0,268	0,097	0,069	0,007	0,000	0,000	0,000	0,010	0,310	2,836
30,65	yellow-brown	0,109	**0,408**	0,050	0,108	0,021	0,007	0,000	0,000	0,000	0,297	3,309
31	yellow-brown	0,248	0,392	0,015	0,000	0,000	0,144	0,000	0,000	0,018	0,183	2,765
34,05	yellow-brown	0,338	0,384	0,030	0,011	0,005	0,029	0,000	0,000	0,000	0,204	
34,15	grey	0,073	**0,495**	0,013	0,068	0,000	0,000	0,000	0,000	0,000	0,351	
34,4	grey	0,067	**0,476**	0,000	0,091	0,003	0,000	0,000	0,000	0,000	0,363	
34,4		0,242	**0,462**	0,005	0,017	0,001	0,001	0,000	0,000	0,000	0,272	
42	yellow-brown	0,380	0,301	0,025	0,017	0,046	0,027	0,002	0,000	0,043	0,158	2,93
42,48	transition	0,310	0,103	0,043	0,022	0,007	0,023	0,066	0,000	0,112	0,315	4,137
42,6	transition	0,039	**0,542**	0,028	0,089	0,094	0,046	0,000	0,000	0,002	0,159	2,832
42,9	transition	0,042	0,142	0,157	0,064	0,000	0,018	0,070	0,000	0,029	**0,478**	5,108

Table 8: XANES based As-species composition and As-bearing minerals (green) and related total As (red) content in core RD54

Corresponding depth level, Munsell colour and aquifer unit is given on the left.

depth & colour	aquifer-unit	As XANES				ED-XRF
		As(III)	As(V)	FeAsS	As_2S_3	As
		[%]				[mg/kg}
20,4		**61**	39			4,894
20,95	grey	**64**	21	15		3,95
23,95	grey	**71**	25		4	
24,2	grey	**85**	15			6,001
26,67	grey	**79**	19	2		3,576
28,1	grey	**50**	20	30		4,081
30,1	yellow-brown	25	**75**			5,589
30,35	yellow-brown	33	**67**			3,609
30,65	yellow-brown	30	**70**			5,856
31	yellow-brown	27	**73**			5,27
34,05	yellow-brown	45	**55**			
34,15	grey	28	**72**			
34,4	grey	38	**62**			
34,4		**50**	**50**			
42	yellow-brown	**76**	18	6		2,52
42,48	transition	43	**57**			3,881
42,6	transition	**77**	23			3,458
42,9	transition		7	**81**	12	4,794

Mossbauer analysis (Fig. 35) of the transition sediments at 20, 21 and 30 m bgs reveal Fe(III)-oxyhydroxides as dominant Fe-phases across all samples and thus reflect the results of the microscopic examination. The samples show differences with regard to the total mineral inventory and composition. The Mossbauer hyperfine parameters from the Fe mineral concretion layer at 19.7 m depth were obtained only at 77 K. The brown to orange sediments with frequent Fe-concretions and the by far highest Fe and As concentration in the aquifer show a well-defined sextet, which is likely ordered Gt (α-FeOOH) (Cornell & Schwertmann 2003) and accounts for about 53 % of the spectra. A narrow Fe(III) doublet matching to short range ordered phases like Lep or Fh (Li et al., 2011) makes up 43 % of the spectra. This corresponds very well to the observed Fe-precipitates. As in the yellow-brown sediments, a distinction between Fh and Lep is difficult but the quadrupole fitting of 0.63 mm/s indicates that Lep is more likely. Since Lep was also detected in the thermomagnetic investigation, it can be assumed that the signal can be assigned to the γ-FeOOH mineral. Furthermore, Mossbauer analysis reveal a minor wide doublet corresponding to Fe(II) in PS (Pollak & Stevenson 1986; Murad 2010) or green rust (Murad & Cashion 2004; Murad 2010) that accounts for 4 % of the spectral area. As the short range ordered Fe(III) doublet masks a potential corresponding Fe(III) component it is not possible to differentiate between the two phases but the PS seem to be more likely than green rust (Pollak & Stevenson 1986). A 5K measurement was not done for the sample. The transition sediments at 21.3 m are dominated by a sextet at 77K, which most likely corresponds to Gt (Cornell & Schwertmann 2003) and accounts for almost 50 % of spectral area. Another poorly defined sextet that accounts for almost 25 % of the spectral area was used to achieve a satisfactory fit, which, however, could not be assigned to any phase. A narrow Fe(III) doublet accounting for 15 % and short range ordered phases like Lep or Fh is present again and coincide with the temperature dependent magnetic susceptibility results which also revealed the presence of Lep. As the Fe(III) doublet considerably decreases at 5 K in spectral area compared to at 77 K and the spectra is best fitted with an additional sextet the presence of a short range ordered Fe(III) mineral phases is very likely. A minor wide doublet corresponding most likely to Fe(II) in PS accounts for 11.5 % of the spectral area in the 77 K measurements. The additional 5 K measurements, which had to be omitted for the first sample, reveal further minor doublets corresponding to Fe(III) (5.5 %) and Fe(II) in PS (5 %). At 5 K, the Fe(III) doublet considerably decreases in spectral area compared to at 77 K, and the spectra is best fitted with an additional sextet, potentially suggesting the presence of a short range ordered Fe(III) mineral phases such as lepidocrocite or ferrihydrite. The same picture can be seen in the following transition sediments where in accordance with increasing silt content, the samples show a strong Fe-bearing PS signal. Doublets corresponding to Fe(III) and Fe(II) are present at 77k and remain prominent at 5k. The amount of Fe(II) and Fe(III) in PS based on the 5 K measurements rises in 30 m depth to about 10 % Fe(II) and 18 % of the spectral area Fe(III). As these two doublets remain prominent when measured at 5 K, also at lower relative abundances, the doublets most likely represent PS as the absence of magnetic ordering is a characteristic behavior for these minerals (Pollak & Stevenson 1986; Murad & Cashion 2004; Murad 2010). The transition zones at a depth of 30m differ from the other transition sediments also due to the detection of Hem, which accounts for around 13 % of the spectral area based on the 77 K measurements. Thus, the composition of the 30 m depth transition sediments is almost identical with the yellow-brown sediments from 36 m. A well-defined sextet, which is likely ordered Gt accounts for about 22 % and narrow Fe(III) doublet matching to short range ordered phases like Lep or Fh account for about a third of the 77 K spectrum. Since Lep could also be identified at this depth level by the magnetic investigations, it can again be assumed that the phase is Lep and not Fh. Two doublets corresponding to Fe(II) in PS account for about 5 and 13 % of the spectral area at the 77 k measurement. Again, a poorly defined sextet that accounts for about 15 % of the spectral area was used to achieve a satisfactory fit but could not be assigned to any phase. What remains to be noted is the great similarity of the Mossbauer spectra between the yellow-brown sediments at 36m depth and

the transition sediments (Fig. 35). An overview of all the results of the 4 Mossbauer measurements can be found in Table 24.

With an average of 395.5 x 10^{-6} SI (287 SD) (n = 15), the **Volume susceptibility (*k*)** in the transition sediments of core RD42 (Fig. 29) are roughly in the range of the aquitards and show a similarly broad range of values with 59-930 x 10^{-6} SI. Distinct layers with *k* values above 500 x 10^{-6} SI indicate a clear contribution of ferrimagnetic Fe minerals like Mt (Tarling & Hrouda 1993). The highest values indicating Mt is present at 19, 22, 26, 28.5, 30 and 41 m bgs. If the exceptional high (up to five times higher) k values in 28 m depth are excluded all samples with high k values are in the transition sediments and correlate with the total Fe content. In core RD54 (Fig. 30) the transition sediments have average k values of 282.6 x 10^{-6} SI (n = 14) with a spread from 106-960 x 10^{-6} SI. In RD54, the magnetic field measurements show significantly higher values at depths of 21, 25, 30 and 31 m and thus provide a comparable picture to RD42, indicating that the highest amount of (ferri-)magnetic Fe minerals are present in the transition sediments. In addition to paramagnetic minerals, such as (phyllo-) silicates and carbonates, the results indicate a higher proportion of ferromagnetic Fe phases such as Gt, Hem or Ilm.

Like in the previous aquifer units, **temperature dependent magnetic susceptibility** (*kt*) was used to specifically identify ferrimagnetic Fe-bearing minerals and their depth distribution. In contrast to the yellow-brown and grey sediments, the transition sediments show no characteristic kt pattern. Rather, the transition sediments are composed of overlapping signals from the two other aquifer units. The low temperature measurements of the transition sediments differ from the yellow-brown sediments by a well-marked Verwey transition (TV) at around -150 °C and resembles the results in the grey sediments. The signal is not as strong as in the grey sediments but still clearly indicates the presence of Mt in the transition sediments. High temperature measurements, indicate the presence of Lep (T_{t1}) and/or Fe-bearing carbonates (T_{t2}), similar to the yellow-brown sediments although the Lep signal at 280 °C is clearly more pronounced than in the yellow-brown sediments. The Curie temperature at around 580 °C, which is characteristic for Mt, is present (Dunlop & Özdemir 1997). In Fig. 37 a) the characteristic T_c clearly indicates the presence of Mt. The kt measurements in the at the upper aquitard-aquifer transition between 19 and 20 m along the laterite layer show a unique pattern in the core profile. In contrast to the other diagrams, the start of the low-temperature measurement shows only a weakly pronounced drop characteristic for Fh (Berquo et al., 2007; Liu et al., 2008). The high temperature measurement shows a shoulder at 300 °C (T_{t1}) and a peak at 500 °C that drops massively up to 600 °C (T_C). T_{t1} indicates the transformation of lepidocrocite into magnetite. The significant increase during the cooling cycle (T_{Ca}), is a clear indication of the presence of iron carbonates such as siderite (Pan et al., 2000). The massive drop during the heating cycle at 600 °C and the congruent increase during the cooling cycle is an indication of magnetite, hematite or maghemite (Dearing 1999; Hunt et al., 2013; Dunlop & Özdemir 2007; Just & Kontny 2012; Petrovsky & Kapicka 2005; Minyuk et al., 2011; Cornell & Schwertmann 2003; Pan et al., 2000). That the increase in the cooling cycle is less pronounced than for the other profiles (b, c, d) can be interpreted as a lower Fe(II) carbonate content in favour of a higher proportion of Fe(III) phases (Mt, Hem, Magh) in the mature laterite layer. In Fig. 37 b) and c) the transformation of lepidocrocite (T_{t1}) and Fe-carbonate (T_{t2}, T_{Ca}) into magnetite is visible. In the cooling curve T_c is much more pronounced and supplemented by T_{t2}. T_c could indicate further primary Mt. Fe-carbonate is seen in the heating curve. The diagrams show a strong drop in magnetic susceptibility at low temperature. Goethite or ferrihydrite and magnetite indicated by Verwey transition (T_V) and Curie temperature (T_C). d) Similar to b) and c) the sample at 40 m depth shows the transformation of lepidocrocite (T_{t1}) and Fe-carbonate (T_{t2}) into magnetite. (e) and (f) show reference curves from lepidocrocite and siderite. Note that siderite is probably not pure but contains some Mt as indicated by the T_C in the cooling curve, which is lower compared to pure magnetite. The

low-temperature curve shows a clearly pronounced drop that indicates Fh (Berquo et al., 2007; Liu et al., 2008). In addition, the low-temperature curves show a weak peak at -155 °C, which is the Verwey transition of magnetite (Dearing 1999). The Verwey transition peaks are pronounced to different extents along the depth profile and increase towards the reduced layers. In the high-temperature curve, the Fe-carbonate signal is much more pronounced in the cooling cycle than in the laterite layer (a). The heating cycle also shows the characteristic shoulder at 300 °C and the peak at 500 °C. In the depth course the peaks are always present but not always equally pronounced. This can be an indication of fluctuating Fe carbonate levels in favour of jacobsite or greigite, which can also lead to a peak at 300 with a subsequent sharp drop (Hunt et al., 1995). Transition kt patters (b, c, d) are best pronounced near the distinct transition sediments, but occur across the entire aquifer at 22, 30, 33, 36 and 40 m depth. They probably represent a redox transition signal related to mineral (trans-) formation and below 30 m they are bound to the appearance of narrow redox fingers along silty layers.

In summary the kt measurements indicate the presence of Fh as in the previous aquifer units. The low temperature curves shown in Fig. 37 (b, c, d) shows a strong drop in k below -190 °C indicative of Fe oxyhydroxides and usually addressed with Fh (Berquo et al., 2007; Liu et al., 2008) or sometimes Gt (Guyodo et al., 2003). It should also be noted that the alleged Fh signal occurs in all samples of the vertical core profile except the beige clays at a depth of 12-14m. Further it should be noted that the kt measurements are not an exclusive method and the results do not reflect the entire Fe mineral inventory. The results of the kt measurements within the transition sediments show a high level of internal variability and often change fundamentally within a few cm. The appearance of layers with a similar kt pattern to that of the yellow-brown indicates that reduced layers cross the transition zones. These sections show the same high and low temperature pattern as the reduced layers in the yellow-brown sediments and are characterized by an absent Verwey transition and a Curie temperature characteristic for Mt and Hem. In the transition sediments at 22, 30 and 41 m bgs, the different patterns lie next to each other. So it can be stated that, based on the kt results, the transition sediments consist, like the yellow-brown sediments, of alternating layers with different mineral properties. On the one hand, the transition sediments are characterized by the presence of various Fe oxyhydroxides including Mt, Lep, Hem and Fe carbonates. The presence of significant amount of Mt indicated by a clear Verwey transition and significant amounts of Lep which are indicated by the significant increase at around 280 °C clearly sets them apart from the yellow-brown sediments. In contrast other samples show only low amount of Mt and Hem. In principle, the transition sediments show the same alternating structure as the yellow-brown sediments, however the differences are much more pronounced on smaller scales.

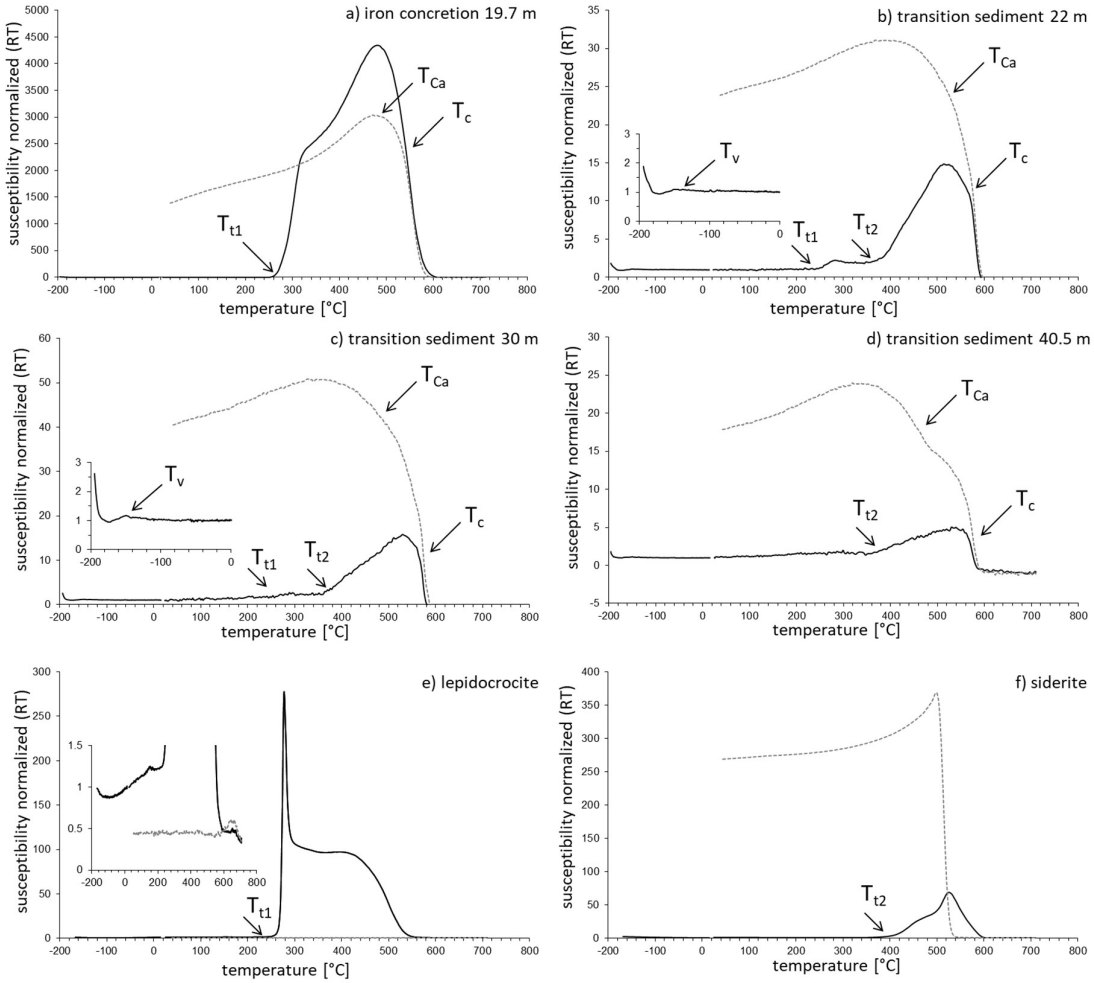

Figure 37: Temperature dependent magnetic susceptibility of the transition sediments

Heating curve is indicated in black and cooling curve in dotted grey. Values are normalized to value at room temperature.

a) *Transformation of lepidocrocite (T_{t1}) and Fe-carbonate (T_{Ca}) into magnetite. b) and c) Transformation of lepidocrocite (T_{t1}) and Fe-carbonate (T_{t2}, T_{Ca}) into magnetite. d) Similar to b) and c) the sample at 40 m depth shows the transformation of lepidocrocite (T_{t1}) and Fe-carbonate (T_{t2}) into magnetite. (e) and (f) show reference curves from lepidocrocite and siderite.*

9.4.3.1 Fe(III) dominated microcrystalline precipitates

Based on microscopic investigations the most distinctive feature of the transition sediments are widespread Fe-precipitates, which form **coatings around primary grains** (Fig. 38) and **extensive cementations across primary particles and pore space** (Fig. 39). Both types of Fe precipitates are present in the transition sediments along the entire redox interface. They represent the largest documented Fe pool across the entire aquifer and dominate the local Fe inventory and correlate with high Fe_2O_3-solid concentrations. In core RD42 Fe precipitates are particularly pronounced in depths of 20, 22, 27, 30 and 41 m bgs and in core RD54 at 20, 30 and 42 m bgs. They usually appear in a sandy matrix with high permeability on the less reduced site of the redox interface. The occurrence of the precipitates in the transition sediments follows a well-defined spatial pattern and is restricted to the immediate vicinity of the redox interface. Coming from the grey sediments towards the redox interface, the amount of precipitates increases continuously. Most widespread are well pronounced multi-layered coatings, which consistently cover the primary grains of the transition sediments. The precipitates show a yellowish to orange colour under the polarization microscope and increase continuously towards the redox interface in size and volume (Fig. 39). The yellow to orange to brown colours indicates the presence of the Fe(III) oxyhydroxides Gt and Hem. However, high-resolution studies show that most precipitates are built up in a very complex manner and the composition can only be determined to a small extent by microscopy.

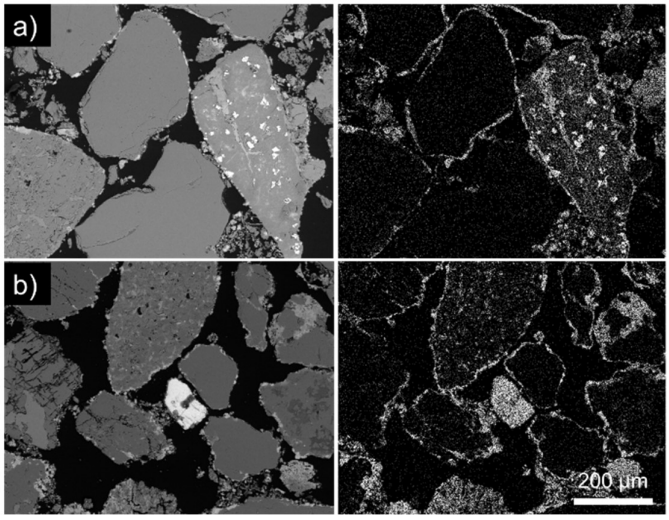

Figure 38: Backscatter micrographs of Fe oxyhydroxide coatings at a) 27 m and b) 30 m depths

The backscatter micrographs and the corresponding Fe Ka1 on the right show the ubiquitous Fe-coatings surround the primary particles.

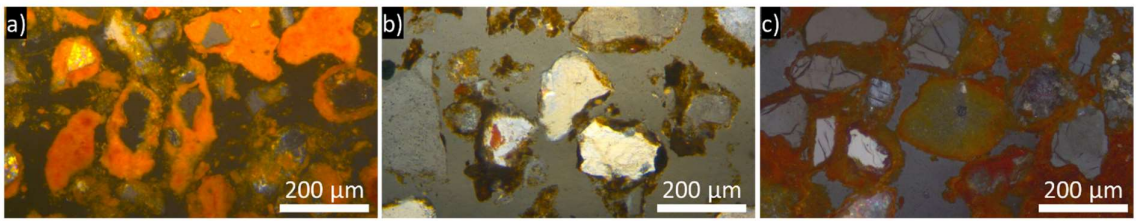

Figure 39: Reflected light (ppl) micrographs of transition sediments

a) Micrograph of the iron concretion at the top aquitard-aquifer transition at 19.7 m bgs in RD42 showing extensive Fe precipitates around primary particles frequently filling the whole pore space in-between the primary grains in strong orange colour. b) Micrograph of the transition sediments at 21 m bgs shows less pronounced yellow precipitations mainly in form of coating around primary particles. c) Micrograph of the transition sediments at 41m bgs showing extensive Fe-precipitate covering primary particles and overgrow pore space.

Near the redox interface the Fe precipitate density increases massively and the coatings gradually expand into cementations. The transition between the features is seamless and is characterized by a colour change to a darker brown and orange. Most noticeable is the massive increase in size and volume of the Fe-precipitates. The precipitates form isolated clusters that expand over several mm and overgrow weathering primary particles (Fig. 40).

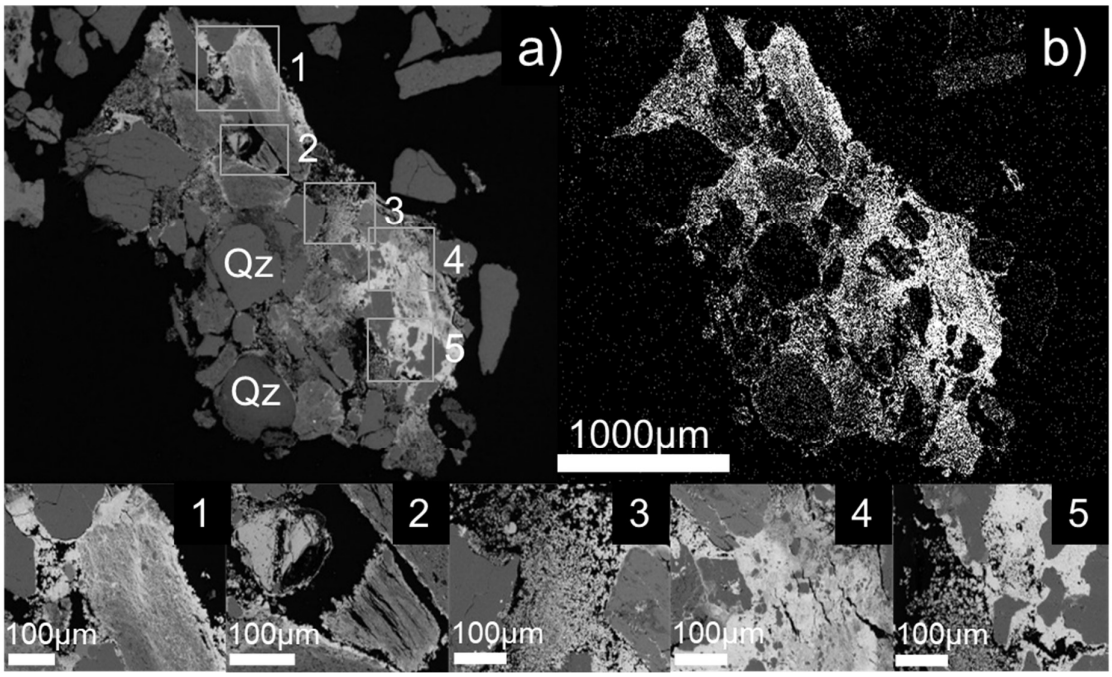

Figure 40: Backscatter micrographs of Fe-cementations at 27 m depth

a) Backscatter micrograph and b) corresponding Fe Ka1 on the right show extensive Fe precipitations covering primary particles and covering pore space. The white frames highlight various features including: 1 iron bended Qtz, 2 weathering PS and 3-5 extensive microcrystalline Fe-O precipitates

The expansion of the cluster gradually increase until the density of precipitates reaches its maximum size at the redox interface and **extensive cementations** form almost coherent structures that can reach several millimetres in diameter (Fig. 41) and length can be seen with the naked eye (Fig. 43a & 48e).

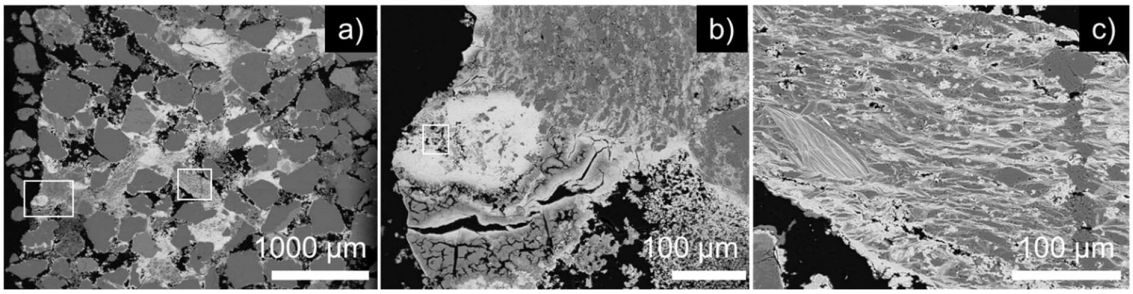

Figure 41: Backscatter micrographs of extensive Fe cementation cluster at 40 m depth.

Backscatter micrographs of a) an extensive Fe-cementation cluster that corresponds to the photomicrograph from Fig. 48 a). The white rectangles mark the area shown in b) and c) as magnification b) corresponds to Fig. 43. b) and the white frame marks the mapping area of the EMPA measurements shown in Fig. 44. c) shows Fe pprecipitates penetrate deep into cracks of primary particles and form iron bended Qtz

Both coatings and cementations of the transition sediments consist of complex and highly heterogeneous Fe-precipitate phase mixtures in variable composition and form crystal grains on the sub-µm scale, which could neither be identified nor quantified microscopically (Fig. 42, 44, 45). The crystals are in the sub-µm range down to nanoparticles with a wide range of morphology and mineralogy. The small crystal size, the complex internal structure and small-scale adhesions of different Fe phases with embedded primary and secondary mineral grains create inconclusive optical properties (colour, extinction angle) and often prevent a clear assignment with the light microscope. In order to discriminate the Fe precipitates and identify the Fe mineral composition high-resolution microscopy was combined with spatial resolved EPMA, SEM-EDX and µXANES measurements. Spatially resolved **µXANES** (Fig. 43 c) revealed that the Fe precipitates are present as crystalline oxyhydroxides, which consist in average of 77 % Gt (59-89 %) 14 % Hem (6-31 %) and 9 % Mt (4-15) (R-factor 0.000194 n=21) (Table 10). The results are largely in accordance with bulk EXAFS, Mossbauer, XRD and kt measurements who also identified Gt as the dominant Fe phase, supplemented by Hem and Mt. Characteristic µXANES spectra clearly indicate a crystalline character although gel-like texture and small crystal size (Fig. 42, 44, 45) suggest amorphous to poorly crystalline phases. The absence of clear microscopically determinable crystal characteristics suggests a composition of Fe phases in the sub-µm range. It is therefore assumed that the precipitates are composed of a complex phase mixtures with variable crystallinity and particle size that most likely corresponds to **microcrystalline Fe(III) and Fe(II/III) oxyhydroxide phases**. This is in line with the results of combined synchrotron-based measurements, Mossbauer and magnetic susceptibility measurements which reveal specific mineral spectra in the absence of visible crystal features. Also the locally characteristic mineral colours observed under the polarizing microscope (Fig. 39 & 50), which indicate at least weakly developed crystalline structures, are in line with this interpretation.

With regard to the mineral composition differences between the coatings and the cementations could be documented. High-resolution backscatter analysis reveal that the **coatings** in the transition sediments are usually 1-20 µm thick and consist of two or more layers with different texture. The coatings differ from the (presumably detrital) coatings in the yellow-brown sediments in their dimensions and their complex multi layered structure and diverse (surface) morphology. Filigree filaments, fibres, twisted stalks and needle-like structures, which form a kind of honeycomb or sponge structures in great variety, follow a massive layer directly on the grain surface with a gel-like appearance (Fig. 42 b-f). The sponge-like structures are composed of nano- to microcrystals and resemble Fe precipitates in microbial mats (Voegelin et al., 2013; Sanchez-Roman et al., 2015). In some places the bacterial cells are still visible (Fig. 42f) and therefore clearly indicate recent microbiological processes. The filigree surface structures also confirm recent processes and the secondary character of the Fe-coatings. Towards the internal layer the filigree structures are continuously condensed. The consolidation corresponds to a recrystallization process and is accompanied by a change in texture, surface area and a decrease of As element concertation. In order to assign the mineralogy of the coatings the biggest challenge was the resolution of the small structures. In this context it must be taken into account that the spot size of the spatially resolved synchrotron measurements is 40 x 30 µm. Therefore, the small-scale structures cannot be resolved individually and it is not possible to assign a specific Fe mineral composition to the different morphologies. To address the mineral composition of the coatings a series of measurements (n=15) was carried out in coating-rich and cementation-free areas (Fig. 43). The µXANES measurements result in an average Fe mineral composition of 80 % (67-89 %) Gt, 12 % (6-20 %) Hem and 8 % (5-15 %) Mt. Based on the assumption that the change in mineralogy is evident in the texture of the coatings the filigree sponge-honeycomb shaped outer structures are most likely Gt dominated. In contrast, the mature inner layer should contain a higher amount of Mt and Hem. This assumption is in accordance with the bright white backscatter contrast and an increasing Fe_2O_3 content towards the center. **EMPA** measurements (n=2) revealed **As concentrations**

< 70 mg/kg (LOD) in the inner most likely Hem/Mt-rich layers, while the As concentration in the outer most likely Gt-rich layers is distinctly higher and reaches 270 mg/kg (Fig. 39d). The decreasing As concertation towards the centre is another hint for progressive crystallization process towards the inside and the presence of less As-affine Fe minerals such as Hem and Mt compared to the high-surface Gt along the outside. The spatially resolved geochemical measurements showed SiO_2 Al_2O_3 P_2O_5, CaO and SO_3 as permanent components in the coatings. With regard to most elements the concentration significantly differs between the inner and out part. Since the measured concentration differences are also influenced by the different precipitate density, the values cannot be compared directly. This is also the reason for the strongly variable Fe_2O_3 content with 50 to 80 wt% between the inner and outer part of the coatings. However, it should be noted that SiO_2, Al_2O_3 and especially P_2O_5 show high concentrations in the range of around 2-3 wt% each. Spatially resolved **µXANES** measurements at the As K-edge revealed an As(III): As(V) ratio of 71:29 (n = 15) across the coatings (Fig. 40 & Table 9).

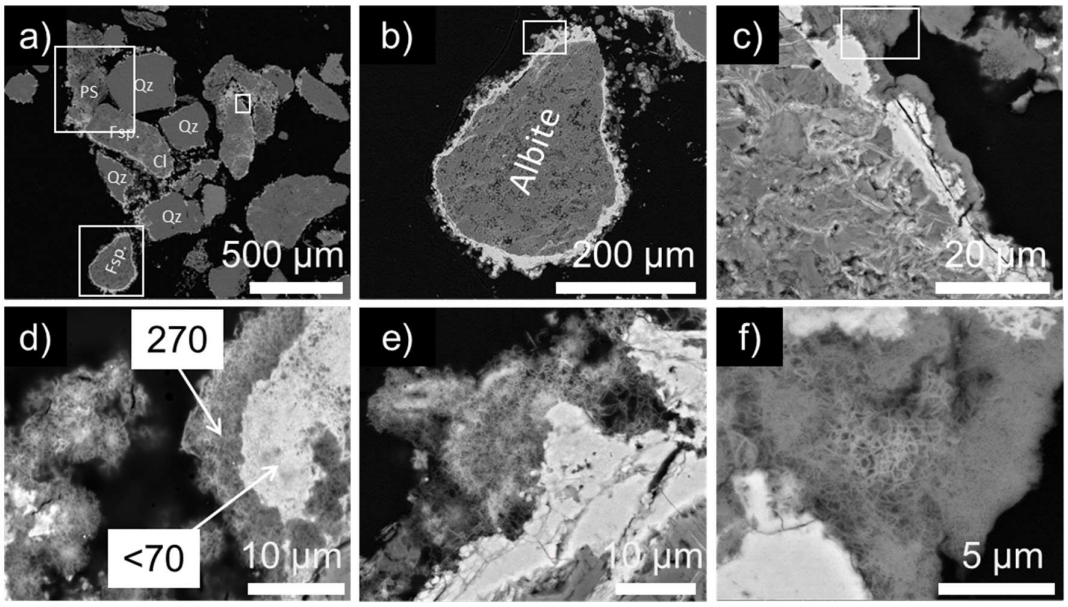

Figure 42: Backscatter micrographs of Fe oxyhydroxide coatings at 40 m depth

a) Shows Fe-coated primary sub-rounded quartz (Qtz), feldspar (Fsp) and phyllosilicate (PS) grains at 40 m depth. b) The primary grains are entirely surrounded by coatings (c) with a two-layer structure. A inner bright white layer, mostly likely composed of Mt/Hem, is covered by a less dense grey rim which is most likely Gt dominated in form of ffiligree filaments, fibres, twisted stalks and needle-like structures, which form a kind of honeycomb or sponge-like structures in great variety (d-f). d) The filaments on the left show a radial growth from a dense core and form radial spheres. Connecting spheres start to from a complex network. The distinct texture suggests small particles as bacterial cell or sub-µm clay minerals as nucleus for Fe precipitation. On the right side, a well-developed honeycomb structure covers older condensed and recrystallized material (white) indicate progressive recrystallization processes of the filigree fibre network. Numbers give mg/kg As. For further elements (given as oxide) see Table 9. e). The texture of the filaments changes continuously but always shows recrystallized areas and filigree sections that must have formed recently. Finally the completely recrystallized material has a homogeneous platy structure f) The delicate mineral fibers show a great morphological diversity and resemble structures formed by bacterial activity and are occasionally accompanied by cemented bacterial cells (right top).

Table 9: Microprobe based elemental composition (given as oxide) of Fig. 42 d)

position	As [mg/kg]	Fe_2O_3 [wt%]	SiO_2 [wt%]	Al_2O_3 [wt%]	P_2O_5 [wt%]	CaO [wt%]	SO_3 [wt%]
centre	< 70	78.60	2.77	2.92	3.34	0.20	0.06
edge	270	47.22	1.59	2.33	1.96	0.13	0.25

High-resolution backscatter analysis across the cementations reveal on the one hand precipitates with a homogeneous massive appearance that penetrate deep into cracks of overgrown and embedded primary Qtz and Fsp grains (Fig. 40-41a). The structures appear in the backscatter images as coherent bright white areas that are composed of crystals in the sub-µm range. On the other hand, heterogeneous structures with alternating layers and thin precipitation bands form a huge variety of multi-layered gel-like to platy structures (Fig. 44 & 45). Comparable multi-layered structures are known from sediments as Liesegang bands and are typical morphologies related to intense precipitation and crystallization processes in context of saturated to supersaturated solutions (Sultan & Abdel-Rhaman 2013). The alternating cementation layers and Liesegang bands indicate oscillating hydrochemical conditions with strongly variable dissolved Fe content. In order the measure the cementation composition a coating-free area was selected to conduct the measurements (Fig. 43 b). **µXANES** measurements (n=6) across the cementations reveal the same mineral inventory with Gt, Hem and Mt although the composition differs slightly compared to the coatings (Table 10). The main difference is a decrease of Gt by 10 % to 70 % (59-80 %) in average. Contrary, the Hem portion rises by 8 % and averages 20 % (12-31 %). The Mt content in the cementations also rises, but at 10 % (8-12 %) it only shows an increase of 2 %. It is assumed that the massive platy recrystallized areas with a high backscatter contrast are Hem-Mt dominated while the darker grey gel-like multi-layered structures are Gt-dominated. Interestingly the precipitations contain no Fe(II) minerals. Based on our EXAFS LC-fit (Table 10) the small Fe(II) content is covered by the presence of Mt and may be supplemented by Fe(II) from mixed valence PS minerals. Despite obviously different textures, **EMPA measurements** across the layered cementations (n=13) show no major differences with regard to the most elements (Fig. 44). Fe_2O_3 accounts for 83 to 93 wt% in all areas and can be considered as relatively constant with an average of 87.2 wt%. The same accounts for P_2O_5 (in average 4.3 %, 3.7-5), Al_2O_3 (2.8 %, 2.3-3.5), SiO_2 (2.9 %, 2.4-3.3), CaO (0.28 %, 0.18-0.46) and SO_3 (0.19 %, 0.01-0.79). While the concentrations of Al_2O_3, SiO_2 and CaO are in a moderate to high range, the P_2O_5 concentrations are remarkably high.

The **As concentration** in the coatings show significant fluctuations and vary between the LOD and almost 500 mg/kg. The As concentration does not follow any general pattern and there is no clear link to the texture. Both the gel-like and the massive platy areas show a broad range of As concentrations. Although As concentrations above 400 mg/kg are limited to the bright platy presumably Gt-dominated cementations, the darker presumably Mt/Hem-rich gels also reach concentrations over 300 mg/kg As. The mapping reveals that increased As concentrations usually go along with increased P_2O_5 and CaO concentrations. As concentrations up to 500 mg/kg, high average concentration of around 300 mg/kg As and high amount of co-adsorbed elements indicate effective sorption and incorporation processes for the precipitates. In contrast to the coatings the cementations show an almost balanced As(III):As(V) ratio of 53:47 (n=6) based on µXANES. SO_3 (0.19 %, 0.01-0.79) shows noteworthy fluctuations across the cementations. The highest SO_3 concentrations occur in the gels, but do not follow a generally applicable pattern. Despite the presence of SO_3, P_2O_5 and CaO, no sulphides, phosphates or carbonates were detected so it can be assumed that the elements are sorbed together with As in the precipitates. The presence of Al_2O_3 and SiO_2 could indicate the presence of sub-µm PS minerals while SO_3 and P_2O_5 suggest the presence of OM as typical elements for organo-mineral structures. However, concrete evidence cannot be provided for either the PS or the organo-mineral structures also lower density indicated by backscatter images (Fig. 42) support their presence. The As concentration reach noteworthy high concentrations of 500 mg/kg and since the concentration hardly falls below 150 mg/kg As, the cementations also contain high average concentrations of around 300 mg/kg As and therefore retain significant amounts of As. Quantitatively the widespread mc Fe precipitates seem to be the most important As carriers in the system. With regard to the As retention, the cementations play the dominant role as the coatings contain in average only half the amount of As.

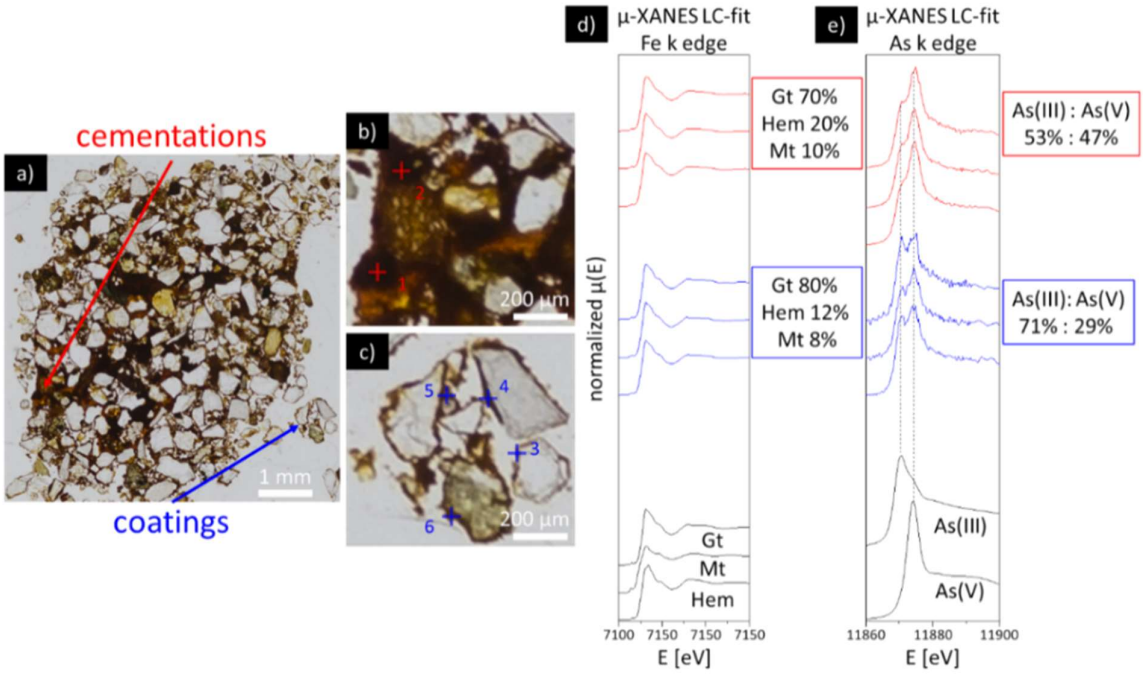

Figure 43: Photomicrograph of an extensive Fe cementation cluster at 40 m depth

a) Fe cementation cluster corresponding to Fig. 41a, b & 48. b) Brown cementations fill up pore space and cover primary grains in the central area in while in the outer areas, orange to yellowish coatings surround the grains. The measuring position on the bottom left in the close-up corresponds to Fig. 41b. c) shows a close-up from the measurement positions of the coatings. Spots for µXANES analyses at the Fe K-edge are marked by red and blue crosses in b) and c). d) shows the results of the Fe K-edge µXANES measurements and the goethite (Gt), magnetite (Mt), hematite (Hem) reference compounds. e) shows As K-edge µXANES spectra of As(III) and As(V) measured at the same positions of the coatings and cementations. The red and blue boxes give the different Gt:Hem:Mt and As(III):As(V) average ratios in the coatings (blue) and cementations (red). Figure was already shown in Kontny et al. (2021).

Table 10: µXANES LC-fit results revealing Fe oxyhydroxide composition, As species distribution and presence of Mn(II) and Mn(III) phases. Measuring points indicated in Fig. 43

position		µ-XANES LC-fit Fe k edge			µ-XANES LC-fit As k edge		µ-XANES LC-fit Mn k edge	
		Mt	Gt	Hem	As3-Gt	As5-Gt	Mn(II)	Mn(III)
		%	%	%	%	%	100 %	45-50 %
cementations	1 a	9.7	58.9	31.4	53.1	46.9	x	
	1 b	7.7	65.7	26.6	55.7	44.3	x	
	1 c	8.9	80.0	11.1	51.2	48.8	x	
	2 a	12.2	66.9	20.9	46.7	53.3	x	
	2 b	10.5	73.0	16.5	55.3	44.7	x	
	2 c	9.9	78.5	11.6	53.7	46.3	-	-
	average	**9.8**	**70.5**	**19.7**	**52.6**	**47.4**	-	-
coatings	3 a	8.9	80.2	10.9	66.0	34.0	x	
	3 b	9.3	78.2	12.5	66.4	33.6	x	
	3 c	9.8	78.7	11.5	67.4	32.6	x	
	3 d	13.8	67.2	19.0	69.4	30.6	x	
	3 e	6.2	73.5	20.3	67.1	32.9	x	
	4 a	6.3	83.3	10.4	76.3	23.7		x
	4 b	15.0	65.2	19.8	67.1	32.9		x
	4 c	4.5	86.9	8.7	72.8	27.2		x
	5 a	5.3	86.6	8.1	78.4	21.6		x
	5 b	9.3	77.6	13.1	70.8	29.2		x
	5 c	5.3	88.5	6.2	-	-		x
	5 d	-	-	-	69.9	30.1	-	-
	5 e	6.1	84.4	9.5	-	-		x
	5 f	7.8	82.5	9.8	65.0	35.0		x
	5 g	12.1	73.3	14.6	72.0	28.0	x	
	6	6.3	83.9	9.8	79.9	20.1	-	-
	average	**8.4**	**79.3**	**12.3**	**70.6**	**29.4**	-	-

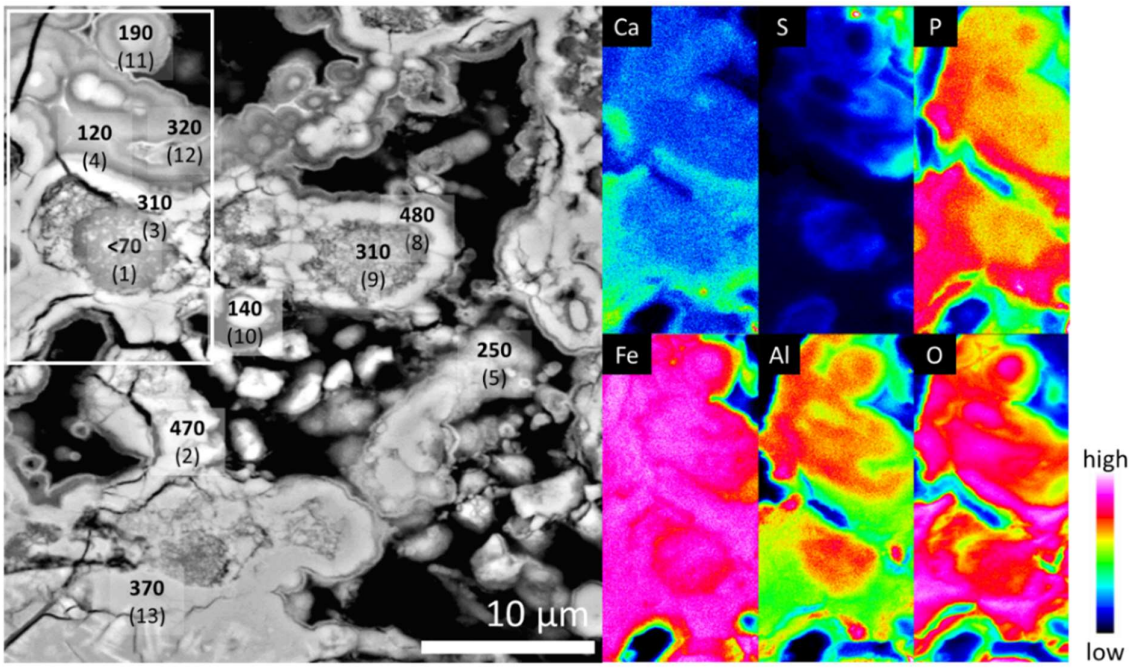

Figure 44: Backscatter micrograph of Fe precipitates occurring as massive cementations at 40 m depth

The section corresponds to the white square from Fig. 41b. The multi morphology precipitates consist of gelic precipitates and platy areas. Based on the contrast of the backscatter image the gel like Fe precipitates in dark grey represent most likely Gt-rich areas while the bright grey to white areas emphasize higher amounts of Mt and Hem. Bold numbers give As concentration in mg/kg and the number in brackets shows the measuring points in Table 11. Elemental mapping images on the right for Ca, S, P, Fe, Al, O are given for the area labelled by white frame.

Table 11: Microprobe based elemental composition (given as oxide) of Fig. 44

position	As [mg/kg]	Fe_2O_3 [wt%]	SiO_2 [wt%]	Al_2O_3 [wt%]	P_2O_5 [wt%]	CaO [wt%]	SO_3 [wt%]
1	< 70	89.56	2.70	2.99	3.94	0.21	0.26
2	470	87.83	2.84	2.28	4.99	0.36	0.01
3	310	87.85	2.91	2.71	4.59	0.33	0.07
4	120	92.51	2.62	3.26	3.96	0.19	0.13
5	250	84.11	3.31	3.04	4.79	0.27	0.14
8	480	82.73	2.86	2.50	4.35	0.33	0.22
9	310	83.41	2.76	2.47	4.01	0.21	0.08
10	160	92.48	3.20	2.57	3.71	0.33	0.07
11	190	87.42	2.75	3.47	4.00	0.22	0.35
12	320	83.11	2.38	2.90	3.77	0.18	0.79
13	370	87.83	3.04	2.49	4.99	0.46	0.02

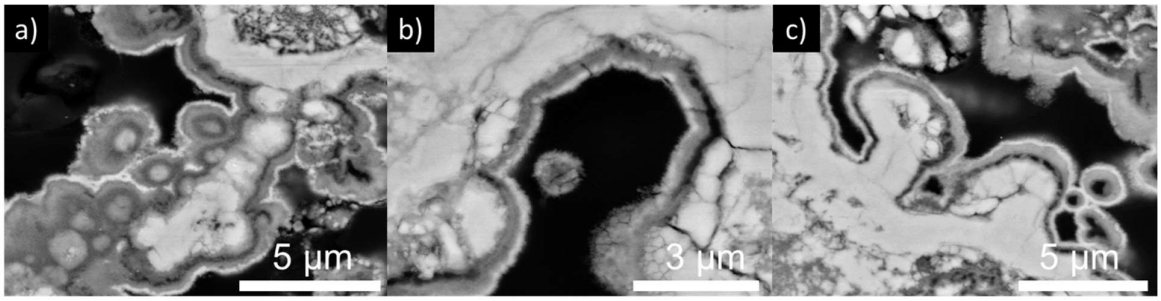

Figure 45: Backscatter micrographs of selected multi layered precipitates at 40 m depth

a) Concentric dark coloured rims indicate organo-mineral complexes around a precipitations nucleus. The white central areas as well as a thin outermost layer indicate pure Fe oxyhydroxide. b) Hexagonal pore resembles the characteristics of a) with an organo-mineral complex in-between pure Fe oxyhydroxide layers. The filigree surface structures indicate the importance of local flow conditions for precipitate growth. c) mushroom-shaped precipitate structures with the same characteristic sequence grow into the pore space.

Mn K edge µ-XANES spectra have been measured at the same positions as As and Fe K XANES spectra in order to check for correlations between Mn and As and Fe oxidations states (Table 10). However, the sample Mn spectra cannot be described satisfactorily by a linear combination with the available reference spectra.

- Mn(II): MnO, $MnSiO_3$ (Rhodonite), $MnCO_3$, $MnSO_4xH_2O$, Mn_2SiO_4 (tephroite), spessartine, olmiite, johannsenite
- Mn(III): α-MnOOH (groutite), γ-MnOOH (manganite), $MnPO_4$ (purpurite) and Mn_2O_3 (bixbyite)
- Mn(IV): MnO_2 (pyrolusite)

Consequently the Mn sample species are of different nature than these compounds. Nevertheless, due to the different edge positions of Mn(II), Mn(II) and Mn(IV) reference spectra a linear combination fit results in semi-quantitative Mn redox fractions for the sample spectra, where edge positions plot between the Mn(II) and Mn(III) reference spectra. The LC fit results give better fits for combinations of Mn(II) and Mn(III) than for Mn(II) and Mn(IV) combinations of reference spectra, and results in about 45-50 % Mn(III) fraction in the coating samples where the highest As(III) and Gt fractions occur. While the Mn(II) content in the cementations is almost 100 %, the Mn(III) content in the coatings is between 25-50 %. Mn(IV) could not be detected.

Another widespread feature of transition sediments are associations of Fe precipitates with (Fe-rich) phyllosilicate minerals. Both coatings and cementations are regularly interspersed with Fe-rich phyllosilicate minerals forming **iron-phyllosilicate complexes (Fe-PS complexes)**. The disintegration of primary Fe-rich PS clearly contributes to Fe dynamic and seems to support the local formation of Fe precipitates as they occur regularly embedded in coatings and cementation structures (Fig. 46).

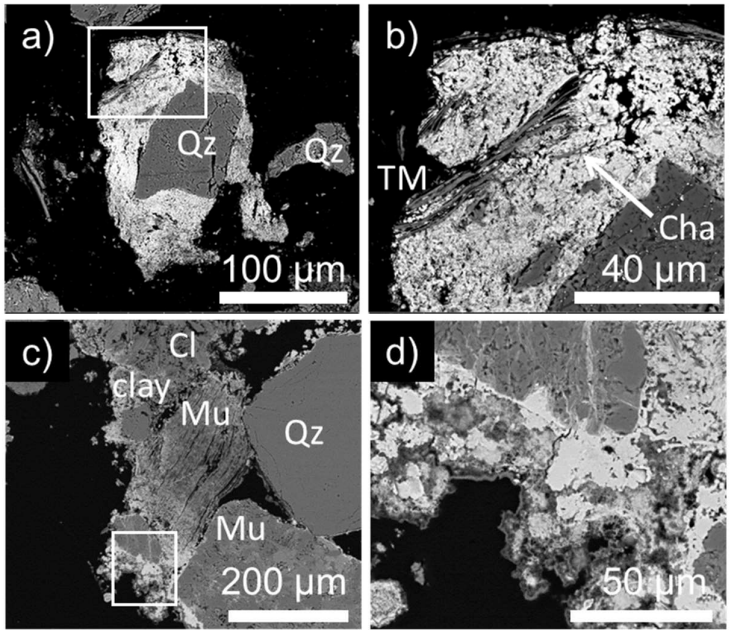

Figure 46: Backscatter micrographs of Fe-PS complexes in the transition sediments

a) Shows a primary Qtz grain surrounded by secondary Fe precipitates and PS in a multi-mineral matrix at 30 m depth in RD42. b) Magnification of weathering o primary iron bearing clay (chamosite), marked by white arrow. c) Locally lithic fragments form adhesions with various PS (e.g. muscovite, chlorite, etc.). The PS show a huge variety and structural heterogeneity and often appear together with small-scale Fe precipitates to form Fe-PS complexes. d) Fe-PS complexes settle along the adhesions and trigger the formation of a complex multi phase mixture and multi texture surface covering.

Furthermore, secondary Fe-rich PS in the sub-µm range are present throughout the precipitates and seem to act as precipitating surface for Fe oxyhydroxide (Fig. 47). The constant Al_2O_3 additions and textures in the sub-µm range and the close spatial association of Fe precipitates and Fe-PS complexes suggests that the weathering and secondary formation of Fe-phases and PS minerals is closely related.

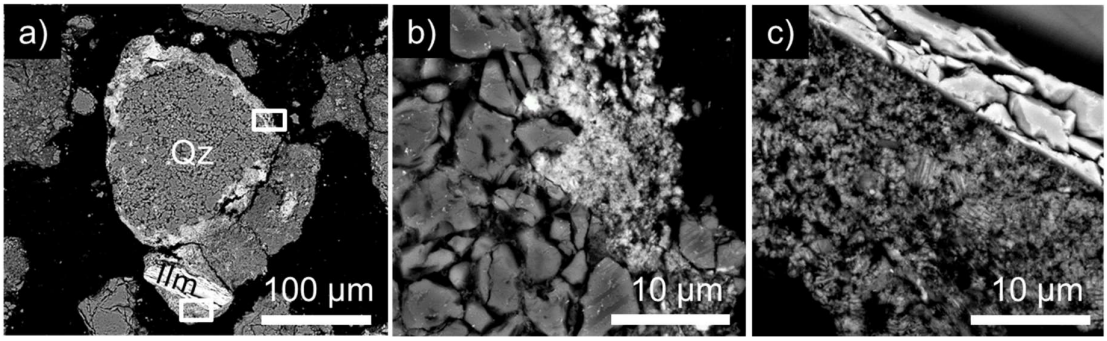

Figure 47: Backscatter micrographs of Fe oxyhydroxide coated Qtz grain in the transition sediments

a) Adjunct disintegrating Ilmenite supports formation of secondary Fe phases at 30 m depth in RD42. b) & c) show sub-µm particles as nucleus for iron precipitation along the surface of primary particles.

The Fe precipitates lead to an enrichment of Fe in the solid phase and trigger the formation of characteristic transition sediments overserved along the redox and GS boundaries. The strong orange to brown colours are related to freshly precipitated Fe oxyhydroxide precipitates. They clearly separate from the surrounding sediments on the macro scale. The transition sediments consist of recurring Fe-precipitate layers of variable thickness at 21 and 30m depth (Fig. 48 b, c) or form coherent concretion-like structures along the lithology boundaries at 20 and 41m bgs(Fig. 48 a, d). Distinct Fe-accumulation through formation of secondary Fe(III) precipitates is a particular feature of the transition sediments and separates the aquifer unit from all other layers of the core.

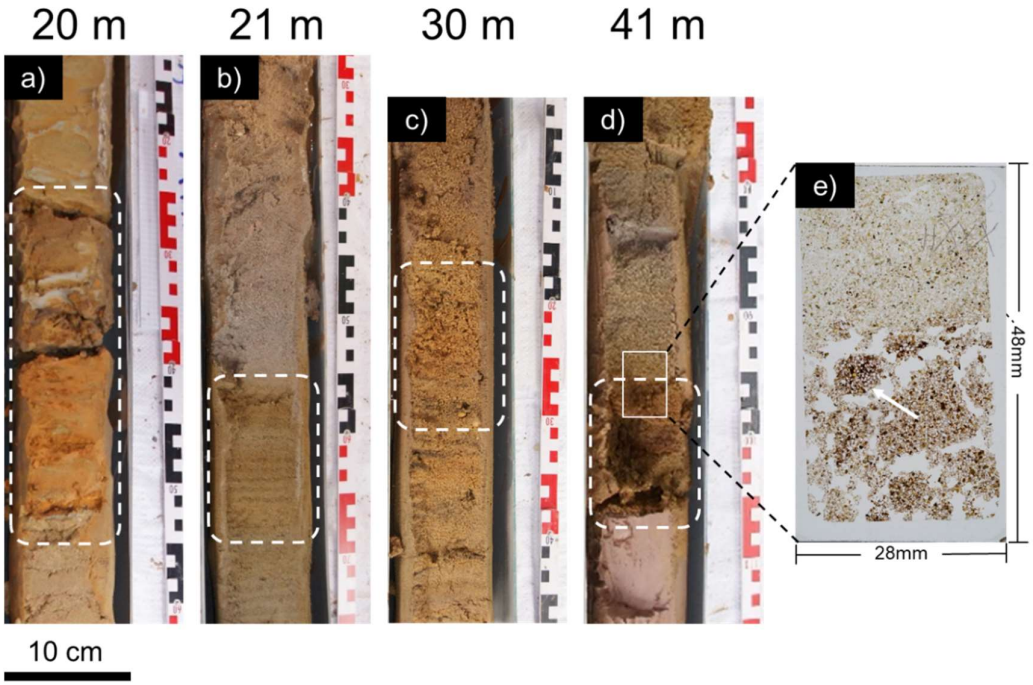

Figure 48: Characteristic orange transition sediments (indicated by dotted square) at 20 a), 21 b) 30 c) and 40m d) bgs. e) shows the corresponding thin section to d) highlighting the strong colour gradient that characterize these sediments.

a) A massive Fe-concretion stretching from 19.6 to 20 m depth marks the transition from the upper aquitard to the aquifer below. The sediments directly boarder the silt layers above and are characterized by brown and strong orange colours over a distance of about 30cm. b) At a depth of 21 m, the transition sediments show a regular layering of brownish and yellowish layers and extend over around 15 cm. c) At a depth of 30 m, the transition sediments clearly separate from the surrounding material over a distance of around 15 cm The characteristic orange colour decreases significantly and turns into greyish colours upwards and yellow-brown colours downwards. d) The transition sediments along the lower aquifer aquitards transition in 40 m depth extend for about 10 cm. They directly adjoin the bottom silt layers and are enclosed on the other side by the lower sandy redox finger. Their strong orange colour clearly distinguishes them from all other sediments. The white frame indicates the position of the thin section shown in e. e) Corresponding thin section from 40 m depth across the sharp colour gradient with well visible Fe oxyhydroxide precipitate cluster (marked by white arrow) next to the redox interface on the less reduced side of the redox interface. The cluster was chosen for combined EMPA and µXANES analysis (Fig. 41, 43). It must be noted that the photos can only partially depict the strong colour gradients. Figure was already shown in Kontny et al. (2021).

With regard to the Fe-precipitate formation in the transition sediments **preferential flow paths** and **hydrological barriers** seem to play a decisive role. The occurrence of the Fe precipitates seems to be mainly controlled by GW flow as secondary Fe phases are clearly pronounced along these features. Fe precipitates appear always where the GW gradients seems to be particularly strong and changes on permeability and therefore flow velocity are to be expected. Frequent variations in grain size control the small-scale hydrology. SEM-EDX and EMPA based element distribution maps reveal the frequent occurrence of preferential flow paths in mm to cm scale throughout the transition sediments. The flow

paths are often well-defined and can be identified with the naked eye as they clearly stand out from the surrounding material (Fig. 49). This flow paths act as hot spots for the Fe-precipitate formation as they are always accompanied by Fe precipitates in various scales. The corresponding elemental maps imply the importance of micro-scale flow paths with regard to the hydrogeochemical processes along the redox interface. The extensive cementations are criss-crossed by mm-scale preferential flow paths (Fig. 50) along which the precipitate density is significantly higher. An increased precipitation density can also be observed along hydrological barriers such as silt layers and especially along the aquifer-aquitard boundaries. Along GW flow boundaries, Fe precipitates form in considerable amounts along the interface (Fig. 51a) or grain size variations (Fig. 51b). The observations highlight the importance of small-scale hydrology and sedimentology with regard to Fe mineral dynamic.

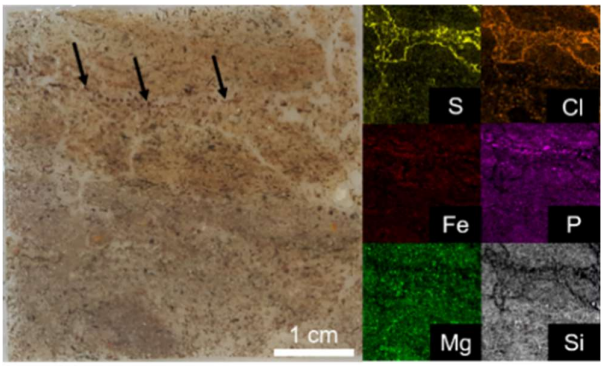

Figure 49: Thin section from 27.5 m bgs (RD42) with well pronounced colour transition and preferential flow path.

Micro Fe-precipitations and Fe-PS complexes are visible as chain of small red dots along the flow path on the less reduced side of the redox interface and marked by black arrow. The preferential flow path is clearly visible in the elemental S, Cl, Si and Mg mappings (µXRF) on the right. while Fe & P are congruent with the micro Fe-precipitations and Fe-PS complexes.

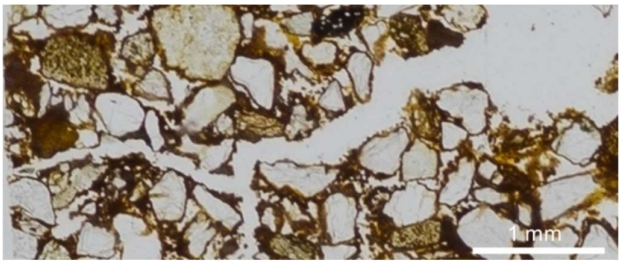

Figure 50: Photomicrograph showing extensive yellow to orange coloured Fe-precipitations along a preferential flow pats in a Qtz dominated matrix in 41 m depth of RD42 (Photo width 4.3 mm).

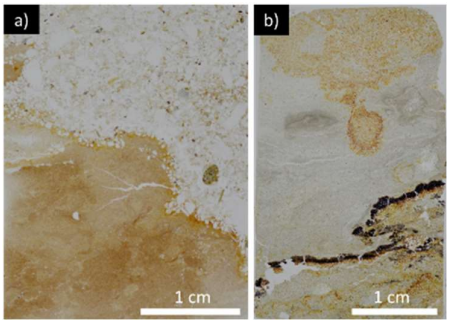

Figure 51:. Transmitted light microscopy of a) Fe mineral precipitate formation along a brown silt (lower left) to grey sand (upper right) interface at 31 m depth in RD54 b) Fe mineral precipitates formation along grain size variations (centre) at 20 m depth in RD54

9.4.3.2 Fe(II)-carbonates

In addition to Fe(III)-dominated oxyhydroxide precipitates, Fe(II) carbonate phases were detected in the transition sediments. Although several bulk methods had already indicated in their presence in the yellow-brown sediments they could not be detected by other methods. In the transition sediments it was possible to identify Fe carbonates microscopically and carry out spatially resolved measurements. Based on the microscopic investigations, Fe carbonates are very common in the transition sediments and are present in three variants that differ with regard to their textural and geochemical properties. Most common are mixed Fe-Mn carbonates. In addition, isolated Fe-Mn carbonate precipitates could be documented which clearly separate by texture and size. Pure skeletal Fe carbonates make up the third carbonate mineral group but are much rarer.

Most widespread are **mixed Fe-Mn carbonates** with a Mn-, Ca- and C-rich core and a Fe and O-dominated rim (Fig. 52). The crystalline Fe-Mn phases are the dominant carbonate phase in the direct vicinity of the redox interface. In contrast to the Fe oxyhydroxide precipitates the mixed Fe-Mn-carbonates appear frequently on the reduced side of the transition zone and could also be documented in slightly greyish flow channels in some distance to the redox interface. However, in completely reduced grey sands or near Fe(III)-dominated precipitations the mixed Fe-Mn-carbonates are absent. The quantity of Fe-carbonates seems to be linked to the occurrence of clay-rich layers as their number increases near fine-grained layers. They are particular frequent in the (organic) carbon-rich transition zones above and below the redox front at 20-22 and 30 m where they occur together with Fe(II)-sulphides (see chapter 9.4.3.3). Due to the clear spatial separation of the Fe and Mn dominated areas, the phases are not true Fe-Mn carbonates such as Ank but rather a sequence of the Mn carbonate rhodochrosite and Fe carbonate the siderite. Most Fe-Mn carbonates in the transition sediments have a macrocrystalline structure and form spherical and irregular shaped grains with a diameter between 20 and 100 µm (Fig. 52. a-c). The distribution of the mixed Fe-Mn carbonates within the sediment does not follow any definable pattern and the carbonates are arranged rather randomly in the sandy matrix. The carbonates usually fill pores and cavities but occasionally they also overgrow transported primary minerals and mineral fragments (Fig. 52. a-c). Towards the rims, the carbonates show signs of dissolution and transformation processes. A thin skin that usually encloses the entire mineral phase and roughened grain surface indicate Fe-carbonate dissolution. Regularly occurring cracks with altered edges confirm the impression of progressive disintegration. The element shift in the altered areas to increased O, Al and Si content to the detriment of C and Ca and occurrence of small sub-µm structures suggest that new minerals are formed within the alteration rims. Changing element composition and small structures with bright backscatter contrast indicate the transformation of carbonate into a Fe, O, and Al, -rich phase. The most reasonable process is the formation of Fe oxyhydroxides and PS as these phases were also able to explain the elemental distribution with regard to the As and P concentrations. Therefore, geochemical results indicate that the carbonate rims get partly dissolved and become transformed or replaced by secondary (Fe-rich) PS minerals and Fe oxyhydroxides. This assumption is in line with the texture of the sub-µm structures. The alteration processes are usually pronounced on one side of the mineral phases suggesting GW-controlled mechanisms. The fact that the occasionally overgrown primary minerals and mineral fragments are linked to these areas might imply growth of the secondary minerals due interaction with GW. That the orientation of the alteration rims does not follow a specific pattern can be traced back to the complex small-scale GW-flow regimes in the heterogeneous sediments. The observation of Fe-rich carbonates is in accordance with previous results and explains very well the increase in magnetic susceptibility above 380 °C in the temperature dependent magnetic susceptibility measurements (Fig. 37). The **As concentrations** are close to the detection limit of 70 mg/kg in the Mn-dominated grain centers and increase towards the alteration rims to around 140 mg/kg with highest concentrations in the strongly altered areas (Fig. 52 a-c).

Position of the highest As concentrations and co-occurrence with P (Table 11) in the mineral rim suggest As sorption on freshly formed Fe oxyhydroxides and (Fe-rich) PS.

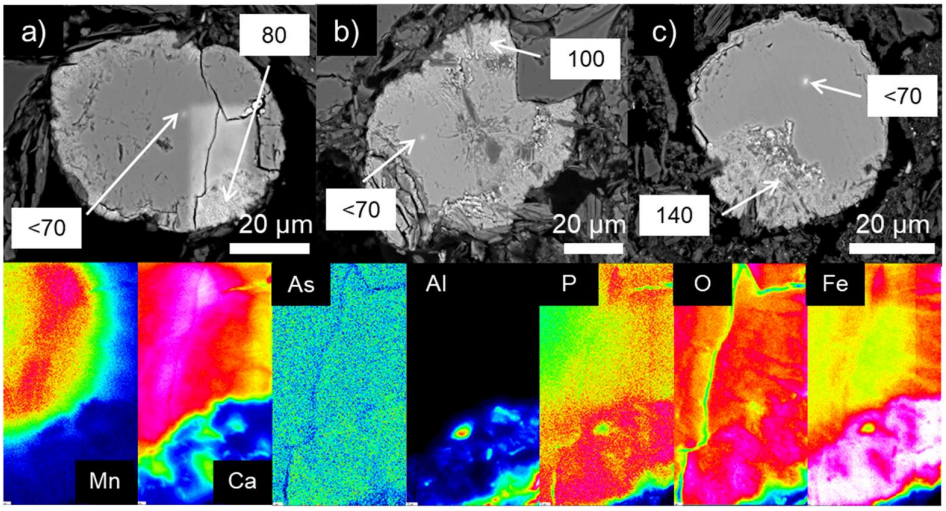

Figure 52: Backscatter micrographs of spherical Fe-Mn carbonate grains with strong alteration rims and inhomogeneous geochemical composition

a) – c) Alteration rims enclose the entire Fe-Mn carbonate surfaces and pronunciation on one side indicate strong influence of local GW-flow conditions on(trans-) formation reactions. The numbers indicate As concentration in mg/kg (Table 12). Elemental mapping images below correspond to the white rectangle in a) and reveal a clear separation with a Mn- and Ca-rich core while the Al, Fe, O, P and As content increases towards the rim.

Table 12: Microprobe based elemental composition (given as oxide) of minerals shown in Fig. 52 & 53c)

Fig.	position	As [mg/kg]	Fe_2O_3 [wt%]	MnO [wt%]	SiO_2 [wt%]	Al_2O_3 [wt%]	P_2O_5 [wt%]	CaO [wt%]	SO_3 [wt%]	CO_2 [wt%]
52a)	centre	< 70	48.58	6.36	0.03	0.01	0.82	10.11	0.01	33.62
	rim	80	76.09	0.63	6.61	3.21	1.57	1.16	0.08	10.23
52b)	centre	100	47.34	6.38	0.06	0.01	0.93	11.40	0.01	33.44
	rim	< 70	75.80	1.03	4.79	2.24	1.59	2.02	0.04	12.14
52c)	centre	< 70	53.90	3.84	0.06	0.04	1.43	9.81	0.01	30.56
	rim	140	60.72	2.28	2.96	1.78	1.43	5.86	0.02	24.51
53c)	centre	< 70	54.79	0.81	0.61	0.22	1.30	8.19	0.00	33.85
	rim	180	65.14	0.93	6.48	3.47	1.36	4.20	0.04	18.09

In addition to the well-defined Fe-Mn carbonate minerals, the microscopic investigation revealed a second class of Fe-Mn carbonates with a precipitation like appearance (Fig. 53). The **Fe-Mn carbonate precipitates** occur in high frequency above and below the redox front in 20-22 and 30 m depth near Mn-rich layers in the immediate vicinity of the redox interface. The Fe-Mn carbonate precipitates form large structures that stretch over 100-500 µm and enclose primary grains. Due to the numerous foreign bodies in the form of overgrown primary minerals or mineral fragments, a petrographic classification was usually difficult but based on the elemental composition the precipitates could be clearly identified as Fe-Mn carbonates (Fig. 53d) despite unclear optical properties (colour, distinction angle). Like the Fe(III)-dominated precipitates the Fe-Mn carbonate precipitates are composed of numerous small minerals of various size and crystallinity and therefore share at least in parts the mc character of the Fe(III) precipitates described before. However, the mineral composition remains unclear as synchrotron based measurements could not be performed to identify the mineral inventory. Since there is again a clear spatial separation of Fe- and Mn-dominated areas, the Fe-Mn carbonate

precipitates probably also consist of the Mn-carbonate rhodochrosite and the Fe-carbonate siderite. Despite size and texture the precipitations share many characteristics of the mixed Fe-Mn carbonates. Although less symmetrical, the inner area of the precipitations has higher Mn concentrations than the rims while the outer area is Fe-dominated and shows a distinct alteration rim (Fig. 53c). The alteration areas show the same textural and geochemical features as described for the mixed Fe-Mn carbonates. Bright spots in the backscatter contrast images and increasing Fe, O, SiO_2 and Al_2O_3 content (Table 11) most likely indicate the formation of Fe(III) oxyhydroxide or Fe-rich PS. The Fe content increases from the centre to the rim from 51 to 69 wt% (n = 4), the Al_2O_3 content from < 0.1 to almost 3 wt% and SiO_2 from < 0.2 to > 5 wt%. In contrast Ca drops from approximately 10 to about 3 wt% and CO_2 from 33 % to less than 17 wt%. Also As and P concentrations follow the trend observed in the mixed Fe-Mn carbonates and the **As concentrations** reach 140-180 mg/kg in the altered rims. Similar to the spherical phases, the highest As concentration occur in the rims and along cracks, which indicates recent As retention from GW. In contrast, the As concentrations in the Mn-rich central areas hardly exceed the detection limit of 70 mg/kg.

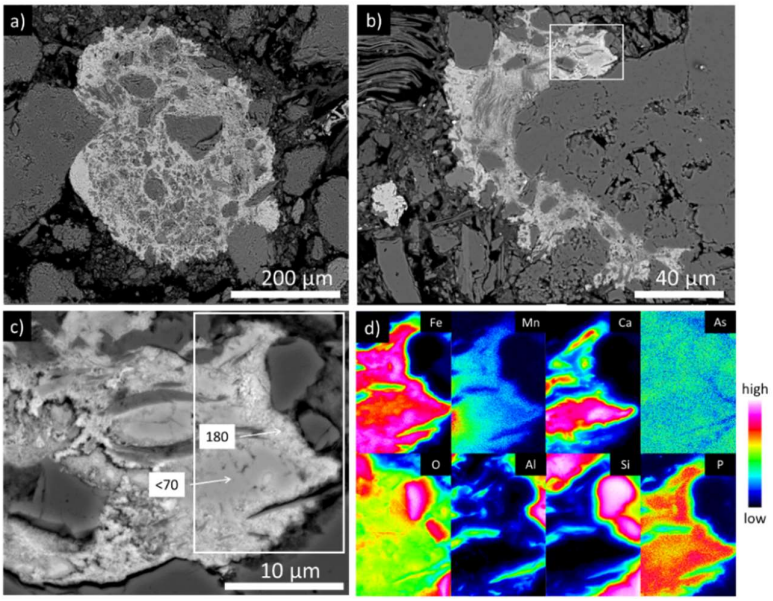

Figure 53: Backscatter micrographs of extensive Fe-Mn carbonate precipitates *cementing primary quartz and feldspar fragments in the redox transition zone*

a) & b) show large Fe(II) precipitates stretching across various 100 µm with well pronounced alteration rims surrounding the entire surface. c) shows the enlargement of the altered area marked by a white frame in b). The numbers indicate local As concentration. The white rectangle in c) marks the mapping area show in d). The mappings reveal the same element separation as in Fig. 52 with a Mn- and Ca-rich central area whereas the rim is enriched with regard to Al, Si and O and indicates the formation of secondary Fe oxyhydroxides and PS and increase As and P sorption/occlusion in the altered area.

In addition, pure Fe carbonates with a characteristic skeletal crystal growth texture are present all across the transition sediments (Fig. 54). Although less common, the **pure skeletal Fe-carbonates** are the most widespread as they occur in all parts of the transition sediments. In contrast to the mixed Fe-Mn carbonates, their presence is not limited to the immediate surrounding of the redox interface and they could also be detected in peripheral areas of the transition sediments towards the yellow-brown sediments. Since the skeletal Fe-carbonates also occur at the outer edge of the redox interface, it is assumed that these phases could display the Fe-carbonates present in the yellow-brown sediments, indicated by Mossbauer and kt measurements (Fig. 35 & 36), but could not be confirmed microscopically. In contrast to the other Fe-carbonates, their texture shows no signs of transformation

or dissolution. The edges are very sharp and show no signs of alteration. On the contrary, the skeletal growth with branches spreading out from the dense core show that the minerals have grown or are still growing. The way in which the primary grains are overgrown by the Fe-carbonates indicates growth processes after deposition. The dense centre of the skeletal Fe-carbonates suggest that the growth processes were more intense in the past and originated in a Fe-rich aquatic environment. Therefore, a coupling to redox process could be possible. The large diameter of the phases, in most cases between 100 and 200µm, and therefore significantly boarder than for the mixed Fe-Mn carbonates points also towards a Fe-rich environment. In contrast to the other Fe-carbonates the element distribution throughout the minerals is homogeneous and essentially consists of Fe, C and O and hardly contains any foreign elements. The **As concentrations** are always below the detection limit (< 70 mg/kg). This aspects could point to rather stable residual primary phases how it could be expected in the yellow-brown sediments. However, the complex GW flow conditions and the sedimentological heterogeneity was shown to create highly variable conditions on small spatial scales and could therefore likely create highly variable hydrogeochemical environments with different precipitation characteristics. Therefore, it is not possible to clearly link the skeletal Fe-carbonates to the recent redox processes.

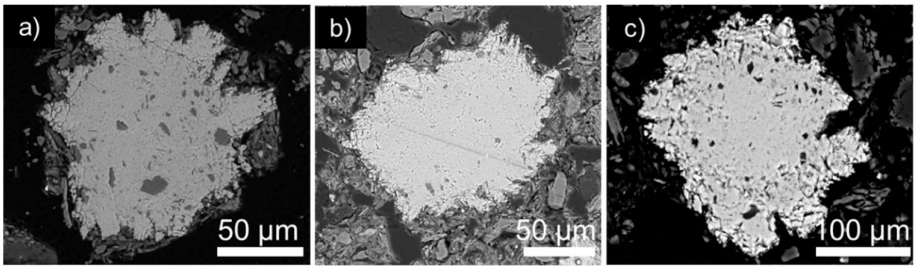

Figure 54: Backscatter micrographs of siderite with skeletal growth at the transition to the yellow-brown sediments

9.4.3.3 Fe(II)-sulphides

Another exclusive feature of the transition sediments are Fe(II)-sulphides. However, the (optical) evidence of the phases is restricted to two depth levels at 22 and 30 m bgs in core RD42 where fine-grained organic-rich layers high in sulphur and (organic) carbon cross the redox interface. Both layers show a strong dark brown colouration. The silty layers clearly set apart from surrounding aquifer sands by grainsize, colour and geochemical composition. Especially the high TS concentrations of 0.019 wt% and TC concentrations between 0.32 and 0.39 wt% stand out and excel the adjunct sediment layers by a factor of about 4 for TS and 10 for TC. The Fe sulphides appear almost exclusively as **framboidal pyrites** (Fig. 55). The characteristic framboidal texture and atomic Fe:S ratio (Table 13) clearly identifies the minerals as Py. Although the Fe:S ratios show slight variations (33:67 to 37:63 for n=10) across various framboids the ratio clearly indicates pyrite stoichiometry rather than mackinawite or greigite. Usually the isolated framboids are lined up at irregular intervals in chains that presumably follow preferential flow paths, which connect the fine-grained transition sediments and the grey sands. Sometimes 2-4 framboids form small clusters (Fig. 55 i). Comparable to the Fe-carbonates the occurrence of the Fe-pyrites is limited to the direct vicinity of the redox and GS interface and the Py occur preferred on the reduced side of the redox transition zone. Most framboids are uniformly sized with 10-20 µm in diameter but show a diverse texture on small spatial scales. Within several 100 µm round (Fig. 55 b-f) and hexagonal (Fig. 55 g-l) shaped framboids co-occur without a specific pattern. The framboids also show a variable internal microarchitecture with microcrystals of cubic or octahedral symmetry. The morphological orientations of the microcrystals is not uniform and the size of microcrystals vary from 0.5–2 µm. The microcrystals appear as well-defined uniform crystals (Fig. 55 a-c) although the majority of the framboids (Fig. 55 d-i) show merging or merged microcrystals. Some framboids show an alteration rim (d-i). The observation is most pronounced on the hexagonal shaped

framboids (Fig. 55 g-i) often accompanied by cracks indicating recent dissolution. Based on these observations, a possible sequence can be defined, which is determined by the framboidal shape, the micro-crystals merging and the appearance of alteration rims and cracks and follows the order of Fig. 54 a-i. The framboids a-c suggest recent formation and the heterogeneous texture indicates very variable geochemical (micro) environments. The framboids d-f display the starting alteration and the highly altered framboids g-i represent the dissolution remains of the presumably oldest phases. The large differences in micro crystal form and size across the various framboids further indicates different geochemical (micro) environments with variable growing conditions within shortest distances. The microcrystals within the majority of the aggregates are homogeneously sized and therefore imply locally stable geochemical conditions for the time of framboid formation. However, disorganised framboids (Fig. 55 a) showing microcrystals with significant variations in form and size located within a range of several 100 µm imply deviating or even fluctuating conditions. In one case, isolated Fe-sulphide microcrystals in irregular order were documented (Fig. 56). The individual microcrystals are randomly oriented, unstructured and separated by large gaps. Further the microcrystals are significantly larger in the framboids The great heterogeneity of framboids and microcrystals shown in Fig. 55 and 56 covering organised, disorganised framboids as well as single-microcrystals indicate a complex sedimentological and hydrochemical setup with a broad range of decoupled microenvironments on small spatial scales. The Py framboids show the largest range and highest total **As concentrations** that vary from below the detection limit (70 mg/kg) to almost 6000 mg/kg. The As concentrations depend strongly on the texture of the framboids and vary greatly within the framboids. The Py rims generally have higher concentrations than the central areas, regardless of whether or not alteration rims have formed. The highest measured concentrations of several 1000 mg/kg are limited to fresh unaltered framboids with isolated microcrystals (Fig. 55 c) and seem to decrease with progressive evolution of the microcrystals (Fig. 55 e-f). With the formation of the alteration rims and the associated recrystallization processes the As concentration seem to increases to 1000 mg/kg (Fig. 55 g-h). This observation could be explained by the formation of Fe(III) oxyhydroxides and/or Fe-rich PS on the Py surface. This hypothesis would be in line with spatial arrangement of the phases showing the most altered framboids in the immediate vicinity of the redox interface and increasing Si and Al concentrations in the rims (Table 13).

Table 13: Microprobe based elemental composition (given as oxide) of Fig. 55 & 56

Fig.	position	As [mg/kg]	Fe_2O_3 [wt%]	MnO [wt%]	SiO_2 [wt%]	Al_2O_3 [wt%]	P_2O_5 [wt%]	CaO [wt%]	SO_3 [wt%]
55a)	SEM image								
55b)	SEM image								
55c)	edge	5770	45.02	0.00	0.55	0.22	0.05	0.15	46.33
	centre	4720	44.50	0.02	0.42	0.07	0.10	0.18	44.54
	hem	680	20.30	0.03	10.53	7.90	0.09	0.30	17.95
55d)	centre	< 70	46.24	0.04	0.11	0.03	0.02	0.01	50.97
55e)	edge	350	44.98	0.00	0.07	0.02	0.02	0.08	50.76
	centre	< 70	44.22	0.00	0.17	0.05	0.04	0.11	49.98
55f)	edge	370	45.57	0.00	1.01	0.11	0.01	0.06	50.01
55g)	centre	< 70	46.68	0.03	0.11	0.02	0.01	0.04	50.59
	edge	430	43.84	0.05	0.41	0.18	0.01	0.03	49.01
55h)	centre	410	45.49	0.05	0.19	0.04	0.00	0.08	50.18
	edge	1010	41.51	0.01	1.25	0.74	0.03	0.14	44.70
55i)	SEM image								
56)	isolated grain	< 70	46.12	0.00	0.08	0.02	0.00	0.02	53.88

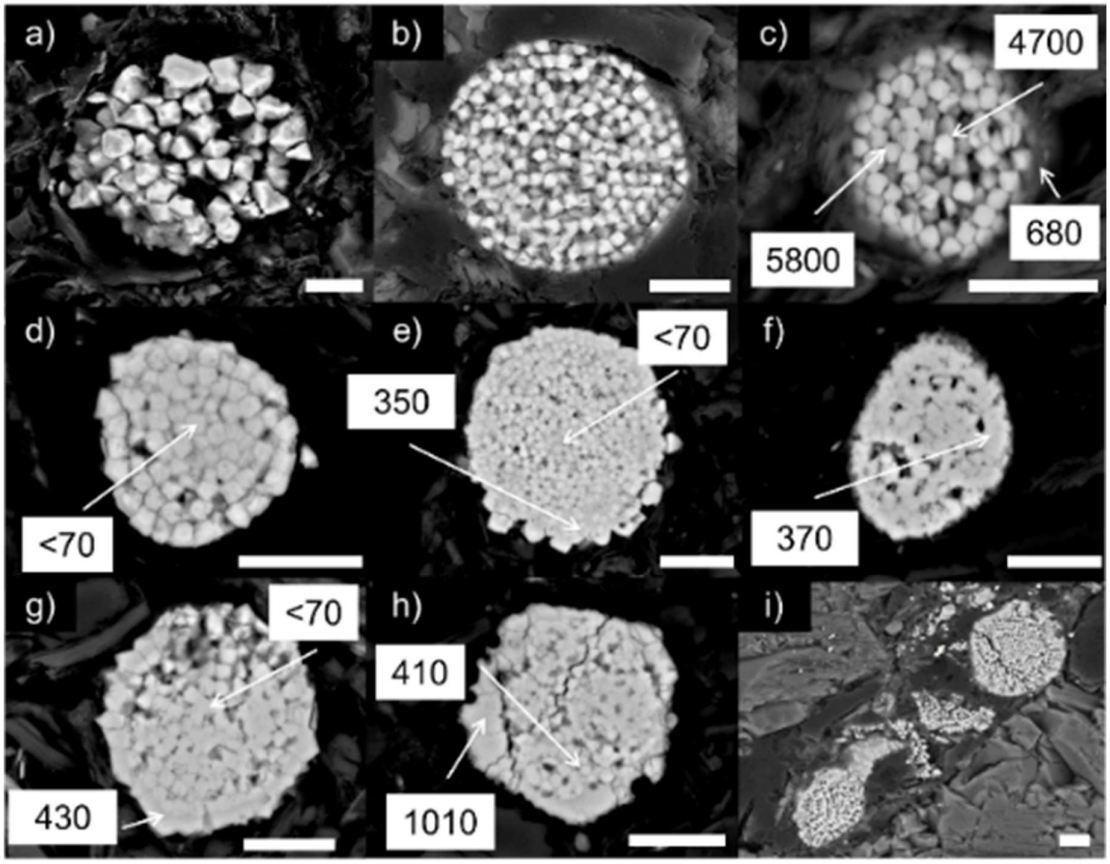

Figure 55: Backscatter micrographs showing the divers pyrite framboid morphology on one thin section from 30m bgs in core RD42.

a) Roundly disorganised single framboid with separated octahedral microcrystals of variable size and two voids, b) Uniform organised round framboid with homogenously sized and separated cubic microcrystals c) small framboid with disordered structure composed of randomly aggregated octahedral microcrystals d) round framboid with merging cubic microcrystals e) large framboid with exceptional small merging microcrystals in the centre and starting ring formation with large microcrystals on the outer edge. f) Processed merging microcrystals and ring formation and voids. g) Hexagonal arrangement of octahedral microcrystals with processed merging and ring formation h) Hexagonal framboid with almost completely merged microcrystals and well-formed alteration rims. Cracks indicating recent dissolution. i) Small framboid cluster aligned along a preferential flow path with recrystallizing rim and cracks. Scale bar 5 µm. Numbers indicate As concentration in the centre and the rim (Table 13).

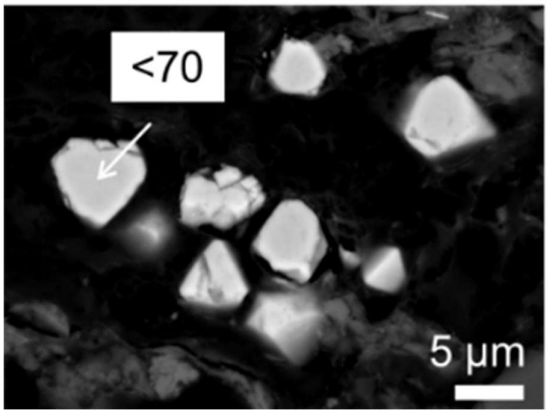

Figure 56: Backscatter micrograph showing an association of irregular pyrite single-microcrystals with high variability in form and size and As concentration below LOD

9.5 Incubation experiment

The visual investigation after three weeks of incubation reveals that most mineral-coated sands are significantly paler compared to the colourful fresh samples before the experiment (Fig. 21). Especially the colouration of the biotic mineral coatings and the poorly crystalline abiotic Fh coating diminished. In contrast the abiotic Gt, Hem and Mt coatings have largely retained their original colour. Visual differences between the depth levels are not recognizable (see also Glodowska et al. (2021b)).

9.5.1 Solid phase geochemistry

ED-XRF based determination of the solid phase geochemistry confirms the visual observations. Quantification of the total **Fe_2O_3** content per g sand provided clear evidence for the loss of some Fe mineral coating in most samples during the experiment (Table 14, Fig. 57). Across both depth levels the Fe_2O_3 content decreased to the same extent by an average of 30 wt% (n = 20). In the highly reduced depth (25 m) the Fe_2O_3 concentration decreased on average by 31 % (n = 10) while in the moderately reduced GW in 32 m depth the Fe_2O_3 concentration decreased on average by 29 % (n = 10). However, across both depth levels the Fe_2O_3 concentration of individual Fe-coatings change significantly. The well crystalline abiotic Fe mineral coatings Gt_{abio}, Hem_{abio} and Mt_{abio} differ from the less crystalline phases (Fh_{abio} and the biotic phases). The well-crystalline abiotic Gt, Hem and Mt phases show minor changes (-8 to + 10 wt%, average 1 wt%, n = 6) with regard to the Fe_2O_3 concentrations in both depths after incubation experiment. In contrast the Fe_2O_3 concentrations in the abiotic Fh and the biotic phases show a clear decrease of in average 47 wt% (-83 to -11 wt%, n = 10) in both depth levels after incubation. The biotic Gt/Lep2 sample, which experiences only minimal changes in the Fe_2O_3 content in both depth levels, is excluded from this trend. The abiotic Gt sample is the only specimen showing an increasing Fe_2O_3 content in both depths during the incubation experiment. In the highly reduced environment at a depth of 25 m the Fe_2O_3 concentration increases around 5 wt%. In the moderately reduced depth of 32 m the increase is 10 % according to an increase of Fe_2O_3 content from 1.9 g/kg to about 2.0 g/kg Fe_2O_3. The Fe_2O_3 content of the abiotic Mt sample remains rather constant in both depth levels. The abiotic Hem sample shows with -3 wt% in 32 depth and -8 wt% in 25m depth also relatively constant to slightly decreasing values. The abiotic Fh sample shows a significant decrease of 56 % at a depth of 25 m and 34 % at a depth of 32 m corresponding to a decreasing Fe_2O_3 concertation from 4.8 g/kg to 2.1 and 3.1 g/kg respectively. The biotic Fh_{bio} shows the largest decrease in Fe_2O_3 concentration with 67 wt% in 25m depth and 83 wt% in 32m depth from 1.6 to 0.5 and 0.3 g/kg Fe_2O_3. The drastic decrease in Fe_2O_3 content indicates reductive dissolution as most likely process. Similar the biogenic minerals were reduced and dissolved as indicated by decreasing Fe_2O_3 concentration. Both Lep/Gt_{1bio} (-58 wt% in 25m and -47 wt% in 32m) and Gt_{bio} (-40 wt% in 25m and -56 wt% in 32m) show a significantly reduced Fe_2O_3 concertation. Lep/Gt_{1bio} contains with 14 g/kg the highest initial Fe_2O_3 concertation which drops to 5.9 g/kg Fe_2O_3 in 25 m depth and 7.4 g/kg Fe_2O_3 in 32 m depth. The Fe content of Gt_{bio} decreases from 0.8 g/kg Fe_2O_3 to 0.5 and 0.3 g/kg Fe_2O_3 in 25 m and 32 m depth respectively. In the Lep/Mt_{bio} sample, the decrease in Fe_2O_3 content is significantly lower at 21 % in 25m and -11 % in 32m depth corresponding to a drop from 1.6 to 1.3 and 1.4 g/kg Fe_2O_3. The Lep/Gt_{2bio} (2 % in 25m and -4 % in 32m) shows almost no changes in the Fe content. With regard to the decrease in the Fe_2O_3concentration, no uniform trend can be identified with regard to the depth levels. Rather, a mineral-specific behaviour is observed in both depth levels.

Noteworthy **As** retention is essentially limited to the highly reduced GW in 25m depth, while in 32m there are hardly any changes in the total As content across all coatings. On average, the net As increase of the different coatings lies around 5.6 mg/kg As (n = 9) at a depth of 25 m while there is an almost balanced As budget at a depth of 32 m (Table 14, Fig. 57). Conspicuous As sequestering is limited to two samples in the highly reduced environment at 25m depth. The by far largest As retention shows the abiotic Fh (22mg/kg) and the biotic Gt/Lep mixture (17 mg/kg). The abiotic Gt and Mt phases at a

depth of 25 m show a minimal As retention of around 2 mg/kg. The abiotic Hem shows a decrease of around 1 mg/kg. In contrast to the abiotic Fh, the biotic Fh shows no As retention. This fact could be explained by the fact that the presumably highly reactive biotic Fh is immediately transferred into more redox-stable phases such as Mt and Hem with a lower As-hosting affinity and capacity in both depth levels. The other biotic phases all show a positive As balance and fix around 3.4 mg/kg As on average (2.3-4.3 mg/kg, n = 3) in 25 m depth. In the moderately reduced environment in 32 m depth the As retention turns out to be significantly lower. In principle, the abiotic phases at this level show a positive As balance, but at around 1 mg/kg (0-1.7, n = 4) the As retention is not as significant as in the highly reduced environment. In contrast, the As balance in 4 of 5 biotic coatings is negative, with an average of -1.6 mg/kg (n = 4, -0.4-3.4). Only Gt/Lep1 shows an As retention of 2 mg/kg at a depth of 32 m. Similar to the Fe_2O_3concentration changes, no common trend can be observed that covers all types of mineral coatings across both depth levels. In contrast to the Fe_2O_3 concentrations, the As retention at a depth of 25 m is significantly more pronounced in the highly reduced aquifer. In general the less crystalline biogenic minerals and the poorly crystalline Fh_{abio} retain more As compared to well crystalline abiogenic minerals, especially in the reduced environment. For the interpretation of the Fe_2O_3 balance it has to be considered that the absolute Fe concentrations of the individual coatings differed significantly before the experiment. There was a factor of 8 between the highest and lowest concentrations (Table 14). The same applies to the As content of the coatings before the experiment. Three out of four abiotic synthesized coatings show low initial As concentrations. For abiotic Gt, Fh and Mt the initial As concertation was between 0 and 0.03 mg/kg while the abiotic Hem and the biotic coatings show As concentrations between 0.4 and 3.5 mg/kg before the start of the experiment (Table 14). Especially the biotic minerals show high initial As concentrations. The origin of the initial As content is unknown. However, it was taken into account with regard to the As flux calculations in Table 14. The uncoated reference sand samples show no increase of Fe_2O_3 or As content at any depth.

Table 14: ED-XRF based total bulk As & Fe_2O_3 content per g sand of individual coatings before and after the experiment in the highly reduced depth at 25m and the moderately reduced environment in 32m bgs

Minerals (coatings)		**Fe_2O_3** [g/kg]	**Fe_2O_3** difference [g/kg]	**Fe_2O_3** difference [%]	**As** [mg/kg]	**As** difference [mg/kg]
original (before experiment)	Fh_{abio}	4,8			0	
	Gt_{abio}	1,9			0	
	Mt_{abio}	6			0,03	
	Hem_{abio}	1,3			2,26	
	Fh_{bio}	1,6			2,02	
	Gt_{bio}	0,8			0,41	
	Lep/Gt_{bio1}	14			3,14	
	Lep/Gt_{bio2}	1,7			1,31	
	Lep/Mt_{bio}	1,6			3,45	
	sand	0,5			0	
highly reduced (25m depth)	Fh_{abio}	2,1	-2,7	-56	22,38	22,38
	Gt_{abio}	2	0,1	5	2,06	2,06
	Mt_{abio}	6	0	0	1,9	1,87
	Hem_{abio}	1,2	-0,1	-8	1,33	-0,93
	Fh_{bio}	0,5	-1,1	-67	0,13	-1,89
	Gt_{bio}	0,5	-0,3	-40	4,72	4,32
	Lep/Gt_{bio1}	5,9	-8,1	-58	19,85	16,7
	Lep/Gt_{bio2}	1,7	0	2	5,09	3,77
	Lep/Mt_{bio}	1,3	-0,3	-21	5,77	2,32
	sand	0,2	-0,3	-63	0	0
moderately reduced (32m depth)	Fh_{abio}	3,1	-1,6	-34	1,75	1,75
	Gt_{abio}	2	0,2	10	0	0
	Mt_{abio}	6,1	0,1	2	1,34	1,3
	Hem_{abio}	1,3	0	-3	3,48	1,22
	Fh_{bio}	0,3	-1,3	-83	0	-2,02
	Gt_{bio}	0,3	-0,4	-56	0	-0,41
	Lep/Gt_{bio1}	7,4	-6,6	-47	2,68	-0,46
	Lep/Gt_{bio2}	1,6	-0,1	-4	3,32	2,01
	Lep/Mt_{bio}	1,4	-0,2	-11	0	-3,45
	sand	0,2	-0,3	-63	0	0

Figure 57: Fe_2O_3 and As concentrations of Fe-coatings before and after the experiment (Table 14)

9.5.2 Mineralogy

Due to the low Fe_2O_3 concentrations it was not possible to identify the Fe minerals of the coatings using XRD. ED-XRF analysis revealed Fe_2O_3-concentrations in the range of 0.02 and 0.8 wt% and therefore far below the detection limit of the method of 3-5 wt%. Consequently, temperature dependent magnetic susceptibility (kt) measurements were used for mineral identification and reconstruction of the mineral transformation schemes. Based on the results (Fig. 58) all samples are characterized by mineral (trans-)formation processes.

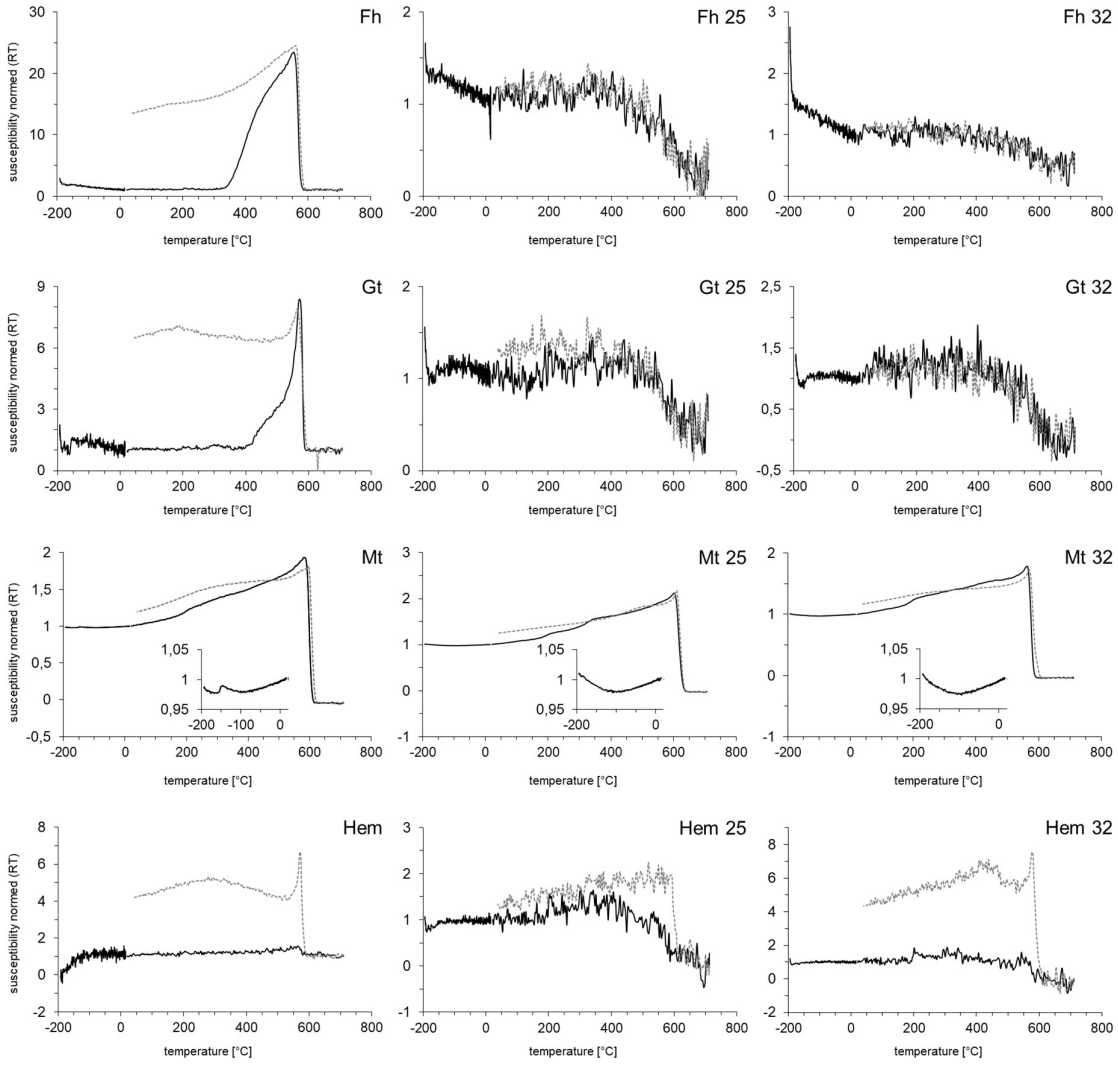

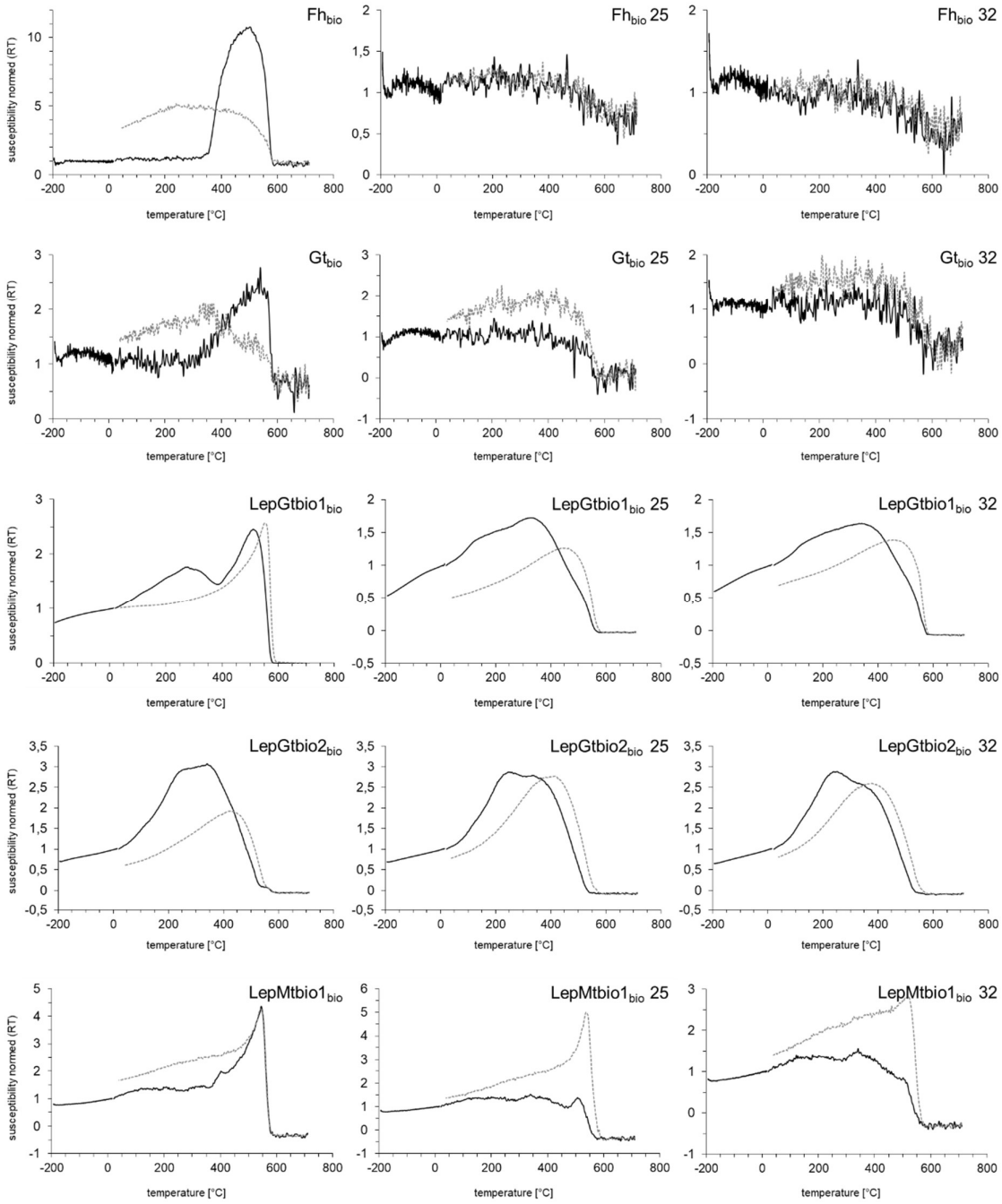

Figure 58: Temperature depended magnetic susceptibility (kt) diagrams of abiogenic and biogenic mineral coatings before and after the experiment in the highly reduced depth at 25 m and the moderately reduced environment in 32 m bgs.

In the majority of analysed samples secondary Mt was identified. The ferrimagnetic mineral was identified based on the characteristic Verwey transition (TV) at about -150 °C and/or its Curie temperature (TC) at 580 °C. That the TV is mostly very weak or even absent is indicative for the very small grain size of the secondary Mt or a significant vacancy concentration in the crystal lattice (Dunlop & Özdemir 2007).

The **abiotic Gt and Hem** coatings show a similar behaviour which can be explained by dissolution transformation of the initial Fe phases into secondary Mt indicated by T_{Curie} at around 580 °C in the high temperature measurements. The Hem_{abio} sample remained almost unchanged in the moderately

reduced aquifer at 32 m depth and only shows a partial conversion into Mt after incubation in the highly reducing GW at 25 m depth. The Hem_{abio}-coated sample shows already little Mt in the original sample. Course and high absolute magnetic susceptibility in the cooling curve indicates that Hem has transformed into Mt during the high-temperature measurement in argon atmosphere. In the highly reduced GW at 25 m bgs, only Mt remained indicating that Hem is either dissolved or entirely transformed into Mt. In moderately reduced GW, no change occurred for Hem. The Gt_{abio} samples indicate an extensive conversion into Mt in both depth levels. During the 30 day exposure also the **abiotic Mt** was at least in part transformed into secondary fine grain Mt which is indicated by the disappearance of the Verwey transition in the low temperature measurements. The relatively good reversibility of heating and cooling curve support rather very small grain sizes than oxidation of Mt. The high temperature measurements are almost unchanged and are defined by the characteristic Mt T_{Curie} at around 580 °C. A Hopkinson peak in the heating curve indicates again very fine-grained Mt (Dunlop & Özdemir 2007) and therefore confirms the previous observations. Further peaks in the heating curve at 200, 400 and 500 °C indicate the presence of other Fe(III)-oxyhydroxide phases such as Lep or Fe-containing phyllosilicate minerals. The **biotic and abiotic Fh** seem to be largely dissolved and the remaining coating was partially (at 32 m depth) or completely (at 25 m depth) transformed to Mt which is indicated by the T_{Curie} at 580 °C. Also the **biogenic Gt** is transformed to fine-grained Mt in both the Holocene and Pleistocene aquifer with Mt formation being more pronounced at 25 m depth. Although for the biogenic Gt and the biogenic and abiogenic Fh samples very little Mt in the original sample cannot be excluded, they are characterized by distinct Mt formation in both, reduced and suboxic waters. This process is more pronounced in the abiogenic samples than in the biogenic samples. Especially in the Fh samples and in the biogenic Gt the transformation into Mt is accompanied by strong dissolution is indicated by the reduced Fe concentration (Table 15, Fig. 57). The **biotic Lep/Mt** samples show dissolution and transformation of initial phases in both aquifer waters with a slightly higher extent at the highly reduced 25 m depth. In the Lep/Mt samples recovered from a depth of 32 m, a T_{Curie} of ca. 280 °C indicates the formation of an additional Fe(III) (oxyhydr)oxide phase, that is most likely Lep. Further grain size decrease in Mt seem to occur, indicated by the disappearance of the Hopkinson peak in the heating curves. The biogenic mixing phase **Gt/Lep_{bio1}** shows a decreasing Gt content in favour of a freshly formed Fe oxyhydroxide phase in both depths. The secondary Fe oxyhydroxide phase is probably Fh. The biogenic mixing phase **Gt/Lep_{bio2}** does not show the formation of further phases. Both samples show no major changes in their course across both depth levels, which suggests that the biogenic mixing phases are relatively stable under both the moderately reduced and the reduced conditions.

In total a set of 6 thin sections could be prepared for **microscopic analysis**. The sample section was based on ED-XRF results and covered the samples with highest As concentration in both depth levels ($Fh_{abio,}$ Gt/Lep_{bio1} & Gt/Lep_{bio2}). **SEM backscatter recordings** show that the Fe-coatings have receded considerably and in most cases have been completely dissolved. The rough surfaces of the sand grains are inhomogeneously coated and the coatings have preceded, especially in protected areas such as cracks crevasse, cavities and between two or more closely spaced sand grains (Fig. 59). The coatings are criss-crossed by numerous cracks and especially the edge areas show strong signs of alteration. **SEM-EDX spectra** confirm Fe and O as major elements (Table 14). Similar to the sediment core samples, Fe-PS complexes seem to have formed within/on top the coatings indicated by the SEM-EDX spectra, which show Al in minor amounts in addition to Fe and O and Si (Table 14 4 & 6). Textural analysis, revealing sub-µm mineral structures (Fig. 59 b, c) support this assumption of recrystallization processes which clearly sets these areas apart from the central, homogeneous areas that consist only of Fe and O. The occasional Si peaks measured in 4 of the 6 samples are presumably related to the overgrown Qtz grains and therefore do not indicate admixing phases. **As concentrations** are below the detection limit for the method of around 1000 mg/kg. The attempt to determine the coatings using SEM-EDX-

based Fe-O ratios did not provide any reliable results. Based on texture the abiogenic Fh-coated sand incubated in the highly reduced GW at 25 shown in Fig. 59 a seem to have transformed into a more crystalline Fe-phase while the abiogenic Fh-coated sand incubated in the moderately reduced GW at 32 m depth (Fig. 59 b) and the biogenic Lep/Gt2-coated sand incubated in the highly reduced GW at 25 m depth (Fig. 59 c) seem to be composed of multiple Fe and Fe-rich phases, with a brighter granular phase and a grey surrounding phase which most likely correspond to Mt and Fh respectively. The abiogenic Fh-coated sand incubated in the highly reduced GW at 25 m depth (Fig. 59 b) and the biogenic Lep/Gt (Fig. 59 c) is characterized by needle-shaped to flaky grain shapes. The Gt/Lep_{bio1} coatings in 25 m an the Gt/Lep_{bio2} in 32m were completely dissolved. The Gt/Lep_{bio1} in 32 m (no shown) resembles the results in Fig. 59 c). Qtz grains coated by biotic Fh in often show intergrowth of two or more phases and resemble the results shown for the abiotic Fh.

Table 15: SEM-EDX based elemental composition (given as oxide) of Fig. 59

Position	Element	Weight %	Atomic %	Formula
1	Silicon	2.348	2.888	SiO_2
	Iron	73.826	45.667	FeO
	Oxygen	23.825	51.444	-
2	Silicon	1.656	2.06	SiO_2
	Iron	74.978	46.911	FeO
	Oxygen	23.366	51.03	-
3	Iron	77.732	50	FeO
	Oxygen	22.268	50	
4	Aluminium	3.475	3.989	Al_2O_3
	Silicon	6.474	7.139	SiO_2
	Iron	61.861	34.305	FeO
	Oxygen	28.189	54.567	-
5	Iron	77.732	50	FeO
	Oxygen	22.268	50	-
6	Aluminium	5.395	5.93	Al_2O_3
	Silicon	7.88	8.32	SiO_2
	Iron	56.704	30.108	FeO
	Oxygen	30.021	55.642	-

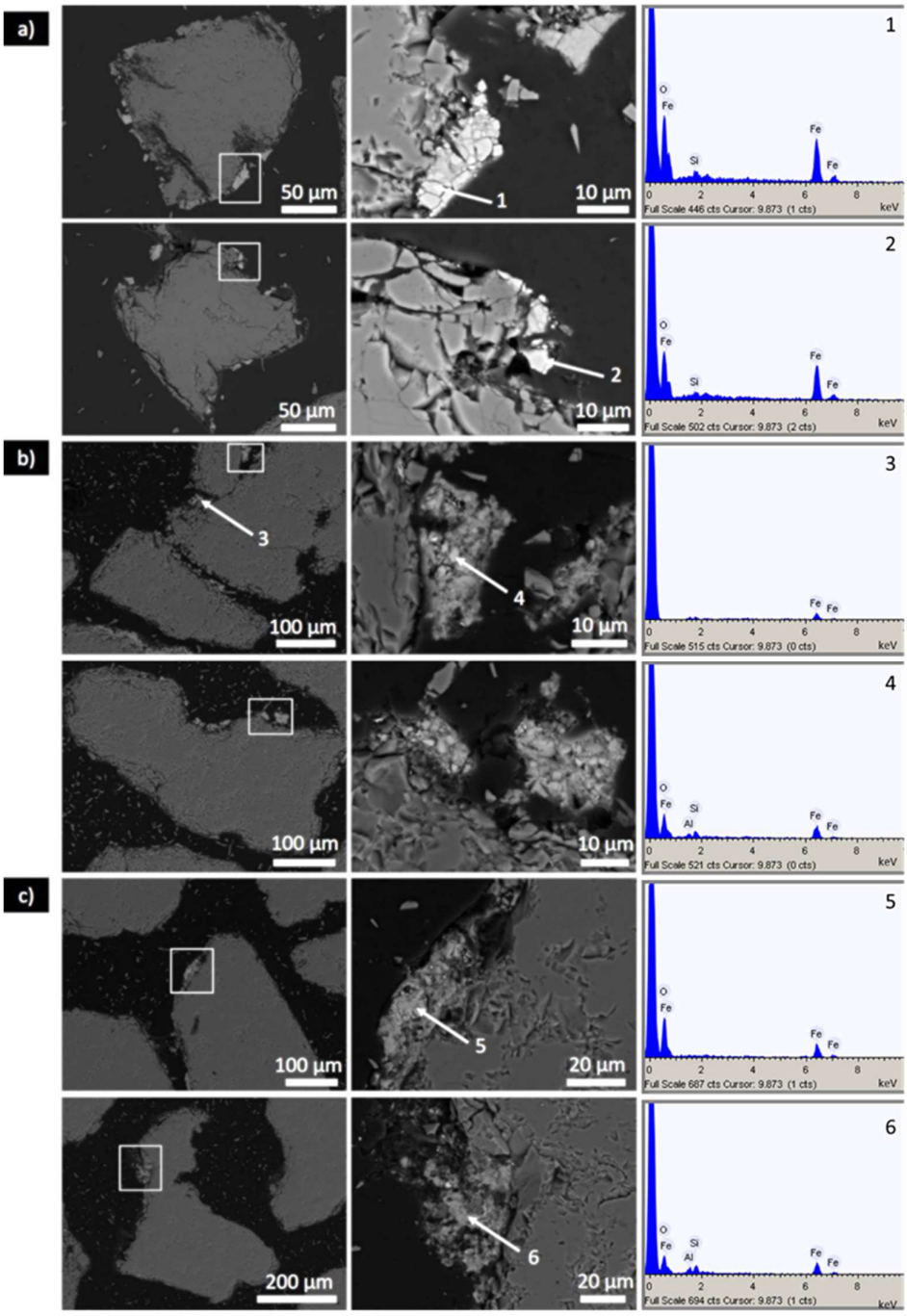

Figure 59: Backscatter micrographs of selected samples from the incubation experiment

a) abiogenic Fh-coated sand incubated in the highly reduced GW at 25 m depth, b) abiogenic Fh-coated sand incubated in the moderately reduced GW at 32 m depth, and c) biogenic Lep/Gt2-coated sand incubated in the highly reduced GW at 25 m depth. The left side shows the extent of the Fe coatings on the Qtz grains. White squares indicate the analysed area which is shown on the right as enlargement. The EDX-spectra on the right were analysed at the position indicated by the arrow (Table 15).

10. Discussion

10.1 Fe mineral dynamic along the redox interface

The documented Fe minerals are typical for present-day sedimentary environments and the mineral formation processes are in accordance with thermodynamical considerations (Curtis & Spear 1968) and other studies in the area (Stopelli et al., 2020; Glodowska et al., 2020 & 2021). The broad variety of Fe minerals in separated hydrogeochemical microenvironments along the core profile is typical for heterogeneous delta sediments and suggests a multitude of coupled and clearly separated hydrogeochemical processes and a diverse microbial activity. The formation of the observed secondary Fe phases along the redox interface represents a sequestering mechanism capable to explain the coupled As and Fe retention documented by Stopelli et al. (2020) based on GW data. The entire redox transition zone is characterized by the formation of secondary Fe minerals including Fe oxyhydroxides, Fe carbonates, Fe sulphides, and Fe-rich (phyllo-) silicates in a distinct spatial and temporal order (Table 6 & 7). The redox interface defined by sediment colour, solid phase geochemistry and mineral inventory acts as hotspot for the secondary Fe mineral formation and largely controls the aquifer Fe dynamic which is ultimately reflected in the formation of the characteristic Fe-rich transition sediments forming a retardation front across the interface.

10.1.1 Fe(III) and Fe(II/III)-phases

The most important process with regard to the Fe dynamic in quantitative terms is the formation of Fe(III) and Fe(II/III)-phases along the actual redox interface. The formation of the Fe(III) and Fe(II/III) phases Gt, Hem and Mt as well as Fe(II/III) containing PS could be identified as the dominant Fe and As retention mechanism along the redox boundary. The mineral inventory is further supplemented by minor amounts of Lep, documented by Mossbauer, temperature dependent magnetic susceptibility and XRD. Although less common Lep is typically found in near surface sediments in sub-micron scale in association with Gt (Cornell & Schwertmann 2003) what very likely resembles the results of this study. Together with Fh and Hem the four minerals represent the most commonly occurring Fe oxyhydroxide minerals in near-surface environments (Benner et al., 2002; Cornell & Schwertmann 2003). The absence of well crystalline secondary Fe(II/III) and Fe(III)-phases is another characteristic of the field site. The few documented well crystalline Fe(III) phases are exclusively primary phases that are only partially involved in the recent Fe dynamic at the redox interface. Altering crystalline Fe(III)-phases seem to function exclusively as Fe source. This is evident in their severely altered external appearance and their low As content. Accordingly, the As and Fe retention across the RTZ is almost entirely controlled by secondary mc structures. Crystalline Fe(III) phases play a subordinate role.

10.1.1.1 Fe(III)-dominated Fe precipitates

The formation of Fe(III)-dominated oxyhydroxide precipitates composed of mc Gt, Hem and Mt was identified as the central Fe retention mechanism across the redox transition zone in Van Phuc. The Fe precipitates are present in large quantities along the entire redox interface and in view of the strongly decreasing Fe(II) GW concentrations across the redox gradients their contribution to recent redox processes can hardly be doubted.

Microcrystalline character

The occurrence of natural microcrystalline Fe oxyhydroxides with very small particle size, which nevertheless exhibit crystalline characteristics in near-surface sediments has been reported for decades (Fordham & Norrish 1983; Bigham et al., 1978; Fordham et al., 1984; Ryan & Gschwend 1994) and amorphous to poorly crystalline Fe oxyhydroxides phases have been postulated as potential As retention mechanism in redox controlled As contaminated near-surface aquifer sediments already in the early 2000s (British Geological Survey 2001; Smedley & Kinniburgh 2002). However, the clear evidence of the mc Fe oxyhydroxide phases could not be provided for a long time. This can essentially

be attributed to the fact that microscopic texture analyses were rarely carried out on undisturbed sediment samples and the mc character of Fe oxyhydroxide phases cannot be identified with standard bulk methods that are usually used for environmental analysis. Only a few methods like synchrotron based XAS measurements and Mossbauer spectroscopy enable statements about the crystallinity of the phases and also in these cases the evidence is often not clear, as mc Fe oxyhydroxide phases often cannot be clearly separated from poorly crystalline hydrous ferric oxide minerals like Fh (Sun et al., 2016). Especially mc Gt has a XAS spectra that is similar to Fh and thus may not be identified and quantified separately. Moreover, it is possible that mc Gt will anomalously fit with Fh due to spectral similarities (Jung et al., 2012). This correspondence makes the interpretation of XAS analyses fundamentally difficult and poses high hurdles to the evaluation. Basically the phases can be distinguished and quantified by EXAFS-LCF but excellent mineral reference spectra are critical to yield consistent results (Sun et al., 2018). As mc phases were hardly mentioned in the past appropriate standards aren't always available. Given the complex and diverse structure and variable composition of Fe oxyhydroxide mixtures in natural systems as well as the high transformation dynamic it is often not possible to apply the appropriate standards that represent the local conditions.

Nevertheless, mc phases have gained increasing attention in the recent past and their importance for the Fe-As cycle in near surface sediments is increasingly discussed. Several studies highlighted the potential importance of mc Fe-phases in comparable near-surface sedimentary aquifer systems during the last two decades (Levy et al., 1999; Soren et al., 2009; Postma et al., 2010; Rotiroti et al., 2015; Kanoua & Merkel 2017; Zachara et al., 2002; Thompson et al., 2006 & 2011; Sun et al., 2018 & 2016) and both environmental analyses and model-based studies indicate that mc phases play an important role in the natural Fe cycle. Especially along strong redox gradients mc phases seem to occur regularly and contribute significantly to the Fe mineral inventory of natural near surface environments. Nanoparticulate to poorly crystalline Fe oxyhydroxides including the documented Gt, Hem and Fh and additionally akaganeite and schwertmannite were documented in near surface sediments (Waychunas et al., 2005). Several XAS studies on sample material from batch experiments (Jung et al., 2012) and natural sediment samples (Sun et al., 2018) indicate the presence of mc Fe oxyhydroxide phases in significant concentrations in environments which likely resemble the conditions in Van Phuc. At the study site in Van Phuc poorly crystalline phases were indicated by sequential extraction analysis (Eiche et al., 2008; Berg et al., 2007). This is in line with previously determined solubilities for Fe(III) oxyhydroxides in a Holocene sand aquifer 30 km north of Hanoi along the Red River by Soren et al. (2009) and Postma et al. (2010) which ranged from Lep and/or poorly crystalline Gt to Hem. Further a recent modelling study of the Van Phuc field site used Fe mineral K logs which correspond to a mc Gt and received good results (Wallis et al., 2020). The occurrence of mc Fe phases is not surprising under the given environmental conditions and agrees with calculated mineral saturation indices in Van Phuc GW by Stopelli et al. (2020). Microcrystalline Fe minerals are common products of weathering and most Fe oxyhydroxides in natural environments display a range of crystallinity that depend on the conditions under which the crystals formed. Although almost all Fe oxyhydroxides are crystalline the degree of structural order and crystal size are variable and range from adequately good to largely amorphous. Only ferrihydrite and schwertmannite are poorly crystalline (Murad 1996; Cornell & Schwertmann 2003). In particular oxic-anoxic boundaries in natural waters and sediments are favoured areas for the precipitation of poorly crystalline Fe oxyhydroxides (Dixit & Hering 2003). Considering the sharp redox gradient and the geochemically heterogeneous microenvironments the precipitation of mc phases along redox interface conditions is plausible.

The mc character of the Fe precipitates is important as mc materials differ from their crystalline counterparts with regard to dissolution, precipitation and reaction kinetics (Voegelin et al., 2013). Microcrystalline and otherwise poorly crystallized phases are characterized by pronounced surface

phenomena and high densities of lattice defects (Stucki et al., 2012). Further the small particle size changes the reactivity and stability of the mc Fe oxyhydroxide phases. It is well known that as the particle size of oxyhydroxide particles decrease, its surface-to-volume ratio increases and surface effects become more important. Due to high reactivity and small size mc phases play s significant role for the biogeochemical cycling. Further small Fe oxyhydroxide particles in the nm to 100 nm range are less stable than their larger counterparts and can be readily dissolved and re-precipitated if the environmental conditions (e.g. Eh) change (Murad 1996). Therefore, their mc nature makes the precipitates highly susceptible to redox changes and changing hydrogeochemistry (Voegelin et al., 2013). Furthermore, the mc character of the Fe- precipitates explains the partially unambiguous results of the magnetic susceptibility measurements and the lack of mineral-specific Gt, Hem and Mt patterns due to missing Curie or Néel temperature. "Magnetic properties of Fe oxides of small particle size" deviate from those of their bulk counterparts and radical changes in their magnetic properties such as Mossbauer spectra, Morin transition or Neel temperature are the consequence (Murad 1996). As the characteristic Neel ordering temperature drops with (micro)crystal size an exact allocation to reference temperatures is no longer possible (Stucki et al., 2012). Murad & Schwertmann 1980 could show that as particle sizes decrease the individual magnetic characteristics of the different Fe oxyhydroxides gradually disappear, until finally only fundamental structural elements of short-range-order common to all Fe oxyhydroxides (i.e. $Fe(O,OH)_6$ octahedra: Fe^{3+} surrounded by six O, OH and/or OH_2) remain. Additional element substitution and other defects affecting crystallinity increase this effect (Rancourt et al., 2001; Thompson et al. (2011). That the precipitates consistently contain impurities and the minerals are quite small, also explains the missing Morin transition of the kt measurements although Hem is definitely present as evidenced by the corresponding high temperature measurements, microscopic examinations and synchrotron measurements. The same mechanism affect the Mossbauer spectra (Murad 1996). Therefore, the identification of specific Fe oxyhydroxides by k-t measurements and Mossbauer spectroscopy is difficult and results are partially ambiguous in complex natural samples with significant concentration of mc phases. As quantity, composition and properties of natural mc phases are hard to determine on a broad scale mc phases were only partially considered to describe and model the Fe mineral dynamic across natural RTZ. Since the spatially resolved XAS measurements enable a clear visual and spatial assignment, the XAS results can be related to the mc texture of the secondary Fe phases. The documented Fe oxyhydroxide precipitations in form of coatings and cementations provide optical evidence for small sized and weakly crystalline Fe phase mixtures that nevertheless exhibit crystalline characteristics and highlight the important role in the local Fe and As cycle across the natural redox interface.

Texture & formation

The combined analyses revealed a broad variety of mc precipitates that differ in size, texture (Fig. 40-42, 44, 45), mineralogical composition as well as As concentration and speciation (Table 10) and quantity of coprecipitated elements (Table 8 & 10). Filigree structures such as twisted stalks and fibres dominate the precipitate surface (Fig. 42) while the inner area is made up of gel-like banded layers and massive and dense platy layers (Fig. 44 & 45). Particular noticeable are the **twisted stalks, fibres and needles that form filigree fibre networks like honeycomb filaments and radial spheres** at the precipitate surfaces (Fig. 42)**.** The filigree surface structures clearly show the recent character of the precipitates and propose biogenic formation processes. Clearly visible cemented bacterial cells along the stalks (Fig. 42 f) proof the connection to present day Fe cycling and highlight the strong influence of biotic activity. In fact, there have been many (review) studies on microbial Fe mineralization (Ferris 2005; Mavrocordatos & Fortin 2002; Chatellier et al., 2004; Ghiorse 1984; Konhauser 1998; Fortin & Langley 2005; Kappler & Straub 2005; Chan et al., 2009) highlighting the strong microbial influence on the sedimentary Fe-cycle. Iron-accumulating bacteria creating long branching Fe filaments of comparable size and shape with a ferruginous and crystalline nature are known from comparable

natural near-surface systems (Nakai & Yashinaga 1980). Iron oxyhydroxide structures with twisted stalk, needle, filament and fibre morphologies are typical Fe biominerals in surface environments (Chan et al., 2009; Schwertmann & Fitzpatrick 1992) and also the wide range of crystal sizes in the sub µm-range is characteristic for biotic processes. As already described in Glodowska et al. (2021b), "sub-µm sized Fe minerals are common products of microbial biomineralization and (bio)minerals formed as a result of direct metabolic activity of bacteria usually occur as nanoparticles or small crystals (2–500 nm) with variable morphology and contain impurities such as sorbed or co-precipitated Si, PO_4^{3-}, SO_4^{2-} ions but also cations such as $Mn^{2+/4+}$, Al^{3+}, etc. (Fortin & Langley 2005)". This resembles type and amount of documented elements in the precipitates (Table 8 & 10) and has been mentioned as characteristic for biogenic Fe-structures multiple times (Voegelin et al., 2010; Suzuki et al., 2011 & 12; Senn et al., 2018; Ahmad et al., 2020; Fortin & Langley 2005). Especially Al_2O_3 and SiO_2 are usually incorporated in the crystal lattice of fibrous Fe oxyhydroxide phases in large quantities and can make up to 33 wt% (Nakai & Yashinaga 1980; Fordham et al., 1984). Additionally, these biominerals are often rich in (cell-derived) organic matter (Hegler et al., 2008; Muehe et al., 2013; Posth et al., 2010) what is in agreement with the results presented here. Also the association of sub-µm sized Fe minerals with (nanocrystalline) PS is typical for microbial biomineralization which is in accordance to the results of this study. In summary, these observations support the assumption that biogenic processes play a key role in the formation of the filigree surface structures. The biogenic formation is crucial as the biogenic minerals show different properties compared to Fe minerals formed by abiotic reactions. As already described in Glodowska et al (2021b) biominerals that contain cell-derived organic matter can possess different properties compared to their abiogenic counterparts (Hegler et al., 2008; Muehe et al., 2013; Posth et al., 2010). The incorporation of various elements (Al, Ca, Si, P) in the crystal lattice weakens the crystal structure und can facilitate dissolution (Voegelin et al., 2010; Suzuki et al., 2011 & 2012; Senn et al., 2018; Ahmad et al., 2020; Nakai & Yashinaga 1980; Fordham et al., 1984). The same applies for the incorporation of organic substances like bacterial cells and the formation of organo-mineral complexes. In general these phases tend to be dissolved more easily (Ferris 2005). This is further reinforced by the small mineral size. Especially biogenic Fe minerals tend to have smaller grain sizes than the abiotic counterparts (Karlin 1990) and can therefore be dissolved more easily and the stability of biogenic minerals is usually lower than their abiotic counterparts.

That **microbially catalysed Fe redox and phase transformations** in sedimentary near surface environments profoundly affect the geochemistry and mineralogy of these environments has widely been accepted for many years (Weber et al., 2006; Emerson et al., 2010 & 2012). Microorganisms from within both the domain Archaea and Bacteria are capable of metabolically exploiting the favourable redox potential between the Fe(III)/Fe(II) couple (Weber et al., 2006). On the one hand oxidized Fe serving as terminal electron acceptor under anaerobic conditions for lithotrophic and heterotrophic **Fe-reducing microorganisms (FRM)** is widely accepted as important mobilization mechanism for Fe and related pollutants such as As (Weber et al., 2006). It was shown that crystalline ferric (Gt, Hem, Lep), ferrous (Si, vivianite), and mixed valence (Mt, green rust) Fe solids are formed in anoxic, circumneutral incubation experiments by dissimilatory metal reducing bacteria (DMRB) (Zachara et al., 2002). On the other hand reduced Fe, can serve as an energy source for lithotrophic **Fe-oxidizing microorganisms (FOM)** under oxic as well as microaerobic and anaerobic conditions (Weber et al., 2006; Emerson & Floyd 2005). Based on Picard et al. (2014) O_2 concentrations as low as 3 µM are sufficient to supply the biogenic Fe(II)-oxidizing process. Glodowska et al. (2020) and (2021) were able to show that a wide range of microorganisms occur in the immediate vicinity of the precipitates involving fermenters, methanotrophs, methanogens as well as iron and sulphate reducing microbes. Fe(II) oxidizers could not be documented in significant quantities. However, with regard to the filigree precipitate surface structures biogenic mediated oxidation processes are very likely to occur. The characteristic morphology is typical for microaerophilic Fe(II)-oxidizing bacteria which are known to

produce twisted stalks or comparable organo-mineral structures (Picard et al., 2014). Especially the precipitate surfaces show the typical texture of organo-mineral structures produced by Fe-(II) oxidizing bacteria (Kappler & Newman 2004; Picard et al., 2014 & 2016; Cismasu et al., 2016; Suzuki et al., 2011 & 12; Banfield et al., 2000). In fact, the filigree structures with their distinct morphologies are strongly reminiscent of twisted stalks formed by Gallionella ferruginea or Mariprofundus ferrooxydans documented by Chan et al. (2011). Some studies even assume that the stalk-like morphologies can be viewed as typical biosignatures for Fe-oxidizing metabolisms (Chan et al., 2011). With regard to the formation of the stalks and filaments two biotic pathways are known. In one pathway, the filaments, composed of regularly arranged microcrystals, are formed directly by Fe-oxidizing bacteria. In the other pathway, the adsorption of inorganically precipitated nanocrystals on the cellular debris trigger a passive growth after the microorganisms have served as a condensation nucleus (Nakai & Yashinaga 1980). The radial spheres with a dense core observed in Fig. 42 (d) likely resemble this description. Visible are small particles such as bacterial cells acting as precipitation surface from where the structures grow radially outward. Microbes are reasonable candidates to act as nucleus for the initial precipitation although it was not possible to identify the small particle in the centre of the spheres. Both pathways can also co-occur which likely resembles the diverse results of the microscopic analyses showing various structures that can be assigned to one or the other category with relative certainty. Despite the morphology also the complex mineralogical composition involving different Fe oxyhydroxides (Gt, Hem, Mt and Lep) in variable size and quantity as well as the incorporation of OM and the high amount of incorporated elements are also typical for phases produced by Fe(II)-oxidizing bacteria (Chan et al., 2011). Furthermore, Fe(III) minerals formed by bacterial Fe(II) oxidation are known to cover a broad range of crystallinities and have a high proportion of poorly to microcrystalline phases (Larese-Casanova et al., 2010). In general the crystalline spectrum of the microbial Fe phases reaches from poorly-crystalline HFO phases to microcrystalline phases. These phases and often occur as complex mixtures which corresponds to the findings of this study. Microcrystalline Fe phases are commonly reported in context of biomineralization (Zachara et al., 2002) and multiple XAS and Mossbauer based studies showed that especially mc Gt tends to form fibrous or needle structures of high electron density (Nakai & Yashinaga 1980; Fordham et al., 1984; Gunnarsson 2002; Guo & Barnard 2013) what is in accordance with the results of this study. µ-XANES results (Table 10) revealed almost 80 % Gt for the precipitate surface structures, supplemented by minor amounts of Hem and Mt. Based on the results of the available methods, it seems therefor most likely that Fe(II) oxidising microbes contribute to the formation of the filigree Gt-dominated surface structures of the Fe oxyhydroxide precipitates. Beside pure Gt also Gt-Mt mixtures in fibrous or needle form have been documented before (Li et al., 2011) which likely match the µ-XANES results as well.

Furthermore, biotic processes are particularly suitable for explaining the formation of the **sub-µm sized Mt phases**. Mt formation as a result of bacterial activity has been known for decades and biogenic Mt in general tend to have smaller grain sizes than the abiotic or detrital counterparts (Karlin 1990) which is most likely related to the truncation of crystal growth by the presence of organic molecules and/or inorganic ligands released by the bacteria (Banfield et al., 2000; Hansel et al., 2003). On the other hand detrital Mt typically occurs in relatively large particles in the range of 10-100s µm (Murad 1996) and abiotic secondary Mt formed by $Fe(II)_{aq}$ that is in contact to Fe(III) oxyhydroxides is also significant larger than the biotic Mt crystals and have about 10-fold the size than biotic Mt (Hansel et al., 2003). Therefore, these phases should be visible under the microscope and easy to detect. The biotic formation of secondary small sized Mt can follow different reactions pathways. Li et al. (2011) showed that poorly crystalline Fh can be reductively transformed by dissimilatory Fe(III)-reducing bacteria to nanocrystalline Mt. This would be a reasonable explanation for the widespread occurrence of very fine-grained Mt in the aquifer sands. A microbial assisted Fh transformation is also in agreement with observations from batch experiments using the same sediments from Van Phuc. The onset of

Fe(III)- reducing conditions resulted only in very little release of Fe(II) (Glodowska et al., 2020). Direct Mt formation would be a suitable explanation for this observation. Alternatively, small-sized Mt phases may also be formed by biotic Fe(II) oxidation. An example for Mt formation by anaerobic bio oxidation of Fe(II) was published by Chaudhuri et al. (2001). The study revealed the natural formation of fine-grained biogenic Mt. In the study, the Fe(II) oxidation was coupled to denitrification but in context of the complex GW hydrochemistry and partially organic-rich sediments other redox couples are conceivable to fuel the reaction in Van Phuc. However, biotic catalysed transformation reactions offer numerous reasonable (trans)formation pathways. Wang et al. (2014) documented Mt nanoparticles as final reaction product from biotic catalysed transformation of Lep to Mt through GR. GR as intermediate phase in the transformation scheme may explain the small amounts of GR documented in the bulk EXAFS measurements (Table 7). Another potential biogenic pathway is Mt formation during the bio reduction of nanoparticulate Hem**.** Behrends & Van Cappellen 2007 described the transformation of nanoparticulate Hem into Mt during dissimilatory Fe reduction. Furthermore, Mt may well form abiotically under favourable physico-chemical conditions. Especially amorphous to poorly crystalline Fe oxyhydroxides are transformed to Mt during reductive dissolution (Fredrickson et al., 1998; Benner et al., 2002). Corresponding processes were described already by Schwertmann (1991) in soils and could likely occur in comparable near-surface systems. Further Mt is known to form abiotically during simultaneous production of soluble Fe(III) and Fe(II) (Behrends & Van Cappellen 2007) related to (reductive) dissolution of Fe(III) minerals during redox oscillations. Especially poorly crystalline to amorphous Fe oxides are known to be transformed into Mt during reductive dissolution (Dixit & Hering 2003). The direct abiotic conversion could also explain why no maghemite as a typical precursor mineral in the dynamic transition zones could be documented. Compared to Fe(III) oxyhydroxides like Gt and Lep the formation of Mt is observed at high $Fe(II)_{aq}$ concentrations with surface loadings greater than 1.0 mmol Fe(II)/g (in the absence of bicarbonate) (Hansel et al., 2005) which is in agreement with hydrochemistry from the study site published by Stopelli et al. (2020). With regard to the mineral composition Hansel et al. (2005) showed that the rate of Mt precipitation is a function of the relative proportions of Gt to Lep which likely explains the low Mt quantity within the precipitations. In contras the formation of nano-micro crystalline Mt phases may be promoted by the high As GW concentration. Wang et al. (2008) observed during the formation of Mt in the presence of arsenite that the secondary products in the absence of As are well-crystallized whereas poorly crystalline phases formed in the presence of As and suggested that As adsorbs on the particles during their nucleation/growth and passivates their surfaces. Mt formation could further be explained by solid state transformation of Fe(III) oxyhydroxides under reducing conditions (British Geological Survey 2001; Smedley & Kinniburg 2002). Therefore, coupled biogenic-abiogenic processes offer a reasonable explanation for the composition of the precipitates with regard to the mc Mt minerals although the complex network of various biotic and abiotic processes which in turn influence each other is hard to disentangle and quantify.

Also with regard to the **Lep formation** coupled biogeochemical processes are suitable to explain the documented results. Lep shares the property of Gt to precipitate over a large Fe(II) concentration range (Hansel et al., 2005). Coupled biomineralization of Gt and Lep by nitrate-reducing Fe(II)-oxidizing bacteria is documented by Larese-Casanova et al. (2010) who showed that Lep and Gt may coexist in aquatic environments through biologically mediated processes. An important aspect which clearly determines the ratio of Lep to Gt formation in an association of these two minerals is the carbonate ion concentration in solution which in turn depends on pH and p $C0_2$. Low amount of Lep compared to dominant Gt can be explained by high carbonate concentrations which are known to suppress Lep formation in favour of Gt (Schwertmann 1991; Schwertmann & Fitzpatrick 1992). As Lep is the more soluble phase related to initial precipitation (Benner et al., 2002; Cornell & Schwertmann 2003) it is also likely to get dissolved again if it is not transformed into a more stable Fe phase. This might explain

the low quantity of Lep in Van Phuc sediments. Furthermore, Hansel et al. (2005) showed that the precipitation of Mt induces the dissolution of Lep in presence of Cl. In summary, these processes are suitable to explain a low quantity of Lep und would fit in the formation scheme of the Fe(III)-dominated precipitates and are in line with local GW data from Stopelli et al. (2020).

With regard to **Hem** the biogenic formation is far less common. Bacterial synthesized Hem nanoclusters (~150 nm) where reported before by Kim et al. (2019) but not in a natural environment. Therefore, it seems to be more likely that Hem formation might be related to abiotic reactions coupled to dehydration and rearrangement processes as described by Posth et al. (2014). According to this model, Hem emerges directly from Gt. This would likely match the observed change in texture from the Gt-dominated surface towards the dense inner sections. Further Hem is known to form directly from natural nanoparticle Mt particles by oxidation (Khan et al., 2015). The phase transformation of nano Mt would agree very well with the local conditions and the composition of the precipitates. Li et al. (2020) showed that that (bi)carbonate promotes the transformation of Fh to Hem and retarded the Gt formation. Therefore, high (bi)carbonate might support Hem formation and govern the relative mineral composition. Finally Fe(II) catalysed growth of Hem was reported for comparable environmental conditions (Rosso et al., 2010). As Literature examples for Hem in in fibrous or needle form could not be found it is reasonable to assume that the filigree surface structures are almost entirely composed of Gt maybe with minor amounts of Mt, Lep or Fh phases. With regard to the µ-XANES analysis this assumption is in line with the results and implies Hem formation within the precipitates is limited to preferably abiotic aging reactions within the inner parts of the precipitates. The presence of Hem in the older precipitate structures might in turn encourage or enable the formation of the filigree surface structures. Secondary formation of acicular needle shaped secondary Gt phases were reported on residual Hem minerals in context of oxide sorbent growth, Fe(II) sorption and subsequent oxidation (Larese-Casanova et al., 2012). In an aqueous Fe(II)–Fe(III) system the poorly soluble Fe(III) products formed as a result of contaminant reduction and Fe(II) oxidation on Fe oxides. The study analysed secondary Fe(III) mineral phases formed after Fe(II) oxidation on variable detrital Fe oxides during heterogeneous contaminant reduction and claimed that Hem may possess a templating ability for the α-FeOOH atom arrangement as opposed to γ-FeOOH. Therefore, the association of the phases within the precipitates could explain the formation of the distinct shaped Gt needles and stalks. With regard to this work, the presence of secondary Hem could take on the role of the residual phases and trigger the formation of the distinct Gt textures. As the proportion of Gt formation on the investigated Hem was linked to number of surface sites the results likely explain the huge filigree Gt-dominated fibre networks formed on top of the mc phases mixture.

In order to understand the **formation of the complex Fe-precipitate phase mixtures**, it is crucial to understand the initial precipitation mechanism from GW und subsequent evolution process. Based on the assumption that the precipitation process remained the same across the entire formation process the filigree precipitate surface structures should represent the initial precipitation process which ultimately leads to the extensive precipitate structures. As described before the initial precipitation and formation of the filaments and stalks is most likely coupled to biotic activity. The filigree fibre networks (Fig. 42) form huge sponge-like 3-dimensional structures along the entire precipitate surface and propose an enormous potential for interaction with GW driving subsequent biotic or abiotic reactions. The usually very high specific surface area of freshly precipitated poorly crystalline Fe oxyhydroxide phases in natural redox environments are known to promote both biotic and abiotic processes (Dixit & Hering 2003) and low density of the 3-dimensional structure and constant GW replenishment should further drive (bio)geochemical processes. With regard to the composition of reactive high-surface minerals and their location in the direct vicinity of strong redox and hydrogeochemistry gradients, the filigree structures offer the ideal conditions for intensive

interactions between the solid phase and the GW in both biotic and abiotic scenarios. In fact, a continuous development of the precipitate textures can be observed. Consolidation and compaction of the structures suggest that interactions with (dissolved) GW compounds transform the filigree primary structures. Successively condensing filaments (Fig. 42 d) suggest progressive recrystallization forms the gelic and plate-like textures inside the cementations. In line with observations is the Al, Si, P content of the precipitates, which decrease from the edge, is associated with an increase in the crystallinity. The filigree biogenic structures get denser and recrystallize. Towards the inner part of the cementations scanning electron backscatter micrographs reveal dark grey gel-like and the white plate-like Fe oxyhydroxide structures. The structures clearly separate from another and especially in the outer area of the cementations the gels and platy sections form a recurring layering while the platy layers dominate the central area of the cementations (Fig. 44 & 45). The less dense **dark grey gel layers** most likely resemble organo-mineral complexes what is in line with higher P_2O_5 and SO_3 concentrations and significantly higher amount of coprecipitated Al_2O_3, SiO_2, and CaO (Table 10) in the gel precipitates compared to the platy structures. Therefore, the less dense character of the gels is most likely related to embedded OM (CHNOPS). In accordance with the geochemical composition the gel-like texture suggest biogenic origin. The concentric gels are typical morphologies for Fe(II) oxidising bacteria (Chan et al., 2009; Schwertmann & Fitzpatrick 1992; Picard et al., 2014 & 2016; Cismasu et al., 2016; Suzuki et al., 2011) and it is known that Fe oxyhydroxide gel precipitations can resemble biofilms or microbial mats that can develop from filigree fibre networks within weeks (Kappler & Newman 2004). Therefore, it can be assumed that the gel formation represents an intermediate transformation step. Within the central parts a completely recrystallized material in form of **white plate-like Fe precipitations** (Fig. 42 e, f) with a homogeneous and dense structure dominates the cementations. It is likely that the progressive re-crystallization and densification of the filaments and gels finally forms the massive Fe cementations with high electron density and therefore white colour in the backscatter SEM images. The decreasing elemental content for coprecipitated Al, Si and P towards these structures fits well with the recrystallization process (Table 10). The associated textural change can be understood as a maturing process where with increasing crystalline order, the co-precipitated elements are removed of the mineral lattice. Observations along the As content and speciation distribution support this hypothesis. Regardless of gel or filament morphology, the outer areas show a high As(III) content between 65 and 80 %. Simultaneously the Hem and Mt content is significant lower in the rim in favor of Gt. In accordance with higher proportion of Hem and Mt in the central area the As(III)/As(V) ratio is almost balanced in the platy precipitates. A trend of increasing crystallinity towards the presumably older precipitations in the center is a reasonable explanation for this observations and points to a continuous ageing gradient ultimately creating the massive plate-like Fe cementations. It can be assumed that the changing morphology represents an ageing gradient and different textures represent different generations of precipitations. This translates to the mineral inventory with more mature phases such as Hem towards the precipitate centre what is shown by the µ-XANES results. For the development of extensive precipitations it can therefore be assumed that the filigree mc Gt-dominated structures represent the starting point and subsequent recrystallization processes form the condensed structures in gelic and platy morphology. Successive growth along the contact surface with the GW continuously expands the precipitates and promote further Fe-accumulation. In consequence, the reactive surface migrates outwards and the precipitates grow. This process is likely to explain the matured Hem, Mt and As(V)-rich inner parts compared to the Gt and As(II)-rich outer areas. However, it is unclear whether the formation of the gelic precipitates within the cementations is a necessary intermediate step or whether it is an alternative (biotic) recrystallization process that ultimately leads to the same dense structures. With regard to the coatings no gel-like Fe oxyhydroxide structures are formed. The filigree fibres are located directly on top of homogeneous and dense precipitates suggesting gelic precipitates may not necessarily be an immediate (re)crystallisation processes and the

platy precipitations may evolve directly from the filigree surface structures. Since the coating structures are more exposed to GW, it can be assumed that the recrystallization processes in the coatings differs from the cementations with regard to the hydrological and biological framework. This would be in agreement with the deviating mineralogical composition of the coatings with a Hem content between 12 and 20 % suggesting that the coatings are not in a juvenile but rather in a more aged state. However, the evidence of Hem in the µ-XANES measurements of the coatings could also be related to the spatial resolution of the method and does not reflect the small-scale precipitate composition visible in texture.

With regard to the maturation process the poorly to mc character of the precipitates, initially most likely composed of mc Gt and/or Fh offer perfect conditions for subsequent biotic reduction reactions towards more stable Fe oxyhydroxide phases such as Hem and Mt. Less crystalline minerals can be metabolized by Fe reducing bacteria much more effectively than crystalline minerals (Benner et al., 2002) and as amorphous to poorly crystalline Fe-phases are the favoured source of Fe(III) for microbes (Lovley & Phillips 1986 & 1987). The poorly crystalline Fe phases should drive microbial activity if other constituents are available and in context of the GW composition subsequent biotic reactions are very likely to be expected and could explain the mineralogical composition of precipitates. Therefore, multiple recrystallization pathways are likely in the complex natural setting. Multiple pathways and **secondary mineralization mechanisms** are well documented and for example Hansel et al. (2003) described the secondary mineralization of Fh via coupled, biotic-abiotic pathways primarily resulting in the production of Mt and Gt with minor amounts of green rust. Subsequent to the initial sorption of ferrous Fe on Fh, Gt (via dissolution/reprecipitation) and/or Mt (via solid-state conversion) precipitation ensues the spatial coupling of both Gt and Mt with the Fh surface (Hansel et al., 2003). This process resembles very well the observed composition of the precipitates. Especially since bulk EXAFS analyses of RD54 (Table 7) showed green rust in minor concentrations in 8 samples along the redox transition zone. The mc Gt documented in this study could replace the Fh with regard to the initial precipitation process and would thus provide a conclusive picture.

Initial precipitation

With regard to the mineralogical composition of the precipitates the analyses revealed partly ambiguous results. Especially the absence of Fh is a remarkable result. Normally the formation of Fh represents the primary Fe mineral precipitation step from GW in both biotic and abiotic scenarios (Schwertmann & Cornell 2000) as initial precipitation generally produces the more soluble short-range ordered (SRO) mineral phases (Benner et al., 2002; Cornell & Schwertmann 2003). Fh formation due abiotic or microbial Fe(II) oxidation (Cornell & Schwertmann 2003) usually poses the typical precursor mineral for development of more crystalline Fe(III) oxyhydroxides such as Gt, Hem or Mt in natural environments (Zachara et al., 2002). However, in the present study µ-XANES analysis revealed no Fh analysing the precipitates. Basically there is the possibility that insufficient Fh concentrations and/or a lack of spatial resolution prevent the detection. Further reasons can be spectral similarities with mc Gt in combination with inappropriate reference material and fast transformation reactions towards more stable mc Fe oxyhydroxide phases (Jung et al., 2012; Sun et al., 2018). Beside methodological limitations the immediate transformation reactions offer a reasonable explanation for the missing Fh proof. Conversion of Fh into more stable phases can likely prevent the detection. This would be in line with the bulk EXAFS data (Table 7) and a comprehensive XAS study by Nghiem et al. (2020) which indicate Fh or amorphous Fe(III) phases as important Fe(III) phase in the study area of Van Phuc. As the evidence of Fh from Mossbauer spectra and thermomagnetic data were not explicit clear and the presence of Fh can neither be ruled out nor confirmed entirely, multiple scenarios for the initial Fe precipitation from the GW are considered.

In the **first scenario**, the **formation of Fh** represents the primary precipitation event of dissolved Fe(II) from GW. Fast transformation reactions are conceivable explanations under both oxic and anoxic conditions. Under oxic conditions Fh likely transforms fast to less hydrated and more stable Fe oxyhydroxides such as Gt and Hem (Cornell & Schwertmann 2003). But also in absence of available O_2 Fh is highly instable and likely to be transformed into more thermodynamically stable phases. A possible Fh transformation mechanism under reducing conditions is the $Fe(II)_{aq}$ catalysed transformation (Tomaszewski et al., 2016; Hansel et al., 2005). It is known that Fh is transformed to more ordered minerals such as Gt, Hem and Mt in the presence of aqueous Fe(II) also in reducing environments as a result of a reaction between dissolved Fe(II) and Fh (Kocar et al., 2006; Benner et al., 2002; Hansel et al., 2003; Hansel et al., 2005; Liu et al., 2005; Rosso et al., 2010). Many laboratory experiments (Hansel et al., 2003; Kocar et al., 2006; Pedersen et al., 2005; Tufano & Fendorf 2008) have demonstrated that dissolved Fe(II) is capable of transforming thermodynamically less stable sedimentary Fe phases rapidly into highly ordered mineral structures (Islam et al., 2005). Fe(II) catalysed transformation of Fh could entirely explain the observed mineralogical composition of the Fe(III) dominated precipitates as Fh is the typical precursors of all documented Fe oxyhydroxides (Cornell & Schwertmann 2003; Zachara et al., 2002) and can be transformed into Lep, Gt, Hem and Mt by Fe(II)-induced transformation reactions (Benner et al., 2002; Liu et al., 2005; Liu et al., 2007). Especially under redox cycling the dissolved Fe(II) concentration is a crucial factor controlling the mineralogical evolution of Fe oxyhydroxides (Hansel et al., 2005; Tomaszewski et al., 2016). As Fe(III) oxyhydroxides undergoing reductive dissolution, release Fe(II) to solution which in turn may induce the transformation of less thermodynamically favourable phases to more thermodynamically stable minerals (Hansel et al., 2003; Benner et al., 2002; Zachara et al., 2002). In this way, redox oscillations can successively increase the crystallinity of Fe oxyhydroxide phases (Thompson et al., 2006). As the Fe(II) catalysed transformation of Fh is promoted by a Fe(II)-rich GW influx and oscillating redox conditions a fast transformation of Fh is a reasonable scenario at the field site and could explain the missing Fh evidence by spatially resolved XAS analyses. Already Schwertmann & Fischer 1973 showed that Fh is very likely a source of dissolved Fe for the crystallization of Gt from the solution phase. Transformation of thermodynamically less stable Fe phases like Fh rapidly into highly ordered mineral structures would be in line with high Fe GW concentrations and would likely explain the formation of the fresh Fe(III)-dominated precipitates. Already small concentrations of Fe(II) promote conversion of 2-line Fh into more crystalline phases (Benner et al., 2002; Hansel et al., 2003 & 2005) According to Hansel et al. (2003), 40 µM of Fe(II) can cause almost complete conversion of the 2- line Fh whereby Fh "undergoes a mineralogical shift to Gt at Fe(II) loadings less than 1 mmol/g (resulting from 0.3 mM aqueous Fe(II)) or to Mt at higher Fe(II) loadings" (Fendorf et al., 2010). Therefore, the absence of Fh in the precipitates could be explained by the immediate formation of Gt and Mt in the precipitates. Ageing reactions promote the transformation of amorphous and poorly crystalline phases into more crystalline minerals and more soluble phases like Fh and Lep will be transformed to the more stable and less soluble forms like Gt, Hem and Mt (Benner et al., 2002; Cornell & Schwertmann 2003). The mc character of the mineral phases can be retained during this process. Handler et al. (2014) showed that Fe(II)-catalysed recrystallization of Gt created negligible change in the Gt mineralogy and morphology and must not necessary create more crystalline phases. Ageing conversation of natural poorly crystalline ferric hydroxides such as Fh are very likely to form Gt minerals under conditions corresponding to the field site (Schwertmann & Fischer 1973) and prevent the detection of the Fe Phase. The same accounts for prolonged anoxic periods (Hansel et al., 2003). So there are many reasons to expect Fh at the study site. The presence of Fh is further obvious as under redox oscillations the coexistence of thermodynamically more and less stable phases is generally common (Kocar et al., 2006). Most likely the spectral similarities of the short range ordered Fh and mc Gt minerals prevent a clear differentiation of the phases. However, It was not possible to document clear evidence of Fh.

Also the presence of Lep is suggested by magnetic measurements and Mossbauer analysis the direct evidence of Fh may be hindered by spatial and quantitative limitations.

Alternatively the formation of the mc Fe precipitates is also conceivable without Fh. **Lep** was documented to be the first neo formed Fe mineral phase under suboxic conditions, despite of Fh, before (Macías & Camps-Arbestain 2020). In this context an initial precipitation scenario around Lep could also explain the absence of Fh and the presumably low Lep content in the precipitates. However, the ambiguous results with regard to Fh and Lep and the characteristic surface texture of the precipitates a scenario where **nanophase Gt** represents the initial precipitation stage may offer the most reasonable scenario with regard to the mineralogical results. As despite preservation of the sensitive precipitate surface structures, no Fh could be detected it seems likely that mc Gt marks the beginning of precipitate formation process instead. Based on calculations a poorly crystalline Gt with a crystal size of 5 nm may well reach the solubility of Fh (Schwertmann 1991) and could therefore explain the leaching experiments done in the field site proposing poorly crystalline Fe oxyhydroxide phases (Berg et al., 2007; Eiche 2010). The bulk EXAFS results suggesting Fh or amorphous Fe(III) phases could be explained by spectral similarities of mc Gt and Fh that make a distinction difficult or impossible (Jung et al., 2012; Sun et al., 2016). As Mossbauer spectra of mc Gt and Fh can also be very similar and hard to distinguish (Sun et al., 2018; Murad 1996) and and thermomagnetic data are only partially able to identify Fh in the nitrogen temperature range anyway the scenario without Fh is also in accordance with the results of this and previous studies. In view of the analytical limitations to separate Fh and mc Gt mentioned at the beginning of chapter, it is also possible that Fh is overrepresented in previous work and that mc Gt phases actually plays a much more important role in biogeochemical cycle in near surface sedimentary environments like Van Phuc. Further Gt precipitates over a large Fe(II) concentration range (Hansel et al., 2005). In context of a presumably varying GW this would likely explain the dominance of Gt. Therefore, the results rather imply re-oxidation of nano-sized to mc Gt as Initial mechanism at the field site. The (nano)minerals, would create crystals of very small shape as observed. Investigations in soil environments exposed to the recurring redox oscillations revealed mc Gt structures, that include mc Hem, are formed by transformation of (Al-bearing) nano-Gt (Thompson et al., 2006). During this process Fh is absent what closely resembles the results of this study. These results indicate that consecutive redox cycles could create an alternative Fe precipitation scheme without Fh. Thompson et al. (2006) further postulated that the frequency and intensity of redox shifts may influence Fe mineral transformation and create multiple transformation scenarios. However, Thompson et al. (2006) showed that redox oscillations during pedogenesis that span the Fe reduction/oxidation threshold can promote the direct conversion of non-Fh SRO material into more crystalline forms. Oscillating GW conditions in the field site of Van Phuc may create comparable effects and likely explain the formation of the mc precipitates. The presence of poorly crystalline Gt ranging from those at the more crystalline end being recognized as mc Gt (Thompson et al., 2011) to progressively less crystalline components that best described as nano-Gt are documented along natural redox gradients in various environments. Up to date it could be shown that across a large variety of lacustrine and marine environments (Van der Zee et al., 2003), mine tailings (Filip et al., 2007) and soils (Thompson et al., 2006) the dominant reactive Fe oxyhydroxide phase is nanophase Gt rather than the assumed two-line Fh. So it is quite possible to find comparable conditions in near surface sediments. Which SRO material ultimately leads to the formation of the mc precipitates remains unclear in this study. Ultimately the complex and oscillating or pulsing hydrobiogeochemical environment will most likely create a range of poorly crystalline phases involving Fh as well as nano-Gt phases. Most likely both phases co-precipitate in and are supplemented by further more soluble phases such as Lep (Benner et al., 2002; Cornell & Schwertmann 2003), depending on the specific conditions. Fh and Gt are closely related and the transformation products of both phases can have very similar crystallinity ranging from poorly crystalline SRO materials to microcrystalline Fe(III)

oxyhydroxide phases. Murad & Schwertmann (1980) stated that individual characteristics of the different Fe oxides gradually disappear as particle sizes decrease and finally only fundamental structural elements of short-range order common to all Fe oxides remain (i.e. the $Fe(O,OH)_6$ octahedra). Therefore, no fundamental differences in the properties of these low-crystalline phases and their function in the environment are to be expected (Fritzsche et al., 2015). Also with regard to the biotic transformation reactions Fh and mc Gt should offer comparable attractiveness towards microbes. The small sized mc Gt minerals should provide good access and effective metabolism capabilities. So it probably does not play a role in the formation of the mc precipitates which SRO mineral marks the beginning. Decisive are the diverse secondary reactions. The formation and mineralogical composition of the mc Fe oxyhydroxide precipitations can be explained regardless whether mc Gt or Fh is formed initially. The presence of the documented mc Fe oxyhydroxide minerals Gt, Hem, Mt and in low concentrations Lep can be entirely explained by secondary transformation reactions related to $Fe(II)_{aq}$ and biotic activity for both initial mineral phases. Both mineral transformation schemes are in line with calculated mineral saturation indices at the field site from Stopelli et al. (2020) who postulated a potential depletion of short range ordered Fe(III) phases towards more crystalline phases and correspond to the standard mineral transformation schemes that are to be expected (Posth et al., 2014). Thompson et al. (2006) showed that redox oscillations that span the Fe reduction/oxidation threshold can promote the direct conversion of SRO material into more crystalline forms with no Fe removal. This process is very much in line with the results auf the study area as it is able to explain ongoing transformation processes that change the mineral composition continuously and the formation of the vast precipitates.

Oscillating conditions

With regard to the high quantity the formation of the vast precipitates structures might be promoted by a further mechanism boosting the mentioned biotic and abiotic pathways. In order to explain the mc character, texture as well as mineralogical and geochemical composition redox and hydrochemical oscillations would offer a comprehensive explanation. Although no studies could be found in comparable near surface sedimentary environments, investigations in soils exposed to redox oscillations show almost identical results as the present thesis. Vogelsang et al. (2016) found ferrous and ferric Fe silicates, nano- to microcrystalline Gt and Hem, as well as a Fh-type phase to be formed in soils under redox oscillations. In accordance to this study mc Gt was the predominating Fe oxyhydroxide phase. The study found that the evolution of the Fe phases was likely linked to the re-crystallization and/or solid-state transformation of of freshly precipitated hydrous Fe(III) mineral phases as initially published by Pedersen et al. (2005). Pedersen et al. (2005) and Vogelsang et al. (2016) describe the process as follows. The secondary transformation is induced by electron transfer between the dissolved Fe(II) and the Fe(III) mineral after adsorption of Fe(II) on the mineral surface (Williams & Scherer 2004). It results in the dissolution of the mineral and the subsequent re-crystallization of the Fe(III) into more stable Fe oxides species (Hansel et al., 2003; Williams & Scherer 2004; Pedersen et al., 2005; Yee et al., 2006). In the absence of organic matter, it promotes structural transformation of weakly crystalline Fe oxides (e.g. Fh) into more crystalline and thermodynamically stable Fe oxide phases, such as Gt, Hem (Jones et al., 2009), and Lep (Pedersen et al., 2005). Thompson et al. (2006) demonstrated in batch experiments that redox oscillations can lead to increasing crystallinity of Gt and Hem due to Fe(II)-catalyzed solid state transformation of Fe(III) oxides. Fe(II) might originate from reduction of Fe(III) minerals in-situ or is replenished by GW. The secondary mineral species formed upon Fe(II)-catalyzed transformation depends on the release rate and the concentration of dissolved Fe(II) (Fredrickson et al., 1998; Benner et al., 2002; Hansel et al., 2003; Zachara et al., 2002; Yee et al., 2006). Since mc Gt is less prone to reductive dissolution than Fh (Hansel et al., 2003), it can, once formed, accumulate along the redox interface becoming the dominant phase. This Fe(II) induced crystallization process in context of redox oscillations offers a reasonable for the

mineral composition and the mc character of the secondary products. Also other studies indicate the great importance redox oscillations of for mc Fe mineral phases. As poorly crystalline Fe oxyhydroxides usually undergo transformation to more crystalline forms over time (Dixit & Hering 2003) the vast presence of mc phases along the redox interface is best explained by cyclic or oscillating conditions as low crystallinity of the is typically related to variable environmental conditions (Stucki et al., 2012). A changing hydrochemical environment with ongoing dissolution, (re)precipitation and transformation reactions prevent continuous recrystallization and aging processes and offer a reasonable explanation for the mc character of the Fe phases along the redox interface. The absence of well crystalline secondary Fe(III)-phases supports this observation. Assuming continuous oscillating hydrogeochemical conditions, well-developed secondary crystalline phases can hardly be expected at the interface. In turn the alternating **multi-layer structure of plate-like and gel-like structures** which follow one another repeatedly across the cementations can easy be related to oscillating GW conditions. Changing hydrogeochemical environments would very likely explain the different re-crystallisation mechanisms creating the gel and the platy Fe oxyhydroxide precipitates. Especially Fe(II) catalysed transformation reactions are known to depend strongly on local $Fe(II)_{aq}$ availability. In column experiments Benner et al. (2002) showed that the $Fe(II)_{aq}$ induced conversion products of Fh depend on dissolved Fe(II) concentrations and convert into Gt under low dissolved Fe(II) concentrations while Mt is formed where Fe(II) concentrations are elevated. This observation was confirmed by other works (Fendorf et al., 2010; Hansel et al., 2003) and is highly interesting as it can explain the variable Gt and Mt concentrations (Table 10) across the precipitations in the context of fluctuating conditions. In addition the occurrence of **sub-µm Mt** also fits well into the picture of oscillating redox conditions. Banfield et al. (2000) showed that biogenic Mt formation in comparable sub-oxic natural environments may depend on the balance between soluble Fe(II) and Fe(III) availability and may, therefore, require the co-occurrence of reductive and non-reductive dissolution of Fe(III) mineral phases. This suggest that fluctuations in GW composition and accompanying redox oscillations are decisive factors for their formation. But it has also to be mentioned that transformation of Fe-bearing minerals under harshly changing redox conditions is still under debate. Although all studies agree that redox oscillations have a strong influence of on Fe mineral transformation some studies suggest preferential accumulation of weakly crystalline Fe oxides while other studies showed that repeated redox cycles favour the presence of crystalline phases (Thompson et al., 2006; Vogelsang et al., 2016). However, most studies describe the formation of mc Fe phases as a consequence of dynamic redox conditions. Especially soil redox oscillations are well investigated and known to promote the formation of mc Fe oxyhydroxides (Thompson et al., 2006 & 2011; Vogelsang et al., 2016).

Also the findings related to the **solid phase geochemistry** point to oscillating conditions. The precipitations (Fig. 42, 44) were show to contain a high amount of coprecipitated ions and cations (Table 8, 10) with in average 4.3 % P_2O_5, 2.9 % SiO_2, 2.8 % Al_2O_3, 0.28 % CaO and 0.19 % SO_3. Dynamic redox changes offer a reasonable explanation for the high amount of ions and cations in the precipitates as they are constantly being re-supplied. In context of oscillating conditions emitting strong hydrochemical gradients cyclic oscillations are capable to force a constant shift in solution chemistry and deploy repeatedly high amounts of dissolved GW compounds and $Fe(II)_{aq}$ to the secondary Fe precipitates and the local biota. This complex oscillating hydrochemistry is likely to support the formation of the mc Fe precipitates and explain the multiple texture and processes presumably involved. The hydrogeochemical conditions (pH, Eh) as well as organic and inorganic GW compounds are known to control biotic and abiotic oxidation and reduction reactions and define the final Fe(III) mineralogy. Especially natural organic matter, silicate, phosphate and carbonate as well as the Fe(II) and Fe(III) concentrations are known to determine transformation reactions and the final mineralogy (Larese-Casanova et al., 2010; Banfield et al., 2000; Benner et al., 2002; Behrends & Van Cappellen 2007). Incorporation of coprecipitated elements, forced by oscillating conditions, might

therefore significantly influence the secondary Fe(II/III) and Fe(III) mineralogy in Van Phuc. Especially silica, phosphate and natural organic matter effect transformation reactions and the properties of secondary Fe(III) minerals. Incorporation of silica, phosphate and natural organic matter is known the hinder crystal growth in both biotic and abiotic mineral formation processes (Jones et al., 2009; Rosso et al., 2010; Chan et al., 2011; Ahmad et al., 2019). From investigation of biogenic mineral formation processes it is known that Fe-binding organics and incorporation of foreign elements during precipitation retard mineral growth (Chan et al., 2011) and decrease the crystallinity (Ahmad et al., 2019). Also for freshly precipitated natural poorly to mc crystalline oxyhydroxides it is documented that further crystallization is greatly retarded by organic and inorganic compounds such as silica, phosphate and OM (Schwertmann & Fischer 1973). Especially Si and natural organic matter are well known to retard Fe mineral crystallization (Francisco et al., 2016). Particularly in context of $Fe(II)_{aq}$-induced transformation reactions this effect is relevant and likely to occur. Jones et al. (2009) showed that the Fe(II)-catalysed transformation of synthetic schwertmannite, ferrihydrite, jarosite and lepidocrocite to more stable, crystalline Fe(III) oxyhydroxides is prevented by high concentrations of Si and natural organic matter. By inhibiting crystal growth, adsorbed Si and OM could explain the mc nature of Fe oxyhydroxides and it could promote aggregation between microcrystals which otherwise might have similar charge and so repel each other. This process was initially described by Fordham et al. (1984) for soil environments and could resemble to the situation at the field site of Van Phuc. Subsequent decomposition of the associated organic compounds would allow the formation of more crystalline Fe phases (Schwertmann & Fischer 1973) but constant supply from oscillating GW would prevent this process at least along the precipitate surfaces. Coprecipitated P, Ca, Si and Al and OM help to explain the mc character of the precipitates as they inhibit mineralization of poorly crystalline Fe oxyhydroxides (Zachara et al., 2002; Carlson & Schwertmann 1981; Fox 1989; Fortin et al., 1993; Perret et al., 2000). The strong effect of OM on Fe crystallization processes are confirmed by findings related to the formation of Fe-OM co-precipitates in soils. Fritzsche et al. (2015) describe Fe-OM co-precipitates composed of very low-crystalline Fh, with a considerable fraction exhibited even lower crystallinity than characteristic of Fh as initial Fe-bearing phase after Fe(II)-oxidation in soil-derived solutions. Since the Fe oxyhydroxide precipitates examined here presumably also contain at least partially high levels of OM, similar mechanisms are also conceivable in Van Phuc and suitable to explain the low crystallinity of the precipitates. The mc character of the Fe(III) precipitates may in part be also related to the high As GW content. High As concentrations are known to supress crystallisation processes and promote the formation of poorly crystalline precipitates. Waychunas et al. (1996) showed that secondary Fe products in the absence of As are well-crystallized, whereas poorly crystalline Fe products are formed in the presence of As. Most likely As adsorbs on the particles during their nucleation/growth and passivates their surfaces (Ona-Nguema et al., 2009; Waychunas et al., 1996). Younger studies confirmed that As suppresses the Fe(II) sorption on Gt and Hem through competitive adsorption processes (Catalano et al., 2011). Therefore, it seems likely that the high As GW content supports the formation of mc Fe phases. Oscillating conditions across the RTZ would enforce strong redox and hydrochemical gradients which may also explain the variable As species ratio across the precipitates The As speciation ratio measured across the Fe oxyhydroxide precipitates show significant variations if central and edge areas are compared. While the As(III) content is significantly higher in the external coatings and averages 71 % the of As(III):As(V) ratio is almost equal in the central part of the cementations. On the one hand, the ratios can represent different GW conditions during the precipitate formation. This would be an indication that the presumably younger coatings were formed under increasingly reduced conditions with higher proportions of As(III). On the other hand, the different As(III):As(V) ratios can be linked to secondary processes that changed the relationship between the two species like aging and recrystallization processes. The presumably older cementations had more time to interact with the GW. Therefore, the more mobile As(III) can be

exchanged preferentially leading to a more balanced species ratio. It is also conceivable that the cementations expressed and lost As(III) in the course of maturation and recrystallization processes. Finally, it is conceivable that the As(III) in the cementations were oxidized to As(V). This can take place abiotic through Fe(III) phases or through biotic processes. Redox transformation of As(III) by electron transfer among Fe(III) is well documented. During these electron transfer, As(III) can be oxidized to As(V) in reducing environment (Oscarson et al., 1980; Oscarson et al., 1981a; Oscarson et al., 1981b; Huang 1982). This process can happen abiotic through Fe(III) oxidation or biotic through microbial processes. These observations agree with changing conditions over time. The presumably older cementations had more time to interact with the GW and the more mobile As(III) can be preferentially exchanged leading to a more balanced As species ratio. Although Ying et al. (2012) showed in a recent study that As(III) oxidation is mostly caused by Mn minerals. That oscillating GW conditions would enforce strong redox and hydrochemical gradients is in line with the local GW data from Stopelli et al. (2020) which show a strong decrease of GW Fe, As, DOC, NH_4^+, S, PO_4^{3-}, Si concentrations. If however the oscillating redox and hydrochemical conditions are linked to oscillating GW is discussed in chapter 10.1.4. However, variable ion and cation GW concentrations due fluctuating GW conditions may explain the variable Gt and Hem concentrations within the Fe oxyhydroxide precipitates. For example Francisco et al. (2016) documented during the crystallization from Fh the proportion of Gt decreases relative to Hem with increasing Si. With regard to the strongly contrasting aquifer bodies up and down-stream the redox interface fluctuating GW would offer a reasonable explanation with regard to the Fe(III) dominated precipitates.

The mc character of the secondary Fe oxyhydroxide phases and the complex texture and mineralogical composition are a clear indication for a dynamic natural environment. Coupled biogenic-abiogenic formation pathways in a complex oscillating hydrochemical environment are capable to explain the complex phase mixtures of variable crystallinity, the broad range in particle size and complex mineralogical and geochemical composition observed. Interplays of microbially mediated and abiotic reactions in the biogeochemical Fe cycle are common to near-surface environments (Melton et al., 2014) and complex mineralization pathways by competing or interactive biotic-abiotic reactions are well documented in literature (Hansel et al., 2003). The mc phase mixtures of Fe(II/III) and Fe(III) phases and PS as well as the high proportion of admixtures of Al, Si, P and presumably organic matter represent most likely the result of an active biologically mediated solid-liquid phase exchange process in a dynamic hydrogeochemical environment. For the Fe(III) dominated mc precipitates it can be assumed that the small mc Gt, Hem and Mt phases show high specific surface areas and strong affinities for surface binding of oxyanions such as As, phosphate or sulphate at the mineral surface (Fendorf et al., 1997; Villalobos & Leckie 2001; Antelo et al., 2005; Granados-Correa et al., 2011; Perelomov et al., 2011; Villacís-García et al., 2015). In particular the small particle size of the mc phases contributes to the high reactivity as the surface area is increased disproportionately (Schwertmann 1991). The large surface areas of the precipitate structures and their location along strong hydrogeochemical and redox gradients offer the perfect conditions for intense GW interaction. Although the reactivity of the mc Gt particles might be decreased through the presence of carbonates and other GW compounds which are known to decrease sorption sites due to changes in the charge and aggregation (Chen et al., 2020) the reactivity of the precipitate structures has to be assessed as high with regard to crystallinity, crystal size and surface area (Roden & Zachara 1996). The **stability of the mc precipitate structures** however has to be assessed as low. Mc Fe phases with small particle size and large surface area are susceptible against variations in GW hydrochemistry and the high amount of coprecipitated and substituted elements is known to destabilize the crystal order. Especially the substitution of Al is known to increase dissolution rates of Gt phases (Schwertmann 1991). For **Al** it is also reported that its association with SRO minerals like Fh during mineral formation may have a considerable effect on the composition, structure, and surface properties of Fh nanoparticles, and thus

impact its reactivity and interaction with pollutant species, bioavailability and as well as sorption reactions (Cismasu et al., 2012). Therefore, the small Gt and Fh particles are usually characterized by high solubility (Bonneville et al., 2004) and low stability (Schwertmann 1991). However, Voegelin et al. (2019) showed that "variations in the structure and composition of amorphous to poorly-crystalline Fe(III) precipitates can lead to substantial variations in their reactivity" and (reductive) dissolution kinetics. In context of the complex mineral composition of the precipitates of several Fe oxyhydroxides in variable amounts significant variations can to be expected. Unfortunately, due to a lack of studies, many question regarding formation and properties of the phase mixtures remain unanswered. Zachara et al. (2002) showed that "a complex combination of thermodynamic and kinetic factors control whether a single, thermodynamically stable solid or a non-equilibrium phase mixture is the final product. Under certain conditions (high or low availability of electron donors) the biomineralization products are predictable and conform to the most thermodynamically stable solid. In other cases, phase mixtures result from the microenvironment or reaction path effects, or poorly resolved competitive kinetic pathways". Zachara et al. (2002) concludes that "current knowledge is generally insufficient to predict which phase or assemblage will result under special chemical conditions or ratios of electron donor to acceptor". With regard to the results of this study the complex mc phase mixtures refer to a highly dynamic hydrogeochemical environment and highlight the role of microenvironments and biomineralization reactions.

Oxidation

A potential trigger for the precipitation of the dissolved Fe(II) phases are **anaerobic oxidation reactions** which are usually coupled to O_2, NO_3^-, NO_2^-, MnO_2, $Fe(OH)_3$ or SO_4^{2-} reduction in natural near surface environments (He et al., 2018). Especially metal-dependent anaerobic oxidation is common and the oxidative behavior of **residual Fe(III) phases** is known to form secondary Fe oxyhydroxides in contact with reducing Fe(II)-rich GW (Larese-Casanova et al., 2012; Bryce et al., 2018). Residual Fe(III) phases were detected in both cores and could have promoted the initial precipitation as well as the precipitate growth. Also the oxidative behaviour **of residual Mn(IV) phases** can trigger to the formation of secondary Fe oxyhydroxides (Lovley 1991; Lovley et al., 2004). Both Fe(III) and Mn(IV) promoted precipitation processes are known to form amorphous to short-range ordered nanoscale Fe(III) precipitates (Voegelin et al., 2010 & 2013; Voegelin et al., 2019; Schaefer et al., 2017; Senn et al., 2018) which can serve as starting point for the formation of the extensive precipitate structures. Larese-Casanova et al. (2012) showed that Fe(III) products formed during heterogeneous Fe(II) oxidation appear to be governed mainly by the identity of the underlying sorbent and partly by the amount of available surface sites. Further Larese-Casanova et al. (2012) observed Lep to form on Mt sorbents due oxidative behaviour of the mineral surfaces. With regard to texture as well as mineral composition of secondary phases the study offers a reasonable pathway to explain the results of this thesis. With regard to the potential influence of Mn(IV) several Mn-rich layers in both sediment cores (Fig. 29 & 30) point to an active inclusion of Mn in the recent redox dynamics. These layers indicate a relocation of Mn in the context of the current redox processes and could represent a redox zonation as the position of the Mn-rich layers, slightly offset the Fe-rich transition layers, suggest that these layers may have formed as a consequence of recent redox mechanisms. However, only residual Fe(III) phases could be detected during this study. Mn(IV) could not be documented although the Mn K edge µ-XANES measurements searched for Mn(IV) phases with a MnO_2 (pyrolusite) reference sample. The precipitates contain significant amounts of Mn(III) (Table 10), which theoretically can have arisen from the reduction of Mn(IV) phases. However, Mn(II) oxidation on mineral surfaces, commonly found in natural environments at neutral pH (Lan et al., 2017) more likely explains the Mn(II)/Mn(III) composition of the precipitates. Therefore, anaerobic oxidation reactions due to the oxidative behaviour of residual Fe(III) or Mn(IV) phases might contribute fundamentally to the formation of the secondary precipitates but Mn(IV) phases could not be documented. However, Fe(III) and Mn(IV)

minerals, especially within fine-grained layers, could represent an important oxidation reservoir along the interface. Due to the lower permeability the intercalated layers could retain oxic phases such as Fe(III) and Mn(IV) and oxidize reduced GW compounds such as Fe(II) and As(III). The local GW data (Stopelli et al., 2020) shows almost no oxygen or other potential oxidants in significant quantity. The aquifer O_2 concentration increases near the coring position vertically from 0.019 mg/L O_2 in 28 m depth (PC43) to 0.474 mg/L O_2 in 38 m depth (PC44). This GW O_2 content is not sufficient to initiate the abiotic precipitation of Fe(II) at the redox interface in the observed scale. Although available O_2 would provide a perfect explanation for the precipitate formation as it could re-oxidise GW Fe(II) in-situ to form a variety of poorly crystalline mineral phases (Heyden & Roychoudhury 2015) abiotic precipitate formation through available O_2 can be excluded based on GW data. However, the **local entry of an oxidant near the coring site** could promote oxidation processes. In order not to contradict the GW data from Stopelli et al. (2020), the access would have to be from above or below the sand aquifer near the coring site. Possible scenarios are the input through upwelling GW from the gravel aquifer from depths greater than 46m bgs or entry through the top aquitard. But there are hardly any hints for this process. The appearance of the bottom silt layer distinguishes the location of the redox interface from all other studies in Van Phuc before and is likely to change local GW hydrology. But it is unlikely that this could introduce the local upwelling of an oxidant containing GW without effect in the surrounding GW wells. The entry of an oxidant from the top aquitard into the sand aquifer seems to be more realistic as there is evidence for a top aquitard – aquifer connection (Stopelli et al., 2020). The lithological analysis revealed rather randomly distributed find sand layers across the top aquitard. If this layers are hydrologically connected migration of surface water towards the redox front could be possible. The inflow of surface water rich in oxygen or another oxidants could be promoted by the local pond and numerous wells. Especially the ubiquitous **agricultural irrigation wells** could introduce atmospheric oxygen directly in the sandy aquifer. During the field work, it was observed that the wells pervade the agricultural fields frequently in a distance of roughly 20 meters and were often not covered if they were not in use. This could introduce a local "ventilation" of the underground. However, the depth distribution of these irrigation wells is unknown but since their minimum depth to the aquifer is around 20 m, it is unlikely that continuous O_2 supply through the wells is possible. However, the potential local entry of an oxidant is a scenario that might explain the formation of the Fe precipitates along the redox boarder.

Another reasonable formation process is the **precipitation from saturated to supersaturated fluids**. Abiotic Fe precipitation reactions resulting from the over and under saturation of GW could likely trigger the precipitate formation along preferential flow paths, hydrological barriers and microenvironments where the hydrogeochemical gradients are maxed out and biological activity is high. The multi-layered cementation structures show the typical morphologies related to intense precipitation and crystallization processes in context of saturated to supersaturated solutions (Sultan & Abdel-Rhaman 2013). Further the alternating cementation layers refer to strongly variable Fe in GW contents. Supersaturated microenvironments in context of oscillating hydrochemical conditions would offer a reasonable framework to promote this circumstances. Especially in separated microenvironments like the observed preferential flow paths precipitation from supersaturated fluids could likely contribute to the extensive precipitate structures. This option is further discussed in chapter 10.1.4. In view of the large quantity of precipitates, the microbial community analyses suggest that the precipitates were not exclusively formed biogenically and that abiotic precipitation mechanisms also contribute to their genesis. Beside coupled biogenic Fe(II) oxidizing reactions and abiogenic reactions related to interaction with $Fe(II)_{aq}$ supplemented by anaerobic oxidation reactions and precipitation from saturated to supersaturated fluids coupled to biotic and abiotic Fe(III) reduction reactions related to oscillating hydrochemical environment create a complex formation pathway.

However, with regard to the reconstruction of the local Fe dynamic it has also to be mentioned the **methodological limitations** set boundaries that are hard to overcome. The different mineralogical analyses sometimes revealed inconsistent results for the same depth levels and different analyses sometimes result in a different composition and indicate the presence of additional Fe phases such as Lep and Fh. There are several explanations for the partly different results. Low quantity and high diversity of Fe minerals push the methods to the limit of detection and make fittings very difficult. Further the methodical sensivity varies for different analyses across the different Fe phases. The magnetic measurements are size dependent and the results can vary depending on crystal size. Heterogeneity of sediments with variations on the mm scale make uniform sampling almost impossible and can lead to different results. The reason that µXANES measurements reveal no Fh or Lep although both Fe phases have been confirmed by bulk EXAFS Mossbauer and kt measurements in the same depth levels can be explained in several ways. One possible cause is the very heterogeneous sediment, even on a small scale. Although the immediately adjacent areas were sampled, there is basically the possibility that the areas have a different mineralogy and Fh and Lep drop below the detection limit. Further there is a possibility that the samples were changed by the measurement itself. The high-energy synchrotron radiation can oxidize metastable Fe phases such as Fh to stable Fe phases during the measurement. Finally, the fact that Fh can be detected in bulk EXAFS analyses, but not in the spatially resolved µ-XANES thin section measurements, could be attributed to the fact that it is not possible to completely protect the samples from oxygen and heat during preparation process. However, the fact that the filigree filaments were preserved is a clear indication that the sample preservation was very good. Finally the selection of available standards for the measurements was limited for all analyses. In view of the complex phase mixtures and transitional forms, however, an evaluation is fundamentally very difficult

10.1.1.2 Fe-phyllosilicates

Microscopy, synchrotron based measurements, Mossbauer and EMPA analyses revealed that large amounts of Fe is bound in in Fe(II)- and Fe(III)-bearing PS highlighting the importance of PS for the total sedimentary Fe budget. However, quantification with regard to the total sedimentary Fe budget is hard to assess but especially in the transition sediments Fe-bearing PS may account for up to one-fourth of the total Fe concentration depending depth level of the core. This is proven by bulk EXAFS data and microscopic analyses, although it must be noted here that the differentiation to the Fe oxyhydroxide minerals, especially in the extensive precipitate structures, is difficult. The same accounts for the Fe-PS complexes and the PS in the alteration rims of primary and secondary Fe minerals (Fig. 46 & 47). Nevertheless, the optical investigations in particular confirm the importance of the Fe-bearing PS for the local redox induced Fe-cycle and underline the importance of Fe-rich PS for the Fe dynamic. The close association of Fe-rich PS and Fe minerals in the extensive precipitate structures, Fe-PS complexes and in the alteration rims of primary and secondary Fe minerals clearly shows how closely related the mineral cycles are in both Fe mobilization and retention processes. There are clear indications that primary and secondary PS phases influence the Fe-cycle and affect the secondary Fe mineral formation along the redox boarder. PS are known to affect the Fe cycle during diagenesis and redox processes in near-surface environments (Stucki & Schwertmann 2012; Stucki 2011; Neumann et al., 2011; Ilgen et al., 2019) and therefore the observations are in accordance with the expectation. However, the study shows the importance of PS may be underestimated in the complex hydrobiogeochemical setups along natural redox boundaries. Based on the results of this study Fe-bearing PS act as **relevant Fe source as well as Fe sink** across the RTZ and may be involved in both abiotic and biotic processes. The high abundance and variety of Fe-rich PS (Table 20) of different Fe valance state involving chamosite, chlorite, illite, clinochlor, glauconite, greenalite and phengite as well as presumably smectite and nontronite not only highlight the importance of PS with regard to the sedimentary Fe-cycle but imply intense dissolution and(trans-) transformation processes (Stucki & Schwertmann 2012) at the field site

of van Phuc in recent time. The presence of embedded weathering PS like chamosite in the precipitates, coatings and Fe-PS complexes prove recent (bio)geochemical processes include PS. Due to methodological limitations and the huge variety of PS in different states of disintegration and formation, often sub-µm particle size frequently in close association with other mineral phases the composition of the Fe-bearing PS is hard to quantify but the PS Fe pool is most likely dominated by mixed valance PS. This estimation is in best agreement with the methodological results as well as literature. Pure Fe(III) PS are usually quite rare in natural environments as Fe^{3+} ions tend to associate with OH rather than silicate ligands (Schwertmann & Fitzpatrick 1992) but most PS formed during weathering incorporate at least some Fe(III) into their structure (Stucki et al., 1996).

Due to relatively high solubility of the Fe(II) containing PS minerals compared to sedimentary Fe(III) phases such as Fe oxyhydroxides (Schwertmann & Fitzpatrick 1992) especially mixed valance PS represent and early and easy accessible Fe pool to form secondary mineral phases or drive biological activity. With regard to Van Phuc it is therefore reasonable to assume that **disintegrating primary PS** are directly involved in the formation of the observed secondary Fe minerals at the redox interface. Disintegration of weathering primary PS all across the profiles clearly demonstrates that alteration of primary PS releases Fe and contributes to secondary Fe mineral formation. Dissolution of Fe-bearing PS coupled to redox oscillations is well-documented and was first proposed by Brinkman (1970) as soil-forming process called Ferrolysis. Brinkman showed that cyclic redox changes promote the destruction of the Fe-rich PS leading to mobilization of Fe. Substitution of exchangeable cations within the PS with Fe(II) and subsequent oxidation of substituted Fe(II) promotes formation of ferric oxyhydroxides and attacks structures of the PS minerals. This is in line with the microscopic observations showing close spatial association of disintegrating PS and formation of coatings, cementations and Fe-PS complexes. The close spatial association of secondary Fe oxyhydroxides and embedded PS clearly demonstrate that the sheet silicate bound Fe fraction contributes to Fe-cycle. Elongated sub-µm structures and ubiquitous Al_2O_3 concentrations in the Fe oxyhydroxide precipitates refer to embedded sub-µm PS minerals. Especially the precipitate surfaces show increased Al, Si, K, Mg and Na and Ca concentrations and characteristic textures which can best be explained by the presence of submicron PS minerals and underline the importance of PS for Fe(III) precipitate growth. The sub-µm PS minerals within the precipitate surface may further serve as nucleus for subsequent precipitation processes and at the same time, the biotic and abiotic reduction of primary PS improves the reaction environment. Cyclic redox changes causing decomposition of PS minerals and release of lattice cations (e.g. Fe, Al, Mg) seems to be a major biogeochemical driver and Fe source at the field site. Especially reactive Fe(II) species originating from the reduction of structural Fe(III) in PS may contribute significantly to the biogeochemical cycling of electrons and therefore trigger subsequent mineral transformation reactions (Hofstetter et al., 2003). Both microbial and abiotic reduction of Fe bearing PS is a common process in sediments and goes along with Fe-liberation, changes in local water chemistry and elemental cycles (Dong et al., 2003; Koo et al., 2014 & 2016). The sorption of Fe(II) to PS is a ubiquitous reaction expected to occur in natural environments (Van Groeningen et al., 2020) and is known to trigger a wide range of secondary reactions including the **precipitation of secondary (Fe) minerals** (Van Groeningen et al., 2020). A significant impact on the complex Fe mineralogy at the redox interface is therefore likely to assume. Especially with regard to the Fe oxyhydroxide precipitate formation a close coupling of the cycles can hardly be denied. The formation of Fe-bearing solid precipitates composed of Fe(III)-bearing PS minerals, Fh, and Lep was documented during redox cycles in periodically anoxic environments as a result of sorption of Fe(II) onto a synthetic montmorillonite recently by Van Groeningen et al. (2020). This process can be easily transferred to Van Phuc in a slightly modified version and suggests that Fe(II) sorption onto PS minerals contribute to the formation of the Fe-rich phase mixtures. This would not only explain the co-occurrence of the mineral phases but would also explain why the presence of the Fe oxyhydroxide precipitates is limited to the surrounding of fine-

grained layers. This finding therefore underlines the importance of mineral-bound Fe(II) and Fe(III) species from fine-crystalline PS phases for mineral dynamic and clarifies the great the influence of the local sedimentology on the Fe mineral dynamic. Also with regard to **oxidation process** necessary to form the extensive Fe(III) dominated precipitate structures PS could play a vital role. Ilgen et al. (2019) showed that "iron that resides in the structures of nano- to micron-scale PS mineral particles was shown to undergo cycling between Fe(II) and Fe(III)". This Fe comprises a **large redox-active pool for transformation reactions** (Hofstetter et al., 2003; Ilgen et al., 2019) and is likely a key player for precipitate formation. Although structural Fe in PS represents only a fraction of the total Fe pool in the aquifers, reactive Fe(II) species originating from the reduction of structural Fe(III) in PS may contribute significantly to the biogeochemical cycling of electrons since it is not subject to depletion by reductive dissolution (Hofstetter et al., 2003). Therefore, it is likely to assume that residual Fe from PS may drive formation of the Fe oxyhydroxide precipitate structures substantially and the PS are involvement in local biogeochemical cycles comprehensively. Also the Mossbauer analysis indicate the importance of PS for the Fe-precipitate formation. The summarized Fe(II) content determined by Mossbauer evolves from 4 % at 19.7 to 16.3 % at 21.3 to 27 % at 30 and back to 17.3 at 36.6m. The high amount between 21,3 and 36.6 m could be related to PS in close association with the precipitates and therefore indicate a close coupling.

Furthermore, the investigations show the strong influence of the local sedimentology on the Fe cycle. Formation of Fe-PS phases mixtures at all redox/grain size interfaces where increased weathering PS are observed show the influence clearly. In addition Fe impregnated clay coatings on primary silicates form at these layers/grain size boundaries. The coatings consist of Fe-PS (Cha) and Fe enriched clay minerals (kaolinite) intergrowths/adhesions with Gt and Hem (eventually traces of P-bearing mineral) and amorphous Fe-phases. These Fe-PS complexes/intergrowths go along with shift of dominant grain size from sand to silt/clay layers and could act as Fe trap and nucleus for Fe mineral precipitation. The complexes could also act as breeding ground for microorganism as the clay-rich layers also go along with increased C & S content. The massive Fe enrichment due cementations, coatings and Fe- PS complexes could also indicate the presence of Fe-rich fluids in recent times.

The presence of disintegrating primary PS only extends the group of potential Fe but also **As sources** in the study site. One the one hand As might be directly released by dissolution of primary PS on the other hand redox induced transformation reactions are known to influence the PS inventory and PS properties and therefore As storage capacity. Recent studies (Szymański et al., 2017) confirm that redox processes influence the qualitative and quantitative PS compositions in near surface environments substantially and especially the transformation of 2:1 clay minerals due to the cyclic reduction and oxidation reactions it is widely accepted to decrease cation exchange capacity, mineral solubility and swelling ability due to the formation of the interlayer space (Rich 1968; Brinkman 1970; Nakao et al., 2009; Szymański et al., 2014). Based on investigations on smectite Stucki et al. (2011) found redox reactions of Fe in clay minerals affect many of the chemical and physical properties. This involves layer charge, cation exchange capacity, cation fixation capacity, specific surface area, hydration energy, reactivity with organic species, and crystal structure. The study showed that redox reactions directly affect the in-situ transformation of PS in natural near surface environments. As the documented PS represent a typical selection for early diagenetic processes and redox induced transformation reactions (Stucki et al., 2012) it can be expected that the As-hosting capacity is significantly reduced.

10.1.2 Fe(II)-phases

The study revealed Fe(II) phases in close spatial association to the Fe(III)-dominated Fe precipitates and Fe-PS complexes. Separated through the sharp redox interface Fe(II) carbonates and Fe(II) sulphides occur along the redox interface and contribute to Fe-inventory. The occurrence of both

Fe(II)-phases seems to be nutrient controlled as both phases are located in the immediate vicinity of sulphur- and carbon-rich fine-grained sediments. The punctual occurrence of the Fe(II) phases indicates a formation due to local particularities such as microenvironments. Both ferrous-bearing solids are typical secondary minerals in sedimentary near-surface systems (Benner et al., 2002; Cornell & Schwertmann 2003) and commonly precipitate after (bio) reduction of Fe oxyhydroxides (Wang et al., 2014). Either Fe(II) phases cover a wide range of textures and involve freshly formed as well as heavily altered phases on small spatial scales which clearly shows that the Fe phases are not stable and are subjected to changing or oscillating conditions. This observation points to a dynamic hydrogeochemical environment and highlights the importance of heterogenic microenvironments for the Fe-cycle.

10.1.2.1 Fe(II)-Sulphides

Pyrites were documented at the top (22 m) and bottom (30 m) redox transition zone of core RD42 and are limited to the direct surrounding (a few centimetres) of the redox and grainsize interface and occur exclusively in framboidal texture. The **formation mechanism** for Py framboids has long been debated and can be clearly linked to biotic processes (Sawlowicz 1993; Ohfuji et al., 2005; Rickard et al., 2019; Rickard 2019¸ Johnson et al., 2015; Sweeney & Kaplan 1973; Graham & Ohmoto 1994; Berner 1970 & 1984; Sawlowicz 1993 & 2000; Cavalazzi et al., 2012; Wei et al., 2012; Weisener & Weber 2010; Large et al., 1999; Wilkin & Barnes 1997; Wilkin et al., 1996; Roberts 1982; Alpers et al., 2002). The observed framboidal shape (Fig. 55) is typical for biogenic Py formation coupled to sulphate reduction and can clearly be attributed to sulphate reducing bacteria. As typical formation products in low-temperature sedimentary environments under reducing conditions secondary framboidal Py are common in alluvial aquifers of SSEA (Smedley & Kinniburgh 2002; Saunders et al., 2008) and to be expected at the field site. The low abundance of Fe(II) sulphides compared to Fe(III) oxyhydroxides is typical for delta aquifer sediments (Bostick et al., 2004; Bostick & Fendorf 2003; Lowers et al., 2007) and the observed framboid size is in typical range for sedimentary Py (Rickard et al., 2019). As a typical accompaniment of anoxic OM decomposition Py commonly form in zones of intense reduction such as around buried and decomposing organic matter or in microenvironments where the sulphate-reducing bacteria generate appreciable amounts of sulphide (Berner 1970 & 1984; Sawlowicz 1993; Wilkin et al., 1996; Roberts 1982; Alpers et al., 2002; Wilkin & Barnes 1997). Therefore, it seems likely that along microenvironments microbially released H_2S reacts with dissolved Fe(II) and precipitates Py (Kirk et al., 2010). The high **importance of separated microenvironments** for Py formation is reflected in the isolated occurrence of the Py and offers an explanation for the strongly variable As concentrations across the different framboids. Further microenvironments are able to create supersaturated conditions where rapid nucleation is able to form the characteristic framboidal texture (Fig. 55) (Butler & Rickard 2000). Chains of Py framboids were observed in pore spaces which seem to be preferential flow paths suggesting Py formation is coupled to local GW flow induced gradients and Fe-rich fluids. The single microcrystal (Fig. 56), which has only been documented once, on the other hand, indicates a significant lower saturation. Separated microenvironments offer a reasonable explanation to explain the large geochemical gradients on small spatial scales necessary to form the observed textures. The single microcrystal may have also be formed on the edge of one of these microenvironments where Py supersaturation is low and rapid Py nucleation is inhibited (Butler & Rickard 2000). In addition to the characteristic framboid texture **microbially mediated sulfate reduction** has been suggested in the Van Phuc transect by a microbial community analysis and hydrogeochemical study of Glodowska et al. (2020). Furthermore, sulfate reduction coupled to Fe sulphide mineral precipitation was reported to occur at the riverbank and in the reduced sands upstream the study site (Wallis et al., 2020). Since the local GW contains practically no SO_4^{2-} (Stopelli et al., 2020) and the occurrence of Fe(II) sulphides is limited to the immediate environment of TS-rich fine-grained layers with high sulphur solid phase concentrations the Py formation is most likely linked to the availability of sulphate in the solid phase.

Both transition zones in 22 and 30 m bgs are characterized by increased amounts of fine sediments and the by far highest aquifer TS concentrations in the solid phase (Fig. 29 & 30). On the other hand traces of dissolved sulfate have been analyzed by Stopelli et al. (2020) in the corresponding depths. Therefore, sulphate entry through oscillating GW could be considered as additional sulphate source. However, a significant increase in GW S concertation is documented by Stopelli et al. (2020) not before 200m horizontal distance away. The distance makes a GW entry of S unlikely even in oscillating conditions and the trace sulphate concentrations documented in GW are more likely related to sulphate-rich microenvironments coupled to sedimentology and microbial activity. However, the distances between the wells are large and the S concentrations in the immediate vicinity of the RTZ are unknown. If the increased S GW concentrations reach close to the RTZ, an entry about oscillating GW is definitely possible. However, S-rich microenvironments along preferential flow paths can also be linked to mobilization from solid phase which would also explain the traces of sulfate documented in GW. Discussing the formation process it must also be noted that in the spatially resolved measurements at core RD42 neither mackinawite nor greigite could be detected, which are assumed to be precursor phases of Py (Wilkin et al., 1996; Hunger & Benning 2007; Rickard & Luther 2007), what indicates matured phases and no recent Fe(II)-sulphide mineral formation. On the other hand some framboids show no signs of alteration and seem to have recently formed or are still growing. Further the bulk EXAFS analysis reveals traces (average 0.07 %, n=6 samples) of mackinawite at the redox boarders in RD54. The presence of mackinawite and detectable but rather low concentration of SO_4^{2-} in GW as well as the presence of microorganisms known to be involved in sulphate reduction and sulphur oxidation (Glodowska et al., 2020), suggest an active S-cycling and recent Py formation and recent dissolution and transformation reactions. The textural and geochemical analysis of the Py framboids in the support this assumption. Altered edges, lobed surfaces and cracks indicate dissolution of the Fe(II)-phase while elemental ratios and small sub-µm structures in the rims suggest recrystallization from exterior and formation of Fe oxyhydroxides or Fe-rich PS minerals in the altered areas. The geochemical mapping support this observation as altered rims generally show increased Fe, O, Al and Si values. Recrystallization processes from the exterior rim are a typical result of framboidal Py alteration during diagenesis and redox reactions. The coarse Py grains in the outer rims and the welding and merging microcrystals are typical morphological characteristics of intermediate dissolution stages (Sawlowicz 2000; Wignall & Newton 1998; Bond & Wignall 2010; Tian et al., 2014 & 2020; Ye et al., 2017). Hence no irregular Py was formed and the complete loss of framboidal texture could not be documented the dissolution process is still at a beginning to intermediate phase. Especially the so called „sunflower" rims (Fig. 55 g, h, i) are typical characteristics of an intermediate stage (Merinero et al., 2008 & 2009 & 2017) and suggest that the dissolution process has just begun. That some framboids don't show these characteristics and appear to have been newly formed or are still growing (Fig. 55 b & c) confirms again the small-scale heterogeneity and the importance of microenvironments supporting previous observations of variable hydrochemical conditions along the redox interface on small spatial scales. The high spatial variability is also confirmed by the differences between the two cores. The documented Py textures and absence of precursor minerals point to a process where along the redox front of RD42, the Py formation has largely ended and the dissolution process has started. In contrast, the process seems to be in full swing at the less reduced edge areas of RD54 where the precursor mackinawite outweighs the Py content. The differences between the two neighbouring cores make clear that the conditions vary significantly within meters.

The coexistence of intact and altered phases and different sized and shaped Py as well as the co-presence of large framboids, euhedral microcrystals and single crystals indicate that the small-scale geochemical environment varies greatly (Blood & Lash 2015). The textural differences of the framboids and microcrystals on small spatial scales and the coexistence of young and altered framboids are a clear indicator of variable GW parameters such as Eh and Fe(II) and SO_4^{2-} concentrations. Random

distribution and high heterogeneity in size and shape of microcrystals and framboids confirm fluctuating or even contrasting hydrochemical conditions. Especially with regard to the Fe_{aq} concentrations considerable variations have to be expected to explain the broad range of textures observed. The large framboid microcrystals (Fig. 55 a, c, j) usually formed by a high rate of growth and a low nucleation rate (Ye et al., 2017) suggest to the temporary occurrence of **Fe-rich fluids**. This assumption is confirmed by the high mean diameter of the Py framboids, which are exclusively over 10 µm (Ding et al., 2014; Blood & Lash 2015). Separated microenvironments along preferential flow paths or biotic hotspots offer a reasonable approach to explain this observations. On the other hand, the uniform shaped and sized microcrystals and the perfectly round framboids (Fig. 55 b & e) distanced only a few mm away indicate conditions with constant Fe and hydrogen sulphide supply in low concentrations (Ding et al., 2014; Blood & Lash 2015). Separated microenvironments could explain the spatial proximity as well as the diverse textures. Another way to explain the contrasting observations are oscillating GW conditions. Even small oscillations could force the formation of strong hydrochemical gradients and therefore explain the multiple textures. Fresh spherical framboids and aged Py with clearly discernible dissolution features occur next to each other and the formation of Fe(III) oxyhydroxides and Fe-rich PS in the alteration rims can both be explained by redox oscillations. GW oscillations are particularly conceivable with regard to the close spatial association of fresh and highly altered phases. Both decoupled microenvironments as well as GW oscillations are capable to cause the temporary occurrence of Fe-rich fluids and with regard to the high importance of supersaturated microenvironments for framboid formation it seems likely that variations in hydrochemistry also trigger the dissolution of framboids by introducing undersaturated GW forcing abiotic dissolution. Since in particular the availability of dissolved reactive iron and hydrogen sulphide are the main factors controlling the framboid formation (Sweeney & Kaplan 1973) changing or fluctuating hydrochemistry is likely to be an important factor for dissolution, too. Undersaturation of sulphide phases in the GW causing dissolution could explain the altered edges, lobed surfaces and cracks. Pulses of undersaturated GW that penetrates into microenvironments along preferential flow paths is a mechanism that could explain the large textural heterogeneity on small spatial scales. S.I. calculations with PHREEQC showed the reduced sediments before the RTZ are SO_4^{2-} oversaturated while the sediments after the RTZ are SO_4^{2-} under saturated. (Stopelli et al., 2020). Therefore, dissolution related to GW saturation seems to be an obvious process for some framboids. However, the process is not able to explain the oxidation reactions related to the transformation reactions in the framboid rims. On the other hand **anaerobic oxidation** process could likely explain the findings. With regard to the high GW Fe and As concentrations and the variable hydrochemistry with oscillating redox conditions oxidation reactions with Fe(III) or As(V) are obvious options. Suib et al. (2017) showed that aqueous As(V) and Fe(III) is able to oxidise As-containing Py in near neutral pH ranges. The work showed that arsenate can act as a major oxidant and form Gt as the main secondary product. Oscillating GW conditions would be able to generate comparable conditions in Van Phuc. Further the study documented (re-)adsorption of As(III) and As(V) on the freshly formed Fe oxyhydroxide phases immediately after release due to the collapse of the crystal Py structure. This would explain why altered Py show high As contents and dissolution of Py is not accompanied by high As and Fe GW concentrations. Also aqueous Fe^{3+} is known as effective oxidant of Py. That Fe^{3+} can act as direct oxidant was already showed Moses et al. (1987) more than 30 years ago and Murphy & Strongin (2009) summarized in a recent review article potential mechanisms in aqueous environments. The close spatial association of various Fe(II), Fe(II/III) and Fe(III) phases along the narrow and distinct redox interface would also allow tiny oscillations to cause intense (trans-)formation processes. It is also known that the sensitivity of Py to oxidation processes can be favored by other factors. For example, high bicarbonate/carbonate ions increase Py oxidation rates in pH ranges from 6 and up (Caldeira et al., 2010). Therefore, oxidation processes are likely supported by local oscillating hydrochemistry. GW

oscillations also offer an possible explanation for available oxygen beside mineral transformation processes. The availability of small amounts of oxygen is reflected in the framboid size. Framboids in the documented dimensions are usually related to oxic and dysoxic environments as strongly anoxic to euxinic conditions are reflected in the greater abundance of small diameter framboids (< 5 µm) (Ding et al., 2014; Blood & Lash 2015). In addition biotic processes such as **S-oxidizing microorganisms** offer an obvious additional biotic pathway for Py dissolution as show by Glodowska et al. (2020). S-oxidizing microbes are present and offer a reasonable process to explain the lobated grain boundaries of aged Py (Fig. 55c). The parallel occurrence of fresh and aged Py framboids with clearly discernable dissolution features indicate successive steps of microbial sulfate and Fe reduction and S oxidation what is best explained by oscillating GW conditions in separated environments. Whatever mechanisms are involved in the complex biotic-abiotic setup the observation confirms an active S cycle and suggest oscillating conditions in a complex sedimentological and hydrological setup with separated microenvironments and complex microbiology. With regard to the Fe- and the As cycle the secondary Fe-sulphides represent the initial Fe and As sink at the reduced site of the redox interface. However, coupled biotic and abiotic dissolution and transformation pathways at least partially convert the Fe sulphides to Fe oxyhydroxides and Fe-rich PS minerals while others will presumably be completely dissolved. Therefore, it can be assumed that the Fe(II)-sulphides are not stable and the formation represent an important intermediate step for the Fe and As at the hydrogeochemical interface.

10.1.2.2 Fe(II)-Carbonates

Most of the findings related to the Fe(II) sulphide phases can be transferred directly to the Fe(II) carbonates. The formation of secondary (Fe) carbonate minerals is common in near-surface GW aquifers across SSEA. Especially along natural redox gradients with strong decrease of dissolved Fe GW concentrations the precipitation of Fe carbonate minerals such as $FeCO_3$ is commonly observed (Guo et al., 200t; Jönsson & Sherman 2008). Fe-carbonates formation in modern sedimentary aquifers can be related to both biotic and/or abiotic processes and is a typical consequence of early diagenesis (Rodrigues et al., 2015). Especially bio-degradation of sedimentary organic carbon through (anaerobic) oxidation coupled to reduction of Fe, Mn, nitrate and sulphate as well as methanogenic fermentation and subsequent accumulation of dissolved inorganic carbon in pore waters commonly results in Fe-carbonate formation in suboxic to anoxic sedimentary environments (Froelich et al., 1979; Lein et al., 2002; Rodrigues et al., 2015; Vuillemin et al., 2019). In particular during microbial reduction of Fe(III)-containing minerals Fe-carbonates are generally known to form, when GW (bi)carbonate concentrations are sufficiently high (Roh et al., 2003; Zavarzina et al., 2004). This process is documented for various Fe(III) and Fe(II/III) phases including Gt, Fh (Johnson et al., 2005), Mt (Kim et al., 2011) as well as various Fe-rich PS minerals (Kim et al., 2004; Koo et al., 2014 & 2016). The results of this study largely coincide with these descriptions although the variety of textural and geochemical characteristics of the documented Fe (dominated) carbonate minerals suggest multiple formation and transformation processes. The Fe(III)-reducing microorganisms documented at the field site in high quantity (Glodowska et al., 2020) are known to use organic carbon as an electron donor for their metabolic processes and produce (bi)carbonate and/or carbon dioxide. In combination with high Fe(II) concentrations in supernatant or pore water the formation of secondary Fe(II) minerals can be promoted (Dong et al., 2003; Koo & Kim 2020). The presence of high bicarbonate concentrations in the aqueous phase and a large CO_2 reservoir to maintain aqueous bicarbonate concentration are essential to enable Fe-carbonate formation in subsurface environments (Lee et al., 2003). At the field site bicarbonate likely originates from sedimentological C degradation via fermentation or/and anaerobic CH_4 oxidation (Reeburgh, 2007; Zhu & Dittrich 2016). The sedimentological C reservoir can easily sustain a continuous C supply and therefore enable high bicarbonate concentrations constantly. The increased presence of Fe(II) carbonates around (organic) carbon-rich layers supports this explanation and suggests that the carbonate formation in the study site is closely related to organic matter

degradation and highlights the importance of local sedimentology for the Fe mineral dynamic. Alternatively bicarbonate can also come from dissolution of carbonates already present in the sediments what can likely be expected at oscillating conditions. Either way, HCO_3^- is the most relevant ion in the GW and based on saturation index calculations, the high alkalinity together with relatively high GW Fe and Ca concentrations (Stopelli et al., 2020) the precipitation of Fe carbonate minerals such as Si according to $Me^{2+} + HCO_3^- \rightarrow MeCO_3 + H^+$, (Me = Ca^{2+}, Fe^{2+} or Mn^{2+}) is reasonable. With regard to the highly reducing and Fe(II) and CH_4-rich GW entering the RTZ related to organic matter degradation by fermentation up-stream the study site (Stopelli et al., 2020; Glodowska et al., 2021) and the high abundance of CH_4 metabolising microbes (Glodowska et al., 2021) it seems likely that the abundant occurrence of Fe- and Mn-bearing carbonates at the redox interface is a direct consequence of the strong microbiological activity. Anaerobic CH_4 oxidation (Beal et al., 2009; Aromokeye et al., 2020) and oxidation of dissolved and sedimentary organic matter (Zhu & Dittrich 2016) coupled to Fe(III) and Mn(IV) reduction (Stopelli et al., 2020; Glodowska et al., 2021) offers a reasonable pathway to explain the presence of Fe carbonates at the field site. With regard to the high abundance of CH_4 metabolising microbes (Glodowska et al., 2021) CH_4 oxidation likely represents a key process in Van Phuc. The anaerobic oxidation of CH_4 coupled to Mn(IV) and Fe(III) reduction is described globally as an important CH_4 sink (Beal et al., 2009) and CH_4 derived carbonates have been documented for a long time (Hein & Koski 1987). Further it was shown that anaerobic microbial oxidation of CH_4 is able to promote local supersaturation with respect to carbonate minerals (Aloisi et al., 2002; Reitner et al., 2005). This would likely explain the heterogenic pattern of the observed Fe carbonates and is particular suitable to explain the various Fe(II) textures. Therefore, **Fe-carbonate formation coupled to CH_4 oxidation** most likely represents a dominant Fe-carbonate formation mechanism in Van Phuc.

Especially for the prevalent **skeletal Fe-carbonates** the inflow of Fe(II)- and HCO_3^--rich GW offers a reasonable formation pathway to explain the position as well as texture and geochemistry of the Fe-carbonate minerals. The skeletal Fe carbonate phases appear in greatest distance from the redox interface and seem to be the first Fe-phases to be formed after reduced GW enters the RTZ. Further they show no textural or geochemical indications of alteration or dissolution along the mineral rims. In contrast the branching texture suggest active mineralization and growth. Therefore, it can be assumed that the skeletal Fe-carbonates were recently formed and are probably still growing. A formation by continuously in-flowing GW offers a coherent explanation for this observations. Although the dense cores could point towards a hydrogeochemical environment with higher Fe(II) concentrations in the past a continuous growth can nevertheless be assumed. Therefore, it seems possible that the skeletal Fe-carbonates result directly from the inflow of Fe-rich GW to the redox transition zone and are completely unrelated to GW oscillations. In context of a fluctuating system it might also be possible that skeletal Fe-carbonates just frame the oscillation window. While the mixed Fe-Mn carbonates are formed in the Mn window in the immediate vicinity of the sharp redox interface the Mn-free skeletal Fe carbonates are formed further away from the redox interface were oscillating GW still contains Fe but Mn already precipitated. This scenario could explain the dense mineral cores and would also explain why the skeletal Fe carbonates show no Fe-Mn zonation. However, it seems more likely that the absence of the distinct geochemical zonation in combination with and the different texture is an indication that these phases were formed in a different temporal or spatial context than the mixed Fe-Mn carbonates and the Fe-Mn carbonate precipitates. Both scenarios could explain why the skeletal Fe carbonate phases were consequently formed as compositionally homogeneous Fe carbonates. The relatively low As content of the skeletal Fe-carbonates is surprising in context of high As GW concentrations but can be explained by increased crystallinity of the skeletal Fe-carbonates compared to the other Fe-carbonate phases and the general high variability of As in the secondary solid phase. Also the Fe sulphides and oxyhydroxides which are clearly related to recent processes show great fluctuations in the As concentration. The most obvious explanation is the heterogeneous

structure of the sediments and the complex hydrology and biological activity. However, the low As content and well crystallinity compared to the other Fe-carbonate types could also point towards primary Fe carbonate phases that were not affected by recent processes. In order to finally clarify this question, further sediment samples outside the RTZ are necessary, which undoubtedly represent the original conditions. Therefore, the formation process of the skeletal Fe-carbonates cannot be conclusively clarified and the skeletal carbonates could also represent the detrital mineral inventory. This would be in assumption with the position of the phases away from the direct vicinity of the redox interface. On the other hand it is unlikely to assume that primary Fe-phases have survived the redox transformation unaltered up to this point in view of the extensive redox-controlled reorganization of the Fe mineral stock along the entire aquifer profile. Therefore, at least for the skeletal Fe-carbonates a formation related to recent GW inflow offers the most conclusive explanation.

However, with regard to the diverse texture and geochemistry of the variable Fe-carbonate phases it seems likely that further processes are involved and it seems likely dissolution and (trans-)formation of Fe-carbonates related to cycling hydrochemical changes adds to Fe carbonate diversity at the field site. With regard to oscillating GW conditions especially the formation of the documented Fe-Mn carbonate precipitates could likely be linked to entry of Fe- and Ca-rich moderately reduced GW into the reduced environment causing rapid and vast precipitation events. Oscillating GW conditions offer a possible pathway to explain this process. Also with regard to the geochemical findings a dynamic GW system offers a coherent picture. The most prominent feature of the **mixed Fe-Mn carbonates and the Fe-Mn carbonate precipitates** is the **distinct Mn-Fe zonation** with a Mn-rich core and a Fe-rich outer areas. The zonation most likely represents a redox sequence and implies Mn(IV)-reducing conditions similar to the uncontaminated Pleistocene aquifer down-stream (Eiche et al., 2008) were prevalent and relocated Mn. Afterwards Fe(III)-reducing conditions relocated Fe and precipitated around the Mn carbonates after reaching the redox boarder. Consequently the Mn carbonates are enclosed by Fe carbonates and form the observed Fe dominated carbonate phases. This sequence represents the redox gradient towards the redox interface and can be related to both constant flow and oscillating conditions. Alternatively, both the zoning of the mixed Fe-Mn carbonates and the Fe-Mn carbonate precipitates and the sequence of the Fe(II) and Fe(III) precipitates could be explained by a successively migrating redox front. However, as the mixed Fe-Mn carbonates and the Fe-Mn carbonate precipitates are characterized by distinctly pronounced alteration areas in a random pattern and a successively migrating redox front should create a continuous alteration sequence oscillating conditions offer the best explanation. Further the alteration of the Fe-Mn phases is shown as a thin hem that encompasses the entire mineral grain or precipitate Although the alteration areas are usually pronounced one hemisphere the altered zones can be found all-around of the minerals (Fig. 52). Oscillating GW conditions and complex flow regime offer the best explanation for this finding. Further this finding underlines the importance of complex small-scale GW regimes on mineral transformation. As the orientations thin sections were preserved relative to each other Fig. 52 demonstrates that the small-scale flow conditions vary significantly on small-scales. The elemental composition and textures in the alteration areas suggest PS and Fe oxyhydroxides (Fh, Gt, Mt) formation on the carbonate surface. Sub-µm mineral structures visible as bright white spots all across the alteration areas (Fig. 52 & 53) demonstrate the secondary formation of Fe(III) phases related to transformation and dissolution of the carbonates. Coupled dissolution-precipitation at mineral-water interface on carbonates are a well-documented feature (Renard et al., 2019) and biogenic oxidation processes are particularly suitable to explain the transformation processes along the rims of the mixed Fe-Mn carbonates and the Fe-Mn carbonate precipitates. Biological Si oxidation by Fe(II)-oxidizing microorganisms coupled to Fe(III) oxyhydroxide formation is known to form Gt, Lep, and Fh and amorphous-looking Fe oxyhydroxide precipitates (Zhang et al., 2009) what could likely contribute to the observed Fe(III) precipitates. Biotic oxidation of Fe(II) carbonates may therefore explain the observed features very well although it is

unclear which oxidant drives the reactions. Biological oxidation would also explain the GW data from Stopelli et al. (2020) showing an increase of Mn and Ca+ and suggest the dissolution of Mn (Fe) carbonates although no Fe crosses the RTZ. Also noticeable in this context is the close association of Fe(II) carbonates and Fe(II) sulphides along the transition zones in 22 and 30 m bgs. The early diagenetic co-authigenesis of Si and Py related bio-degradation of sedimentary organic carbon highlights the importance of organic-rich intercalated fine-grained layers and the complex sub-surface build for the Fe mineral dynamic (Rodrigues et al., 2015) and offers an approach to explain the formation of the different Fe carbonate types. Additional transformation processes related to changes in GW hydrochemistry and biological activity might be involved. For instance in a recent study Bobo et al. (2020) showed that changes in the pH – CO_2 system related to organic matter decay can promote the transformation from Si to Gt. Also changes in GW proton and bicarbonate concentrations related to microbial metabolic reactions can were shown to trigger Fe carbonate dissolution and transformation (Borch et al., 2010; Chapelle 2000; Mc Mahon & Chapelle 2008). In a complex natural setup a large number of processes that also interact with each other must be expected. Therefore, multiple pathways are possible. However, the recurrently changing GW conditions would create a dynamic system that can comprehensively explain the large variety of Fe carbonates characteristics.

In context of oscillating conditions it seems further possible that the **Fe(II) and Fe(III) precipitates could be directly coupled by cyclic GW movement** across the redox interface. The extensive Fe(II) and Fe(III) precipitates on both sides of the redox interface suggest fast and massive precipitations events and precipitation in contrasting supersaturated environments in immediate vicinity. GW oscillations across the redox interface offers a reasonable mechanism to explain the strong hydrochemical gradients and link the multiple findings. In fact, the mutual influence of the Fe(II) and Fe(III) precipitates offers an approach to explain the formation of both Fe precipitate structures in the depth levels were the Fe-carbonates are present. Recurring changes in redox conditions and hydrogeochemistry can explain the texture, size and the close spatial association of the various Fe(II) and Fe(III) precipitates. Furthermore, the interaction might also help to explain the formation of the extensive size of the Fe(III) (oxyhydr)oxides. After change in GW flow direction reduced Fe(II)-rich GW may cause secondary **siderite to coat the surface of highly reactive Fe(III) (oxyhydr)oxides precipitates** at the redox interface limiting the reductive dissolution sensitivity and protect the Fe(III)-precipitates. This mechanism was described by Zhu & Dittrich (2016) and might explain how the extensive Fe(III) cementations reach their size and why no Fe(II) leaves the redox interface despite recurring redox changes. Microcosm batch experiments using in-situ organic matter and sandy sediments from 30 m depth of the RD42 core showed that Fe(III) reduction took place, but only a small amount of the Fe(II) was actually released to solution while the majority of Fe(II) remained in the solid phase (Glodowska et al., 2020). These results fit very well to the observation of an in-situ (re-)formation of Fe (and Mn) carbonates within the redox transition zone and explain why mobilized Fe(II) is caught at the latest along the Fe(III) precipitates. Due to the sharp redox interface that only extends over a few centimeters, only small distances are required after the Fe (re-)mobilization to trigger (re-)precipitation. This also explains why the GW data do not show the oscillations. The high spatial and temporal resolution necessary to record these processes and cannot be captured in GW well sampling. The process is capable to explain the presence of large Fe-Mn carbonate precipitates and mc oxyhydroxide precipitates next to each other separated only by a sharp redox gradient. However, it is difficult to differentiate between biotic and abiotic dissolution and precipitation processes in the complex natural setup. Further it must be noted that no Fe(II) mineral coating could be detected at the Fe(III) dominated precipitates. Nevertheless, the process is possible with regard to the methodological limitations. Immediate transformation to Fe(III) phases may further prevent the detection. Especially when their occurrence in limited to a small temporal window related to an oscillating thrust. The similar texture of the Fe(II) and Fe(III) precipitates could be another indication for ongoing oscillations

and suggests that the carbonate precipitates share the mc character of the Fe(III) precipitates. This finding is typical for rapid precipitation during microbial reduction reactions (Dong et al., 2000; Fredrickson et al., 1998; Zachara et al., 2002; Islam et al., 2005; Handley et al., 2013) but can also be linked to oscillating GW conditions at the field site. Despite strongly variable hydrogeochemical conditions and highly heterogenic sedimentology and microbial activity, the high As GW concentration may promote the presence of mc Fe(II) carbonate precipitates. As with oxyhydroxide precipitates, high GW As concentrations are known to promote the formation of poorly crystalline carbonate precipitates. Most likely As adsorbs on the particles during their nucleation/growth and passivates their surfaces (Ona-Nguema et al., 2009). This agrees with the geochemical results and also indicates mc phases.

A **combined formation scenario** with inflowing GW and recuring oscillations across the interface closely resemble the microscopic results which show that the pure Fe carbonates and Fe-Mn carbonates are spatially ordered and form a sequence with mixed Fe-Mn carbonates near the actual redox interface while the pure skeletal Fe carbonates also appear in greater distance to the interface. The textural and geochemical characterises highlight the recent character of the carbonates and confirm dynamic conditions. While the mixed Fe-Mn carbonates and the Fe-Mn carbonate precipitates are clearly exposed to recent dissolution and transformation processes the pure skeletal Fe-carbonates seem to be still growing. The complex GW flow conditions and the sedimentological heterogeneity was shown to create highly variable conditions on small spatial scales. Therefore, the contrasting observations across a few centimetres can be explained by the complex hydrobiogeochemical setting of the overserved sediments. The fact that unaltered presumably freshly formed Fe carbonates and dissolving/transforming Fe carbonates occur next to each other shows the variability of the hydrogeochemical setting and suggest that GW redox oscillations further add to different GW flow regimes on microenvironments. Complex hydrogeochemical setups were shown to promote the formation of comparable Fe-carbonate textures in siliciclastic sediments. Rodrigues et al. (2015) showed that the occurrence of microcrystalline and macrocrystalline Fe-carbonates with variable texture and geochemical composition with regard to Ca and Mg is strongly related to local redox state and Fe(II) availability. The studies illustrates that the Fe-carbonate mineralogy implies a field side characterized by highly variable to contrasting hydrogeochemical conditions on small spatial scales. Therefore, the carbonates confirm previous observations related to the Fe-sulphides and Fe oxyhydroxides. The study provides insight into the highly dynamic Fe-cycling in redox interfaces where secondary Fe minerals like Py and Fe-bearing carbonates can be formed and dissolved again, or transformed into Fe oxyhydroxides by coupled biogeochemical redox processes. The (trans)formation reactions related to the Fe(II) carbonates require strong hydrogeochemical gradients and imply separated microenvironments governed by biological, sedimentological and hydrological framework and therefore confirm and complement the findings gained analyzing the Fe(III) and Py phases. However, in an oscillating environment the Fe carbonates cannot be defined as stable and therefore match the Fe(II) sulphides.

10.1.3 In-situ transformation processes

With regard to mineral evolution of As-hosting Fe minerals until now the majority of studies focused on experiments in controlled and simplified lab environments and most of studies used abiogenic synthetic minerals (Dixit & Hering 2003; Farquhar et al., 2002; Gimenez et al., 2007; Manning et al., 1998). Very little work has been done using biogenic Fe(III) minerals formed as external or internal precipitates (Ferris 2005; Fortin & Langley 2005; Kleinert et al., 2011; Muehe et al., 2016). Already in Glodowska et al. (2021b) we mentioned that this is surprising as microbially driven processes are an integral part of Fe cycling in natural environments. Fe(III) reduction and Fe(II) oxidation as well as subsequent Fe mineral (trans-)formation or dissolution are known to be strongly influenced by

microbial activity (Posth et al., 2014; Kappler et al., 2021). Further it is known that biotic phases have different characteristics compared to synthetic minerals and behave differently with regard to both biotic and abiotic processes. Especially in complex natural environments significant differences with regard to mineral properties and evolution have to be expected that have not been targeted by previous studies. Therefore, it is still difficult to correctly address their impact on As dynamic in natural setups. A few previous studies have investigated the role of biogenic Fe(III) minerals in the context of As sorption in the laboratory (Hohmann et al., 2010; Kleinert et al., 2011; Muehe et al., 2016) but in general, the number of studies is limited. The small number of studies used biogenic Fe minerals is likely related to the difficulty to synthesize biogenic minerals in sufficient quantity (see Glodowska et al. (2021b)). The hurdles for meaningful experiments in natural (GW) environments are also high. In addition to the complex test setup and the great effort that has to be made to set up an experiment in the natural GW environment it is almost impossible the record the hydrogeochemical and biotic framework conditions in dynamic natural systems in an adequate temporal and spatial resolution. As biotic and abiotic variations can hardly be traced, evaluation is in general difficult. Therefore, there is still a lack of knowledge when it comes to transferring results from lab experiments to aquifer systems and understanding of process dynamics under natural conditions. In order to address these knowledge gaps, the in-situ incubation experiment was developed.

In Glodowska et al. (2021b) we described that higher numbers of **bacteria and archaea** were associated with the minerals incubated in the As-contaminated aquifer in Van Phuc compared to the non-contaminated aquifer and all Fe(III) minerals were mainly colonized by Fe(III)-reducing bacteria, with Geobacter being the most abundant taxon. Additionally, fermenting microorganisms were abundant on minerals incubated in the As-contaminated reducing aquifer, while methanotrophs were found on the minerals incubated in the As-free aquifer, implying involvement of these microorganisms in Fe(III) reduction. However, Geobacter and Holophagaceae taxa seem to be the key players in Fe(III) reduction in both hydrochemical environments. Nevertheless, the large number of Fe-metabolizing microorganisms documented in Glodowska et al. (2020b) clearly demonstrates that biogenic processes have a major influence on the Fe dynamic in Van Phuc.

With regard to the **Fe mineral dynamics** it was shown that most of abiogenic and biogenic Fe(III) minerals are transformed in-situ into Mt, at least to some extent (Glodowska et al., 2021b). However, **biogenic Fe(III) minerals** generally tend to become more reduced and when incubated in the As-contaminated aquifer. At the end of incubation biogenic Fe(III) minerals sorbed slightly more As than the abiogenic ones (with the exception of abiogenic Fh). Overall the biogenic minerals are more prone to be colonized by (Fe(III)-reducing) microorganisms and host a higher relative abundance of Fe(III) reducers. Further biogenic minerals (except for Fh) are more prone to transformation and reductive dissolution, although similar secondary minerals are formed during Fe(III) reduction (Glodowska et al., 2021b). However, the biogenic mixed phases of Lep/Gt and Lep/Mt are not subjected to visible transformation. Also the **abiogenic Fe(III) minerals** show a heterogenic response to the field site conditions. While Fh will more likely get reduced Gt, Hem and Mt behave differently. Based on solid phase Fe and colour changes the crystalline abiotic Gt, Mt and Hem samples are more resistant to the in-situ hydrogeochemical conditions and showed a rather stable Fe_2O_3 content. The Fe_2O_3 concentrations before and after the experiment of the less crystalline phases (Fh_{abio} and the biotic phases) show a clear decrease indicating intense dissolution within the short time frame of the experiment (Glodowska et al., 2021b). Fading colours and decreasing Fe_2O_3 content clearly show that some mineral coatings were transformed, dissolved or washed away during the incubation experiment. To which extent this loss is related to abiotic dissolution or biotic activity or if the artificial coatings were simply washed out by the GW flow cannot be determined but based on combined geochemical and mineralogical results most of the Fe(III) minerals exposed to moderately and strongly

reducing GW were subjected to dissolution and transformation processes. Intensive dissolution of Fe(III) minerals was further confirmed by SEM which revealed that Fe(III) mineral coatings remained mainly in the protected areas such as cracks, crevasse, cavities and between closely spaced sand grains. The coatings are criss-crossed by numerous cracks and especially the edge areas showed strong signs of alteration. This applies to all samples in both depth levels although in the uncontaminated aquifer the conditions were less reducing and shows clearly the intense dissolution and transformation reactions affecting the minerals. This is further confirmed by formation of sub-µm scaled secondary minerals which were detected in all samples. It is surprising that all remaining minerals are greatly reduced at both depths during the incubation experiment. While this is obvious for the strongly reduced environment, Fe(III) phases should be partly resistant in the moderately reduced environment. This observations reinforces the impression that that the stability range of secondary Fe(III) minerals is limited to a narrow band along the redox interface with a sharp border where strong geochemical gradients separate the two hydrogeochemical units and where microbiology is highly active.

In summary it can be stated that all samples are characterized by dissolution and/or transformation processes und there are distinct differences in transformation of biogenic vs. abiogenic Fe(III) minerals under the environmental conditions examined during this field experiment (see Glodowska et al. (2021b)). The most interesting observation of the study is the in-situ secondary Mt formation within the short exposure time and that mixed biogenic Lep/Gt and Lep/Mt are less susceptible for Fe mineral transformations and dissolution in these environments. The experiment suggests that **Mt formation** in the natural environment of Van Phuc is most likely coupled to transformation of Fe(III) phases like Fh and Gt into secondary sub-µm Mt particles. This process is in line with the microbial community present and as it applies for most biogenic and abiogenic phases. This not only agrees with the drill core analyses, but confirms fine-grained Mt as the final phase of the transformation and dissolution and secondary biogenic formation of fine-grained Mt as prominent transformation process. Hem as further secondary transformation product could be documented for both Fh samples (biotic and abiotic) and biogenic Gt. This (trans)formation is also in agreement with previous results and is a typical transformation reaction for low crystalline minerals. That no secondary mineral formation could be documented at the coating-free reference sand samples reinforces the assumption that the formation of secondary phases is entirely related to transformation reactions.

With regard to the **Fe mineral dissolution** the outcome is not as clear. The fact that the abiotic Gt, Hem and Mt samples don't show a negative Fe balance is most likely explained by the crystallinity retarding the reductive dissolution within the time frame of the experiment. In contrast the intense dissolution of biotic and abiotic Fh is most likely linked to its low crystallinity and good availability to microorganisms. However, with regard to the biogenic Lep/Gt and Lep/Mt the results clearly demonstrate that biosynthesized phase mixtures can show substantial variations with regard to their stability and bioavailability. The experiment suggests that biosynthesized minerals such as biogenic Lep/Gt produced by native microbial communities may have a comparable dissolution kinetic as the abiotic Gt, Hem and Mt samples under natural conditions. Whether this characteristic is related to a high crystallinity or other factors could not be determined due to low sample quantity and methodological limitations. Therefore, the assumption cannot be proved and it remains unclear which properties or surface reactions keep the minerals stable. However, as biogenic phases usually are more prone to dissolution these phases were expected to be dissolved and transformed quickly. The fact that phases that are not dissolved or get transformed towards more redox stable secondary phases is an unexpected outcome. The behaviour of the biogenic Lep/Gt and Lep/Mt phases resembles the results of the core analysis in many aspects. Since the biotic minerals of the incubation experiment were generated with the local microorganisms that are also present in the sediment it is likely that the

biosynthesized phase mixtures do closely correspond to the complex Fe(III) precipitate mixtures from the core analysis. Especially the surface processes along the extensive Fe(III) precipitates could likely resemble the processes documented in the incubation experiment. With regard to the Fe mineral dynamics at the field site the results might help to explain the formation of the large Fe(III) precipitates documented in the sediment. The documentation of complex Fe(III) phase mixtures formed by intense microbiological activity being relatively stable in moderately and reduced environments might well explain the precipitate growth in context of oscillating redox conditions. If formed on the precipitate surface these biogenic phases might protect the extensive Fe(III) precipitate structures from dissolution. However, the mechanism retarding the dissolution of the biogenic Lep/Gt and Lep/Mt could not be identified during this experiment but both the Mt formation and the behaviour of the biogenic Lep/Gt phases demonstrate the great importance of biogenic processes in the study area. With regard to the Fe mineral evolution in natural aquifer systems it can clearly be stated that microbial activity is a key driver and biotic minerals may have deviating characterises with regard to redox stability or bioavailability. The experiment showed that biogenic and abiogenic minerals behave differently in the natural environment of Van Phuc. This outcome must be considered when evaluating Fe dynamic and the fate of As under reducing conditions in aquifers. It is a clear hint that properties derived from laboratory experiments with synthetic Fe phases may differ from biosynthesized minerals. As these circumstances are unconsidered in most modelling approaches further studies with biogenic minerals are necessary to expand the understanding of Fe dynamic in natural systems. With regard to the hydrogeochemical processes the results of the incubation experiment support the previous observations of an dynamic environment with intense dissolution and transformation reactions and confirms the sharp contours of the redox interface and the importance of microenvironments for Fe mineral formation. As the in-situ experiments show an intensive dissolution dynamic almost directly at the redox interface (~ 2m) stability of secondary Fe phases could be limited to a small window of constant transformation reactions along the interface where the interaction of biotic and abiotic surface processes cause a stabilization of the normally redox-sensitive phases. The formation of relatively redox stable and dissolution resistant biogenic surface minerals might an essential mechanism to form the extensive secondary Fe precipitates.

With regard to the **As dynamics** the incubation experiments reveal that the As retention occurs in phases that show a strong decrease in the Fe_2O_3 content. This indicates that secondary phases which have formed in the context of an active conversion dynamic are largely responsible for the As retention. The in-situ observations only show fine-grained Mt as a newly formed phase. However, this occurs in almost all samples and thus only partially provides an explanation for the significantly increased As retention in the two samples Fh_{abio} and Lep/Gt_{bio1}. Especially since there is no evidence that more secondary Mt is formed than in other samples. However, the biotic phases could tend to form more fine-grained secondary Mt. This would explain the increased As retention. Otherwise the incubation experiment also revealed secondary Fe-PS formation. As this finding is in accordance with the core analysis very fine Fe-rich PS might offer an additional approach to explain the As-retention at the field site. With regard to the result in the sediment drill core, organo-mineral structures would offer an additional explanation for the As fixation, although they could not be directly detected. However, the Fe(IIII) oxyhydroxide coatings offer the perfect conditions for their formation. The sediment drill core has shown that they occur frequently and have the potential to fix significant amounts of As and the weakly crystalline and biogenic phases in the natural environment of Van Phuc offer the perfect conditions for their formation.

10.1.4 Conceptual model on Fe mineral (trans-)formation

Diverse Fe mineralogy, complex sedimentology, variable hydrochemistry and diversified microbial communities in variable quantities suggest that a broad range of processes are involved in the Fe

mineral (trans-) formation processes at the macro and micro scale of the RTZ. The broad assortment of secondary Fe phases along the redox interface involving thermodynamically less-stable Fe phases such as Lep as well as more stable phases such as Gt, Hem and Mt and the characteristic surface morphologies of the precipitates highlight the **importance of an oscillating hydrogeochemical environment for the Fe dynamics.** A fluctuating hydrochemical setup is most favourable to support both biotic and abiotic mineral dissolution and (trans-) formation reactions and is presumably fundamental to explain the mc character of the phases. The presence of mc Fe precipitates composed of complex phase mixtures and altering surface structures clearly point towards a dynamic GW system and an oscillating hydrogeochemical setup offers a reasonable scenario to explain the observed composition, frequency, distribution of the Fe mineralogy and the various textural features that all point to a high redox dynamic. In fact, the stability of the interface minerals might be directly linked to the **continuous transformation reactions** coupled to biotic and abiotic processes in context of fluctuating conditions. If formed on the precipitate surface the biogenic phases documented in the in-situ experiment and the secondary Fe(II) carbonates potentially formed during oscillations on the precipitate surfaces might protect the extensive Fe(III) precipitate structures from (re)dissolution. Constant transformation and rearrangement of the surface phases might therefore be essential for the formation of the vast Fe precipitates and accumulation of secondary minerals along the interface.

One option to explain the oscillating conditions are recurring GW pulses with and against main GW flow direction. The contrasts between the two GW bodies up- and down-stream the redox interface are distinct with regard to redox conditions and hydrochemistry (Stopelli et al., 2020). As the Fe mineral stability is strongly dependent on the ambient redox properties of the surrounding sediment intense Fe mineral transformations can be expected along a fluctuating sub-oxic and anoxic interface. While the highly recued GW contains 13 mg Fe/L only trace amounts are present in the moderately reduced GW. The highly reducing GW has As up to 500 µg/L and CH_4 concentrations of approximately 51 mg/L while the moderately reduced GW contains As concentrations well below 10 µg/L and no detectable CH_4 (Glodowska et al., 2020; Stopelli et al., 2020). The same trend applies for most other aqueous elements relevant for biotic and abiotic processes including DOC, NH_4^+, S, PO_4^{3-} and Si. The strong redox and hydrochemical gradients during GW oscillations would offer favourable conditions for Fe mineral (trans-) formation through recurring redox changes. Contrasting GW conditions of the highly and moderately reduced GW introduced to the transition sediments during GW oscillations are likely to initiate the formation of a broad range of Fe-phases of variable crystallinity and have the potential to trigger a cascade of geochemical reactions to create of the observed series of secondary Fe-phases. Especially pulses of Fe(II)-rich GW after a period of consolidation would be able to trigger intense (trans) formation processes (Fendorf et al., 2010; Zachara et al., 2002; Hansel et al., 2003). Oscillating GW between the two adjacent aquifers that just passes the interface might also be in line with the strict extent of the RTZ. The transition sediments, framed by the secondary Fe(II) and F(III) minerals, would therefore represent the oscillating window. This assumption was already indicated during the discussion of the Fe(II) phases but there is no clear evidence, yet. However, GW oscillations in As contaminated aquifers related to monsoon (seasonal oscillations) and GW abstraction (short-term oscillations) from shallow GW resources are common all across SSEA (Chakraborty et al., 2015; Ni et al., 2017; Parsons et al., 2013). The Southeast Asian monsoon regime with wet and dry periods creates drastic water level changes in the Red River and accompanying aquifers. An influence on the local GW flow regimes of Van Phuc would be expectable. In addition anthropogenic influence on local GW flow due to GW abstraction in the village of Van Phuc and intense pumping below the city of Hanoi. Short term variations in local GW flow dynamic can further be expected related to agricultural irrigation during the dry season. Near surface GW abstraction across different depths on both sides of the transition zones has the potential to affect the local GW dynamic fundamentally in both directions. Constantly changing redox conditions and hydrochemistry should therefore be considered for both,

biotic and abiotic mineral reactions. Repeatedly exposure to contrasting hydrogeochemical environments would shape the transition sediments consistently as the oscillating GW conditions would introduce strong redox and hydrochemistry gradients to the interface sediments and promote biological activity and abiotic reactions. Coupled biotic and abiotic mineral (trans-)formation reactions would change in recurring order depending on prevailing conditions. Especially to describe the extensive Fe(II) and Fe(III) precipitate formation and the often mc characteristics fluctuating GW flow offers a reasonable approach. Cyclic intrusion of moderately and highly reduced GW with contrasting hydrochemical composition and different redox states are likely to stimulate a broad range of dissolution, transformation and (re-)precipitation events able to explain the complex mineral assemblage and offer a coherent explanation for the mc character of the extensive precipitates. However, the lack of GW data in high temporal and spatial resolution leaves open the question of possible small-scale oscillations.

Oscillating hydrochemical conditions may also be introduced to the redox interface without changes in GW flow. Especially at the micro scale, the broad range of mineralogical, chemical and biological reactions documented at the study area are capable to change the hydrochemical and redox environment locally without GW oscillations. That oscillating redox and hydrochemistry changes may be spatially confined and restricted to microenvironments and preferential flow paths explains the close spatial association of Fe(II), Fe(II/III) and Fe(III) minerals with variable crystallinity, contrasting redox attributes and mineral properties. Microscale fluctuations are further able to explain the presence of thermodynamically unstable phases along more mature Fe phases. The complex sedimentological sub surface structure is capable to provide sharply separated microenvironments with specific porewater composition and explain the variety of documented Fe-phases in close spatial association across the interface sediments. The fact that the phases continuously occur in different compositions reinforces the impression of dynamic processes in heterogeneous microenvironments. In context of separated microenvironments a continuous intrusion of reduced Fe(II)-rich GW during constant GW flow is capable to drive local transformation reactions independent of possible GW fluctuations. Moreover, a constant replenishment of Fe(II)-rich reduced GW together with nutrients mobilized from the solid phase up-stream offers favourable conditions for an active Fe cycling through Fe(II) oxidizing and Fe(III) reducing bacteria. The typically biogenic Py framboids (Fig. 55), the bacterial cells embedded in the secondary precipitates (Fig. 42f) and characteristic morphology of the filigree Fe oxyhydroxide fibres and gels (Fig. 44 & 45) documented in this thesis and described in Glodowska et al. (2020) & (2021) proof an active and diverse microbial community that has significant influence on the Fe-flux towards the redox interface. That sedimentary Fe cycling is often driven by microbial processes has been accepted since many years (Benner et al., 2002). Glodowska et al. (2020) documented a broad variety and quantity of Fe mediating microorganisms further highlighting the importance of biotic reactions. This biotic activity might be sufficient to introduce small-scale fluctuating hydrochemical an redox conditions independent from GW flow conditions. The various microorganisms provide numerous potential biochemical pathways for both oxidation and reduction reactions. The high diversity of microbial communities present in local GW and in sediments not only enable diverse processes but unexplored metabolic potential of unknown taxa may further provide yet undocumented pathways with regard to Fe(II) oxidation and Fe(III) reduction (Glodowska et al., 2020 & 2020b). As biogeochemical Fe cycles are known to spatially overlap and compete with each other biotic oxidation and reduction of Fe can occur cyclically or simultaneously (Kappler et al., 2021). Variable supply of possible electron donors or acceptors might further add to variable biotic activity. Spatial and temporal variations in microbial activity might therefore contribute significantly to an interface characterized by oscillating conditions. As poorly crystalline large surface area phases are thermodynamically more favourable for microorganism than crystalline phases (Weber et al., 2006) they are preferentially utilized by microorganisms for dissimilatory and fermentation-linked Fe

reduction (Munch & Ottow 1980 & 1983; Lovley & Phillips 1986 & 1987; Lovley 1991; Roden & Zachara 1996; Schwertmann & Taylor 2018). Especially the dominant mc precipitates should provide bio accessible phases that drive intense biological reactions. The accumulation of large Fe(II) and Fe(III) precipitates and line up of Py further showed that Fe-rich fluids move locally along preferential flow paths across the redox interface. Especially the formation of the filigree structures requires a constant supply of dissolved $Fe(II)_{aq}$ in moderate to high concentrations (Nakai & Yashinaga 1980). The locally and temporally restricted Fe-rich fluids may be coupled to microbial activity what explains why the formation of secondary Fe minerals is increased in the immediate vicinity of fine-grained TS- and TC-rich layers were intense microbiological activity might even cause supersaturation conditions. Highly enriched or even supersaturated porewater in separated microenvironments at the RTZ offers a prerequisite explanation for intense precipitations events in locally confined areas. The drastic variations in local Fe(II) concentrations also helps to explain the variety of observed Fe phases as aqueous Fe(II) concentrations are known to dictate the resulting mineral phase at a given pH and alkalinity (Benner et al., 2002). This suggests that Fe oxidation and reduction occur cyclically or simultaneously in separated microenvironments along the redox interface are widely governed by microbial activity. Recently Lightfoot et al. (2022) suggested for Van Phuc that gas phases related to the intense biotic activity within the aquifer form bubbles which cause local GW flow disruptions. Such hydrogeological obstacles would result in reduced and re-directed GW transport and could vastly increase GW residence time. The in-aquifer gas production linked to degassing of CH_4 as results of local oversaturation could likely contribute to the formation of hydrochemical microenvironments and explain the formation of Fe-rich fluids. Overall, these observations suggest a strong influence of microbiology on Fe dynamic at the field site.

In context of in the complex and dynamic environment of the redox interface the **combination of biotic and abiotic processes** has the potential to fundamentally change the local hydrogeochemical environment within short temporal scales. Although the process dynamics could not be deciphered, the field study offers an approach to explain the small-scale Fe dynamic through constant fluctuations in separated microenvironments. Through the interaction of mineralogical, chemical and biological reactions the hydrochemical and redox conditions can oscillate on a small scale. Conclusively this can explain the considerable small-scale diversity of the Fe(II) and Fe(III) mineralogy and often contrasting textural characteristics both, with or without oscillating GW. However, GW oscillation is possible as long as the fluctuations don't exceed a spatially confined window defined by the RTZ. If GW fluctuations occur and add to oscillating conditions they are limited to a restricted oscillating window defined by the sharply demarcated area of the secondary minerals. Otherwise the characteristic mineral order on the macro scale cannot be explained. Slight GW oscillations across the redox interface however are reasonable to assume and trigger mineral transformation reactions and add to the variety of secondary Fe phases and diverse morphology. The importance of isolated microenvironments was documented for all secondary minerals in the study and only small-scale variations in the sub-surface conditions offer a comprehensive explanation in order to explain the different hydrochemical and biological processes in view of the close spatial association of the phases. The fact that secondary Fe minerals form particularly along destined flow paths or other confined areas where biotic and abiotic reactions are promoted through the interaction with the solid phase reinforces the impression that local peculiarities determine the small-scale processes. Accumulation of Fe phases along preferential flow paths and hydraulic barriers suggests that mineral dissolution and re-precipitation are coupled to specific conditions of spatially confined areas. In summary, the study shows that the Fe mineral dynamic within the redox interface is most likely controlled by **repeated micro-scale dissolution-(re)precipitation and transformation reactions** related to strong redox and hydrochemistry gradients. Therefore, decoupled microenvironments are particularly important to explain the high small-scale variety of the secondary Fe phases revealed by the spatially resolved investigations. A highly complex

and heterogeneous sedimentology with variable depositional origin is essential to promote different hydrobiogeochemical microenvironments. The contrasting hydrochemical conditions with regard to As and Fe(II), dissolved TEA (NO_3^-, SO_4^{2-}), DOC and reactive metabolic products (H_2S, acetate) offer a huge reaction spectrum and hence, it is nearly impossible to strictly distinguish between abiotic and biotic processes that affect the Fe dynamic in the aquifer. As all processes and mechanisms are inseparably connected and feedback effects create a highly complex setup and especially in local microenvironments it is extremely difficult to identify and quantify the processes due to the large variety of potentially superimposing mechanisms. It can be stated that especially on the microscale the complex and heterogeneous sedimentology creates numerous hydrobiogeochemical microenvironments across the RTZ**.** Separated small-scale environments with strong redox and hydrochemical gradients and specific biotic and abiotic processes are likely to develop a heterogenic Fe mineralogy as observed. Due to the dynamic conditions the microenvironments may change and over overlap and therefore offer an explanation for the occurrence, distribution and variety of the secondary Fe minerals and offer a coherent approach to explain the multi generation Fe(III)precipitates observed in this study.

The conceptual model combines all before discussed influences on Fe mineralogy along the RTZ. As part of a dynamic system, the model has to include a larger part of the aquifer, especially up-stream the GW flow. Starting point is the **Fe mobilization** that takes place up-stream of the RTZ and is induced by the onset of reducing conditions due to microbiological activity. Reductive biogeochemical reactions, notably organic matter degradation, cause a rapid decrease in the redox potential and thereby affecting Fe mineral stability upstream the RTZ (Glodowska et al., 2020). Glodowska et al. (2020b) showed that especially microbialy produced CH_4 triggers Fe reduction and mobilization. Several other recent studies demonstrated that anaerobic CH_4-oxidizing archaea are able to use Fe(III) as electron acceptor (Aromokeye et al., 2020; Cai et al., 2018; Egger et al., 2015; Ettwig et al., 2016) support this assumption. Additional microorganisms such as Geobacter spp. (Islam et al., 2005), Shewanella spp. (Cummings et al., 1999) and Geothrix spp. (Islam et al., 2005) present at the study site (Glodowska et al., 2020) add to this process. Based on carbon isotope signatures ($\delta^{13}C$ - CH_4, $\delta^{13}C$ -DOC, $\delta^{13}C$ -DIC) Stopelli et al. (2021) provided further evidence that fermentation, methanogenesis and methanotrophy are actively contributing to the Fe dynamic at the study site and are largely responsible for the mobilisation and subsequent fate of Fe towards the redox interface. Considering many other microorganisms have been shown to be capable of dissimilatory Fe(III) reduction and most Fe(III)-reducing bacteria and archaea can use either organic C (e.g. short chain fatty acids, CH_4) or hydrogen (H) as electron donor (Esther et al., 2015) multiple additional biogeochemical pathways can be expected to be involved, that were not covered by microbial investigations at the field site. Especially fermenters are extremely versatile organisms that can use a wide range of different organic substrates but also various electron acceptors such as Fe(III), Mn(IV), NO_3^- and NO_2^- and many species have been recorded yet (Esther et al., 2015). Therefore, the microbial communities across redox transition zone might influence the Fe mobilization in additional unknown ways. However, reductive processes cause dissolution of primary Fe oxyhydroxide coatings (Fig. 60 1) and releases Fe(II) to the GW. Basic requirement for this process is the assumption that the now grey aquifer material was initially coated with Fe oxyhydroxide coatings as we observed it in the yellow-brown sediment (Kontny et al., 2021) and which was proven by previous studies in the field site (Eiche 2010; Berg et al., 2007).

Following reductive dissolution up-stream the RTZ, Fe(II) is released and migrates with GW flow towards the redox front. When the highly reduced Fe(II)-rich GW enters the RTZ, **precipitation of secondary Fe phases** is initiated due to drastic change in redox conditions. Dissolution, transformation and (re-) precipitation of Fe minerals across the redox gradient leads to a redistribution of Fe along the redox interface. In consequence the severely Fe enriched transition sediments are formed as distinct

retardation front. It is obvious that the strong decrease of GW Fe(II) concertation down-stream the RTZ (Stopelli et al., 2020) is mainly related to the precipitation process that form the secondary Fe minerals of the redox interface with the mc precipitates being quantitatively most important. The formation of the distinct retardation front is a direct consequence of the net Fe accumulation in the solid phase along the redox interface. The presumably microbial-driven formation of mc Fe precipitates leads to a considerable sequestration of Fe, As, Al, Si, S, C and P. Consequently, these precipitates characterize the redox interfaces as active hotspots and zones of enhanced immobilization. The development of **natural reactive Fe barriers** characterized by massive Fe-accumulation in form of Fe(III) dominated precipitates have been reported before in near surface sediments and soils along strong redox gradients (Johnston et al., 2010 & 2011). The secondary products at the interface of strongly (methanogenic-sulphate reducing conditions) and weakly (NO_3^- and Mn reducing) reduced GW bodies described by Johnston et al. (2010) & (2011) formed a "wall" of reactive Fe phases that share many features to the precipitations observed in this study. In general the Fe-precipitation of the reduced Fe(II) at redox boundaries is described as a typical process in these environments (Heyden & Roychoudhury 2015). However, the scale of the retardation front documented in this thesis is remarkable as the natural reactive-Fe barrier largely controls the local GW hydrochemistry across two contrasting aquifer bodies. As soon as the GW reaches the RTZ redox and hydrochemistry gradients gradients across the RTZ cause secondary Fe phases to precipitate in a specific order and form a **characteristic mineral pattern on the macro scale**. Before the GW actually reaches the redox interface Fe(II) phases form at the reduced side of the beginning RTZ. These are mainly Fe-Mn carbonates as pyrites are restricted to S-rich sediment layers. The fact that the Fe(II) phases form near the redox interface and not earlier can be attributed to kinetic and thermodynamic conditions that favour formation at geochemical transition zones (Schwertmann & Cornell 2000; Haese 2000). As soon as the GW crosses the redox interface the Fe(III) dominated microcrystalline precipitates form as counterpart to the Fe(II) phases on the moderately reduced side of the RTZ and form the specific mineral sequence overserved in the thin sections. The characteristic spatial order of the Fe(Mn)-carbonate, Fe-sulphide (Fig. 60 2) and the Fe oxyhydroxide formation (Fig. 60 3) on the macro scale is shown in Fig. 60. can therefore be seen as a direct consequence of the changing redox conditions under advective flow conditions. The macro scale assortment of the secondary phases clearly points to an advective flow controlled system and additional micro fluctuations with regard to microenvironments.

Based on a conceptual model integrating established mechanisms (Horneman et al., 2004; Lowers et al., 2007; van Geen et al., 2013) the Fe dynamic with regard to the **Fe(Mn)-carbonate and Fe-sulphide formation** (Fig. 60 2) can be described as follows. The frequent presence of Fe- and Mn-bearing carbonates at the redox interfaces is presumably related to various formation processes. However, anaerobic CH_4 oxidation (Beal et al., 2009; Zhu & Dittrich 2016; Aromokeye et al., 2020) and microorganism-mediated CH_4 oxidation of fermented organic matter coupled to Fe(III) and Mn(IV) reduction (Glodowska et al., 2021) are certainly important. The anaerobic oxidation of CH_4 coupled to Mn(IV) and Fe(III) reduction associated with formation of rhodocrosite ($MnCO_3$) has been described before (Hein & Koski 1987). The in-situ formation of Fe (and Mn) carbonates coupled to Fe(III) reduction was also indicated by the microcosm batch experiments from (Glodowska et al., 2020). In context of the inflowing Fe(II)-rich GW and the documented Mn oxides another reasonable process to consider is the oxidation of Fe(II) coupled with MnO_2 reduction (Kontny et al., 2021). Especially in context of the formation of the mixed Fe-Mn carbonates the process offers a reasonable pathway as the released Mn^{2+} can precipitate with remaining Fe^{2+} and Ca^{2+} to form the characteristic structures (chapter 9.4.3.2). Elevated concentration of dissolved Ca^{2+}, Mn^{2+} and Fe^{2+} are reported from an upstream well close to the redox transition zone (Stopelli et al., 2020) supporting the idea of multiple coupled redox and precipitation-dissolution processes. That the secondary Fe-bearing carbonates can be redissolved or transformed into Fe oxyhydroxides supports the idea of closely coupled redox

processes in a highly dynamic setting. Distinct changing redox conditions in the past are also suggested by the distinct Mn-Fe zonation of the Fe(II) carbonates. With regard to the Fe(II) sulphides microbially mediated sulfate reduction was suggested by microbial community analysis, the hydrogeochemical study of Glodowska et al. (2020b) and the characteristic framboid morphology. Biotic sulfate reduction coupled to Fe sulphide mineral precipitation is commonly accepted as formation mechanism and Glodowska et al. (2020b) has shown that sulfate-reducing are present. Beside, fermentation, methanogenesis and methanotrophy SO_4^{2-} reduction seems to be the most abundant metabolic pathway in sediments. The assembly of recent framboids and altered Py with clearly discernable dissolution features next to each other show the metastable character of the Fe(II) phases that could either point to fluctuating hydrochemical and redox conditions causing undersaturation and dissolution of Py or point to microbial S oxidation. S oxidizing microorganisms documented by Glodowska et al. (2020b) can also explain the lobate grain boundaries of the altered Py. The dominance of Fe(II) oxidizing bacteria in some parts of the local sediments (Glodowska et al., 2020) underline the importance of microbial Fe(II) oxidation for the study site. However, the observation suggest an active S cycle and confirm oscillation conditions on small spatial scales.

The **Fe oxyhydroxide formation** (Fig. 60 3) coupled to reduction of primary Fe(III) and Mn(IV) might be a coherent approach to explain initial or local Fe(II) oxidation reactions but it is still in question whether this mechanism is able to explain the extensive mc Fe oxyhydroxide precipitates. Although it is unquestionable that the oxidation of aqueous Fe(II) is able to form amorphous to short-range ordered nanoscale Fe(III)- precipitates composed of Gt, Hem and Mt in variable amounts (Voegelin et al., 2010 & 2013 & 2019; Schaefer et al., 2017; Senn et al., 2018) the study was not able to proof the presence of primary Fe(III) and Mn(IV) in sufficient quantity. Nevertheless, the Mn(IV) phases offer a realistic option to explain the oxidation reactions. There are both sedimentological and mineralogical indications of active Mn cycling coupled to hydrochemical and redox oscillations. The presence of Mn(IV) phases in sufficient quantity would be suitable to explain the observed structures. Also primary Fe(III)-rich PS offer a large oxidation potential and certainly contribute significantly to the processes. Whether the combined oxidation potential of the Fe(III), Mn(IV) and Fe(III)-containing PS is sufficient to form the Fe(III)-dominated precipitates would have to be investigated by a stoichiometric modelling. However, additional oxidants introduced by unknown pathways or unidentified microbiological reactions cannot be ruled out. In particular biotic processes offer a large undiscovered field of unknown oxidation and reduction reactions that might explain the extensive size of the secondary Fe(III) precipitates.

The study clearly showed that after the formation of the various Fe(III) phases a further reduction to **Mt** takes place. Especially microbially mediated reduction of ferric Fe as described by Benner et al. (2002) offers a reasonable explanation for Mt formation although both abiotic and biotic formation mechanisms are convincible and in fact and coupled processes are presumably most likely. Also studies like Li et al. (2011) showed that dissimilatory Fe(III)-reducing bacteria are particularly suitable to explain the nano/microcrystalline Mt formation as the biogenic Mt production is known to form small particle size in the sub-µm range (Roh et al., 2003; Behrends & Van Cappellen 2007; Vali et al., 2004; Hansel et al., 2003). Alternatively Mt can be formed in-situ abiotically for example at the expense of Gt or Lep via reduction when the conditions are suitable (high Fe(II) surface loadings) (Hansel et al., 2005). Combined reduction reactions offer a reasonable explanation for the widespread occurrence of Mt and the subordinate occurrence of Fh. In-situ transformation reactions however, appear to be the dominant mechanism for the secondary Mt. The in-situ formation of Mt coupled to Fe(III) reduction was indicated by the microcosm batch experiments that showed that the transformation to Fe(II) or mixed Fe(II/III) solid phases such as Si or Mt, can happen without releasing of dissolved Fe to the GW. The incubation experiments with NOM (Glodowska et al., 2020) or CH_4 (Glodowska et al., 2020b) as

electron donor revealed biogenic mediated Fe(III) reduction but in both cases, only a limited amount of Fe(II) was released as $Fe(II)_{aq}$ to GW and the majority of it remained in the sediments. Immediate re-precipitation or re-sorption of $Fe(II)_{aq}$ onto remaining Fe(III) mineral phases offer the best explanation for this finding. The in-situ formation of Fe(II)-bearing or mixed-valent Fe minerals such as Si and Mt is also suggested by other results. Spatially resolved µXANES also revealed Si and Mt in close spatial association. Also with regard to the susceptibility measurements the in-situ formation of very fine Mt offers the best explanation for the results. The limited amount of Mt found by any spatially resolved method (microscopy, SEM, EMPA, µXANES) is insufficient to explain the clear Mt peak of the kt measurements but fine-grained secondary Mt phases on mineral surfaces offer an obvious explanation in an active redox environment. The small particle size of the transformation phases can explain why, despite the clear kt signal, no secondary Mt minerals could be detected microscopically. This assumption is further reinforced by individual microscopical analyses with ferrofluid that suggested the presence of fine-grained Mt in the matrix and along primary minerals in the grey sediments at 25m bgs without a visually recognizable counterpart. However, the observed Mt in-situ formation suggests high rates of Fe(III) reduction, at least on a short time period and locally restricted. In combination with the varying Mt content across the precipitates supports the impression of oscillating conditions most likely related to microbial activity. This shows that Mt formation plays an important role in the local biogeochemical cycle what is further confirmed by the fact that previous studies have showed that Mt accelerates CH_4 production in methanogenic environments, accompanied by the enrichment of Geobacter and Methanosarcina. This is attributed to enhanced electron transfer through Mt to methanogens (Zheng et al., 2017) and resembles what was observed by Glodowska et al. (2020b) at the field site.

However, with regard to the **evolution of the RTZ** it is unclear to what extent the results from the different aquifer units can be used in a process description and to infer from mineral transformation reactions to the evolution of the study. Merging and interpretation of the results from the different depth levels (orange, grey, transition sediments) is very difficult as the large hydrogeochemical framework is still unclear. Whether the RTZ is a moving redox or stagnant front and what, if any, determines the position of the front is still under debate. Therefore, linking the residual Fe(II/III) phases in the reduced environment to the processes along the RTZ is prone to some uncertainty. Assuming a moving front the results would suggest that fine-grained secondary Mt phases remain as most redox stable phase. The consequence is a low-iron setting where mostly nano/microcrystalline Mt with low As sorption capacity remains as it was determined in the grey aquifer unit. Alternatively, a process without a migrating redox front is plausible where the secondary Mt formation is based on the reduction of the primary coatings, presumably initially present all over the grey sediments. Based on the assumption that the evolution of the primary Fe(III) coatings of the now grey sediments and the transformation processes documented for the Fe(III) precipitates at the recent RTZ are comparable the same result could be achieved. Therefore, it can be concluded that **Mt represents the final stage** in the Fe oxyhydroxide transformation. This process was already reported in Hornemann et al. (2004) and points to Mt as long-term Fe(II) sink while all other documented phases have a metastable character. This assumption also explains the magnetic and EXAFS bulk analyses that show the highest aquifer Mt concentration in the central grey sediments. However, as the study only covers a relatively short period of time it can be questioned whether the Fe(II/III) phases are also permanently stable in view of the strong presence of Fe(II) and/or Fe(III) mediating microorganisms.

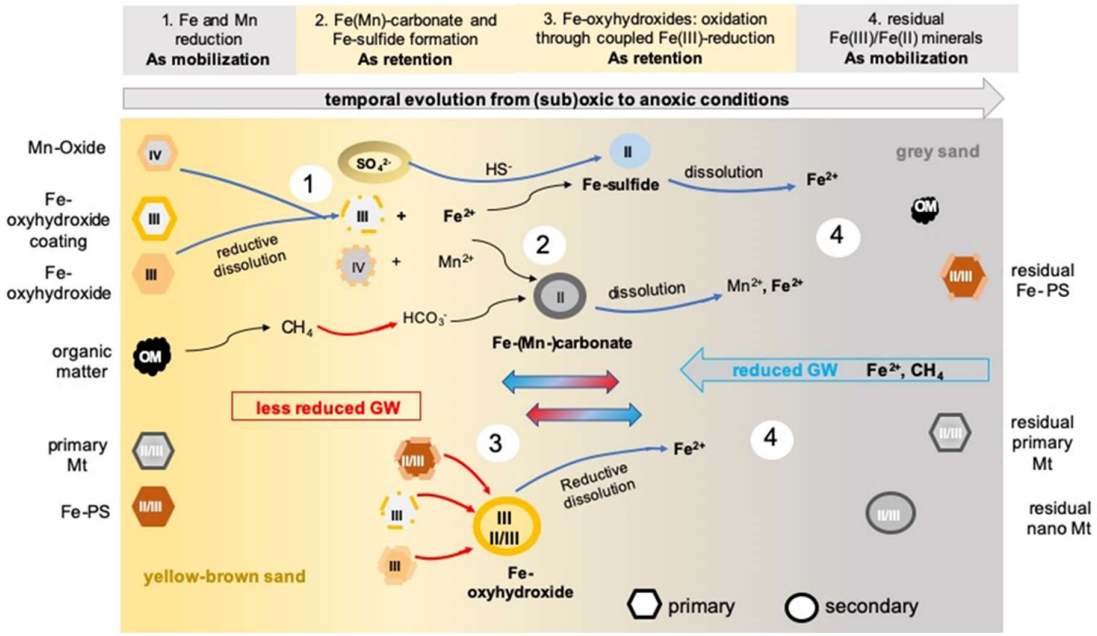

Figure 60: Conceptual model of Fe mineral transformation

Conceptual model of Fe mineral transformations in the redox transition zone based on known mechanisms (Horneman et al., 2004; Lowers et al., 2007; van Geen et al., 2013) and the results of this study presented in Kontny et al. (2021). 1. Reductive dissolution causes dissolution of primary Fe oxyhydroxide coatings. 2. Fe(Mn)-carbonate and Fe-sulphide formation. 3. Fe oxyhydroxide formation coupled to reduction of primary Fe(III) and Mn(IV). 4. Residual Fe(II/III) phases in the reduced environment. Blue arrows indicate reduction, red arrow oxidation. Numbers in sketch refer to numbers in the header. Primary refers to minerals that are present in the yellow-brown sand, secondary refers to minerals that were formed in the redox transition zone.

10.2 Formation, structure and extent of the RTZ

To describe the shape and extent of the documented RTZ and to predict the future development of the retardation front it is indispensable to decipher the complex sub-surface processes. However, in order to classify the results and incorporate the sedimentological, mineralogical and geochemical observations into a process model, a comprehensive understanding of the study area is necessary. The evolution of the redox front is still under debate and the insufficient knowledge of the complex sedimentological and hydrological framework poses great challenges with regard to the interpretation of the results. In this context, the study has to deal with information gaps that cannot be filled by the results of this thesis or previous works in Van Phuc.

10.2.1 Sedimentological and hydrological framework

First of all the **large-scale sedimentological subsurface structure** is unknown as the limited number of sediment drill cores is not sufficient to reliably reconstruct the heterogeneous study area. Consequently hydrology and lithology can hardly be interpolated to the whole Van Phuc area. However, a comprehensive understanding of the sedimentological and hydrological framework is essential to establish a process model. It is still unclear whether the position of the redox interface is stagnant or if the front is successively moving in the main GW flow direction, which however is elementary for interpreting the development of the interface sediments. Although the field site has been monitored for almost 20 years, there are still uncertainties with regard to the temporal evolution of the redox front over several decades. The GW monitoring program covering the last 15 years presented by Stopelli et al. (2020) documented no movement. However, lack of temporal and spatial resolution of the study does not exclude slow movement and also leaves room for the possibility of a cyclic movement. The question of a fixed or moving front is also inextricably linked to the question of

the recent **position of the front**. A firmly anchored front might be related to a depositional change from Holocene to Pleistocene sediments as postulated by Van Geen et al. (2013) or is coupled to other local peculiarities like inflowing surface water or sedimentological anomalies. Based on the results of this study the recent stability and growth of the RTZ seems to be caused by ongoing transformation reactions, but since no locally restricted control mechanism could be identified, it is difficult to predict how the RTZ will develop. Whether the sedimentological boundary mentioned by Van Geen et al. (2013) is responsible for the position of the RTZ remains unclear because age and expansion of the sub-surface structure remains largely unknown due lack of sediment cores and dating information. The transfer from grey to yellow-brown sediments might entirely be related to the strong redox effect without the need of a sedimentological boundary. The fine grey fingers documented in the yellow-brown sediments could indicate that the intrusion of reduced water into the Pleistocene aquifer and reduction of primary Fe(III) coatings is responsible for the colour change of the sediments from yellow-brown to grey, and not a former sedimentological boundary. Given the constant GW flow and the high permeability of the aquifer sediments a migrating front is therefore very likely.

However, the sediments analysed in this work do provide some sedimentological results that support the fixed position of the RTZ. One possible explanation is a locally restricted availability of organic matter or other oxidation and reduction couples. The importance of sedimentary OM and DOC for the Fe mineral dynamic at the field site was highlighted by Glodowska et al. (20210b) as well as Stopelli et al. (2021). In this context the core analysis revealed significant bioavailable carbon reservoirs within several fine-grained layers of the sand aquifer. These so far **undocumented OC-rich sediment layers** explain the intense microbiological activity across the RTZ and might even be prerequisite for the position of the redox interface. However, since only sediment samples from the two cores at the interface are available, it cannot be determined whether the sedimentary carbon is a local peculiarity. However, their occurrence could well be associated with the sedimentological boundary mentioned by Van Geen et al. (2013) and explain a fixed position over 15 years of GW monitoring.

In addition to the sedimentological carbon further **input of dissolved OC could from the top aquitard** is conceivable at the position of the RTZ (Stopelli et al., 2020). The upper aquitard consists of clayey silt. Although believed to be rather impermeable, could be hydraulically connected in some places to the underlying sandy aquifer by fine sandy layers and lenses that penetrate the aquitard. This observation is substantial as it supports the presence of the various groups of microorganisms involved in C turnover (fermenters, methanogens and methanotrophs). In consequence a variety of organic acids such as acetate, lactate, propionate or formate, produced as a result of fermentation (Chapelle 2000; Mc Mahon & Chapelle 2008), can be transported to the aquifer providing bioavailable C which fuels microbial activity (Glodowska et al., 2021). Dissolved organic molecules are mainly mobile and can be easily transported along flow paths. While slowly percolating through the aquitard, pore waters become enriched in DOC and other metabolic relevant GW compounds. Therefore, the finding that the fine sandy layers within the top aquitard could represent a vertical connection towards the aquifer that could deliver DOC or other metabolic relevant GW compounds is a substantial outcome as it might provide additional oxidation and reduction reactions. Reduced humic substances function as important electron shuttles and often dominate the dissolved organic carbon (DOC) fraction in Fe(III)-reducing aquifer parts (Mladenov et al., 2010). Hence, DOC plays a dual role depending on the degradability. Labile DOC serves as electron donor in microbial respiration, while persistent humic substances are used as electron shuttles during Fe(III) reduction. During the slow percolation and decomposition of sedimentary OM the formation of highly reducing conditions with high dissolved As and Fe concentrations might add to the aquifer dynamic**.** This could explain the massive precipitation events along the aquifer borders and might be a key explanation for the position of the redox front. Also the exceptional high dissolved As GW concentrations detectable within short distances pose the question

of additional input beside the aquifer itself. A connection to overlying aquitard could contribute significantly to the dissolved aquifer As, Fe and CHNOPS concentration and likely explain the drastic change in GW hydrochemistry. If the availability of DOC, either through sedimentological peculiarities or an aquitard-aquifer connection, is unique to the position of the RTZ it would likely explain site as well as stability of the retardation front. Whether the aquitard-aquifer interaction is actually possible and to which extent a hydraulic connection links the two sedimentological units remains unclear. The top aquitard is penetrated by narrow (mm to cm scale) sand layers in both horizontal and vertical direction and cm-scale sand lenses appear at irregular intervals. These structures appear completely random and are most likely related to biological activity within the delta sediments. Plant roots or digging organisms are the most obvious explanations. The sandy cavity fillings should provide a significantly increased permeability but it is very difficult to assess whether and to what extent this potential sandy flow paths are connected. Based on sedimentological results of the two cores it seems unlikely that the upper 12m of the aquitard with high solid Fe, As and TC concentrations are directly connected to the aquifer given the clay layers between 12 and 16 m. The clay layer which was also mentioned by van Geen et al. (2013) is probably a paleosol dating to the last sea level low-stand about 20.000 years ago (McArthur et al., 2008; Funabiki et al., 2007) while the organic-rich deposits (often referred to as peat) have most likely their origin in mangrove forests in the Holocene, which led to the accumulation of huge amounts of organic matter (Mathers et al., 1996). These organic-rich layers might play a decisive role in local Fe and As cycle if they are connected to the recent processes. The constantly decreasing element concentrations in the aquitard towards the aquifer could point to an interaction. Also formation of the massive laterite layer at the aquitard-aquifer border in around 20m depth points to an aquitard-aquifer connection. With a constant thickness above 10 cm, composed of extensive secondary Fe cementations and characterized by the highest Fe (11 wt%) and As (16.5 mg/kg) concentrations in the entire aquifer, the laterite layer suggests a strong interaction. The bottom aquifer-aquitard border from 40.0-41.5 m depth is characterized by massive Fe cementations resulting in 4-5 wt% Fe_2O_3. These are much higher concentrations compered to the other aquifer samples. Therefore, an aquitard-aquifer interaction along both aquifer-aquitard boundaries are likely to contribute to the redox driven aquifer element dynamics. This is also in line with the huge amount of strongly weathered PS along the lithological boundaries. A connection to the silty aquitards through progressive biogeochemical weathering offers a mobilization potential for As, Fe and OM and other GW compounds that can massively enhance biogeochemical aquifer processes. Whether the mobilization of bioavailable C is also associated with the reduction of the now grey sediments up-stream of the RTZ is hard to assess. In this context a **top aquitard-aquifer connection** could explain why the upper grey aquifer, to which bioavailable C can likely percolate, is already reduced (20-30 m depth), while the lower aquifer (30-42.5 m), to which the DOC transportation was limited, is not strongly reduced yet. The volatile fatty acids analysis from sediment porewater collected at the same site confirmed increased concentrations of acetate, lactate and propionate at the depth between 24 and 27 m (Table S2) (Glodowska et al., 2021). However, Stopelli et al. (2020) identified different GW flow regimes along the vertical axes that might offer a more reasonable explanation for the highly reduced area from 20-30 m bgs and the moderately reduced section from 30-40 m bgs. In case of an aquitard-aquifer connection also surface-water bodies (ponds) and intense agricultural activity could influence the local hydrochemistry fundamentally. Possible effects of connected surface water bodies were documented by Kuroda et al. (2017) and likely matches many observations of this study. With regard to the massive clay layers in the upper part of the top aquitard a direct impact of agriculture seems unlikely but a local pond could affect the aquifer of the field site. The ponds in the area that are used for coupled duck breeding and fish farming are extraordinarily rich in nutrients. Pond-derived OC import into near surface GW aquifers across several meters thick silt/clay aquitards affecting local As dynamic has been documented in comparable deltaic regions of Asia before (Lawson et al., 2013; Kocar

et al., 2008). Kocar et al. (2008) showed that ponds and agricultural fields may serve as important sources of infiltrating OM. However, since nothing is known about the depth and structure of the pond, little can be said about its potential influence but given the depth of the clay layers between 12 and 16 m and since the local is located slightly downstream, a direct impact on the RTZ seems unlikely. All other ponds in Van Phuc are located in some distance which minimizes the chance of a connection to the RTZ analyzed here.

River-aquifer interaction are commonly discussed as drivers for aquifer reactions. Stopelli et al. (2020) and Wallis et al. (2020) showed that the study site is embedded in a system of hydrogeochemical zones stretching from the RR in the SE towards NW. The importance of river-aquifer interactions for near-surface aquifer dynamic was show by many studies including more recently Stahl et al. (2016) and Stopelli et al. (2020). In general sold As and Fe are known to accumulate in riverbank deposits (Bone et al., 2006; Charette & Sholkovitz 2002). Flow reversals caused by GW pumping may pull the As contaminated water into the GW system. Riverbank deposits can contain thousands of mg As/kg (Datta et al., 2009) and are therefore a particularly important source for aquifer As pollution (Stahl et al., 2016). Beside As and Fe intrusion of river water can also import other metabolically relevant compounds and thus effect the biogeochemical aquifer processes. For van Phuc, however, this process can be ruled out based on the comprehensive GW monitoring program by Stopelli et al. (2020). River-aquifer interactions only play a long-term role in the evolution of the RTZ. With regard to the study site long-term changes in land and water management practices up-stream are able to change sediment delivery and therefore affect the river-aquifer interaction during the last decades. A decreasing sediment delivery, affecting the Red River bed and thus exchange between the aquifer and river was reported by Le et al. (2006) and could likely affect the aquifer. Also the dam construction during the last decades to shield the city of Hanoi against the Red River could have affected sediment and flow dynamic along the Van Phuc meander peninsula. As the process falls in the same period as the increasing GW abstraction below the city of Hanoi it is impossible to assess and differentiate the effect of the different influencing factors.

Another basic information gap are the **unknown starting conditions** of the mineralogical evolution. The process model introduced by Berg et al. (2007) and Eiche (2010) assumed that the initial Fe mobilization is related to the dissolution of detrital Fe-coatings around primary minerals. However, the two studies did not include a mineralogical characterization. The coring campaign of this study was hoping to unlock undisturbed yellow brown sediments in the core profile, which correspond to the sediments of "site L" from Eiche (2010) and represent the initial mineralogical situation before the onset of reducing conditions. On the one hand the results of the solid phase geochemistry and mineralogy is comparable to other sediments in SSEA that are usually considered to represent the initial conditions and match in many aspects the descriptions from Berg et al. (2007) and Eiche (2010). Both the total Fe_2O_3 content and the (partially) preserved characteristic coatings around detrital grains in the depth section from 30 to 40 m the sediment is comparable to the description from previous work in less reduced areas (Site L Eiche 2010). This could suggest original conditions, unaffected by recent redox processes. Especially the local presence of crystalline Gt and distinct Fe-coatings correspond to previous descriptions and could represent the original (pre-redox) conditions. However, these observations are restricted to a few locations while the majority of the yellow-brown sediments seem to have been exposed to at least slight redox processes. There are several indicators that the sedimentological conditions of the majority of the yellow-brown sediments do not correspond to the original circumstances and thus do not represent the starting conditions and have already been influenced by (moderately) redox processes. The thin coatings in most parts of the yellow-brown sediments are far less frequent and distinct to match the description of the initial pre-redox conditions described by Eiche (2010) The coatings are much rarer, thinner and usually do not enclose the entire

grain and seem to be partially dissolved what clearly implies a redox influence. In some parts of the yellow-brown sediments the coatings are completely absent. On a close look fluctuating colour and variable solid phase geochemistry within the yellow-brown sediments indicate at least locally occurring reductive dissolution processes. It must be noted that the supposedly homogeneous section from 30 to 40 m is very complex on a small scale. Along the depth profile of 30 to 40 m, yellowish moderately reduced and more reduced greyish layers alternate. This could indicate starting or ongoing redox processes related to the permeability of the individual layers. Although GS analyses cannot cover this resolution colour and microscopic impression support this assumption. This suggestion is also in agreement with the geochemical results. From a geochemical perspective the initial conditions, that most closely represent the original conditions, should be characterised by relatively high and homogeneous spread Fe/As content across continuously coated detrital grains. However, the investigation reveals significant variations for Fe (1.0-3.6 wt%) and As (1.3-5.1 mg/kg) within the yellow-brown sediments (within the resolution of the bulk samples). In addition to inhomogeneous distribution some coatings show a characteristic layering. These results could be related to a subsequent redox overprinting. Also the occasional presence of Fe-PS complexes and Fe-carbonates imply an active Fe dynamic in the yellow-brown sediments between 30 and 40 m bgs. Based on colour and solid phase geochemistry the yellow brown sediments are at least partially overprinted. Active Fe dynamic and redox processes are also in agreement with a recent XAS study by Nghiem et al. (2020). The study reported for the sediments from 30-40 m (called orange in this study) show a great mineralogical similarity to the transition zone sediments of this study. Therefore, it can be suggested that the yellow-brown sediments are about to become transitional sediments but that the transition has not been sufficient to change their appearance yet. However, it must be noted that due to the high heterogeneity of the field site, the samples of Nghiem et al. (2020) are not identical to the core profiles presented here and the overprinting is presumably more advanced in the samples from Nghiem et al. (2020). This is supported by the presence of presumably primary Fe(III) oxyhydroxides in the core samples and the absence of Fe mineral phases like Lep and Viv which are limited to the transition sediments. Both observation indicate an initial overprinting state. Assuming the original conditions at the location of the borehole were identical to those described in Eiche (2010) it must be concluded that the sediments from 20-30 m bgs has been at least partly reductively overprinted. Based on the observations most parts of the yellow-brown sediments have been subjected to redox processes of slight to moderate intensity and do not represent the initial conditions. As the initial conditions cannot be reconstructed other Fe mobilization mechanisms cannot be ruled out. However, all the results point to the dissolution of primary coatings as dominant Fe source for the RTZ and the unclear starting conditions is no obstacle for the interpretation of the results with regard to the evolution of the RTZ.

10.2.2 Impact of sedimentology & hydrology

Due to complex depositional history and the limited amount of core profiles the reconstruction of the subsurface structure and the shape and expansion of the redox front is difficult. However, with regard to **macro scale sub-surface structure of the RTZ** the core data suggest that the extension of the redox front is mainly controlled by local GW flow regimes and sedimentology and compared to previous studies in the field site, the coring revealed a different subsurface build. This study revealed an approximately 4 m thick bottom silt layer stretching from 42 to 46 m bgs which separates the sandy aquifer from the gravel aquifer below. The layer was not clearly visible in the cores described in Eiche (2009) that were taken in a distance of less than 200m. The **four-storied core structure** (top aquitard, aquifer, bottom aquitard, gravel aquifer) documented in both cores stands in contrast to previous works in the field site (Berg et al., 2007; Eiche 2010). Consequently, the sandy aquifer is not hydraulicly connected to the gravel aquifer below at the position of the RTZ and different GW flow conditions along the sand-gravel aquifer boarder have to be expected. Stopelli et al. (2020) and Wallis et al. (2020) describe a complex GW environment with different GW flow regimes along the vertical aquifer profile

and, in addition, presumably pockets with fossil GW. Based on the colour and thus the inferred redox state of the sediment highly reduced Fe- and As-rich GW enters the RTZ mainly in the depth from 20 to 30 bgs from Eastern to South-Easter direction. This observation is in accordance with the study of Stopelli et al. (2020) who recorded highly reduced GW especially in the range from 22-25 m depth. As the sediment colours map the shape and expansion of the redox front a reconstruction of the aquifer subsurface structure based the documented core profiles points towards a central redoxfront from about 20-30m bgs and a redox finger along the bottom aquifer-aquitard boundary at around 40 m bgs (Fig. 63). Therefore, the sandy aquifer is separated into an upper grey, highly reduced sand dominated part between 20 and 30 m, and a yellow-brown, less reduced sand dominated part between 30 and 40 m. The existence of the bottom redox finger at a depth of 40 m is unique to the coring site and most likely related to the bottom silt layer and suggests that the reduced area in front of the RTZ extends over the entire vertical profile, but has not yet spread as widely in the depth range of the yellow-brown sediments from 30-40 m bgs. Micro scale variations across the yellow-brown sediments imply starting reduction at layers with higher permeability and therefore reinforce the impression that the front covers the whole aquifer. The central redoxfront is interrupted by several less reduced layers at around 20-22, 27 and 30 bgs. The finger-like structures are formed along the grain size boundaries and map the local permeability. These layers indicate that the redox front does not spread in a straight line but rather sediment layers of variable permeability create a fringy redox front. The congruent colour and GS gradient suggests that the expansion and shape of the redoxfront between 20 and 30 m bgs is controlled by the permeability of local the sedimentology. The top and bottom boarder of the redoxfront at 20 and 30 m bgs as well as the oxic fingers at 21.5 and 27.5 m bgs show finer grainsize with higher clay and silt content. The interface layer at 30m bgs is classified as sand, but with 6 % clay, 44 % silt and 49 % sand the layer shows a significantly higher silt and lower sand content than the surrounding grey or yellow-brown layers. In combination with a series of fine GS layers stretching from 27-30 m bgs this section is able to decrease vertical permeability and separate aquifer GW flow regimes. A series of low permeable layers stretching from 27-30 m bgs offers a reasonable explanation for the distinct separation of the flow regimes as the comparison of GS composition of grey aquifer samples above (n=18) and yellow-brown below (n=17) 30 m reveals no major differences. The sand content (70 % sand, 27 % silt, 3 % clay) is slightly higher in the lower part while the silt and clay content (66 % sand, 30 % silt, 4 % clay) is slightly higher in the upper part of the aquifer. However, the redox properties differ significantly, although the sedimentological properties of the two areas are relatively similar. A low permeable barrier layer explains why the bottom area between 30 and 40 m bgs shows no reduced colours on the macro scale until the grey finger direct above to bottom clay layer around 41 m bgs appears. The reduced permeability of the barrier layer limit the spread of the redox front and separates the well-permeable sandy aquifer units. As redox and grain size boarders largely coincide throughout both core profiles sedimentological conditions seem to be the main control mechanism on the extent of the redox front in the aquifer. Based on both core data several low-permeability barrier layers separate the GW flow regimes and support the formation of **vertically separated hydrogeochemical zones** with different redox and hydrochemical conditions within the aquifer (Fig. 63). Therefore, it is reasonable to assume the decreased permeability of the fine-grained layers separating the different GW-flow regimes are largely responsible for the vertical redox structure observed in both cores and guides the shape and expansion of the various GW flow regimes.

It can be assumed that secondary minerals form along the entire redox interface but the position of the extensive mc precipitates and the Fe-PS complexes along four transition areas (Fig. 63 1-4) where highly and moderately reduced GW and sediment adjoin each other along fine-grained layers clearly demonstrates the importance of local sedimentology for secondary Fe mineral formation. The documented Fe accumulation along these transition sediments surpasses by far the other aquifer samples. The transition sediments between yellow-brown and grey sands are always related to silt-

sand interfaces that show a particular different elemental composition. For both As and Fe the total and average concentrations for the aquifer as well as the aquitards is in a typical range for sedimentary delta sediments composed of siliciclastic and argillaceous deposits (Cornell & Schwertmann 2003, Garelick et al., 2008; Reimann & Caritat 1998; Smedley & Kinniburgh 2002; Bowell et al., 2014). The documented As concentrations in the range 1–20 mg/kg and a Fe_2O_3 content between 1 and 5 wt% for most samples are within the typical range for floodplain and stream deposits. Both the absolute and the average concentrations largely similar to the previous studies in the area (Berg et al., 2007; Eiche 2010). The aquifer average for As is 4 mg /kg As. Towards the finer aquitard deposits the average concentrations increase up to about 14 mg/kg As what is related to their higher proportion of sulphide minerals, organic matter and clay minerals which typically contain more As (Garelick et al., 2008). The average Fe content is 2.2 wt% in the aquifer and between 5.0 and 6.5 wt% in the two aquitards. However, whenever grey and yellow-brown sediments lie next to each other and orange transition sediments are formed and the colour change goes along with a significant change in geochemistry. The average Fe content of 1.5 wt.% (n=9) in the reduced aquifer is significantly lower compared to aquifer average of 2.5 wt% (n=24) while transition zones (n=6) show an average Fe content of 4.6 wt% that is three times higher. As shows same tendency. Reduced layers are depleted by factor of 2 (2.3 mg/kg, n=9) compared to moderately reduced aquifer layers (4.6 mg/kg, n=24). Within the transition zone sediments the average concentrations of 8 mg/kg (n=6) is almost four times higher for As. In consequence the secondary Fe minerals investigated in this thesis study show the highest quantity near the aquifer-aquitard boundaries and along fine-grained layers within the aquifer. This can be related to low permeability barrier layers maintained a less reduced state and could therefore provide residual Fe(III) and Mn(IV) phases for oxidation reactions or metabolic compounds driving biotic oxidation reactions. The results underline the importance of local sedimentology for secondary Fe mineral formation and show that microenvironments where mineral (trans) formations are promoted in spatially confined areas is responsible for the formation of the secondary Fe(II) and Fe(III) phases.

The dissolved Fe concentration along hydraulic barriers further suggests that the **Fe dynamic is flow-controlled** and the Fe-accumulation along the redox interface is related to inflowing of Fe(II)-rich GW. Especially the extensive precipitates along the redox and grain size boarders of the interface require a continuous supply and indicate local supersaturation. The location at the sediment-GW interface offers the best conditions for coupled biotic and abiotic processes resulting in secondary mineral formation. The supply of electron donors and acceptors is supported by the nearby silty layers and sub-µm PS particles support the crystallization process as they can serve as a nucleus to initiate (biogenic) precipitation and provide numerous elements including Fe(III). The combined micromorphology, geochemistry and mineralogy underlined the important role of microenvironments for the local Fe dynamic as all secondary Fe(II) and Fe(III) phases occur along the redox interface only in specific clearly delimited areas related to depositional conditions. Analyses of the micro-texture in µm to cm scale revealed preferential flow path and micro-concretions all along lithological variations. Here, strong hydrochemical gradients can be achieved on a small scale and the interaction between the solid and the liquid phase is enhanced. Especially the elemental mappings showed that preferential flow paths and separated microenvironments are of particular importance for the Fe mineral dynamic. Near the redox boundaries, strong colour changes on mm- to cm-scales and highly variable solid phase geochemistry and mineralogy characterize the sediments and indicate that sharp gradients in grain size play a significant role in establishing the redox interface on the micro scale. The congruent course of the colour, solid phase geochemistry and mineralogy is a clear indication of a redox-driven dynamic and suggests that the interplay of local lithology composition and permeability with local GW flow conditions regulate the formation of the secondary Fe phases. In consequence the observed Fe mineral inventory and course of the redox interface developed the distinct redox zonation documented on the macro as well micro scale. The micro (mineral) scale evidence for a distinct redox zonation (chapter

10.1.2.2) are analogously visible in the sediment on the macro (sediment core) scale. Geochemical analyses revealed isolated Mn-rich layers dominated by Mn precipitates. The texture of the Mn precipitates is very similar to the secondary Fe precipitates and refers to mc phases that are probably related to recent redox processes (Fig. 61 & 62).

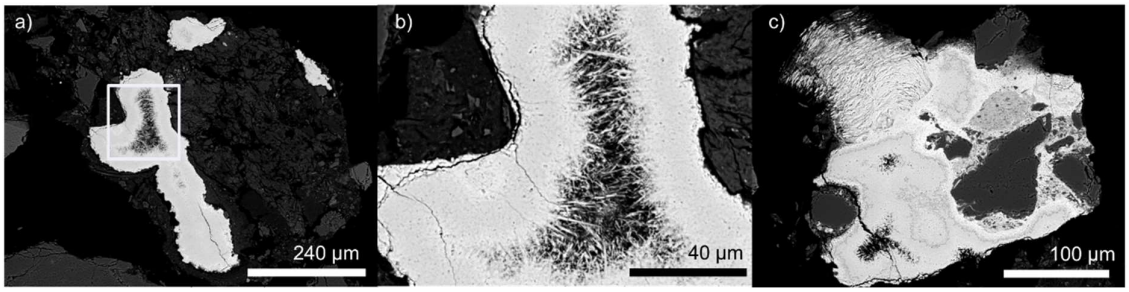

Figure 61: Backscatter micrographs of large Mn precipitates at 21 m depth in core RD42

a) Based on Atom%: (Mn 44, O 50 Al 3, K 2.5, Ba 0.5) the phase could be identified as Mn oxide. b) shoes the magnification indicated by white rectangle. The needle shaped mineral fibers clearly suggest recent formation. c) The large Mn precipitate structure stretch above several 100 µm and cover primary particles. Dimension und texture clearly resemble Fe(III)-dominated precipitates. The Atom% is Mn 43, O 51, Al 3, Ba 2, K 2, Si1.

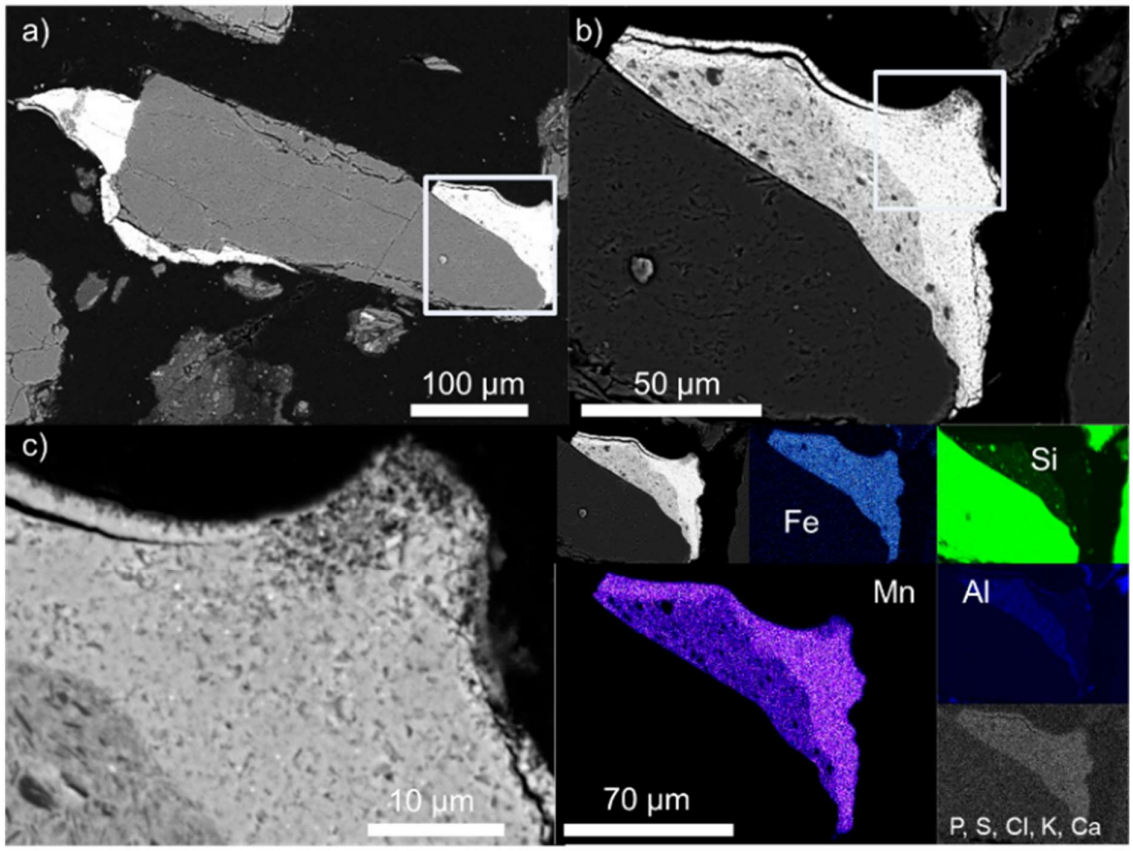

Figure 62: Backscatter micrographs of Mn precipitates covering surfaces of primary grains at 21 m depth in core RD42

Mn oxide is clearly indicated by Atom%: Mn 20-25, O 56-59 and Al, Si, K < 2

A distinct Mn-rich layer is located at a depth of around 21 m in core RD42 (Fig. 29). In core RD54 isolated Mn-rich layers were documented at depths of around 19, 30 and 39 m bgs (Fig. 30). The Mn-rich layer in core RD42 at 21m and in RD54 at 30m depth are located next to Fe-rich layers presumably formed due secondary processes. The position of the Mn-rich sediments, slightly offset the Fe precipitate layers, reinforces the impression of a vertical redox zonation related to recent redox processes. The fact that the depth of the Fe-and Mn-rich layers in core RD42 and in RD54 are not identical order can be attributed to various vertically separated flow regimes described by Stopelli et al. (2020). In this setup multiple possibly overlapping redox zones along the core profile can be expected depending on course of the flow regimes. In consequence multiple hydrogeochemical gradients can pervade the sediments and form Fe and Mn-rich sediments along the core profile. The fact that the top Mn-rich layers in core RD42 (21m) and RD54 (19m) are separated by 2 m in depth might illustrate the small-scale heterogeneity at the field site and the influence of local sediments on course of GW flow regimes. Based in atomic ratio the Mn precipitates could be identified as Mn-oxide phases. Taking into account the importance of Mn-phases for oxidation process in slightly reduced aquifers, the mineralogy of Mn-phases, addressing the Mn(IV) and Mn(III) composition and influence of the Mn phases on the Fe dynamic, should be further clarified.

In summary, the sedimentological observations match the micro-scale results. The diverse core structures with frequent changes in colour, grainsize and mineralogical and geochemical composition confirm the image of a complex underground and the sedimentological heterogeneity documented in-between the adjacent sediment cores RD42 and RD54 clarifies the complex sub-surface conditions. The fact that the two cores have a vertical offset for similar sediment layers of up to two meters over a horizontal distance of 10 m shows how quickly the subsurface conditions change (Fig. 23). Further corresponding sediment layers in the two cores usually show a different thickness and slightly variable colour and grain size composition. The aquifer structure of RD54 is more heterogeneous and the redox processes do not seem to be as advanced. That is expressed in less bold colours and a less homogeneous redoxfront. In RD42 there is a sharp transition to a homogeneous grey part which spreads for almost 10 m from 20-30 m bgs. In RD54 the transition is not as sharp and the grey front is regularly interrupted by less bleached horizons. The absolute reduced grey layers spread only for 1.5 m from 26.8 – 28.2m bgs while the surrounding layers show grey-brown to grey-beige colours and are interrupted by fine brownish layers. So the two neighbouring cores show fundamental differences with regard to subsurface structure and redox evolution and highlight the complex sub-surface conditions. However, integrating the heterogeneous sedimentology and the complex GW regimes, the results of the joint lithological, mineralogical and geochemical description suggest that that sharp grainsize gradients within the aquifer control the expansion of the redox redoxfront. The reconstructed shape and expansion of the redox front based on lithology and colour matches the mineralogical and geochemical results and thus represents a realistic approach to describe the subsurface processes. The clear vertical separation of the different GW flow regimes through fine-grained layers and the significant quantitative increase of secondary Fe phases along these areas clearly demonstrates the importance of the interface sediments for the solid-liquid exchange processes controlling local Fe dynamic. The fine-grained layers act as reservoir for Fe(III), Mn(IV), carbon, sulphur and OM and in combination with the local presence of PS-rich layers the formation of secondary phases is reinforced. In addition, the selection of documented PS, the (pseudo-) matrix, overgrowths on Qtz, Fsp and other primary particles, alternating Ti-(Fe-) minerals and Fe oxyhydroxides transformation clearly indicate diagenetic processes in addition to the redox processes. Solid geochemistry and Fe mineralogy along the colour and GS boundaries prove that the observed gradients mark the local redox boundary and the transition sediments represent the recent redox interface position. The GW data from Stopelli et al. (2020) are in line with these results. The results on hand can explain the massive drop in GW concentrations across the redox interface reported from (Stopelli et al., 2020) for various GW

compounds. Therefore, genesis, composition, extent, texture and mineralogy of the RTZ can be described as interplay of depositional conditions and different GW flow regimes driving hydrobiogeochemical reactions. In consequence the redox boundary dominated by secondary Fe phases is formed and separates the As-contaminated and As-free GW. With regard to the vertical extension of the RTZ GW data from Stopelli et al. (2020) already indicated that the entire retention dynamic takes place in the narrow RTZ with a maximum horizontal extension of about 35 m. Based on the two core profiles, the extent of the RTZ cannot be determined exactly, but the results of the drilling campaign indicate a further spatial concentration of the retention dynamics along a narrow band along the actual redox interface. With regard to the spatially resolved results of the thins section analyses, the formation of the secondary Fe minerals is concentrated in a zone a few tens of centimetres wide along the actual redox interface (Fig. 63).

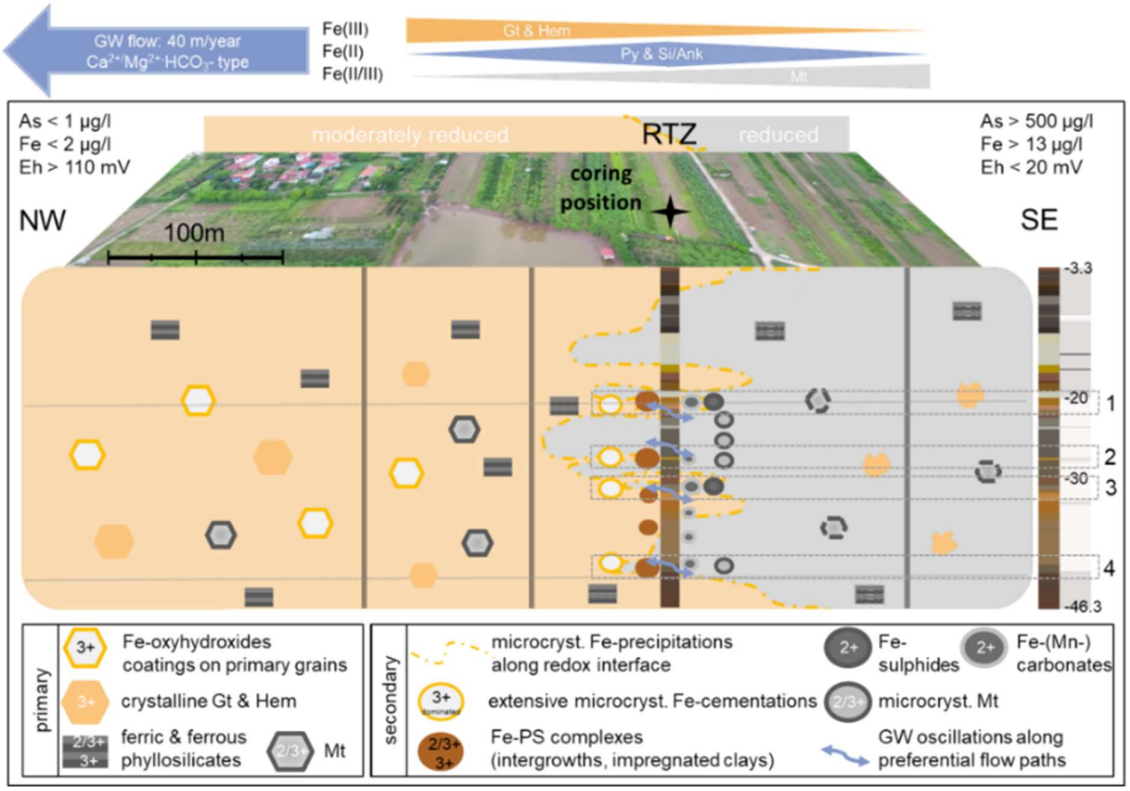

Figure 63: Reconstruction of the subsurface structure based the documented core profiles

The figure illustrates the distribution of primary and secondary Fe phases in consequence of the inflowing highly reduced GW and the formation of the fringy RTZ as result of the local sedimentological conditions, especially in the 4 key areas in about 20, 27, 30 and 42 m bgs where secondary mineral formation is increased along fine grained layers. The blue arrow in the top left indicates GW flow direction and type of inflowing GW. As, Fe and respective Eh of the highly and moderately reduced GW bodies are given in the corners below. The central figure on the top indicates Fe mineral distribution across the RTZ, demonstrated on core RD42.

11. Conclusion

Based on the combined mineralogical and geochemical characterization of two sediment cores this study is able to explain formation, structure and extent of the RTZ as well as occurrence, distribution and quantity of secondary Fe mineral phases related to sedimentology and hydrology on the micro (µm) and macro (m) scale. After reductive dissolution of primary Fe(III) oxyhydroxide minerals and coatings up-stream of the study site GW transport of dissolved Fe(II) and co-released dissolved As to the RTZ is induced. As soon as the As and Fe-rich GW reaches the redox boundary Fe(II) minerals and Fe(III)-dominated microcrystalline precipitates form in close proximity along the redox interface in a specific order. The study reveals a large variability of Fe(II) and Fe(III)-bearing minerals. While the mineral sequence on the macro scale corresponds to the redox conditions the local sedimentology, GW flow regimes and microbiotic activity create multiple micro milieus and control local (trans-) formation of secondary Fe minerals on the micro scale. The spatially resolved measurements revealed the **importance of separated microenvironments** formed as result of the heterogenic subsurface structure for the local Fe cycle. Mineralogy and geochemistry reveals the strong impact of microbial activity on the Fe dynamic and indicate a highly dynamic and heterogeneous aquifer dynamic on the micro scale. Changing or oscillating hydrogeochemical conditions related to the interaction of sedimentological, hydrochemical and biotic processes create a complex interplay of processes with strong interdependency. The study shows that on the micro scale the occurrence, distribution, stability and quantity of secondary phases is widely by through the interaction of these processes in spatially confined areas. These areas of secondary mineral formation are of critical importance to the biogeochemical cycle and therefore largely influence the Fe and As flux across the RTZ. Therefore, the study demonstrates the **importance of local sedimentology** for the formation of secondary Fe phases and might explain the position of the natural reactive-Fe barrier. Local availability of SOM and presence of residual Fe(III) and Mn(IV) phases may be sufficient to explain the co-accumulation of Fe and As at the redox interface in the observed sequence of secondary Fe minerals. With regard to primary Fe(III) phases the study documented an extensive involvement of PS in the recent Fe dynamic. The role of ferric and ferrous PS with regard to the Fe cycle might have been underestimated in the past. A re-evaluation is essential for understanding and modelling the evolution of Fe-phases in complex near-surface sediments. The same applies to primary Mn-phases. The study has provided clear indications that the Mn phases are involved in the recent redox processes. Their specific role will have to be clarified in further studies. In combination, the residual Fe(III) and Mn(IV) phases offer a realistic approach to explain the anaerobic oxidation reactions that must be assumed to explain the observed Fe precipitates. If, however, these phases alone are capable to explain the large quantity of the Fe(III)-dominated precipitates is still unclear. Nevertheless, the study highlights the importance of a distinct sedimentological analysis to conclusively understand the Fe mineral dynamic in a complex natural setup. To explain how the RTZ acts as As and Fe sink and buffers the transport of these elements due to accumulation in secondary Fe phases at the redox boundary cannot be explained by a mineralogical description alone. The comprehensive description of the two core profiles demonstrated the importance of the multiple sediment and GS boarders on various scales. Continuous exchange process along the aquifer-fingers and along the aquifer-aquitard boarders were shown to offer additional pathways for Fe and CHNOPS into the aquifer. When the redox interface coincides with less reduced CHNOPS-rich layers, the mineral (trans-) formation develops the greatest dynamic and strong hydrogeochemical gradients force enhanced secondary mineral formation by coupled biotic and abiotic processes. If, however, the aquitard-aquifer connection and the embedded fine-grained layers in the aquifer are unique to the RTZ remains unclear due a lack of sediment cores. Therefore, it cannot be clearly proven that the position of the RTZ is directly linked to presence of fine-grained sediments layers. However, the thesis underlines the large variety of biotic and abiotic processes related to a complex natural sedimentary system. As a heterogenic near surface geology is characteristic for clastic

delta sediments with alternating fluviatile and marine depositional conditions the processes described in this study are assumed to be representative for multiple comparable field sites in SSEA. Therefore, the work provides new insides into the redox controlled As and Fe dynamic across sharp natural redox boundaries.

The most important outcome, however, is the **importance for microcrystalline Fe(III)-dominated precipitates** for the As and Fe cycle in natural environments. This result is entirely related to the detailed description and the broad range of methods used in this study and highlights the importance of comprehensive mineralogical investigations by microscopy and spatially resolved measurements to understand the dynamics in natural systems. The work underlines that determination of crystallinity, texture and (micro-)morphology, in context of the sedimentological framework, is essential to explain structure and evolution of a natural RTZ. Since frequently practiced X-ray based bulk measurements of homogenized samples which are done in most studies cannot provide information about crystallinity, texture and spatial distribution of Fe phases actual field site conditions can only be derived to a limited extent. However, the study showed that addressing the mc nature and large mineralogical variability of the mc precipitates is essential to describe to local Fe dynamic. Voegelin et al. (2019) showed that "variations in the structure and composition of amorphous to poorly-crystalline Fe(III) precipitates can lead to substantial variations in their reactivity" and (reductive) dissolution kinetics. The consequence is a large, presumably field site specific, or even small-scale reaction diversity which has not sufficiently been taken into account in recent models. Therefore, the results suggest a Fe dynamic that differs significantly from most models that assume crystalline Fe minerals. The mineralogical characterization revealed that well crystalline Fe(III) minerals are rare whereas mc Fe(III)-dominated precipitates play the dominant role in regulating the fate of As and Fe in Van Phuc. In this context, the results of this study may help to improve modelling approaches by providing an impression of the actual mineral conditions in a natural environment. Since Van Phuc might be representative for many field sites in SSEA the Fe mineral characteristics documented in this thesis may apply for many natural redox boundaries. The fact that this discrepancy has rarely been reported before also highlights the importance of drilling campaigns. Laboratory experiments like column, batch or microcosm experiments can never cover the full range of naturally occurring processes due the high complexity of natural aquifer systems and will therefore never reproduce the mineral properties accordingly. Another important outcome of the study is the stability of the mc Fe(III)-dominated precipitates in the complex and fluctuating environment. The study clearly showed that mc Fe(III)-dominated precipitates are the most important Fe sink and primarily responsible for Fe accumulation along the redox boarders. However, low crystallinity and high amounts of incorporated elements make it very unlikely, that these phase-complexes resist fluctuating hydrogeochemical conditions and develop a distinct quantity. The thesis identified two processes that might have the potential to preserve the sensitive precipitate phases and explain continuous growth during oscillating conditions. The biogenic phases documented in the incubation experiment and the Fe(II) carbonates potentially forming during oscillations on the precipitate surfaces offer a reasonable mechanism capable to protect the extensive Fe(III) precipitate surface structures from (re)dissolution. Therefore, the results imply that constant transformation and rearrangement of the surface Fe phases might therefore be essential for the formation of the vast mc Fe precipitates and accumulation of secondary Fe phases along the interface in the observed quantity. However, the documented protection mechanisms enhancing the stability of the mc Fe(III)-dominated precipitates are presumably limited to a fluctuation range and could not resist a drastic change of the environmental conditions. On the other hand **oscillating conditions** causing repeated precipitation and dissolution sequences, at least along microenvironments, might be a prerequisite to explain the observed findings. Fluctuations not only explain the formation of the extensive precipitates, but also the (oxidative) dissolution of the secondary Fe(II) minerals (pyrites and Fe-bearing carbonates). Furthermore, fluctuating conditions enable to link Fe precipitate formation,

Fe(II) mineral re-dissolution and impact of residual Fe(III) and Mn(IV) phases, sedimentology and microbiology.

With regard to the **As dynamic** along the redox interface the formation of secondary Fe(II) carbonates, sulphides and especially the Fe(III)-dominated precipitates is the decisive factor as it largely controls the As mobility. All secondary Fe(III), Fe(II/III) and Fe(II) minerals provide a high hosting capacity for As and can immobilize significant amounts of As, either as As(III) or As(V) species. Especially the mc Fe mineral precipitates have shown to adsorb and incorporate considerable amounts of both As species with up to 480 mg As/kg. The complex Fe(III)-dominated phase mixtures comprise the dominant As sink at the RTZ and by far exceed the other As retardation phases. Although Py showed the highest As concentration among all identified Fe-phases (up to 5800 mg/kg) it only occurs in minor amounts coupled to the local availability of SO_4^{2-}. The secondary Fe- and Mn-bearing carbonates are more frequent but have a relatively low As retention capacity (< 180 mg/kg). However, the combined As immobilization along the natural RTZ is a powerful natural retardation mechanism and the presented redox-dependent sequence of secondary Fe(II) and Fe(III) phases across the RTZ is suggested to generally play a significant role for As retardation in sandy aquifers of deltaic regions in SSEA. All identified As hosting phases showed a high reactivity and sensivity to changes in the hydrobiochemical environment and revealed a metastable character in context of the dynamic environment. Despite the Fe(II) phases and Fe(III) precipitates along a RTZ comprises an considerable As and Fe sink the retention capacity of the documented Fe phases for oxyanions like As is high the (long-term) stability has to be assessed as rather low. The vulnerability of the phases to variations in the biogeochemical and hydrochemical conditions enables relatively fast Fe mineral dissolution and therefore bears the danger of sudden release of As into GW when certain thresholds are exceeded. Especially the extensive mc Fe precipitates are able to influence the As and Fe cycle on short temporal scales. They have the potential to respond almost immediately to changes in advective flow or hydrochemical variations. Changes in advective flow, the GW level or the biogeochemical framework could destabilize the precipitates and release the stored contaminants. As the As-free GW down-stream the RTZ is used at least in agriculture and still partially as drinking water the As accumulation along the retardation front has to be evaluated as potentially dangerous and should carefully be taken into account with regard to local GW use. Dominance of As(III) species across the secondary precipitates (Table 10) implies a high mobility, toxicity and bioavailability of the toxic element should the secondary Fe carrier minerals disintegrate. As despite locally high As and P concentrations no phosphate or As minerals were found across the precipitations suggests As is entirely sorbed and embedded in the secondary Fe(III)-dominated precipitates. This finding is supported by various As-element correlations (Table 5). If the grey sands represent the final stage of the Fe mineral transformation sequence and only Mt remains as end product of the advancing redox front, the dissolution of the main As carrier phases would release almost all As into the GW. With regard to the biogeochemical cycle, the use of Fe as electron donor and acceptor most likely coupled to CH_4 and Mn cycling represents the dominant process controlling the aquifer As dynamic.

References

Abejón, R. & Garea, A. (2015). A bibliometric analysis of research on arsenic in drinking water during the 1992–2012 period: An outlook to treatment alternatives for arsenic removal. *Journal of water process engineering*, *6*, 105–119. https://doi.org/10.1016/j.jwpe.2015.03.009

Abernathy, C. R., Liu, Y. W., Longfellow, D., Aposhian, H. V., Beck, B., Fowler, B. A., Goyer, R. A., Menzer, R., Rossman, T., Thompson, C. & Waalkes, M. P. (1999). Arsenic: health effects, mechanisms of actions, and research issues. In *Environmental Health Perspectives* (Bd. 107, Nummer 7, S. 593–597). National Institute of Environmental Health Sciences. https://doi.org/10.1289/ehp.99107593

Acharyya, S. K., Chakraborty, P., Lahiri, S. K., Raymahashay, B. C., Guha, S. & Bhowmik, A. (1999). Arsenic poisoning in the Ganges delta. *Nature*, *401*(6753), 545. https://doi.org/10.1038/44052

Agusa, T., Kubota, R., Kunito, T., Minh, T. B., Trang, P. T. K., Chamnan, C., Iwata, H., Viet, P. H., Tana, T. S. & Tanabe, S. (2007). Arsenic Pollution in Groundwater of Vietnam and Cambodia : A Review. *Biomedical research on trace elements*, *18*(1), 35–47. https://doi.org/10.11299/brte.18.35

Agusa, T., Kunito, T., Kubota, R., Inoue, S., Fujihara, J., Minh, T. B., Ha, N. N., Tu, N. T., Trang, P. T. K., Chamnan, C., Takeshita, H., Iwata, H., Tuyen, B. C., Viet, P. H., Tana, T. S. & Tanabe, S. (2010). Exposure, Metabolism and Health effects of Arsenic in Residents of Arsenic-Contaminated Groundwater Areas of Vietnam and Cambodia: A Review. *Reviews on environmental health*, *25*(3). https://doi.org/10.1515/reveh.2010.25.3.193

Agusa, T., Trang, P. T. K., Lan, V. M., Anh, D. T., Tanabe, S., Viet, P. H. & Berg, M. (2014). Human exposure to arsenic from drinking water in Vietnam. *Science of The Total Environment*, *488–489*, 562–569. https://doi.org/10.1016/j.scitotenv.2013.10.039

Ahmad, A., Rutten, S., Eikelboom, M., De Waal, L., Bruning, H., Bhattacharya, P. & Van Der Wal, A. (2020). Impact of phosphate, silicate and natural organic matter on the size of Fe(III)

precipitates and arsenate co-precipitation efficiency in calcium containing water. *Separation and Purification Technology*, *235*, 116117. https://doi.org/10.1016/j.seppur.2019.116117

Ahmad, A., Van Der Wal, A., Bhattacharya, P. & Van Genuchten, C. M. (2019). Characteristics of Fe and Mn bearing precipitates generated by Fe(II) and Mn(II) co-oxidation with O2, MnO4 and HOCl in the presence of groundwater ions. *Water Research*, *161*, 505–516. https://doi.org/10.1016/j.watres.2019.06.036

Ahmed, K. M., Bhattacharya, P., Hasan, M. A., Akhter, S. H., Alam, S., Bhuyian, M., Imam, M. B., Khan, A. A. & Sracek, O. (2004). Arsenic enrichment in groundwater of the alluvial aquifers in Bangladesh: an overview. *Applied Geochemistry*, *19*(2), 181–200. https://doi.org/10.1016/j.apgeochem.2003.09.006

Akai, J., Izumi, K., Fukuhara, H., Masuda, H., Nakano, S., Yoshimura, T., Ohfuji, H., Anawar, H. M. & Akai, K. (2004). Mineralogical and geomicrobiological investigations on groundwater arsenic enrichment in Bangladesh. *Applied Geochemistry*, *19*(2), 215–230. https://doi.org/10.1016/j.apgeochem.2003.09.008

Akbar, A. (1998, 4. September). Arsenic-tainted water from Unicef wells is poisoning half of Bangladesh | The Independent. *The Independent*. https://www.independent.co.uk/news/arsenictainted-water-from-unicef-wells-is-poisoning-half-of-bangladesh-1196091.html

Alam, M. O., Shaikh, W. A., Chakraborty, S., Avishek, K. & Bhattacharya, T. (2016). Groundwater Arsenic Contamination and Potential Health Risk Assessment of Gangetic Plains of Jharkhand, India. *Exposure and health*, *8*(1), 125–142. https://doi.org/10.1007/s12403-015-0188-0

Alam, M. S., Allinson, G., Stagnitti, F., Tanaka, A. & Westbrooke, M. (2002). Arsenic contamination in Bangladesh groundwater: A major environmental and social disaster. *International Journal of Environmental Health Research*, *12*(3), 235–253. https://doi.org/10.1080/0960312021000000998

Aloisi, G., Bouloubassi, I., Heijs, S. K., Pancost, R. D., Pierre, C., Damsté, J. S. S., Gottschal, J. C., Forney, L. J. & Rouchy, J. (2002). CH 4 -consuming microorganisms and the formation of carbonate crusts at cold seeps. *Earth and Planetary Science Letters*, *203*(1), 195–203. https://doi.org/10.1016/s0012-821x(02)00878-6

Alpers, C. E., Nordstrom, D. K. & Spitzley, J. (2003). Extreme acid mine drainage from a pyritic massive sulfide deposit, the Iron Mountain end-member. *) Environmental Aspects of Mine Wastes (2003), Mineralogical Association of Canada Short-Course*, *v. 31, S. 407–430*, 407–430.

Amini, M., Abbaspour, K. C., Berg, M., Winkel, L. H. E., Hug, S. J., Hoehn, E., Yang, H. & Johnson, C. L. (2008). Statistical Modeling of Global Geogenic Arsenic Contamination in Groundwater. *Environmental Science & Technology*, *42*(10), 3669–3675. https://doi.org/10.1021/es702859e

An, B., Steinwinder, T. R. & Zhao, D. (2005). Selective removal of arsenate from drinking water using a polymeric ligand exchanger. *Water Research*, *39*(20), 4993–5004. https://doi.org/10.1016/j.watres.2005.10.014

Anderson, L. & Bruland, K. W. (1991). Biogeochemistry of arsenic in natural waters: the importance of methylated species. *Environmental Science & Technology*, *25*(3), 420–427. https://doi.org/10.1021/es00015a007

Antelo, J., Avena, M. J., Fiol, S., López, R. Q. & Arce, F. (2005). Effects of pH and ionic strength on the adsorption of phosphate and arsenate at the goethite–water interface. *Journal of Colloid and Interface Science*, *285*(2), 476–486. https://doi.org/10.1016/j.jcis.2004.12.032

Apata, M., Arriaza, B., Llop, E. & Moraga, M. (2017). Human adaptation to arsenic in Andean populations of the Atacama Desert. *American Journal of Physical Anthropology*, *163*(1), 192–199. https://doi.org/10.1002/ajpa.23193

Appelo, C. & Postma, D. J. (2004). Geochemistry, Groundwater and Pollution. *CRC Press eBooks*. https://doi.org/10.1201/9781439833544

Argos, M., Kalra, T., Rathouz, P. J., Chen, Y., Pierce, B. L., Parvez, F., Islam, T., Ahmed, A., Rakibuz-Zaman, M., Hasan, M. R., Sarwar, G., Slavkovich, V., Van Geen, A., Graziano, J. H. & Ahsan, H. (2010). Arsenic exposure from drinking water, and all-cause and chronic-disease mortalities in Bangladesh (HEALS): a prospective cohort study. *The Lancet*, *376*(9737), 252–258. https://doi.org/10.1016/s0140-6736(10)60481-3

Aromokeye, D. A., Kulkarni, A., Elvert, M., Wegener, G., Henkel, S., Coffinet, S., Eickhorst, T., Oni, O. E., Richter-Heitmann, T., Schnakenberg, A., Taubner, H., Wunder, L. C., Yin, X., Zhu, Q., Hinrichs, K., Kasten, S. & Friedrich, M. W. (2020). Rates and Microbial Players of Iron-Driven Anaerobic Oxidation of Methane in Methanic Marine Sediments. *Frontiers in Microbiology*, *10*. https://doi.org/10.3389/fmicb.2019.03041

Atkinson, C. A., Jolley, D. F. & Simpson, S. L. (2007). Effect of overlying water pH, dissolved oxygen, salinity and sediment disturbances on metal release and sequestration from metal contaminated marine sediments. *Chemosphere*, *69*(9), 1428–1437. https://doi.org/10.1016/j.chemosphere.2007.04.068

Banfield, J. F., Welch, S., Zhang, H., Ebert, T. T. & Penn, R. L. (2000). Aggregation-Based Crystal Growth and Microstructure Development in Natural Iron Oxyhydroxide Biomineralization Products. *Science*, *289*(5480), 751–754. https://doi.org/10.1126/science.289.5480.751

Banning, A., Rüde, T. R. & Dölling, B. (2013). Crossing redox boundaries—Aquifer redox history and effects on iron mineralogy and arsenic availability. *Journal of Hazardous Materials*, *262*, 905–914. https://doi.org/10.1016/j.jhazmat.2012.12.015

Battling Arsenic Poisoning in Southeast Asia. (2018, 22. September). Columbia University Irving Medical Center. https://www.cuimc.columbia.edu/news/battling-arsenic-poisoning-southeast-asia

Bauer, M. & Blodau, C. (2006). Mobilization of arsenic by dissolved organic matter from iron oxides, soils and sediments. *Science of The Total Environment*, *354*(2–3), 179–190. https://doi.org/10.1016/j.scitotenv.2005.01.027

Beal, E. J., House, C. H. & Orphan, V. J. (2009). Manganese- and Iron-Dependent Marine Methane Oxidation. *Science*, *325*(5937), 184–187. https://doi.org/10.1126/science.1169984

Behrends, T. & Van Cappellen, P. (2007). Transformation of Hematite into Magnetite During Dissimilatory Iron Reduction—Conditions and Mechanisms. *Geomicrobiology Journal*, *24*(5), 403–416. https://doi.org/10.1080/01490450701436497

Benner, S. G. & Fendorf, S. (2010). Arsenic in South Asia Groundwater. *Geography Compass*, *4*(10), 1532–1552. https://doi.org/10.1111/j.1749-8198.2010.00387.x

Benner, S. G., Hansel, C. M., Wielinga, B. W., Barber, T. M. & Fendorf, S. (2002). Reductive Dissolution and Biomineralization of Iron Hydroxide under Dynamic Flow Conditions. *Environmental Science & Technology*, *36*(8), 1705–1711. https://doi.org/10.1021/es0156441

Berg, M. (2007). Arsenic Contamination of Groundwater and Drinking Water in the Red River Delta, Vietnam: Geochemical Investigations and Mitigation Measures. *DISSERTATION*. https://doi.org/10.5445/ir/1000007320

Berg, M., Luzi, S., Trang, P. T. K., Viet, P. H., Giger, W. & Stüben, D. (2006). Arsenic Removal from Groundwater by Household Sand Filters: Comparative Field Study, Model Calculations, and Health Benefits. *Environmental Science & Technology*, *40*(17), 5567–5573. https://doi.org/10.1021/es060144z

Berg, M., Stengel, C., Trang, P. T. K., Viet, P. H., Sampson, M. L., Leng, M., Samreth, S. & Fredericks, D. F. (2007). Magnitude of arsenic pollution in the Mekong and Red River Deltas — Cambodia and Vietnam. *Science of The Total Environment*, *372*(2–3), 413–425. https://doi.org/10.1016/j.scitotenv.2006.09.010

Berg, M., Tran, H. N., Nguyen, T. H. O., Pham, H., Schertenleib, R. & Giger, W. (2001). Arsenic Contamination of Groundwater and Drinking Water in Vietnam: A Human Health Threat. *Environmental Science & Technology*, *35*(13), 2621–2626. https://doi.org/10.1021/es010027y

Berg, M., Trang, P. T. K., Stengel, C., Buschmann, J., Viet, P. H., Van Dan, N., Giger, W. & Stüben, D. (2008). Hydrological and sedimentary controls leading to arsenic contamination of groundwater in the Hanoi area, Vietnam: The impact of iron-arsenic ratios, peat, river bank deposits, and excessive groundwater abstraction. *Chemical Geology*, *249*(1–2), 91–112. https://doi.org/10.1016/j.chemgeo.2007.12.007

Berner, R. A. (1970). Sedimentary pyrite formation. *American Journal of Science*, *268*(1), 1–23. https://doi.org/10.2475/ajs.268.1.1

Berner, R. A. (1984). Sedimentary pyrite formation: An update. *Geochimica et Cosmochimica Acta*, *48*(4), 605–615. https://doi.org/10.1016/0016-7037(84)90089-9

Berquó, T. S., Imbernon, R. A. L., Blot, A., Franco, D. R., De Toledo, M. C. M. & De Moya Partiti, C. S. (2007). Low temperature magnetism and Mössbauer spectroscopy study from natural goethite. *Physics and Chemistry of Minerals*, *34*(5), 287–294. https://doi.org/10.1007/s00269-007-0147-9

Bhattacharya, P., Chatterjee, D. & Jacks, G. (1997). Occurrence of Arsenic-contaminatedGroundwater in Alluvial Aquifers from Delta Plains, Eastern India: Options for Safe Drinking Water Supply. *International Journal of Water Resources Development*, *13*(1), 79–92. https://doi.org/10.1080/07900629749944

Bhumbla, D. K. & Keefer, R. F. (1994). Arsenic mobilization and bioavailability in soils. *J. O. Nriagu, Ed., Arsenic in the Environment*, *Part I: Cycling and Characterization*.

Bigham, J. M., Golden, D. C., Bowen, L. H., Buol, S. W. & Weed, S. B. (1978). Iron Oxide Mineralogy of Well-drained Ultisols and Oxisols: I. Characterization of Iron Oxides in Soil Clays by Mössbauer Spectroscopy, X-ray Diffractometry, and Selected Chemical Techniques. *Soil Science Society of America Journal*, *42*(5), 816–825. https://doi.org/10.2136/sssaj1978.03615995004200050033x

Biswas, A., Biswas, S., Das, A. & Roychowdhury, T. (2018). Spatial variability and competing dynamics of arsenic, selenium, iron and bioavailable phosphate from ground water and soil to paddy

plant parts. *Groundwater for Sustainable Development*, *7*, 328–335. https://doi.org/10.1016/j.gsd.2018.08.001

Blood, D. K. & Lash, G. G. (2015). Dynamic redox conditions in the Marcellus Shale as recorded by pyrite framboid size distributions. *Special papers*, 153–168. https://doi.org/10.1130/2015.2515(08

Bobo, X., Graham, N. & Yu, W. (2020). Transformation of siderite to goethite by humic acid in the natural environment. *Communications chemistry*, *3*(1). https://doi.org/10.1038/s42004-020-0284-3

Bond, D. & Wignall, P. B. (2010). Pyrite framboid study of marine Permian–Triassic boundary sections: A complex anoxic event and its relationship to contemporaneous mass extinction. *Geological Society of America Bulletin*, *122*(7–8), 1265–1279. https://doi.org/10.1130/b30042.1

Bone, S. E., Gonneea, M. E. & Charette, M. A. (2006). Geochemical Cycling of Arsenic in a Coastal Aquifer. *Environmental Science & Technology*, *40*(10), 3273–3278. https://doi.org/10.1021/es052352h

Bonneville, S., Van Cappellen, P. & Behrends, T. (2004). Microbial reduction of iron(III) oxyhydroxides: effects of mineral solubility and availability. *Chemical Geology*, *212*(3–4), 255–268. https://doi.org/10.1016/j.chemgeo.2004.08.015

Borch, T., Kretzschmar, R., Kappler, A., Van Cappellen, P., Ginder-Vogel, M., Voegelin, A. & Campbell, K. M. (2010). Biogeochemical Redox Processes and their Impact on Contaminant Dynamics. *Environmental Science & Technology*, *44*(1), 15–23. https://doi.org/10.1021/es9026248

Borggaard, O. K. (1983). Effect of Surface Area and Mineralogy of Iron Oxides on Their Surface Charge and Anion-Adsorption Properties. *Clays and Clay Minerals*, *31*(3), 230–232. https://doi.org/10.1346/ccmn.1983.0310309

Bostick, B. C., Chen, C. & Fendorf, S. (2004). Arsenite Retention Mechanisms within Estuarine Sediments of Pescadero, CA. *Environmental Science & Technology*, *38*(12), 3299–3304. https://doi.org/10.1021/es035006d

Bostick, B. C. & Fendorf, S. (2003). Arsenite sorption on troilite (FeS) and pyrite (FeS2). *Geochimica et Cosmochimica Acta*, *67*(5), 909–921. https://doi.org/10.1016/s0016-7037(02)01170-5

Bostick, B. C., Harvey, C. F., Stahl, M., Oates, P. M., L, V., Nguyen, M., Viet, P. H., Trang, P., Berg, M. P., Stengel, C. & Van Geen, A. (2010). Distribution of Arsenic Sulfides in Van Phuc, Vietnam, and Their Relationship to Aquifer Arsenic Concentrations. *AGUFM*, *2010*. http://adsabs.harvard.edu/abs/2010AGUFM.H41H1200B

Botto, I. L., González, M. J. G., Gazzoli, D. & Soto, E. L. (2013). Iron Activation of Natural Aluminosilicates to Remove Arsenic from Groundwater. *Journal of environmental science & engineering*. https://doi.org/10.17265/2162-5298/2013.12.006

Bowell, R. (1994). Sorption of arsenic by iron oxides and oxyhydroxides in soils. *Applied Geochemistry*, *9*(3), 279–286. https://doi.org/10.1016/0883-2927(94)90038-8

Bowell, R., Alpers, C. E., Jamieson, H. E., Nordstrom, D. K. & Majzlan, J. (2014). The Environmental Geochemistry of Arsenic -- An Overview --. *Reviews in mineralogy and geochemistry*, *79*(1), 1–16. https://doi.org/10.2138/rmg.2014.79.1

Bowen, H. J. M., Ure, A. M. & Berrow, M. L. (1982). The elemental constituents of soils. *The Royal Society of Chemistry eBooks*, 94–204. https://doi.org/10.1039/9781847555991-00094

Boyle, R. & Jonasson, I. R. (1973). The geochemistry of arsenic and its use as an indicator element in geochemical prospecting. *Journal of Geochemical Exploration*, *2*(3), 251–296. https://doi.org/10.1016/0375-6742(73)90003-4

Brannon, J. M. & Patrick, W. L. (1987). Fixation, transformation, and mobilization of arsenic in sediments. *Environmental Science & Technology*, *21*(5), 450–459. https://doi.org/10.1021/es00159a005

Bretzler, A., Lalanne, F., Nikiema, J., Podgorski, J., Pfenninger, N., Berg, M. & Schirmer, M. (2017). Groundwater arsenic contamination in Burkina Faso, West Africa: Predicting and verifying regions at risk. *Science of The Total Environment*, *584–585*, 958–970. https://doi.org/10.1016/j.scitotenv.2017.01.147

Brinkel, J., Khan, M. H. & Kraemer, A. (2009). A Systematic Review of Arsenic Exposure and Its Social and Mental Health Effects with Special Reference to Bangladesh. *International Journal of Environmental Research and Public Health*, *6*(5), 1609–1619. https://doi.org/10.3390/ijerph6051609

Brinkman, R. (1970). Ferrolysis, a hydromorphic soil forming process. *Geoderma*, *3*(3), 199–206. https://doi.org/10.1016/0016-7061(70)90019-4

British Geological Survey. (1996). *The effect of urbanisation on the groundwater quality beneath the city of Hanoi, Vietnam - NERC Open Research Archive*. https://nora.nerc.ac.uk/id/eprint/21403/

British Geological Survey (BGS). (2001). *Arsenic Contamination of Groundwater in Bangladesh: Final report*.

Bryce, C., Blackwell, N., Schmidt, C., Otte, J. M., Huang, Y., Kleindienst, S., Tomaszewski, E. J., Schad, M., Warter, V., Peng, C., Byrne, J. M. & Kappler, A. (2018). Microbial anaerobic Fe(II) oxidation - Ecology, mechanisms and environmental implications. *Environmental Microbiology*, *20*(10), 3462–3483. https://doi.org/10.1111/1462-2920.14328

Bundschuh, J., Farias, B., Martin, R. M., Del R Storniolo, A., Bhattacharya, P., Cortes, J. E., Bonorino, G. G. & Albouy, R. (2004). Groundwater arsenic in the Chaco-Pampean Plain, Argentina. *Applied Geochemistry*, *19*(2), 231–243. https://doi.org/10.1016/j.apgeochem.2003.09.009

Bundschuh, J. & Maity, J. P. (2015). Geothermal arsenic: Occurrence, mobility and environmental implications. *Renewable & Sustainable Energy Reviews*, *42*, 1214–1222. https://doi.org/10.1016/j.rser.2014.10.092

Butler, I. S. & Rickard, D. (2000). Framboidal pyrite formation via the oxidation of iron (II) monosulfide by hydrogen sulphide. *Geochimica et Cosmochimica Acta*, *64*(15), 2665–2672. https://doi.org/10.1016/s0016-7037(00)00387-2

Cai, C., Leu, A. O., Xie, G., Guo, J., Feng, Y., Zhao, J., Tyson, G. W., Yuan, Z. & Hu, S. (2018). A methanotrophic archaeon couples anaerobic oxidation of methane to Fe(III) reduction. *The ISME Journal*, *12*(8), 1929–1939. https://doi.org/10.1038/s41396-018-0109-x

Caldeira, C. L., Ciminelli, V. S. T. & Osseo-Asare, K. A. (2010). The role of carbonate ions in pyrite oxidation in aqueous systems. *Geochimica et Cosmochimica Acta*, *74*(6), 1777–1789. https://doi.org/10.1016/j.gca.2009.12.014

Callegari, A., Torretta, V., Rada, E. C. & Capodaglio, A. G. (2018). Assessment of arsenic removal efficiency by an iron oxide-coated sand filter process. *Environmental Science and Pollution Research*, *25*(26), 26135–26143. https://doi.org/10.1007/s11356-018-2674-y

Campbell, K. M. & Nordstrom, D. K. (2014). Arsenic Speciation and Sorption in Natural Environments. *Reviews in mineralogy and geochemistry*, *79*(1), 185–216. https://doi.org/10.2138/rmg.2014.79.3

Carlson, L. & Schwertmann, U. (1981). Natural ferrihydrites in surface deposits from Finland and their association with silica. *Geochimica et Cosmochimica Acta*, *45*(3), 421–429. https://doi.org/10.1016/0016-7037(81)90250-7

Catalano, J. G., Luo, Y. & Otemuyiwa, B. (2011). Effect of Aqueous Fe(II) on Arsenate Sorption on Goethite and Hematite. *Environmental Science & Technology*, *45*(20), 8826–8833. https://doi.org/10.1021/es202445w

Cavalazzi, B., Barbieri, R., Cady, S. L., George, A. D., Gennaro, S., Westall, F., Lui, A., Canteri, R., Rossi, A. P., Ori, G. G. & Taj-Eddine, K. (2012). Iron-framboids in the hydrocarbon-related Middle Devonian Hollard Mound of the Anti-Atlas mountain range in Morocco: Evidence of potential microbial biosignatures. *Sedimentary Geology*, *263–264*, 183–193. https://doi.org/10.1016/j.sedgeo.2011.09.007

Chakraborti, D., Rahman, M. M., Das, B., Prakash, S., Das, D., Nayak, B., Pal, A. K., Chowdhury, U. K., Ahmed, S., Biswas, B. K., Sengupta, M. K., Hossain, A., Samanta, G., R., Dutta, R. N., Saha, K. C., Mukherjee, S., Pati, S., Kar, P. B., . . . Sharma, M. (2017). Groundwater arsenic contamination and its health effects in India. *Hydrogeology Journal*, *25*(4), 1165–1181. https://doi.org/10.1007/s10040-017-1556-6

Chakraborti, D., Rahman, M. M., Mukherjee, A., Alauddin, M., Hassan, M. M., Dutta, R. N., Pati, S., Mukherjee, S. C., Roy, S., Quamruzzman, Q., Rahman, M., Morshed, S., Islam, T., Sorif, S. M., Selim, M., Islam, M. R. & Hossain, M. M. (2015). Groundwater arsenic contamination in Bangladesh—21 Years of research. *Journal of Trace Elements in Medicine and Biology*, *31*, 237–248. https://doi.org/10.1016/j.jtemb.2015.01.003

Chakraborty, M., Mukherjee, A. & Ahmed, K. M. (2015). A Review of Groundwater Arsenic in the Bengal Basin, Bangladesh and India: from Source to Sink. *Current pollution reports*, *1*(4), 220–247. https://doi.org/10.1007/s40726-015-0022-0

Chakraborty, S., Nath, B., Chatterjee, D. & Charlet, L. (2014). Retardation of arsenic transport by oxidized Holocene aquifer sediments of West Bengal, India. *Journal of Hydrology*, *518*, 460–463. https://doi.org/10.1016/j.jhydrol.2013.07.028

Chan, C. C., Fakra, S. C., Edwards, D., Emerson, D. R. & Banfield, J. F. (2009). Iron oxyhydroxide mineralization on microbial extracellular polysaccharides. In *Geochimica et Cosmochimica Acta* (Bd. 73, Nummer 13, S. 3807–3818). Elsevier BV. https://doi.org/10.1016/j.gca.2009.02.036

Chan, C. C., Fakra, S. C., Emerson, D. R., Fleming, E. J. & Edwards, K. J. (2011). Lithotrophic iron-oxidizing bacteria produce organic stalks to control mineral growth: implications for biosignature formation. *The ISME Journal*, *5*(4), 717–727. https://doi.org/10.1038/ismej.2010.173

Chapelle, F. H. (2000). *Ground-Water Microbiology and Geochemistry*. John Wiley & Sons.

Charette, M. A. & Sholkovitz, E. R. (2002). Oxidative precipitation of groundwater-derived ferrous iron in the subterranean estuary of a coastal bay. *Geophysical Research Letters*, *29*(10), 85–4. https://doi.org/10.1029/2001gl014512

Charlet, L., Morin, G., Rose, J., Wang, Y., Auffan, M., Burnol, A. & Fernandez-Martinez, A. (2011). Reactivity at (nano)particle-water interfaces, redox processes, and arsenic transport in the environment. In *Comptes Rendus Geoscience* (Bd. 343, Nummern 2–3, S. 123–139). Elsevier BV. https://doi.org/10.1016/j.crte.2010.11.005

Charlet, L. & Polya, D. A. (2006). Arsenic in Shallow, Reducing Groundwaters in Southern Asia: An Environmental Health Disaster. *Elements*, *2*(2), 91–96. https://doi.org/10.2113/gselements.2.2.91

Châtellier, X., West, M. M., Rose, J., Fortin, D., Leppard, G. G. & Ferris, F. G. (2004). Characterization of Iron-Oxides Formed by Oxidation of Ferrous Ions in the Presence of Various Bacterial Species and Inorganic Ligands. *Geomicrobiology Journal*, *21*(2), 99–112. https://doi.org/10.1080/01490450490266343

Chatterjee, S., Moogoui, R. & Gupta, D. K. (2017). Arsenic: Source, Occurrence, Cycle, and Detection. *Springer eBooks*, 13–35. https://doi.org/10.1007/978-3-319-54356-7_2

Chaudhuri, S. K., Lack, J. G. & Coates, J. D. (2001). Biogenic Magnetite Formation through Anaerobic Biooxidation of Fe(II). *Applied and Environmental Microbiology*, *67*(6), 2844–2848. https://doi.org/10.1128/aem.67.6.2844-2848.2001

Chen, C., Chen, C., Wu, M. C. & Kuo, T. (1992). Cancer potential in liver, lung, bladder and kidney due to ingested inorganic arsenic in drinking water. *British Journal of Cancer*, *66*(5), 888–892. https://doi.org/10.1038/bjc.1992.380

Chen, C. & Wu, H. (1962). Epidemiologic studies on blackfoot disease. 2. A study of source of drinking water in relation to the disease. *Journal of the Formosan Medical Association*, *61*, 611–618.

Chen, G., Hofstetter, T. B. & Gorski, C. A. (2020). Role of Carbonate in Thermodynamic Relationships Describing Pollutant Reduction Kinetics by Iron Oxide-Bound Fe2+. *Environmental Science & Technology*, *54*(16), 10109–10117. https://doi.org/10.1021/acs.est.0c02959

Chen, M., Mai, L. & Harris, W. G. (2002). Arsenic Concentrations in Florida Surface Soils. *Soil Science Society of America Journal*, *66*(2), 632–640. https://doi.org/10.2136/sssaj2002.6320

Chen, Y., Wu, F., Liu, M., Parvez, F., Slavkovich, V., Eunus, M., Ahmed, A., Argos, M., Islam, T., Rakibuz-Zaman, M., Hasan, M. R., Sarwar, G., Levy, D., Graziano, J. H. & Ahsan, H. (2013). A Prospective Study of Arsenic Exposure, Arsenic Methylation Capacity, and Risk of Cardiovascular Disease in Bangladesh. *Environmental Health Perspectives*, *121*(7), 832–838. https://doi.org/10.1289/ehp.1205797

Chiban, M., Zerbet, M., Carja, G. & Sinan, F. (2012). Application of low-cost adsorbents for arsenic removal: A review. *Journal of Environmental Chemistry and Ecotoxicology*, *4*(5). https://doi.org/10.5897/jece11.013

Chowdhury, T. R., Basu, G., Mandal, B. K., Biswas, B. K., Samanta, G., Chowdhury, U. K., Chanda, C. R., Lodh, D., Roy, S., Saha, K. C., Roy, S., Kabir, S., Quamruzzaman, Q. & Chakraborti, D. (1999). Arsenic poisoning in the Ganges delta. *Nature*, *401*(6753), 545–546. https://doi.org/10.1038/44056

Cismasu, A. C., Michel, F., Stebbins, J. F., Levard, C. & Brown, G. E. (2012). Properties of impurity-bearing ferrihydrite I. Effects of Al content and precipitation rate on the structure of 2-line ferrihydrite. *Geochimica et Cosmochimica Acta*, *92*, 275–291. https://doi.org/10.1016/j.gca.2012.06.010

Cismasu, A. C., Williams, K. S. & Nico, P. S. (2016). Iron and Carbon Dynamics during Aging and Reductive Transformation of Biogenic Ferrihydrite. *Environmental Science & Technology*, *50*(1), 25–35. https://doi.org/10.1021/acs.est.5b03021

Clark, M. R., Schoenbohm, L. M., Royden, L. H., Whipple, K. X., Burchfiel, B. C., Zhang, X. Y., Tang, W. W., Wang, E. & Chen, L. Q. (2004). Surface uplift, tectonics, and erosion of eastern Tibet from large-scale drainage patterns. *Tectonics*, *23*(1), n/a. https://doi.org/10.1029/2002tc001402

Cornell, R. M. & Giovanoli, R. (1988). The influence of copper on the transformation of ferrihydrite (5Fe2O3 · 9H2O) into crystalline products in alkaline media. In *Polyhedron* (Bd. 7, Nummer 5, S. 385–391). Elsevier BV. https://doi.org/10.1016/s0277-5387(00)80487-8

Cornell, R. M. & Schwertmann, U. (2003). *The Iron Oxides: Structure, Properties, Reactions, Occurrences and Uses*. John Wiley & Sons.

Cozzarelli, I. M. & Weiss, J. (2007). Biogeochemistry of Aquifer Systems. *Manual of Environmental Microbiology*, 843–859. https://doi.org/10.1128/9781555815882.ch68

Cullen, W. R. & Reimer, K. J. (1989). Arsenic speciation in the environment. *Chemical Reviews*, *89*(4), 713–764. https://doi.org/10.1021/cr00094a002

Cummings, D. E., Caccavo, F., Fendorf, A. S. & Rosenzweig, R. F. (1999). Arsenic Mobilization by the Dissimilatory Fe(III)-Reducing Bacterium *Shewanella alga* BrY. *Environmental Science & Technology*, *33*(5), 723–729. https://doi.org/10.1021/es980541c

Curtis, C. D. & Spears, D. A. (1968). The formation of sedimentary iron minerals. *Economic geology and the bulletin of the Society of Economic Geologists*, *63*(3), 257–270. https://doi.org/10.2113/gsecongeo.63.3.257

Dang, V. H., Doubre, C., Weber, C., Gourmelen, N. & Masson, F. (2014). Recent land subsidence caused by the rapid urban development in the Hanoi region (Vietnam) using ALOS InSAR data. *Natural Hazards and Earth System Sciences*, *14*(3), 657–674. https://doi.org/10.5194/nhess-14-657-2014

Das, D., Samanta, G., Mandal, B. N., T, R. C., Chanda, C. R., Chowdhury, P., Basu, G. & Chakraborti, D. (1996). Arsenic in groundwater in six districts of West Bengal, India. *Environmental Geochemistry and Health*, *18*(1), 5–15. https://doi.org/10.1007/bf01757214

Datta, S., Mailloux, B. J., Jung, H., Hoque, M., Stute, M., Ahmed, K. M. & Zheng, Y. H. (2009). Redox trapping of arsenic during groundwater discharge in sediments from the Meghna riverbank in Bangladesh. *Proceedings of the National Academy of Sciences of the United States of America*, *106*(40), 16930–16935. https://doi.org/10.1073/pnas.0908168106

Dearing, J. (1999). Environmental Magnetic Susceptibility. Using the Bartington MS2 System (Second Edition). *Hi Publishing, England*, *54 pp*.

Devi, R. R., Umlong, I. M., Das, B., Borah, K., Thakur, A. J., Raul, P. K., Banerjee, S. & Singh, L. (2014). Removal of iron and arsenic (III) from drinking water using iron oxide-coated sand and limestone. *Applied Water Science*, *4*(2), 175–182. https://doi.org/10.1007/s13201-013-0139-5

Ding, H., Yao, S. & Chen, J. (2014). Authigenic pyrite formation and re-oxidation as an indicator of an unsteady-state redox sedimentary environment: Evidence from the intertidal mangrove sediments of Hainan Island, China. *Continental Shelf Research*, *78*, 85–99. https://doi.org/10.1016/j.csr.2014.02.011

Dixit, S. & Hering, J. G. (2003). Comparison of Arsenic(V) and Arsenic(III) Sorption onto Iron Oxide Minerals: Implications for Arsenic Mobility. *Environmental Science & Technology*, *37*(18), 4182–4189. https://doi.org/10.1021/es030309t

Dong, H., Fredrickson, J. K., Kennedy, D. N., Zachara, J. M., Kukkadapu, R. K. & Onstott, T. C. (2000). Mineral transformations associated with the microbial reduction of magnetite. *Chemical Geology*, *169*(3–4), 299–318. https://doi.org/10.1016/s0009-2541(00)00210-2

Dong, H., Kukkadapu, R. K., Fredrickson, J. K., Zachara, J. M., Kennedy, D. N. & Kostandarithes, H. M. (2003). Microbial Reduction of Structural Fe(III) in Illite and Goethite. *Environmental Science & Technology*, *37*(7), 1268–1276. https://doi.org/10.1021/es020919d

Dowdle, P. R., Laverman, A. M. & Oremland, R. S. (1996). Bacterial Dissimilatory Reduction of Arsenic(V) to Arsenic(III) in Anoxic Sediments. *Applied and Environmental Microbiology*, *62*(5), 1664–1669. https://doi.org/10.1128/aem.62.5.1664-1669.1996

Dowling, C., Poreda, R. J., Basu, A. R., Peters, S. L. & Aggarwal, P. (2002). Geochemical study of arsenic release mechanisms in the Bengal Basin groundwater. *Water Resources Research*, *38*(9), 12–18. https://doi.org/10.1029/2001wr000968

Drahota, P. & Filippi, M. (2009). Secondary arsenic minerals in the environment: A review. *Environment International*, *35*(8), 1243–1255. https://doi.org/10.1016/j.envint.2009.07.004

Du Bui, D., Kawamura, A., Tong, T. N., Amaguchi, H. & Trinh, T. T. (2012). Aquifer system for potential groundwater resources in Hanoi, Vietnam. *Hydrological Processes*, *26*(6), 932–946. https://doi.org/10.1002/hyp.8305

Duker, A. A., Carranza, E. J. M. & Hale, M. (2005). Arsenic geochemistry and health. *Environment International*, *31*(5), 631–641. https://doi.org/10.1016/j.envint.2004.10.020

Dunlop, D. J. & Özdemir, Ö. (1997). Rock Magnetism. *Fundamentals and Frontiers. Cambridge University Press, Cambridge.* https://doi.org/10.1017/cbo9780511612794

Dunlop, D. J. & Özdemir, Ö. (2007). Magnetizations in Rocks and Minerals. *Elsevier EBooks*, 277–336. https://doi.org/10.1016/b978-044452748-6.00093-6

Eary, L. E. & Schramke, J. A. (1990). Rates of Inorganic Oxidation Reactions Involving Dissolved Oxygen. *Acs Symposium Series*, 379–396. https://doi.org/10.1021/bk-1990-0416.ch030

Egger, M., Lenstra, W. K., Jong, D., Meysman, F. J. R., Sapart, C., Van Der Veen, C., Röckmann, T., Gonzalez, S. F. & Slomp, C. P. (2016). Rapid Sediment Accumulation Results in High Methane Effluxes from Coastal Sediments. *PLOS ONE*, *11*(8), e0161609. https://doi.org/10.1371/journal.pone.0161609

Eiche, E. (2009). *Arsenic Mobilization Processes in the Red River Delta, Vietnam: Towards a Better Understanding of the Patchy Distribution of Dissolved Arsenic in Alluvial Deposits*. KIT Scientific Publishing.

Eiche, E. (2010). Arsenic mobilization processes in the red river delta, Vietnam: towards a better understanding of the patchy distribution of dissolved arsenic in alluvial deposits. *Karlsruher*

Mineralogische Und Geochemische Hefte Schriftenreihe Des Instituts Für Mineralogie Und Geochemie.

Eiche, E., Neumann, T., Berg, M., Weinman, B., Van Geen, A., Norra, S., Berner, Z., Trang, P. T. K., Viet, P. H. & Stüben, D. (2008). Geochemical processes underlying a sharp contrast in groundwater arsenic concentrations in a village on the Red River delta, Vietnam. *Applied Geochemistry*, *23*(11), 3143–3154. https://doi.org/10.1016/j.apgeochem.2008.06.023

Elizalde-González, M. P., Mattusch, J., Einicke, W. & Wennrich, R. (2001). Sorption on natural solids for arsenic removal. *Chemical Engineering Journal*, *81*(1–3), 187–195. https://doi.org/10.1016/s1385-8947(00)00201-1

Emerson, D. R., Fleming, E. J. & McBeth, J. (2010). Iron-Oxidizing Bacteria: An Environmental and Genomic Perspective. *Annual Review of Microbiology*, *64*(1), 561–583. https://doi.org/10.1146/annurev.micro.112408.134208

Emerson, D. R. & Floyd, M. (2005). Enrichment and Isolation of Iron-Oxidizing Bacteria at Neutral pH. *Methods in Enzymology*, 112–123. https://doi.org/10.1016/s0076-6879(05)97006-7

Esther, J., Sukla, L. B., Pradhan, N. & Panda, S. (2015). Fe (III) reduction strategies of dissimilatory iron reducing bacteria. *Korean Journal of Chemical Engineering*, *32*(1), 1–14. https://doi.org/10.1007/s11814-014-0286-x

Ettwig, K. F., Zhu, B., Speth, D. R., Keltjens, J. T., Jetten, M. S. M. & Kartal, B. (2016). Archaea catalyze iron-dependent anaerobic oxidation of methane. *Proceedings of the National Academy of Sciences of the United States of America*, *113*(45), 12792–12796. https://doi.org/10.1073/pnas.1609534113

Farquhar, M., Charnock, J. M., Livens, F. R. & Vaughan, D. G. (2002). Mechanisms of arsenic uptake from aqueous solution by interaction with goethite, lepidocrocite, mackinawite, and pyrite: an X-ray absorption spectroscopy study. *Environmental Science & Technology*, *36*(8), 1757–1762. https://doi.org/10.1021/es010216g

Fendorf, S., Eick, M. J., Grossl, P. R. & Sparks, D. L. (1997). Arsenate and Chromate Retention Mechanisms on Goethite. 1. Surface Structure. *Environmental Science & Technology*, *31*(2), 315–320. https://doi.org/10.1021/es950653t

Fendorf, S., Michael, H. A. & Van Geen, A. (2010). Spatial and Temporal Variations of Groundwater Arsenic in South and Southeast Asia. *Science*, *328*(5982), 1123–1127. https://doi.org/10.1126/science.1172974

Fendorf, S., Nico, P. S., Kocar, B. D., Masue, Y. & Tufano, K. J. (2010). Arsenic Chemistry in Soils and Sediments. *Elsevier eBooks*, 357–378. https://doi.org/10.1016/s0166-2481(10)34012-8

Ferris, F. G. (2005). Biogeochemical Properties of Bacteriogenic Iron Oxides. *Geomicrobiology Journal*, *22*(3–4), 79–85. https://doi.org/10.1080/01490450590945861

Filippi, M., Doušová, B. & Machovič, V. (2007). Mineralogical speciation of arsenic in soils above the Mokrsko-west gold deposit, Czech Republic. *Geoderma*, *139*(1–2), 154–170. https://doi.org/10.1016/j.geoderma.2007.01.015

Fitz, W. J. & Wenzel, W. W. (2002). Arsenic transformations in the soil–rhizosphere–plant system: fundamentals and potential application to phytoremediation. *Journal of Biotechnology*, *99*(3), 259–278. https://doi.org/10.1016/s0168-1656(02)00218-3

Fordham, A., Merry, R. & Norrish, K. (1984). Occurrence of microcrystalline goethite in an unusual fibrous form. *Geoderma*, *34*(2), 135–148. https://doi.org/10.1016/0016-7061(84)90018-1

Fordham, A. & Norrish, K. (1983). The nature of soil particles particularly those reacting with arsenate in a series of chemically treated samples. *Soil Research*. https://doi.org/10.1071/sr9830455

Fortin, D. & Langley, S. (2005). Formation and occurrence of biogenic iron-rich minerals. *Earth-Science Reviews*, *72*(1–2), 1–19. https://doi.org/10.1016/j.earscirev.2005.03.002

Fortin, D., Leppard, G. G. & Tessier, A. (1993). Characteristics of lacustrine diagenetic iron oxyhydroxides. *Geochimica et Cosmochimica Acta*, *57*(18), 4391–4404. https://doi.org/10.1016/0016-7037(93)90490-n

Fox, L. E. (1989). A model for inorganic control of phosphate concentrations in river waters. *Geochimica et Cosmochimica Acta*, *53*(2), 417–428. https://doi.org/10.1016/0016-7037(89)90393-1

Francisco, P. W., Sato, T., Otake, T. & Kasama, T. (2016). Kinetics of Fe3+mineral crystallization from ferrihydrite in the presence of Si at alkaline conditions and implications for nuclear waste disposal. *American Mineralogist*, *101*(9), 2057–2069. https://doi.org/10.2138/am-2016-5589

Frankenberger, W. T. (2002). Environmental Chemistry of Arsenic. *CRC Press eBooks*. https://doi.org/10.1201/9781482271102

Fredrickson, J. K., Zachara, J. M., Kennedy, D. N., Dong, H., Onstott, T. C., Hinman, N. W. & Li, S. (1998). Biogenic iron mineralization accompanying the dissimilatory reduction of hydrous ferric oxide by a groundwater bacterium. *Geochimica et Cosmochimica Acta*, *62*(19–20), 3239–3257. https://doi.org/10.1016/s0016-7037(98)00243-9

Fritzsche, A., Schröder, C., Wieczorek, A. K., Händel, M., Ritschel, T. & Totsche, K. U. (2015). Structure and composition of Fe–OM co-precipitates that form in soil-derived solutions. *Geochimica et Cosmochimica Acta*, *169*, 167–183. https://doi.org/10.1016/j.gca.2015.07.041

Froelich, P. N., Klinkhammer, G. P., Bender, M. L., Luedtke, N. A., Heath, G., Cullen, D., Dauphin, P., Hammond, D., Hartman, B. & Maynard, V. (1979). Early oxidation of organic matter in pelagic sediments of the eastern equatorial Atlantic: suboxic diagenesis. *Geochimica et Cosmochimica Acta*, *43*(7), 1075–1090. https://doi.org/10.1016/0016-7037(79)90095-4

Funabiki, A., Haruyama, S., Van Quy, N., Pham, V. H. & Mai, D. T. T. (2007). Holocene delta plain development in the Song Hong (Red River) delta, Vietnam. *Journal of Asian Earth Sciences*, *30*(3–4), 518–529. https://doi.org/10.1016/j.jseaes.2006.11.013

Gallegos-Garcia, M., Ramirez-Muñiz, K. & Song, S. (2012). Arsenic Removal from Water by Adsorption Using Iron Oxide Minerals as Adsorbents: A Review. *Mineral Processing and Extractive Metallurgy Review*, *33*(5), 301–315. https://doi.org/10.1080/08827508.2011.584219

Garelick, H., Jones, H., Dybowska, A. & Valsami-Jones, E. (2008). Arsenic Pollution Sources. *Reviews of Environmental Contamination and Toxicology*, 17–60. https://doi.org/10.1007/978-0-387-79284-2_2

Ghiorse, W. (1984). Biology of Iron- and Manganese-Depositing Bacteria. *Annual Review of Microbiology*, *38*(1), 515–550. https://doi.org/10.1146/annurev.micro.38.1.515

Giménez, J., Martínez, M. J., De Pablo, J., Rovira, M. & Duro, L. (2007). Arsenic sorption onto natural hematite, magnetite, and goethite. *Journal of Hazardous Materials*, *141*(3), 575–580. https://doi.org/10.1016/j.jhazmat.2006.07.020

Glodowska, M., Schneider, M., Eiche, E., Kontny, A., Neumann, T., Straub, D., Berg, M., Prommer, H., Bostick, B. C., Nghiem, A. A., Kleindienst, S. & Kappler, A. (2021a). Fermentation, methanotrophy and methanogenesis influence sedimentary Fe and As dynamics in As-affected aquifers in Vietnam. *Science of The Total Environment*, *779*, 146501. https://doi.org/10.1016/j.scitotenv.2021.146501

Glodowska, M., Schneider, M., Eiche, E., Kontny, A., Neumann, T., Straub, D., Kleindienst, S. & Kappler, A. (2021b). Microbial transformation of biogenic and abiogenic Fe minerals followed by in-situ incubations in an As-contaminated vs. non-contaminated aquifer. *Environmental Pollution*, *281*, 117012. https://doi.org/10.1016/j.envpol.2021.117012

Glodowska, M., Stopelli, E., Schneider, M., Lightfoot, A., Rathi, B., Straub, D., Patzner, M. S., Duyen, V. T., Berg, M. P., Kleindienst, S. & Kappler, A. (2020a). Role of in Situ Natural Organic Matter in Mobilizing As during Microbial Reduction of FeIII-Mineral-Bearing Aquifer Sediments from Hanoi (Vietnam). *Environmental Science & Technology*, *54*(7), 4149–4159. https://doi.org/10.1021/acs.est.9b07183

Glodowska, M., Stopelli, E., Schneider, M., Rathi, B., Straub, D., Lightfoot, A., Kipfer, R., Van Den Berg, M., Jetten, M. S. M., Kleindienst, S. & Kappler, A. (2020b). Arsenic mobilization by anaerobic iron-dependent methane oxidation. *Communications earth & environment*, *1*(1). https://doi.org/10.1038/s43247-020-00037-y

Goh, K. & Lim, J. W. (2004). Geochemistry of inorganic arsenic and selenium in a tropical soil: effect of reaction time, pH, and competitive anions on arsenic and selenium adsorption. *Chemosphere*, *55*(6), 849–859. https://doi.org/10.1016/j.chemosphere.2003.11.041

Goldberg, S. (1986). Chemical Modeling of Arsenate Adsorption on Aluminum and Iron Oxide Minerals. *Soil Science Society of America Journal*, *50*(5), 1154–1157. https://doi.org/10.2136/sssaj1986.03615995005000050012x

Goldberg, S. & Glaubig, R. A. (1988). Determination of Inorganic Arsenic (III) and Arsenic (III Plus V) Using Automated Hydride-Generation Atomic-Absorption Spectrometry. *Soil Science Society of America Journal*, *52*(2), 536–537. https://doi.org/10.2136/sssaj1988.03615995005200020044x

Goldberg, S. & Johnston, C. T. (2001). Mechanisms of Arsenic Adsorption on Amorphous Oxides Evaluated Using Macroscopic Measurements, Vibrational Spectroscopy, and Surface Complexation Modeling. *Journal of Colloid and Interface Science*, *234*(1), 204–216. https://doi.org/10.1006/jcis.2000.7295

Goldhaber, M. B., Lee, R. W., Hatch, J. R., Pashin, J. C. & Treworgy, J. (2003). Role of Large Scale Fluid-Flow in Subsurface Arsenic Enrichment. *Kluwer Academic Publishers eBooks*, 127–164. https://doi.org/10.1007/0-306-47956-7_5

Goyer, R. (2001). Toxic effects of metals. *Casarett and Doull's Toxicology, The Basic Science of Poison*, 811–867.

Gräfe, M., Eick, M. J. & Grossl, P. R. (2001). Adsorption of Arsenate (V) and Arsenite (III) on Goethite in the Presence and Absence of Dissolved Organic Carbon. *Soil Science Society of America Journal*, *65*(6), 1680–1687. https://doi.org/10.2136/sssaj2001.1680

Gräfe, M., Eick, M. J., Grossl, P. R. & Saunders, A. (2002). Adsorption of Arsenate and Arsenite on Ferrihydrite in the Presence and Absence of Dissolved Organic Carbon. *Journal of Environmental Quality*, *31*(4), 1115–1123. https://doi.org/10.2134/jeq2002.1115

Graham, U. M. & Ohmoto, H. (1994). Experimental study of formation mechanisms of hydrothermal pyrite. *Geochimica et Cosmochimica Acta*, *58*(10), 2187–2202. https://doi.org/10.1016/0016-7037(94)90004-3

Granados-Correa, F., Corral-Capulin, N., Olguín, M. & Acosta-León, C. (2011). Comparison of the Cd(II) adsorption processes between boehmite (γ-AlOOH) and goethite (α-FeOOH). *Chemical Engineering Journal*, *171*(3), 1027–1034. https://doi.org/10.1016/j.cej.2011.04.055

Guerin, W. & Blakemore, R. J. (1992). Redox Cycling of Iron Supports Growth and Magnetite Synthesis by Aquaspirillum magnetotacticum. *Applied and Environmental Microbiology*, *58*(4), 1102–1109. https://doi.org/10.1128/aem.58.4.1102-1109.1992

Guillot, S. & Charlet, L. (2007). Bengal arsenic, an archive of Himalaya orogeny and paleohydrology. *Journal Of Environmental Science And Health, Part A*, *42*(12), 1785–1794. https://doi.org/10.1080/10934520701566702

Guillot, S., Garçon, M., Weinman, B., Gajurel, A. P., Tisserand, D., France-Lanord, C., Van Geen, A., Chakraborty, S., Huyghe, P., Upreti, B. N. & Charlet, L. (2015). Origin of arsenic in Late Pleistocene to Holocene sediments in the Nawalparasi district (Terai, Nepal). *Environmental Earth Sciences*, *74*(3), 2571–2593. https://doi.org/10.1007/s12665-015-4277-y

Gunnarsson, M. (2002). *Surface Complexation at the Iron Oxide/water Interface: Experimental Investigations and Theoretical Developments*.

Guo, H. & Barnard, A. S. (2013). Naturally occurring iron oxide nanoparticles: morphology, surface chemistry and environmental stability. *Journal of materials chemistry. A, Materials for energy and sustainability*, *1*(1), 27–42. https://doi.org/10.1039/c2ta00523a

Guo, H., Stüben, D. & Berner, Z. (2007). Removal of arsenic from aqueous solution by natural siderite and hematite. *Applied Geochemistry*, *22*(5), 1039–1051. https://doi.org/10.1016/j.apgeochem.2007.01.004

Guo, H., Yang, S., Tang, X., Li, Y. & Shen, Z. (2008). Groundwater geochemistry and its implications for arsenic mobilization in shallow aquifers of the Hetao Basin, Inner Mongolia. *Science of The Total Environment*, *393*(1), 131–144. https://doi.org/10.1016/j.scitotenv.2007.12.025

Guo, H., Zhang, Y., Xing, L. & Jia, Y. (2012). Spatial variation in arsenic and fluoride concentrations of shallow groundwater from the town of Shahai in the Hetao basin, Inner Mongolia. *Applied Geochemistry*, *27*(11), 2187–2196. https://doi.org/10.1016/j.apgeochem.2012.01.016

Gupta, A., Yunus, M. & Sankararamakrishnan, N. (2012). Zerovalent iron encapsulated chitosan nanospheres – A novel adsorbent for the removal of total inorganic Arsenic from aqueous systems. In *Chemosphere* (Bd. 86, Nummer 2, S. 150–155). Elsevier BV. https://doi.org/10.1016/j.chemosphere.2011.10.003

Gupta, V. K., Saini, V. & Jain, N. (2005). Adsorption of As(III) from aqueous solutions by iron oxide-coated sand. *Journal of Colloid and Interface Science*, *288*(1), 55–60. https://doi.org/10.1016/j.jcis.2005.02.054

Gustafsson, J. P. & Bhattacharya, P. (2007). Geochemical modelling of arsenic adsorption to oxide surfaces. *Elsevier eBooks*, 159–206. https://doi.org/10.1016/s1875-1121(06)09006-7

Guyodo, J., Banerjee, S. K. & Penn, R. L. (2003). Rock Magnetic and HRTEM Study of Iron Oxyhydroxide Nanoparticles. *Conference Paper: AGU Fall Meeting*.

Haese, R. R. (2000). The Reactivity of Iron. *Springer eBooks*, 233–261. https://doi.org/10.1007/978-3-662-04242-7_7

Hafeznezami, S., Zimmer-Faust, A. G., Hoek, E. M., Rugh, M., Haro, H. L., Park, A., Suh, J., Najm, T., Reynolds, M. R., Davis, J., Parhizkar, T. & Jay, J. A. (2017). Remediation of groundwater contaminated with arsenic through enhanced natural attenuation: Batch and column studies. *Water Research*, *122*, 545–556. https://doi.org/10.1016/j.watres.2017.06.029

Hai, P. & Yamaguchi, Y. (2008). Characterizing the Urban Growth of Hanoi, Nagoya, and Shanghai City using Remote Sensing and Spatial Metrics. *International Geoscience and Remote Sensing Symposium*. https://doi.org/10.1109/igarss.2008.4780014

Halder, D., Biswas, A., Šlejkovec, Z., Chatterjee, D., Nriagu, J. O., Jacks, G. & Bhattacharya, P. (2014). Arsenic species in raw and cooked rice: Implications for human health in rural Bengal. *Science of The Total Environment*, *497–498*, 200–208. https://doi.org/10.1016/j.scitotenv.2014.07.075

Hall, G. E., Pelchat, J. & Gauthier, G. (1999). Stability of inorganic arsenic (III) and arsenic (V) in water samples. *Journal of Analytical Atomic Spectrometry*, *14*(2), 205–213. https://doi.org/10.1039/a807498d

Handler, R., Frierdich, A. J., Johnson, C. M., Rosso, K. M., Beard, B. L., Wang, C., Latta, D. E., Neumann, A., Pasakarnis, T., Premaratne, W. & Scherer, M. M. (2014). Fe(II)-Catalyzed Recrystallization of Goethite Revisited. *Environmental Science & Technology*, *48*(19), 11302–11311. https://doi.org/10.1021/es503084u

Handley, K. M., McBeth, J., Charnock, J. M., Vaughan, D. G., Wincott, P. L., Polya, D. A. & Lloyd, J. R. (2013). Effect of iron redox transformations on arsenic solid-phase associations in an arsenic-rich, ferruginous hydrothermal sediment. *Geochimica et Cosmochimica Acta*, *102*, 124–142. https://doi.org/10.1016/j.gca.2012.10.024

Hanna, K. (2007). Adsorption of aromatic carboxylate compounds on the surface of synthesized iron oxide-coated sands. *Applied Geochemistry*, *22*(9), 2045–2053. https://doi.org/10.1016/j.apgeochem.2007.05.005

Hansel, C. M., Benner, S. G. & Fendorf, S. (2005). Competing Fe(II)-Induced Mineralization Pathways of Ferrihydrite. *Environmental Science & Technology*, *39*(18), 7147–7153. https://doi.org/10.1021/es050666z

Hansel, C. M., Benner, S. G., Neiss, J., Dohnalkova, A., Kukkadapu, R. K. & Fendorf, S. (2003). Secondary mineralization pathways induced by dissimilatory iron reduction of ferrihydrite under advective flow. *Geochimica et Cosmochimica Acta*, *67*(16), 2977–2992. https://doi.org/10.1016/s0016-7037(03)00276-x

Harvey, C. F., Ashfaque, K. N., Yu, W., Badruzzaman, A. B. M., Ali, M. A. B., Oates, P. J., Michael, H. A., Neumann, R. B., Beckie, R., Islam, S. & Ahmed, M. H. (2006). Groundwater dynamics and arsenic contamination in Bangladesh. *Chemical Geology*, *228*(1–3), 112–136. https://doi.org/10.1016/j.chemgeo.2005.11.025

Harvey, C. F., Swartz, C. L., Badruzzaman, A. B. M., Keon-Blute, N., Yu, W., Ali, M. A. B., Jay, J. A., Beckie, R., Niedan, V., Brabander, D. J., Oates, P. J., Ashfaque, K. N., Islam, S., Hemond, H. F. & Ahmed, M. H. (2002). Arsenic Mobility and Groundwater Extraction in Bangladesh. *Science*, *298*(5598), 1602–1606. https://doi.org/10.1126/science.1076978

Hassellöv, M. & Von Der Kammer, F. (2008). Iron Oxides as Geochemical Nanovectors for Metal Transport in Soil-River Systems. In *Elements* (Bd. 4, Nummer 6, S. 401–406). Mineralogical Society of America. https://doi.org/10.2113/gselements.4.6.401

He, J. & Charlet, L. (2013). A review of arsenic presence in China drinking water. *Journal of Hydrology*, *492*, 79–88. https://doi.org/10.1016/j.jhydrol.2013.04.007

He, Z., Zhang, Q., Feng, Y., Luo, H., Pan, X. & Gadd, G. M. (2018). Microbiological and environmental significance of metal-dependent anaerobic oxidation of methane. *Science of The Total Environment*, *610–611*, 759–768. https://doi.org/10.1016/j.scitotenv.2017.08.140

Hegler, F., Posth, N. R., Jiang, J. & Kappler, A. (2008). Physiology of phototrophic iron(II)-oxidizing bacteria: implications for modern and ancient environments. *FEMS Microbiology Ecology*, *66*(2), 250–260. https://doi.org/10.1111/j.1574-6941.2008.00592.x

Hein, J. R. & Koski, R. A. (1987). Bacterially mediated diagenetic origin for chert-hosted manganese deposits in the Franciscan Complex, California Coast Ranges. *Geology*, *15*(8), 722. https://doi.org/10.1130/0091-7613(1987)15

Higham, C. (1989). *The Archaeology of Mainland Southeast Asia: From 10,000 B.C. to the Fall of Angkor*. Cambridge University Press.

Hindmarsh, J. & McCurdy, R. (1986). Clinical and Environmental Aspects of Arsenic Toxicity. *CRC critical reviews in clinical laboratory sciences*, *23*(4), 315–347. https://doi.org/10.3109/10408368609167122

Hingston, F. J., Posner, A. M. & Quirk, J. P. (1971). Competitive adsorption of negatively charged ligands on oxide surfaces. *Discussions of the Faraday Society*, *52*, 334. https://doi.org/10.1039/df9715200334

Hoa, N. D., Postma, D., Trang, P. T. K., Jessen, S., Viet, P. H. & Larsen, F. (2014). Adsorption and desorption of arsenic to aquifer sediment on the Red River floodplain at Nam Du, Vietnam. *Geochimica et Cosmochimica Acta*, *142*, 587–600. https://doi.org/10.1016/j.gca.2014.07.014

Hofstetter, T. B., Schwarzenbach, R. P. & Haderlein, S. B. (2003). Reactivity of Fe(II) Species Associated with Clay Minerals. *Environmental Science & Technology*, *37*(3), 519–528. https://doi.org/10.1021/es025955r

Hohmann, C., Winkler, E. C., Morin, G. & Kappler, A. (2010). Anaerobic Fe(II)-Oxidizing Bacteria Show As Resistance and Immobilize As during Fe(III) Mineral Precipitation. *Environmental Science & Technology*, *44*(1), 94–101. https://doi.org/10.1021/es900708s

Hong, Y. J., Song, K. B. & Chung, J. W. (2014). Health Effects of Chronic Arsenic Exposure. *Journal of preventive medicine and public health*, *47*(5), 245–252. https://doi.org/10.3961/jpmph.14.035

Hopenhayn, C. (2006). Arsenic in Drinking Water: Impact on Human Health. *Elements*, *2*(2), 103–107. https://doi.org/10.2113/gselements.2.2.103

Horneman, A. J., Van Geen, A., Kent, D. V., Mathé, P., Zheng, Y. H., Dhar, R., O'Connell, S., Hoque, M. A., Aziz, Z., Shamsudduha, M., Seddique, A. A. & Ahmed, K. M. (2004). Decoupling of As and Fe release to Bangladesh groundwater under reducing conditions. Part I: Evidence from sediment profiles. *Geochimica et Cosmochimica Acta*, *68*(17), 3459–3473. https://doi.org/10.1016/j.gca.2004.01.026

Hsu, C., Han, S., Kao, Y. & Liu, C. (2010). Redox characteristics and zonation of arsenic-affected multi-layers aquifers in the Choushui River alluvial fan, Taiwan. *Journal of Hydrology*, *391*(3–4), 351–366. https://doi.org/10.1016/j.jhydrol.2010.07.037

Hu, Q., Sun, G. X., Gao, X. Y. & Zhu, Y. S. (2012). Conversion, sorption, and transport of arsenic species in geological media. *Applied Geochemistry*, *27*(11), 2197–2203. https://doi.org/10.1016/j.apgeochem.2012.01.012

Hu, Z. & Gao, S. (2008). Upper crustal abundances of trace elements: A revision and update. *Chemical Geology*, *253*(3–4), 205–221. https://doi.org/10.1016/j.chemgeo.2008.05.010

Huang, J. (2014). Impact of Microorganisms on Arsenic Biogeochemistry: A Review. *Water Air and Soil Pollution*, *225*(2). https://doi.org/10.1007/s11270-013-1848-y

Huang, P. M., Oscarson, D. W., Liaw, W. K. & Hammer, U. T. (1982). Dynamics and mechanisms of arsenite oxidation by freshwater lake sediments. *Hydrobiologia*, *91–92*(1), 315–322. https://doi.org/10.1007/bf02391948

Hug, S. J., Winkel, L. H. E., Voegelin, A., Berg, M. & Johnson, C. L. (2020). Arsenic and Other Geogenic Contaminants in Groundwater – A Global Challenge. *Chimia*, *74*(7–8), 524. https://doi.org/10.2533/chimia.2020.524

Hunger, S. & Benning, L. G. (2007). Greigite: a true intermediate on the polysulfide pathway to pyrite. *Geochemical Transactions*, *8*(1). https://doi.org/10.1186/1467-4866-8-1

Hunt, C. H., Moskowitz, B. M. & Banerjee, S. K. (2013). Magnetic Properties of Rocks and Minerals. *American Geophysical Union eBooks*, 189–204. https://doi.org/10.1029/rf003p0189

Huq, E., Su, C., Xie, X. & Sarven, M. S. (2018). Arsenic enrichment and mobilization in the Holocene alluvial aquifers of Prayagpur of Southwestern Bangladesh. *International Biodeterioration & Biodegradation*, *128*, 186–194. https://doi.org/10.1016/j.ibiod.2018.01.008

Ilgen, A. G., Kukkadapu, R. K., Leung, K. & Washington, R. E. (2019). “Switching on” iron in clay minerals. *Environmental science. Nano*, *6*(6), 1704–1715. https://doi.org/10.1039/c9en00228f

Irgolic, K. J. (1994). Determination of total arsenic and arsenic compounds in drinking water. *Science and Technology Letters*, *in Arsenic: Exposure and Health*, Pp. 51-60.

Islam, F., Gault, A. G., Boothman, C., Polya, D. A., Charnock, J. M., Chatterjee, D. & Lloyd, J. R. (2004). Role of metal-reducing bacteria in arsenic release from Bengal delta sediments. *Nature*, *430*(6995), 68–71. https://doi.org/10.1038/nature02638

Islam, F. & Medraj, M. (2005). Thermodynamic Modelling of the Mg-Al-Ca System. *Canadian Metallurgical Quarterly*, *44*(4), 523–536. https://doi.org/10.1179/cmq.2005.44.4.523

Islam, S. & Islam, M. R. (2011). *Arsenic in Bangladesh Rice*. LAP Lambert Academic Publishing.

Jackson, C. J., Langner, H., Donahoe-Christiansen, J., Inskeep, W. P. & McDermott, T. R. (2001). Molecular analysis of microbial community structure in an arsenite-oxidizing acidic thermal spring. *Environmental Microbiology*, *3*(8), 532–542. https://doi.org/10.1046/j.1462-2920.2001.00221.x

Jain, A., Raven, K. P. & Loeppert, R. H. (1999). Arsenite and Arsenate Adsorption on Ferrihydrite: Surface Charge Reduction and Net OH- Release Stoichiometry. *Environmental Science & Technology*, *33*(8), 1179–1184. https://doi.org/10.1021/es980722e

Jambor, J. L. & Dutrizac, J. E. (1998). Occurrence and Constitution of Natural and Synthetic Ferrihydrite, a Widespread Iron Oxyhydroxide. In *Chemical Reviews* (Bd. 98, Nummer 7, S. 2549–2586). American Chemical Society. https://doi.org/10.1021/cr970105t

Johnson, C. M., Roden, E. E., Welch, S. & Beard, B. L. (2005). Experimental constraints on Fe isotope fractionation during magnetite and Fe carbonate formation coupled to dissimilatory hydrous ferric oxide reduction. *Geochimica et Cosmochimica Acta*, *69*(4), 963–993. https://doi.org/10.1016/j.gca.2004.06.043

Johnson, D. L. & Pilson, M. E. Q. (1975). The Oxidation of Arsenite in Seawater. *Environmental Letters*, *8*(2), 157–171. https://doi.org/10.1080/00139307509437429

Johnson, T. E., Kilburn, M. R., Saunders, M., Cliff, J. B., Kong, C., Liu, A. G., Matthews, J. J. & Brasier, M. D. (2015). Uncovering framboidal pyrite biogenicity using nano-scale CNorg mapping. *Geology*, *43*(1), 27–30. https://doi.org/10.1130/g36048.1

Johnston, S. G., Keene, A. F., Burton, E. D., Bush, R. T. & Sullivan, L. A. (2011). Iron and Arsenic Cycling in Intertidal Surface Sediments during Wetland Remediation. *Environmental Science & Technology*, *45*(6), 2179–2185. https://doi.org/10.1021/es103403n

Johnston, S. G., Keene, A. F., Burton, E. D., Bush, R. T., Sullivan, L. A., McElnea, A. E., Ahern, C. R., Smith, C. D., Powell, B. & Hocking, R. K. (2010). Arsenic Mobilization in a Seawater Inundated Acid Sulfate Soil. *Environmental Science & Technology*, *44*(6), 1968–1973. https://doi.org/10.1021/es903114z

Jones, A., Collins, R., Rose, J. C. & Waite, T. D. (2009). The effect of silica and natural organic matter on the Fe(II)-catalysed transformation and reactivity of Fe(III) minerals. *Geochimica et Cosmochimica Acta*, *73*(15), 4409–4422. https://doi.org/10.1016/j.gca.2009.04.025

Jönsson, J. & Sherman, D. H. (2008). Sorption of As(III) and As(V) to siderite, green rust (fougerite) and magnetite: Implications for arsenic release in anoxic groundwaters. *Chemical Geology*, *255*(1–2), 173–181. https://doi.org/10.1016/j.chemgeo.2008.06.036

Jovanovic, M. B., Vukasinovic-Pesic, L. V., Veljovic, N. D. & Rajakovic, V. L. (2011). Arsenic removal from water using low-cost adsorbents: A comparative study. *Journal of The Serbian Chemical Society*, *76*(10), 1437–1452. https://doi.org/10.2298/jsc101029122j

Jung, H., Bostick, B. C. & Zheng, Y. (2012). Field, Experimental, and Modeling Study of Arsenic Partitioning across a Redox Transition in a Bangladesh Aquifer. *Environmental Science & Technology*, *46*(3), 1388–1395. https://doi.org/10.1021/es2032967

Jusseret, S., Baeteman, C. & Dassargues, A. (2010). The tratigraphical architecture of the quaternary deposits as support for hydrogeological modelling of the central zone of Hanoi (Vietnam). *Geologica Belgica*, *13*(1), 77–90. http://orbi.ulg.ac.be/bitstream/2268/28471/1/publi182-2009.pdf

Just, J. & Kontny, A. (2012). Thermally induced alterations of minerals during measurements of the temperature dependence of magnetic susceptibility: a case study from the hydrothermally altered Soultz-sous-Forêts granite, France. *International Journal of Earth Sciences*, *101*(3), 819–839. https://doi.org/10.1007/s00531-011-0668-9

Kabata-Pendias, A. (2010). Trace Elements in Soils and Plants. *CRC Press eBooks*. https://doi.org/10.1201/b10158

Kanoua, W. & Merkel, B. J. (2017). Hydrochemical evolution and arsenic release in shallow aquifer in the Titas Upazila, Eastern Bangladesh. *Arabian Journal of Geosciences*, *10*(13). https://doi.org/10.1007/s12517-017-3063-4

Kapaj, S., Peterson, H. G., Liber, K. & Bhattacharya, P. (2006). Human Health Effects From Chronic Arsenic Poisoning–A Review. *Journal Of Environmental Science And Health, Part A*, *41*(10), 2399–2428. https://doi.org/10.1080/10934520600873571

Kappler, A., Bryce, C., Mansor, M., Lueder, U., Byrne, J. M. & Schoenberg, R. (2021). An evolving view on biogeochemical cycling of iron. *Nature Reviews Microbiology*, *19*(6), 360–374. https://doi.org/10.1038/s41579-020-00502-7

Kappler, A. & Newman, D. K. (2004). Formation of Fe(III)-minerals by Fe(II)-oxidizing photoautotrophic bacteria 1 1Associate editor: L. G. Benning. *Geochimica et Cosmochimica Acta*, *68*(6), 1217–1226. https://doi.org/10.1016/j.gca.2003.09.006

Kappler, A. & Straub, K. (2005). Geomicrobiological Cycling of Iron. In *Reviews in mineralogy and geochemistry* (Bd. 59, Nummer 1, S. 85–108). Mineralogical Society of America. https://doi.org/10.2138/rmg.2005.59.5

Karagas, M. R., Gossai, A., Pierce, B. L. & Ahsan, H. (2015). Drinking Water Arsenic Contamination, Skin Lesions, and Malignancies: A Systematic Review of the Global Evidence. *Current Environmental Health Reports*, *2*(1), 52–68. https://doi.org/10.1007/s40572-014-0040-x

Karlin, R. (1990). Magnetic mineral diagenesis in suboxic sediments at Bettis Site W-N, NE Pacific Ocean. *Journal of Geophysical Research*, *95*(B4), 4421. https://doi.org/10.1029/jb095ib04p04421

Khan, U., A., Manan, A., Khan, N., Mahmood, A. & Rahim, A. (2015). Transformation mechanism of magnetite nanoparticles. *Materials Science Poland*, *33*(2), 278–285. https://doi.org/10.1515/msp-2015-0037

Kim, J. W., Dong, H., Seabaugh, J. L., Newell, S. Y. & Eberl, D. D. (2004). Role of Microbes in the Smectite-to-Illite Reaction. *Science*, *303*(5659), 830–832. https://doi.org/10.1126/science.1093245

Kim, K., Chanpiwat, P., Hanh, H. T., Phan, K. & Sthiannopkao, S. (2011). Arsenic geochemistry of groundwater in Southeast Asia. *Frontiers of Medicine*, *5*(4), 420–433. https://doi.org/10.1007/s11684-011-0158-2

Kim, M., Nriagu, J. O. & Haack, S. K. (2000). Carbonate Ions and Arsenic Dissolution by Groundwater. *Environmental Science & Technology*, *34*(15), 3094–3100. https://doi.org/10.1021/es990949p

Kim, T., Park, S., Yoon, Y., Lee, J., Jeon, J., Kim, M., Kim, Y., Kim, E. K. & Hur, H. (2019). Biogenic Hematite from Bacteria: Facile Synthesis of Secondary Nanoclusters for Lithium Storage Capacity. *ACS Applied Materials & Interfaces*, *11*(7), 6948–6957. https://doi.org/10.1021/acsami.8b18894

Kirk, M. F., Roden, E. E., Crossey, L. J., Brealey, A. J. & Spilde, M. N. (2010). Experimental analysis of arsenic precipitation during microbial sulfate and iron reduction in model aquifer sediment reactors. *Geochimica et Cosmochimica Acta*, *74*(9), 2538–2555. https://doi.org/10.1016/j.gca.2010.02.002

Kleinert, S., Muehe, E. M., Posth, N. R., Dippon, U., Daus, B. & Kappler, A. (2011). Biogenic Fe(III) Minerals Lower the Efficiency of Iron-Mineral-Based Commercial Filter Systems for Arsenic

Removal. *Environmental Science & Technology*, *45*(17), 7533–7541. https://doi.org/10.1021/es201522n

Knowles, F. & Benson, A. J. (1983). The biochemistry of arsenic. *Trends in Biochemical Sciences*, *8*(5), 178–180. https://doi.org/10.1016/0968-0004(83)90168-8

Kocar, B. D. & Fendorf, S. (2009). Thermodynamic Constraints on Reductive Reactions Influencing the Biogeochemistry of Arsenic in Soils and Sediments. *Environmental Science & Technology*, *43*(13), 4871–4877. https://doi.org/10.1021/es8035384

Kocar, B. D., Herbel, M. J., Tufano, K. J. & Fendorf, S. (2006). Contrasting Effects of Dissimilatory Iron(III) and Arsenic(V) Reduction on Arsenic Retention and Transport. *Environmental Science & Technology*, *40*(21), 6715–6721. https://doi.org/10.1021/es061540k

Kocar, B. D., Polizzotto, M. L., Benner, S. G., Ying, S. C., Ung, M., Ouch, K., Samreth, S., Suy, B., Phan, K., Sampson, M. J. & Fendorf, S. (2008). Integrated biogeochemical and hydrologic processes driving arsenic release from shallow sediments to groundwaters of the Mekong delta. *Applied Geochemistry*, *23*(11), 3059–3071. https://doi.org/10.1016/j.apgeochem.2008.06.026

Konhauser, K. O. (1998). Diversity of bacterial iron mineralization. *Earth-Science Reviews*, *43*(3–4), 91–121. https://doi.org/10.1016/s0012-8252(97)00036-6

Konhauser, K. O. (2009). *Introduction to Geomicrobiology*. John Wiley & Sons.

Konhauser, K. O., Kappler, A. & Roden, E. E. (2011). IRON IN MICROBIAL METABOLISMS. *Elements*, *7*(2), 89–93. https://doi.org/10.2113/gselements.7.2.89

Kontny, A., Schneider, M., Eiche, E., Stopelli, E., Glodowska, M., Rathi, B., Göttlicher, J., Byrne, J. M., Kappler, A., Berg, M., Thi, D., DO, Trang, P. T. K., Viet, P. H. & Neumann, T. (2021). Iron mineral transformations and their impact on As (im)mobilization at redox interfaces in As-contaminated aquifers. *Geochimica et Cosmochimica Acta*, *296*, 189–209. https://doi.org/10.1016/j.gca.2020.12.029

Koo, T. & Kim, J. W. (2020). Controls on the Formation and Stability of Siderite (FeCO3) and Chukanovite (Fe2(CO3)(OH)2) in Reducing Environment. *Minerals*, *10*(2), 156. https://doi.org/10.3390/min10020156

Koo, T. Y., Jang, Y. P., Kogure, T., Kim, J. N., Park, B. J., Sunwoo, D. & Kim, J. (2014). Structural and chemical modification of nontronite associated with microbial Fe(III) reduction: Indicators of "illitization". *Chemical Geology*, *377*, 87–95. https://doi.org/10.1016/j.chemgeo.2014.04.005

Koo, T. Y., Lee, G. & Kim, J. (2016). Biogeochemical dissolution of nontronite by Shewanella oneidensis MR-1: Evidence of biotic illite formation. *Applied Clay Science*, *134*, 13–18. https://doi.org/10.1016/j.clay.2016.03.030

Kuroda, K., Hayashi, T., Thuan, A., DO, Canh, V. D., Nga, T. V. T., Funabiki, A. & Takizawa, S. (2017). Groundwater recharge in suburban areas of Hanoi, Vietnam: effect of decreasing surface-water bodies and land-use change. *Hydrogeology Journal*, *25*(3), 727–742. https://doi.org/10.1007/s10040-016-1528-2

Langner, H. & Inskeep, W. P. (2000). Microbial Reduction of Arsenate in the Presence of Ferrihydrite. *Environmental Science & Technology*, *34*(15), 3131–3136. https://doi.org/10.1021/es991414z

Larese-Casanova, P., Haderlein, S. B. & Kappler, A. (2010). Biomineralization of lepidocrocite and goethite by nitrate-reducing Fe(II)-oxidizing bacteria: Effect of pH, bicarbonate, phosphate, and humic acids. *Geochimica et Cosmochimica Acta*, *74*(13), 3721–3734. https://doi.org/10.1016/j.gca.2010.03.037

Larese-Casanova, P., Kappler, A. & Haderlein, S. B. (2012). Heterogeneous oxidation of Fe(II) on iron oxides in aqueous systems: Identification and controls of Fe(III) product formation. *Geochimica et Cosmochimica Acta*, *91*, 171–186. https://doi.org/10.1016/j.gca.2012.05.031

Large, D., Sawłowicz, Z. & Spratt, J. (1999). A cobaltite-framboidal pyrite association from the Kupferschiefer: possible implications for trace element behaviour during the earliest stages of diagenesis. *Mineralogical Magazine*, *63*(3), 353–361. https://doi.org/10.1180/002646199548574

Larsen, F., Pham, N. T., Dang, N. T. T., Postma, D., Jessen, S., Pham, V. H., Nguyen, T. D., Trieu, H., Tran, L. M., Nguyen, H. A., Chambon, J. C. C., Van Nguyen, H., Ha, D. T. M., Hue, N. T., Duc, M. T. & Refsgaard, J. C. (2008). Controlling geological and hydrogeological processes in an arsenic contaminated aquifer on the Red River flood plain, Vietnam. *Applied Geochemistry*, *23*(11), 3099–3115. https://doi.org/10.1016/j.apgeochem.2008.06.014

Lawati, W. M. A., Rizoulis, A., Eiche, E., Boothman, C., Polya, D. A., Lloyd, J. R., Berg, M., Vasquez-Aguilar, P. & Van Dongen, B. E. (2012). Characterisation of organic matter and microbial communities in contrasting arsenic-rich Holocene and arsenic-poor Pleistocene aquifers, Red River Delta, Vietnam. *Applied Geochemistry*, *27*(1), 315–325. https://doi.org/10.1016/j.apgeochem.2011.09.030

Lawson, M. J., Polya, D. A., Boyce, A. J., Bryant, C., Mondal, D., Shantz, A. A. & Ballentine, C. J. (2013). Pond-Derived Organic Carbon Driving Changes in Arsenic Hazard Found in Asian Groundwaters. *Environmental Science & Technology*, *47*(13), 7085–7094. https://doi.org/10.1021/es400114q

Le, T. P. Q., Garnier, J., Gilles, B., Sylvain, T. & Van Minh, C. (2007). The changing flow regime and sediment load of the Red River, Viet Nam. *Journal of Hydrology*, *334*(1–2), 199–214. https://doi.org/10.1016/j.jhydrol.2006.10.020

Lear, G., Song, B., Gault, A. G., Polya, D. A. & Lloyd, J. (2007). Molecular Analysis of Arsenate-Reducing Bacteria within Cambodian Sediments following Amendment with Acetate. *Applied and Environmental Microbiology*, *73*(4), 1041–1048. https://doi.org/10.1128/aem.01654-06

Lee, S. Y., Lee, I. & Roh, Y. (2003). Biomineralization of a poorly crystalline Fe(III) oxide, akaganeite, by an anaerobic Fe(III)-reducing bacterium (Shewanella alga) isolated from marine environment. *Geosciences Journal*, *7*(3), 217–226. https://doi.org/10.1007/bf02910288

Lein, A. Y., Ivanov, M. V., Pimenov, N. V. & Gulin, M. B. (2002). Geochemical Peculiarities of the Carbonate Constructions Formed during Microbial Oxidation of Methane under Anaerobic Conditions. *Microbiology*, *71*(1), 78–90. https://doi.org/10.1023/a:1017906501726

Leloup, P. H., Tapponnier, P., Lacassin, R. & Searle, M. P. (2007). Discussion on the role of the Red River shear zone, Yunnan and Vietnam, in the continental extrusion of SE Asia *Journal* , Vol. 163, 2006, 1025–1036. *Journal of the Geological Society*, *164*(6), 1253–1260. https://doi.org/10.1144/0016-76492007-065

Lenoble, V., Bouras, O., Deluchat, V., Serpaud, B. & Bollinger, J. (2002). Arsenic Adsorption onto Pillared Clays and Iron Oxides. In *Journal of Colloid and Interface Science* (Bd. 255, Nummer 1, S. 52–58). Elsevier BV. https://doi.org/10.1006/jcis.2002.8646

Levy, D., Schramke, J. A., Esposito, K., Erickson, T. A. & Moore, J. (1999). The shallow ground water chemistry of arsenic, fluorine, and major elements: Eastern Owens Lake, California. *Applied Geochemistry*, *14*(1), 53–65. https://doi.org/10.1016/s0883-2927(98)00038-9

Li, Y., Yang, M., Pentrák, M., He, H. & Arai, Y. (2020). Carbonate-Enhanced Transformation of Ferrihydrite to Hematite. *Environmental Science & Technology*, *54*(21), 13701–13708. https://doi.org/10.1021/acs.est.0c04043

Li, Y., Zhu, S. & Deng, K. (2011). Mössbauer hyperfine parameters of iron species in the course of Geobacter-mediated magnetite mineralization. *Physics and Chemistry of Minerals*, *38*(9), 701–708. https://doi.org/10.1007/s00269-011-0443-2

Li, Z., Saito, Y., Matsumoto, E., Wang, Y., Tanabe, S. & Vu, Q. H. (2006). Climate change and human impact on the Song Hong (Red River) Delta, Vietnam, during the Holocene. *Quaternary International*, *144*(1), 4–28. https://doi.org/10.1016/j.quaint.2005.05.008

Lightfoot, A. F., Brennwald, M. S., Prommer, H., Stopelli, E., Berg, M., Glodowska, M., Schneider, M. & Kipfer, R. (2022). Noble gas constraints on the fate of arsenic in groundwater. *Water Research*, *214*, 118199. https://doi.org/10.1016/j.watres.2022.118199

Lin, H., Wang, M. & Li, G. (2004). Complexation of arsenate with humic substance in water extract of compost. *Chemosphere*, *56*(11), 1105–1112. https://doi.org/10.1016/j.chemosphere.2004.05.018

Litter, M. I., Nicolli, H. B., Meichtry, M., Quici, N., Bundschuh, J., Bhattacharya, P. & Naidu, R. (2014). *One Century of the Discovery of Arsenicosis in Latin America (1914-2014) As2014: Proceedings of the 5th International Congress on Arsenic in the Environment, May 11-16, 2014, Buenos Aires, Argentina*. CRC Press.

Liu, H., Li, P., Zhu, M., Wei, Y. & Sun, Y. (2007). Fe(II)-induced transformation from ferrihydrite to lepidocrocite and goethite. *Journal of Solid State Chemistry*, *180*(7), 2121–2128. https://doi.org/10.1016/j.jssc.2007.03.022

Liu, H., Wei, Y. & Sun, Y. (2005). The Formation of hematite from ferrihydrite using Fe(II) as a catalyst. *Journal of Molecular Catalysis A-chemical*, *226*(1), 135–140. https://doi.org/10.1016/j.molcata.2004.09.019

Liu, Q., Barrón, V., Torrent, J., Eeckhout, S. G. & Deng, C. (2008). Magnetism of intermediate hydromaghemite in the transformation of 2-line ferrihydrite into hematite and its paleoenvironmental implications. *Journal of Geophysical Research*, *113*(B1). https://doi.org/10.1029/2007jb005207

Livesey, N. T. & Huang, P. M. (1981). Adsorption of Arsenate by Soils and its relation to selected chemical properties and anions. *Soil Science*, *131*(2), 88–94. https://doi.org/10.1097/00010694-198102000-00004

Lovley, D. R. (1991). Dissimilatory Fe(III) and Mn(IV) reduction. *Microbiological reviews*, *55*(2), 259–287. https://doi.org/10.1128/mr.55.2.259-287.1991

Lovley, D. R. (1995). Microbial Reduction of Iron, Manganese, and other Metals. *Elsevier eBooks*, 175–231. https://doi.org/10.1016/s0065-2113(08)60900-1

Lovley, D. R. (1997). Microbial Fe(III) reduction in subsurface environments. *Fems Microbiology Reviews*, *20*(3–4), 305–313. https://doi.org/10.1111/j.1574-6976.1997.tb00316.x

Lovley, D. R., Holmes, D. E. & Nevin, K. P. (2004). Dissimilatory Fe(III) and Mn(IV) Reduction. *Elsevier eBooks*, 219–286. https://doi.org/10.1016/s0065-2911(04)49005-5

Lovley, D. R. & Phillips, E. J. (1986). Organic Matter Mineralization with Reduction of Ferric Iron in Anaerobic Sediments. *Applied and Environmental Microbiology*, *51*(4), 683–689. https://doi.org/10.1128/aem.51.4.683-689.1986

Lovley, D. R. & Phillips, E. J. (1987). Rapid Assay for Microbially Reducible Ferric Iron in Aquatic Sediments. *Applied and Environmental Microbiology*, *53*(7), 1536–1540. https://doi.org/10.1128/aem.53.7.1536-1540.1987

Lovley, D. R., Phillips, E. J. & Lonergan, D. J. (1989). Hydrogen and Formate Oxidation Coupled to Dissimilatory Reduction of Iron or Manganese by *Alteromonas putrefaciens*. *Applied and Environmental Microbiology*, *55*(3), 700–706. https://doi.org/10.1128/aem.55.3.700-706.1989

Lowers, H. A., Breit, G. N., Foster, A. L., Whitney, J. C., Yount, J. C., Uddin, M. N. & Muneem, A. A. (2007). Arsenic incorporation into authigenic pyrite, Bengal Basin sediment, Bangladesh. *Geochimica et Cosmochimica Acta*, *71*(11), 2699–2717. https://doi.org/10.1016/j.gca.2007.03.022

Luu, T. L. (2019). Remarks on the current quality of groundwater in Vietnam. *Environmental Science and Pollution Research*, *26*(2), 1163–1169. https://doi.org/10.1007/s11356-017-9631-z

Luxton, T. P., Eick, M. J. & Rimstidt, D. J. (2008). The role of silicate in the adsorption/desorption of arsenite on goethite. *Chemical Geology*, *252*(3–4), 125–135. https://doi.org/10.1016/j.chemgeo.2008.01.022

Luzi, Berg, M., Trang, P. T. K., Viet & Schertenleib, R. (2014). Household Sand Filters for Arsenic Removal : An option to mitigate arsenic from iron-rich groundwater. *Technical Report*. https://www.ircwash.org/sites/default/files/Luzi-2004-Household.pdf

Macías, F. & Camps-Arbestain, M. (2020). A biogeochemical view of the world reference base soil classification system. *Advances in Agronomy*, 295–342. https://doi.org/10.1016/bs.agron.2019.11.002

Madhukar, M., Murthy, S. & Udayashankara, T. H. (2016). Sources of Arsenic in Groundwater and its Health Significance-A Review. *Nature Environment & Pollution Technology*, *15.3*.

Mahimairaja, S., Bolan, N., Adriano, D. C. & Robinson, B. (2005). Arsenic Contamination and its Risk Management in Complex Environmental Settings. *Elsevier eBooks*, 1–82. https://doi.org/10.1016/s0065-2113(05)86001-8

Mailloux, B. J., Alexandrova, E., Keimowitz, A. R., Wovkulich, K., Freyer, G. A., Herron, M. C., Stolz, J. F., Kenna, T. C., Pichler, T., Polizzotto, M. L., Dong, H., Bishop, M. R. & Knappett, P. S. (2009). Microbial Mineral Weathering for Nutrient Acquisition Releases Arsenic. *Applied and Environmental Microbiology*, *75*(8), 2558–2565. https://doi.org/10.1128/aem.02440-07

Mamindy-Pajany, Y., Hurel, C., Marmier, N. & Roméo, M. (2009). Arsenic adsorption onto hematite and goethite. *Comptes Rendus Chimie*, *12*(8), 876–881. https://doi.org/10.1016/j.crci.2008.10.012

Manceau, A. & Gates, W. P. (1997). Surface Structural Model for Ferrihydrite. *Clays and Clay Minerals*, *45*(3), 448–460. https://doi.org/10.1346/ccmn.1997.0450314

Mandal, B. K. & Suzuki, K. (2002). Arsenic round the world: a review. *Talanta*, *58*(1), 201–235. https://doi.org/10.1016/s0039-9140(02)00268-0

Manning, B. B., Fendorf, S., Bostick, B. C. & Suarez, D. L. (2002). Arsenic(III) Oxidation and Arsenic(V) Adsorption Reactions on Synthetic Birnessite. *Environmental Science & Technology*, *36*(5), 976–981. https://doi.org/10.1021/es0110170

Manning, B. B., Fendorf, S. & Goldberg, S. (1998). Surface Structures and Stability of Arsenic(III) on Goethite: Spectroscopic Evidence for Inner-Sphere Complexes. *Environmental Science & Technology*, *32*(16), 2383–2388. https://doi.org/10.1021/es9802201

Manning, B. B. & Goldberg, S. (1996). Modeling Competitive Adsorption of Arsenate with Phosphate and Molybdate on Oxide Minerals. *Soil Science Society of America Journal*, *60*(1), 121–131. https://doi.org/10.2136/sssaj1996.03615995006000010020x

Manning, B. B. & Goldberg, S. (1997). Adsorption and Stability of Arsenic(III) at the Clay Mineral−Water Interface. *Environmental Science & Technology*, *31*(7), 2005–2011. https://doi.org/10.1021/es9608104

Masscheleyn, P. H., DeLaune, R. D. & Patrick, W. L. (1991). Effect of redox potential and pH on arsenic speciation and solubility in a contaminated soil. *Environmental Science & Technology*, *25*(8), 1414–1419. https://doi.org/10.1021/es00020a008

Masue, Y., Loeppert, R. H. & Kramer, T. A. (2007). Arsenate and Arsenite Adsorption and Desorption Behavior on Coprecipitated Aluminum:Iron Hydroxides. *Environmental Science & Technology*, *41*(3), 837–842. https://doi.org/10.1021/es061160z

Mathers, S. (1996). *The Red River Delta of Vietnam: A Demonstration of the Applicability of Sedimentology to the Investigation of Unconsolidated Sedimentary Aquifers: Bd. TECHNICAL REPORT WC/96/02*.

Mathers, S. & Zalasiewicz, J. (1999). Holocene Sedimentary Architecture of the Red River Delta, Vietnam. *Journal of Coastal Research*, *15*(2), 314–325. https://journals.flvc.org/jcr/article/download/80504/77737

Matis, K. A., Zouboulis, A. I., Malamas, F. M., Afonso, M. R. & Hudson, M. (1997). Flotation removal of As(V) onto goethite. *Environmental Pollution*, *97*(3), 239–245. https://doi.org/10.1016/s0269-7491(97)00091-2

Matisoff, G., Khourey, C. J., Hall, J. E., Varnes, A. W. & Strain, W. D. (1982). The Nature and Source of Arsenic in Northeastern Ohio Ground Watera. *Ground Water*, *20*(4), 446–456. https://doi.org/10.1111/j.1745-6584.1982.tb02765.x

Matschullat, J. (2000). Arsenic in the geosphere — a review. *Science of The Total Environment*, *249*(1–3), 297–312. https://doi.org/10.1016/s0048-9697(99)00524-0

Mavrocordatos, D. & Fortin, D. (2002). Quantitative characterization of biotic iron oxides by analytical electron microscopy. *American Mineralogist*, *87*(7), 940–946. https://doi.org/10.2138/am-2002-0717

McArthur, J. M., Banerjee, D., Hudson-Edwards, K. A., Mishra, R., Purohit, R., Ravenscroft, P., Cronin, A., Howarth, R. W., Chatterjee, A., Talukder, T., Lowry, D., Houghton, S. & Chadha, D. (2004). Natural organic matter in sedimentary basins and its relation to arsenic in anoxic ground water: the example of West Bengal and its worldwide implications. *Applied Geochemistry*, *19*(8), 1255–1293. https://doi.org/10.1016/j.apgeochem.2004.02.001

McArthur, J. M., Ravenscroft, P., Banerjee, D., Milsom, J., Hudson-Edwards, K. A., Sengupta, S., Bristow, C. S., Sarkar, A., Tonkin, S. & Purohit, R. (2008). How paleosols influence groundwater flow and arsenic pollution: A model from the Bengal Basin and its worldwide implication. *Water Resources Research*, *44*(11). https://doi.org/10.1029/2007wr006552

McArthur, J. M., Ravenscroft, P., Safiulla, S. & Thirlwall, M. F. (2001). Arsenic in groundwater: Testing pollution mechanisms for sedimentary aquifers in Bangladesh. *Water Resources Research*, *37*(1), 109–117. https://doi.org/10.1029/2000wr900270

McCarty, K. M., Hanh, H. T. & Kim, K. (2011). Arsenic geochemistry and human health in South East Asia. *Reviews on environmental health*, *26*(1), 71–78. https://doi.org/10.1515/reveh.2011.010

McCleskey, R. B., Nordstrom, D. K., Hurwitz, S., Colman, D. R., Roth, D. A., Johnson, M. & Boyd, E. S. (2022). The source, fate, and transport of arsenic in the Yellowstone hydrothermal system - An overview. *Journal of Volcanology and Geothermal Research*, *432*, 107709. https://doi.org/10.1016/j.jvolgeores.2022.107709

McMahon, P. L. & Chapelle, F. H. (2008). Redox Processes and Water Quality of Selected Principal Aquifer Systems. *Ground Water*, *46*(2), 259–271. https://doi.org/10.1111/j.1745-6584.2007.00385.x

Medunić, G., Fiket, Ž. & Ivanić, M. (2020). Arsenic Contamination Status in Europe, Australia, and Other Parts of the World. *Springer eBooks*, 183–233. https://doi.org/10.1007/978-981-13-8587-2_6

Meharg, A. A., Williams, P., Adomako, E., Lawgali, Y. F., Deacon, C., Villada, A., Cambell, R. C. J., Sun, G., Zhu, Y., Feldmann, J., Raab, A., Zhao, F., Islam, R., Hossain, S. A. & Yanai, J. (2009). Geographical Variation in Total and Inorganic Arsenic Content of Polished (White) Rice. *Environmental Science & Technology*, *43*(5), 1612–1617. https://doi.org/10.1021/es802612a

Meliker, J. R. & Nriagu, J. O. (2007). Arsenic in drinking water and bladder cancer: review of epidemiological evidence. *Trace Metals and other Contaminants in the Environment*, 551–584. https://doi.org/10.1016/s1875-1121(06)09021-3

Melton, E. D., Schoenberg, R., Behrens, S., Schmidt, C. & Kappler, A. (2014). The interplay of microbially mediated and abiotic reactions in the biogeochemical Fe cycle. *Nature Reviews Microbiology*, *12*(12), 797–808. https://doi.org/10.1038/nrmicro3347

Meng, X., Jing, C. & Korfiatis, G. P. (2002). A Review of Redox Transformation of Arsenic in Aquatic Environments. *ACS symposium series*, 70–83. https://doi.org/10.1021/bk-2003-0835.ch006

Meng, Y., Liu, Z. & Rosen, B. P. (2004). As(III) and Sb(III) Uptake by GlpF and Efflux by ArsB in Escherichia coli. In *Journal of Biological Chemistry* (Bd. 279, Nummer 18, S. 18334–18341). American Society for Biochemistry and Molecular Biology. https://doi.org/10.1074/jbc.m400037200

Menon, M., Dong, W., Chen, X., Hufton, J. & Rhodes, E. J. (2021). Improved rice cooking approach to maximise arsenic removal while preserving nutrient elements. *Science of The Total Environment*, *755*, 143341. https://doi.org/10.1016/j.scitotenv.2020.143341

Merinero, R., Cárdenes, V., Lunar, R., Boone, M. & Cnudde, V. (2017). Representative size distributions of framboidal, euhedral, and sunflower pyrite from high-resolution X-ray tomography and scanning electron microscopy analyses. *American Mineralogist*, *102*(3), 620–631. https://doi.org/10.2138/am-2017-5851

Merinero, R., Lunar, R., Martínez-Frías, J., Somoza, L. & Díaz-Del-Río, V. (2008). Iron oxyhydroxide and sulphide mineralization in hydrocarbon seep-related carbonate submarine chimneys, Gulf of

Cadiz (SW Iberian Peninsula). *Marine and Petroleum Geology*, *25*(8), 706–713. https://doi.org/10.1016/j.marpetgeo.2008.03.005

Merinero, R., Lunar, R., Somoza, L., Díaz-Del-Río, V. & Martinez-Frias, J. (2009). Nucleation, growth and oxidation of framboidal pyrite associated with hydrocarbon-derived submarine chimneys: lessons learned from the Gulf of Cadiz. *European Journal of Mineralogy*, *21*(5), 947–961. https://doi.org/10.1127/0935-1221/2009/0021-1956

Minyuk, P. S., Subbotnikova, T. V. & Plyashkevich, A. S. (2011). Measurements of thermal magnetic susceptibility of hematite and goethite. *Izvestiya-physics of The Solid Earth*, *47*(9), 762–774. https://doi.org/10.1134/s1069351311080052

Mladenov, N., Zheng, Y., Miller, M. J., Nemergut, D. R., Legg, T. M., Simone, B., Hageman, C., Rahman, M. M., Ahmed, K. M. & McKnight, D. M. (2010). Dissolved Organic Matter Sources and Consequences for Iron and Arsenic Mobilization in Bangladesh Aquifers. *Environmental Science & Technology*, *44*(1), 123–128. https://doi.org/10.1021/es901472g

Mladenov, N., Zheng, Y., Simone, B., Bilinski, T. M., McKnight, D. M., Nemergut, D. R., Radloff, K. A., Rahman, M. M. & Ahmed, K. M. (2015). Dissolved Organic Matter Quality in a Shallow Aquifer of Bangladesh: Implications for Arsenic Mobility. *Environmental Science & Technology*, *49*(18), 10815–10824. https://doi.org/10.1021/acs.est.5b01962

Mohan, D. & Pittman, C. U. (2007). Arsenic removal from water/wastewater using adsorbents—A critical review. *Journal of Hazardous Materials*, *142*(1–2), 1–53. https://doi.org/10.1016/j.jhazmat.2007.01.006

Mondal, D., Banerjee, M., Kundu, M., Banerjee, N., Bhattacharya, U., Giri, A. P., Ganguli, B., Roy, S. S. & Polya, D. A. (2010). Comparison of drinking water, raw rice and cooking of rice as arsenic exposure routes in three contrasting areas of West Bengal, India. *Environmental Geochemistry and Health*, *32*(6), 463–477. https://doi.org/10.1007/s10653-010-9319-5

Moore, J. N., Ficklin, W. H. & Johns, C. M. (1988). Partitioning of arsenic and metals in reducing sulfidic sediments. *Environmental Science & Technology*, *22*(4), 432–437. https://doi.org/10.1021/es00169a011

Moses, C. O., Nordstrom, D., Herman, J. S. & Mills, A. L. (1987). Aqueous pyrite oxidation by dissolved oxygen and by ferric iron. *Geochimica et Cosmochimica Acta*, *51*(6), 1561–1571. https://doi.org/10.1016/0016-7037(87)90337-1

Mozumder, M. R. H., Bostick, B. C., Selim, M., Islam, M. A., Shoenfelt, E. L., Ellis, T., Mailloux, B. J., Choudhury, I. A., Ahmed, K. M. & Van Geen, A. (2020). Similar retardation of arsenic in gray Holocene and orange Pleistocene sediments: Evidence from field-based column experiments in Bangladesh. *Water Research*, *183*, 116081. https://doi.org/10.1016/j.watres.2020.116081

Muehe, E. M. & Kappler, A. (2014). Arsenic mobility and toxicity in South and South-east Asia – a review on biogeochemistry, health and socio-economic effects, remediation and risk predictions. *Environmental Chemistry*, *11*(5), 483–495. https://doi.org/10.15496/publikation-1578

Muehe, E. M., Morin, G., Scheer, L., Pape, P. L., Esteve, I., Daus, B. & Kappler, A. (2016). Arsenic(V) Incorporation in Vivianite during Microbial Reduction of Arsenic(V)-Bearing Biogenic Fe(III) (Oxyhydr)oxides. *Environmental Science & Technology*, *50*(5), 2281–2291. https://doi.org/10.1021/acs.est.5b04625

Muehe, E. M., Scheer, L., Daus, B. & Kappler, A. (2013). Fate of Arsenic during Microbial Reduction of Biogenic versus Abiogenic As–Fe(III)–Mineral Coprecipitates. *Environmental Science & Technology*. https://doi.org/10.1021/es400801z

Mukhopadhyay, R., Rosen, B. P., Phung, L. T. & Silver, S. (2002). Microbial arsenic: from geocycles to genes and enzymes. *Fems Microbiology Reviews*, *26*(3), 311–325. https://doi.org/10.1111/j.1574-6976.2002.tb00617.x

Müller, K., Ciminelli, V. S. T., Dantas, M. V. O. & Willscher, S. (2010). A comparative study of As(III) and As(V) in aqueous solutions and adsorbed on iron oxy-hydroxides by Raman spectroscopy. *Water Research*, *44*(19), 5660–5672. https://doi.org/10.1016/j.watres.2010.05.053

Munch, J. C. & Ottow, J. C. G. (1980). Preferential reduction of amorphous to crystalline iron oxides by bacterial activity. *Soil Science*, *129*(1), 15–21. https://doi.org/10.1097/00010694-198001000-00004

Munch, J. C. & Ottow, J. C. G. (2016). Reductive Transformation Mechanism of Ferric Oxides in Hydromorphic Soils. *Environmental Biogeochemistry*, *35 S. 383–394*.

Murad, E. (1996). Magnetic properties of microcrystalline iron (III) oxides and related materials as reflected in their Mossbauer spectra. *Physics and Chemistry of Minerals*, *23*(4–5). https://doi.org/10.1007/bf00207766

Murad, E. (2010). Mössbauer spectroscopy of clays, soils and their mineral constituents. *Clay Minerals*, *45*(4), 413–430. https://doi.org/10.1180/claymin.2010.045.4.413

Murad, E. & Cashion, J. D. (2004). Mössbauer Spectroscopy of Environmental Materials and Their Industrial Utilization. *Springer eBooks*. https://doi.org/10.1007/978-1-4419-9040-2

Murad, E. & Schwertmann, U. (1980). The Möessbauer spectrum of ferrihydrite and its relations to those of other iron oxides. *American Mineralogist*, *65 (9-10): 1044–1049.*

Murcott, S. (2012). *Arsenic Contamination in the World*. IWA Publishing.

Murphy, R. & Strongin, D. R. (2009). Surface reactivity of pyrite and related sulfides. *Surface Science Reports*, *64*(1), 1–45. https://doi.org/10.1016/j.surfrep.2008.09.002

Nakai, M. & Yoshinaga, N. (1980). Fibrous goethite in some soils from Japan and Scotland. *Geoderma*. https://doi.org/10.1016/0016-7061(80)90040-3

Nakao, A., Funakawa, S. & Kosaki, T. (2009). Hydroxy-Al polymers block the frayed edge sites of illitic minerals in acid soils: studies in southwestern Japan at various weathering stages. *European Journal of Soil Science*, *60*(1), 127–138. https://doi.org/10.1111/j.1365-2389.2008.01097.x

Naujokas, M. F., Anderson, B., Ahsan, H., Aposhian, H. V., Graziano, J. H., Spilki, F. R. & Suk, W. A. (2013). The Broad Scope of Health Effects from Chronic Arsenic Exposure: Update on a Worldwide Public Health Problem. *Environmental Health Perspectives*, *121*(3), 295–302. https://doi.org/10.1289/ehp.1205875

Neidhardt, H. (2014). Arsenic in groundwater of West Bengal: Implications from a field study. KIT *Scientific Publishing. Karlsruher Mineralogische und Geochemische Hefte: Schriftenreihe des Instituts für Mineralogie und Geochemie Band 39.* https://doi.org/10.5445/KSP/1000030868

Neidhardt, H., Berg, M., Stengel, C., Winkel, L., Pham, T. & Viet, P. H. (2014). Arsenic adsorption on iron mineral phases under reducing conditions. *One Century of the Discovery of Arsenicosis in Latin America*, 947–983. https://doi.org/10.1201/b16767-32

Neidhardt, H., Norra, S., Tang, X., Guo, H. & Stüben, D. (2012). Impact of irrigation with high arsenic burdened groundwater on the soil–plant system: Results from a case study in the Inner Mongolia, China. In *Environmental Pollution* (Bd. 163, S. 8–13). Elsevier BV. https://doi.org/10.1016/j.envpol.2011.12.033

Neidhardt, H., Winkel, L. H. E., Kaegi, R., Stengel, C., Trang, P. T. K., Lan, V. M., Viet, P. H. & Berg, M. (2018). Insights into arsenic retention dynamics of Pleistocene aquifer sediments by in situ sorption experiments. *Water Research*, *129*, 123–132. https://doi.org/10.1016/j.watres.2017.11.018

Neumann, A., Petit, S. & Hofstetter, T. B. (2011). Evaluation of redox-active iron sites in smectites using middle and near infrared spectroscopy. *Geochimica et Cosmochimica Acta*, *75*(9), 2336–2355. https://doi.org/10.1016/j.gca.2011.02.009

Neumann, T., Scholz, F., Kramar, U., Ostermaier, M., Rausch, N. & Berner, Z. (2013). Arsenic in framboidal pyrite from recent sediments of a shallow water lagoon of the Baltic Sea. *Sedimentology*, n/a. https://doi.org/10.1111/sed.12031

Nghiem, A. A., Shen, Y., Stahl, M., Sun, J., Haque, E., DeYoung, B., Nguyen, K. V., Thi, T. M., Trang, P. T. K., Pham, H., Mailloux, B. J., Harvey, C. F., Van Geen, A. & Bostick, B. C. (2020). Aquifer-

Scale Observations of Iron Redox Transformations in Arsenic-Impacted Environments to Predict Future Contamination. *Environmental Science and Technology Letters*, *7*(12), 916–922. https://doi.org/10.1021/acs.estlett.0c00672

Nguyen, T. H. L. (2006). *Holocene Evolution of the Central Red River Delta, Northern Vietnam: Lithological and Mineralogical Investigations* (DISSERTATION). https://doi.org/10.23689/fidgeo-197

Ni, P., Guo, H., Yuan, R. & Huang, Q. (2017). Arsenic Migration and Transformation in Aquifer Sediments under Successive Redox Oscillations. *Procedia Earth and Planetary Science*, *17*, 384–387. https://doi.org/10.1016/j.proeps.2016.12.097

Nickson, R., McArthur, J. M., Burgess, W., Ahmed, K. M., Ravenscroft, P. & Rahman, M. M. (1998). Arsenic poisoning of Bangladesh groundwater. *Nature*, *395*(6700), 338. https://doi.org/10.1038/26387

Nickson, R., McArthur, J. M., Ravenscroft, P., Burgess, W. & Ahmed, K. M. (2000). Mechanism of arsenic release to groundwater, Bangladesh and West Bengal. *Applied Geochemistry*, *15*(4), 403–413. https://doi.org/10.1016/s0883-2927(99)00086-4

Nicomel, N. R., Leus, K., Folens, K., Van Der Voort, P. & Du Laing, G. (2015). Technologies for Arsenic Removal from Water: Current Status and Future Perspectives. *International Journal of Environmental Research and Public Health*, *13*(1), 62. https://doi.org/10.3390/ijerph13010062

Nitzsche, K. S., Lan, V. M., Trang, P. T. K., Viet, P. H., Berg, M., Voegelin, A., Planer-Friedrich, B., Zahoransky, J., Müller, S., Byrne, J. M., Schröder, C., Behrens, S. & Kappler, A. (2015). Arsenic removal from drinking water by a household sand filter in Vietnam — Effect of filter usage practices on arsenic removal efficiency and microbiological water quality. *Science of The Total Environment*, *502*, 526–536. https://doi.org/10.1016/j.scitotenv.2014.09.055

Nollet, L. M. L. & Lambropoulou, D. A. (2019). *Chromatographic Analysis of the Environment: Mass Spectrometry Based Approaches, Fourth Edition*. CRC Press.

Nordstrom, D. K. (2000). An overview of arsenic mass-poisoning in Bangladesh and West Bengal, India. *Society for Mining, Metallurgy, and Exploration*, 21–30.

Norrman, J., Sparrenbom, C., Berg, M., Nhan, D., Nhan, P. Q., Rosqvist, H., Jacks, G., Sigvardsson, E., Baric, D., Moreskog, J., Harms-Ringdahl, P. & Van Hoan, N. (2008). Arsenic mobilisation in a new well field for drinking water production along the Red River, Nam Du, Hanoi. *Applied Geochemistry*. https://doi.org/10.1016/j.apgeochem.2008.06.016

Nriagu, J. O., Bhattacharya, P. K., Mukherjee, A., Bundschuh, J., Zevenhoven, R. & Loeppert, R. H. (2007). Arsenic in soil and groundwater: an overview. *Trace Metals and other Contaminants in the Environment*, 3–60. https://doi.org/10.1016/s1875-1121(06)09001-8

O'Day, P. A. (2006). Chemistry and Mineralogy of Arsenic. *Elements*, *2*(2), 77–83. https://doi.org/10.2113/gselements.2.2.77

Ohfuji, H., Boyle, A., Prior, D. L. & Rickard, D. (2005). Structure of framboidal pyrite: An electron backscatter diffraction study. *American Mineralogist*, *90*(11–12), 1693–1704. https://doi.org/10.2138/am.2005.1829

Ona-Nguema, G., Morin, G., Juillot, F., Calas, G. & Brown, G. E. (2005). EXAFS Analysis of Arsenite Adsorption onto Two-Line Ferrihydrite, Hematite, Goethite, and Lepidocrocite. *Environmental Science & Technology*, *39*(23), 9147–9155. https://doi.org/10.1021/es050889p

Ona-Nguema, G., Morin, G., Wang, Y., Menguy, N., Juillot, F., Olivi, L., Aquilanti, G., Abdelmoula, M., Ruby, C., Bargar, J. R., Guyot, F., Calas, G. & Brown, G. E. (2009). Arsenite sequestration at the surface of nano-Fe(OH)2, ferrous-carbonate hydroxide, and green-rust after bioreduction of arsenic-sorbed lepidocrocite by Shewanella putrefaciens. *Geochimica et Cosmochimica Acta*, *73*(5), 1359–1381. https://doi.org/10.1016/j.gca.2008.12.005

Oremland, R. S., Newman, D. K., Kail, B. W. & Stolz, J. F. (2002). Bacterial Respiration of Arsenate and Its Significance in the Environment. *CRC Press eBooks*, 293–316. https://doi.org/10.1201/9781482271102-18

Oremland, R. S. & Stolz, J. F. (2003). The Ecology of Arsenic. *Science*, *300*(5621), 939–944. https://doi.org/10.1126/science.1081903

Oremland, R. S. & Stolz, J. F. (2005). Arsenic, microbes and contaminated aquifers. *Trends in Microbiology*, *13*(2), 45–49. https://doi.org/10.1016/j.tim.2004.12.002

Oscarson, D., Huang, P., Defosse, C. & Herbillon, A. (1981). Oxidative power of Mn(IV) and Fe(III) oxides with respect to As(III) in terrestrial and aquatic environments. *Nature*, *291*(5810), 50–51. https://doi.org/10.1038/291050a0

Oscarson, D. W., Huang, P. M. & Liaw, W. K. (1980). The Oxidation of Arsenite by Aquatic Sediments. *Journal of Environmental Quality*, *9*(4), 700–703. https://doi.org/10.2134/jeq1980.00472425000900040032x

Oscarson, D. W., Huang, P. M. & Liaw, W. K. (1981). Role of Manganese in the Oxidation of Arsenite by Freshwater Lake Sediments1. *Clays and Clay Minerals*, *29*(3), 219–225. https://doi.org/10.1346/ccmn.1981.0290308

Pan, Y., Zhu, R., Banerjee, S. K., Gill, J. B. & Williams, Q. (2000). Rock magnetic properties related to thermal treatment of siderite: Behavior and interpretation. *Journal of Geophysical Research*, *105*(B1), 783–794. https://doi.org/10.1029/1999jb900358

Parsons, C. A., Couture, R., Omoregie, E. O., Bardelli, F., Greneche, J., Roman-Ross, G. & Charlet, L. (2013). The impact of oscillating redox conditions: Arsenic immobilisation in contaminated calcareous floodplain soils. *Environmental Pollution*, *178*, 254–263. https://doi.org/10.1016/j.envpol.2013.02.028

Pedersen, H. B., Postma, D. J. & Jakobsen, R. (2006). Release of arsenic associated with the reduction and transformation of iron oxides. *Geochimica et Cosmochimica Acta*, *70*(16), 4116–4129. https://doi.org/10.1016/j.gca.2006.06.1370

Pedersen, H. B., Postma, D. J., Jakobsen, R. & Larsen, O. H. (2005). Fast transformation of iron oxyhydroxides by the catalytic action of aqueous Fe(II). *Geochimica et Cosmochimica Acta*, *69*(16), 3967–3977. https://doi.org/10.1016/j.gca.2005.03.016

Perelomov, L., Cozzolino, V., Pigna, M. & Violante, A. (2011). Adsorption of Cu and Pb on Goethite in the Presence of Low-Molecular Mass Aliphatic Acids. *Geomicrobiology Journal*. https://doi.org/10.1080/01490451.2011.559303

Perret, D., Gaillard, J. F., Dominik, J. & Atteia, O. (2000). The Diversity of Natural Hydrous Iron Oxides. *Environmental Science & Technology*, *34*(17), 3540–3546. https://doi.org/10.1021/es0000089

Peterson, M. L. & Carpenter, R. (1983). Biogeochemical processes affecting total arsenic and arsenic species distributions in an intermittently anoxic fjord. *Marine Chemistry*, *12*(4), 295–321. https://doi.org/10.1016/0304-4203(83)90058-0

Petrovský, E. & Kapička, A. (2005). Comments on "The use of field dependence of magnetic susceptibility for monitoring variations in titanomagnetite composition - a case study on basanites from the Vogelsberg 1996 drillhole, Germany" by de Wall and Nano, Stud. Geophys. Geod., 48, 767–776. *Studia Geophysica Et Geodaetica*. https://doi.org/10.1007/s11200-005-0008-2

Phan, K., Phan, S., Heng, S., Huoy, L. & Kim, K. (2014). Assessing arsenic intake from groundwater and rice by residents in Prey Veng province, Cambodia. *Environmental Pollution*, *185*, 84–89. https://doi.org/10.1016/j.envpol.2013.10.022

Phan, V. N., Bardelli, F., Pape, P. L., Couture, R., Fernandez-Martinez, A., Tisserand, D., Bernier-Latmani, R. & Charlet, L. (2019). Interplay of S and As in Mekong Delta sediments during redox oscillations. *Geoscience frontiers*, *10*(5), 1715–1729. https://doi.org/10.1016/j.gsf.2018.03.008

Phi, T. H. & Strokova, L. A. (2015). Prediction maps of land subsidence caused by groundwater exploitation in Hanoi, Vietnam. *Resource-Efficient Technologies*, *1*(2), 80–89. https://doi.org/10.1016/j.reffit.2015.09.001

Picard, A., Gartman, A. & Girguis, P. R. (2016). What Do We Really Know about the Role of Microorganisms in Iron Sulfide Mineral Formation? *Frontiers in Earth Science*, *4*. https://doi.org/10.3389/feart.2016.00068

Picard, A., Kappler, A., Schmid, G. F., Quaroni, L. & Obst, M. (2015). Experimental diagenesis of organo-mineral structures formed by microaerophilic Fe(II)-oxidizing bacteria. *Nature Communications*, *6*(1). https://doi.org/10.1038/ncomms7277

Podgorski, J. & Berg, M. (2020). Global threat of arsenic in groundwater. *Science*, *368*(6493), 845–850. https://doi.org/10.1126/science.aba1510

Pollak, H. & Stevens, J. G. (1986). Phyllosilicates: A Mössbauer evaluation. *Hyperfine Interactions*, *29*(1–4), 1153–1156. https://doi.org/10.1007/bf02399439

Polizzotto, M. L., Kocar, B. D., Benner, S. G., Sampson, M. J. & Fendorf, S. (2008). Near-surface wetland sediments as a source of arsenic release to ground water in Asia. *Nature*, *454*(7203), 505–508. https://doi.org/10.1038/nature07093

Posth, N. R., Canfield, D. E. & Kappler, A. (2014). Biogenic Fe(III) minerals: From formation to diagenesis and preservation in the rock record. *Earth-Science Reviews*, *135*, 103–121. https://doi.org/10.1016/j.earscirev.2014.03.012

Posth, N. R., Huelin, S., Konhauser, K. O. & Kappler, A. (2010). Size, density and composition of cell–mineral aggregates formed during anoxygenic phototrophic Fe(II) oxidation: Impact on modern and ancient environments. *Geochimica et Cosmochimica Acta*, *74*(12), 3476–3493. https://doi.org/10.1016/j.gca.2010.02.036

Postma, D. & Jakobsen, R. (1996). Redox zonation: Equilibrium constraints on the Fe(III)/SO4-reduction interface. *Geochimica et Cosmochimica Acta*, *60*(17), 3169–3175. https://doi.org/10.1016/0016-7037(96)00156-1

Postma, D., Jessen, S., Hue, N. T., Duc, M. T., Koch, C., Viet, P. H., Nhan, P. Q. & Larsen, F. (2010). Mobilization of arsenic and iron from Red River floodplain sediments, Vietnam. *Geochimica et Cosmochimica Acta*, *74*(12), 3367–3381. https://doi.org/10.1016/j.gca.2010.03.024

Postma, D., Larsen, F., Hue, N. T., Duc, M. T., Viet, P. H., Nhan, P. Q. & Jessen, S. (2007). Arsenic in groundwater of the Red River floodplain, Vietnam: Controlling geochemical processes and reactive transport modeling. *Geochimica et Cosmochimica Acta*, *71*(21), 5054–5071. https://doi.org/10.1016/j.gca.2007.08.020

Postma, D., Larsen, F., Thai, N. Q., Trang, P. T. K., Jakobsen, R., Nhan, P. Q., Long, T. K., Viet, P. H. & Murray, A. S. (2012). Groundwater arsenic concentrations in Vietnam controlled by sediment age. *Nature Geoscience*, *5*(9), 656–661. https://doi.org/10.1038/ngeo1540

Quicksall, A. N., Bostick, B. C. & Sampson, M. (2008). Linking organic matter deposition and iron mineral transformations to groundwater arsenic levels in the Mekong delta, Cambodia. *Applied Geochemistry*, *23*(11), 3088–3098. https://doi.org/10.1016/j.apgeochem.2008.06.027

Radu, T., Subacz, J. L., Phillippi, J. M. & Barnett, M. A. (2005). Effects of Dissolved Carbonate on Arsenic Adsorption and Mobility. *Environmental Science & Technology*, *39*(20), 7875–7882. https://doi.org/10.1021/es050481s

Rahman, M. M., Naidu, R. & Bhattacharya, P. (2009). Arsenic contamination in groundwater in the Southeast Asia region. *Environmental Geochemistry and Health*, *31*(S1), 9–21. https://doi.org/10.1007/s10653-008-9233-2

Rahman, M. M., Ng, J. C. & Naidu, R. (2009). Chronic exposure of arsenic via drinking water and its adverse health impacts on humans. *Environmental Geochemistry and Health*, *31*(S1), 189–200. https://doi.org/10.1007/s10653-008-9235-0

Raiswell, R., Reinhard, C. T., Derkowski, A., Owens, J. D., Bottrell, S. H., Anbar, A. D. & Lyons, T. W. (2011). Formation of syngenetic and early diagenetic iron minerals in the late Archean Mt. McRae Shale, Hamersley Basin, Australia: New insights on the patterns, controls and paleoenvironmental implications of authigenic mineral formation. In *Geochimica et Cosmochimica Acta* (Bd. 75, Nummer 4, S. 1072–1087). Elsevier BV. https://doi.org/10.1016/j.gca.2010.11.013

Rancourt, D., Fortin, D., Pichler, T., Thibault, P., Lamarche, G., Morris, R. W. & Mercier, P. P. (2001). Mineralogy of a natural As-rich hydrous ferric oxide coprecipitate formed by mixing of hydrothermal fluid and seawater: Implications regarding surface complexation and color banding in ferrihydrite deposits. *American Mineralogist*, *86*(7–8), 834–851. https://doi.org/10.2138/am-2001-0707

Rancourt, D. G. & Ping, J. (1991). Voigt-based methods for arbitrary-shape static hyperfine parameter distributions in Mössbauer spectroscopy. *Nuclear Instruments & Methods in Physics Research Section B-beam Interactions With Materials and Atoms*, *58*(1), 85–97. https://doi.org/10.1016/0168-583x(91)95681-3

Rangin, C., Klein, M., Roques, D., Pichon, X. L. & Van Trong, L. (1995). The Red River fault system in the Tonkin Gulf, Vietnam. *Tectonophysics*, *243*(3–4), 209–222. https://doi.org/10.1016/0040-1951(94)00207-p

Rathi, B., Neidhardt, H., Berg, M., Siade, A. J. & Prommer, H. (2017). Processes governing arsenic retardation on Pleistocene sediments: Adsorption experiments and model-based analysis. *Water Resources Research*, *53*(5), 4344–4360. https://doi.org/10.1002/2017wr020551

Raven, K. P., Jain, A. A. & Loeppert, R. H. (1998). Arsenite and Arsenate Adsorption on Ferrihydrite: Kinetics, Equilibrium, and Adsorption Envelopes. *Environmental Science & Technology*, *32*(3), 344–349. https://doi.org/10.1021/es970421p

Ravenscroft, P., Brammer, H. & Richards, K. (2009). *Arsenic Pollution: A Global Synthesis*. Wiley-Blackwell.

Ravenscroft, P., McArthur, J. M. & Hoque, B. (2001). Geochemical and palaeohydrological controls on pollution of groundwater by arsenic. *Elsevier Science B.V. eBooks*. https://discovery.ucl.ac.uk/id/eprint/562/

Redman, A. D., Macalady, D. L. & Ahmann, D. (2002). Natural Organic Matter Affects Arsenic Speciation and Sorption onto Hematite. *Environmental Science & Technology*, *36*(13), 2889–2896. https://doi.org/10.1021/es0112801

Reeburgh, W. S. (2007). Oceanic Methane Biogeochemistry. *Chemical Reviews*, *107*(2), 486–513. https://doi.org/10.1021/cr050362v

Reich, M. & Becker, U. (2006). First-principles calculations of the thermodynamic mixing properties of arsenic incorporation into pyrite and marcasite. *Chemical Geology*, *225*(3–4), 278–290. https://doi.org/10.1016/j.chemgeo.2005.08.021

Reimann, C. & De Caritat, P. (1998). *Chemical Elements in the Environment: Factsheets for the Geochemist and Environmental Scientist*. Springer.

Reimann, C., Matschullat, J., Birke, M. & Salminen, R. (2009). Arsenic distribution in the environment: The effects of scale. *Applied Geochemistry*, *24*(7), 1147–1167. https://doi.org/10.1016/j.apgeochem.2009.03.013

Reitner, J., Peckmann, J., Reimer, A., Schumann, G. & Thiel, V. (2005). Methane-derived carbonate build-ups and associated microbial communities at cold seeps on the lower Crimean shelf (Black Sea). *Facies*, *51*(1–4), 66–79. https://doi.org/10.1007/s10347-005-0059-4

Renard, F., Røyne, A. & Putnis, C. V. (2019). Timescales of interface-coupled dissolution-precipitation reactions on carbonates. *Geoscience frontiers*, *10*(1), 17–27. https://doi.org/10.1016/j.gsf.2018.02.013

Rich, C. I. (1968). Hydroxy Interlayers in Expansible Layer Silicates*. *Clays and Clay Minerals*, *16*(1), 15–30. https://doi.org/10.1346/ccmn.1968.0160104

Rickard, D. (2019a). How long does it take a pyrite framboid to form? *Earth and Planetary Science Letters*, *513*, 64–68. https://doi.org/10.1016/j.epsl.2019.02.019

Rickard, D. (2019b). Sedimentary pyrite framboid size-frequency distributions: A meta-analysis. *Palaeogeography, Palaeoclimatology, Palaeoecology*, *522*, 62–75. https://doi.org/10.1016/j.palaeo.2019.03.010

Rickard, D. & Luther, G. W. (2007). Chemistry of Iron Sulfides. *Chemical Reviews*, *107*(2), 514–562. https://doi.org/10.1021/cr0503658

Roberts, F. I. (1982). Trace element chemistry of pyrite: A useful guide to the occurrence of sulfide base metal mineralization. *Journal of Geochemical Exploration*, *17*(1), 49–62. https://doi.org/10.1016/0375-6742(82)90019-x

Robinson, G. R. & Ayotte, J. D. (2006). The influence of geology and land use on arsenic in stream sediments and ground waters in New England, USA. *Applied Geochemistry*, *21*(9), 1482–1497. https://doi.org/10.1016/j.apgeochem.2006.05.004

Rochette, E. A., Li, G. C. & Fendorf, S. (1998). Stability of Arsenate Minerals in Soil under Biotically Generated Reducing Conditions. *Soil Science Society Of America Journal*, *62*(6), 1530–1537. https://doi.org/10.2136/sssaj1998.03615995006200060008x

Roden, E. E. & Zachara, J. M. (1996). Microbial Reduction of Crystalline Iron(III) Oxides: Influence of Oxide Surface Area and Potential for Cell Growth. *Environmental Science & Technology*, *30*(5), 1618–1628. https://doi.org/10.1021/es9506216

Rodrigues, A. K. B. F., De Ros, L. F., Neumann, R. & Borghi, L. (2015). Paleoenvironmental implications of early diagenetic siderites of the Paraíba do Sul Deltaic Complex, eastern Brazil. *Sedimentary Geology*, *323*, 15–30. https://doi.org/10.1016/j.sedgeo.2015.04.005

Rodríguez-Lado, L., Sun, G., Berg, M., Zhang, Q., Xue, H., Zheng, Q. & Johnson, C. A. (2013). Groundwater Arsenic Contamination Throughout China. *Science*, *341*(6148), 866–868. https://doi.org/10.1126/science.1237484

Roh, Y., Zhang, C. C., Vali, H., Lauf, R. J., Zhou, J. & Phelps, T. J. (2003). BIOGEOCHEMICAL AND ENVIRONMENTAL FACTORS IN Fe BIOMINERALIZATION: MAGNETITE AND SIDERITE FORMATION. *Clays and Clay Minerals*, *51*(1), 83–95. https://doi.org/10.1346/ccmn.2003.510110

Rosso, K. M., Yanina, S., Gorski, C. A., Larese-Casanova, P. & Scherer, M. M. (2010). Connecting Observations of Hematite (α-Fe2O3) Growth Catalyzed by Fe(II). *Environmental Science & Technology*, *44*(1), 61–67. https://doi.org/10.1021/es901882a

Rotiroti, M., Jakobsen, R., Fumagalli, L. & Bonomi, T. (2015). Arsenic release and attenuation in a multilayer aquifer in the Po Plain (northern Italy): Reactive transport modeling. *Applied Geochemistry*, *63*, 599–609. https://doi.org/10.1016/j.apgeochem.2015.07.001

Ryan, J. N. & Gschwend, P. M. (1994). Effect of Solution Chemistry on Clay Colloid Release from an Iron Oxide-Coated Aquifer San. *Environ. Sci. Technol.*, *28, 1717–1726*.

Saha, K. C. (1984). Melanokeratosis from arsenic contaminated tubewell water. *Indian Journal of Dermatology*, *29*(4), 37–46.

Salmassi, T., Venkateswaren, K., Satomi, M., Nealson, K. H., Newman, D. K. & Anastas, P. T. (2002). Oxidation of Arsenite by Agrobacterium albertimagni , AOL15, sp. nov., Isolated from Hot Creek, California. *Geomicrobiology Journal*, *19*(1), 53–66. https://doi.org/10.1080/014904502317246165

Sánchez-Román, M., Puente-Sánchez, F., Parro, V. & Amils, R. (2015). Nucleation of Fe-rich phosphates and carbonates on microbial cells and exopolymeric substances. In *Frontiers in Microbiology* (Bd. 6). Frontiers Media. https://doi.org/10.3389/fmicb.2015.01024

Sanders, J. O. (1980). Arsenic cycling in marine systems. *Marine Environmental Research*, *3*(4), 257–266. https://doi.org/10.1016/0141-1136(80)90038-0

Sarkar, A. & Paul, B. (2016). The global menace of arsenic and its conventional remediation - A critical review. *Chemosphere*, *158*, 37–49. https://doi.org/10.1016/j.chemosphere.2016.05.043

Saunders, J. C., Pritchett, M. A. & Cook, R. L. (1997). Geochemistry of biogenic pyrite and ferromanganese coatings from a small watershed: A bacterial connection? *Geomicrobiology Journal*, *14*(3), 203–217. https://doi.org/10.1080/01490459709378044

Saunders, J., Lee, M. J., Shamsudduha, M., Dhakal, P., Uddin, A., Chowdury, M. & Ahmed, K. M. (2008). Geochemistry and mineralogy of arsenic in (natural) anaerobic groundwaters. *Applied Geochemistry*, *23*(11), 3205–3214. https://doi.org/10.1016/j.apgeochem.2008.07.002

Saunders, J., Lee, M. J., Uddin, A., Mohammad, S., Wilkin, R. T., Fayek, M. & Korte, N. (2005). Natural arsenic contamination of Holocene alluvial aquifers by linked tectonic, weathering, and

microbial processes. *Geochemistry Geophysics Geosystems*, *6*(4), n/a. https://doi.org/10.1029/2004gc000803

Saunders, J., Mohammad, S., Korte, N., Lee, M. J., Fayek, M., Castle, D. J. & Barnett, M. O. (2005). Groundwater Geochemistry, Microbiology, and Mineralogy in Two Arsenic-Bearing Holocene Alluvial Aquifers from the United States. *Acs Symposium Series*, 191–205. https://doi.org/10.1021/bk-2005-0915.ch014

Sawłowicz, Z. (1993). Pyrite framboids and their development: a new conceptual mechanism. *Acta Diabetologica*, *82*(1), 148–156. https://doi.org/10.1007/bf00563277

Sawłowicz, Z. (2000). Framboids: from their origin to application. *Polska Akademia Nauk – Oddzial W Krakowie Komisja Nauk Mineralogicznych Prace Mineralogiczne*, *88*, 83-86726-73–3.

Schaefer, M., Handler, R. & Scherer, M. M. (2017). Fe(II) reduction of pyrolusite (β-MnO2) and secondary mineral evolution. *Geochemical Transactions*, *18*(1). https://doi.org/10.1186/s12932-017-0045-0

Scheidegger, A., Borkovec, M. & Sticher, H. (1993). Coating of silica sand with goethite: preparation and analytical identification. *Geoderma*, *58*(1–2), 43–65. https://doi.org/10.1016/0016-7061(93)90084-x

Schwertmann, U. (1991). Solubility and dissolution of iron oxides. *Plant and Soil*, *130*(1–2), 1–25. https://doi.org/10.1007/bf00011851

Schwertmann, U. & Cornell, R. M. (2000). *Iron Oxides in the Laboratory: Preparation and Characterization*. John Wiley & Sons.

Schwertmann, U. & Fischer, W. R. (1973). Natural “amorphous” ferric hydroxide. *Geoderma*, *10*(3), 237–247. https://doi.org/10.1016/0016-7061(73)90066-9

Schwertmann, U. & Fitzpatrick, R. (1992). Iron minerals in surface environments. *Skinner, H.C.W. & Fitzpatrick, R.W. (eds.) „Biomineralization“. Catena Suppl.*, *21*, 7–30.

Schwertmann, U. & Taylor, R. J. K. (2018). Iron Oxides. *Soil Science Society of America book series*, 379–438. https://doi.org/10.2136/sssabookser1.2ed.c8

Senn, A., Hug, S. J., Kaegi, R., Anastas, P. T. & Voegelin, A. (2018). Arsenate co-precipitation with Fe(II) oxidation products and retention or release during precipitate aging. *Water Research*, *131*, 334–345. https://doi.org/10.1016/j.watres.2017.12.038

Sherman, D. H. & Randall, S. (2003). Surface complexation of arsenic(V) to iron(III) (hydr)oxides: structural mechanism from ab initio molecular geometries and EXAFS spectroscopy. *Geochimica et Cosmochimica Acta*, *67*(22), 4223–4230. https://doi.org/10.1016/s0016-7037(03)00237-0

Siivola, J. & Schmid, R. (2007). Recommendations by the IUGS Subcommissionon the Systematics of Metamorphic Rocks: List of mineral abbreviations. Webversion 01.02.07. *IUGS Commission on the Systematics in Petrology*. https://ttp://www.bgs.ac.uk/scmr/docs/papers/paper_12.pdf

Simons, G., Bastiaanssen, W. G., Ngô, L. A., Hain, C., Anderson, M. C. & Senay, G. B. (2016). Integrating Global Satellite-Derived Data Products as a Pre-Analysis for Hydrological Modelling Studies: A Case Study for the Red River Basin. *Remote Sensing*, *8*(4), 279. https://doi.org/10.3390/rs8040279

Smedley, P. & Kinniburgh, D. G. (2002). A review of the source, behaviour and distribution of arsenic in natural waters. *Applied Geochemistry*, *17*(5), 517–568. https://doi.org/10.1016/s0883-2927(02)00018-5

Smith, A. H., Hopenhayn-Rich, C., Bates, M. N., Goeden, H. M., Hertz-Picciotto, I., Duggan, H. M., Wood, R., Kosnett, M. J. & Smith, M. T. (1992). Cancer risks from arsenic in drinking water. *Environmental Health Perspectives*, *97*, 259–267. https://doi.org/10.1289/ehp.9297259

Smith, A. H., Lingas, E. O. & Rahman, M. (2000). Contamination of drinking-water by arsenic in Bangladesh: a public health emergency. *Bulletin of The World Health Organization*, *78*(9), 1093–1103.

Smith, A. H. & Smith, M. M. H. (2004). Arsenic drinking water regulations in developing countries with extensive exposure. *Toxicology*, *198*(1–3), 39–44. https://doi.org/10.1016/j.tox.2004.02.024

Smith, E., Naidu, R. & Alston, A. M. (1998). Arsenic in the Soil Environment: A Review. *Elsevier eBooks*, 149–195. https://doi.org/10.1016/s0065-2113(08)60504-0

Smith, S. S. & Edwards, M. (2005). The influence of silica and calcium on arsenate sorption to oxide surfaces. *Aqua*, *54*(4), 201–211. https://doi.org/10.2166/aqua.2005.0019

Sø, H. U., Postma, D., Hoang, V. T., Mai, L. V., Kim, T. P. T., Hung, V. P. & Jakobsen, R. (2018). Arsenite adsorption controlled by the iron oxide content of Holocene Red River aquifer sediment. *Geochimica et Cosmochimica Acta*, *239*, 61–73. https://doi.org/10.1016/j.gca.2018.07.026

Sø, H. U., Postma, D., Lan, M. T., Pham, T. T. H., Kazmierczak, J., Dao, V. T., Pi, K., Koch, C., Pham, H. & Jakobsen, R. (2018). Arsenic in Holocene aquifers of the Red River floodplain, Vietnam: Effects of sediment-water interactions, sediment burial age and groundwater residence time. *Geochimica et Cosmochimica Acta*, *225*, 192–209. https://doi.org/10.1016/j.gca.2018.01.010

Søren, J. (2009). *Groundwater arsenic in the Red River delta, Vietnam Regional distribution, release, mobility and mitigation options* (DISSERTATION). https://backend.orbit.dtu.dk/ws/portalfiles/portal/5034320/ENV2009-208.pdf

Squibb, K. & Fowler, B. A. (1983). The toxicity of arsenic and its compounds. *Elsevier eBooks*, 233–269. https://doi.org/10.1016/b978-0-444-80513-3.50011-6

Stachowicz, M., Hiemstra, T. & Van Riemsdijk, W. (2008). Multi-competitive interaction of As(III) and As(V) oxyanions with Ca2+, Mg2+, PO3−4, and CO2−3 ions on goethite. *Journal of Colloid and Interface Science*, *320*(2), 400–414. https://doi.org/10.1016/j.jcis.2008.01.007

Stahl, M., Harvey, C. F., Van Geen, A., Sun, J., Trang, P. T. K., Lan, V. M., Phuong, T. T., Viet, P. H. & Bostick, B. C. (2016). River bank geomorphology controls groundwater arsenic concentrations in aquifers adjacent to the Red River, Hanoi Vietnam. *Water Resources Research*, *52*(8), 6321–6334. https://doi.org/10.1002/2016wr018891

Steefel, C. I. & Van Cappellen, P. (1990). A new kinetic approach to modeling water-rock interaction: The role of nucleation, precursors, and Ostwald ripening. *Geochimica et Cosmochimica Acta*, *54*(10), 2657–2677. https://doi.org/10.1016/0016-7037(90)90003-4

Stopelli, E., Duyen, V. T., Mai, T. T., Trang, P. T. K., Viet, P. H., Lightfoot, A. F., Kipfer, R., Schneider, M., Eiche, E., Kontny, A., Neumann, T., Glodowska, M., Patzner, M. S., Kappler, A., Kleindienst, S., Rathi, B., Cirpka, O. A., Bostick, B. C., Prommer, H., . . . Berg, M. (2020). Spatial and temporal evolution of groundwater arsenic contamination in the Red River delta, Vietnam: Interplay of mobilisation and retardation processes. *Science of The Total Environment*, *717*, 137143. https://doi.org/10.1016/j.scitotenv.2020.137143

Stopelli, E., Duyen, V. T., Prommer, H., Glodowska, M., Kappler, A., Schneider, M., Eiche, E., Lightfoot, A. F., Schubert, C. J., Trang, P. T. K., Viet, P. H., Kipfer, R., Winkel, L. H. E., Berg, M. & Members, A. T. (2021). Carbon and methane cycling in arsenic-contaminated aquifers. *Water Research*, *200*, 117300. https://doi.org/10.1016/j.watres.2021.117300

Stuckey, J. W., Schaefer, M., Benner, S. G. & Fendorf, S. (2015). Reactivity and speciation of mineral-associated arsenic in seasonal and permanent wetlands of the Mekong Delta. *Geochimica et Cosmochimica Acta*, *171*, 143–155. https://doi.org/10.1016/j.gca.2015.09.002

Stuckey, J. W., Schaefer, M., Kocar, B. D., Benner, S. G. & Fendorf, S. (2016). Arsenic release metabolically limited to permanently water-saturated soil in Mekong Delta. *Nature Geoscience*, *9*(1), 70–76. https://doi.org/10.1038/ngeo2589

Stucki, J., Goodman, B., Goodman, B. A. & Schwertmann, U. (1988). *Iron in Soils and Clay Minerals*. Springer.

Stucki, J., Goodman, B. & Schwertmann, U. (2012). *Iron in Soils and Clay Minerals*. Springer Science & Business Media.

Stucki, J. W. (2011). A review of the effects of iron redox cycles on smectite properties. *Comptes Rendus Geoscience*, *343*(2–3), 199–209. https://doi.org/10.1016/j.crte.2010.10.008

Stucki, J. W., Bailey, G. S. & Gan, H. (1996). Oxidation-reduction mechanisms in iron-bearing phyllosilicates. *Applied Clay Science*, *10*(6), 417–430. https://doi.org/10.1016/0169-1317(96)00002-6

Suib, S. L., Gao, T., Hong, J. S., Tan, W., Liu, F. & Zheng, L. (2017). Mechanisms of arsenic-containing pyrite oxidation by aqueous arsenate under anoxic conditions. *Geochimica et Cosmochimica Acta*, *217*, 306–319. https://doi.org/10.1016/j.gca.2017.08.030

Sullivan, K. & Aller, R. C. (1996). Diagenetic cycling of arsenic in Amazon shelf sediments. *Geochimica et Cosmochimica Acta*, *60*(9), 1465–1477. https://doi.org/10.1016/0016-7037(96)00040-3

Sultan, R. & Abdel-Rahman, A. M. (2013). On dynamic self-organization: examples from magmatic and other geochemical systems. *Latin American Journal of Solids and Structures*, *10*(1), 59–73. https://doi.org/10.1590/s1679-78252013000100006

Sun, J., Chillrud, S. N., Mailloux, B. J., Stute, M., Singh, R., Dong, H., Lepre, C. J. & Bostick, B. C. (2016). Enhanced and stabilized arsenic retention in microcosms through the microbial oxidation of ferrous iron by nitrate. *Chemosphere*, *144*, 1106–1115. https://doi.org/10.1016/j.chemosphere.2015.09.045

Sun, J., Prommer, H., Siade, A. J., Chillrud, S. N., Mailloux, B. J. & Bostick, B. C. (2018). Model-Based Analysis of Arsenic Immobilization via Iron Mineral Transformation under Advective Flows. *Environmental Science & Technology*, *52*(16), 9243–9253. https://doi.org/10.1021/acs.est.8b01762

Suzuki, T., Hashimoto, H., Itadani, A., Matsumoto, N., Kunoh, H. & Takada, J. (2012). Silicon and Phosphorus Linkage with Iron via Oxygen in the Amorphous Matrix of Gallionella ferruginea Stalks. *Applied and Environmental Microbiology*, *78*(1), 236–241. https://doi.org/10.1128/aem.05913-11

Suzuki, T., Hashimoto, H., Matsumoto, N., Furutani, M., Kunoh, H. & Takada, J. (2011). Nanometer-Scale Visualization and Structural Analysis of the Inorganic/Organic Hybrid Structure of

Gallionella ferruginea Twisted Stalks. *Applied and Environmental Microbiology*, *77*(9), 2877–2881. https://doi.org/10.1128/aem.02867-10

Swartz, C. L., Blute, N., Badruzzman, B., Ali, A., Brabander, D. J., Jay, J. A., Besancon, J., Islam, S., Hemond, H. F. & Harvey, C. F. (2004). Mobility of arsenic in a Bangladesh aquifer: Inferences from geochemical profiles, leaching data, and mineralogical characterization. *Geochimica et Cosmochimica Acta*, *68*(22), 4539–4557. https://doi.org/10.1016/j.gca.2004.04.020

Sweeney, R. E. & Kaplan, I. R. (1973). Pyrite Framboid Formation; Laboratory Synthesis and Marine Sediments. *Economic geology and the bulletin of the Society of Economic Geologists*, *68*(5), 618–634. https://doi.org/10.2113/gsecongeo.68.5.618

Szymański, W., Skiba, M. & Błachowski, A. (2017). Influence of redox processes on clay mineral transformation in Retisols in the Carpathian Foothills in Poland. Is a ferrolysis process present? *Journal of Soils and Sediments*, *17*(2), 453–470. https://doi.org/10.1007/s11368-016-1531-1

Szymański, W., Skiba, M., Nikorych, V. A. & Kuligiewicz, A. (2014). Nature and formation of interlayer fillings in clay minerals in Albeluvisols from the Carpathian Foothills, Poland. *Geoderma*, *235–236*, 396–409. https://doi.org/10.1016/j.geoderma.2014.08.001

Tamaki, S. & Frankenberger, W. T. (1992). Environmental Biochemistry of Arsenic. *Reviews of Environmental Contamination and Toxicology*, 79–110. https://doi.org/10.1007/978-1-4612-2864-6_4

Tanabe, S. I. (2003). Song Hong (Red River) delta evolution related to millennium-scale Holocene sea-level changes. *Quaternary Science Reviews*, *22*(21–22), 2345–2361. https://doi.org/10.1016/s0277-3791(03)00138-0

Tanabe, S., Saito, Y., Vu, Q. H., Hanebuth, T. J. J., Ngo, Q. M. & Kitamura, A. (2006). Holocene evolution of the Song Hong (Red River) delta system, northern Vietnam. *Sedimentary Geology*, *187*(1–2), 29–61. https://doi.org/10.1016/j.sedgeo.2005.12.004

Tarling, D. H. & Hrouda, F. (1995). The Magnetic Anisotropy of Rocks. *Geological Magazine*. https://doi.org/10.1017/s0016756800021543

Thakur, J. K., Thakur, R. K., Ramanathan, A., Kumar, M. & Singh, S. K. (2010). Arsenic Contamination of Groundwater in Nepal—An Overview. *Water*, *3*(1), 1–20. https://doi.org/10.3390/w3010001

Thanabalasingam, P. & Pickering, W. (1986). Arsenic sorption by humic acids. *Environmental Pollution Series B, Chemical and Physical*, *12*(3), 233–246. https://doi.org/10.1016/0143-148x(86)90012-1

The Groundwater Project. *The Importance of Groundwater - The Groundwater Project* (27.10.2020). https://gw-project.org/the-importance-of-groundwater/

The microbial ferrous wheel: iron cycling in terrestrial, freshwater, and marine environments. (2012). *Frontiers research topics*. https://doi.org/10.3389/978-2-88919-074-4

Thompson, A., Chadwick, O. A., Rancourt, D. & Chorover, J. (2006). Iron-oxide crystallinity increases during soil redox oscillations. *Geochimica et Cosmochimica Acta*, *70*(7), 1710–1727. https://doi.org/10.1016/j.gca.2005.12.005

Thompson, A., Rancourt, D., Chadwick, O. A. & Chorover, J. (2011). Iron solid-phase differentiation along a redox gradient in basaltic soils. *Geochimica et Cosmochimica Acta*, *75*(1), 119–133. https://doi.org/10.1016/j.gca.2010.10.005

Thu, T. M. & Fredlund, D. G. (2000). Modelling subsidence in the Hanoi City area, Vietnam. *Canadian Geotechnical Journal*, *37*(3), 621–637. https://doi.org/10.1139/cgj-37-3-621

Thuan, A., DO, Kuroda, K., Hayashi, T., Nga, T. V. T., Oguma, K. & Takizawa, S. (2014). Household survey of installation and treatment efficiency of point-of-use water treatment systems in Hanoi, Vietnam. *Aqua*, *63*(2), 154–161. https://doi.org/10.2166/aqua.2013.011

Tian, L., Song, H., Ye, Q., Hu, J., An, Z., Zhao, X., Bottjer, D. J. & Tong, J. (2020). Recurrent anoxia recorded in shallow marine facies at Zhangcunping (western Hubei, China) throughout the

Ediacaran to earliest Cambrian. *Precambrian Research*, *340*, 105617. https://doi.org/10.1016/j.precamres.2020.105617

Tian, L., Tong, J., Algeo, T. J., Song, H., Song, H., Chu, D., Shi, L. & Bottjer, D. J. (2014). Reconstruction of Early Triassic ocean redox conditions based on framboidal pyrite from the Nanpanjiang Basin, South China. *Palaeogeography, Palaeoclimatology, Palaeoecology*, *412*, 68–79. https://doi.org/10.1016/j.palaeo.2014.07.018

Tobias, R. & Berg, M. (2011). Sustainable Use of Arsenic-Removing Sand Filters in Vietnam: Psychological and Social Factors. *Environmental Science & Technology*, *45*(8), 3260–3267. https://doi.org/10.1021/es102076x

Tomaszewski, E. J., Cronk, S. S., Gorski, C. A. & Ginder-Vogel, M. (2016). The role of dissolved Fe(II) concentration in the mineralogical evolution of Fe (hydr)oxides during redox cycling. *Chemical Geology*, *438*, 163–170. https://doi.org/10.1016/j.chemgeo.2016.06.016

Tseng, W. (1977). Effects and dose-response relationships of skin cancer and blackfoot disease with arsenic. *Environmental Health Perspectives*, *19*, 109–119. https://doi.org/10.1289/ehp.7719109

Tseng, W., Chu, H. M., How, S., Fong, J. J., Lin, C. & Yeh, S. D. (1968). Prevalence of Skin Cancer in an Endemic Area of Chronic Arsenicism in Taiwan2. *Journal of the National Cancer Institute*. https://doi.org/10.1093/jnci/40.3.453

Tufano, K. J. & Fendorf, S. (2008). Confounding Impacts of Iron Reduction on Arsenic Retention. *Environmental Science & Technology*, *42*(13), 4777–4783. https://doi.org/10.1021/es702625e

Tufano, K. J., Reyes, C., Saltikov, C. W. & Fendorf, S. (2008). Reductive Processes Controlling Arsenic Retention: Revealing the Relative Importance of Iron and Arsenic Reduction. *Environmental Science & Technology*, *42*(22), 8283–8289. https://doi.org/10.1021/es801059s

Tufo, A. E., Afonso, M. D. S. & Sileo, E. E. (2016). Arsenic adsorption onto aluminium-substituted goethite. *Environmental Chemistry*, *13*(5), 838. https://doi.org/10.1071/en15154

UN World Water Development Report 2020 | UN-Water. (2022, 24. August). United Nations. https://www.unwater.org/publications/un-world-water-development-report-2020

Van Der Zee, C., Roberts, D. R., Rancourt, D. & Slomp, C. P. (2003). Nanogoethite is the dominant reactive oxyhydroxide phase in lake and marine sediments. *Geology*, *31*(11), 993. https://doi.org/10.1130/g19924.1

Van Geen, A. (2011). International Drilling to Recover Aquifer Sands (IDRAs) and Arsenic Contaminated Groundwater in Asia. *Scientific Drilling*, *12, September 2011*. https://doi.org/10.2204/iodp.sd.12.06.2011

Van Geen, A., Bostick, B. C., Trang, P. T. K., Lan, V. M., Mai, N., Manh, P. D., Viet, P. H., Radloff, K. A., Aziz, Z., Mey, J. L., Stahl, M., Harvey, C. F., Oates, P. J., Weinman, B., Stengel, C., Frei, F., Kipfer, R. & Berg, M. (2013). Retardation of arsenic transport through a Pleistocene aquifer. *Nature*, *501*(7466), 204–207. https://doi.org/10.1038/nature12444

Van Geen, A., Zheng, Y. H., Cheng, Z., Aziz, Z., Horneman, A. J., Dhar, R., Mailloux, B. J., Stute, M., Weinman, B., Goodbred, S. L., Seddique, A. A., Hoque, M. & Ahmed, K. M. (2006). A transect of groundwater and sediment properties in Araihazar, Bangladesh: Further evidence of decoupling between As and Fe mobilization. *Chemical Geology*, *228*(1–3), 85–96. https://doi.org/10.1016/j.chemgeo.2005.11.024

Van Geen, A., Zheng, Y. H., Versteeg, R., Stute, M., Horneman, A., Dhar, R., Steckler, M. S., Gelman, A. E., Small, C., Ahsan, H., Graziano, J. H., Hussain, I. & Ahmed, K. M. (2003). Spatial variability of arsenic in 6000 tube wells in a 25 km2area of Bangladesh. *Water Resources Research*, *39*(5). https://doi.org/10.1029/2002wr001617

Van Groeningen, N., ThomasArrigo, L. K., Byrne, J. M., Kappler, A., Christl, I. & Kretzschmar, R. (2020). Interactions of ferrous iron with clay mineral surfaces during sorption and subsequent oxidation. *Environmental Science: Processes & Impacts*, *22*(6), 1355–1367. https://doi.org/10.1039/d0em00063a

Villacís-García, M., Ugalde-Arzate, M., Vaca-Escobar, K., Villalobos, M., Zanella, R. & Martínez-Villegas, N. (2015). Laboratory synthesis of goethite and ferrihydrite of controlled particle sizes. *Boletín de la Sociedad Geológica Mexicana*, *67*(3), 433–446. https://doi.org/10.18268/bsgm2015v67n3a7

Villalobos, M. & Leckie, J. O. (2001). Surface Complexation Modeling and FTIR Study of Carbonate Adsorption to Goethite. *Journal of Colloid and Interface Science*, *235*(1), 15–32. https://doi.org/10.1006/jcis.2000.7341

Violante, A. & Pigna, M. (2002). Competitive Sorption of Arsenate and Phosphate on Different Clay Minerals and Soils. *Soil Science Society of America Journal*, *66*(6), 1788–1796. https://doi.org/10.2136/sssaj2002.1788

Voegelin, A., Kaegi, R., Frommer, J., Vantelon, D. & Hug, S. J. (2010). Effect of phosphate, silicate, and Ca on Fe(III)-precipitates formed in aerated Fe(II)- and As(III)-containing water studied by X-ray absorption spectroscopy. *Geochimica et Cosmochimica Acta*, *74*(1), 164–186. https://doi.org/10.1016/j.gca.2009.09.020

Voegelin, A., Senn, A., Kaegi, R. & Hug, S. J. (2019). Reductive dissolution of As(V)-bearing Fe(III)-precipitates formed by Fe(II) oxidation in aqueous solutions. *Geochemical Transactions*, *20*(1). https://doi.org/10.1186/s12932-019-0062-2

Voegelin, A., Senn, A., Kaegi, R., Hug, S. J. & Mangold, S. (2013). Dynamic Fe-precipitate formation induced by Fe(II) oxidation in aerated phosphate-containing water. *Geochimica et Cosmochimica Acta*, *117*, 216–231. https://doi.org/10.1016/j.gca.2013.04.022

Vogelsang, V., Kaiser, K., Wagner, F. E., Jahn, R. & Fiedler, S. (2016). Transformation of clay-sized minerals in soils exposed to prolonged regular alternation of redox conditions. *Geoderma*, *278*, 40–48. https://doi.org/10.1016/j.geoderma.2016.05.013

Von Der Heyden, B. P. & Roychoudhury, A. N. (2015). Application, Chemical Interaction and Fate of Iron Minerals in Polluted Sediment and Soils. *Current pollution reports*, *1*(4), 265–279. https://doi.org/10.1007/s40726-015-0020-2

Vuillemin, A., Wirth, R., Kemnitz, H., Schleicher, A. M., Friese, A., Bauer, K. W., Simister, R. L., Nomosatryo, S., Ordóñez, L. G., Ariztegui, D., Henny, C., Crowe, S. A., Benning, L. G., Kallmeyer, J., Russell, J. A., Bijaksana, S. & Vogel, H. (2019). Formation of diagenetic siderite in modern ferruginous sediments. *Geology*, *47*(6), 540–544. https://doi.org/10.1130/g46100.1

Wagner, F., Berner, Z. A. & Stueben, D. (2005). Arsenic in groundwater of the Bengal Delta Plain. *Natural Arsenic in Groundwater: Occurrence, Remediation and Management*, 3–15. https://doi.org/10.1201/9780203970829.sec1

Wallis, I., Prommer, H., Berg, M., Siade, A. J., Sun, J. & Kipfer, R. (2020). The river–groundwater interface as a hotspot for arsenic release. *Nature Geoscience*, *13*(4), 288–295. https://doi.org/10.1038/s41561-020-0557-6

Wang, C. & Stoffella, P. J. (2005). Trace elements in agroecosystems and impacts on the environment. *Journal of Trace Elements in Medicine and Biology*, *19*(2–3), 125–140. https://doi.org/10.1016/j.jtemb.2005.02.010

Wang, H., Byrne, J., Perez, J. P. H., Thomas, A. W., Göttlicher, J., Höfer, H. E., Mayanna, S., Kontny, A., Kappler, A., Guo, H., Benning, L. G. & Norra, S. (2020). Arsenic sequestration in pyrite and greigite in the buried peat of As-contaminated aquifers. *Geochimica et Cosmochimica Acta*, *284*, 107–119. https://doi.org/10.1016/j.gca.2020.06.021

Wang, S. & Mulligan, C. N. (2006). Effect of natural organic matter on arsenic release from soils and sediments into groundwater. *Environmental Geochemistry and Health*, *28*(3), 197–214. https://doi.org/10.1007/s10653-005-9032-y

Wang, Y., Morin, G., Ona-Nguema, G. & Brown, G. E. (2014). Arsenic(III) and Arsenic(V) Speciation during Transformation of Lepidocrocite to Magnetite. *Environmental Science & Technology*, *48*(24), 14282–14290. https://doi.org/10.1021/es5033629

Wang, Y., Morin, G., Ona-Nguema, G., Menguy, N., Juillot, F., Aubry, E., Guyot, F., Calas, G. & Brown, G. E. (2008). Arsenite sorption at the magnetite–water interface during aqueous

precipitation of magnetite: EXAFS evidence for a new arsenite surface complex. *Geochimica et Cosmochimica Acta*, *72*(11), 2573–2586. https://doi.org/10.1016/j.gca.2008.03.011

Wang, Y., Pi, K., Fendorf, S., Deng, Y. & Xie, X. (2017). Sedimentogenesis and hydrobiogeochemistry of high arsenic Late Pleistocene-Holocene aquifer systems. *Earth-Science Reviews*, *189*, 79–98. https://doi.org/10.1016/j.earscirev.2017.10.007

Wasiuddin, N. M., Tango, M. & Islam, M. R. (2002). A Novel Method for Arsenic Removal at Low Concentrations. *Energy Sources*, *24*(11), 1031–1041. https://doi.org/10.1080/00908310290086914

Waychunas, G. A., Fuller, C. C., Rea, B. A. & Davis, J. C. (1996). Wide angle X-ray scattering (WAXS) study of "two-line" ferrihydrite structure: Effect of arsenate sorption and counterion variation and comparison with EXAFS results. *Geochimica et Cosmochimica Acta*, *60*(10), 1765–1781. https://doi.org/10.1016/0016-7037(96)89830-9

Waychunas, G. A., Kim, C. & Banfield, J. F. (2005). Nanoparticulate Iron Oxide Minerals in Soils and Sediments: Unique Properties and Contaminant Scavenging Mechanisms. *Journal of Nanoparticle Research*, *7*(4–5), 409–433. https://doi.org/10.1007/s11051-005-6931-x

Weber, K. A., Achenbach, L. A. & Coates, J. D. (2006). Microorganisms pumping iron: anaerobic microbial iron oxidation and reduction. *Nature Reviews Microbiology*, *4*(10), 752–764. https://doi.org/10.1038/nrmicro1490

Webster, J. G. (1999). The source of arsenic (and other elements) in theMarbel–Matingao river catchment, Mindanao, Philippines. *Geothermics*, *28*(1), 95–111. https://doi.org/10.1016/s0375-6505(98)00046-7

Wei, H., Chen, D., Wang, J., Yu, H. & Tucker, M. E. (2012). Organic accumulation in the lower Chihsia Formation (Middle Permian) of South China: Constraints from pyrite morphology and multiple geochemical proxies. *Palaeogeography, Palaeoclimatology, Palaeoecology*, *353–355*, 73–86. https://doi.org/10.1016/j.palaeo.2012.07.005

Weinman, B. (2010). The evolution of aquifers and arsenic in Asia: A study of the fluvio-deltaic processes leading to aquifer formation and arsenic cycling and heterogeneity in Bangladesh, Vietnam, and Nepal. *DISSERTATION*.

Weisener, C. G. & Weber, P. (2010). Preferential oxidation of pyrite as a function of morphology and relict texture. *New Zealand Journal of Geology and Geophysics*, *53*(2–3), 167–176. https://doi.org/10.1080/00288306.2010.499158

Welch, A. H. & Stollenwerk, K. G. (2007). *Arsenic in Ground Water*. Springer Science & Business Media.

Whitney, D. L. & Evans, B. W. (2010). Abbreviations for names of rock-forming minerals. *American Mineralogist*, *95*(1), 185–187. https://doi.org/10.2138/am.2010.3371

Wignall, P. B. & Newton, R. U. (1998). Pyrite framboid diameter as a measure of oxygen deficiency in ancient mudrocks. *American Journal of Science*, *298*(7), 537–552. https://doi.org/10.2475/ajs.298.7.537

Wilkin, R. T. & Barnes, H. (1997). Formation processes of framboidal pyrite. *Geochimica et Cosmochimica Acta*, *61*(2), 323–339. https://doi.org/10.1016/s0016-7037(96)00320-1

Wilkin, R. T., Barnes, H. & Brantley, S. L. (1996). The size distribution of framboidal pyrite in modern sediments: An indicator of redox conditions. *Geochimica et Cosmochimica Acta*, *60*(20), 3897–3912. https://doi.org/10.1016/0016-7037(96)00209-8

Wilkin, R. T. & Ford, R. C. (2006). Arsenic solid-phase partitioning in reducing sediments of a contaminated wetland. *Chemical Geology*, *228*(1–3), 156–174. https://doi.org/10.1016/j.chemgeo.2005.11.022

Wilkin, R. T., Wallschläger, D. & Ford, R. C. (2003). Speciation of arsenic in sulfidic waters. *Geochemical Transactions*, *4*(1), 1–7. https://doi.org/10.1039/b211188h

Williams, A. M. & Scherer, M. M. (2004). Spectroscopic Evidence for Fe(II)−Fe(III) Electron Transfer at the Iron Oxide−Water Interface. *Environmental Science & Technology*, *38*(18), 4782–4790. https://doi.org/10.1021/es049373g

Winkel, L. H. E., Berg, M., Amini, M., Hug, S. J. & Johnson, C. L. (2008). Predicting groundwater arsenic contamination in Southeast Asia from surface parameters. *Nature Geoscience*, *1*(8), 536–542. https://doi.org/10.1038/ngeo254

Winkel, L. H. E., Trang, P. T. K., Lan, V. M., Stengel, C., Amini, M., Ha, N. N., Viet, P. H. & Berg, M. (2011). Arsenic pollution of groundwater in Vietnam exacerbated by deep aquifer exploitation for more than a century. *Proceedings of the National Academy of Sciences of the United States of America*, *108*(4), 1246–1251. https://doi.org/10.1073/pnas.1011915108

Wolf, M., Kappler, A., Jiang, J. & Meckenstock, R. U. (2009). Effects of Humic Substances and Quinones at Low Concentrations on Ferrihydrite Reduction by *Geobacter metallireducens*. *Environmental Science & Technology*, *43*(15), 5679–5685. https://doi.org/10.1021/es803647r

World Health Organization (WHO). (2008, 2. Dezember). *Guidelines for Drinking-water Quality: Incorporating First and Second Addenda to Third Edition. Vol. 1—Recommendations. Geneva:WHO Press.*. https://www.who.int/publications/i/item/9789241547611

World Health Organization (WHO). (2019, 18. Juni). *1 in 3 people globally do not have access to safe drinking water – UNICEF, WHO*. https://www.who.int/news/item/18-06-2019-1-in-3-people-globally-do-not-have-access-to-safe-drinking-water-unicef-who#:~:text=Some%202.2%20billion%20people%20around,lack%20basic**%20handwashing%20facilities.

World Health Organization (WHO). (2022, 7. Dezember). *Arsenic*. https://www.who.int/news-room/fact-sheets/detail/arsenic

Xie, X., Wang, Y., Su, C., Liu, H., Duan, M. & Xie, Z. (2008). Arsenic mobilization in shallow aquifers of Datong Basin: Hydrochemical and mineralogical evidences. *Journal of Geochemical Exploration*, *98*(3), 107–115. https://doi.org/10.1016/j.gexplo.2008.01.002

Xu, H., Allard, B. & Grimvall, A. (1991). Effects of acidification and natural organic materials on the mobility of arsenic in the environment. *Water Air and Soil Pollution*, *57–58*(1), 269–278. https://doi.org/10.1007/bf00282890

Xu, X. P., McGrath, S. P. & Zhao, F. (2007). Rapid reduction of arsenate in the medium mediated by plant roots. *New Phytologist*, *176*(3), 590–599. https://doi.org/10.1111/j.1469-8137.2007.02195.x

Yamazaki, C., Ishiga, H., Ahmed, F., Itoh, K., Suyama, K. & Yamamoto, H. (2003). Vertical distribution of arsenic in ganges delta sediments in Deuli Village, Bangladesh. *Soil Science and Plant Nutrition*, *49*(4), 567–574. https://doi.org/10.1080/00380768.2003.10410046

Ye, Y., Wu, C., Zhai, L. & An, Z. (2017). Pyrite morphology and episodic euxinia of the Ediacaran Doushantuo Formation in South China. *Science China-earth Sciences*, *60*(1), 102–113. https://doi.org/10.1007/s11430-016-0066-0

Yee, N. K., Shaw, S., Benning, L. G. & Nguyen, T. H. (2006). The rate of ferrihydrite transformation to goethite via the Fe(II) pathway. *American Mineralogist*, *91*(1), 92–96. https://doi.org/10.2138/am.2006.1860

Ying, S. C., Kocar, B. D. & Fendorf, S. (2012). Oxidation and competitive retention of arsenic between iron- and manganese oxides. *Geochimica et Cosmochimica Acta*, *96*, 294–303. https://doi.org/10.1016/j.gca.2012.07.013

Zachara, J. M., Kukkadapu, R. K., Fredrickson, J. K., Gorby, Y. A. & Smith, S. M. (2002). Biomineralization of Poorly Crystalline Fe(III) Oxides by Dissimilatory Metal Reducing Bacteria (DMRB). *Geomicrobiology Journal*, *19*(2), 179–207. https://doi.org/10.1080/01490450252864271

Zaldívar, R. & Ghai, G. (1980). Clinical epidemiological studies on endemic chronic arsenic poisoning in children and adults, including observations on children with high- and low-intake of dietary arsenic. *Zentralblatt Fur Bakteriologie. 1. Abt. Originale B, Hygiene, Krankenhaushygiene, Betriebshygiene, Praventive Medizin*, *170*(5–6), 409–421. https://pubmed.ncbi.nlm.nih.gov/7424281/

Zavarzina, D. G., Tourova, T. P., Kolganova, T. V., Boulygina, E. S. & Zhilina, T. N. (2009). Description of Anaerobacillus alkalilacustre gen. nov., sp. nov.—Strictly anaerobic diazotrophic bacillus

isolated from soda lake and transfer of Bacillus arseniciselenatis, Bacillus macyae, and Bacillus alkalidiazotrophicus to Anaerobacillus as the new combinations A. arseniciselenatis comb. nov., A. macyae comb. nov., and A. alkalidiazotrophicus comb. nov. *Microbiology*, *78*(6), 723–731. https://doi.org/10.1134/s0026261709060095

Zhang, D., Guo, H., Xiu, W., Ni, P., Zheng, H. & Wei, C. (2017). In-situ mobilization and transformation of iron oxides-adsorbed arsenate in natural groundwater. *Journal of Hazardous Materials*, *321*, 228–237. https://doi.org/10.1016/j.jhazmat.2016.09.021

Zhang, G., Dong, H., Jiang, H., Kukkadapu, R. K., Kim, J. W., Eberl, D. D. & Xu, Z. (2009). Biomineralization associated with microbial reduction of Fe3+ and oxidation of Fe2+ in solid minerals. *American Mineralogist*, *94*(7), 1049–1058. https://doi.org/10.2138/am.2009.3136

Zhang, P., Najman, Y., Mei, L., Millar, I. L., Sobel, E. R., Carter, A., Barfod, D. N., Dhuime, B., Garzanti, E., Govin, G., Vezzoli, G. & Hu, X. (2019). Palaeodrainage evolution of the large rivers of East Asia, and Himalayan-Tibet tectonics. *Earth-Science Reviews*, *192*, 601–630. https://doi.org/10.1016/j.earscirev.2019.02.003

Zhang, W., Singh, P. K., Paling, E. & Delides, S. (2004). Arsenic removal from contaminated water by natural iron ores. *Minerals Engineering*, *17*(4), 517–524. https://doi.org/10.1016/j.mineng.2003.11.020

Zhang, Z., Guo, H., Zhao, W., Liu, S., Cao, Y. & Jia, Y. (2018). Influences of groundwater extraction on flow dynamics and arsenic levels in the western Hetao Basin, Inner Mongolia, China. *Hydrogeology Journal*, *26*(5), 1499–1512. https://doi.org/10.1007/s10040-018-1763-9

Zheng, S., Wang, B., Liu, F. & Wang, O. (2017). Magnetite production and transformation in the methanogenic consortia from coastal riverine sediments. *Journal of Microbiology*, *55*(11), 862–870. https://doi.org/10.1007/s12275-017-7104-1

Zhu, J., Pigna, M., Cozzolino, V., Caporale, A. G. & Violante, A. (2011). Sorption of arsenite and arsenate on ferrihydrite: Effect of organic and inorganic ligands. *Journal of Hazardous Materials*, *189*(1–2), 564–571. https://doi.org/10.1016/j.jhazmat.2011.02.071

Zhu, M., Graham, S. A. & McHargue, T. (2009). The Red River Fault zone in the Yinggehai Basin, South China Sea. *Tectonophysics*, *476*(3–4), 397–417. https://doi.org/10.1016/j.tecto.2009.06.015

Zhu, T. & Dittrich, M. (2016). Carbonate Precipitation through Microbial Activities in Natural Environment, and Their Potential in Biotechnology: A Review. *Frontiers in Bioengineering and Biotechnology*, *4*. https://doi.org/10.3389/fbioe.2016.00004

Zhu, Y., Yoshinaga, M., Zhao, F. & Rosen, B. P. (2014). Earth Abides Arsenic Biotransformations. *Annual Review of Earth and Planetary Sciences*, *42*(1), 443–467. https://doi.org/10.1146/annurev-earth-060313-054942

Zobrist, J., Dowdle, P. R., Davis, J. & Oremland, R. S. (2000). Mobilization of Arsenite by Dissimilatory Reduction of Adsorbed Arsenate. *Environmental Science & Technology*, *34*(22), 4747–4753. https://doi.org/10.1021/es001068h

Appendix

Table 16: RD42 and RD54 depth profile involving grain size, colour, sedimentological features, segment length and core loss

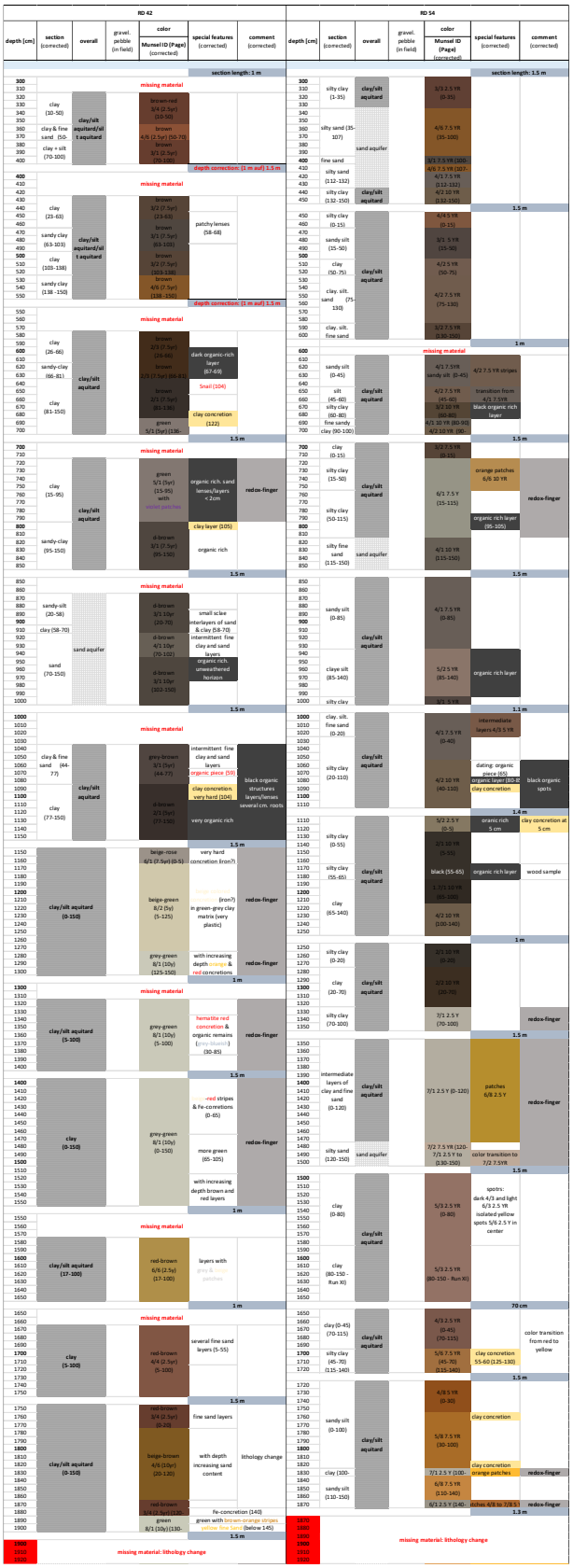

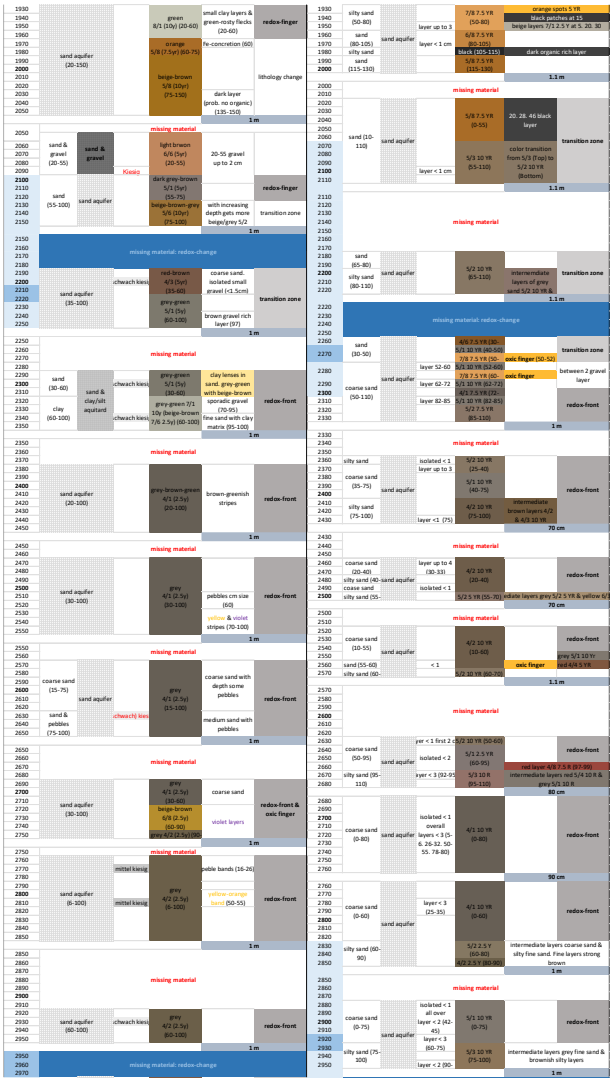

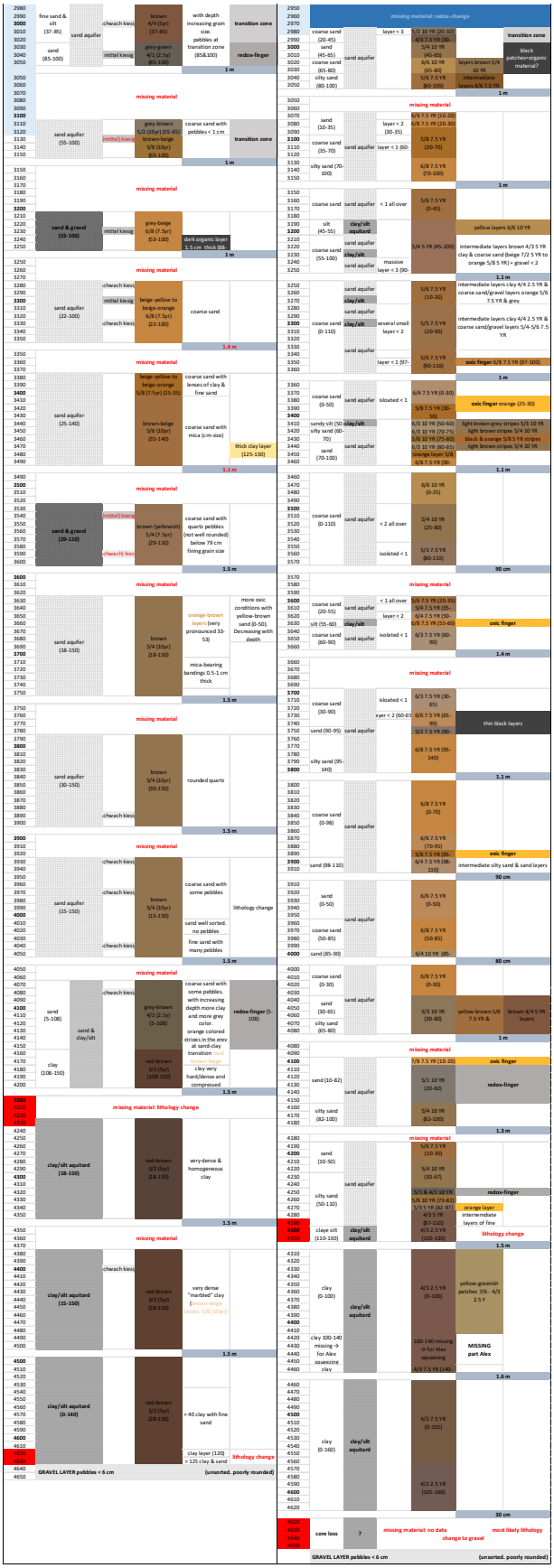

Table 17: RD42 colour, grain size and geochemistry (CSA, IRMS, ED-XRF)

colour	grain size	Depth [m]	CSA			IRMS			ED-XRF
			TC [%]	TOC [%]	TS [%]	TN [%]	TOC/TN	$\delta^{13}C$ [‰]	As [mg/kg]
	Ut3	3,3	0,28		0,005				15,63
	Us	3,6	0,07		0,002				6,26
	Us	3,9	0,50		0,004				10,13
	Ut2	4,4	1,33	0,98	0,011	0,10	11	-24,18	13,61
	Us	4,8	1,05		0,013				12,33
	Ut2	5,2	0,60		0,006				9,07
	Ut2	5,9	1,14	0,80	0,008	0,09	10	-25,11	11,75
	Us	6,2	0,58	0,37	0,003	0,04	12	-25,89	8,02
	Ut4	6,6	1,48	1,17	0,057	0,12	11	-24,83	18,01
	Ut4	7,0	0,38		0,017				12,25
	Ut4	7,4	0,51	0,50	0,080	0,06	9	-27,47	18,80
	Us	8,2	2,02	1,90	0,252	0,09	26	-28,37	14,20
	Ut2	9,1	4,96	4,80	0,305	0,18	34	-28,71	20,20
	Us	9,5	5,39	5,46	0,542	0,20	33	-29,00	16,71
	Ut2	10,8	5,08	5,10	0,365	0,15	42	-28,91	17,67
	Ut2	11,2	8,57	8,52	0,538	0,23	47	-28,86	28,88
		11,3	9,68	9,48	0,913	0,22	53	-28,57	30,32
		11,6	0,67		0,018				12,74
		11,9	0,34		0,019				8,56
	Ut4	12,4	0,95	0,14	0,009	0,06	3	-22,27	23,59
	Ut4	13,0	0,54	0,10	0,005	0,04	2	-22,81	23,63
	Ut4	13,5	0,13		0,004				22,26
	Tu4	14,8	0,10		0,005				5,78
	Ut3	15,5	0,08		0,005				5,88
	Tu4	16,1	0,10	0,11	0,007	0,04	2	-25,95	5,82
	Ut2	17,3	0,09		0,008				5,18
	Ut2	18,2	0,07		0,005				4,79
	Ut2	18,8	0,06		0,003				5,65
	Ut2	19,4	0,05		0,005				7,24
	Uls	19,7	0,07	0,11	0,008	0,05	2	-24,46	16,47
	Uls	20,1	0,04		0,008				3,72
		20,4	0,03		0,006				4,46
		20,7	0,06	0,07	0,007	0,02	3	-24,44	3,52
	Su2	20,8	0,03		0,005				2,58
	Su3	21,2	0,05		0,006				0,85
	Su3	21,3	0,08	0,04	0,006	0,01	4	-26,88	5,44
	Su3	22,0	0,32	0,24	0,019	0,03	10	-25,59	7,14
	Su3	22,4	0,04		0,005				3,09
	Su4	23,3	0,04		0,004				3,42
	Su3	24,2	0,03		0,005				1,33
	Su4	25,5	0,03	0,03	0,006				2,57
	Su2	25,9	0,03		0,005				3,35
	Su3	26,3	0,02		0,004				2,90

	Us	27,4	0,04		0,005				4,18
	Su2	28,1	0,05		0,006				4,92
	Su3	28,5	0,03		0,006				1,87
	Su4	29,4	0,04		0,005				4,57
	Su4	30,1	0,39	0,30	0,019	0,03	10	-24,58	9,88
		30,3	0,19	0,15	0,012	0,02	9	-24,85	5,45
	Su3	30,4	0,03		0,006				1,33
	Su3	31,4	0,03		0,006				1,25
	Su3	32,4	0,03		0,005				4,35
	Su2	33,1	0,03		0,005				1,42
	Su2	33,3	0,10	0,09	0,007	0,01	10	-25,10	5,13
	Us	33,8	0,06		0,004				4,64
	Su3	34,5	0,02		0,005				3,68
	Su3	35,4	0,02		0,005				1,42
	Slu	35,9	0,03		0,005				2,30
	Su3	36,4	0,03	0,04	0,003				1,86
		36,9	0,03		0,005				4,25
	Su4	37,3	0,04		0,005				2,00
	Su3	38,2	0,03		0,005				1,70
	Su2	39,7	0,04		0,007				5,90
	Su3	40,4	0,12		0,009				6,01
	Su2	40,8	0,03		0,004				1,99
		40,9	0,03		0,005				4,72
	Su3	41,4	0,03		0,006				2,15
	Ut3	41,7	0,09	0,10	0,005	0,04	2	24,07	4,96
		42,3	0,14		0,005				8,76
	Ut4	43,3	0,12		0,006				8,10
	Ut4	44,5	0,12		0,004				14,68
	Ut4	45,3	0,31		0,006				8,65
	Ut2	45,8	0,06		0,007				4,31
	Ut2	46,3	0,53	0,09	0,009	0,04	3	23,61	4,86
from 46.3 m: GRAVEL → no further coring possible									

Table 18: RD42 colour, grain size and geochemistry (WD-XRF)

colour	grain size	Depth [m]	WD-XRF									
			MnO [%]	Fe_2O_3 [%]	Al_2O_3 [%]	TiO_2 [%]	SiO_2 [%]	MgO [%]	Na_2O [%]	P_2O_5 [%]	K_2O [%]	CaO [%]
	Ut3	3,3	0,09	5,71	14,72	0,83	68,26	1,45	0,67	0,10	2,77	0,65
	Us	3,6	0,04	3,72	9,37	0,64	82,07	0,96	0,84	0,08	2,28	0,69
	Us	3,9	0,09	5,27	12,79	0,85	73,00	1,38	0,78	0,12	2,44	1,39
	Ut2	4,4	0,08	6,33	15,14	0,92	63,88	1,61	0,66	0,16	2,68	1,43
	Us	4,8	0,09	5,35	12,63	0,85	68,32	1,38	0,75	0,13	2,38	1,67
	Ut2	5,2	0,08	5,16	12,35	0,81	71,57	1,34	0,75	0,12	2,38	1,42
	Ut2	5,9	0,08	6,09	15,37	0,94	63,72	1,66	0,67	0,15	2,68	1,53
	Us	6,2	0,05	4,30	10,49	0,74	75,84	1,19	0,82	0,10	2,27	1,18
	Ut4	6,6	0,09	6,53	17,00	0,92	60,28	1,62	0,57	0,14	2,87	0,98
	Ut4	7,0	0,04	4,15	19,52	0,93	62,35	1,54	0,56	0,07	3,21	0,39
	Ut4	7,4	0,04	4,58	19,08	0,92	62,68	1,56	0,57	0,07	3,19	0,41
	Us	8,2	0,06	5,42	14,53	0,85	74,22	1,46	0,77	0,11	2,77	0,77
	Ut2	9,1	0,09	7,24	16,05	0,87	69,73	1,77	0,74	0,18	2,97	1,07
	Us	9,5	0,08	6,75	17,80	0,97	69,87	1,90	0,73	0,14	3,15	1,01
	Ut2	10,8	0,08	6,21	16,85	0,88	70,49	1,65	0,62	0,11	2,92	0,76
	Ut2	11,2	0,05	5,15	20,25	0,97	66,74	1,91	0,52	0,10	3,32	0,81
		11,3	0,03	4,09	14,58	0,89	76,27	1,20	0,29	0,06	2,16	0,65
		11,6	0,05	7,97	12,79	0,81	68,78	0,55	0,08	0,12	1,58	0,17
		11,9	0,03	3,31	14,78	0,92	72,33	0,68	0,11	0,05	1,98	0,14
	Ut4	12,4	0,06	9,18	17,94	0,95	59,72	0,85	0,13	0,07	2,55	0,17
	Ut4	13,0	0,03	5,64	17,47	0,92	65,32	0,80	0,12	0,05	2,39	0,15
	Ut4	13,5	0,02	3,71	20,60	1,01	64,27	0,98	0,15	0,04	3,07	0,12
	Tu4	14,8	0,02	1,48	17,69	1,04	69,83	0,82	0,13	0,04	2,79	0,09
	Ut3	15,5	0,02	1,80	11,44	0,98	79,15	0,48	0,08	0,04	1,77	0,06
	Tu4	16,1	0,02	2,14	15,99	1,00	72,12	0,71	0,11	0,06	2,38	0,07
	Ut2	17,3	0,03	3,19	15,83	0,85	71,08	0,81	0,16	0,06	2,56	0,06
	Ut2	18,2	0,04	5,50	12,64	0,81	73,26	0,74	0,17	0,11	2,27	0,07
	Ut2	18,8	0,04	4,05	12,65	0,84	74,40	0,76	0,18	0,08	2,31	0,07
	Ut2	19,4	0,03	2,80	12,62	0,77	76,38	0,69	0,17	0,05	2,32	0,08
	Uls	19,7	0,07	10,95	10,41	0,79	70,77	0,54	0,15	0,04	2,00	0,08
	Uls	20,1	0,04	2,28	9,62	0,56	81,66	0,49	0,18	0,04	2,23	0,09
		20,4	0,04	1,73	8,91	0,50	83,46	0,42	0,15	0,04	1,98	0,09
		20,7	0,79	1,85	9,50	0,58	80,63	0,46	0,18	0,04	2,14	0,10
	Su2	20,8	0,07	1,06	6,36	0,35	88,15	0,29	0,13	0,03	1,81	0,08
	Su3	21,2	0,03	1,06	5,24	0,27	90,10	0,26	0,12	0,02	1,66	0,08
	Su3	21,3	0,11	2,62	6,10	0,28	86,79	0,27	0,14	0,09	1,82	0,11
	Su3	22,0	0,04	2,99	9,04	0,51	81,01	0,68	0,35	0,07	2,13	0,39
	Su3	22,4	0,01	1,43	6,38	0,31	87,91	0,33	0,17	0,04	1,93	0,14
	Su4	23,3	0,02	1,64	7,08	0,44	87,00	0,35	0,16	0,04	1,93	0,10
	Su3	24,2	0,00	1,31	6,02	0,25	89,39	0,32	0,19	0,03	1,93	0,09
	Su4	25,5	0,01	1,97	6,30	0,32	87,68	0,36	0,22	0,03	1,92	0,11
	Su2	25,9	0,02	2,02	6,88	0,42	87,03	0,41	0,23	0,03	1,94	0,13
	Su3	26,3	0,01	1,90	6,27	0,38	88,10	0,34	0,22	0,04	1,88	0,12
	Us	27,4	0,04	2,34	8,82	0,53	83,79	0,59	0,31	0,03	2,26	0,17

	Su2	28,1	0,01	1,54	5,02	0,22	90,05	0,24	0,20	0,05	1,76	0,11
	Su3	28,5	0,00	1,35	4,10	0,17	91,99	0,17	0,17	0,03	1,64	0,09
	Su4	29,4	0,01	1,37	5,42	0,24	90,44	0,28	0,25	0,03	1,83	0,10
	Su4	30,1	0,07	3,91	9,76	0,59	77,93	1,05	0,54	0,09	2,20	0,66
		30,3	0,03	2,36	6,75	0,36	85,18	0,57	0,39	0,05	1,93	0,38
	Su3	30,4	0,00	1,08	4,62	0,18	91,55	0,21	0,22	0,03	1,77	0,10
	Su3	31,4	0,01	1,57	5,13	0,24	90,36	0,28	0,29	0,03	1,69	0,15
	Su3	32,4	0,05	1,73	4,93	0,19	90,48	0,22	0,35	0,06	1,73	0,13
	Su2	33,1	0,00	1,57	4,12	0,16	89,94	0,18	0,26	0,04	1,55	0,14
	Su2	33,3	0,00	1,67	4,56	0,22	88,62	0,30	0,29	0,04	1,52	0,23
	Us	33,8	0,04	3,56	11,61	0,71	74,74	0,79	0,46	0,08	2,36	0,22
	Su3	34,5	-0,01	1,55	5,69	0,27	85,00	0,35	0,37	0,03	1,75	0,17
	Su3	35,4	0,00	1,33	5,22	0,23	88,55	0,30	0,32	0,03	1,86	0,15
	Slu	35,9	0,01	1,96	6,64	0,35	85,14	0,47	0,44	0,03	1,93	0,23
	Su3	36,4	0,01	2,15	7,05	0,36	83,87	0,50	0,45	0,03	2,03	0,21
		36,9	0,01	1,85	7,24	0,38	84,17	0,53	0,48	0,03	2,08	0,23
	Su4	37,3	0,02	2,20	7,03	0,37	85,54	0,51	0,48	0,03	2,05	0,24
	Su3	38,2	0,01	2,20	7,17	0,39	85,63	0,53	0,49	0,03	2,06	0,25
	Su2	39,7	0,00	1,82	5,24	0,25	90,20	0,33	0,39	0,04	1,83	0,20
	Su3	40,4	0,02	2,22	6,37	0,33	86,48	0,51	0,43	0,04	1,90	0,32
	Su2	40,8	0,00	2,02	5,83	0,29	88,26	0,42	0,44	0,03	1,86	0,24
		40,9	0,01	2,29	5,55	0,28	88,47	0,39	0,43	0,05	1,83	0,22
	Su3	41,4	0,01	2,22	6,29	0,36	87,47	0,49	0,52	0,04	1,79	0,32
	Ut3	41,7	0,05	4,93	16,23	0,89	67,96	1,50	0,39	0,07	2,91	0,25
		42,3	0,06	6,34	15,92	0,88	67,18	1,51	0,39	0,13	2,86	0,29
	Ut4	43,3	0,05	6,25	18,30	0,90	62,59	1,65	0,30	0,12	3,19	0,26
	Ut4	44,5	0,07	8,58	19,87	0,86	57,41	1,53	0,21	0,21	3,31	0,20
	Ut4	45,3	0,15	7,61	15,87	0,86	64,61	1,28	0,36	0,12	2,76	0,27
	Ut2	45,8	0,03	3,48	11,96	0,71	76,41	1,03	0,60	0,06	2,43	0,33
	Ut2	46,3	0,14	6,96	13,21	0,81	68,82	1,14	0,51	0,07	2,52	0,34
from 46.3 m: GRAVEL → no further coring possible												

Table 19: RD54: colour, grain size and geochemistry (CSA, ED-XRF)

colour	Depth [m]	CSA		ED-XRF					
		TC [%]	TS [%]	As [mg/kg]	MnO [%]	Fe_2O_3 [%]	TiO_2 [%]	K_2O [%]	CaO [%]
	3,40	0,11	0,014	8,26	0,06	4,27	0,71	2,83	0,83
	4,25	0,24	0,041	8,79	0,09	4,13	0,74	2,78	1,52
	4,40	1,65	0,090	14,79	0,02	1,16	0,21	0,68	0,44
	4,90	1,25	0,045	11,55	0,10	5,23	0,82	2,56	1,76
	5,90	0,43	0,013	9,88	0,07	6,10	0,96	2,83	1,31
	6,30	1,49	0,044	13,95	0,11	5,97	0,93	2,78	1,94
	6,65	1,44	0,167	15,77	0,07	5,90	0,95	2,84	1,62
	7,70	1,19	0,315	24,06	0,04	7,57	1,01	3,45	0,77
	8,40	3,43	0,559	17,42	0,18	8,81	0,85	3,05	1,14
	9,00	5,85	0,411	23,02	0,10	6,99	0,93	3,26	1,16
	9,90	3,43	0,441	15,43	0,09	7,24	0,96	3,26	1,15
	10,80	5,63	0,749	19,15	0,07	6,54	0,97	3,60	0,81
	10,90	7,11	0,990	22,32	0,04	5,94	0,98	3,51	0,80
	11,50	6,60	0,626	19,79	0,04	5,17	1,02	3,21	0,72
	12,30	0,66	0,015	6,01	0,01	2,04	1,14	1,45	0,31
	13,10	0,72	0,007	4,64	0,01	1,68	0,99	1,60	0,30
	13,45	0,09	0,008	6,11	0,00	1,01	0,80	1,49	0,19
	13,90	0,67	0,007	8,25	0,01	6,60	0,96	2,79	0,25
	14,95	0,17	0,005	7,51	0,01	1,94	1,10	2,43	0,18
	15,40	0,17	0,006	8,76	0,01	3,15	1,08	2,97	0,20
	16,40	0,12	0,006	6,97	0,01	3,87	0,98	3,26	0,16
	17,10	0,09	0,007	16,79	0,02	23,68	0,76	2,40	0,14
	17,70	0,06	0,005	6,78	0,02	9,18	0,82	2,77	0,16
	19,70	0,04	0,006	3,15	0,06	3,64	0,55	3,05	0,18
	20,40	0,04	0,004	4,89	0,03	2,02	0,42	2,38	0,16
	20,95	0,03	0,005	3,95	0,03	1,95	0,41	2,41	0,19
	22,15	0,03	0,006	1,25	0,03	1,62	0,43	2,72	0,22
	24,20	0,03	0,005	6,00	0,03	2,65	0,50	2,62	0,24
	24,80	0,03	0,006	4,12	0,01	2,19	0,39	2,54	0,20
	25,30	0,15	0,017	3,39	0,04	2,39	0,43	2,52	0,39
	26,67								
	26,67	0,03	0,004	3,58	0,01	2,03	0,43	2,57	0,26
	26,90	0,03	0,007	2,18	0,02	1,94	0,41	2,81	0,23
	27,95								
	28,10	0,02	0,007	4,08	0,01	1,37	0,25	2,24	0,19
	29,00	0,02	0,003	4,27	0,01	1,21	0,24	2,29	0,21
	29,30	0,02	0,006	1,92	0,02	2,06	0,43	2,16	0,32
	30,10	0,05	0,006	5,59	0,23	2,40	0,57	2,42	0,37
	30,35	0,03	0,007	3,61	0,16	2,84	0,64	2,62	0,37
	30,65	0,03	0,005	5,86	0,03	3,31	0,53	2,51	0,33
	30,75	0,03	0,005	14,23	0,07	6,54	0,50	2,25	0,33
	31,00	0,02	0,005	5,27	0,02	2,77	0,24	2,02	0,25

	31,35	0,03	0,007	3,66	0,02	3,46	0,38	2,52	0,30
	31,80	0,03	0,005	1,69	0,02	1,59	0,28	2,05	0,25
	32,35	0,03	0,005	3,14	0,02	2,26	0,44	2,55	0,29
	33,50	0,03	0,007	2,41	0,03	2,34	0,43	2,53	0,32
	34,15								
	34,90	0,02	0,004	1,03	0,01	1,06	0,19	2,01	0,20
	35,60	0,03	0,006	3,60	0,01	1,38	0,25	2,59	0,24
	36,10	0,03	0,005	1,02	0,01	1,38	0,27	2,04	0,24
	37,73	0,02	0,006	2,91	0,01	2,23	0,35	2,36	0,28
	37,90	0,02	0,007	2,62	0,12	2,02	0,40	2,50	0,30
	38,30	0,03	0,004	2,03	0,01	2,13	0,29	2,26	0,28
	39,00	0,03	0,006	2,44	0,01	2,68	0,41	2,62	0,34
	39,70	0,02	0,004	2,33	0,01	1,26	0,08	1,91	0,17
	40,00	0,04	0,006	1,24	0,01	1,02	0,17	1,95	0,23
	40,55	0,03	0,005	1,82	0,01	1,97	0,26	2,21	0,32
	41,45	0,03	0,004	1,65	0,01	1,79	0,35	2,38	0,34
	42,00	0,03	0,006	2,52	0,01	2,93	0,33	2,31	0,33
	42,45	0,03	0,007	3,88	0,01	4,14	0,48	2,74	0,37
	42,50	0,05	0,008	3,46	0,01	2,83	0,46	2,67	0,37
	42,60	0,04	0,008	4,79	0,01	5,11	0,42	2,49	0,36
	42,62	0,04	0,006	3,12	0,01	2,41	0,57	2,87	0,41
	42,70	1,74	0,150	11,60	0,02	2,77	0,67	3,07	0,43
	42,80	0,15	0,033	4,04	0,02	2,37	0,62	2,90	0,45
	42,90	0,11	0,045	11,07	0,03	6,08	1,02	3,61	0,32
	43,65	0,13	0,013	10,35	0,05	7,35	1,00	3,59	0,32
	44,90	0,55	0,012	12,88	0,18	10,02	0,95	3,60	0,32
	45,90	0,17	0,012	4,62	0,07	4,56	0,82	3,01	0,42
from 45.9 m: GRAVEL → no further coring possible									

Table 20: All documented Fe- & As-bearing minerals and the method(s) used for their identification

valence		minerals	formula	aquifer unit			methods				
				yellow-brown	transition	grey	Microscopy/ SEM/EMPA	XRD	XAS	Magnetic	Mössbauer
	major minerals: oxyhydroxides, carbonates & sulphides										
ferrous Fe^{2+}	Fe-(Mn)-Carbonates	**Siderite (Si)**	$Fe^{2+}CO_3$	+	+++		+	+	+	+	-
		Ankerite (Ank)	$Ca(Fe^{2+},Mg,Mn)(CO_3)_2$	+	+++		+	-	-		-
	Fe-sulphides	**Pyrite (Py)** Mackinawite (Mack)	$Fe^{2+}S_2$ $(Fe^{2+},Ni)_{1+x}S_{(x\,=\,0-0.07)}$		+++		+	+	+	-	-
	Fe-Ti-oxides	**Ilmenite (Ilm)**	$Fe^{2+}Fe^{3+}TiO_3$	++	+	+	+	-	-	-	-
mixed valence $Fe^{2+/3+}$	Fe-oxyhydroxides	**Magnetite (Mt)**	$Fe^{2+}Fe^{3+}{}_2O_4$	++	+	+	+	+	+	+	-
		Green rust (Greru)	$Fe^{2+}{}_6Fe^{3+}{}_2(OH)_{16}CO_3{\cdot}3H_2O$	+	+	‡	-	-	+	?	?
	Fe-sulphides	*Greigite (Grei)*	$Fe^{2+}Fe^{3+}{}_2S_4$		+		-	-	+	?	-
ferric Fe^{3+}	Fe-oxyhydroxides	**Goethite (Gt)**	alpha-$Fe^{3+}O(OH)$	++	+	+	+	+	+	+	+
		Lepidocrocite (Lep)	gamma-$Fe^{3+}O(OH)$	+	++		-	+	-	?	?
		Ferrihydrite (Fh)	$Fe^{3+}{}_{10}O_{14}(OH)_2$	+	++		+		+	?	?
		Hematite (Hem)	$Fe^{3+}{}_2O_3$	++	+	+	+	+	+	+	+
		Maghemite (Mgh)	$Fe^{3+}{}_{2.67}O_4$	+	+		-	-	-	?	?
	minor Fe-minerals: inosilicates & three-layer silicates (micas, chlorites, clays)		The frequency of phyllosilicates is linked to the occurrence of fine-grained layers. The following three-layer silicates were detected:								not further differentiable
Ferrous Fe^{2+}	Fe-phyllosilicates	**Clinochlor (Clc)**	$(Mg,Fe^{2+})_5Al[Si_3Al]O_{10}(OH)_8$		+++		+	+	-		
		Biotite (Bt)	$K(Mg,Fe^{2+})_3(Si_3Al)O_{10}(OH,F)_2$		+		+	-	+		
		Phengite (Phg)	$KAl_{1.5}(Mg,Fe^{2+})_{0.5}(Al_{0.5}Si_{3.5}O_{10})(OH)_2$		+		-	+	-		
mixed valence $Fe^{2+/3+}$	Fe-phyllosilicates	**Illite (Ill)**	$(K,H_3O)(Al,Mg,Fe^{2/3+})_2(Si,Al)_4O_{10}[(OH)_2,(H_2O)]$		++		+	+	-		
		Chamosite (Chm)	$(Fe^{2+},Mg,Fe^{3+})_5Al(Si_3Al)O_{10}(OH,O)_8$		+++		+	+	-		
		Smectite (Sme)	$A0.3D2{\cdot}3[T4O10]Z2{\cdot}nH2O$		+		?	-	-		
		Greenalite (Gre)	$(Fe^{2+},Fe^{3+})_{2\text{-}3}Si_2O_5(OH)_4$		+		?	+	-	+	?
	Inosilicates: Amphiboles	**Hornbende (Hbl)**	$(Ca,Na,K)_{2\text{-}3}(Mg,Fe^{2/3+},Al)_5[(OH,F)_2/(Si,Al)_2Si_8O_{22}$		+++		+	-	+		
ferric Fe^{3+}	Fe-phyllosilicates	**Glauconite (Glt)**	$(K,Na)(Fe^{3+},Al,Mg)_2(Si,Al)_4O_{10}(OH)_2$		++		+	-	-		
		Nontronit (Non)	$Na_{0.3}Fe^{3+}{}_2(Si,Al)_4O_{10}(OH)_2{\cdot}4H_2O$		+		?	-	-		
		Vermiculit (Vrm)	$Mg_{0.7}(Mg,Fe^{3+},Al)_6(Si,Al)_8O_{20}(OH)_4{\cdot}8H_2O$		+		?	-	-		
	As-minerals										
	As-sulphides	Arsenopyrit (Aspy)	FeAsS		+		-	+	+	-	-
		Auripigment (Aspi)	As_2S_3		+		-	+	+	-	-
	As-phosphates	*Svabite (Sva)*	$Ca_5(AsO_4)_3F$	ocurance limited to top 11m silt aquitard			-	+	-	-	-

+	rare
++	regularly
+++	frequently
primary	secondary

+	proven
?	not exactly identifiable by used method
-	not proven

Table 21: RD42 XRD (sulphides, oxides and hydroxides, carbonates, borates, sulphates, phosphates, arsenates & vanadates)

Depth [m]	Sulfides		Oxides and Hydroxides							Carbonates			Borates	Sulfates		Phosphates, Arsenates & Vanadates				
	Pyrite FeS_2	Arsenopyrite $FeAsS$	Hematite Fe_2O_3	Goethite α-$Fe^{3+}O(OH)$	Lepidocrocite γ-$Fe^{3+}O(OH)$	Magnetite $Fe^{2+}Fe^{3+}{}_2O_4$	Rutile TiO_2	Anatase TiO_2	Wulfenite $PbMoO_4$	Siderite $FeCO_3$	Rhodochrosite $MnCO_3$	Dolomite $CaMg(CO_3)_2$	Calcite $CaCO_3$	Yuanfuliite $NaBe_4^{3+}(PO_4)(OH)_3$	Despujolsite $Ca_3Mn^{3+}Cl(IO_3)(OH)_6 \cdot 2H_2O$	Gypsum $CaSO_4 \cdot 2H_2O$	Agrellite $NaCa_2Si_4O_{10}F$	Svabite $Ca_5(AsO_4)_3F$	Loellingite $FeAs_2$	Arsenolite As_4O_6	Cornubite $Cu_5(AsO_4)_2(OH)_4$
3.3													2				8			
3.6													2				2			
3.9			1									2	1				3			
4.4				1									1				3		1	
4.8			1	1									1				3			
5.2				3									1				2			
5.9				18									1				2			
6.2												1	1							
6.6			1				1					1	1				3			
7.0																	4			
7.4																	4			
8.2																	3			
9.1											1									
9.5	1	1		3		4						1	4			1				
10.8				2												1		3		
11.2				3								1						1		
11.3						1				1										
11.6		5				1														
11.9						18										18				
12.4											1									
13.0						2		1												2
13.5								1												
14.8								1												
15.5			1					1												
16.1			1					1												
17.3			1	1	1		1								4					3
18.2			1	1																
18.8																				
19.4				1			3		1											
19.7					1		2													
20.1									1											
20.4																				
20.7			1				2											1		
20.8																				
21.2																				
21.3			1																	
22.0																		3		
22.4																				
23.3							3													
24.2																		2		
25.5																				
25.9			1																	
26.3									1											
27.4									1											
28.1																				
28.5																				
29.4																				
30.1				8														3		
30.3																				
30.4																				
31.4														4						
32.4																				
33.1							1											1		
33.3							1													
33.8																				
34.5																				
35.4																				
35.9																				
36.4																				
36.9																				
37.3																				
38.2																				
39.7																				
40.4																				
40.8																				
40.9																				
41.4																				
41.7			1																	
42.3			1	1																
43.3			1																	
44.5			1																	
45.3			1			1														
45.8																				
46.3			1																	

Table 22: RD42 XRD (silicates I: nesosilicates, sorosilicates, cyclosilicates, phyllosilicates)

Depth [m]	Silicates																		
	Nesosilicates		Sorosilicates	Cyclosilicates	Phyllosilicates														
	Andradite	Titanite	Ilmenite	Kummerkoite	Phengite	Muscovite	Kaolinite	Illite	Chlorite	Clinochlore	Chamosite	Lepidolite	Greenalite	Sudoite	Sepiolite				
	$Ca_3Fe^{3+}_2Si_3O_{12}$	$CaTiSiO_5O$	$Na_xCa(Mg,Ti)(SiO_3)_2(O,OH)_2.1H_2O$	$K_2Mn^{2+}Ti_6Na_2Si_8O_{28}(OH)_2(O,OH)_6.5.5H_2O$	$KAl_2(AlSi_3O_{10})(OH)_2$	$KAl_2(AlSi_3O_{10})(OH)_2$	$Al_2Si_2O_5(OH)_4$	$K_{0.65}Al_{2.0}Al_{0.65}Si_{3.35}O_{10}(OH)_2$	$(Mg,Fe)_3(Si,Al)_4O_{10}(OH)_2(Mg,Fe)_3(OH)_6$	$(Mg,Al,Fe)_6(Si,Al)_4O_{10}(OH)_8$	$(Fe^{2+},Mg,Al)_6(Si,Al)_4O_{10}(OH)_8$	$K(Li,Al)_3(Si,Al)_4O_{10}(OH)_2$	$Fe^{2+}_3Si_2O_5(OH)_4$	$Mg_3Al_2Si_3O_{10}(OH)_8$	$Mg_4Si_6O_{15}(OH)_2.6H_2O$				
3.3						22	3		5	6					1				
3.6						15	2		2										
3.9		3	1			17			3	3	3		1						
4.4						21				5									
4.8						23					3	7	1						
5.2						15		25					1						
5.9						18				4	2								
6.2						20				11	2								
6.6						21				5	4								
7.0						23				6	5								
7.4						17				6	3								
8.2						25				5	3								
9.1		2				20				2	3	8							
9.5						27	2			2	3	7							
10.8						22	3	16		5	3								
11.2					13	16				1	1	3							
11.3						7	2												
11.6						17	5			5									
11.9						27	4												
12.4						28	5							5					
13.0						27	5			5				5					
13.5						25	5							9					
14.8						26	3												
15.5						12	5			1									
16.1						16	5			1									
17.3						20	6			1									
18.2						28	2			1									
18.8						23	3			1					1				
19.4						20	3			1					1				
19.7						26	5												
20.1				2		18	2			1									
20.4						27	2			1									
20.7						19	2			1									
20.8						17	9												
21.2						16	2			1									
21.3						23	2			1									
22.0		2				22	2			1	2								
22.4						25	3												
23.3						10	1			1									
24.2						18	8			1									
25.5						24	1			1									
25.9						17	2			1									
26.3						25	2			1									
27.4						19	2												
28.1						22	2												
28.5		4				17	1												
29.4						16	2												
30.1						18	8		2	1	2								
30.3						18	2												
30.4						17	2			1									
31.4						12	1	37		1									
32.4						10	3	37											
33.1						26	5												
33.3						16	5				1								
33.8						15	2				1								
34.5						15	5												
35.4						17	7												
35.9						18	2												
36.4						14	4												
36.9						21	5				2								
37.3						16	3				1								
38.2						12	1				1								
39.7						12					12								
40.4						13													
40.8						16													
40.9						27					3								
41.4						22					6								
41.7						28					6								
42.3		2				28					4								
43.3		2				32					6								
44.5		3				32													
45.3						17	3												
45.8		2				24													
46.3						19													

Table 23: RD42 XRD (silicates II: inosilicates, tectosilicates)

Depth [m]	Silicates														
	Inosilicates			Tectosilicates											
	Manganpyrosmalite $(Mn^{2+},Fe^{2+},Mg)_8Si_6O_{15}(OH)_{18}Cl_2$	Tremolite $Ca_2(Mg,Fe)_5Si_8O_{22}(OH)_2$	Leucophanite $NaMgLiF_2BSi_2O_6$	Quartz SiO_2	Microcline $KAlSi_3O_8$	Orthoclase $KAlSi_3O_8$	Sanidine $KAlSi_3O_8$	Anabite $(Na,K)AlSi_2O_6$	Albite $NaAlSi_3O_8$	Anorthite $CaAl_2Si_2O_8$	Gaultite $Na_2Zn_2Si_5O_{13}\cdot 2H_2O$
3,3				36	7				10		
3,6				48	14		5		9		
3,9				42	16				7		
4,4		3		53			3		7		
4,8				51			3		8		
5,2				42	13	3			9		
5,9				37					7		
6,2				46				6	7		
6,6				50	5				10		
7,0				50	5				7		
7,4				46	8				8		
8,2				51	13				7		
9,1			3	50	5				10		
9,5				42	12				7		
10,8				46	10				6		
11,2				39	3				5		
11,3				40	16				5		
11,6				58	3				2		
11,9				37	2				3		
12,4				55	4			4			
13,0				56	5	3					
13,5				52	5	4					
14,8				57	4						
15,5				61	5	3			4		
16,1				72	6						
17,3				61	13						
18,2				60	8						
18,8				56	6	6					
19,4				52	18					2	
19,7				65	10						
20,1				51	11						
20,4				60	10						
20,7				54	16					9	
20,8				66	7		4				
21,2			2	62	11						
21,3				60	10	11					
22,0				56	9				4		
22,4				54	7	9			4		
23,3				66	13	5			3		
24,2				62	7	7			4		
25,5				64					3		2
25,9				63	10	9			6		
26,3				68	6				4		
27,4				61	10				5		
28,1				64	7				6		
28,5				55	8				6		
29,4				64	7				5		
30,1				63	8				3		
30,3				69	7				4		
30,4				37	4	5			3		
31,4				38	4	5			3		
32,4				55	6	6			4		
33,1				58	12				8		
33,3				69	8	8			6		
33,8				56	9				6		
34,5				57	7	6			5		
35,4				65		9			5		
35,9				58	8	10			5		
36,4				54	7	4			5		
36,9				54	7	10			6		
37,3				61	10	9			5		
38,2				56	9	10			6		
39,7				61	9	24			5		
40,4				65	7	5			5		
40,8			1	50	5	12			8		
40,9				56	5				6		
41,4				57	9				5		
41,7				56	7						
42,3				58	26						
43,3				49	7						
44,5				57	7				7		
45,3				62	7				9		
45,8											
46,3											

Table 24: RD42 Fitting results of Mossbauer spectroscopy

*CS – center shift, QS – quadrupole splitting, S(QS) – standard deviation of QS, Qshift – quadrupole shift, H – hyperfine magnetic field, S(H) – standard deviation of H, R.A. – Relative abundance determined by integration under the curve. The goodness of fit (χ2) was below 1 for all fitted spectra. *Phase identification is a best guess and is open to interpretation. Lep – lepidocrocite, Fh – ferrihydrite, Gt – goethite, Hem – hematite, Phyl – phyllosilicate, pSxt – poorly ordered sextet. Table was already shown in Kontny et al. (2021).*

Depth [m]	T [K]	Phase*	CS [mm/s]	QS [mm/s]	*S(QS)* [mm/s]	Qshift [mm/s]	H [T]	*S(H)* [T]	R.A. [%]	±
19,7	77	Lep/Fh + Phyl?	0,49	0,63	*0,29*				43,2	0,9
		Fe(II)	1,32	2,74	*0,2*				4	0,4
		Gt	0,48			-0,12	46,3	*5*	52,8	1
21,3	77	Lep/Fh + Phyl?	0,48	0,62	*0,32*				14,8	1,4
		Fe(II)	1,25	2,82	*0,3*				11,5	1,3
		Gt	0,47			-0,13	47,5	*2,2*	48,9	3,7
		pSxt	0,57			-0,12	37,4	*16,7*	24,8	5,4
	5	Fe(II)-Phyl?	1,3	2,95	*0,24*				4,8	1,1
		Fe(III)-Phyl?	0,48	0,65	*0,33*				5,5	1,3
		Gt	0,5			-0,14	49,7	*0,7*	37,4	3,5
		Lep/Fh	0,46			-0,06	49,4	*3,3*	30,1	3,5
		pSxt/Phyl	1,64			1,43	17,3	*13,1*	22,3	3,7
30,0	77	Lep/Fh + Phyl?	0,41	0,78	*0,43*				31,9	3,3
		Fe(II)	1,53	2,48	*0,05*				4,8	5,2
		Fe(II)	1,21	2,81	*0,21*				12,6	5,1
		Gt	0,47			-0,13	47,5	*2,7*	22,1	3,4
		Hem	0,48			-0,09	53,2	*0,4*	13,2	2,4
		pSxt	0,28			-0,57	25,9	*14,7*	15,5	3,5
	5	Fe(II)-Phyl?	1,27	2,9	*0,16*				9,6	0,9
		Fe(III)-Phyl?	0,45	0,75	*0,45*				17,9	1,6
		Hem	0,48			-0,11	53	*0,5*	12,7	1,5
		Gt	0,49			-0,14	49,7	*0,6*	16,1	2,5
		Lep/Fh	0,47			-0,03	49,5	*3,6*	19,8	3,3
		pSxt/Phyl	0,89			0,64	13,9	*10,5*	23,9	2,1
36,4	77	Lep/Fh + Phyl?	0,37	0,9	*0,41*				33,4	3,9
		Fe(II)	1,47	2,51	*0,14*				9,6	1,4
		Gt	0,48			-0,13	46,5	*2,4*	23,9	3,4
		Hem	0,48			-0,09	53,2	*0,3*	8,9	1,5
		pSxt	0,84			-0,01	35,1	*21,4*	24,3	8,3
	5	Fe(III)-Phyl?	0,45	0,77	*0,41*				26,2	5,3
		Fe(II)-Phyl?	1,24	2,94	*0,2*				7,7	2,2
		Hem	0,49			-0,13	53,3	*0*	7,1	2,5
		Gt	0,48			-0,15	49,6	*0,9*	20,9	5,1
		Lep/Fh	0,42			0,02	48,3	*3,9*	15,1	6
		pSxt/Phyl	1,74			0,75	35,2	*23,5*	23	13